Journal of Fluids Engineering

Published Bimonthly by ASME

VOLUME 126 • NUMBER 5 • SEPTEMBER 2004

TECHNICAL PAPERS

(Contents continued on inside back cover)

Transactions of the ASME, Journal of Fluids Engineering (ISSN 0098-2202) is published bimonthly (Jan., Mar., May, July, Sept., Nov.) by The American Society of Mechanical Engineers, Three Park Avenue, New York, NY 10016. Periodicals postage paid at New York, NY and additional mailing offices.
POSTMASTER: Send address changes to Transactions of the ASME, Journal of Fluids Engineering, c/o THE AMERICAN SOCIETY OF MECHANICAL ENGINEERS, 22 Law Drive, Box 2300, Fairfield, NJ 07007-2300.
CHANGES OF ADDRESS must be received at Society headquarters seven weeks before they are to be effective. Please send old label and new address.
STATEMENT from By-Laws. The Society shall not be responsible for statements or opinions advanced in papers or ... printed in its publications (B7.1, Par. 3).

INDEXED by Applied Mechanics Reviews and Engineering Information, Inc. Canadian Goods & Services Tax Registration #126148 048.

Journal of Fluids Engineering Volume 126, Number 5 SEPTEMBER 2004

TECHNICAL BRIEFS

The ASME Journal of Fluids Engineering is abstracted and indexed in the following:

Applied Science & Technology Index, Chemical Abstracts, Chemical Engineering and Biotechnology Abstracts (Electronic equivalent of Process and Chemical Engineering), Civil Engineering Abstracts, Computer & Information Systems Abstracts, Corrosion Abstracts, Current Contents, Ei EncompassLit, Electronics & Communications Abstracts, Engineered Materials Abstracts, Engineering Index, Environmental Engineering Abstracts, Environmental Science and Pollution Management, Excerpta Medica, Fluidex, Index to Scientific Reviews, INSPEC, International Building Services Abstracts, Mechanical & Transportation Engineering Abstracts, Mechanical Engineering Abstracts, METADEX (The electronic equivalent of Metals Abstracts and Alloys Index), Petroleum Abstracts, Process and Chemical Engineering, Referativnyi Zhurnal, Science Citation Index, SciSearch (The electronic equivalent of Science Citation Index), Shock and Vibration Digest, Solid State and Superconductivity Abstracts, Theoretical Chemical Engineering

Hironori Horiguchi
Graduate School of Engineering Science,
Osaka University,
Toyonaka, Osaka, 560-8531, Japan
e-mail: horiguti@me.es.osaka-u.ac.jp

Souhei Arai
Business Logistics Division,
Mazda Motor Corporation,
Hiroshima, 730-8670, Japan
e-mail: arai.so@mazda.co.jp

Junichiro Fukutomi
e-mail: fukutomi@me.tokushima-u.ac.jp

Yoshiyuki Nakase
e-mail: nakase@me.tokushima-u.ac.jp

Faculty of Engineering,
The University of Tokushima,
Tokushima, 770-8506, Japan

Yoshinobu Tsujimoto
Graduate School of Engineering Science,
Osaka University,
Toyonaka, Osaka, 560-8531, Japan
e-mail: tujimoto@me.es.osaka-u.ac.jp

Quasi-Three-Dimensional Analysis of Cavitation in an Inducer

A method for the prediction of steady cavitation in turbopumps is proposed on the assumption that the fluid is inviscid and the stream surface is rotationally symmetric. The analysis in the meridian plane is combined with that in a blade-to-blade stream surface where a singularity method based on a closed cavity model is used. The present method is applied to a helical inducer and it is found that the influence of the three-dimensionality of the flow on cavitation mainly appears as the change of angle of attack associated with the change of meridional velocity caused by the movement of meridian streamline in radial direction. [DOI: 10.1115/1.1789526]

Introduction

Various types of cavitation instabilities occur when steady cavity length reaches about 65% of blade spacing in high-speed turbomachinery, such as turbopumps for rocket engines [1]. This fact indicates that the onset of cavitation instability can be predicted by estimating the steady cavitation. So, the prediction of the steady cavitation is important also from the viewpoint of the prediction of the cavitation instabilities.

Recently, it is becoming possible to predict three-dimensional steady and unsteady cavitating flows in turbopumps by numerically solving the Navier–Stokes equations [2–4]. On the other hand, the alternate blade cavitation [5] was simulated by a linear analysis of two-dimensional, steady potential flow in cascades [6] or by a two-dimensional numerical calculation [7].

In the present study, a method for the prediction of the steady, quasi-three-dimensional flow with cavitation in turbopumps is proposed, in which the analysis in the meridian plane is combined with that in the rotationally symmetric blade-to-blade stream surface with a circumferentially averaged meridional velocity. The analysis in the stream surface is performed by a singularity method based on a closed cavity model, which can simulate the alternate blade cavitation on the assumption of steady flow. The present method is applied to a helical inducer and the effects of the three-dimensionality of the flow on cavitation are discussed by comparing the results obtained by the present method with those of the linear analysis of two-dimensional flow.

Basic Equation

Analysis in the Meridian Plane. Although the method proposed in the present study can be applied to various kind of turbomachinery, it is applied to a helical inducer shown in Fig. 1 in the present study. The number of the blades is 2, the diameters of the hub and tip are 50.0 and 158.0 ($=D_T$) mm, respectively, the blade angle at the tip is 14.0°, and the solidity is 2.0. Tip clearance is not considered. Figure 2 shows the sketch of the meridian plane. The lines drawn vertically from the hub toward the casing represent the q-coordinate lines, and the number of them, N_q, is 33 in the present study. The first and 33rd q-coordinate lines, q_1 and q_{33}, are set on the inflow boundary at $z=-D_T$ and the outflow boundary at $z=D_T$ of the computational domain, respectively. The other q_j-coordinate lines ($j=2,\ldots,32$) between q_1 and q_{33} are arranged with almost equal intervals. Thirteen q-coordinate lines are placed in the impeller region. The coordinate m is defined along the streamlines in the meridian plane. A meridional velocity is represented by w_m and the angle between w_m and the z axis is shown by α. In the analysis of the meridional flow, all variables in the blade-to-blade stream surface are circumferentially averaged.

On the assumption that the flow is steady and the fluid is inviscid, the following differential equation is derived from Euler's equation and the energy equation [8] for a relative velocity w in the meridian plane on each q_j-coordinate line:

$$\frac{dw}{dq_j}=wK_1+K_2+\frac{1}{w}K_3, \tag{1}$$

where

$$K_1=\left(\frac{\cos^2\beta\cos\alpha}{r_c}-\frac{\sin^2\beta}{r}\right)\frac{dr}{dq_j}+\cos\beta\sin\alpha\sin\beta\frac{d\theta}{dq_j}-\frac{\cos^2\beta\sin\alpha}{r_c}\frac{dz}{dq_j},$$

Contributed by the Fluids Engineering Division for publication in the JOURNAL OF FLUIDS ENGINEERING. Manuscript received by the Fluids Engineering Division March 19, 2003; revised manuscript received March 31, 2004. Associate Editor: J. Katz.

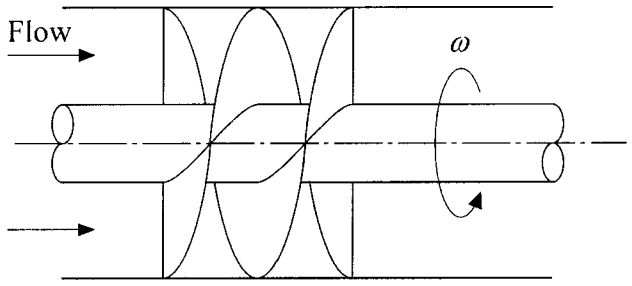

Fig. 1 Inducer geometry

$$K_2=\left(\cos\beta\sin\alpha\frac{dw_m}{dm}-2\omega\sin\beta\right)\frac{dr}{dq_j}+r\cos\beta\left(\frac{dw_\theta}{dm}+2\omega\sin\alpha\right)\frac{d\theta}{dq_j}+\cos\alpha\cos\beta\frac{dw_m}{dm}\frac{dz}{dq_j},\tag{2}$$

$$K_3=\frac{dH_i}{dq_j}-\omega\frac{d(r_i v_{\theta i})}{dq_j},$$

where β is the angle between the relative velocity w and the meridian plane, r_c is a curvature radius, and θ is an angle around the z axis. H_i and $v_{\theta i}$ are the total enthalpy and circumferential component of absolute velocity at the inlet of the impeller respectively. Since the q_j-coordinate line is normal to the hub and the casing in the present study, the differentiations of r, θ, z by q_j can be expressed as follows:

$$\frac{dr}{dq_j}=1,\quad \frac{d\theta}{dq_j}=\frac{dz}{dq_j}=0.\tag{3}$$

Assuming that the fluid is incompressible and the flow upstream of the impeller is without prerotation, we obtain

$$K_3=\frac{dH_i}{dq_j}-\omega\frac{d(r_i v_{\theta i})}{dq_j}=0.\tag{4}$$

By substituting Eqs. (3) and (4) into Eq. (1), Eq. (1) is simplified to

$$\frac{dw}{dq_j}=w\left(\frac{\cos^2\beta\cos\alpha}{r_c}-\frac{\sin^2\beta}{r}\right)+\cos\beta\sin\alpha\frac{dw_m}{dm}-2\omega\sin\beta.\tag{5}$$

Equation (5) is an equilibrium equation on q_j-coordinate line.

The continuity equation can be expressed as follows, by requiring that the flow rate through the surface obtained by rotating q_j-coordinate line around z axis equals the prescribed total flow rate Q_0,

$$Q_0=\int_{q_{\text{hub}}}^{q_{\text{casing}}} w\cos\beta\cos\alpha\,2\pi r\,dq_j.\tag{6}$$

The meridian streamline is determined by w satisfying Eqs. (5) and (6) so that the flow rates between adjacent streamlines are equal.

Analysis in the Blade-to-Blade Stream Surface. It is assumed that the stream surface is rotationally symmetric and the absolute flow in it is irrotational. The assumption of the irrotational flow requires

$$\frac{\partial(v_\theta r)}{\partial m}-\frac{\partial(v_m)}{\partial\theta}=0.\tag{7}$$

The relations between the absolute and relative velocities are

$$v_m=w_m,\quad v_\theta=w_\theta+r\omega.\tag{8}$$

By substituting Eq. (8) into Eq. (7), we obtain

$$\frac{\partial(w_\theta r)}{\partial m}-\frac{\partial(w_m)}{\partial\theta}=-2\omega r\frac{\partial r}{\partial m}.\tag{9}$$

The stream function Ψ' is defined as follows in consideration of the continuity equation

$$\frac{\partial\Psi'}{\partial m}=-bw_\theta,\quad \frac{\partial\Psi'}{\partial\theta}=brw_m,\tag{10}$$

where b is the interval between adjacent stream surfaces. Substituting Eq. (10) into Eq. (9), the following equation is obtained:

$$\frac{1}{r^2}\frac{\partial^2\Psi'}{\partial\theta^2}+\frac{\partial^2\Psi'}{\partial m^2}-\frac{1}{r^2}\frac{\partial(\ln b)}{\partial\theta}\frac{\partial\Psi'}{\partial\theta}+\left\{\frac{1}{r}\sin\alpha+b\frac{\partial}{\partial m}\left(\frac{1}{b}\right)\right\}\frac{\partial\Psi'}{\partial m}=2b\omega\sin\alpha.\tag{11}$$

The coordinates (m,r,θ) can be transformed to the polar coordinates (R,Θ) by a conformal mapping using the following equations.

$$\Theta=\theta,\quad R=R_0\exp\left(\int_0^m\frac{1}{r}dm'\right),\tag{12}$$

where R_0 is an constant. Assuming that the interval b does not change with the flow, Eq. (11) transformed by Eq. (12) can be expressed as the following Poisson equation:

$$\frac{1}{R^2}\frac{\partial^2\Psi}{\partial\Theta^2}+\frac{\partial^2\Psi}{\partial R^2}+\frac{1}{R}\frac{\partial\Psi}{\partial R}=2\omega\sin\alpha\left(\frac{r}{R}\right)^2,\tag{13}$$

where

$$\Psi=\Psi'/b.\tag{14}$$

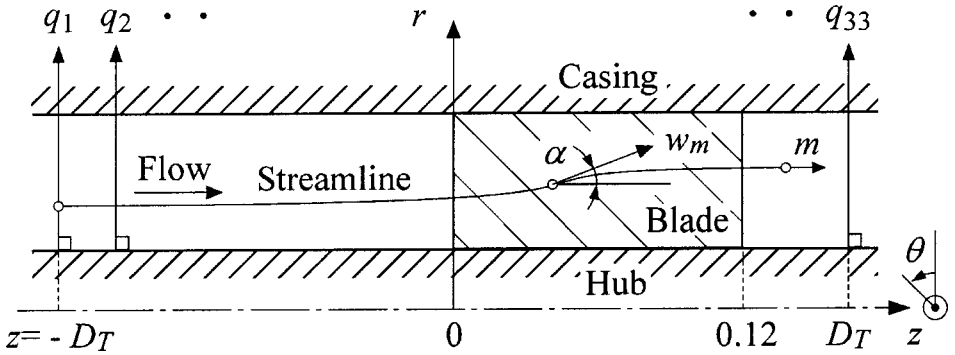

Fig. 2 Meridian plane

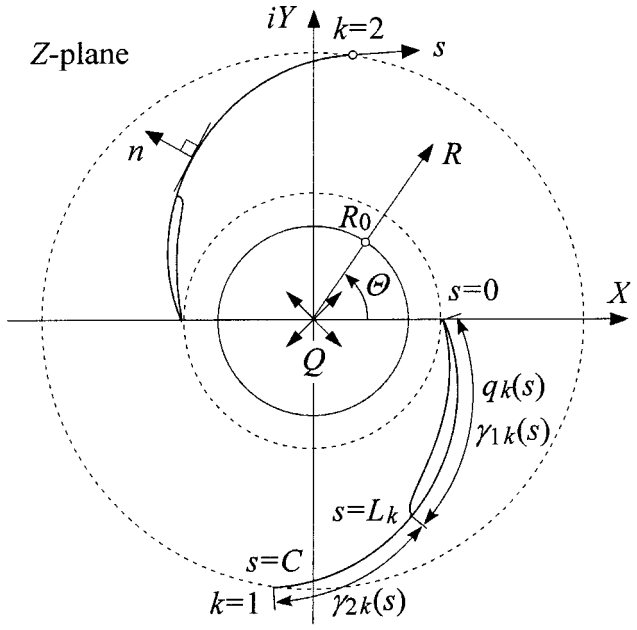

Fig. 3 Mapping plane

Defining a stream function Ψ_0 that satisfies the Laplace equation, the solution of Eq. (13) is as follows:

$$\Psi = \Psi_0 + \Psi^*, \tag{15}$$

where

$$\Psi^* = \int \frac{1}{2\pi R} \int_0^R 2\omega \sin\alpha \left(\frac{r}{R'}\right)^2 2\pi R' dR' dR. \tag{16}$$

Thus, the relative flow in the mapping plane can be represented by superposing the potential and rotational flows whose stream functions are Ψ_0 and Ψ^*, respectively. The above fundamental equations are the same as those used in Ref. [9], so we do not provide details in the present paper.

We use the mapping plane as shown in Fig. 3. The coordinate along the blade is s and the coordinate normal to the blade is n. The blade length is C and the cavity length on the kth blade is L_k $(k=1,2)$ in the mapping plane.

The velocity disturbances due to the cavities and the blades are represented by source distributions $q_k(s)$ on the cavity, vortex distributions $\gamma_{1k}(s)$ and $\gamma_{2k}(s)$ on the blade. Then, the complex velocity can be expressed as follows:

$$W = W_X - iW_Y = \frac{Q}{2\pi Z} + \frac{1}{2\pi}\sum_{k=1}^{2}\left[\int_0^{L_k}\frac{q_k(s)}{Z-\zeta_k(s)}ds - \int_0^{L_k}\frac{i\gamma_{1k}(s)}{Z-\zeta_k(s)}ds - \int_{L_k}^{C}\frac{i\gamma_{2k}(s)}{Z-\zeta_k(s)}ds\right] + i\frac{r^2\omega}{R}\exp(-i\Theta), \tag{17}$$

where $\zeta_k(s)$ is a complex number that represents the blade. Q is a concentrated source at the origin and defined as

$$Q = 2\pi r w_m. \tag{18}$$

The last term of the right-hand side of Eq. (17) is derived from Eq. (16) and it physically means the relative circumferential velocity caused by the rotation of the impeller.

The following boundary conditions (a)–(d) are applied to determine the values of the unknowns, $q_k(s)$, $\gamma_{1k}(s)$, $\gamma_{2k}(s)$, and L_k in Eq. (17). The cavity is assumed to be thin, and all boundary conditions are applied on the blades.

(a) The boundary condition on cavity surface: In the case in which the flow is without prerotation and the pressure on the cavity is equal to the vapor pressure p_v, the Bernoulli equation is

$$p_{ti} = p_v + \tfrac{1}{2}\rho w^2 - \tfrac{1}{2}(r\omega)^2, \tag{19}$$

where p_{ti} is a total pressure at the inlet of the impeller. Equation (19) can be expressed as follows in terms of w:

$$w = U_T\sqrt{\sigma + (r/r_T)^2}, \quad U_T = r_T\omega, \tag{20}$$

where r_T is the radius of the impeller. σ is a cavitation number and defined as

$$\sigma = 2(p_{ti} - p_v)/(\rho U_T^2). \tag{21}$$

We define the relative velocity components W_R and W_Θ in R and Θ directions respectively, in the mapping plane

$$\frac{\partial\Psi}{\partial R} = -W_\Theta, \quad \frac{\partial\Psi}{\partial\Theta} = RW_R. \tag{22}$$

The relation between the relative velocity w in the physical plane and the relative velocity W in the mapping plane is determined by Eqs. (10), (12), (14), and (22) and can be expressed as

$$W_R = \frac{r}{R}w_m, \quad W_\Theta = \frac{r}{R}w_\theta, \quad |W| = \frac{r}{R}w. \tag{23}$$

Therefore, the velocity on the cavity surface in the mapping plane is

$$|W| = \frac{r}{R}U_T\sqrt{\sigma + (r/r_T)^2}. \tag{24}$$

(b) The boundary condition on wetted surface: The condition that the velocity normal to the blade is equal to 0 can be expressed as

$$W_n = -\mathrm{Im}[W\exp(i\Theta')] = 0, \tag{25}$$

where Θ' is the angle between the tangent of the blade and X axis.

(c) The cavity closure condition: The thickness of cavity $\eta_k(s)$ should satisfy the following kinematic condition:

$$\frac{\partial(W_s\eta_k)}{\partial s} = W_n, \tag{26}$$

where W_s is the tangential velocity on the blade. Equation (26) is integrated to give

$$\eta_k(s) = -\frac{1}{W_s}\int_0^s q_k(s')ds' \tag{27}$$

[therefore $(W_n = -q_k(s)$ on the cavity surface)]. Hence, the cavity closure condition that the cavity thickness is equal to 0 at the cavity trailing edge is given by

$$\eta_k(L_k) = -\frac{1}{W_s}\int_0^{L_k} q_k(s')ds' = 0. \tag{28}$$

(d) Kutta's condition: Assuming that the pressure difference across the blade vanishes at the trailing edge, the following equation can be obtained:

$$\gamma_{2k}(C) = 0. \tag{29}$$

The values of unknowns, $q_k(s)$, $\gamma_{1k}(s)$, and $\gamma_{2k}(s)$, are specified at discrete points S_j and they are considered to be unknowns. It is assumed that the distribution between them is linear. The locations of the discrete points are defined as follows so that they distribute densely near the leading and trailing edge of the cavity and the blade:

$$S_j = \frac{L_k}{2}\left[1 - \cos\left(\frac{j-1}{N_C - 1}\pi\right)\right], \quad 0 \le s \le L_k, \quad j = 1,2,\ldots,N_C \tag{30}$$

$$S_{j+N_C} = L_k + \frac{(C-L_k)}{2}\left[1-\cos\left(\frac{j}{N_B}\pi\right)\right],$$

$$L_k < s \leqq C, \quad j = 1,2,\ldots,N_B \tag{31}$$

where N_C and N_B are the number of discrete points on the cavity and wetted surface, respectively. In the present study, N_C and N_B are set to be 40. The singular behavior of linearized cavitating flow obtained by Geurst [10] is taken into account near the leading and trailing edges of cavity: it is assumed that $q_k(s) \sim s^{-1/4}$ and $\gamma_{1k}(s) \sim s^{-1/4}$ near the leading edge of the cavity and the blade, $q_k(s) \sim (L_k - s)^{-1/2}$ and $\gamma_{2k}(s) \sim (s-L_k)s^{-1/2}$ near the trailing edge of the cavity. The boundary conditions are applied at the middle between these discrete points.

By evaluating the integrals in Eq. (17) using the unknowns at discrete points, the boundary conditions can be expressed as follows:

$$A(L_k)\begin{pmatrix} q_k(S_1) \\ \vdots \\ \gamma_{1k}(S_1) \\ \vdots \\ \gamma_{2k}(S_1) \\ \vdots \end{pmatrix} = B, \tag{32}$$

where $A(L_k)$ is a coefficient matrix and B is a constant vector. Since the coefficient matrix includes the unknown cavity length L_k, the following procedure is employed. By assuming the values of L_k, other unknowns are determined from Eq. (32) without closure condition. This result generally does not satisfy the closure condition. Then the correction is made on the values of L_k and the above process is repeated until the closure condition is satisfied.

Cooper proposed an approximate method for the analysis of 3D, cavitating flow in turbomachinery [11]. In the method, the analysis in the meridional plane where the effect of streamline curvature was neglected was coupled with the analysis in a blade-to-blade stream surface. In the blade-to-blade stream surface, the direction of relative flow was assumed to be that of the blade mean line, flow angles were specified in the neighborhood of exit, and the distribution of relative velocity was assumed to be linear in circumferential direction. In the present study the effect of streamline curvature in meridional plane is taken into consideration and there is no assumption about the velocity distribution in the blade-to-blade stream surface. Therefore, we think that the present method can predict the flow more properly.

Analytical Procedure

1. Fifteen meridian streamlines ($N_{st}=15$) are assumed including those on the hub and the casing.
2. The stream surface obtained by rotating the meridian streamline around z axis is mapped to the Z plane using Eq. (12). The analysis in the mapping plane Z is carried out by the singularity method. Initial values of cavity length are given, which are equal in all blades for the equal length cavitation and different alternately from blade to blade for the alternate blade cavitation. The values of the unknowns which satisfy Eq. (32) are determined through the iteration of calculation.
3. The relative velocity w are calculated by Eq. (23) using the circumferentially averaged values of W_R and W_θ obtained by Eq. (17). The values of dw_m/dm and the angle β between the relative velocity w and the meridian plane are calculated.
4. Assuming the relative velocity w at the hub, the distribution of w on q_j-coordinate line is determined by the numerical calculation of Eq. (5), in which the values of dw_m/dm and β obtained in step 3 are used.

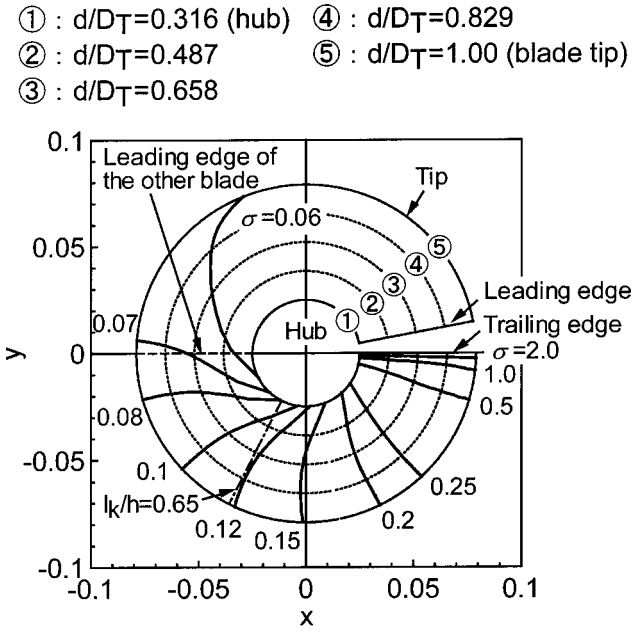

Fig. 4 Cavity shapes. ϕ=0.213

5. The flow rate through the surface obtained by rotating q_j-coordinate line around the z axis is calculated. If the continuity equation, Eq. (6), is not satisfied, the values of w are corrected in step 4. Steps 4 and 5 are repeated until the continuity equation is satisfied.
6. The meridian streamlines are determined by w obtained in the above steps. If the obtained meridian streamlines agree with those by the last calculation, the calculation is finished. If they do not agree, the meridian streamlines are corrected and the steps 2–6 are repeated.

In the present study, the calculation was finished when the amount of movement of meridian streamline on q_j-coordinate line became 0.1% or less of the impeller radius in one iteration. The procedure mentioned above is performed for the equal length cavitation. For the alternate blade cavitation, only step 2 is carried out using the stream surface in the case of the equal length cavitation because it is difficult to converge the calculation of the stream surface in the case of the alternate blade cavitation. As a result, the equilibrium equation, Eq. (5), is not satisfied in the calculation of the alternate blade cavitation.

The cavity length in the present calculations with $N_q=33$, $N_{st}=15$, $N_C=N_B=40$ agrees with the results with $N_q=65$, $N_{st}=29$, $N_C=N_B=80$ to second or third places of decimals. Thus, $N_q=33$, $N_{st}=15$, and $N_C=N_B=40$ are considered to be sufficient for the discussion in the present paper.

Results and Discussion

The analysis by the present method, which is called the quasi-three-dimensional analysis in the present study, was carried out for the case in which the flow coefficient ϕ defined as v_{zi}/U_T is 0.213. In this case the angle of attack at the tip is about 2.0°.

Shapes and Length of Cavity. Figure 4 shows the cavity shapes on a blade for the case of equal length cavitation, for which the cavity shapes on all blades are the same. The cavity shapes are represented by projecting the outline of the cavities to a perpendicular plane to the z axis. Figure 4 also shows the cylindrical planes (1–5) equally spaced between the hub and the tip. The diameter of the planes d/D_T is shown in the upper part of the figure. The cavity length measured from the leading edge in the planes (1–5) is defined as l_k $(k=1,2)$.

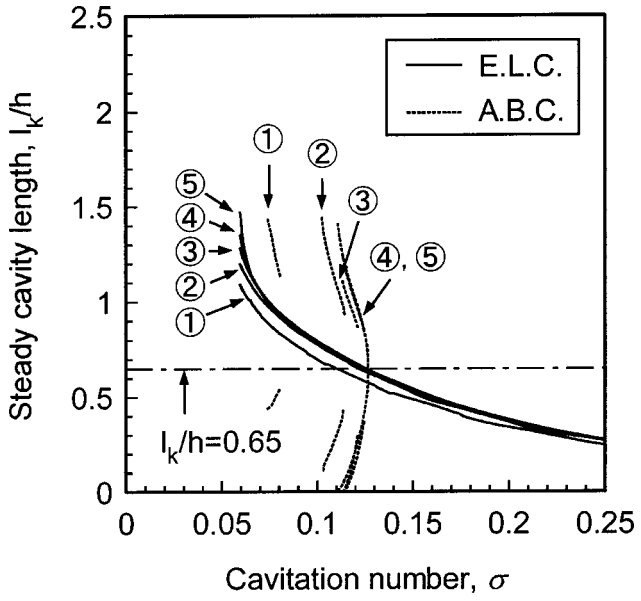

Fig. 5 Steady cavity length. ϕ=0.213

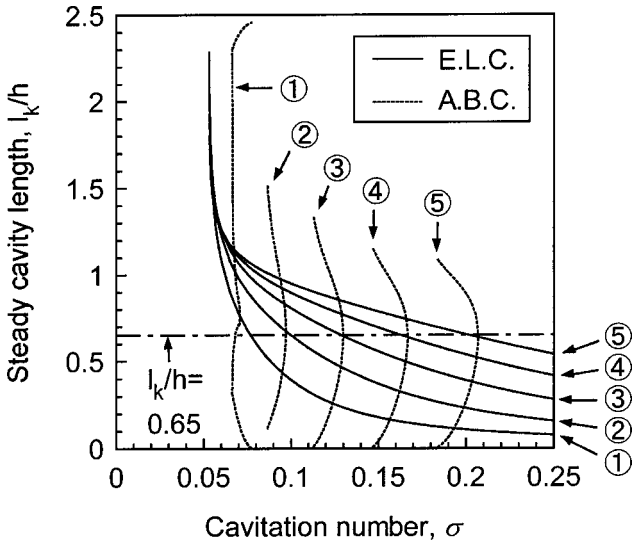

Fig. 7 Steady cavity length obtained by the 2D analysis, ϕ=0.213

The values of l_k normalized by the blade spacing h ($=\pi r$) are shown in Fig. 5. The solid and dotted lines show the solutions of the equal length cavitation and the alternate blade cavitation, respectively. In the alternate blade cavitation, the cavity length changes alternately from blade to blade and a couple of the cavity length is shown in the figure.

When the cavity length l_k/h of the equal length cavitation reaches about 65% of the blade spacing, the solutions of the alternate blade cavitation appears. Though we cannot determine which cavitation occurs in the cavitation number where the both solutions exist, it has been observed in some experiments [12,13] that the alternate blade cavitation occurs when the cavity length of the equal length cavitation reaches about 65% of the blade spacing, as shown in Fig. 6.

Effect of Three-Dimensionality of Flow. Figure 7 shows the results of the two-dimensional flow analysis on the cylindrical planes (1–5). The solid and dotted lines show the solutions of the equal length cavitation and the alternate blade cavitation, respectively. It is found that the cavity length is quite different from that in Fig. 5. This is due to the effect of three-dimensionality of the flow.

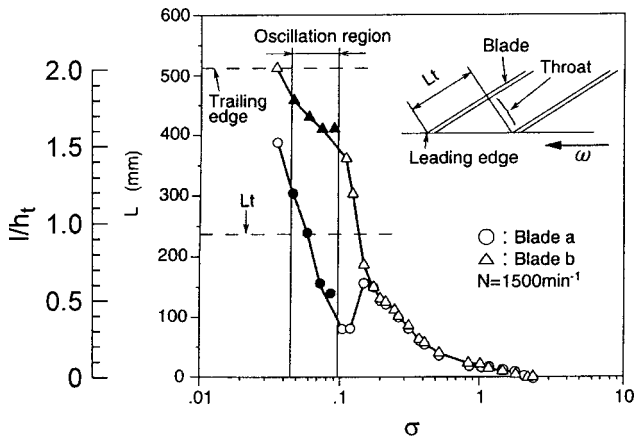

Fig. 6 Steady cavity length in experiment [12]

Then, we discuss about the effect of the three-dimensionality of the flow on cavitation. Two-dimensional linear analysis [14] shows that the cavity length is a function of $\sigma^*/(2\alpha)$, where σ^* is a local cavitation number defined as $2(p_{ti}-p_v)/(\rho w^2)$ and α is an angle of attack, both evaluated at each radial location. As the values of $\sigma^*/(2\alpha)$ decreases, the cavity length in the equal length cavitation increases in the cascade with larger solidity over about 1.5 [6]. Table 1 shows the values of α, σ^*, and $\sigma^*/(2\alpha)$ at the hub and the tip in the inlet of the impeller ($z/D_T=-0.0625$). In the two-dimensional analysis, the values of α and σ^* at the tip are smaller than those at the hub because the rotational speed of the impeller is larger at the tip due to its geometry. If the angle of attack is smaller, we should have shorter cavity. On the other hand, we should have longer cavity if the cavitation number is smaller. Since the value of $\sigma^*/(2\alpha)$ is smaller, the cavity length is larger at the tip, as shown in the results obtained by the two-dimensional analysis in Fig. 7. The value of α in the quasi-three-dimensional analysis is larger at the hub and smaller at the tip in comparison with that in the two-dimensional analysis, though the value of σ^* is almost the same as for the case of 2D analysis. As a result, the value of $\sigma^*/(2\alpha)$ is smaller at the hub and larger at the tip and the difference of the values of $\sigma^*/(2\alpha)$ at the hub and the tip becomes smaller, as compared with the case of 2D analysis. This partially explains the smaller difference of the cavity length at the hub and tip, of the results in the quasi-3D analysis.

Figure 8 shows the meridian streamlines in the equal length cavitation at σ=0.150 and 10.0. It is shown that the streamlines move radially outward near the leading edge of the blade. Though the amount of their movement at the smaller cavitation number is larger than that at the larger cavitation number, the difference of them is small. The meridional velocity changes due to the move-

Table 1 The values of the angle of attack, the local cavitation number and $\sigma^*/(2\alpha)$ at $z/D_T=-0.0625$, σ=0.150, ϕ=0.213

		Angle of attack, α	Local cavitation number, σ*	σ*/(2α)
Quasi 3-D	Hub	6.85°	1.09	4.56
	Tip	1.49°	0.143	2.74
2-D	Hub	4.29°	1.03	6.88
	Tip	2.04°	0.143	2.02

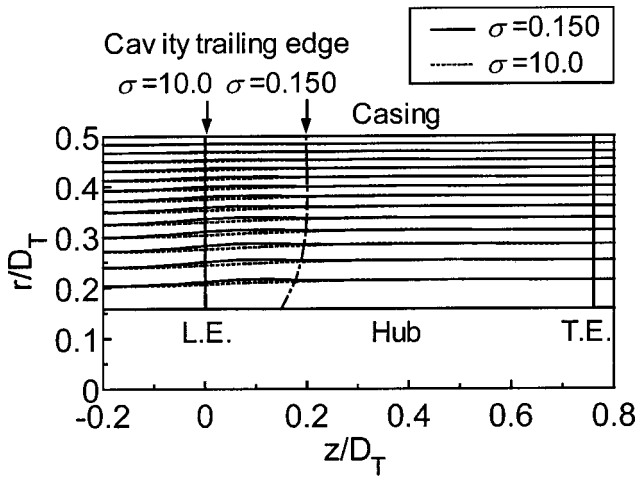

Fig. 8 Meridian streamline. σ=0.150, ϕ=0.213

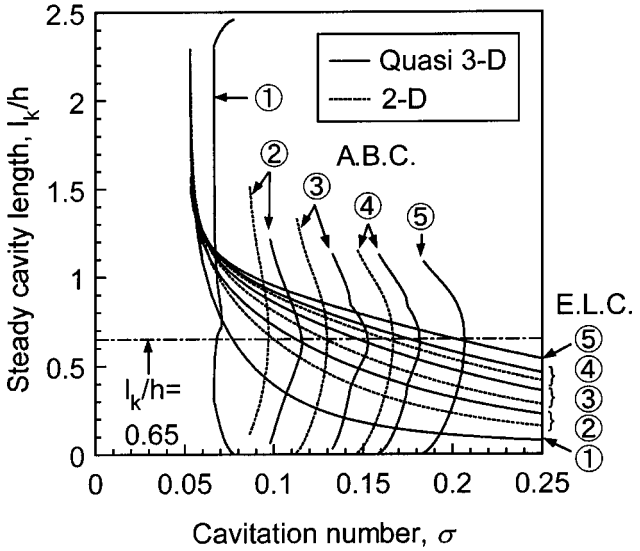

Fig. 10 Steady cavity length by the quasi-3D analysis assuming constant meridional velocity, compared with the 2D analysis. ϕ=0.213

ment of the meridian streamlines. Figure 9 shows the meridional velocity w_m at the inlet of the impeller ($z/D_T=-0.0625$). The value of w_m is smaller at the hub and larger at the tip in comparison with that in the 2D analysis. As a result, the angle of attack α is larger at the hub and smaller at the tip in the quasi-3D analysis, as shown in Table 1.

The above discussions can be summarized as follows. Due to the movement of the meridian streamlines to the radial direction, the meridional velocity becomes larger at the tip. The increase of the meridional velocity decreases the angle of attack α and the local cavitation number σ^* at the tip. As the rate of the decrease of α, which has the effects to shorten the cavity, is larger than that of the decrease of σ^*, which has the effect to lengthen the cavity, the cavity length becomes uniform over the span, as compared with the results of 2D analysis. The region of σ where the alternate blade cavitation occurs is smaller in the quasi-3D analysis than that in the 2D analysis. This can be explained by the effect of the movement of meridian streamlines.

Effect of the Meridional Velocity. In the present method the effect of the three-dimensionality of the flow appears through (a) the change in the meridional velocity caused by the shift of the meridian streamline and (b) the change in the tangential velocity caused by the shift of the meridian streamline. In order to identify those effects, calculations are made assuming that the meridional velocity is constant in each radial location. The cavity length obtained under this assumption is shown in Fig. 10. The curves denoted by E.L.C. and A.B.C. in Fig. 10 show the solutions of the equal length cavitation and the alternate blade cavitation, respectively. At the hub and the tip, the cavity length agrees with that of the 2D analysis because the flow there is identical from the assumption. In the location except the hub and the tip, the cavity length in the equal length cavitation is larger at a given σ in comparison with the result of the 2D analysis. Such results are quite different from the complete results shown in Fig. 5. This shows that the change of meridional velocity due to the change of interval between adjacent stream surfaces gives the large effect in the development of the cavity.

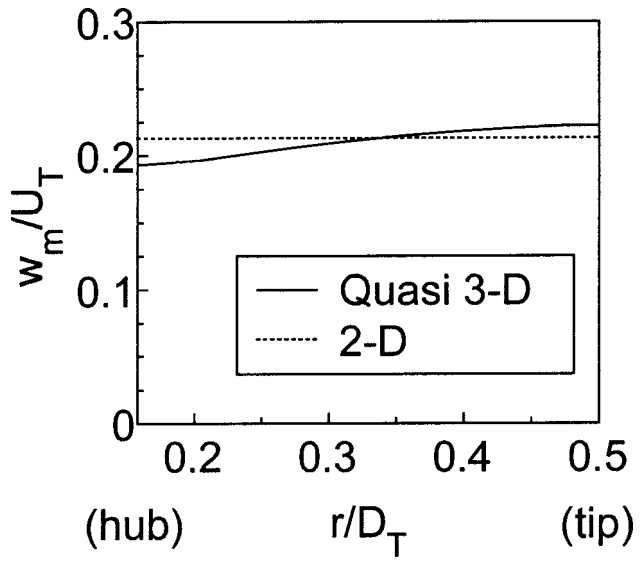

Fig. 9 Meridional velocity at $z/D_T=-0.0625$, σ=0.150, ϕ=0.213

Applicability

The application of the present method should be made for lower incidence angles in which the effects of backflow and tip leakage flow are smaller because the present method does not take these effects into account. In addition, it is difficult to obtain the convergence of the calculation for larger incidence angles (for example, we could not obtain the results for the incidence angles larger than about 3.5°, which corresponds to the flow rate smaller than about 0.185, at σ=0.2).

Even at low incidence angles, there will be a loss that occurs downstream of the cavity closure for larger cavity in actual turbopumps. We should keep in mind that the velocity distribution might be altered by the losses which are not included in the present calculations.

From a designer's perspective, it is thought to be useful to know the behavior of the head coefficient with cavitation number and the performance. In 1998, we estimated the performance by a 2D analysis in consideration of a loss near the cavity trailing edge [15]. Though the flow model was 2D, the head drop at the transition to the alternate blade cavitation from the equal length cavitation could be predicted qualitatively. The estimated performance did not agree with the performance in experiment quantitatively. Although the performance can be estimated if the model of loss is

introduced, we did not consider the model of loss and did not discuss the performance in the present study because the loss depended on its model.

Generally, a backflow is observed at the inlet of real inducers and a tip leakage flow occurs in the impeller with tip clearance and their effects cannot be ignored. The present study shows that the three-dimensionality of the flow considerably affects the development of the cavity even if the backflow and the tip leakage flow are not taken into consideration.

Conclusions

1. A method for the prediction of the steady, quasi-three-dimensional flow with cavitation in turbopumps was proposed, in which the analysis in the meridian plane was combined with that in the rotationally symmetric stream surface with the circumferentially averaged velocity.
2. The alternate blade cavitation occurs when the cavity length of equal length cavitation reaches about 65% of the blade spacing. This is the same as the results of two-dimensional flow analysis.
3. The three-dimensionality of the flow has a significant effect on the development of the cavity. The effect appears as the change of angle of attack accompanied with the change of meridional velocity, caused by the radially outward movement of the stream surface.

Acknowledgments

This study was supported by the Grant-in-Aid for Encouragement of Young Scientists from the Japan Society for the Promotion of Science.

Nomenclature

b = Interval between adjacent stream surfaces
C = Blade length in mapping plane
D_T = Diameter of impeller
d = Diameter
h = Blade spacing
h_t = Blade spacing at tip
i = Imaginary unit
L = Cavity length in mapping plane
l = Cavity length
m = Coordinate along meridian streamline
N_C, N_B = Number of discrete points on cavity and wetted surface, respectively
N_q, N_{st} = Number of q-coordinate lines and meridian streamlines, respectively
n = Coordinate normal to blade in mapping plane
p_t = Total pressure
p_v = Vapor pressure
Q = Concentrated source at the origin in mapping plane
q = Coordinate from hub to casing, or strength of source
R = Radial coordinate in mapping plane
r = Radial coordinate
r_T = Radius of impeller
S = Location of discrete point
s = Coordinate along blade in mapping plane
U_T = Peripheral speed of the impeller
v = Absolute velocity
w = Relative velocity
Z = Complex coordinate in mapping plane, $=X+iY$
z = Axial coordinate
α = Angle between w_m and z axis, or angle of attack
β = Angle between relative velocity and meridian plane
γ = Strength of vortex
η = Cavity thickness in mapping plane
Θ = Angular coordinate in mapping plane
θ = Angular coordinate
ρ = Density of fluid
σ = Cavitation number, $=2(p_{ti}-p_v)/(\rho U^2)$
σ^* = Local cavitation number, $=2(p_{ti}-p_v)/(\rho w^2)$
ϕ = Flow coefficient, $=v_{zi}/U_T$
Ψ, Ψ' = Stream function
ω = Rotational angular velocity of impeller

Subscripts

1, 2 = Index of cavitating and noncavitating region in s coordinates
casing = Casing
hub = Hub
I = Index of discrete point
i = Inlet of impeller
j = Index of q coordinate
k = Index of blade
m, r, θ = Components in m, r, θ directions, respectively
R, Θ = Components in R, Θ directions, respectively
s, n = Components in s, n directions, respectively
X, Y = Components in X, Y directions, respectively
z = Component in z direction

References

[1] Tsujimoto, Y., 2001, "Simple Rules for Cavitation Instabilities in Turbomachinery," Proceeding, 4th International Symposium on Cavitation (CAV2001), Pasadena, California, lecture.006, pp. 1–16.
[2] Dupont, P., and Okamura, T., 2002, "Cavitating Flow Calculations in Industry," Proceedings, 9th International Symposium on Transport Phenomena and Dynamics of Rotating Machinery (ISROMAC-9), Honolulu, Hawaii, FD-ABS-146, pp. 1–8.
[3] Coutier-Delgosha, O., Morel, P., Fortes-Patella, R., and Reboud, J. L., 2002, "Numerical Simulation of Turbopump Inducer Cavitating Behavior," FD-ABS-127, Proceedings, 9th International Symposium on Transport Phenomena and Dynamics of Rotating Machinery (ISROMAC-9), Honolulu, Hawaii, pp. 1–12.
[4] Okita, K., and Kajishima, T., 2002, "Three-Dimensional Computation of Unsteady Cavitating Flow in a Cascade," FD-ABS-076, Proceedings, 9th International Symposium on Transport Phenomena and Dynamics of Rotating Machinery (ISROMAC-9), Honolulu, Hawaii, pp. 1–8.
[5] Acosta, A. J., 1958, "An Experimental Study of Cavitating Inducers," ONR/ACR-38, Proceedings, 2nd Symposium on Naval Hydrodynamics, pp. 533–557.
[6] Horiguchi, H., Watanabe, S., Tsujimoto, Y., and Aoki, M., 2000, "A Theoretical Analysis of Alternate Blade Cavitation in Inducers," ASME J. Fluids Eng., **122**, pp. 156–163.
[7] Joussellin, F., Courtot, Y., Coutier-Delgosha, O., and Reboud, J. L., 2001, "Cavitating Inducer Instabilities: Experimental Analysis and 2D Numerical Simulation of Unsteady Flow in Blade Cascade," session B8.002, Proceeding, 4th International Symposium on Cavitation (CAV2001), Pasadena, California, pp. 1–8.
[8] Senoo, Y., and Nakase, Y., 1972, "An Analysis of Flow Through a Mixed Flow Impeller," ASME J. Eng. Power, **94**, pp. 43–50.
[9] Senoo, Y., and Nakase, Y., 1971, "A Blade Theory of an Impeller With an Arbitrary Surface of Revolution," ASME J. Eng. Power, **93**, pp. 454–460.
[10] Geurst, J. A., 1959, "Linearized Theory for Partially Cavitated Hydrofoils," International Shipbuilding Progress, **6**, pp. 369–384.
[11] Cooper, P., 1967, "Analysis of Single- and Two-Phase Flows in Turbopump Inducers," ASME J. Eng. Power, **89**, pp. 577–588.
[12] Huang, J., Aoki, M., and Zhang, J., 1998, "Alternate Blade Cavitation on Inducer," JSME Int. J., Ser. B, **41**, pp. 1–6.
[13] Yoshida, Y., Tsujimoto, Y., Kataoka, D., Horiguchi, H., and Wahl, F., 2001, "Effects of Alternate Leading Edge Cutback on Unsteady Cavitation in 4-Bladed Inducers," ASME J. Fluids Eng., **123**, pp. 762–770.
[14] Watanabe, S., Sato, K., Tsujimoto, Y., and Kamijo, K., 1999, "Analysis of Rotating Cavitation in a Finite Pitch Cascade Using a Closed Cavity Model and a Singularity Method," ASME J. Fluids Eng., **121**, pp. 834–840.
[15] Horiguchi, H., Watanabe, S., Tsujimoto, Y., and Aoki, M., 1998, "A Theoretical Analysis of Alternate Blade Cavitation in Inducers," FEDSM98-5057, Proceedings. 1998 ASME Fluids Engineering Division Summer Meeting, Washington, D.C., pp. 834–840.

An Experimental Investigation of Thermal Effects in a Cavitating Inducer

Jean-Pierre Franc
LEGI, Grenoble, France
Jean-Pierre.Franc@hmg.inpg.fr

Claude Rebattet
CREMHYG, Grenoble, France
Claude.Rebattet@hmg.inpg.fr

Alain Coulon
SNECMA, Vernon, France
alain.coulon@snecma.fr

The thermal effects which affect the development of leading edge cavitation in an inducer were investigated experimentally using refrigerant R114. For different operating conditions, the evolution of the cavity length with the cavitation parameter was determined from visualizations. The tests were conducted up to two-phase breeding. The comparison of tests in R114 and in cold water allowed us to estimate the amplitude of the thermodynamic effect. The results show that the B-factor depends primarily upon the degree of development of cavitation but not significantly upon other parameters such as the inducer rotation speed or the fluid temperature, at least in the present domain of investigation. These trends are qualitatively in agreement with the classical entrainment theory. In addition, pressure fluctuations spectra were determined in order to detect the onset of cavitation instabilities and particularly of alternate blade cavitation and rotating cavitation. If the onset of alternate blade cavitation appeared to be connected to a critical cavity length, the results are not so clear concerning the onset of rotating cavitation.
[DOI: 10.1115/1.1792278]

1 Introduction

When cavitation occurs in a liquid flow, part of the liquid changes into vapor in the low pressure regions. The latent heat of vaporization involved in the phase change makes that the two-phase medium is somewhat colder than the oncoming liquid. The temperature difference ΔT between the liquid at infinity and the cavitating region is usually made nondimensional using the characteristic temperature difference:

$$\Delta T^* = \frac{\rho_v L}{\rho_\ell c_{p\ell}} \tag{1}$$

This reference quantity depends only upon the nature of the fluid. The nondimensional temperature difference:

$$B = \frac{\Delta T}{\Delta T^*} \tag{2}$$

is the classical *B*-factor of Stepanoff [1–2]. Assuming that, a volume $\dot{\mathcal{V}}_v$ of vapor is formed per unit time and that the latent heat of vaporization is taken from a volume $\dot{\mathcal{V}}_\ell$ of liquid, the heat balance gives

$$B = \frac{\dot{\mathcal{V}}_v}{\dot{\mathcal{V}}_\ell} \tag{3}$$

If the cavitating region is considered as a two-phase mixture of void fraction α and typical thickness e, and assuming, in a basically dimensional approach, that the two-phase mixture is entrained with the general flow velocity V (Fig. 1), we have per unit span length:

$$\dot{\mathcal{V}}_v \approx \alpha e V \tag{4}$$

$$\dot{\mathcal{V}}_\ell \approx (1-\alpha) e V \tag{5}$$

so that

$$B \approx \frac{\alpha}{1-\alpha} \tag{6}$$

This very simple approach shows that the *B*-factor is of order unity unless the cavity is full of vapor ($\alpha=1$). In other words, the characteristic temperature difference ΔT^* can usually be considered as a reasonable estimate of the actual temperature difference ΔT.

In the case of water at room temperature, $\Delta T^* \cong 0.01$ K whereas $\Delta T^* \cong 1.2$ K for liquid hydrogen at 22.2 K. Thus, if thermal effects can be considered as negligible in water, it is not the case in LH_2 used in rocket engines.

For a full vapor cavity, only the surrounding liquid can supply the heat for vaporization since there is no liquid inside the cavity. This situation was analyzed by several investigators including Holl, Billet, and Weir [3], Kato [4], and Fruman, Reboud, and Stutz [5]. Still from a dimensional viewpoint, the vapor is assumed to be entrained at a flow velocity of the order of the liquid flow, so that (Fig. 2)

$$\dot{\mathcal{V}}_v \approx e V \tag{7}$$

The liquid concerned by heat transfer is contained in a thermal boundary layer of thickness δ which develops on the interface, so that

$$\dot{\mathcal{V}}_\ell \approx \delta V \tag{8}$$

and thus

$$B \approx \frac{e}{\delta} \tag{9}$$

As the transit time along the cavity of length ℓ is ℓ/V, the boundary layer thickness can be estimated by

$$\delta \approx \sqrt{a \frac{\ell}{V}} \tag{10}$$

where a is the thermal diffusivity. Kato [4] shows that turbulent mixing may very significantly enhance heat transfer in comparison with pure conduction. The thermal diffusivity to be considered is then an eddy diffusivity. Fruman et al. [6] proposed to

Contributed by the Fluids Engineering Division for publication in the JOURNAL OF FLUIDS ENGINEERING. Manuscript received by the Fluids Engineering Division December 15, 2003; revised manuscript received May 12, 2004. Associate Editor: Y. Tsujimoto.

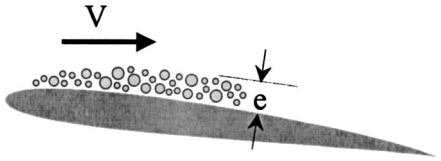

Fig. 1 Typical two-phase cavity

estimate it, considering that the liquid flow on the cavity is analogous to that on a rough wall. In the case of a full vapor cavity, the *B*-factor can therefore be estimated by

$$B \approx \frac{e}{\sqrt{a\,\frac{\ell}{V}}} \tag{11}$$

This relation is very similar to that which is found in the case of a single spherical bubble whose radius grows from a negligible value to R [cf., e.g., Brennen [7] or Eq. (28)]:

$$B \approx \frac{R}{\sqrt{at}} \tag{12}$$

where t is the growth time.

In practical applications, a major problem is to estimate the amplitude of the thermodynamic effect, i.e., of the *B*-factor. Several researchers such as Hord [8], Billet [9], Fruman, Reboud, and Stutz [5] have measured the temperature depression on ogives, hydrofoils or venturis for different operating conditions and different fluids. These data have been used either to derive semi-empirical correlations or to adjust predictive models. As an example, Fruman et al. [6] developed a model based on the entrainment theory which gives a reasonable prediction of the thermodynamic effect for two-dimensional sheet cavitation.

In the case of a rotating machinery as a rocket engine inducer, the direct measurement of the temperature depression on a rotating blade is more difficult. It is the reason why we tried to estimate the *B*-factor without measuring directly the temperature inside the cavitating region. Preliminary experiments [10] showed that this is possible from visualizations of the extent of the sheet cavity. The principle is elementary and based upon classical scaling rules in terms of the cavitation parameter.

There are two different ways to define the cavitation parameter. It can be calculated from the vapor pressure computed at the liquid temperature at infinity T_∞:

$$\sigma = \frac{p_{\text{ref}} - p_v(T_\infty)}{\frac{1}{2}\rho V^2} \tag{13}$$

or from the actual cavity pressure p_c equal to the vapor pressure at the actual temperature of the cavity T_c:

$$\sigma_c = \frac{p_{\text{ref}} - p_c}{\frac{1}{2}\rho V^2} = \frac{p_{\text{ref}} - p_v(T_c)}{\frac{1}{2}\rho V^2} \tag{14}$$

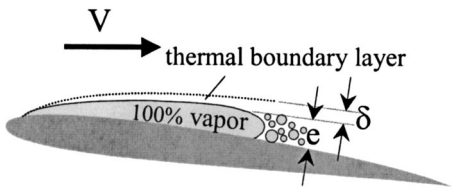

Fig. 2 Typical full vapor cavity

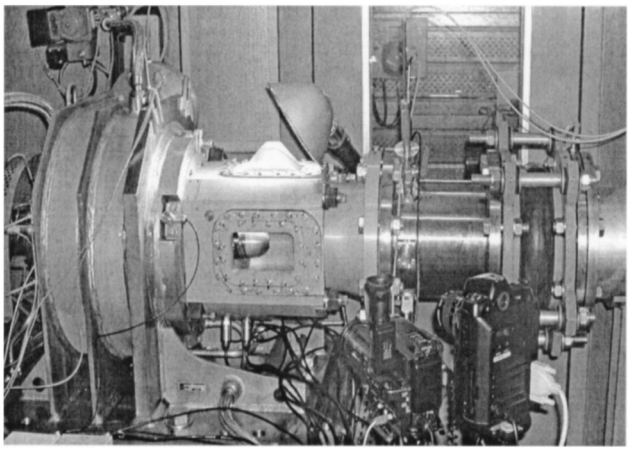

Fig. 3 View of the pump together with the inlet pipe. The flow is from right to left. The front window allows the observation of cavitation on the blades.

Both cavitation numbers are connected by

$$\frac{1}{2}\rho V^2(\sigma_c - \sigma) = \frac{dp_v}{dT}\Delta T. \tag{15}$$

This relation shows that the thermodynamic effect ΔT on the right-hand side can be estimated from the difference in cavitation numbers $\sigma_c - \sigma$. The value σ is determined from the general operating conditions, whereas σ_c is estimated from reference tests conducted in cold water, i.e., without thermal effects. The method consists in assuming that the cavity length is a function of the only cavitation number σ_c whatever may be the fluid. This is a classical scaling rule which is further discussed in Sec. 5. The value σ_c can then be obtained from a test in water leading to the same development of cavitation.

2 Experimental Facility

The fluid used for the tests is the refrigerant R114 (dichlorotetrafluoroethane $C_2Cl_2F_4$) between 20 and 40°C. The corresponding vapor pressure varies between 1.8 and 3.4 bar. The characteristic temperature difference ΔT^* increases from about 1.2 to 2.0 in this temperature range. Such values are very comparable to that of liquid hydrogen. Hence, it is expected that the thermodynamic effect in LH2 can be reasonably well approached by tests in R114. However, other parameters are significantly different such as the Prandtl number which is about 1 for LH2 and 5 for R114, so that deviations can also be expected. The problem of the transposition from R114 to LH2 is not addressed in the present work.

The experimental facility includes a resorption tank of 2.6 m^3, a pressure control device, a heat exchanger for the control of the fluid temperature, a variable head-loss and the pump to be tested (cf. [10] for a scheme of the facility). The inducer has four blades and its diameter is 182 mm. A flowmeter and several transducers allow the control of the operating conditions: flowrate, rotation speed, pressures, and temperatures. The fluid quality is controlled by means of a special degassing device which allows the removal of any noncondensable gas dissolved in the liquid before the facility is filled. Figure 3 presents a view of the inlet pipe and the pump.

The inlet pipe is equipped with an optical probe in order to measure the void fraction in case of two-phase breeding. Figure 4 presents a typical example of the signal given by the probe. Two-phase flow occurs naturally when the inlet pressure reaches the vapor pressure. The core of the flow remains generally liquid whereas the vapor structures develop in a boundary layer whose thickness is of the order of 3 cm. The void fraction was measured at a depth of 1.5 cm inside the pipe. It has to be noticed that such

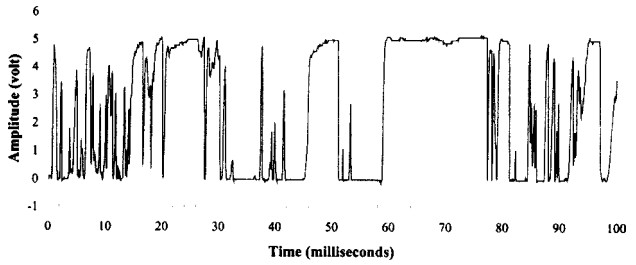

Fig. 4 Typical signal given by the optical probe. The lower level (0 V) corresponds to the liquid whereas the higher level (5 V) corresponds to the vapor. The void fraction is estimated from the ratio of the cumulative "vapor time" above a given threshold to the total acquisition time.

a local measurement is not representative of the mean void fraction throughout the whole pipe. It is only used here to give a qualitative indication on the quality of the oncoming flow with respect to its two-phase nature. The operation of the inducer in two-phase flow is beyond the scope of the present paper.

This study focused on sheet cavitation. The cavity length was measured using a grid drawn directly on each blade and visible on Fig. 5. It was measured along a unique radius corresponding to the mean radius between hub and casing. At this location, the cavity length is not significantly altered by tip-leakage cavitation. The three-dimensional features of the cavity were not investigated. For each operating condition, the cavity length was measured on each of the four blades and the mean value was computed. This procedure allows us to take into account possible differences in cavity

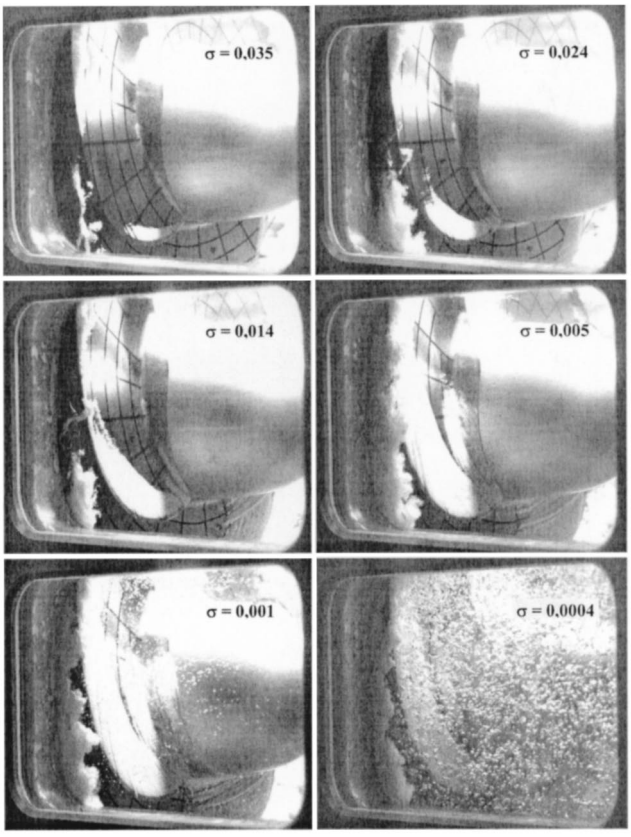

Fig. 5 Visualizations of the leading edge cavity for different values of the cavitation parameter up to two-phase breeding. Operating conditions: nominal flow rate, 4000 rpm, R114 at 20°C.

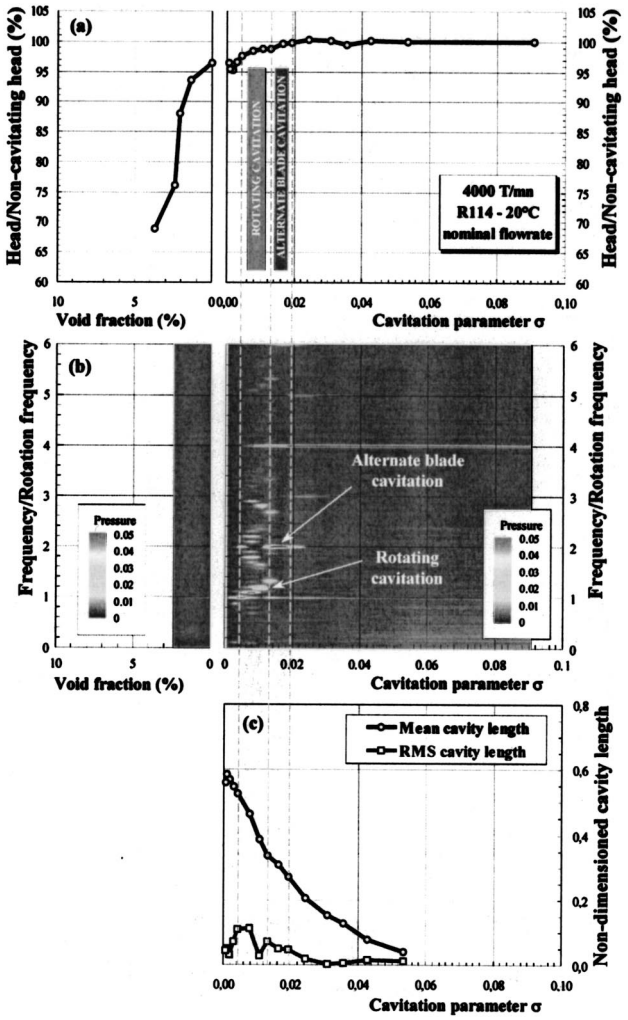

Fig. 6 Typical example of (a) efficiency of the inducer (b) map of pressure fluctuations spectra and (c) cavity length as a function of the cavitation parameter (right-hand side) or indicative void fraction (left-hand side). Operating conditions: nominal flow rate, 4000 rpm, R114 at 20°C.

lengths from a blade to another which may occur when cavitation instabilities develop. Figure 5 presents typical visualizations of the leading edge cavity during a cavitation test. When the cavitation parameter approaches 0, two-phase breeding occurs as explained later.

Cavitation instabilities were identified from a spectral analysis of pressure fluctuations. Several flush mounted pressure transducers were available at different locations along the casing. The cavitation instabilities are most easily detected from the pressure transducer located close to the leading edge of the blades. Figure 6(b) presents a typical example of the pressure fluctuations spectra. Alternate blade cavitation is easily identified at a frequency twice the rotation frequency. The observation through the windows confirms the alternation of a short and a long cavity. This is the first regime of instability observed as the cavitation parameter is decreased. A further decrease leads to the extinction of alternate blade cavitation and the onset of rotating cavitation. The latter is characterized by a frequency slightly greater that the rotation frequency. This frequency is progressively shifted toward the rotation frequency as the cavitation parameter continues to decrease. During rotating cavitation, a relatively short cavity rotates from a blade to the next one, whereas the three other blades have longer cavities. For low values of the cavitation parameter, any cavitation

instabilities disappear. Four cavities of equal length develop on each blade and the cavitation regime is balanced.

The ratio of head to noncavitating head is given in Fig. 6(a). It appears that the head does not drop significantly as long as the inlet flow remains purely liquid. The limit of two-phase flow corresponds to $\sigma=0$ since the inlet pressure is here chosen as the reference pressure [see Eq. (13)]. For two-phase breeding, the inlet pressure remains equal to the vapor pressure, so that the cavitation parameter remains equal to zero. In order to represent the head loss in two-phase flow, the void fraction is used instead of the cavitation parameter. The corresponding diagram is shown on the left-hand side. Due to the nonhomogeneous nature of the oncoming two-phase flow, the void fraction considered here is not an estimate of the mean void fraction as already mentioned. However, Fig. 6(a) clearly shows that the head drops mainly because of two phase breeding while the development of the leading edge cavities does not significantly alter the head. This is probably due to the relatively high thermodynamic effect in R114 which significantly delays the development of leading edge cavities. In fact, in case of negligible thermodynamic effect as in cold water, the head drops because of leading edge cavitation before the flow changes to vapor at the inlet. On the contrary, if thermal effects are important, the development of leading edge cavitation is greatly delayed and phase change is expected at the pump inlet whereas leading edge cavitation remains rather limited on the blades.

A typical evolution of the cavity length with the cavitation parameter is shown in Fig. 6(c). The cavity length is made nondimensional using the blade spacing, so that a cavity length equal to 1 corresponds to a cavity which extends up to the next blade. The behavior of the graph $\ell(\sigma)$ is quite usual. The rms value of the cavity length is more important in case of cavitation instabilities, as expected. From the consideration of Fig. 6(c) and similar graphs $\ell(\sigma)$ obtained for all other operating conditions, it appeared that the present inducer exhibits alternate blade cavitation for a critical cavity length of about 25%. This value has to be compared to the critical value of 65% that Tsujimoto found from a linear stability analysis of a two-dimensional cascade [11]. It has to be emphasized that, in the present work, the cavity length was measured along a unique radius corresponding to the mean value between hub and casing. The critical value of 25% obtained here would probably be different if the cavity length were measured at another location and especially near the tip. The actual three-dimensional nature of the cavity may then be one reason for the difference. Another one may be connected to tip cavitation which has not been considered in the present analysis which focuses on sheet cavitation. On the other hand, the onset of rotating cavitation did not prove to be correlated to a critical cavity length. This point is further discussed in the next section.

3 Thermodynamic Effect

When the fluid temperature is increased, all other parameters including the cavitation number σ being kept constant, the leading edge cavity shrinks as shown in Fig. 7. This effect is typical of a thermal delay due to the thermodynamic effect. In order to quantify the phenomenon, the variations of the cavity length with the cavitation parameter were systematically investigated. Figure 8 presents a comparison of the graphs $\ell(\sigma)$ for R114 at two different temperatures. Reference tests in cold water are also indicated. They result of former runs for which the scattering in cavity length was significantly greater than presently. Anyway, the thermodynamic effect is clearly visible since, for a given cavitation number, the cavity is longer in water than in R114 and, moreover, it is longer in R114 at 20 than at 40°C.

On the basis of the procedure presented in the introduction [cf. Eq. (13)], the temperature depression was computed for all operating conditions. The fluid temperature was varied between 20 and 40°C and the rotation speed between 3000 and 5000 rpm. All data were obtained at nominal flowrate. The results are presented in Fig. 9. The temperature depression increases with the cavity

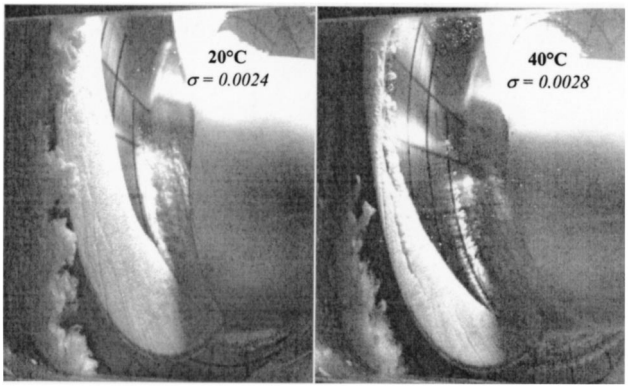

Fig. 7 Effect of the temperature on the development of cavitation at a nearly constant cavitation number S. Operating conditions: nominal flow rate, 5000 rpm, R114.

length. This is a common trend (cf., e.g., Ref. [12]) and in the present case, the increase is almost linear. Besides the cavity length, ΔT depends primarily upon the fluid temperature but does not depend significantly upon the rotation speed in the range 3000 to 5000 rpm. The *B*-factor defined by Eq. (2) was also computed. Results are presented in Fig. 10. It is remarkable to observe that all curves tend to collapse in a unique one. In other words, the thermodynamic effect in terms of *B*-factor is almost independent of the fluid temperature and of the rotation speed of the inducer in the present domain of investigation. It depends nearly exclusively upon the degree of development of the cavitation. The dependency is nearly linear with the cavity length.

Concerning cavitation instabilities, Fig. 8 shows that the onset of alternate blade cavitation has an approximately horizontal limit. This suggests that alternate blade cavitation appears for a critical value of the cavity length of the order of 25% of blade spacing. This observation holds for all other operating conditions investigated in the present work. Referring to Fig. 10, this critical development of cavitation corresponds to a value of the *B*-factor close to 2. It can then be concluded that the onset of alternate blade cavitation is affected by a thermodynamic effect whose amplitude

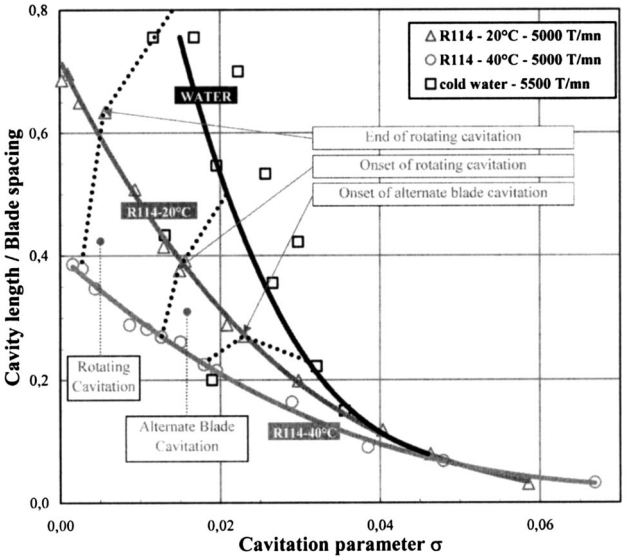

Fig. 8 Variation of the cavity length with the cavitation parameter for cold water and for R114 at two different temperatures

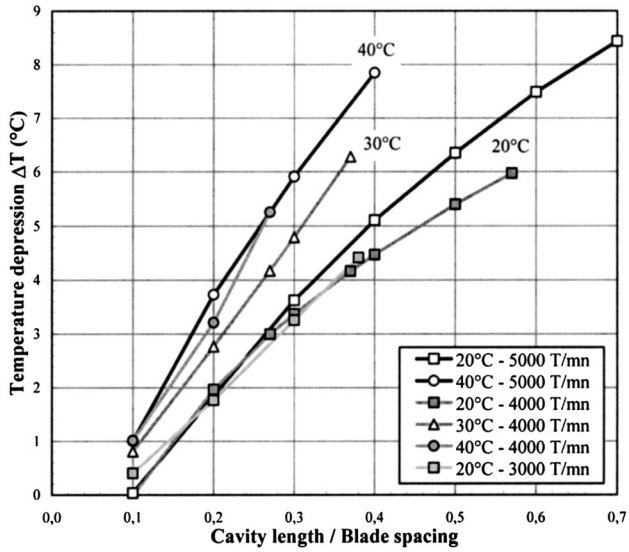

Fig. 9 Estimated temperature depression as a function of the cavity length for the inducer working in R114 at different operating conditions and nominal flow rate

is given by a *B*-factor of the order of 2. This observation can be used to predict the delay on the occurrence of the first cavitation instabilities due to thermal effects.

As for the transition from alternate blade cavitation to rotating cavitation, the limit in Fig. 8 is no longer horizontal. The present results lead then to supposing that the onset of rotating cavitation should not be simply connected to a critical degree of development of the leading edge cavities. Tip-leakage cavitation, whose development is no longer negligible for such regimes, might also contribute to the onset of rotating cavitation together with blade cavitation. It can be conjectured that the key factor is the total volume of vapor inside the inducer and that blade cavitation represents only part of it.

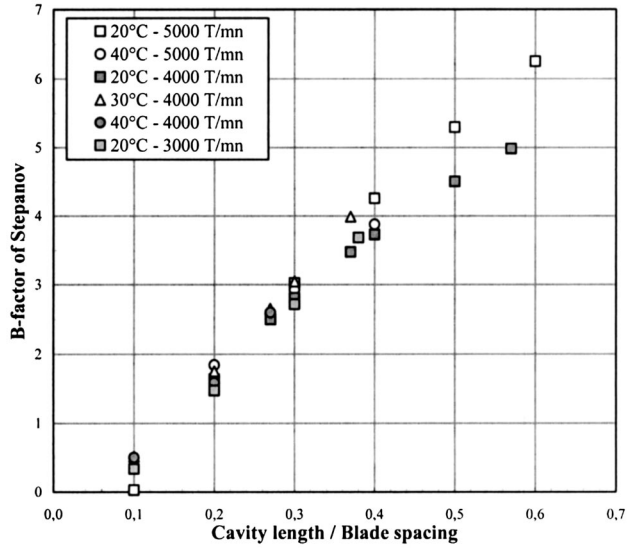

Fig. 10 *B*-factor of Stepanoff as a function of the cavity length for the inducer working in R114 at different operating conditions and nominal flow rate

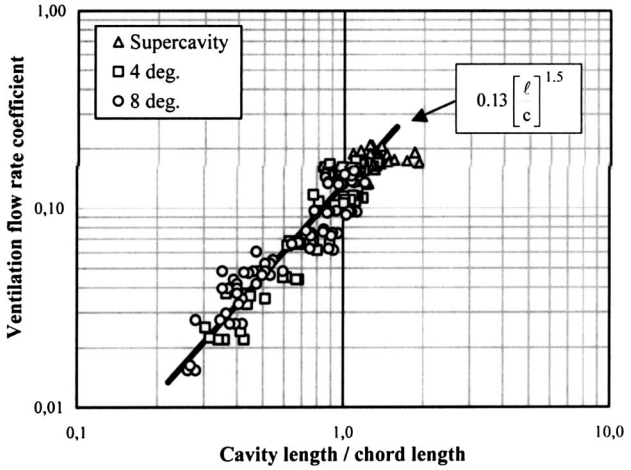

Fig. 11 Evolution of the flow rate coefficient with the cavity length for a foil named EN foil (data adapted from Kamono et al. [13]). The flow rate coefficient was made nondimensional using the foil thickness.

4 Analysis of Results

The trends observed in the present experimental study are analyzed on the basis of the entrainment theory (Holl et al. [3]). In Sec. 1, the *B*-factor for a vapor cavity was determined using a conductive type approach. In order to switch to a convective type approach as proposed by Holl et al., we simply identify the expressions of the heat flux given by both theories:

$$q \approx h \cdot \Delta T \approx \lambda \cdot \frac{\Delta T}{\delta} \tag{16}$$

This allows one to compute the equivalent boundary layer thickness δ:

$$\frac{\delta}{\ell} \approx \frac{h}{\rho_\ell c_{p\ell} V} = \frac{\mathrm{Nu}_\ell}{\mathrm{Re}_\ell \,\mathrm{Pr}} \tag{17}$$

where Nu_ℓ and Re_ℓ are the Nusselt and Reynolds numbers based on the cavity length ℓ and Pr the Prandtl number. Taking into account this expression of δ, Eq. (9) gives

$$B \approx \frac{e}{\ell} \frac{\mathrm{Re}_\ell \,\mathrm{Pr}}{\mathrm{Nu}_\ell} \tag{18}$$

Introducing the usual flow rate coefficient of vapor entrained at the rear of the cavity:

$$C_{Q\ell} = \frac{\dot{\mathcal{V}}_v}{\ell V} \approx \frac{e}{\ell} \tag{19}$$

we finally obtain

$$B \approx C_{Q\ell} \frac{\mathrm{Re}_\ell \,\mathrm{Pr}}{\mathrm{Nu}_\ell} \tag{20}$$

This is the classical relation of the entrainment theory as derived by Holl et al. [3]. To estimate the influence of the cavity length on the flow rate coefficient, we refer to experimental data of ventilation obtained by Kamono et al. [13]. Their data were re-plotted in logarithmic scales in order to reveal the exponent of the power law for the evolution of the flow rate coefficient versus the cavity length. From Fig. 11, it appears that the flow rate coefficient based on the foil thickness varies approximately as the power 1.5 of the cavity length, so that the flow rate coefficient based on the cavity length as defined by Eq. (19) should vary like the square root of the cavity length:

$$C_{Q\ell} \approx \sqrt{\frac{\ell}{c}} \tag{21}$$

As for the Nusselt number, we suggest to use, in a first approach, traditional correlations as the one proposed by Dittus and Boetler for convection heat transfer on a wall in fully developed turbulent flow (see, e.g., Holman [14]):

$$\mathrm{Nu} = 0.023\,\mathrm{Re}^{0.8}\,\mathrm{Pr}^{0.3} \tag{22}$$

Fruman et al. [5] showed that heat transfer through the liquid vapor interface can be reasonably well approximated by considering the interface as a solid wall.

By introducing Eq. (22) into Eq. (20), we obtain

$$B \approx C_{Q\ell}\,\mathrm{Re}_\ell^{0.2}\,\mathrm{Pr}^{0.7} \tag{23}$$

For the present experiments, the Prandtl number varies very little with the fluid temperature, from 5.5 at 20°C to 5.0 at 40°C. It is then impossible to estimate the exponent of the Prandtl number from this work. As for the rotation speed, it appears with exponent 0.2 in Eq. (23). This small value indicates a small dependency of the *B*-factor with the rotation speed. From 3000 to 5000 rpm, the term $\mathrm{Re}^{0.2}$ increases of 11% only. This observation is consistent with the present experimental results which show a small influence of the rotation speed on the *B*-factor. Equation (23) shows that the major parameter of influence is the cavity length. The above simplified approach suggests that the *B*-factor varies as the power 0.7 of the cavity length [from Eqs. (21) and (23)]. The present work actually demonstrates a major influence of the cavity length on the *B*-factor. It was observed on Fig. 10 that the *B*-factor is almost proportional to the cavity length. This is not so far from the power 0.7 expected from the entrainment theory. On the whole, the present results appear to be consistent with this theory which shows that the *B*-factor depends primarily upon the cavity length.

5 Scaling Rules With Thermodynamic Effect

The present results are based upon the assumption that cavitating flows are similar provided the cavitation number σ_c based on the real cavity pressure is constant, whatever may be the thermal effects. This assumption is re-examined here, on the basis of the Rayleigh-Plesset equation.

The classical Rayleigh-Plesset equation in which, for simplicity, the effects of surface tension, viscosity and noncondensable gases are not considered, writes:

$$\rho_\ell \left[R\ddot{R} + \frac{3}{2}\dot{R}^2 \right] = p_v(T_c) - p \tag{24}$$

R is the bubble radius and p is the time-dependent pressure applied to the bubble. Introducing the temperature difference $\Delta T = T_\infty - T_c$, this can be written:

$$\rho_\ell \left[R\ddot{R} + \frac{3}{2}\dot{R}^2 \right] + \frac{dp_v}{dT}\Delta T = p_v(T_\infty) - p \tag{25}$$

The second term on the left-hand side accounts for the thermodynamic effect. The determination of the temperature depression requires the solution of the heat equation in the liquid. For a mainly dimensional analysis, a simplified approach can be used to approximate this term (see, e.g., Brennen [7]). It consists in assuming that the thermal boundary layer around the bubble has the typical thickness $\sqrt{at}$ after time t, so that the heat flux on the bubble wall can be approximated by

$$q = \lambda \frac{\Delta T}{\sqrt{at}} \tag{26}$$

If conduction only is involved, λ is the usual thermal conductivity. As mentioned in the introduction, if heat transfer is enhanced by turbulence, the corresponding thermal diffusivity a has to be considered as an eddy thermal diffusivity (Kato [4]). Within this approximation, the heat balance for the bubble writes:

$$q[4\pi R^2] = \rho_v L \frac{d}{dt}\left[\frac{4}{3}\pi R^3 \right] \tag{27}$$

Combination of Eqs. (26) and (27) gives the order of magnitude of the thermodynamic effect for the bubble:

$$\Delta T \approx \frac{\dot{R}\sqrt{t}}{\sqrt{a}} \frac{\rho_v L}{\rho_\ell c_{p\ell}}. \tag{28}$$

The introduction of the previous estimate of the temperature depression into the Rayleigh-Plesset equation gives (cf. Brennen [7]):

$$\left[R\ddot{R} + \frac{3}{2}\dot{R}^2 \right] + \Sigma \dot{R}\sqrt{t} = \frac{p_v(T_\infty) - p}{\rho_\ell} \tag{29}$$

where Σ is the parameter defined by

$$\rho_\ell \sqrt{a}\,\Sigma = \frac{\rho_v L}{\rho_\ell c_{p\ell}} \frac{dp_v}{dT} \tag{30}$$

This Σ-parameter has been originally introduced by Brennen [7]. A very similar parameter (named α in Ref. [4]) was defined by Kato. It is connected to Σ by

$$\alpha = \sqrt{\frac{\rho_\ell}{\rho_v}}\,\Sigma \tag{31}$$

Both authors have shown that this parameter is a relevant one for the analysis of thermodynamic effect. In particular, Kato has shown that Hord's data on cavitation inception and desinence on a hydrofoil and ogives in cryogenic liquids are satisfactorily correlated to this parameter [4].

If this approach is not limited to the case of pure conduction but generalized to turbulent heat transfer, the Σ parameter depends no longer on the only fluid temperature but also on the fluid flow itself and its turbulence. In order to exhibit scaling rules, the time dependence is replaced by a space dependence using $x = Vt$ where x is the distance along the streamline followed by the bubble. Equation (29) is made nondimensional using a characteristic diameter D of the inducer and a characteristic velocity V. The following equation is obtained:

$$\left[\bar{R}\ddot{\bar{R}} + \frac{3}{2}\dot{\bar{R}}^2 \right] + \Sigma \sqrt{\frac{D}{V^3}}\,\dot{\bar{R}}\sqrt{\bar{s}} = -\frac{C_p + \sigma}{2}. \tag{32}$$

In this equation, the derivatives are no longer time derivatives but derivatives with respect to the nondimensioned distance $\bar{x} = x/D$. $\bar{R}$ is the nondimensioned bubble radius R/D and C_p the usual pressure coefficient. σ is the cavitation number defined by Eq. (11). For two geometrically similar flows characterized then by the same pressure distribution C_p, the solution $\bar{R}(\bar{x})$ is the same provided two scaling rules are satisfied.

As usually assumed for cavitating flows without thermal effects, the classical scaling rule on the cavitation number σ must first be fulfilled. In addition, the similarity of the thermal effects requires an additional scaling law. This consists in the conservation of the nondimensioned parameter $\Sigma\sqrt{D/V^3}$ as proposed by Brennen [15] and also by Kato [4]. This law must be used to ensure the scaling of two cavitating flows with thermodynamic effect. For example, if a different fluid is used to simulate the real fluid flow (e.g., a refrigerant instead of liquid hydrogen), it indicates how to change the length scale or the velocity so that both flows remain similar. Now, if one flow is without thermodynamic effect ($\Sigma = 0$) as is the case for cold water, the solution of Eq. (32) is obviously different from that with thermodynamic effect. There cannot then be a perfect scaling between two cavitating flows, with and without thermal effects. The differences in the solutions

$\overline{R}(\overline{x})$ mean that the bubbles do not present geometrically similar developments along the blades. If generalized to the case of attached cavities, it can be expected that the cavities are not geometrically similar which may result in differences in their relative thickness for instance. In a recent numerical work, Tani and Nagashima [16] have shown that the cavitation zone in liquid nitrogen is thicker than that in water. They observe that this might have consequences on cavitation instabilities and blockage. Strictly speaking, there is no complete scaling possible between two cavitating flows, with and without thermal effects. This is mainly due to the variations in temperature inside the cavity along the blade which induces variations in vapor pressure. The free streamline is then no longer at constant pressure as it is the case without thermodynamic effect. It is difficult to quantify the deviation which can be expected and, for limited thermodynamic effects, it can be conjectured that the classical scaling law on σ_c leads to a reasonable scaling of the flows. This was the assumption used in the present work.

6 Conclusion

The present paper reports the results of tests on a cavitating inducer conducted in refrigerant 114. This fluid was chosen to simulate the thermodynamic effect encountered in liquid hydrogen. The comparison of results in R114 and in cold water (i.e., without thermal effects) shows that, at a constant cavitation number, the leading edge cavities are less developed in the case of R114 than in the case of water. Moreover, an increase of the liquid temperature leads to shorter cavities, as can be expected from the theory on thermodynamic effect.

From the consideration of the Rayleigh-Plesset equation, it is shown that the scaling of cavitation development between two geometrically similar flows requires two scaling laws to be satisfied. The first one is the classical conservation of the cavitation number σ based on a reference pressure at infinity. The second one is relative to thermal effects and requires the conservation of an additional nondimensional parameter $\Sigma\sqrt{D/V^3}$ where Σ is a thermodynamic parameter classically introduced in most analysis of thermal effects [see Eq. (30)] and D and V characteristic scales of length and velocity. Hence, there is no exact scaling possible between tests in cold water and in a thermosensible fluid as R114. Deviations in the geometries of the cavities are expected due to temperature changes along the cavity. The comparison of tests in R114 and in cold water is then not so simple. However, assuming that thermal effects are not too important, the cavity pressure can be considered as approximately constant and both flows can be considered as almost similar provided the cavitation number σ_c based on the actual cavity pressure is kept constant. This scaling law is used here to compare tests in water and R114.

To observe the same development of cavitation in R114 than in cold water, it is necessary to lower the cavitation number. Using the scaling law on σ_c, it is then possible to estimate the temperature depression inside the cavity from this measured shift in cavitation number. The results are presented in terms of the B-factor of Stepanoff. It is shown that the B-factor does not depend significantly on the fluid temperature or on the rotation speed of the inducer in the present domain of investigation. It depends mainly upon the degree of development of the cavitation and is nearly proportional to the cavity length. These trends are consistent with the entrainment theory in which basic assumptions are made concerning the convection heat transfer coefficient and the flow-rate of vapor entrained at the rear of the cavity.

During the tests, the development of cavitation instabilities is also detected from the analysis of pressure fluctuations. On the present inducer, it is observed that alternate blade cavitation starts for a critical development of the leading edge cavities characterized by a length (measured along the mean radius between hub and casing) of about 25% of blade spacing. The onset of alternate blade cavitation is affected by a thermal delay given by a value of the B-factor of the order of 2. On the other hand, the transition from alternate blade cavitation to rotating cavitation could not be correlated to a critical development of sheet cavities so that it is supposed that tip-leakage cavitation also plays an important role in the onset of rotating cavitation.

Present estimates of the temperature depression are deduced from visualizations and basic scaling laws. The only way to validate the approach would be to measure directly the temperature or the pressure inside the cavities which develop on the rotating blades.

Acknowledgments

We would like to thank our colleagues R. Brillault, E. Janson and M. Riondet for providing support in the preparation and running of tests. We would also like to acknowledge the contribution of P. Morel (SNECMA) in the initiation of the present research. Useful discussions, suggestions and information were provided by several colleagues, especially D. H. Fruman and Y. Lecoffre, in the framework of the COSCAV meeting. This research was partly supported by CNES.

Nomenclature

a = thermal diffusivity or eddy diffusivity
B = B-factor of Stepanoff (Eq. 2)
C_p = pressure coefficient
$c_{p\ell}$ = liquid heat capacity
D = characteristic diameter of the inducer
e = cavity thickness
ℓ = cavity length
h = convection heat transfer coefficient
L = latent heat of vaporization
Nu_ℓ = Nusselt number based on cavity length
p = pressure
p_c = cavity pressure
p_{ref} = reference pressure
p_v = vapor pressure
Pr = Prandtl number
q = heat flux
R = bubble radius
$\dot{R}$ = bubble wall velocity
Re_ℓ = Reynolds number based on cavity length
t = time
T = temperature
T_c = temperature of cavity
T_∞ = liquid temperature at infinity
V = flow velocity
$\dot{\mathcal{V}}_\ell$ = volume flow rate of liquid
$\dot{\mathcal{V}}_v$ = volume flow rate of vapor
x = distance
α = void fraction [except in Eq. (31)]
δ = thermal boundary layer thickness
ΔT = thermodynamic effect
ΔT^* = characteristic temperature difference [Eq. (1)]
λ = thermal conductivity
ρ_v = vapor density
ρ_ℓ = liquid density
σ = cavitation number [Eq. (13)]
σ_c = cavitation number based on cavity pressure [Eq. (14)]
Σ = thermodynamic parameter [Eq. (30)]

References

[1] Stahl, H. A., Stepanoff, A. J., and Phillipsburg, N. J., 1956, "Thermodynamic Aspects of Cavitation in Centrifugal Pumps," ASME J. Basic Eng., 1691–1693.
[2] Stepanoff, A. J., 1964, "Cavitation Properties of Liquids," J. Eng. Power, 195–200.
[3] Holl, J. W., Billet, M. L., and Weir, D. S., 1975, "Thermodynamic Effects on Developed Cavitation," J. Fluids Eng., 507–514.
[4] Kato, H., 1984, "Thermodynamic Effect on Incipient and Developed Sheet

Cavitation,'' International Symposium on Cavitation Inception, FED-Vol. 16, New Orleans, LA, 9–14 December, pp. 127–136.
[5] Fruman, D. H., Reboud, J. L., and Stutz, B., 1999, ''Estimation of Thermal Effects in Cavitation of Thermosensible Liquids,'' Int. J. Heat Mass Transfer, **42**, 3195–3204.
[6] Fruman, D. H., Benmansour, I., and Sery, R., 1991, ''Estimation of the Thermal Effects on Cavitation of Cryogenic Liquids,'' Cavitation and Multiphase Flow Forum, ASME FED, **109**, 93–96.
[7] Brennen, C. E., 1995, *Cavitation and Bubble Dynamics*, Oxford University Press, New York.
[8] Hord, J., ''Cavitation in Liquid Cryogens,'' NASA Report Nos. CR-2054, CR-2156 (1972), CR-2242 (1973), CR-2448 (1974).
[9] Billet, M. L., 1970, ''Thermodynamic Effects on Developed Cavitation in Water and Freon 113,'' Master of Science thesis, The Pennsylvania State University, March 1970.
[10] Franc, J. P., Janson, E., Morel, P., Rebattet, C., and Riondet, M., 2001, ''Visualizations of Leading Edge Cavitation in an Inducer at Different Temperatures,'' Fourth International Symposium on Cavitation, Pasadena, CA, 20–23 June.
[11] Tsujimoto, Y., 2001, ''Simple Rules for Cavitation Instabilities in Turbomachinery,'' Fourth International Symposium on Cavitation, Pasadena, CA, 20–23 June.
[12] Billet, M. L., Holl, J. W., and Weir, D. S., 1981, ''Correlations of Thermodynamic Effects for Developed Cavitation,'' J. Fluids Eng., **103**, 534–542.
[13] Kamono, H., Kato, H., Yamaguchi, H., and Miyanaga, M., 1993, ''Simulation of Cavity Flow by Ventilated Cavitation on a Foil Section,'' *Cavitation and Multiphase Flow, FED-Vol. 153*, ASME, pp. 183–189.
[14] Holman, J. P., 1997, *Heat Transfer*, McGraw-Hill, New York.
[15] Brennen, C. E., 1994, *Hydrodynamics of Pumps*, Concepts ETI Inc. and Oxford University Press, New York.
[16] Tani, N., and Nagashima, T., 2002, ''Numerical Analysis of Cryogenic Cavitating Flow on Hydrofoil—Comparison Between Water and Cryogenic Fluids,'' 4th Int. Conf. on Launcher Technology, 3–6 December, Liege (Belgium).

R. Latorre
Naval Architecture & Marine Engineering,
University of New Orleans, LA 70148 USA

A. Muller

J. Y. Billard

A. Houlier

Hydrodynamic Laboratory,
Ecole Navale, Brest, 29240 France

Investigation of the Role of Polymer on the Delay of Tip Vortex Cavitation

Cavitation tunnel measurements have shown tip vortex cavitation inception is delayed when polymers are injected from the hydrofoil tip. Experiments with polymers have also shown that the polymers cause the cavitation to become more violent. To better understand the role of polymer in the delay of tip vortex cavitation, a theoretical analysis of tip vortex cavitation inception in pure water and in polymer solution is presented. The analysis shows that while polymer injection causes instability in small bubbles, its main effect is an increase in tip vortex core radius, resulting in the delay of tip vortex cavitation inception. [DOI: 10.1115/1.1792260]

Introduction

Fruman and Aflafo, [1] and Fruman et al. [2], reported that injecting a polymer solution from an elliptic hydrofoil lowered the tip vortex cavitation inception number σ_i (Fig. 1). Their LDV measurements downstream of the hydrofoil tip showed a 28% increase in tip vortex radius from polymer injection. The tests also revealed that polymer injection increased the tip vortex radius as well as reduced the tip vortex tangential velocity and hydrofoil lift [1].

In explaining the tip vortex cavitation (TVC) inception test results, they linked the delay to the increase of the tip vortex radius. This TVC inception delay has also been observed when the tip vortex radius is increased by roughening the blade pressure side (McCormick [3], Latorre, [4]) and by modification of the foil tip using bulbs and plates (Platzer and Sounders, [5], Green, [6]).

The influence of polymers on cavitation bubble dynamics was studied by Shima and Tsujino [7]. Their experiments showed that using an ultrasonic vibratory rig polymers increased noise and cavitation collapse. The polymer solution was shown to reduce the surface tension, resulting in bubble cavitation at greater cavitation numbers than in tests with pure water.

The results of Shima and Tsujino [7] indicate that instead of delaying the TVC inception, the polymers' influence could cause TVC inception at higher cavitation numbers. Since this wasn't observed, Fruman's results suggest a filtering process occurs where the tip vortex cavitation inception is limited to the larger cavitation nuclei population which is unaffected by the polymer injection.

As a contribution to clarifying whether the filtering process occurs, this paper presents the results from a theoretical study to clarify tip vortex cavitation inception with and without polymer injection. A theoretical model of the bubble capture by the tip vortex is used to study the TVC inception with and without polymers. The results show filtering and the larger bubbles play a dominant role in the TVC inception.

To further support this view, the results of bubble stability analysis in water with and without polymers is presented. The results again show that the inception cavitation number of the larger bubbles is unaffected by the presence of polymers. This leads to the conclusion that the filtering process occurs, and the main influence of the polymer is to increase tip vortex core radius, which delays TVC inception σ_i.

Contributed by the Fluids Engineering Division for publication in the JOURNAL OF FLUIDS ENGINEERING. Manuscript received by the Fluids Engineering Division June 23, 1999; revised manuscript received April 29, 2004. Associate Editor: B. Schiavello.

Analysis of Elliptic Foil Experiments

The elliptic hydrofoil design used in the TVC inception experiments is summarized in Table 1. The theoretical analysis requires an estimate of the foil circulation Γ and tip vortex radius without polymers R_1, and with polymers R_1', which are summarized in Table 2 for the test conditions shown in Fig. 1.

McCormick [3] introduced the following semi-empirical relation to characterize the TVC inception:

$$\sigma_i = \mathrm{Re}_c^{0.4} \tag{1}$$

Latorre and Ligneul [8] showed that the cavitation number σ at which TVC appeared could be estimated using the tip vortex radius R_1 in a Rankine vortex at the core center, $R=0$:

$$\sigma_i \approx C_{p\ \min} = \frac{\Gamma^2}{4\pi^2 V^2 R_1^2} \tag{2}$$

Since Γ is unchanged by the polymer injection, the main polymer influence is on the vortex radius R_1. Since R_1 is estimated as equal to a turbulent boundary layer thickness, it follows that $R_{1\ no\ polymer} \approx 1/\mathrm{Re}_c^{0.2}$ and $R_{1\ polymer} \approx 1/\mathrm{Re}_c^{\beta}$. The exponent β value depends on the polymer injection solution. This leads to the approximation

$$R_{1\ no\ polymer}/R_{1\ polymer} \approx \mathrm{Re}_c^{\beta-0.2} \tag{3}$$

Introducing this expression in Eq. (2) results in a semi-empirical expression of tip vortex inception in the presence of polymers.

$$\sigma_{i\ polymer} \approx \mathrm{Re}_c^{0.4-2\beta} \tag{4}$$

For the data in Fig. 1, the value of $\beta = 0.193$.

This format can be useful in reporting the results of future tip vortex cavitation tests with/without polymer injection.

Theoretical Model of Tip Vortex Cavitation Inception

To investigate the influence of polymers on the inception of tip vortex cavitation, the theoretical model of tip vortex cavitation capture and inception noise developed by Latorre [4] is adopted. This model consists of

1. modeling of nuclei as spherical bubbles,
2. idealization of tip vortex as a Rankine vortex,
3. analytical specification of the vortex circulation Γ,
4. vortex core R_1 equal to equivalent flat plate foil boundary layer thickness, and
5. model of bubble trajectory using Johnson-Hsieh formulation [4].

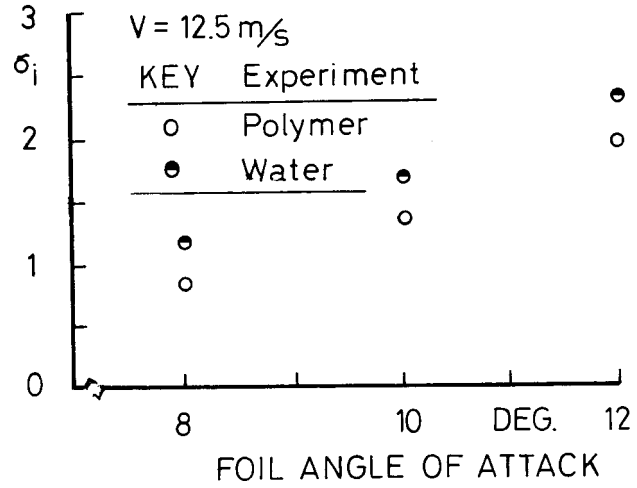

Fig. 1 Delay of elliptical foil tip vortex calculation inception (foil details in Table 1) $R_e=10^6$, polymer concentration: 1000 ppm, cavitation number uncertainty estimated to be <±2.5% [2].

The nuclei are assumed as spherical gas filled bubbles with radius R. The variation of the radius R with change in pressure P taken at the bubble center is given by the Rayleigh–Plesset formulation Eq. (5):

$$\rho(R\ddot{R}+3/2\dot{R}^2)=P_V-P-2S/R+G/R^3-4\mu\dot{R}/R \tag{5}$$

The noise generated by the change in the bubble radius R at a distance r from the bubble center is estimated using the Fitzpatrick–Strassberg formulation [4]:

$$P_a(t')=p(t')-P_0=\frac{\rho_0 R}{r}[R(t')\ddot{R}(t')+2(\dot{R}(t'))^2] \tag{6}$$

The trajectory of the spherical cavitation nuclei around the tip vortex pressure field is determined by the Johnson–Hsieh formulation. This neglects the buoyancy force in the forces acting on the bubble:

Table 1 Elliptic hydrofoil used in tip vortex cavitation inception tests with polymer injection (Fruman et al. [2])

Item	Units	Value
Hydrofoil	···	Elliptic
Base chord	mm	80
Semi-span	mm	120
Aspect ratio	···	3.8
Foil section	···	NACA 16.020

Table 2 Tip vortex cavitation inception simulation data-elliptical foil in Table 1

Item	Unit	Case I	Case II	Case III	Notes
Angle α	Deg.	8	10	12	
Speed V	m/s	12.5	12.5	12.5	···
Circulation Γ	m^2/s	0.0675	0.09	0.1125	···
TipVortex Radius R_1	mm	1.34	1.34	1.34	Water
Polymer Tip Vortex Radius R_1	mm	1.7	1.7	1.7	
Cavitation σ	···	1.0–1.5	1.5–2.0	2.0–2.5	···
Bubble R_o	μm	25	25	25	Average
Background noise level	dB	80	80	80	Assumed

$$\text{Force}=F_{Drag}+F_{\text{Pressure}}+F_{Inertial\ and\ virtual\ mass} \tag{7}$$

This is written in vector form:

$$\frac{dW_b}{dt}=\frac{3}{4}(\overline{W}-\overline{W}_b)|\overline{W}-\overline{W}_b|\frac{C_D}{R}-\frac{3\nabla P}{\rho}+\frac{3}{R}(\overline{W}-\overline{W}_b)\frac{dR}{dt} \tag{8}$$

The drag coefficient C_D of the spherical nuclei is determined using Haberman's empirical equation:

$$\frac{C_D\,\mathrm{Re}_B}{24}=1.0+0.197\,\mathrm{Re}_B^{0.63}+2.6\times10^{-4}\,\mathrm{Re}_B^{1.38} \tag{9}$$

The model of the tip vortex flow field is a combined Rankine vortex with a characteristic radius R_1 and circulation Γ. In the case of Fruman's experiment [1] the value of R_1 was measured. When the R_1 value is not reported, it can be estimated as the equivalent flat plate boundary layer thickness:

$$R_{1/\eta\neq0}=\frac{0.37(C_0\sqrt{1-\eta^2})}{[V_\infty C_o\sqrt{1-\eta^2}/v]} \tag{10}$$

where $\eta=0.75$ for hydrofoils with elliptic platform shape.

The value of the maximum circulation Γ_1 at $R=R_1$ was taken to be equal to $\frac{1}{2}$ the maximum foil Γ_0 value:

$$\Gamma=1/2\Gamma_0 \tag{11}$$

where the maximum foil circulation Γ_0

$$\Gamma_0=1/2\mathrm{C_L}\mathrm{U}_\infty\mathrm{C_o} \tag{12}$$

At radial position $R_t\geqslant R_1$ the bubble is in the irrotational vortex flow with a tangential velocity V_{tang}.

$$V_{Tang}=\frac{\Gamma}{2\pi R_t},\quad R_t\geqslant R_1 \tag{13}$$

The corresponding pressure coefficient at R_t can be written as

$$C_p=\frac{P-P_\infty}{1/2\rho V^2}=-\frac{\Gamma_1^2}{4\pi^2R_t^2V^2},\quad R_t\geqslant R_1 \tag{14}$$

At the core center, $R_t=0$, the pressure is at its minimum value, and $C_{p\,\min}$ is given by

$$C_{p\,\min}=\frac{\Gamma_1^2}{4\pi^2V^2R_1^2} \tag{15}$$

In the simulation of the nucleus trajectory these equations are evaluated for each instantaneous trajectory radius R_t. The equations of bubble trajectory [Eq. (8)] and bubble radius [Eq. (5)] were integrated using the Runga–Kutta method, employing a time step of 5×10^{-7} s. This gives an accuracy of ±2.0% on the bubble radius, trajectory, and sound pressure P_a SPL. The superposition of bubble translation along the X_1 axis and the radial motion around the vortex center results in a three-dimensional spiral trajectory shown in Fig. 2. This spiral bubble trajectory and bubble capture is similar to earlier results of Latorre [4], Levkovskii [9], and Ligneul and Latorre [10,11].

Example of Tip Vortex Cavitation Inception for Pure Water for Case II

The theoretical analysis of TVC inception was investigated using the numerical simulation described in the previous selection, for a range of bubble radii. The analysis was done for the following conditions, $\sigma=2.0$:

1. Bubble growth in pure water with $S=8.125\times10^{-2}$ N/m for pure water
2. Bubble growth with large vortex core $R_1'=R_1\times1.28$ and $S=8.125\times10^{-2}$ N/m for pure water

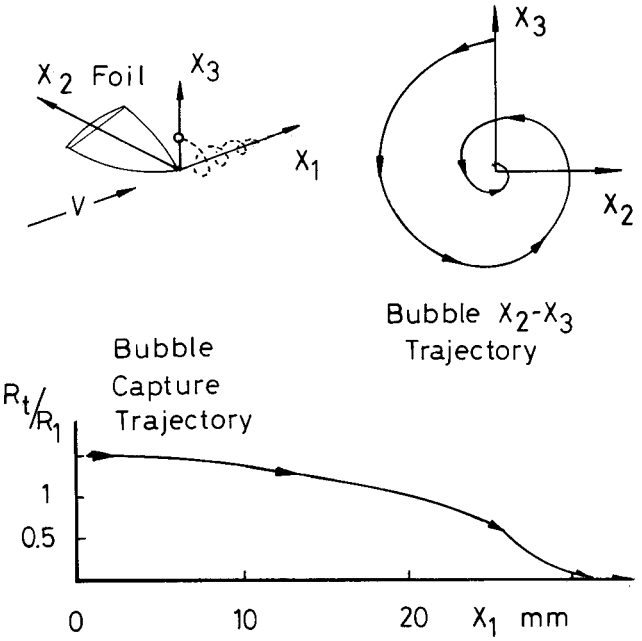

Fig. 2 Foil geometry and simulated bubble trajectory radius R_t/R_1 during bubble capture α=10 deg (case II in Table 2) σ=2.0

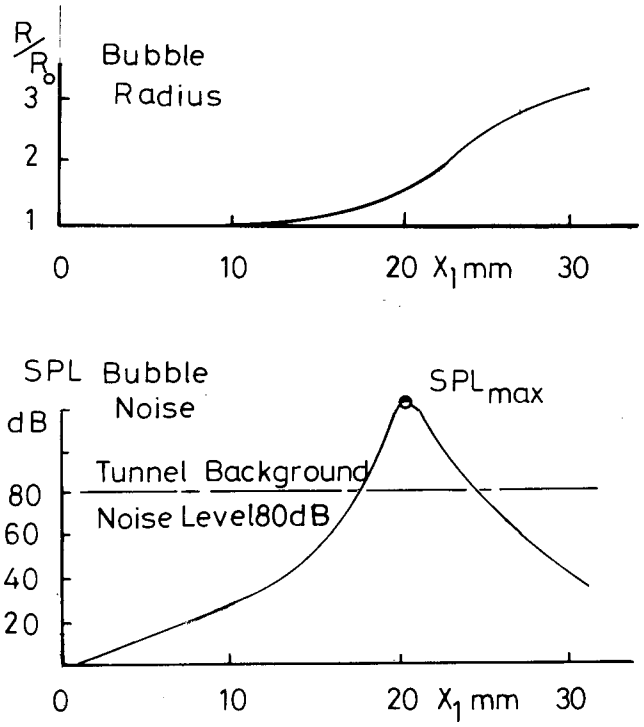

Fig. 3 Bubble radius and corresponding bubble capture noise (bubble is stable)

3. Bubble growth with large vortex core $R_1' = R_1 \times 1.28$ and $S = 6.5 \times 10 - 2$ N/m for polymer solution [12]

Simulations 2 and 3 were done to understand the influence of surface tension on the bubble growth. Simulation 2 reflects the influence of the tip vortex radius on TVC inception.

To illustrate the analysis, the pure water results for case II in Table 2, the results for $\Gamma = 0.09$ m^2/s, with pure water of $R_1 = 1.34$ mm, are shown for an initial bubble radius $R_o = 25\ \mu$m. The results are shown in Figs. 2–4. Figure 2 shows the spiral bubble trajectory which ends in capture by the vortex at $X_1 = 30$ mm. The corresponding non-dimensional bubble radius R/R_o in Fig. 3 reaches a value of 3 by the point of capture. Since the value of $\sigma > \sigma_{ins} = 1.5$, corresponding to the limiting cavitation number for stable bubble growth for initial bubble radius $R_o = 25\ \mu$m. Following earlier results, the visible inception of tip vortex cavitation can be estimated when the corresponding sound pressure level, SPL, of the bubble equals the background SPL of the cavitation tunnel.

$$\mathrm{SPL}_{\mathrm{Bubble}} \geqslant \mathrm{SPL}_{\mathrm{Tunnel}} \tag{16}$$

where

$$\mathrm{SPL} = 20 \log (P_a / P_o) \mathrm{dB}$$

From the analysis of the results, the value of $\mathrm{SPL}_{\mathrm{Tunnel}}$ is 80 dB. Systematic results of the maximum SPL value are plotted as a function of the initial bubble radius $5 < R_o < 25\ \mu$m in Fig. 4. This figure shows several interesting points, namely for a given cavitation number σ.

1. The maximum bubble SPL is dependant on the initial bubble radius, R_o.
2. Small initial bubble radii, R_o, do not generate large values of SPL as shown in Fig. 4

Stability Analysis of Cavitation Bubbles

To clarify the results from the TVC inception study, the bubble stability analysis was performed as part of this study. The Rayleigh–Plesset equation describes the variation of the radius gas filled bubble with changing external pressure:

$$\rho\left(R \frac{d^2R}{dt^2} + \frac{3}{2}\left(\frac{dR}{dt}\right)^2 \right) = P_v - P - \frac{2S}{R} + \frac{G}{R^3} - \frac{4\mu}{R}\frac{dR}{dt} \tag{17}$$

Considering the static case, the time dependent derivative terms drop out of this equation leaving

$$P_v - P - \frac{2S}{R} + \frac{G}{R^3} = 0 \tag{18}$$

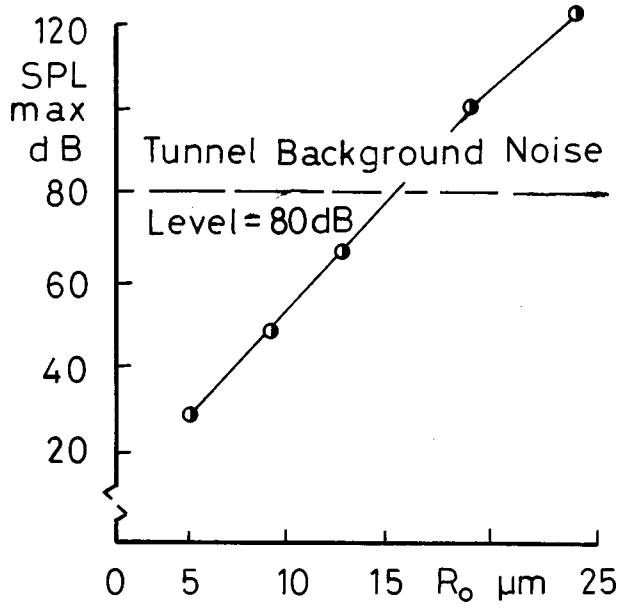

Fig. 4 Determination of the cavitation noise inception using background noise and the simulated bubble capture noise (±2.0% numerical accuracy) for a given cavitation number σ=2.0

or

$$P - P_v = \frac{2S}{R} + \frac{G}{R^3} \tag{19}$$

As $(P-P_v)$ approaches a minimum, i.e., as the fluid pressure approaches the vapor pressure, the bubble becomes unstable. The minimum value of $(P-P_v)$ in Eq. (19) can be found by taking the first derivative with respect to R and equating it to zero to find its roots. The procedure is as follows:

$$\begin{gathered}\frac{d}{dR}(GR^{-3}-2SR^{-1}) = -3GR^{-4}+2SR^{-2}=0 \\ R^{-2}(-3GR^{-2}+2S)=0 \\ (-3GR^{-2}+2S)=0 \Rightarrow R^2=\frac{3G}{2S} \\ R=\pm\sqrt{\frac{3G}{2S}}\end{gathered} \tag{20}$$

Taking the positive root and substituting this value for R back into Eq. (19) yields:

$$(P-P_v) = \frac{-4S}{3}\sqrt{\frac{2S}{3G}} \tag{21}$$

for $G>0$. Rewriting this in terms of minimum pressure coefficient, $C_{p\,\min}=(P-P_\infty)/\frac{1}{2}\rho V^2$, yields

$$\frac{1}{2}\rho V_\infty^2 C_{p\,\min} + P_\infty - P_v = \frac{-4S}{3}\sqrt{\frac{2S}{3G}} \tag{22}$$

for $G>0$.

Equation (22) can be rewritten by squaring both sides as follows:

$$\left(\frac{1}{2}\rho V_\infty^2 C_{p\,\min} + P_\infty - P_v\right)^2 = \frac{32}{27}\frac{S^3}{G} \tag{23}$$

Equation (23) can now be written in terms of cavitation number, $\sigma=(P-P_v)/\frac{1}{2}\rho V^2$, by letting

$$P=P_\infty; \quad V=V_\infty; \quad (P-P_v)=\tfrac{1}{2}\rho V^2\sigma$$

and combining terms gives

$$\frac{1}{4}\rho^2 V^4 C_{p\,\min}^2 + \frac{1}{2}\rho^2 V^4 C_{p\,\min}\sigma + \frac{1}{4}\rho^2 V^4\sigma^2 = \frac{32}{27}\frac{S^3}{G} \tag{24}$$

Now, multiplying both sides of Eq. (24) by G and substituting the expression for G,

$$G = \tfrac{1}{2}\rho V^2\sigma R_o^3 + 2SR_o^2$$

into the resulting equation yields

$$\begin{aligned}(\tfrac{1}{2}\rho V^2\sigma R_o^3 + 2SR_o^2)\cdot(\tfrac{1}{4}\rho^2 V^4 C_{p\,\min}^2 + \tfrac{1}{2}\rho^2 V^4 C_{p\,\min}\sigma \\ + \tfrac{1}{4}\rho^2 V^4 C_{p\,\min}\sigma^2) = \tfrac{32}{27}S^3\end{aligned} \tag{25}$$

Expanding the multiplication, regrouping terms, and multiplying the resulting equation by 216 yields the bubble instability equation:

$$\begin{aligned}(27\rho^3 V^6 R_o^3)\sigma^3 + 54\rho^2 V^4 R_o^2(\rho V^2 R_o C_{p\,\min} + 2S)\sigma^2 \\ + 27\rho^2 V^4 C_{p\,\min} R_o^2(\rho V^2 R_o C_{p\,\min} + 8S)\sigma \\ + 108\rho^2 V^4 C_{p\,\min}^2 S R_o^2 - 256S^3 = 0\end{aligned} \tag{26}$$

The results of this analysis show that for bubbles larger than 10 μm, the threshold stability/instability value of σ can be estimated by $\sigma_{ins}=-C_{p\,\min}$. It is useful to compare the stability limit σ for the bubbles in pure water and polymer solution. The stability boundary σ_{ins} from Eq. (26) was calculated for tunnel test conditions of $5<V<15$ m/s and $-3.2<Cp_{\min}<-1.6$. The polymer surface tension is $S_{Polymer}=6.5\times10^{-2}$ N/m which is 80% the pure water value [12]. The similarity of the stability boundary σ_{ins} results allows the introduction of $\Delta\sigma$:

$$\Delta\sigma_{ins} = \frac{\text{Water}\ \ \sigma_{ins} - \text{Polymer}\ \ \sigma_{ins}}{\text{Water}\ \ \sigma_{ins}} \times 100\% \tag{27}$$

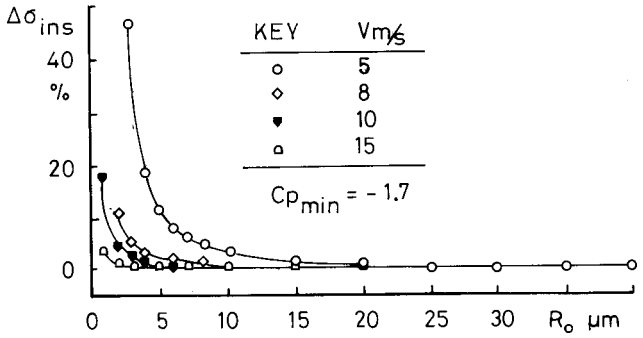

Fig. 5 Change of bubble stability bounding $\Delta\sigma$ by introduction of lower surface tension from polymer solution (numerical uncertanty estimated to be $<\pm1.25\%$)

The overall results in Fig. 5 indicate significant polymer influence on small bubbles with radius $R_o<15\,\mu$m. This supports the earlier TVC results in that the polymer does not have a significant influence on the larger bubbles.

Comparison of Theoretical Prediction With Experimentally Observed TVC Inception With/Without Polymers

The tip vortex cavitation inception simulations were made for Cases I–III. These simulations were made for 25 μm bubble-capture using the tip vortex circulation Γ and radius R_1 values in Table 2.

The inception value σ is taken as the value when $\text{SPL}_{\max}=80$ dB as shown in Fig. 4. The TVC simulations were essentially the same for cases II and III. The results for case I (water) and case III (polymer) are plotted in Fig. 6 with Fruman's experimental σ_i measurements. The simulations tend to have a higher inception cavitation number σ_i than the measured σ_i values. The lower value of the tip vortex cavitation inception value σ_i with the polymer can be understood from an examination of the numerical simulation results. For cases I–III in Table 2 the simulations showed two interesting points:

1. The introduction of the smaller value of surface tension (Table 2) representing the polymer solution only modified the SPL values for the smaller bubbles ($R_o<15\,\mu$m) but had no effect on the larger bubble radius. This corresponds to the stability analysis results shown in Fig. 5.
2. The increase in the tip vortex core radius $R_1'=1.28\,R_1$ formed in the polymer fluid (Table 2) had the opposite effect of lowering the SPL value obtained in fresh water and delaying the inception of the tip vortex cavity.

The calculations show reduced surface tension-polymer induced instability observed by Shima and Tsujino [7] is present in the smaller bubbles $R_o<15\,\mu$m. The SPL level of these smaller bubbles failed to exceed the 80 dB tunnel SPL level, therefore they were not significant in the tip vortex cavitation inception bubble capture process. In contrast the enlargement of the tip vortex core radius R' by the polymer delayed the bubble capture resulting in the experimentally observed delay in the tip vortex cavitation inception. This reflects the fact that the bubble becomes unstable at $\sigma_{ins}=-Cp_{\min}$ while the tip vortex cavitation noise spikes occur at higher cavitation numbers σ.

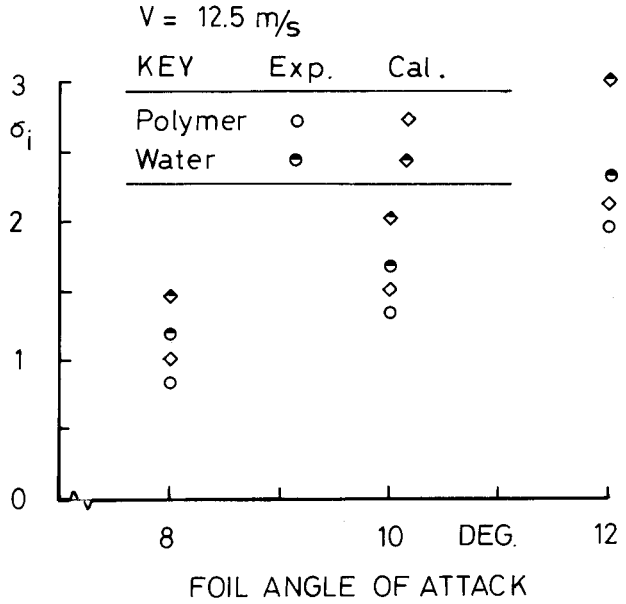

Fig. 6 Comparison of tip vortex cavitation inception σ_i from simulations with measurements of Fruman et al. [2] (experimental cavitation number uncertainty estimated to be <±2.5%; numerical uncertainty estimated to be <±1.25%)

Conclusions

This paper has presented the results of a theoretical study of the influence of polymer on the inception of tip vortex cavitation in pure water and in polymer solution. The results are interesting as they reveal the main role that the larger bubbles play in the inception of tip vortex cavitation. The tip vortex investigation results aid subsequent bubbles stability analysis.

These results support the view of Latorre [4] and Ligneul and Latorre [8] that the small bubbles are not significant noise generators. The tip vortex cavitation inception involves a screening process where the larger bubbles play the dominant role. The main conclusion of the investigation is that the influence of polymer is to increase the tip vortex core radius and delay the inception of tip vortex cavitation that occurs at a lower cavitation number σ. Specifically:

1. The polymer influences the stability of small bubbles.
2. In the bubble capture by tip vortex, only the larger bubbles are significant.
3. The increase in the tip vortex core radius leads to the delay of the bubble capture and a lower value of tip vortex cavitation inception σ_i.
4. There is relatively good agreement between the theoretical and experimental results for tip vortex cavitation inception in polymers.

Acknowledgments

The authors are grateful for the support of the French Navy for funding the study visit of Ensigns Houlier and Muller in fall, 1999.

Nomenclature

AR = foil aspect ratio—Chord/Span
b_o = foil semi-span
c = speed of sound
C_D = bubble drag coefficient
C_L = lift coefficient
C_p = pressure coefficient
C_o = base chord
D = constant
G = gas constant, $G=R_o^3(P_o-P_v+2S/R_o)$
K = constant
P = test pressure
P_a = sound pressure
P_o = local pressure
P_v = fluid vapor pressure
Q = polymer injection rate
Re_B = bubble Reynolds number, $Re_B=2R|\overline{W}-\overline{W_b}|/\nu$
Re_c = foil chord Reynolds number
R_1 = tip vortex radius,
R_1' = tip vortex radius with polymer
Ro = radial position of bubble
R = bubble radius
R^* = critical bubble radius, $R^*=3g/3S$
R_1 = tip vortex radius
R_t = trajectory radius, $R_t=\sqrt{X_2^2+X_3^2}$
R_o, R_t = initial bubble radius
r = distance from sound receiver to bubble center
S, S' = surface tension, surface tension with polymer
SPL = sound pressure level
TVC = tip vortex cavitation
t = time
t' = time, $t'=(t-r-R/c)$
t^* = nondimensional time
V = velocity
W = velocity vector of fluid particle
W_b = velocity vector of spherical nuclei
X_1 = axial distance
X_2 = horizontal distance from foil tip
X_3 = vertical distance from foil tip
α = angle of attack
β = polymer exponent
Γ = tip vortex circulation
Γ_o = 2-D foil circulation
ρ = density
η = span-wise location
σ = cavitation number, $\sigma=P-P_V/\frac{1}{2}\rho V^2$
σ_i = inception cavitation number
σ_{ins} = cavitation number at bubble stable/unstable limit
ν = kinematic viscosity
μ = viscosity$=\nu/\rho$
$\bar{}$ = (upper bar) nondimensional values
$'$ = indicates value with polymer
$^\circ$ = reference condition

References

[1] Fruman, D., and Aflalo, S., 1989, "Tip Vortex Cavitation Inhibition by Drag Reducing Polymer Solution," ASME J. Fluids Eng., **111**, pp. 211–216.
[2] Fruman, D. H., Pichon, T., and Cerrutti, P., 1995, "Effect of Drag-Reducing Polymer Solution Ejection on Tip Vortex Cavitation," SNAJ J. Marine Sci. Technol., **1**, pp. 13–23.
[3] McCormick, W. B., 1962, "On Cavitation Produced by a Vortex Trailing From a Lifting Surface," ASME J. Basic Eng., **84**, pp. 369–379.
[4] Latorre, R., 1980, "Study of Tip Vortex Cavitation Noise From Foils and Propellers," Int. Shipbuilding Prog., **27**, pp. 66–85.
[5] Platzer, G. P., and Souders, W. G., 1981, "Tip Vortex Cavitation Characteristics-Delay on a Three Dimensional Hydrofoil," Proc. 19th ATTC Meeting, Univ. of Michigan, Ann Arbor, pp. 989–1022.
[6] Green, I., Acosta J., and Akbar, R., 1988, "The Influence of Tip Geometry on Trailing Vortex Roll-up and Cavitation," Proceedings 1988 ASME Cavitation and Multiphase Flow Forum, FED 64, pp. 76–80.
[7] Shima, A., and Tsujino, T., 1994, "The Dynamics of Cavity Clusters in Polymer Aqueous Solutions Subject to an Oscillating Pressure," Proc. Bubble Dynamics and Interface Phenomena, Kluwer Academic Publications, Dordrecht, Netherlands, pp. 81–92.
[8] Latorre, R., and Ligneul, P., 1993, "Acoustic Considerations in Tip Vortex Cavitation Inception," Acustica, **79**, pp. 266–273.

[9] Levkovskii, Y. L., 1978, Structure of Cavitation Flows, Sudostroyeniye, Leningrad, pp. 153, 203 (in Russian).
[10] Latorre, R., and Ligneul, P., 1989, ''Study of the Capture Noise of Spherical Nuclei in the Presence of Tip Vortex of Hydrofoils and Propellers,'' Acustica, **68**, pp. 1–13.
[11] Ligneul, P., and Latorre, R., 1993, ''Study of Nuclei Distribution and Vortex Diffusion Influence on Nuclei Capture by a Tip Vortex and Nuclei Captive Noise,'' ASME J. Fluids Eng., **115**, pp. 504–507.
[12] Hoyt, J. W., 1976, ''Effect of Polymer Additives on Jet Cavitation,'' ASME J. Fluids Eng., **98**, pp. 106–112.

John M. Sankovic*

Dept. of Biomedical Engineering,
Case Western Reserve University,
10900 Euclid Ave.,
Cleveland, Ohio 44106

National Aeronautics and Space Administration,
John H. Glenn Research Center,
21000 Brookpark Rd.,
M/S 77-5,
Cleveland, Ohio 44135

Jaikrishnan R. Kadambi

Mehul Mehta

Dept. of Mechanical and Aerospace Engineering,
Case Western University,
10900 Euclid Ave.,
Cleveland, Ohio 44106

William A. Smith

Dept. of Biomedical Engineering,
The Lerner Research Center,
The Cleveland Clinic Foundation,
9500 Euclid Ave.,
Cleveland, Ohio 44195

Mark P. Wernet

National Aeronautics and Space Administration,
John H. Glenn Research Center,
21000 Brookpark Rd.,
M/S 77-1,
Cleveland, Ohio 44135

PIV Investigations of the Flow Field in the Volute of a Rotary Blood Pump

A full-size acrylic model of a rotary blood pump was developed in order to utilize Particle Image Velocimetry (PIV) to make measurements of the fluid velocities and turbulent stresses throughout the device. The development of an understanding of the hemodynamics within the blood pump is critical to the development and validation of computational models. A blood analog solution, consisting of sodium iodide solution and glycerin, was developed to match physiological kinematic viscosity. The refractive indecies of the fluid, the pump casing, and the impeller were matched to facilitate the use of PIV to make velocity measurements. Velocity measurements made in the volute exit/diffuser region are presented for pumps speeds of 3000–3850 rpm. At each speed data were obtained at a physiological pressure of 12 kPa and at a maximum flow condition. Four hundred data pairs were used for each resultant mean velocity vector value, representing greater than an order of magnitude more data pairs than reported previously in the literature on similar devices and resulting in velocity uncertainty levels of approximately $\pm 2.9\%$. [DOI: 10.1115/1.1789529]

Introduction

Mechanical assistance in blood pumping varies widely depending on the application. For example hundreds of thousands of open-heart surgeries are performed in the U.S. yearly, and in those cases the patient is placed on a blood pump along with an oxygenator. The duration of use of this type of blood pump is limited to hours and beyond the concern for hemolysis and thrombosis, the engineering constraints, although difficult, are not nearly as challenging as for the incorporeal applications. Incorporeal applications or so-called artificial heart applications are extremely challenging. Not only must the device not cause hemolysis and thrombosis, but also the reliability must be high, the power consumption low, and the package size must be compact.

The predominant current uses of mechanical circulatory support devices are as a bridge to transplantation and to provide temporary pumping assistance after cardiac surgery in cases where the heart tissue needs to have the pumping work load removed to allow for healing. In the U.S. approximately 6000 receive support devices after cardiac surgery with a survival rate of 20%–40% in the hospital. Bridging for transplantation occurs in 300–400 patients yearly with a discharge rate of 50%–70% after transplantation. Regarding the devices, several factors are not yet clear: (1) the need for biventricular versus univentricular support, (2) a total artificial heart versus a ventricular assist device, and (3) the duration of support is not defined and depends on donor organ availability, time to myocardial recovery, potential outpatient therapy, and unpredictability of adverse events regarding the new technology [1].

One of the major advantages of a rotary pump over pulsatile technology is the reduced physical pump volume. Rotary pumps can be designed to occupy one-tenth the volume of a pulsatile pump, allowing the insertion of the pump inside the existing left ventricle. When compared to industrial pumps, blood pumps operate in a unique flow regime. The Reynolds number (based on the impeller diameter, is on the order of 10^3-10^4. This is on the low end of commercial pumps, which have focused mainly on the high end of the Reynolds number range of $2\times10^4-10^8$, since the hydraulic losses increase dramatically below a knee at $\mathrm{Re}=1\times10^5$ [2]). Sparse literature exists in the high loss regime of blood pump operation. To complicate matters further, blood is a dense, high particle concentration, solid–liquid slurry, which exhibits non-Newtonian characteristics at low shear rates. Gopalakrishnan [3] presents an excellent overview of U.S. pump research and development and summarizes the state-of-art of pump CFD, ''While CFD holds the promise of becoming a useful tool for pump design, it must be noted that a major unknown in fluid dynamics today is a realistic model for turbulence—pump designers will use some of the existing turbulence models and calibrate their CFD

*Corresponding author. Tel.: 216-977-7429; Fax: 216-433-8050; e-mail: john.m.sankovic@nasa.gov

Contributed by the Fluids Engineering Division for publication in the JOURNAL OF FLUIDS ENGINEERING. Manuscript received by the Fluids Engineering Division March 10, 2003; revised manuscript received January 21, 2004. Associate Editor: Y. Tsujimoto.

results against test data thereby introducing some empiricism into their analysis.'' The need for experimental flow field data is still necessary for industrial pump model development and validation. For blood pumps, with their extremely complex flow regime, the need is even greater. Obtaining information across the entire flow field can be extremely laborious. Particle image velocimetry (PIV) has the advantage of providing instantaneous velocity information over an entire plane. An excellent overview of the technique is provided by Raffel et al. [4].

Several researchers have applied PIV to the study of rotary pumps. Dong et al. [5] used PIV in a 25.4 cm diameter; 890 rpm pump. The flow regime was inertially dominant with water as the working fluid and the use of acrylic pump parts. Fluorescent particles were used with an autocorrelation technique. The technique uses a laser light sheet to illuminate particles in the flow. Double exposures recorded on a single image can be autocorrelated to obtain velocity information since the time between light source pulses is known. One drawback of the autocorrelation technique is that direction is not known. This can be overcome by obtaining pairs of single exposure images and using a cross-correlation technique, as has been used to study complex flows in the Laser Flow Diagnostics Laboratory at Case Western Reserve University [6]. Dong et al. [5] found that the flow was pulsating and depended on the location of the blade relative to tongue. Sites prone to high velocity fluctuations included blade wake, interface between the jet and the wake, and near the tongue. A follow-on study by Chu et al. [7] used the same setup as Dong et al. [5].

The paper did not mention the number of sets of data averaged for turbulence measurements; however, 35 mm film was used for data collection making data reduction of multiple sets arduous. That study found that slight increases in the space between impeller and tongue caused significant changes in flow structure. The impact was significant as long as the gap was less than 20% of impeller radius. Large vortex trains associated with jet/wake phenomena dominated variations in total pressure. A more recent study by Sinha and Katz [8] reported the inclusion of digital data acquisition with the same pump hardware. They discuss the issues of the commonly used RANS in commercial CFD codes, including the validity of turbulence closure.

Attempts at using several flow visualization techniques for artificial organs have been reported in the literature. Particle streak imaging using fluorescence was used by Kerrigan et al. [9] in the Nimbus Axipump and by Kerrigan et al. [10] in a prototype SUN Medical Technology pump. Laser Doppler anemometry (LDA) has been used successfully to obtain velocity information on the popular BP-80 by Pinotti and Paone [11]; however, the technique is limited to instantaneous point measurement. Particle tracking was reported by Sakuma et al. [12,13] and by Asztalos et al. [14]. Asztalos et al. [14] used a $3\times$ scale pump operating at 126 rpm and 9 l/min, which corresponded to a full scale pump operating at 1900 rpm and 5 l/min. A 256×256 bit 4500 frame/s camera was used, with no image-to-image variance or turbulence data reported. Subramanian et al. [15] applied PIV to the study of heart valves and Wernet et al. [16] compared the advantages of PIV with respect to LDA as applied to heart valves. Mussivand et al. [17] applied PIV to a HeartSaver pulsatile VAD by using a 300 W halogen lamp and camera with frame rate of 1000/s, but was limited to 100–200 micron diameter particles due to the light source. That paper reported Reynolds shear stresses (RSS) based on the measured instantaneous velocity fluctuation using a 25 velocity data point ensemble in 5 mm region to obtain the mean velocity. No estimate of uncertainty was presented. Peak RSS levels of >0.9 kPa reported. Day et al. [18] have applied PIV to investigate the gap between housing and rotor centrifugal blood pump manufactured by HeartQuest/MedQuest Products Inc. pump. The velocities presented in that work were the average of 20 image pairs. Most recently, Day et al. [19] have reported recent progress in applying PIV to an acrylic model of the HeartQuest pump and have presented velocity field data for the pump inlet; however, no mention is made regarding number of data pairs or the measurement uncertainty.

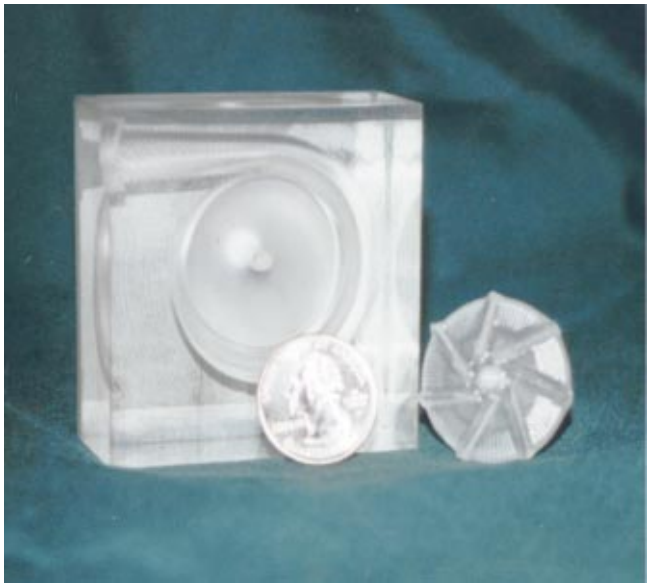

Fig. 1 Impeller and casing of acrylic model of blood pump

The overall goal of our work is to obtain a better understanding of the flow field inside a rotary blood pump, in order to improve efficiency and to decrease damage to blood cellular components. Experimental measurements of the flow field throughout a rotary blood pump are required to understand the underlying fluid physics. These measurements require a high enough fidelity to allow the development and validation of computational design tools. Because of the extreme challenges of making measurements in a small centrifugal pump, to date that data has been lacking in the literature. We have successfully developed an optically clear rotary blood pump test-bed and have obtained measurements of the velocities and turbulent shear stress using particle image velocimetry in the volute exit and diffuser at various operating conditions. The data presented herein provide insight into the importance of the interaction of the discharge flow of the impeller with the flow along the outer wall of the volute and the cutwater.

Experimental Apparatus and Procedure

Pump and Flow Loop. In order to enable the use of PIV for all areas of the pump, the pump housing, and impeller were fabricated from acrylic as shown in Fig. 1. The pump housing was fabricated in two sections, which bisected the volute and diffuser. The pump design had heritage to those reported previously by Bernstein et al. [20], Golding and Smith [21], and Veres et al. [22]. The nominal design operation condition for the pump was 5 l/min at a pressure rise of 13.3 kPa and a speed of 3000 rpm. The impeller consisted of seven straight blades which are offset from the centerline with an outside diameter of 35 mm. The impeller described by Golding and Smith [21] and Veres et al. [22], consisted of an open center section, where the blades were mounted on a ring and a stationary center shroud provided a gradual transition from the axial flow near the inlet to the radial impeller flow. To facilitate fabrication, the impeller used in this study had a solid center section that incorporated the center shroud with the ring holding the blades.

The working fluid used for this study was a mixture of water, sodium iodide, and glycerin with a specific gravity of 1.69. The sodium iodide/water solution was selected such that the refractive index of acrylic was matched, and was measured to be 1.485 ±0.001. Silver-coated glass spheres, 15 μm in diameter were

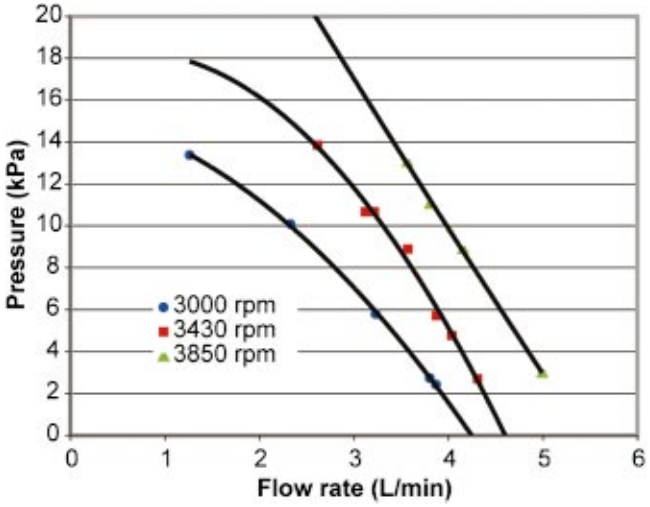

Fig. 2 Pressure-flow curves for pump operating at various speeds utilizing sodium iodide solution

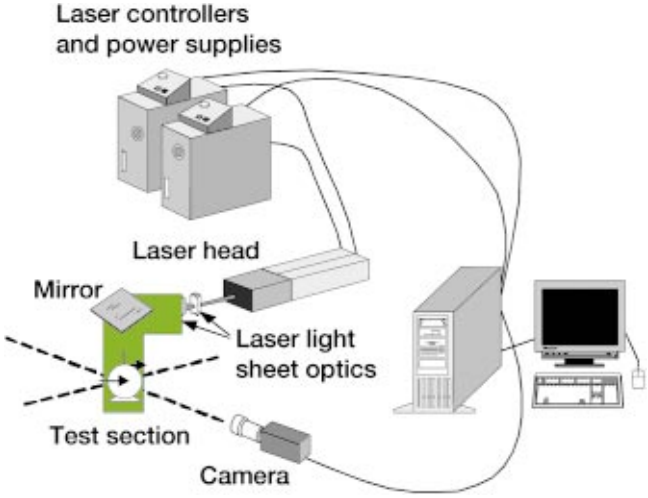

Fig. 3 Schematic diagram of PIV experimental setup

used as the particles and were neutrally buoyant. The pump design and operating conditions were chosen to maintain similarity with those reported earlier. The geometry was maintained at actual scale and the speed range was duplicated. In order to maintain Reynolds number similarity, glycerin was used to increase the viscosity of the fluid such that the kinematic viscosity of the fluid was similar to that of blood. In this case, the measured kinematic viscosity was 3.2 cSt.

The flow loop consisted of a reservoir, which was open to atmosphere, to which a 13 mm ID inlet tube was connected. The height of the fluid in the reservoir was equal to the height of the discharge. After passing through the pump, the fluid passed through an exit tube also with a 13 mm ID and returned to the supply reservoir. The pump pressure rise was measured by the use of a simple manometer located downstream of the diffuser. Flow regulation was accomplished by the use of a pinch clamp valve located at the exit tube near the discharge to the fluid reservoir.

The flow rate was calibrated by fixing both the output pressure of the pump and speed, and then measuring the volume of fluid pumped for a set time interval. Calibration was performed using the sodium iodide solution. This measurement was taken over the entire range of operating conditions. Performance curves of the pump are presented in Fig. 2. The data show that the achieved flow rates at a given speed are lower than those reported by Golding and Smith [21]. It is believed that the inlet and outlet fittings used in this study contributed an increased pressure drop not seen in the published results, and caused a decrease in flow. Further improvements in the transition from the pump to the test loop should decrease these effects.

PIV System. The PIV setup was similar to that used by Kadambi et al. [6]. The PIV hardware consists of a 50 mJ/pulse Nd:YAG laser (532 nm wavelength), laser light sheet optics, a CCD camera (Dantec DoubleImage 700 cross-correlation camera; resolution: 768×484 pixels) equipped with a 60 mm Micro Nikkor lens (Nikon). The laser beam (3.5 mm diameter) is formed into a light sheet (0.37 mm thick; 256 mm wide) using a combination of cylindrical and spherical lenses. In order to eliminate distortion at the pump housing seam, the light sheet was aligned parallel to the seam and passed entirely through the half containing the inlet section. For each of the operating conditions 400 pairs of single exposure image frames were obtained and analyzed using cross-correlation data processing. The image pairs are processed into vector maps, in real-time, by the DantecFlowMap PIV 2000 processor. The image pair acquisition was synchronized to the impeller rotation using a once per rev signal, which then triggered the digital delay generator (DDG). The DDG in turn sent a signal to the PIV 2000 processor, which then fired the laser and acquires the images from the PIV camera. Figure 3 shows a schematic diagram of the PIV setup.

The camera lens is operated at f/No. 8 and the field of view (FOV) was 24.1×17.8 mm. Images were analyzed using a subregion size of 32×32 pixels with 50% overlap. This resulted in 47 ×29 vectors in the FOV with a spatial resolution of 0.51 ×0.61 mm/vector. The FOV included both the volute exit/diffuser and the interblade region; however, large differences in velocity in those regions precluded the use of a 32×32 subregion size across the entire FOV. This was due to the fact that the hardware was constrained at the lower level of time between laser pulses. Analysis of the higher velocity flow in the interblade region was limited to a 64×64 pixel subregion size in order to not have the particles travel farther than 0.25 of the subregion dimension between the image pairs.

Data reported herein consist of 18×29 vectors representing the volute exit/diffuser region. Postprocessing of the data was performed on the 400 image pairs to determine mean velocities and relative uncertainties to a 95% confidence level and RSS levels. Chauvenet's criterion was used to remove spurious points during analysis.

Results and Discussion

Data were obtained at three rotational speeds of 3000, 3430, and 3850 rpm. In addition, at each speed two pump operating points were investigated. The first condition sought to maintain a constant output pressure of 12 kPa to simulate a physiologically relevant condition: 1.8, 3.0, and 3.7 l/min at 3000, 3430, and 3850 rpm, respectively. This was accomplished via adjustment of the downstream tube clamp, which served as a flow restriction. The second operating point was the maximum flow condition for that speed: 4.0 l/min (1.55 kPa), 4.4 l/min (1.87 kPa), and 5.1 l/min (2.01 kPa) at 3000, 3430, and 3850 rpm, respectively. It is believed that those two conditions would be representative of the high pressure differential/lower flow region and the low pressure differential/high flow region of the pump pressure/flow curve. Using the 400 data pairs, the average over the 18×29 vector matrix of the uncertainty in the mean velocity ranged between 2.4% and 2.9%, which includes uncertainty estimates for both random and bias effects.

A sample PIV image is presented in Fig. 4 in order to illustrate the coordinate system used and the orientation of blades. All data were obtained with one blade perpendicular to the cutwater as shown in Fig. 4.

Figure 5 provides velocity vector plots in the volute/diffuser region for maximum flow conditions for the three speeds. Varia-

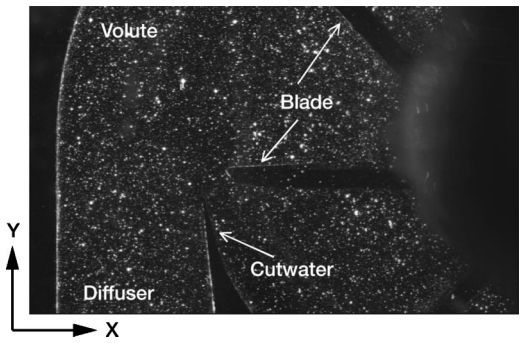

Fig. 4 Sample PIV image showing impeller blade position, volute exit, and diffuser

tions in velocity magnitude are presented as color variations in the figure. What is evident is the influence of the cutwater (tongue) on the velocity profile and the boundary layer growth on the outer volute wall immediately opposite the cutwater as the flow is slowed. Although the magnitude of the velocity vectors increase with rotational speed as expected, the vector angles also appear similar. This point was investigated more fully by looking at the velocity vectors at a Y location of 16.5 mm. At that horizontal location the flow conditions are both influenced by the incoming volute flow (from the top of Fig. 4 and the additional mass from the blade passage (on the right-hand side of Fig. 4). Figure 6 provides plots of the velocity vector angle relative to the vertical and the magnitude of the velocity normalized to the tip speed. The figure shows that over an axial position of 3.5–9.0 mm the velocity vectors scale directly with tip speed. This leads to the prediction that the velocity triangles are similar for the three flow conditions. Direct measurements in the interblade region will serve to validate that hypothesis.

Figure 7 provides related velocity vector plots for the three

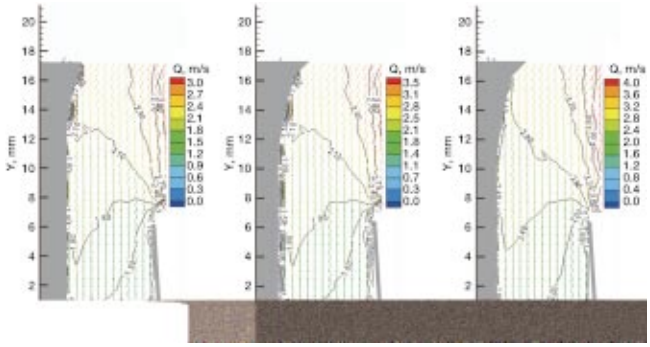

Fig. 5 Velocity vector maps of volute exit and diffuser region at various impeller speeds at maximum flow condition: (*a*) 3000 rpm, (*b*) 3430 rpm, (*c*) 3850 rpm.

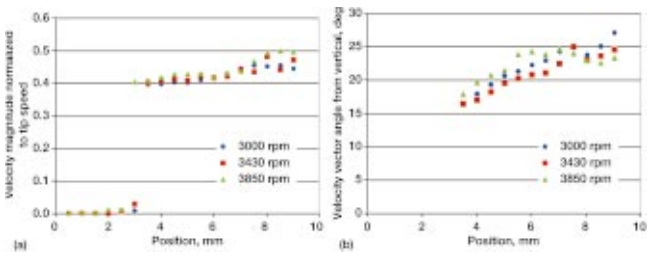

Fig. 6 Similarity of velocity vectors at various points across the volute at location $Y=16.5$ mm: (*a*) Velocity magnitude normalized to tip speed, (*b*) velocity vector angle relative to diffuser axis.

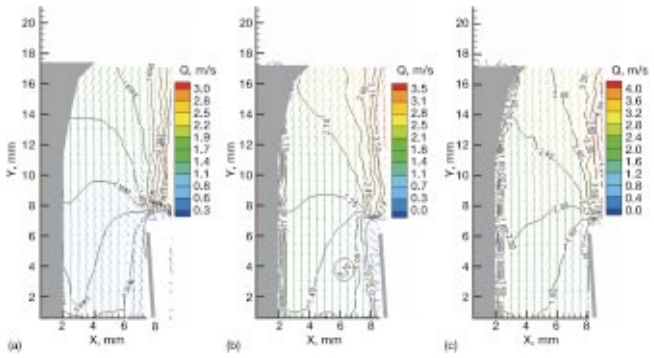

Fig. 7 Velocity vector maps of volute exit and diffuser region at various impeller speeds at 90 mmHg pressure rise: (*a*) 3000 rpm, (*b*) 3430 rpm, (*c*) 3850 rpm

speeds at a constant pressure of 90 mmHg. Again, variations in velocity magnitude are presented as color variations in the figure. The flow rates for these operating conditions were significantly lower than the data sets presented in the previous section. In this flow regime recirculation losses are important. The 3000 rpm data clearly show the flow reentering the impeller passage upstream of the cutwater. This flow is essentially repumped causing the losses to multiply. Also, of interest is that the trajectory of the particles is such that significant impingement may occur on the cutwater surface, which could be of significance for cell-wall energy transfer effects. As the speed increases from 3000 to 3430, and finally to 3850 rpm, the operating point moves in the direction of the best efficiency point. Since the pressure is being held constant, it would be expected that the losses would decrease. As shown in Fig. 7 the entrainment of the flow steadily decreases as the speed (and hence volumetric flow) increases, signifying a decrease in recirculation losses.

Knowledge of the shear stresses in the flow field of a blood pump is of critical importance. Often in blood pump literature, little attention is paid to the RSS caused by turbulence in the flow. The use of PIV offers a powerful tool to obtain direct measurements of the turbulence level of the flow and a measurement of the RSS from the mean of $u'v'$.

Figure 8 shows a color contour plot of the mean of $u'v'$ (m^2/s^2) for the volute/diffuser region for the highest flow rate tested 5.1 l/min at (3850 rpm and an outlet pressure of 2.11 kPa). Using the fluid density of 1.69 kg/m^3, the RSS was calculated to reach 47 kPa and occurred at the exit of the blade passage 8 mm upstream of the cutwater. Looking at the other extreme in flow

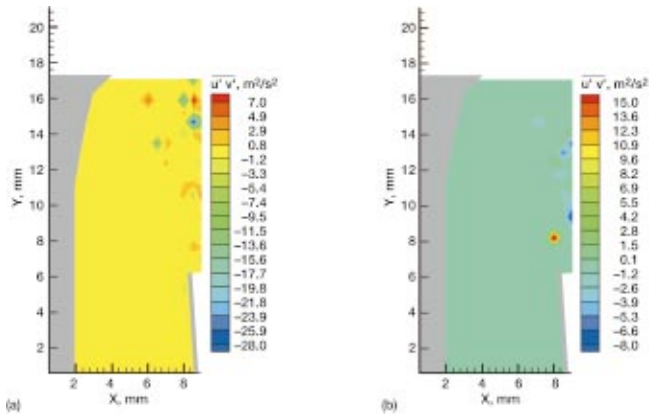

Fig. 8 Reynolds shear stress levels depicted as mean $u'v'$ ($m2/s2$): (*a*) 3850 rpm, 5.1/min/15.8 mmHg. (*b*) 3000 rpm, 1.8/min/90 mmHg

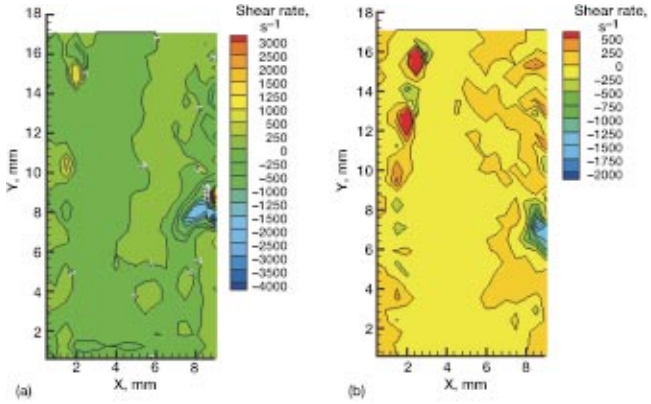

Fig. 9 Shear rate levels in volute ($s-1$)

conditions, the minimum flow case of 1.8 l/min, which occurred at a speed of 3000 rpm and a pressure of 90 mmHg, the highest RSS occurred immediately upstream of the cutwater. Although, peak RSS values near the impeller discharge and cutwater region were found to be very high, the levels in the majority of the volute were found to be below 0.1 kPa. The turbulent stresses measured are significant for a rotary blood pump and warrant further investigation utilizing a higher resolution.

Figure 9 provides plots of the shear rate levels corresponding to the conditions in Fig. 8. These levels are important in blood pump development, since many researchers often look at the viscous shear rate levels and assume Newtonian behavior above $100-500\ s^{-1}$. Figure 9 shows that the highest shear rates occur near the cutwater where the flow is being entrained back into the impeller ($2000-4000\ s^{-1}$), and where the flow discharged from the impeller enters the volute ($500\ s^{-1}$). The flow along the outside surface of the volute, is subject to very low shear rates, $<250\ s^{-1}$. The viscous shear stress can be obtained from the shear rate by multiplication by the viscosity. This allows comparison of the viscous stress levels with the Reynolds shear stress. Throughout the volute, the RSS levels are significantly higher than the viscous shear stresses. Upstream of the cutwater where the flow from the impeller discharges into the end of the volute, the RSS levels are three orders of magnitude greater that the viscous shear stresses.

Concluding Remarks

The development of efficient and reliable rotary blood pumps that do not cause hemolysis and thrombosis is a significant engineering challenge. As the technology advances, so does the need for engineering tools such as computational modeling. Particle image velocimetry offers a powerful experimental method to develop an understanding of the flow field in order to develop and validate such models. This work presented the results of the initial phase of obtaining experimental measurements throughout a rotary blood pump. Measurements in the volute exit/diffuser section were obtained at pumps speeds ranging from 3000 to 3850 rpm. Over the range of operating conditions tested, various flow phenomena were noted. At the extreme operating condition of 12.0 kPa and 1.8 l/min, significant reentry of the flow back into the impeller was observed, signifying increased recirculation losses. At the opposite extreme of 2.11 kPa and 5.1 l/min, the influence of the cutwater is evident. In addition at the maximum flow conditions the velocity vectors in the volute scaled directly with impeller tip speed over the entire speed range. Reynolds shear stress measurements showed regions of significant stress levels that warrant further investigation.

Acknowledgments

The authors would like to acknowledge Jason Bradshaw and Sam Cordero of Case Western Reserve University and Jonathan Rupp of Cornell University for assistance in the development and fabrication of the acrylic pump.

References

[1] Stevenson, L. W., and Kormos, R. L., 2001, "Mechanical Cardiac Support 2000: Current applications and future trial design," J. Thorac. Cardiovasc. Surg., **121**, pp. 418–24.
[2] Soundranayagam, S., and Ramarajan, V., 1986, "Scale Effects in a Mixed Flow Pump: Part 2," Proc. Inst. Mech. Eng., **200**, pp. 180–186.
[3] Gopalakrishnan, S., 1999, "Pump Research and Development: Past, Present, and Future- An American Perspective," J. Fluids Eng., **121**, pp. 237–247.
[4] Raffel, M., Willert, C.E., and Kompenhaus, J., 1998, *Particle Image Velocimetry: A Practical Guide*, Springer, Berlin.
[5] Dong, R., Chu, S., and Katz, J., 1992, "Quantitative Visualization of the Flow Within the Volute of a Centrifugal Pump. Part B: Results and Analysis," J. Fluids Eng., **114**, pp. 396–403.
[6] Kadambi, J.R., Mehta, M., Charoenngam, P., Wernet, M., Sankovic, J., and Addie, A., 2003, "Particulate Velocity Measurements in the Intra-Blade Passages of a Centrifugal Slurry Pump," FEDSM2003-45504, Proceedings of the 2003 ASME Fluids Engineering Division Summer Meeting, Honolulu, HI, July 6–10.
[7] Chu, S., Dong, R., and Katz, J., 1995, "Relationship between unsteady flow, pressure fluctuations, and noise in a centrifugal pump-part A: use of PDV data to compute the pressure field," J. Fluids Eng., **117**, pp. 24–29.
[8] Sinha, M., and Katz, J., 2000, "Quantitative visualization of the flow in a centrifugal pump with diffuser vanes-1:on flow structures and turbulence," J. Fluids Eng., **122**, pp. 997–1007.
[9] Kerrigan, J. P., Shaffer, F. D., Maher, T. R., Dennis, T. J., Borovetz, H. S., and Antaki, J. F., 1993, "Fluorescent Image Tracking Velocimetry of the Nimbus AxiPump," ASAIO J., **39**, pp. M639–M643.
[10] Kerrigan, J. P., Yamazaki, K., Meyer, R. K., Mori, T., Otake, Y., Outa, E., Umezu, M., Borovetz, H. S., Kormos, R. L., Griffith, B. P., Koyanagi, H., and Antaki, J. F., 1996, "High-Resolution Fluorescent Particle-Tracking Flow Visualization Within an Intraventricular Axial Flow Left Ventricular Assist Device," Artif. Organs, **20**, pp. 534–540.
[11] Pinotti, M., and Paone, N., 1996, "Estimating Mechanical Blood Trauma in a Centrifugal Blood Pump: Laser Doppler Anemometer Measurements of the Mean Velocity Field," Artif. Organs, **20**, pp. 546–552.
[12] Sakuma, I., Tadokoro, H., Fukui, Y., and Dohi, T., 1995, "Flow Visualization Study on Centrifugal Blood Pump Using a High Speed Video Camera," Artif. Organs, **19**, pp. 665–670.
[13] Sakuma, I., Fukui, Y., and Dohi, T., 1996, "Study of Secondary Flow in Centrifugal Blood Pumps Using a Flow Visualization Method with a High-Speed Video Camera," Artif. Organs, **20**, pp. 541–545.
[14] Asztalos, B., Yamane, T., and Nishida, M., 1999, "Flow Visualization Analysis for Evaluation of Shear and Recirculation in a New Closed-Type, Monopivot Centrifugal Blood Pump," Artif. Organs, **23**, pp. 939–946.
[15] Subramanian, A., Mu, H., Kadambi, J. R., Wernet, M. P., Brendzel, A. M., and Harasaki, H., 2000, "Particle Image Velocimetry Investigation of Intravalvular Flow Fields of a Bileaflet Mechanical Heart Valve in a Pulsatile Flow," J. Heart Valve Dis., **9**, pp. 721–731.
[16] Wernet, M. P., Subramanian, A., Mu, H., and Kadambi, J. R., 2000, "Comparison of particle image velocimetry and laser Doppler anemometry measurements in turbulent fluid flow," Ann. Biomed. Eng., **28**, pp. 1393–1396.
[17] Mussivand, T., Day, K. D., and Naber, B. C., 1999, "Fluid Dynamic Optimization of a Ventricular Assist Device Using Particle Image Velocimetry," ASAIO J., **45**, pp. 25–31.
[18] Day, S. W., McDaniel, J. C., Wood, H. G., Allaire, P. E., Landrot, N., and Curtas, A., 2001, "Particle Image Velocimetry Measurements of Blood Velocity in a Continuous Flow Ventricular Assist Device," ASAIO J., **47**, pp. 406–411.
[19] Day, S. W., McDaniel, J. C., Wood, H. G., Allaire, P. E., Song, X., Lemire, P. P., and Miles, S. D., 2002, "A Prototype HeartQuest Ventricular Assist Device for Particle Image Velocimetry Measurements," Artif. Organs, **26**, pp. 1002–1005.
[20] Bernstein, E. F., Cosentino, L. C., Reich, S., Stasz, P., Levine, I. D., Scott, D. R., Dorman, F. D., and Blackshear, Jr., P. L., 1974, "A compact, low hemolysis, non-thrombogenic system for non-thoracotomy prolonged left ventricular bypass," Trans. Am. Soc. Artif. Intern. Organs, **20**, pp. 645–654.
[21] Golding, L. A., and Smith, W. A., 1996, "Cleveland Clinic Rotodynamic Pump," Ann. Thorac. Surg., **61**, pp. 457–462.
[22] Veres, J. P., Golding, L. A., Smith, W. A., Horvath, D., and Medvedev, A., 1997, "Flow Analysis of the Cleveland Clinic Centrifugal Pump," ASAIO J., **43**, pp. M778–M881.

Shape Optimization of Forward-Curved-Blade Centrifugal Fan with Navier-Stokes Analysis

Kwang-Yong Kim[1]
Professor
e-mail: kykim@inha.ac.kr

Seoung-Jin Seo
Graduate Student

Department of Mechanical Engineering,
Inha University,
Incheon 402-751, Republic of Korea

In this paper, the response surface method using a three-dimensional Navier-Stokes analysis to optimize the shape of a forward-curved-blade centrifugal fan is described. For the numerical analysis, Reynolds-averaged Navier-Stokes equations with the standard k-ϵ turbulence model are discretized with finite volume approximations. The SIMPLEC algorithm is used as a velocity–pressure correction procedure. In order to reduce the huge computing time due to a large number of blades in forward-curved-blade centrifugal fan, the flow inside of the fan is regarded as steady flow by introducing the impeller force models. Four design variables, i.e., location of cutoff, radius of cutoff, expansion angle of scroll, and width of impeller, were selected to optimize the shapes of scroll and blades. Data points for response evaluations were selected by D-optimal design, and a linear programming method was used for the optimization on the response surface. As a main result of the optimization, the efficiency was successfully improved. Effects of the relative size of the inactive zone at the exit of impeller and momentum fluxes of the flow in scroll on efficiency were further discussed. It was found that the optimization process provides a reliable design of this kind of fan with reasonable computing time.
[DOI: 10.1115/1.1792256]

1 Introduction

Forward-curved-blade centrifugal fans have been widely used in air-conditioning devices due to relatively high flow rates, low noise, and high efficiency. These centrifugal fans have several main features that distinguish them from the other types of centrifugal fans: a larger diameter ratio of impeller, larger relative width of impeller, and larger number of forward-curved blades.

In order to design a fan of high performance, it is necessary to obtain detailed information about flow field of the fan. Some experimental studies on the flow inside of forward-curved-blade fan were carried out with five-hole probe [1,2] and spark tracing method [3]. The results commonly show that the separation zone is formed at the front of the impeller. In the scroll, strong three-dimensional flows were also observed.

Recent development of computational fluid dynamics for three-dimensional viscous flow fields provides efficient tools for analysis and design. Flow analysis techniques using Reynolds-averaged Navier-Stokes equations (RANS) have made remarkable progress in the applications to turbomachinery. As for forward-curved-blade centrifugal fans, Guo and Kim [4] performed both steady and unsteady three-dimensional RANS analysis for a forward-curved-blade centrifugal fan, and found that, except in the vicinity of the volute tongue, the steady results with frozen rotor condition are in good agreements with unsteady results. In order to reduce the huge computing time for RANS analysis of this flow, Seo, Kim, and Kang [5] developed simplified models of impeller forces, and a steady calculation with the models gave the results for velocity components, static pressure, and flow angles at the exit of the impeller in good agreement with experimental data at relatively high flow coefficients.

The recent enhancement of the computing environment has made numerical optimizations using three-dimensional RANS analysis as a tool for design of turbomachinery. As a technique of aerodynamic numerical optimization, gradient-based optimization methods have been most widely used in design optimizations [6]. However, the largest disadvantage of these methods is the possibility to fall into a local minimum with nonsmooth and noisy objectives and constraints. The adjoint variable method [7], developed recently, is regarded as one of most efficient gradient-based methods, but needs significant reprogramming in the analysis routine. On the other hand, the response surface method [8], as a global optimization method, has many advantages over the gradient-based methods. Local sensitivity analysis is not required. The information is collected from various sources and by different tools. Multiple criteria as well as multiple design point optimizations can be handled. Parallel computations can be easily performed. And, it smooths out the high-frequency noise of the objective function and is thus expected to find a solution near the global optimum. Recently, with these advantages, the response surface methods have been applied to many single- and multidisciplinery optimization problems [9,10].

Ahn and Kim [11] applied the response surface method based on three-dimensional thin-layer Navier-Stokes analysis to the design of blade section of axial compressor rotor. In this work, the optimum stacking line was found to design a custom-tailored three-dimensional blade for maximum efficiency with other parameters fixed. And a gradient-based optimization method was presented by Lee and Kim [6] to find an optimum shape of a stator blade in an axial compressor through calculations of single-stage rotor-stator flow. For forward-curved-blade centrifugal fans, Han, Maeng, and Yoo [12] studied the characteristics of the inactive zone, and optimized the shape of cutoff by using a two-dimensional RANS analysis and response surface method. However, due to the strong three-dimensional structure of the flow in the scroll, the validity of the two-dimensional analysis is still in doubt.

In this study, the response surface method using three-dimensional Navier-Stokes analysis was applied to the aerodynamic design of a forward-curved-blade centrifugal fan to maxi-

[1]Author to whom correspondence should be addressed.

Contributed by the Fluids Engineering Division for publication in the JOURNAL OF FLUIDS ENGINEERING. Manuscript received by the Fluids Engineering Division October 27, 2003; revised manuscript received April 4, 2004. Associate Editor: Yoshinobu Tsujimoto.

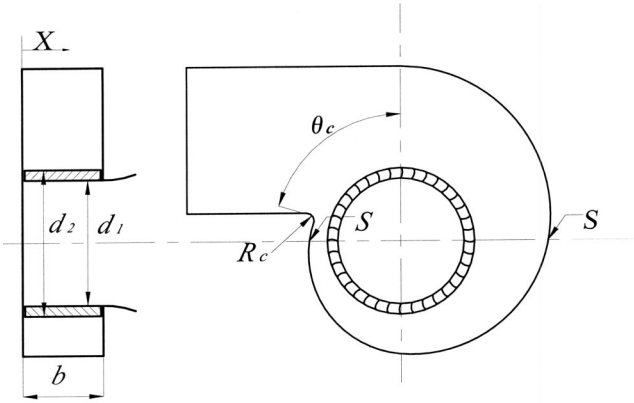

Fig. 1 Geometry of a forward-curved-blade centrifugal fan

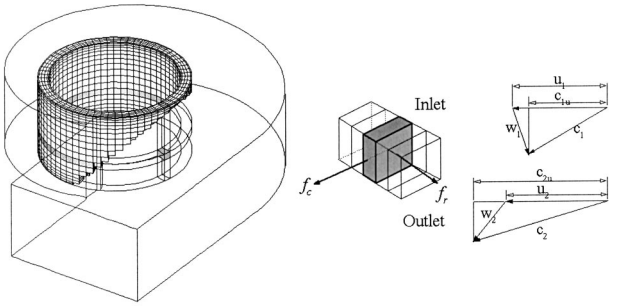

Fig. 2 Grid system of the impeller block, diagram of forces acting on the cell, and velocity triangles

mize the flow efficiency. To reduce computing time for RANS analysis of the complicated three-dimensional unsteady flow in this fan, a steady approximation using the simplified mathematical model of impeller forces [5] was employed. Four design variables, i.e., location of cutoff, radius of cutoff, expansion angle of scroll, and width of impeller, were selected as design variables to optimize the shapes of scroll and blades.

2 Flow Analysis

For steady incompressible turbulent flows, the continuity and Reynolds-averaged Navier-Stokes equations are as follows:

$$\frac{\partial}{\partial x_i}(\rho u_i)=0, \tag{1}$$

$$\frac{\partial}{\partial x_j}(\rho u_i u_j)=-\frac{\partial p}{\partial x_i}+\frac{\partial}{\partial x_j}\left[\mu\left(\frac{\partial u_i}{\partial x_j}+\frac{\partial u_j}{\partial x_i}-\frac{2}{3}\frac{\partial u_k}{\partial x_k}\delta_{ij}\right)-\rho\overline{u_i' u_j'}\right]+\overline{s_i^u}, \tag{2}$$

where u_i and u_i' are mean and fluctuating velocities, respectively, and $\overline{s_i^u}$ is source term. Governing equations with standard $k-\epsilon$ turbulence model [13] are transformed to non-orthogonal curvilinear coordinates, and are discretized with finite volume approximations. As a numerical scheme for the convection terms, a linear upwind differencing scheme is used, and for the diffusion terms, a central differencing scheme is used. The strongly implicit procedure (SIP) [14] was used to solve linear algebraic equations. Also the SIMPLEC algorithm is used to match pressure and velocities.

Various boundary conditions have to be imposed for calculations of the forward-curved-blade centrifugal fan shown in Fig. 1. In this work, since no experimental data are available for inlet velocities and turbulent quantities, uniform profiles are assumed at the inlet. At the exit boundary of each block, Neumann conditions are used. A no-slip condition is adopted at the solid walls. Also, the implementation of wall boundary conditions in turbulent flows is completed by use of the empirical wall function to calculate the mean velocity, turbulent kinetic energy, and dissipation rate in the logarithmic wall layer.

In the presented work, a multiblock system is employed for the grids. The whole computational domain is divided into three blocks: core, impeller, and scroll. The grid points along the adjacent block boundaries are coincident with each other, and therefore a simple overlapping coupling procedure can be applied to facilitate the transfer of aerodynamic information between blocks. In case of a multiblock system, pressure gradient affects the transport of momentum at the interface between different blocks. Therefore, the pressure gradients as well as the pressures must be joined between different blocks.

Flow through the impeller experiences forces by moving blades, which change the direction and the angular momentum of the flow. Therefore, in the numerical calculation, the action of the moving blade, i.e., the ''blade force,'' can be simulated by a body force introduced to the computational cells in the impeller block. With this concept, the impeller force models proposed in Ref. [5] are used in this work to reduce the computing time. In these models, circumferential and radial forces (f_c and f_r, respectively) in the impeller block, shown in Fig. 2, are derived as functions of flow rate and flow conditions at inlet and exit of the impeller, as follows:

$$f_c=\dot{m}[d_2(d_2\omega/2-c_{2r}\cot\beta_2)\varepsilon-d_1 c_{1u}]/\overline{d}, \tag{3}$$

$$f_r=\tfrac{1}{2}\overline{A}\rho\{c_{2u}[(1+\eta_{\mathrm{im}})u_2-c_{2u}]-c_{1u}[(1+\eta_{\mathrm{im}})u_1-c_{1u}]\}-\sum\frac{\Delta V\rho}{r}c_u^2, \tag{4}$$

where $\dot{m}$, d, ω, β, ε, ρ, $\overline{A}$, c, u, r, ΔV, and η_{im} are the mass flow rate, diameter of impeller, angular velocity, blade angle, slip factor, density, average flow area, flow velocity, blade speed, radial coordinate, volume of cell, and efficiency of impeller, respectively, and subscripts 1 and 2 indicate the inlet and outlet of the blade, respectively. As shown in Fig. 2, the impeller block consists of a number of computational cells. The body forces f_c and f_r in the above equations are calculated with the local velocities at inlet and outlet of blade: c_{1u}, c_{1r}, c_{2u}, and c_{2r}. Thus, the body forces are functions of both axial and circumferential coordinates. Then, in the radial direction, the forces at specified axial and circumferential locations are distributed as proportional to the cell volume, and stored in the source terms of discretized momentum equations for each computational cell in the impeller block. Therefore, physical information concerning the blade forces included in the cell is not uniform in the block and changes with iteration step. Thus, the nonaxisymmetric three-dimensional flow field in the impeller block can be calculated with these impeller models.

To stabilize the solutions, each component of the force is calculated by blending the local force (f^{local}) with the averaged force (f^{av}) with a weighting factor (w), as follows:

$$f_c=w_c f_c^{\mathrm{av}}+(1-w_c)f_c^{\mathrm{local}}, \tag{5}$$

$$f_r=w_r f_r^{\mathrm{av}}+(1-w_r)f_r^{\mathrm{local}}. \tag{6}$$

The average force, f^{av} indicates the force averaged in circumferential direction and is calculated with the average velocities: $\overline{c_{1u}}$ and $\overline{c_{1r}}$ at the inlet of impeller, and $\overline{c_{2u}}$ and $\overline{c_{2r}}$ at the outlet of impeller, which are obtained from the flow coefficient ϕ and the velocity diagram. In the above models of impeller force, the slip factor and the efficiency must be prescribed. In this work, these values are obtained from the experimental results provided by Kim and Kang [2].

Table 1 Geometric data for the forward-curved-blade centrifugal fan (reference shape)

Impeller		Blade		Scroll	
d_2	160 mm	β_1	87.0°	α	4.7°
d_1/d_2	0.80	β_2	151.3°	$r_3=r_2e^{\theta\tan\alpha}$	
b	100 mm	Shape	Circular arc	θ_c	77°
Number of blades	36	Thickness	1.2 mm	R_c	5 mm

3 Numerical Optimization

3.1 Response Surface Method. Optimization using the response surface method (RSM) [8] is a series of statistical and mathematical techniques, which is useful for optimization processes: generation of data by numerical computations or experiments, construction of response surface by interpolating the data, and optimization of the objective function on the surface. Although the RSM was devised to obtain empirical correlation from the experimental data, the ability to reduce the number of experiments let this method be applied widely to the optimization problems [15].

The polynomial-based response surfaces are commonly employed in RSM. Unknown coefficients of the polynomial are obtained from a regression process. The response model is usually assumed as a second-order polynomial, which can be written as follows:

$$F=\beta_0+\sum_{j=1}^{n}\beta_j x_j+\sum_{j=1}^{n}\beta_{jj}x_j^2+\sum\sum_{i\neq j}\beta_{ij}x_i x_j, \qquad (7)$$

where n is the number of design variables, and the number of regression coefficients (β_o, β_l, etc.) is $n_t=(n+1)(n+2)/2$. To determine the coefficients, standard least-squares regression can be used. In this case, the number of data must be larger than the number of coefficients.

In order to reduce the number of data needed for constructing response surface and to improve the representation of the design space, the design of experiment (DOE) is important for selecting design points. Among the different types of DOE techniques, D-optimal design [16] is employed in this work for the representation of design space. With the number of design points only 1.5–2.5 times the number of coefficients in the response model, reliable results can be obtained [17]. Guinta [18] showed that this technique constructs the response surface with sufficient reliability in case with five design variables.

To estimate the significance of any individual in the quadratic polynomial coefficient, analysis of variance (ANOVA) and regression analysis yield a measure of the uncertainty in the coefficients to increase the efficiency of the response surface. This uncertainty estimation is provided by using the t statistic [19]. The reciprocal of the t statistic is an estimate of the standard deviation of each coefficient as a fraction of its value. Accordingly, coefficients with low values for the t statistic are not accurately estimated. This test forms the basis for model optimization by adding or deleting coefficients. A common statistical measure of significance of a response surface model is the adjusted R^2 value, R^2_{adj} [19]. The maximum value for R^2_{adj} is 1.0, which occurs when all of the variation in the observed response values is described by the trends of the response surface polynomial model.

3.2 Objective Function and Design Variables. The following objective function is minimized in the optimization process:

$$F=1-\eta. \qquad (8)$$

The efficiency is defined as follows:

$$\eta=\frac{P_{t,\text{ex}}-P_{t,\text{in}}}{\rho(u_2c_{2u}-u_1c_{1u})}, \qquad (9)$$

where P_t is total pressure, and the subscripts, in and ex indicate the inlet and exit of the fan, respectively.

Figure 1 shows the design variables for impeller and scroll: location of the cutoff (θ_c), radius of the cutoff (R_c), and width of the impeller (b). Another design variable is the expansion angle of scroll (α) shown in Table 1.

4 Results and Discussions

A sectional view of the fan is shown in Fig. 1, and geometric data of the reference fan are summarized in Table 1. The computational grid system used for the present calculations is shown in Fig. 3. The numbers of grids in computational blocks are $30\times18\times18$, $6\times66\times20$, and $96\times12\times20$ at the core, impeller, and scroll, respectively. The working fluid is 20°C air of 1.22 kg/m^3 density and 1.8×10^{-5} N s/m^2 viscosity. The rotational speed of the impeller is 1140 rpm, and the mass flow rate is 7.66 m^3/min. The CPU time to obtain the converged solution for single-flow analysis is about 2 h with a 2-GHz Pentium-IV processor.

The results with the impeller force models [Eqs. (3) and (4)] were validated in comparison with the measurements of Kim and Kang [2] in the previous work [5]. For example, in Fig. 4, axial distributions of radial velocity component at the exit of impeller (θ=270°) for three different flow coefficients, are compared with the measurements [2]. In case of higher flow rates, ϕ=2.4 and 4.0, negative velocities occur near the front plate. Except in this region of reverse flow, the computational profile for ϕ=4.0 shows reasonably good agreement with experiment, while for the lower flow coefficients the magnitudes of this velocity component are slightly overpredicted. In this work, the clearance between impeller and casing is not considered in the analyses, and thus the leakage flow through the clearance and associated losses are ignored. Therefore, the computational errors are partly attributed to

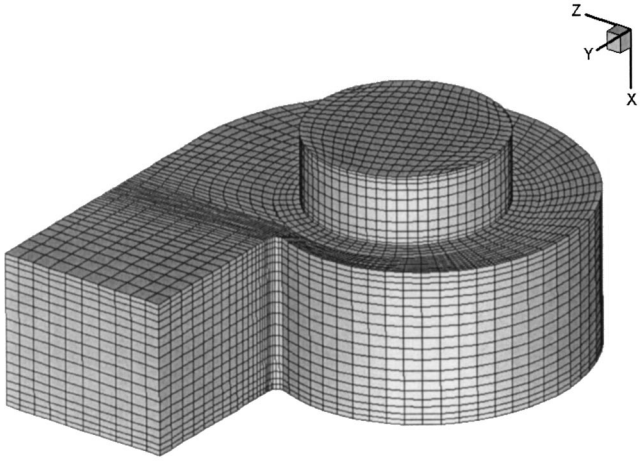

Fig. 3 Surface grids of computational domain

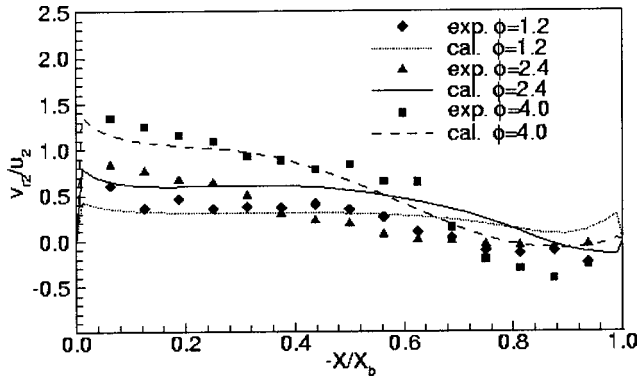

Fig. 4 Comparisons of computational results with measurements at the impeller exit (Seo, Kim, and Kang [5])

this assumption. However, accuracy of the prediction is generally acceptable even with the approximated models of the impeller.

Guo and Kim [4] performed a three-dimensional unsteady calculation using a commercial CFD code for a multiblade fan, which is similar to the model used in this work. Due to a large number of forward curved blades in the impeller, they used 794,435 grid points, which is an order of magnitude larger than the number of grid points, 40,680 used in this work. Therefore, it is found that large computing time and memory can be reduced with the mathematical model for the impeller forces presented in this work.

The ranges of design variables for selection of evaluation points are shown in Table 2. To construct the response surface, each range of design variables is normalized, so that the dimensionless variable varies from -1 to 1. For four design variables, there are $n_t=(n+1)(n+2)/2$, namely, 15 unknown coefficients in the polynomial. To determine these coefficients, 42 points for response evaluations were selected by using the D-optimal design. The values of unknown coefficients were obtained with the data at the selected points by the commercial statistics software, the statistical package for the social sciences (SPSS), which is used to perform ANOVA and regression analysis along with other statistical analyses in the wide field. The reliability of the response surface is improved by the t statistics and adjusted R^2 method. The coefficients of response surface function were determined by ANOVA and regression analysis, the results of which are summarized in Table 3. Guinta [18] suggested that the typical values of R^2_{adj} are in the range $0.9 \leqslant R^2_{\text{adj}} \leqslant 1.0$, when the observed response values are accurately predicted by the response surface model. In this respect, the present response surface is quite reliable. The optimum point on the response surface was found by a linear programming method.

The optimizations with and without constraint, as shown in Table 4, were carried out. The constraint was imposed on the fan static pressure, P_s, i.e., the difference between inlet and exit static pressures of the fan, in order to prevent the pressure from being lowered below specified level. One of the advantages of response surface optimization method is the ability to test multiple objective functions and/or constraints without additional analyses of the flow field.

Since the fan static pressure is dependent on design variables, in order to impose the constraint, the response surface for the static pressure should also be constructed. The results of regression analysis for this surface are shown in Table 5.

Figure 5 shows the results of sensitivity analysis of each design variable for the reference and the first optimum shapes. Here, dv indicates the percent change of each design variable. As shown in this figure, the objective function is more sensitive to location of the cutoff and expansion angle of the scroll than the radius of the cutoff and width of the impeller near the optimum point.

As the main result of the optimizations, shown in Table 6, the efficiency was successfully increased. In the first optimization without constraint, the maximum efficiency of 96.9% was obtained, while the fan static pressure was reduced by 37% in comparison with the reference fan. The constraints on static pressure reduced the efficiency by only 1–2%, but guaranteed specified minimum static pressures at given flow rate.

Due to the intrinsic error of response surface, the value of static pressure on the surface, in general, does not coincide with the value obtained from the flow analysis, but agrees with the value in specified error bounds. Thus, even if the constraint is satisfied on the response surface, it may not in the calculation. This is the reason why, in Table 6, the fan static pressure in second optimi-

Table 2 Ranges of design variables for selection of the points for response evaluation

Variables	Lower bounds	Upper bounds
Location of cutoff θ_c (deg)	70	84
Radius of cutoff R_c (mm)	4.0	6.0
Expansion angle of scroll α (deg)	3.7	5.7
Width of impeller b/d_2	0.4	0.7

Table 3 Quality of the second-order response surface for the objective function

Model	R^2	R^2_{adj}	Std. error of the estimate
1	0.983	0.973	2.08×10^{-2}

Table 4 Cases of optimization

	First optimization	Second optimization	Third optimization
Constraint P_o $(P_s \geqslant P_o)$		100.0 Pa	130.0 Pa

Table 5 Quality of the second-order response surface for the fan static pressure

Model	R^2	R^2_{adj}	Std. error of the estimate
1	0.996	0.994	6.99

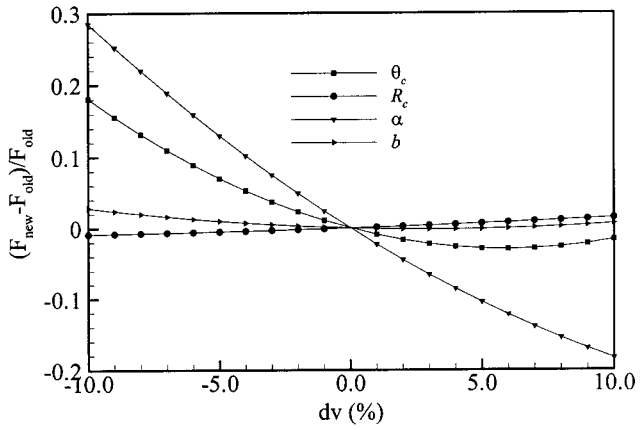

(a) reference

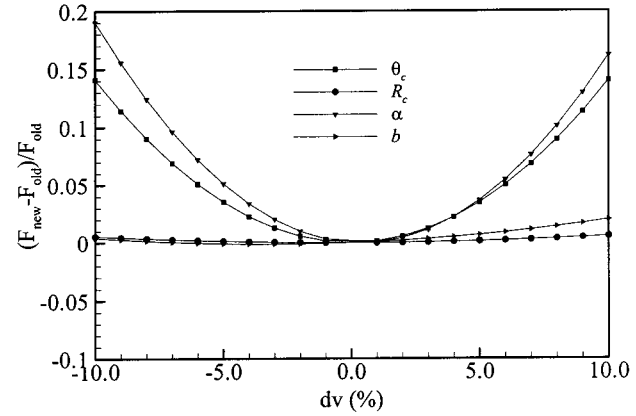

(b) 1st optimum

Fig. 5 Sensitivity analyses for reference and first optimum shapes

zation does not satisfy exactly the specified constraint. It is one of the weak points of response surface method that this kind of constraint cannot be imposed exactly.

Since the flow rate is fixed in the optimizations, each optimum point may not be the maximum efficiency point of the corresponding performance curve. Thus, it would be interesting, in the future, to find the maximum efficiency by employing flow rate as one of design parameters.

The optimum values of design variables are listed in Table 7. It is found that several optimum values are out of bounds shown in Table 2. However, since the range of each variable shown in Table 2 is not a constraint for the variable but a range for selection of evaluation points, the optimum value of the variable can be out of this range if it is located within the distance from the bound, which is less than the distance between adjacent evaluation points. The optimal values of the location and the radius of the cutoff are similar to the results of Han, Maeng, and Yoo [12]. The optimum value of the ratio of exit to inlet flow area, $4b/d_1=1.71$ in the first optimization, is less than a half of the value for reference shape, 3.47. This is consistent with the result obtained by Roth [20], which shows that efficiency increases as the width of impeller decreases. However, it is found in Table 7 that the relationship between impeller width and efficiency is far from linearity. Optimum locations of cutoff are around 75°. And, as the radius of the cutoff increases or as the expansion angle of the scroll decreases, the static pressure increases with a decrease of efficiency at optimum point. As Kind and Tobin [1] suggested and also shown in Figs. 6 and 7, reduction of impeller width (b) reduces the relative extent of flow recirculation zone through the impeller, the so-called inactive zone, from 18.4% to 13.4% of the total exit surface area of impeller.

At this moment, it is thought to be meaningful to discuss about the relationship between the efficiency and the relative size of inactive zone at the exit of impeller based on the database obtained by the flow calculations. Figure 8 shows the plot of efficiencies versus the sizes of the inactive zone. It is found that the efficiency is not directly correlated with the relative size of inactive zone. That is, enlargement of this inactive zone, in general, does not result in a decrease of efficiency. And, it is also noted that the size of inactive zone is strongly dependent on impeller width. As impeller width reduces, the size of the inactive zone also reduces and becomes less dependent on design variables other than the impeller width. For the impeller width of $b/d_2=0.40$, size of the inactive zone is nearly independent of the other variables. In contrast, as the impeller width increases, the efficiency becomes less dependent on the other design variables.

To find the correlation of momentum in the scroll with efficiency, two kinds of dimensionless momentum flux, i.e., C_{Mt} and C_{Ms}, are defined as follows:

$$C_{Mt}=\frac{\int_A V_t \rho V_c dA}{\rho V_{\text{in}}^2 A_{\text{in}}}, \quad C_{Ms}=\frac{\int_A V_s \rho V_c dA}{\rho V_{\text{in}}^2 A_{\text{in}}}$$

where

$$V_t=\sqrt{V_a^2+V_r^2+V_c^2}, \quad V_s=\sqrt{V_a^2+V_r^2}$$

A is the cross-sectional area of the scroll, which is normal to circumferential direction. V_a, V_r, and V_c indicate axial, radial, and circumferential components of velocity vector in the scroll, respectively. V_{in} and A_{in} are the velocity and flow area at the inlet of the fan, respectively. Then, these momentum fluxes are averaged in the scroll as follows:

Table 6 Results of optimizations

	Reference	First optimization	Second optimization	Third optimization
Efficiency	87.6%	96.9%	95.7%	94.6%
Static pressure	97.6 Pa	61.4 Pa	95.11Pa	139.0Pa

Table 7 Optimal values of design variables

Variables	Reference	First optimization	Second optimization	Third optimization
Location of cutoff, θ_c (deg)	77.0	74.99	75.88	75.42
Radius of cutoff, R_c (mm)	5.0	5.094	5.196	5.617
Expansion angle of scroll, α (deg)	4.7	6.521	6.465	6.190
Width of scroll, b/d_2	0.625	0.3438	0.3934	0.5606

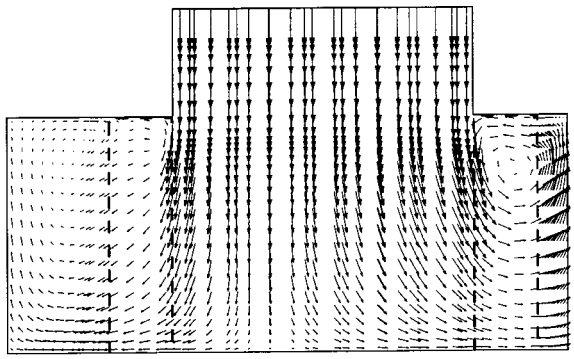

(a) reference

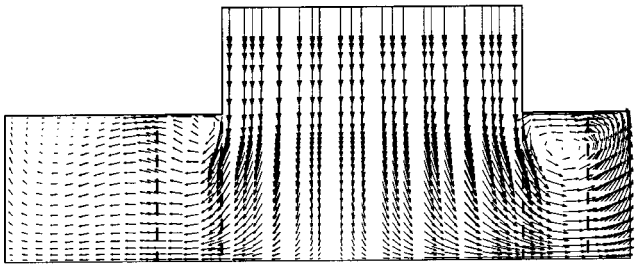

(b) 1st optimum

Fig. 6 Velocity vectors in reference and first optimum shapes (S-S cross section in Fig. 1)

$$\overline{C_{Mt}} = \frac{1}{\text{Vol}} \int C_{Mt} d\text{Vol}, \quad \text{and} \quad \overline{C_{Ms}} = \frac{1}{\text{Vol}} \int C_{Ms} d\text{Vol},$$

where the integrations are performed for the scroll volume (Vol) in the range from θ=90° to 360°. Circumferential variations of dimensionless momentum fluxes are shown in Figs. 9(*a*) and 9(*b*). Figures 10(*a*) and 10(*b*) are plots of efficiency versus averaged momentum fluxes. It is found in these figures that, although both momentum fluxes in the scroll are correlated with the efficiency,

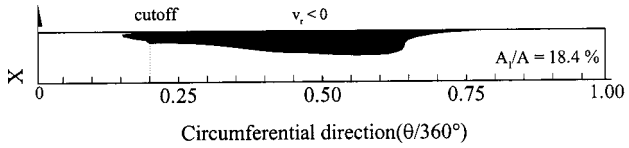

(a) reference

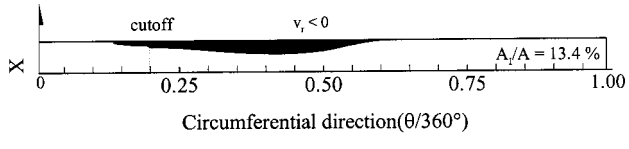

(b) 1st optimum

Fig. 7 Inactive zones at the exit of impeller for reference and first optimum shapes

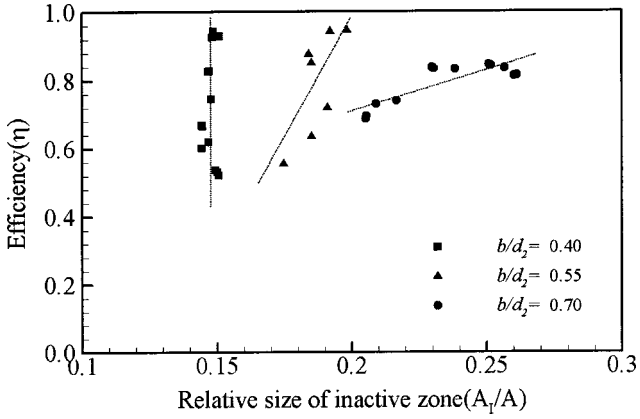

Fig. 8 Efficiency versus relative size of inactive zone

$\overline{C_{Ms}}$ is correlated more strongly than $\overline{C_{Mt}}$. Since $\overline{C_{Ms}}$ is related to the strength of three-dimensional motion in the scroll, the results indicate that the stronger three-dimensional motion in the scroll is related to the higher level of the efficiency, which is defined by Eq. (9) based on total pressures. However, if we define the efficiency (η_s) based on static pressures, the efficiency reduces rapidly as averaged momentum fluxes increase as shown in Fig. 11.

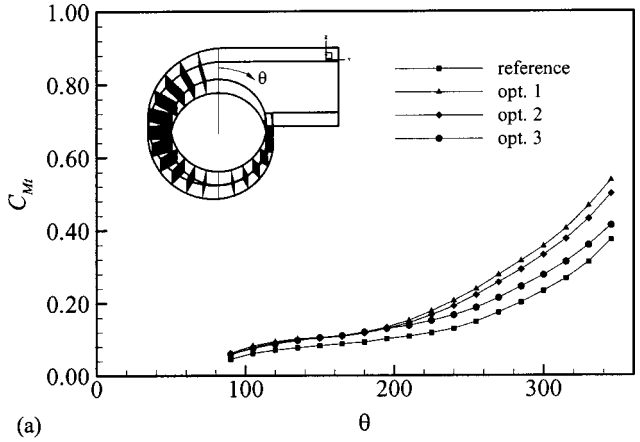

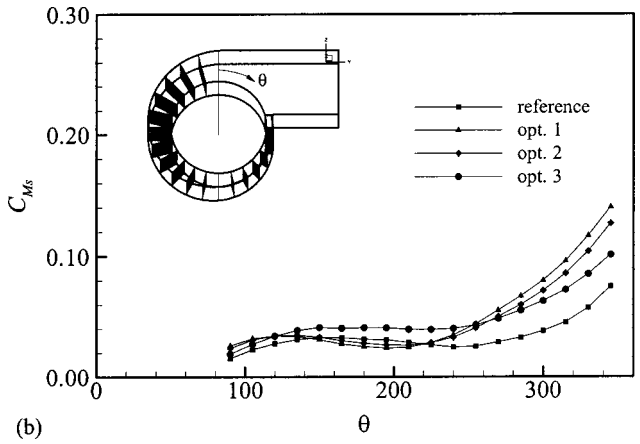

Fig. 9 Circumferential variations of momentum fluxes in scroll: (*a*) C_{Mt}, (*b*) C_{Ms}

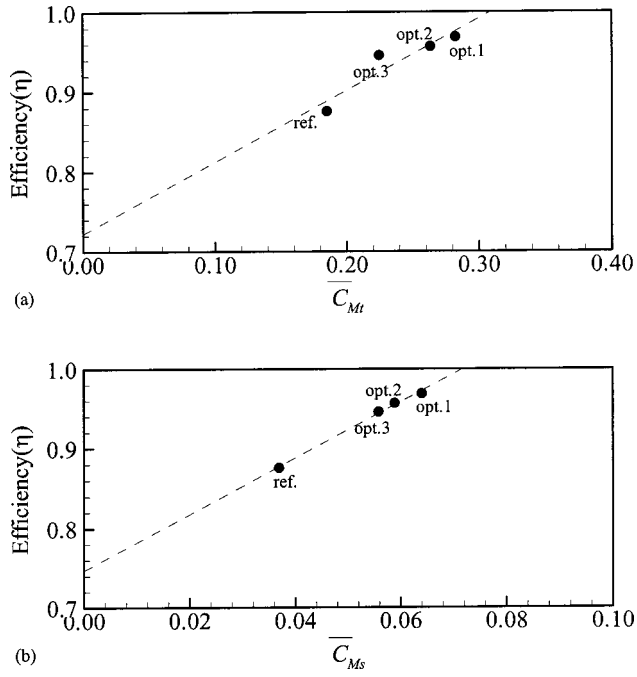

Fig. 10 Correlations between efficiency and averaged momentum fluxes in the scroll: (*a*) $\overline{C_{Mt}}$, (*b*) $\overline{C_{Ms}}$

5 Conclusions

In order to maximize the efficiency, using location and radius of the cutoff, the expansion angle of the scroll and width of impeller as design variables, the response surface optimization method with three-dimensional Navier-Stokes analysis was successfully applied to the aerodynamic design of forward-curved-blade centrifugal fan. Navier-Stokes analysis using a mathematical model of impeller forces is very effective to reduce computing time. With only 42 points for response evaluations, the main objective, i.e., the efficiency is improved effectively in comparison with the reference fan. With the restriction to guarantee the level of reference fan static pressure, the reduction in efficiency is not large. From the results of sensitivity analysis, it is found that the efficiency is more sensitive to the location of the cutoff and the expansion angle of the scroll than the other design variables. Further analyses of computational results indicate that the efficiency is not directly correlated with the relative size of inactive zone at the exit of impeller, which is strongly dependent on impeller width, and also that the stronger three-dimensional motion in the scroll is related to the higher level of total efficiency, but to the lower level of static efficiency.

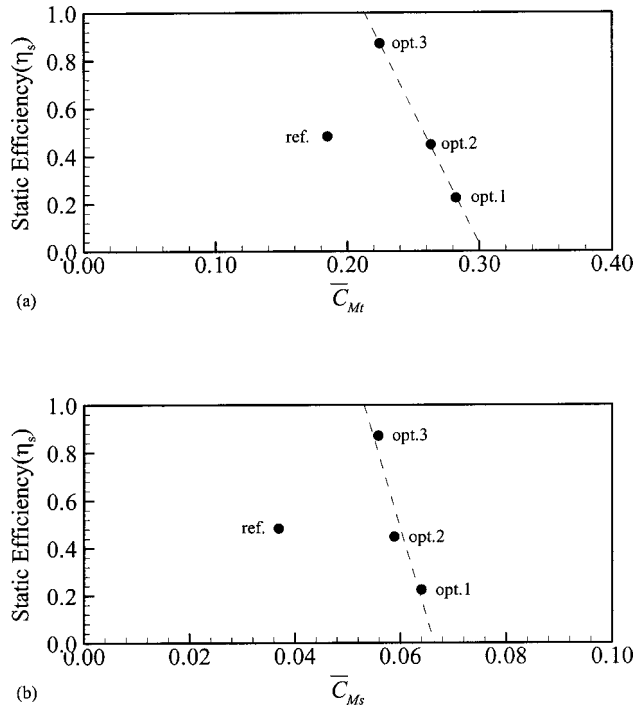

Fig. 11 Correlations between static efficiency and averaged momentum fluxes in the scroll: (*a*) $\overline{C_{Mt}}$, (*b*) $\overline{C_{Ms}}$

Nomenclature

A = Flow area
b = Width of impeller
c_r, c_u = Radial and tangential components of flow velocity, respectively
C_{Ms}, C_{Mt} = Dimensionless momentum fluxes in scroll
d = Diameter of impeller
F = Response function or objective function
f = Blade force
$\dot{m}$ = Mass flow rate
n = Number of regression coefficients
P_t, P_s = Total and static pressures, respectively
r_2, r_3 = Radii of impeller exit and scroll surface, respectively
R_c = Radius of cutoff
u_i = Cartesian velocity component
u = Blade speed
w = Weighting factor
V = Flow velocity
x_i = Cartesian coordinate or design variable
X, X_b = Axial coordinate and width of impeller, respectively
α = Expansion angle of scroll
β = Blade angle
β_i = Coefficient of response polynomial
δ_{ij} = Kronecker delta
ε = Slip factor
ϕ = Flow coefficient
η, η_s = Total and static efficiencies, respectively
η_{im} = Efficiency of impeller
θ_c = Location of cutoff
ρ = Fluid density
ω = Angular velocity

Subscripts

1, 2 = Inlet and outlet of blade, respectively
a, *c*, *r* = Axial, circumferential, and radial directions, respectively
in, ex = Inlet and exit of the fan

Diacritic

Overbar = Average value

References

[1] Kind, R. J., and Tobin, M. G., 1990, "Flow in a Centrifugal Fan of the Squirrel-Cage Type," ASME J. Turbomach., **112**, pp. 84–90.
[2] Kim, J. K., and Kang, S. H., 1997, "Effects of the Scroll on the Flow Field of a Sirocco Fan," ISROMAC-7, Hawaii, pp. 1318–1327.
[3] Kadota, S., Kawaguchi, K., Suzuki, M., Matsui, K., and Kikuyama, K., 1994, "Experimental Study on Low-Noise Multiblade Fan" (First Report, Visualization of Three-Dinensional Flow Between Blades), JSME Int. J., Ser. B, **60**, pp. 102–113.
[4] Guo, E. M., and Kim, K. Y., 2004, "Three-Dimensional Flow Analysis and Improvement of Slip Factor Model for Forward-Curved Blades Centrifugal Fan," KSME Int. J., **18**, pp. 302–312.
[5] Seo, S. J., Kim, K. Y., and Kang, S. H., 2003, "Calculations of Three-

Dimensional Viscous Flow in a Multi-Blade Centrifugal Fan by Modeling Blade Forces,'' Proc. Inst. Mech. Eng., Part A: Journal of Power and Energy, **217**, pp. 287–297.
[6] Lee, S. Y., and Kim, K. Y., 2000, ''Design Optimization of Axial Flow Compressor Blades With Three-Dimensional Navier-Stokes Solver,'' KSME Int. J., **14**, pp. 1005–1012.
[7] Jameson, A., Schmidt, W., and Turkel, E., 1981, ''Numerical Solutions of the Euler Equation by Finite Volume Methods Using Runge-Kutta Time Stepping Schemes,'' AIAA 81-1259.
[8] Shyy, W., Papila, N., Vaidyanathan, R., and Tucker, K., 2001, ''Global Design Optimization Aerodynamics and Roket Propulsion Components,'' Prog. Aerosp. Sci., **37**, pp. 59–118.
[9] Kim, K. Y., and Kim, S. S., 2002, ''Shape Optimization of Rib-Roughened Surface to Enhance Turbulent Heat Transfer,'' Int. J. Heat Mass Transfer, **45**, pp. 2719–2727.
[10] Sevant, N. E., Bloor, M. I. G., and Wilson, M. J., 2000, ''Areodynamic Design of a Flying Wing Using Response Surface Methodology,'' J. Aircr., **37**, pp. 562–569.
[11] Ahn, C. S., and Kim, K. Y., 2003, ''Aerodynamic Design Optimization of an Axial Flow Compressor Rotor,'' Proc. Inst. Mech. Eng., Part A: Journal of Power and Energy, **217**, pp. 179–184.
[12] Han, S. Y., Maeng, J. S., and Yoo, D. H., ''Shape Optimization of Cutoff in A Multiblade Fan/Scroll System Using Response Surface Methodology,'' Numer. Heat Transfer, Part B, **42**, pp. 1–12.
[13] Launder, B. E., and Spalding, D. B., 1974, ''The Numerical Computational of Turbulent Flows,'' Comput. Methods Appl. Mech. Eng., **3**, pp. 269–289.
[14] Fletcher, C. A., 1991, *Computational Techniques for Fluid Dynamics I*, Springer, Berlin.
[15] Myers, R. H., 1999, ''Response Surface Methodology-Current Status and Future Direction,'' J. Quality Technol., **31**, pp. 30–44.
[16] Box, M. J., and Draper, N. R., 1971, ''Fractional Designs, the $|X^TX|$ Criterion, and Some Related Matters,'' Technometrics, **13**, pp. 731–742.
[17] Venter, G., Haftka, R. T., and Starnes, J. H. Jr., 1996, ''Construction of Response Surfaces for Design Optimization Applications,'' AIAA 96-4040-CP.
[18] Guinta, A. A., 1997, ''Aircraft Multidisciplinary Design Optimization Using Design of Experimental Theory and Response Surface Modeling Methods,'' Ph.D. thesis, Department of Aerospace Engineering, Virginia Polytechnic Institute and State University, Blacksburg, VA.
[19] Myers, R. H., and Montgomery, D. C., 1995, *Response Surface Methodology: Process and Product Optimization Using Designed Experiments*, Wiley, New York.
[20] Roth, H. W., 1981, ''Optimierung von Trommelläufer,-Ventilatoren,'' Strömungsmechanik und Strömungsmaschinen, **29**, pp. 1–45.

On Cross-Flow Fan Theoretical Performance and Efficiency Curves: An Energy Loss Analysis on Experimental Data

Andrea Toffolo[1]
Department of Mechanical Engineering,
University of Padova,
Via Venezia, 1-35131
Padova, Italy
e-mail: andrea.toffolo@unipd.it

Contrary to conventional turbomachinery, cross-flow fan flow field is non-axisymmetrical and its complex configuration strongly affects performance and efficiency characteristic curves. The formulation of a theory on cross-flow fan operation is made even tougher since the strength and the eccentricity of the vortex that forms within the impeller are deeply influenced by the geometry of the impeller and of the casing as well. In this paper, a numerical reconstruction of the flow field, validated against an extensive systematic database of global and local experimental measurements, is analyzed. The aim is to achieve a general interpretation of performance and efficiency curves, and to lead them back to one theoretical archetype, whatever the fan configuration being considered.
[DOI: 10.1115/1.1792268]

1 Introduction

Cross-flow fan operation differs from conventional turbomachinery because both suction and discharge occur radially. A typical configuration of the resulting flow field is illustrated in Fig. 1. Its main features are the double passage of the air across the blade row and the formation of an eccentric vortex inside the impeller due to the motion of the blades themselves. The fluid-dynamic equilibrium between throughput and recirculating flow, which exerts a significant and complicated influence on fan performance and efficiency, is mainly governed by the position and the strength of this vortex. It is apparent that, in turn, the characteristics of the vortex are affected by the geometry of the impeller and of the casing as well. This makes it difficult not only to predict performance and efficiency for a given set of design parameters, but also to analyze the aerodynamics and the loss mechanisms of this category of fans and formulate a general theory on their operation.

This paper is part of an extensive research by the same group of authors. Systematic experimental studies on cross-flow fan operation were performed to investigate the validity of the similarity laws [1], to determine performance and efficiency curves [2], and to explore the flow field pattern [3] as the most significant design parameters defined by an original effective criterion to describe fan geometry [4] are varied. Numerical simulations validated against the experimental measurements were also performed to analyze the link between the flow field pattern and fan performance and efficiency [5]. Finally, a multi-objective optimization based on the available data has led to the definition of some design guidelines according to different possible choices of design criteria [6].

In this work, a theoretical approach is presented to analyze systematically the experimental results in order to come to a unified interpretation of the characteristic curves for all fan configurations. In fact, different and well-defined trends of performance and efficiency have been identified according to different choices of the design parameters [2]: now, the aim is to find a common theoretical explanation for all of them. First, theoretical and analytical methods previously proposed in the literature [7–13] to retrieve performance and efficiency curves are concisely reviewed and the actual sources of energy losses in cross-flow fan operation are discussed. Then, the fan configurations considered in this work are presented and the experimental results obtained in [2,3] about the relationships between performance, flow field pattern, and main design parameters are briefly recalled. Finally, a normalized stream function, which is a powerful tool to analyze the integrals of the local quantities of the flow fields [5], is introduced and applied to reveal the theoretical archetype of performance and efficiency curves.

2 Theoretical and Analytical Models of Cross-Flow Fan Operation and Analysis of Energy Losses

The main theoretical efforts to interpret and/or reproduce performance and efficiency characteristic curves are based on one-dimensional Eulerian analysis.

Eck's model [7] of the energy transfer mechanism in a cross-flow fan impeller assumes that the blade row is unrolled into a straight line, so that a generic streamline crosses two planar cascades. The resulting theoretical characteristic curve Ψ_t-Φ is a straight line with positive slope (Fig. 2). The actual characteristic curve is then estimated by subtracting friction losses (that are considered proportional to the square of the flow coefficient) and incidence losses (that are considered zero at the design flow coefficient and proportional to the square of the difference between actual and design flow rates). The ascending–descending shape of the actual characteristic curve obtained (Fig. 2) can be experimentally recognized in some cross-flow fan configurations, among which the fan patented by Eck himself [14].

In Moore's model [8], the theoretical characteristic curve Ψ_t-Φ is calculated by evaluating the energy transfer across the impeller along a mean line, which is determined after an estimation of the actual suction and discharge arcs according to the assumption that that the flow field is governed by a Rankine vortex. The experimental values of Ψ_t/η_t are close to those estimated by this approach only for some of the analyzed configurations [8]. In particular, the difference becomes significant when fans having a descending (stable) characteristic curve are considered.

Other authors have tried to predict analytically the characteristic curve of a particular fan configuration using simplifying assumptions to describe the flow field within and around the impeller. Coester [9] and Tramposch [10] used a potential flow generated by a single vorticity source lying on the inner periphery of the impeller, whereas Ilberg and Sadeh [11] modeled the flow

[1]Corresponding author.

Contributed by the Fluids Engineering Division for publication in the JOURNAL OF FLUIDS ENGINEERING. Manuscript received by the Fluids Engineering Division January 7, 2004; revised manuscript received May 12, 2004. Associate Editor: Y. Tsujmoto.

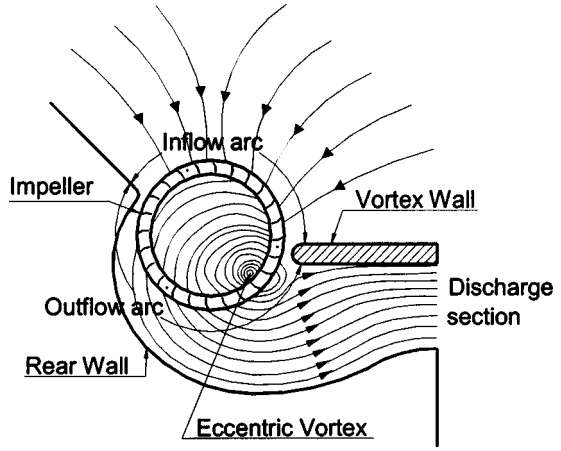

Fig. 1 A cross-flow fan configuration

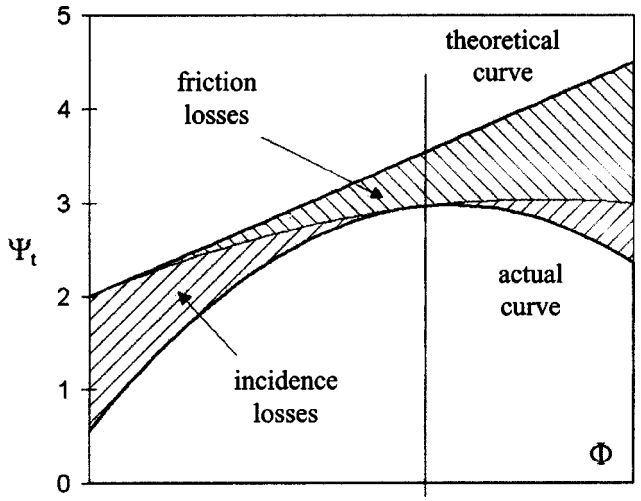

Fig. 2 Theoretical and actual characteristic curve according to Eck's theory [7]

with a Rankine vortex. Ikegami and Murata [12] evaluated the theoretical total pressure coefficient for different vortex eccentricities and external blade angles using a potential flow model featuring two vorticity sources, one inside and the other outside the impeller. Yamafuji [13] suggested the use of an actuator-driven vortical flow and calculated the characteristic curves for several vortex positions and impeller geometries.

The main reason why all the mentioned theoretical and analytical approaches fail to reproduce and/or predict theoretical and/or actual cross-flow fan characteristic curves is the lack of reliable models for taking into account the losses that occur in the energy transfer mechanism. On the other hand, the sources of these losses cannot be simply considered as in conventional turbomachinery because of the complexity of the non-axisymmetric flow field. Energy losses in cross-flow fan operation can be classified as follows:

- *Volumetric losses:* As mentioned previously, only part of the flow that passes through the impeller reaches the discharge section. Part of that flow is entrained in the recirculation zone formed by the eccentric vortex and another part may return to suction. Total efficiency depends in a complex way on these fractions of the overall flow rate. In particular, the fraction associated with the recirculation zone depends on the strength and the eccentricity of the vortex [13].
- *Incidence losses:* The tangential and radial components of the velocity vary considerably along the inner and outer peripheries of the impeller due to the streamline curvature induced by the vortical flow. As a consequence, a flow rate resulting in ideal incidence conditions along the entire inlet arcs at both blade passages does not exist. Most of the incidence losses occur in the portion of the suction arc that is adjacent to the vortex wall, where radial velocities are higher [3,15], and in the portions affected by stall phenomena (which may even persist at all flow rates [16]).
- *Friction losses:* According to Eck [7] and Clayton [17], cross-flow fan total efficiencies in the field of low Reynolds numbers are higher than those of centrifugal and axial fans. In fact, viscous losses would remain limited as Re_D diminishes because most of the flow tends to stay close to the boundary of the recirculation zone, where the highest velocities are generated, and this results in local Reynolds numbers higher than Re_D [10]. Moreover, it is worth noting that during each impeller revolution the flow on a generic blade inverts twice. In such conditions the flow is turbulent even at low velocities, since the formation of a laminar boundary layer is greatly hindered.
- *Unstable operation losses:* Cross-flow fan pressure and velocity flow fields often show large pulsations in time that are not due to ordinary rotor-stator interaction. These pulsations are generated by stall phenomena that may occur in some portions of the suction arc and in particular by the intrinsic instability of the eccentric vortex within the impeller. In fact, the vortex core is surrounded by a nonuniform pressure boundary that makes it cyclically migrate towards quasi-stable equilibrium positions. Stability in operation is often achieved at the expenses of performance, and is generally improved at intermediate flow coefficients.
- *Three-dimensional losses:* Cross-flow fan flow field is only ideally two-dimensional in planes perpendicular to machine axis. Secondary flows involving axial velocities can be caused by the rotation of the impeller discs if the length to diameter ratio L/D_2 is below 0.5 [11], and even in ''long'' runners (L/D_2 greater than 4) three-dimensional effects make the flow not uniform in the axial direction and may even cause a vortex breakdown.

When the energy transfer mechanism is analyzed just in two dimensions (i.e., the losses for three-dimensional effects are neglected) it is suggested here to subdivide the aforementioned sources of losses in two categories. Volumetric losses alone can be taken into account through a volumetric efficiency η_{vol}, defined here as

$$\eta_{vol}=\frac{mechanical\ energy\ transferred\ by\ the\ impeller\ to\ the\ only\ throughflow}{overall\ mechanical\ energy\ supplied\ by\ the\ impeller} \tag{1}$$

The other three sources (incidence, friction, and unstable operation) can be comprised in a hydraulic efficiency η_{hyd}, defined, as usual, as

$$\eta_{hyd}=\frac{energy\ (total\ pressure)\ gained\ by\ the\ throughflow}{mechanical\ energy\ transferred\ by\ the\ impeller\ to\ the\ only\ throughflow} \tag{2}$$

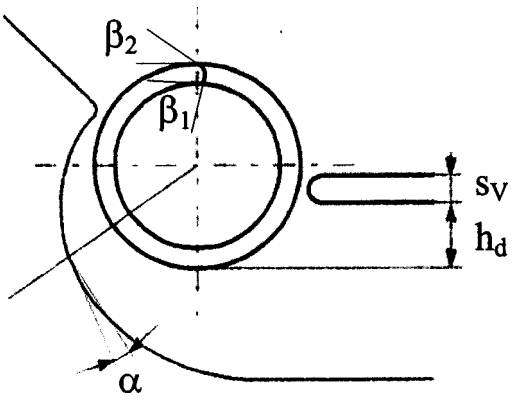

Fig. 3 The most significant parameters affecting fan performance and efficiency

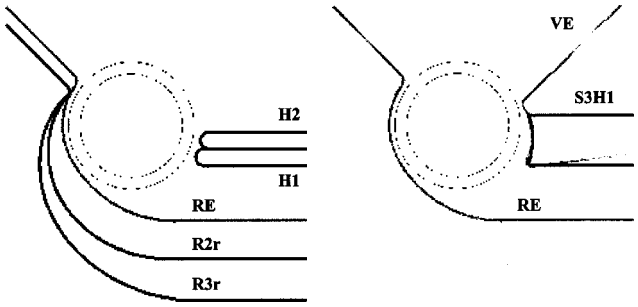

Fig. 4 The casing shapes selected for the analysis

Thus the product of the volumetric and the hydraulic efficiency is equal to the total efficiency:

$$\eta_t = \eta_{hyd}\,\eta_{vol} \tag{3}$$

Such definitions will prove to be powerful tools in the analysis of the integral quantities of the flow field that will be performed in Secs. 4 and 5.

3 The Fan Configurations Considered

A representative set of fan configurations has been selected for the analysis using different values of the design parameters that were identified in [2,4] as the most significant according to the influence exerted on performance and efficiency. These are the circular arc blade angles β_1 and β_2 for the impeller and, for the casing, the angle α of the logarithmic spiral that controls the radial width of the rear wall, the height h_d, and the thickness s_V of the vortex wall (Fig. 3).

The tests to determine fan performance and efficiency were carried out in [2] using a facility of type A (free suction and plenum chamber at the delivery) according to the UNI 10531 standard [18] on industrial fan test methods and acceptance conditions (equivalent to ISO 5801 [19]). Pressure measurements in the airway sections were performed by water micromanometers and fan total efficiency was determined by torque measurement with a load cell. All tests were performed at a rotational speed of 1000 rpm and with impellers having an external diameter D_2 equal to 152.4 mm and an axial length L equal to 228.6 mm. The estimated uncertainty for the total pressure coefficient is within 1.5%, whereas for total efficiency is within 3%, since more measured quantities are involved in its calculation.

A systematic program of tests showed that the radial width of the rear wall is the fundamental geometrical feature in determining the shape of the characteristic curve [2]: small, intermediate, and large radial widths result in ascending, nearly flat, and descending Ψ_t-Φ curves, respectively. The three rear walls considered in this work are shown in Fig. 4 as

1. RE (small radial width Eck's patented rear wall made up of two circular arcs, one of which centered on impeller axis),
2. R2r (intermediate radial width log spiral rear wall, α=17.2 deg) and
3. R3r (large radial width log spiral rear wall, α=23.6 deg).

Vortex wall geometry can be subdivided in two main categories according to thickness. Characteristic curve stability tends to improve if the height of thin vortex walls is increased. A flat thin vortex wall ($s_V/D_2=0.13$) is combined with all the three rear walls in the two lowest positions tested in [2] [indicated as H1 ($h_d/D_2=0.185$) and H2 ($h_d/D_2=0.316$) in Fig. 4], for which high performance and efficiencies are obtained. The matching with thick vortex walls is convenient only when small radial width rear walls are used, but this combination leads to the highest total efficiencies with ascending Ψ_t-Φ curves [2,6]. The two thick vortex walls considered (Fig. 4) are the modular vortex wall S3H1 already used in [2] ($s_V/D_2=0.39$, $h_d/D_2=0.185$) and Eck's patented vortex wall VE, and are both matched to the rear wall RE. The experimental results showed that impeller blade angles do not substantially alter the trends of the characteristic curves in the ranges of high performance and efficiency [2]. In particular, the internal blade angle mainly affects the maximum value of the η_t-Φ curve and of the free blowing flow rate (both these quantities show a maximum for $\beta_2=90°$), whereas higher external blade angles improve just slightly the stability of the Ψ_t-Φ curves. The impeller used in this study is the one for which the validity of the similarity laws was verified in [1], having $\beta_2=38$ deg and $\beta_1=70$ deg.

The flow fields inside the impeller of the resulting fan configurations were experimentally investigated in [3] using a three-dimensional aerodynamic probe. This measurement technique of the local flow quantities was chosen to investigate both pressure and velocity fields on a predefined grid of points which lie on circumferences of different radii at half of the impeller axial length L. The pressure signals of the five-hole ''cobra'' probe were collected by pressure transducers, amplified, and sent to a computer which calculates total, static, and dynamic pressures, according to the calibration curves provided by the manufacturer of the probe. Outside the stall zone, the uncertainty on the final measurements are within $\pm$2% for pressure (total and static), within $\pm$2.5% for velocity magnitude and within $\pm$1 deg for the yaw angle. The tests were performed for each fan configuration at the flow rates corresponding to flow coefficients equal to 0.2, 0.4, 0.6, 0.8, and 1.0, provided that these values are lower than the free-blowing flow coefficient.

The flow fields for the whole fan were finally reconstructed in [5] using a commercial CFD code (FLUENT by Fluent Inc.). Unsteady numerical simulations of the selected fan configurations were performed using the RNG k-ε turbulence model and a ''sliding mesh'' rotating grid with about 100,000 cells. The results of these simulations were validated against the global and local experimental measurements collected in [2,3], showing that real performance and flow fields are reproduced with satisfactory accuracy [5].

4 Definition of a Normalized Stream Function

It was shown in [5] that it is not convenient to analyze the simulated flow fields according to the angular coordinate. In fact, the nonuniform distribution of the flow rate along the effective suction arc would make it difficult to evaluate the average values of the local quantities. Conversely, the introduction of a normalized stream function f (defined as illustrated in Fig. 5) allows

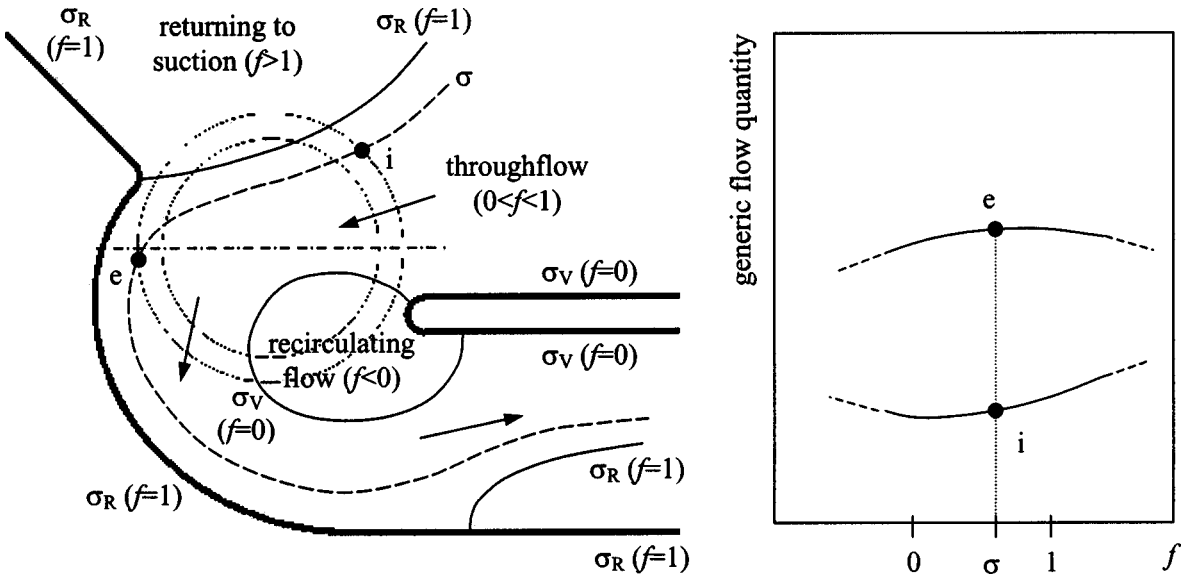

Fig. 5 Definition of the normalized stream function *f*

easier comparisons among different fan configurations or at different flow coefficients. The normalization of the stream function σ is done by assigning the value 0 to the streamline that coincides with the vortex wall and envelopes the recirculating flow ($\sigma = \sigma_V$), and the value 1 to the streamline that coincides with the rear wall ($\sigma = \sigma_R$). The value of f for a generic streamline σ is defined as

$$f(\sigma) = (\sigma - \sigma_V)/(\sigma_R - \sigma_V) \tag{4}$$

Consequently, the streamlines of the throughflow correspond to a number between 0 and 1, a streamline of the recirculating flow to a negative number, and a streamline of the portion of the flow that returns to suction to a number greater than 1.

Some characteristic quantities of the flow field along the external circumference of the impeller are plotted in Figs. 6 and 7 for a sample configuration (R2r-H1) and flow coefficient (0.4) to illustrate how hydraulic, volumetric, and total efficiencies can be evaluated. In both figures two values of the ordinate are associated with a single abscissa, since each of the represented streamlines crosses the impeller twice (see the example in Fig. 5 for a generic streamline σ). In Figs. 6 and 7, the lower value of the ordinate corresponds to the streamline entering the impeller, whereas the upper one corresponds to the streamline leaving the impeller.

Figure 6 shows the local total pressure coefficient (Ψ_t) along the external circumference of the impeller. At impeller inlet, the values of Ψ_t for the streamlines coming from suction are null ($f > 0$, lower values of ordinate), even if some perturbing effects due to blade motion appear. Therefore, the average value of Ψ_t for the throughflow streamlines at impeller exit ($0 < f < 1$, upper values of the ordinate) is the total pressure rise of the throughflow across the impeller and, apart from the viscous losses occurring between impeller exit and discharge section, across the fan itself. The total pressure of the streamlines that returns to suction is also raised by the impeller ($f > 1$, upper values of the ordinate), but this energy is completely lost. Finally, it can be observed that all the energy transferred to the recirculating streamlines is dissipated since the total pressure coefficient does not change across the impeller (upper and lower values of the ordinate are practically superimposed for $f < 0$).

Figure 7 shows the ratio between the tangential component of the absolute velocity (c_{u2}) and the peripheral speed u_2 along the

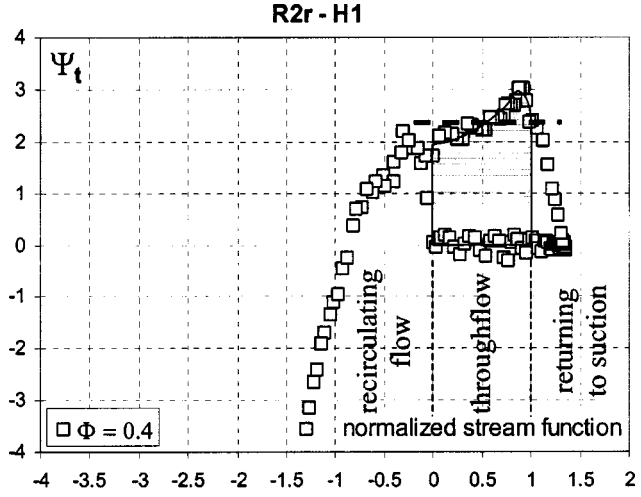

Fig. 6 Example of the local total pressure coefficient along the external circumference of the impeller

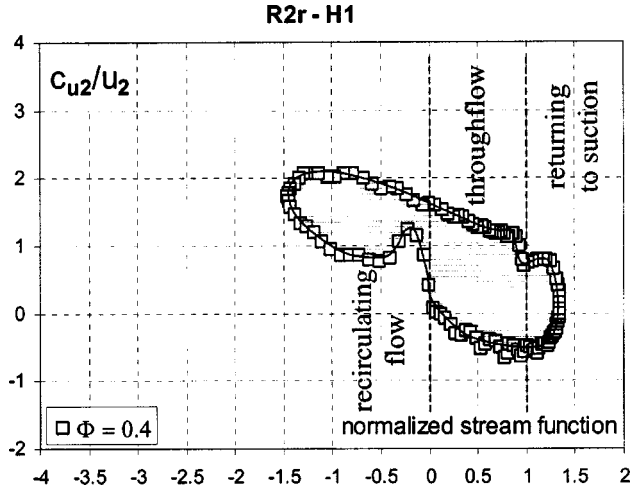

Fig. 7 Example of the ratio between the tangential velocity and the peripheral speed along the external circumference of the impeller

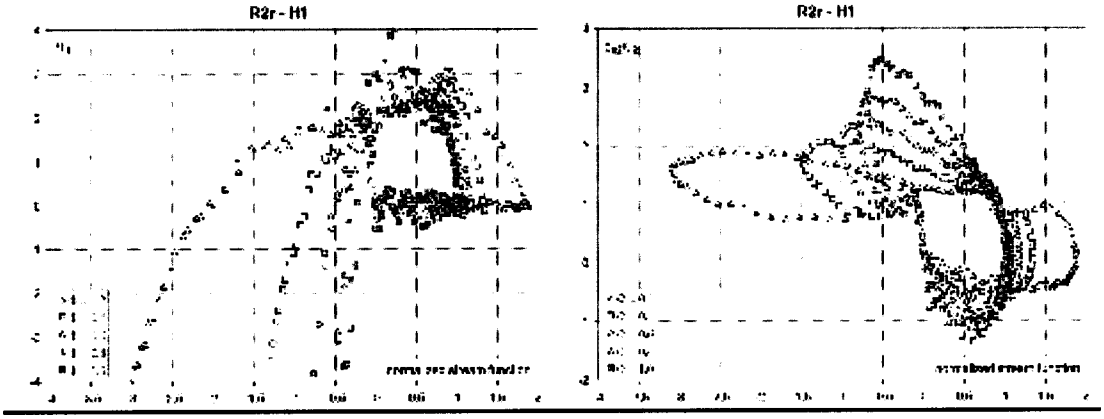

Fig. 8 The total pressure coefficient and the ratio c_{u2}/u_2 along the impeller external circumference at different flow coefficients for a sample configuration

external circumference of the impeller. The area bounded by the upper and lower values of the ordinate is the average of variation of c_{u2}/u_2 between impeller inlet and exit and is therefore a measure of the mechanical energy transferred from the impeller to the flow. Actually, the complete expression of the specific energy transferred to a single streamline is

$$e = c_{u2}{}^{\mathrm{II}}u_2 - c_{u1}{}^{\mathrm{II}}u_1 + c_{u1}{}^{\mathrm{I}}u_1 - c_{u2}{}^{\mathrm{I}}u_2 \tag{5}$$

but the contributions of the tangential components on the inner circumference of the impeller can be neglected since they almost annul each other.

The portions of mechanical energy that are transferred to the recirculating flow, the throughflow, and the flow returning to suction can be determined by dividing the area of the diagram along the abscissae $f=0$ and $f=1$. Volumetric efficiency, according to the definition given in Sec. 2, can be evaluated in Fig. 7 as the ratio between the area of the diagram between $f=0$ and $f=1$ (the mechanical energy transferred to the only throughflow) and the area of the overall diagram (the overall mechanical energy available). Hydraulic efficiency can be evaluated in Figs. 6 and 7 by comparing the average of the upper values of the ordinate for $0<f<1$ in Fig. 6 (the total pressure rise of the throughflow) and the area of the diagram between $f=0$ and $f=1$ in Fig. 7 (the mechanical energy transferred to the only throughflow). As already mentioned in Sec. 2, the product of the volumetric and the hydraulic efficiency is equal to the total efficiency, that is the ratio between the energy (total pressure) gained by the throughflow and the mechanical energy supplied by the impeller. Figure 8 shows how the local total pressure coefficient and the ratio c_{u2}/u_2 vary at different flow coefficients for the same sample configuration (R2r-H1).

5 Results of the Analysis

The concepts introduced in the previous section have been applied to the flow fields of the fan configurations considered in Sec. 3. The resulting estimations of the volumetric and hydraulic efficiencies are reported in Fig. 9, together with the total efficiency curves. Figure 10 shows the real (Ψ_t) and theoretical (Ψ_t/η_t) performance curves. A third curve (Ψ_t/η_{hyd}) is also plotted to separate the effects of volumetric and hydraulic energy losses.

Efficiency Curves. It is apparent that for a generic configuration the ascending–descending shape of the total efficiency curve is determined by the opposite trends of volumetric and hydraulic energy losses (Fig. 9).

Volumetric efficiency always increases with the throughput flow rate (Fig. 9). The energy associated with the flow returning to suction, and this portion of flow itself, quickly vanish when the flow coefficient is increased, whereas the unavoidable energy transfer to the recirculating flow is affected by a more complicated mechanism (Fig. 8). In fact, the stronger interaction between the vortex inside the impeller and the blade row due to the increased eccentricity and intensity of the vortex core makes the energy transferred to each recirculating streamline increase with the flow coefficient (see, e.g., Fig. 8). However, at the same time the number of such streamlines is reduced, so that the energy fraction associated with the recirculating flow increases less than proportionally to the energy fraction associated with the throughput flow (see Fig. 8 and [5]).

On the other hand, hydraulic efficiency always decreases with the throughput flow rate (Fig. 9) because the nonuniformity of the radial velocity profile along the suction arc becomes more marked as the flow coefficient grows. This results in higher radial velocities at the boundary with the recirculating flow, leading to higher hydraulic losses in the blade passages, and in lower radial velocities (higher incidence angles) in the portion of the suction arc adjacent to the rear wall, leading to stall phenomena (see also [3,5]).

In summary: At low flow coefficients, total efficiency is limited by the high volumetric losses due to both the significant fractions of the flow recirculating inside the impeller and returning to suction. At intermediate flow coefficients, a maximum of the η_t-Φ curve is found because of a substantial equilibrium between the decay of volumetric losses and the increase in hydraulic losses. At high flow coefficients, the further improvement of volumetric efficiency does not counterbalance the increasing hydraulic losses due to high radial velocities and stall, so that the total efficiency curve drops.

The highest total efficiencies are obtained using thick vortex walls matched with the small radial width rear wall (RE-S3H1 and RE-VE) because both volumetric and hydraulic efficiencies are at their maximum values, up to about 80% and over 50%, respectively (Fig. 9). In fact, the lower extension of the suction arc and the larger space occupied by the thick vortex wall itself are the key geometrical features that dramatically reduce volumetric losses and enhance hydraulic efficiency, limiting vortex eccentricity and strength and making the velocity profile more uniform.

Using thin vortex wall configurations, both volumetric and hydraulic efficiencies are penalized by the largest portion of the flow returning to suction and by the stronger and more eccentric recirculation caused by the small vortex wall thickness. In general, higher volumetric efficiencies are obtained using smaller radial width rear walls (+5 points from R3r to R2r and from R2r to RE, on average) and lower positions of the thin vortex wall (+1 point from H2 to H1, on average) (Fig. 9). This is because the fluid-dynamic equilibrium between the throughput and the recirculating flow does not allow the latter to expand too much inside the machine. The reduction in the flow returning to suction for higher

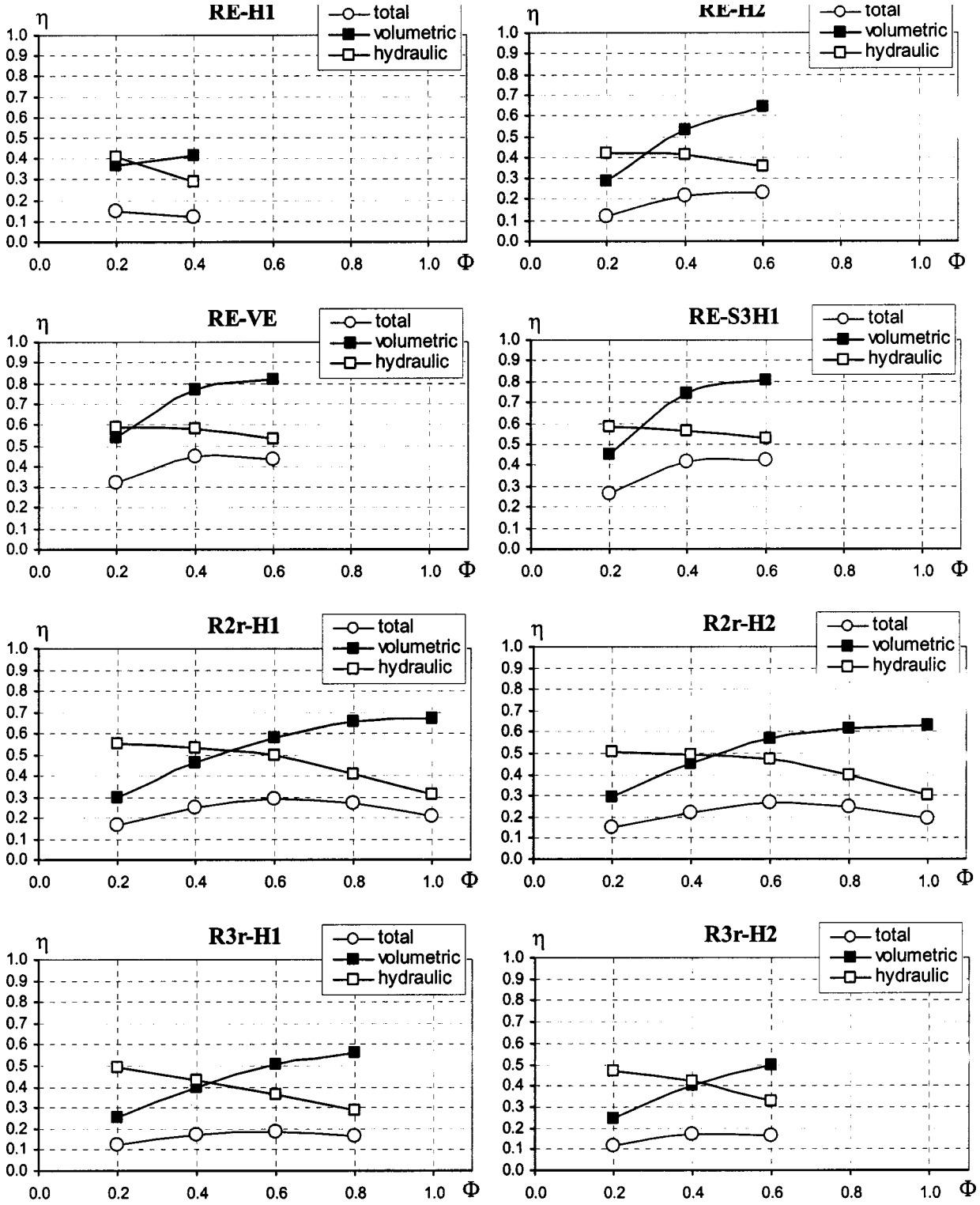

Fig. 9 Total efficiency and estimation of the volumetric and hydraulic efficiencies for the considered configurations at different flow coefficients

positions of the vortex wall seems to be only a secondary effect [5]. Hydraulic efficiencies rapidly drop with larger rear wall radial widths (−5 to −10 points from R2r to R3r) and higher positions of the thin rear wall (−1 to −5 points on average from H1 to H2). The drop becomes more marked as the rear wall radial width, the vortex wall height, and the flow coefficient increase (Fig. 9). In fact, all these factors cause an increase in the mean and/or local radial velocity across the impeller and/or the promotion of stall at lower flow rates [3,5]. The unfavorable combinations of the small radial width rear wall with the thin vortex wall (configurations RE-H1 and RE-H2) partially turn away from these trends because a strong and eccentric recirculating flow is confined in a small space in front of the vortex wall, reducing both volumetric and hydraulic efficiencies.

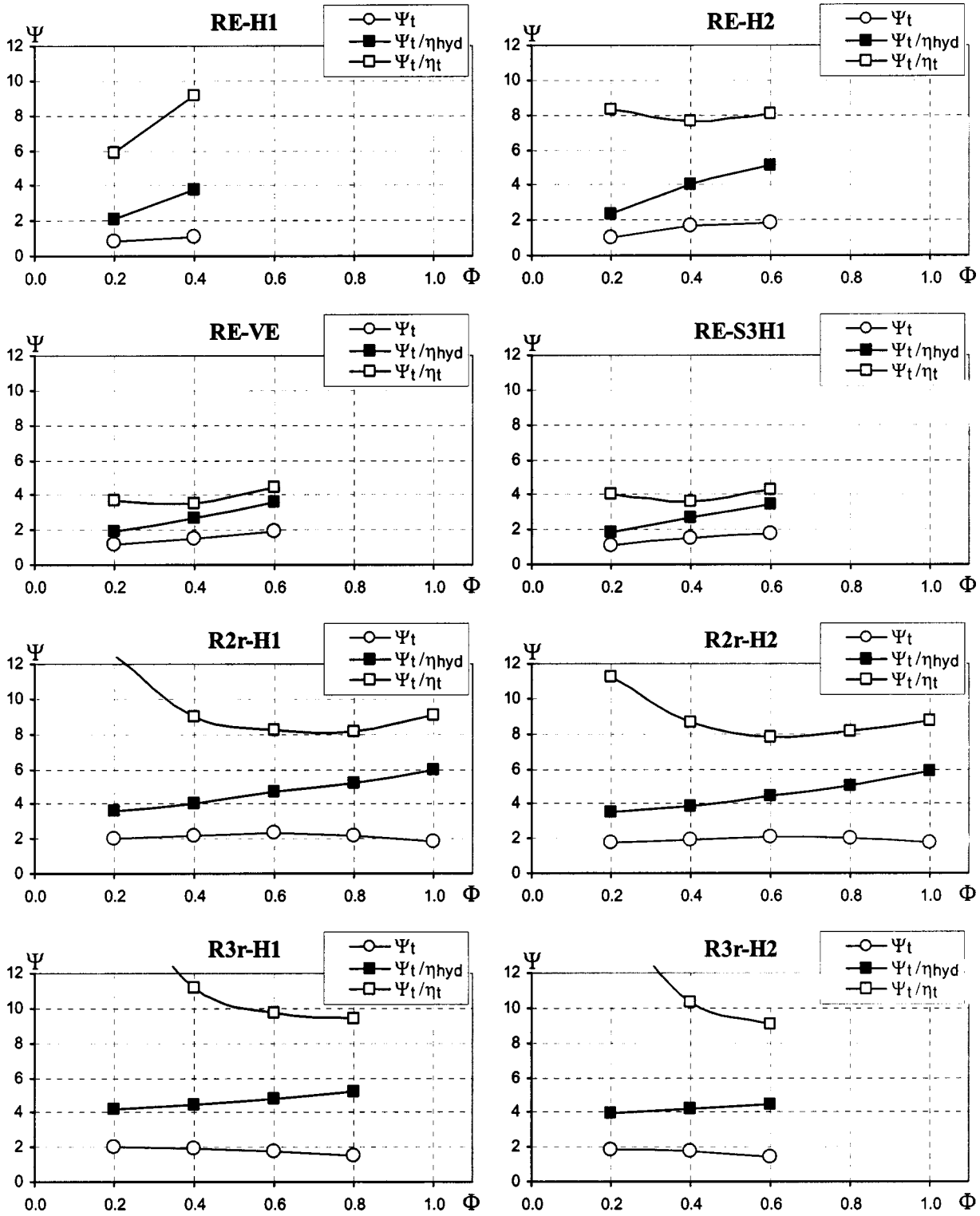

Fig. 10 Actual and theoretical performance curves of the considered configurations at different flow coefficients

Performance Curves. It is apparent in Fig. 8 that the *energy transferred by the impeller to the only throughflow* $(0<f<1)$ *increases almost linearly with the flow coefficient*. Figure 10 reveals that this relationship can be extended to all the considered configurations, since all the Ψ_t/η_{hyd} curves show an almost constant positive slope. This trend is in agreement with the predictions of the one-dimensional Eulerian theory, but it considers the energy losses of the throughput flow only (hydraulic efficiency). Contrary to Eck and Moore's analyses [7,8], volumetric losses are still to be added to obtain the overall energy supplied by the impeller (Ψ_t/η_t curve).

The slope and the intercept at zero flow rate of the Ψ_t/η_{hyd} curves mainly depend on the radial width of the rear wall (Fig. 10): Small radial widths correspond to lower intercepts and steeper slopes, and vice versa. This relationship can be explained considering that the energy available to the throughput flow

(Ψ_t/η_{hyd}) increases with the strength and the eccentricity of the vortex inside the impeller. In fact, according to the one-dimensional Eulerian theory, radial and then tangential components of velocities across the impeller increase when a stronger and more eccentric vortex forms, and so does the theoretical energy transfer between the impeller and the throughflow. Therefore, low intercepts and steep slopes of the Ψ_t/η_{hyd} curve are obtained using small radial width rear walls since vortex strength and eccentricity are limited at low flow rates but grow rapidly with the flow coefficient (see [3,5]). On the contrary, using larger radial widths, vortex strength and eccentricity are already higher at low flow rates and do not grow much with the flow coefficient. Secondary effects can be attributed to vortex wall height and thickness. Higher positions of the vortex wall slightly decrease both the slope and the intercept because, the rear wall being equal, more streamlines with a lower theoretical energy transfer available become part of the throughflow (see [5]). On the other hand, a thick vortex wall significantly decreases the slope of the curve since vortex strength and eccentricity increase at a slower rate versus the flow coefficient (see [3,5]).

The discovery of this archetypal theoretical curve, together with the analysis of hydraulic efficiency, finally allows us to explain how different shapes of the Ψ_t-Φ characteristic curves are obtained depending on the rear wall radial width (Fig. 10). For small radial widths of the rear wall, the vortex is forced to be not very strong and eccentric at low flow rates, and the available theoretical performance of the throughflow is not very high (Ψ_t/η_{hyd} near 2 at $\Phi=0.2$). Therefore, the total pressure coefficient cannot be much higher than 1, in spite of the highest hydraulic efficiencies obtained. As flow rate grows, the increase in the variation of the tangential components of the velocity overweights the small drop in hydraulic efficiency (that is still very high if a thick vortex wall is used) and results in an ascending characteristic curve. In configurations featuring an intermediate radial width rear wall, at low flow rates the vortex is already eccentric and strong enough to make a high theoretical performance available (Ψ_t/η_{hyd} near 3.5 at $\Phi=0.2$). Then, as flow rate grows, a substantial equilibrium occurs between the increasing theoretical performance and the more marked hydraulic drop, resulting in an almost constant characteristic curve. For large rear wall radial widths, the reduction in hydraulic efficiency becomes dramatic because of the high radial velocities and the insurgence of stall, and is not counterbalanced by the further increase in the theoretical throughflow performance (Ψ_t/η_{hyd} higher than 4 at $\Phi=0.2$). This results in a descending trend of the characteristic curve.

Higher positions of the thin vortex wall tend to make the characteristic curve more stable because the resulting flow fields are characterized by a lower theoretical throughflow performance Ψ_t/η_{hyd} and by lower values of hydraulic efficiency.

6 Conclusions

This study has presented a qualitative and quantitative analysis of energy losses in cross-flow fan operation. A representative set of fan configurations has been considered according to the main design parameters that were highlighted in the experimental investigations by the same group of authors. Experimental and numerical data on the corresponding flow fields at different flow coefficients have been analyzed to investigate the trends of performance and efficiency. A volumetric and an hydraulic efficiency have been defined to separate the different sources of the total energy losses. It was shown that these two efficiencies have an opposite behavior as flow rate increases, the volumetric one improving while the hydraulic one progressively decays. The separate effects of these energy losses on the theoretical performance has been examined and a common behavior of all the considered fan configurations has been found. This archetypal theoretical curve can be referred to as the only throughput flow rate, since the variation of volumetric losses is far too complicated to be included in a theoretical analysis. The throughflow theoretical performance, i.e., the energy transferred by the impeller to the only throughflow, shows a linear trend that is mainly affected by the rear wall radial width. This finding has finally allowed us to explain theoretically how different shapes of the characteristic curves can be obtained by varying this parameter, which can be regarded as the most significant in cross flow fan design.

Acknowledgments

The author wishes to thank Professor Andrea Lazzaretto and Professor Antonio Dario Martegani for the helpful discussions and their useful suggestions.

Nomenclature

c = absolute velocity (m/s)
D = diameter (m)
e = specific energy (J/kg)
f = normalized stream function
h = height (m)
L = axial length (m)
p = pressure (Pa)
Q = volumetric flow rate (m^3/s)
$\mathrm{Re}_D=u_2D_2\rho/\mu$ = Reynolds number
u = peripheral speed (m/s)
α = log spiral angle (deg)
β = angle of relative velocity (deg)
η = efficiency
μ = dynamic viscosity (kg/ms)
ρ = density (kg/m^3)
σ = stream function
$\Phi=\mathrm{Q}/(\mathrm{LD_2u_2})$ = flow coefficient
$\Psi=\Delta\mathrm{p}/(0.5\rho\mathrm{u_2^2})$ = pressure coefficient

Subscripts and superscripts

1 = internal
2 = external
I = first blade passage
II = second blade passage
d = discharge
hyd = hydraulic
R = rear wall
r = radial
t = total
th = theoretical
u = tangential component
V = vortex wall
vol = volumetric

References

[1] Lazzarotto, L., Lazzaretto, A., Macor, A., and Martegani, A. D., 2001, "On Cross-Flow Fan Similarity: Effects of Casing Shape," ASME J. Fluids Eng., **123**, pp. 523–531.
[2] Lazzaretto, A., Toffolo, A., and Martegani, A. D., 2003, "A Systematic Experimental Approach to Cross-Flow Fan Design," ASME J. Fluids Eng., **125**, pp. 684–693.
[3] Toffolo, A., Lazzaretto, A., and Martegani, A. D., 2004, "An Experimental Investigation of the Flow Field Pattern Within the Impeller of a Cross-Flow Fan," accepted for publication in Experimental Thermal and Fluid Science, available on-line at www.sciencedirect.com.
[4] Lazzaretto, A., 2003, "A Criterion to Define Cross-Flow Fan Design Parameters," ASME J. Fluids Eng., **125**, pp. 680–683.
[5] Toffolo, A., 2004, "On the Theoretical Link Between Design Parameters and Performance in Cross-Flow Fans: a Numerical and Experimental Study," accepted for publication in Computers and Fluids, available on-line at www.sciencedirect.com.
[6] Toffolo, A., Lazzaretto, A., and Martegani, A. D., 2004, "Cross-Flow Fan Design Guidelines for Multi-Objective Performance Optimization," J. Power Energy (PIME part A), **218**, pp. 33–42.
[7] Eck, B., 1973, *Fans*, Pergamon, New York.
[8] Moore, A., 1972, "The Tangential Fan—Analysis and Design," *Conference on Fan Technology and Practice*, 18–19 April, London, IMechE, pp. 66–82.
[9] Coester, R., 1959, "Theoretische und Experimentelle Untersuchungen an Querstromgeblase," Mitteilungen aus dem Institut fur Aerodynamic ETH, 28.
[10] Tramposch, H., 1964, "Cross-Flow Fan," ASME Paper No. 64-WA/FE-25.

[11] Ilberg, H., and Sadeh, W. Z., 1965, ''Flow Theory and Performance of Tangential Fans,'' Proc. Inst. Mech. Eng., **180**, Part 1, p. 19.
[12] Ikegami, H., and Murata, S. A., 1966, ''Study of Cross Flow Fan. I. A Theoretical Analysis,'' Technol. Rep. Osaka Univ., **16**, pp. 557–578.
[13] Yamafuji, K., 1975, ''Studies on the Flow of Cross-Flow Impellers—2nd Report, Analytical Study,'' Bull. JSME, **18**, No. 126, pp. 1425–1431.
[14] Porter, A. M., and Markland, E., 1970, ''A Study of the Cross Flow Fan,'' J. Mech. Eng. Sci., **12**, No. 6, pp. 421–431.
[15] Tuckey, P. R., Holgate, M. J., and Clayton, B. R., 1982, ''Performance and Aerodynamics of a Cross Flow Fan,'' International Conference on Fan Design and Applications, September 7–9, Guilford, England, Paper No. J3.
[16] Allen, D. J., 1982, ''The Effect of Rotor and Casing Design on Cross-Flow Fan Performance,'' International Conference on Fan Design and Applications, September 7–9, Guilford, England, Paper No. J1.
[17] Clayton, B. R., 1975, ''A Review and Appraisal of Crossflow Fans,'' Building Services Engineer, **42**, pp. 230–247.
[18] UNI 10531, Ventilatori Industriali-Metodi di Prova e Condizioni di Accettazione (in Italian), Milan, 1995.
[19] ISO 5801, Industrial Fans-Performance Testing using Standardized Airways, 1993.

P. K. Papadopoulos
e-mail: p.papado@des.upatras.gr

P. M. Hatzikonstantinou

Department of Engineering Science,
University of Patras,
GR 26500 Patras, Greece

Numerical Analysis of Fully Developed Flow in Curved Square Ducts With Internal Fins

The laminar incompressible flow in a curved square duct with two or four internal longitudinal fins is studied numerically with the SIMPLE method. The results show an increase of the friction factor depending on the fin height and the Dean number. The visualization of the flow reveals the existence of complex flow patterns in the transverse plane of the channel, where up to ten vortices are found to form. The effect of the curvature on the friction factor is examined and a functional relation for the latter is developed in terms of the Dean number and the fin height. [DOI: 10.1115/1.1792269]

Introduction

A large part of the applications of flow inside ducts in modern engineering is targeted for heat transfer, such as in heat exchangers, nuclear reactors, jet engines, etc. Due to its significance, this flow has been studied extensively in order to optimize the heat transfer rates. There are several ways to accomplish this and the most common are use of curved or helical ducts and use of fins inside the duct. Therefore a study of the hydrodynamic characteristics of the flow which occurs inside a curved square duct with longitudinal fins is considered useful to the design of heat exchanging apparatuses.

Studies of flow inside curved square and rectangular ducts as well as in straight ducts with internal fins can be found in the literature. Concerning the first class of problems, relevant works have been produced by Cheng et al. [1], Hwang et al. [2], and Ghia et al. [3] who have used numerical methods based on the stream function-vorticity formalism, Tangham [4] who employed the SIMPLE method, and Sakalis et al. [5] who employed the recently developed CVP method. Experimental data about developing and fully developed flows in curved square ducts have been published by Hille et al. [6] and Bara et al. [7]. Large attention has also been drawn to the bifurcations of the transverse velocities in a curved square duct (Winters et al. [8], Shantini et al. [9], Soh [10]). Regarding the problem of internally finned straight ducts, information can be found in the work of Sakalis et al. [11], where four symmetrical fins, each on every side of a square duct, are considered, and in Aggarwala et al. [12] who examined rectangular ducts with fins from opposite walls.

The curved duct flow far from the entrance is considered as fully developed due to the smooth surface and the constant curvature of the duct, as well as the range of the low Dean numbers considered. This hypothesis is supported by the numerical and experimental study of Mori [13] which is related with the flow in a curved circular duct and a helical tube with marginal pitch.

In the present study, fully developed flow in a curved square duct with and without fins was examined with use of the SIMPLE method. This can be done either by taking into account the upper or lower half of the duct's cross-section with symmetry boundary conditions imposed on the middle, or by considering the full cross-section. In our computations the second approach was followed. It has been stated by Bolinder [14] that when the whole cross-section is used, numerical instabilities are encountered appearing as an inability of the method to converge to solutions with four vortices in the secondary flow. In the present study instabilities occurred during the computational procedure, without, however, leading to nonconvergence. The solution converged to either two or four vortices, depending on the Dean number, until the method reached its limitations for high De.

Concerning the finned duct, calculations of the Dean number and of the friction factor were conducted for various fin heights and curvatures. Graphical illustrations of the secondary flow formations are presented, where due to the complex geometry many vortices exist. Furthermore, a functional relation for the friction factor of the curved square duct with four longitudinal fins is given in terms of the fin height and the Dean number.

Analysis

The problem under consideration is the steady, laminar, fully developed flow inside a curved square duct with internal longitudinal fins. For the study of the flow a toroidal coordinate system was used with its center positioned at the center of the cross-section as shown in Fig. 1, and the new coordinates are denoted by (X',Y',Z') with the corresponding velocities being (U,V,W). Thus the governing equations with the dimensionless variables which have been defined in the nomenclature can be expressed as follows: Continuity equation

$$\frac{\partial u}{\partial x}+\frac{\partial v}{\partial y}+\kappa J u=0 \tag{1}$$

Momentum equation in the x axis

$$\frac{\partial u^2}{\partial x}+\frac{\partial(uv)}{\partial y}=-\frac{\partial p}{\partial x}+\frac{\partial^2 u}{\partial x^2}+\frac{\partial^2 u}{\partial y^2}+\kappa J\frac{\partial u}{\partial x}-(\kappa J)^2 u+\kappa J(w^2-u^2) \tag{2}$$

Momentum equation in the y axis

$$\frac{\partial(uv)}{\partial x}+\frac{\partial v^2}{\partial y}=-\frac{\partial p}{\partial y}+\frac{\partial^2 v}{\partial x^2}+\frac{\partial^2 v}{\partial y^2}+\kappa J\frac{\partial v}{\partial x}-\kappa J u v \tag{3}$$

Axial momentum equation in the z axis

$$\frac{\partial(uw)}{\partial x}+\frac{\partial(vw)}{\partial y}=-J\frac{dp_a}{dz}+\frac{\partial^2 w}{\partial x^2}+\frac{\partial^2 w}{\partial y^2}+\kappa J\frac{\partial w}{\partial x}-(\kappa J)^2 w-2\kappa J u w \tag{4}$$

where $J=1/(\kappa x+1)$.

The boundary conditions applied in our computations are:

$$u,v,w=0 \quad \text{at the walls} \tag{5}$$

Contributed by the Fluids Engineering Division for publication in the JOURNAL OF FLUIDS ENGINEERING. Manuscript received by the Fluids Engineering Division January 13, 2003; revised manuscript received April 8, 2004. Associate Editor: I. Celik.

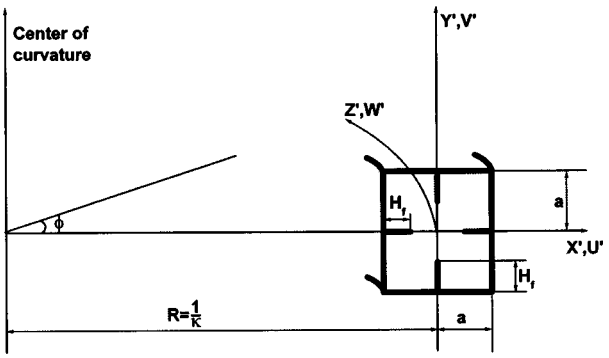

Fig. 1 Toroidal coordinate system

In internal flows for small transversal velocities the variation of the pressure in the transverse plain is small and its dependence on the axial direction can be ignored from the transverse momentum equations. Thus the pressure p_0 may be split into two parts, the axial part p_a and the transversal pressure distribution p [$p_0 = p_a(z) + p(x,y)$] and with the assumption of the fully developed flow it is concluded that the axial pressure gradient can be regarded as uniform over the cross-section and constant in the longitudinal direction. The mean axial velocity, which in the current nondimensional form coincides with the Reynolds number, is given by

$$\overline{w} = \frac{\int_A w\, dA}{\int_A dA} \tag{6}$$

where A is the area of the cross-section and $\mathrm{Re} = \overline{w}$.

The characteristic quantities of the flow, the Dean number, and the product of the friction factor with the Reynolds number are given by the formulas

$$\mathrm{De} = \mathrm{Re}\sqrt{\kappa}, \quad f\,\mathrm{Re} = -\left(\frac{dp_a}{dz}\right) \Big/ (2\overline{w}) \tag{7}$$

In the case of the duct with four fins of height $H=1$, the problem could be considered as that of four separated ducts without fins. In this case, if we indicate the quantities referring to each of the minor ducts by the subscript $\frac{1}{4}$ (e.g., $D_{h1/4}$ is the minor hydraulic diameter) and consider the case of a straight duct, then a relation can be deduced between the results for the finless duct and the one with fins of height $H=1$. If we denote the equivalent area of the duct by A_e, then

$$A_e = \frac{\pi D_h^2}{4} = 4\,\frac{\pi D_{h1/4}^2}{4} \Rightarrow D_h = 2D_{h1/4}$$

Thus, according to the present nondimensionalization, the relations amongst the main variables for the finless duct and the one with four fins of $H=1$ are as follows:

$$\frac{dp_a}{dz} = 8\left(\frac{dp_a}{dz}\right)_{1/4}, \quad \overline{w} = 2\overline{w}_{1/4}, \quad \kappa = 2\kappa_{1/4},$$

$$\mathrm{De} = 2\sqrt{2}\,\mathrm{De}_{1/4}, \quad f\,\mathrm{Re} = 4 f\,\mathrm{Re}_{1/4} \tag{8}$$

In a similar manner for the duct with two fins on opposite walls, it is found that

$$D_h = \sqrt{2}D_{h1/2}, \quad \frac{dp_a}{dz} = 2\sqrt{2}\left(\frac{dp_a}{dz}\right)_{1/2}, \quad \overline{w} = \sqrt{2}\overline{w}_{1/2},$$

$$\kappa = \sqrt{2}\kappa_{1/2},$$

$$\mathrm{De} = \sqrt[4]{8}\,\mathrm{De}_{1/2}, \quad f\,\mathrm{Re} = 2 f\,\mathrm{Re}_{1/2} \tag{9}$$

Table 1 Friction factor product for a straight duct with various fin heights

H	f Re present	f Re Ebadian [17]	% Divergence
0	14.2	14.26	0.4
0.125	15.0	15.28	1.8
0.25	17.75	18.28	2.9
0.375	22.76	23.63	3.7
0.5	30.56	31.88	4.1
0.625	40.79	42.53	4.1
0.75	50.55	52.34	3.4
1	56.53	56.92	0.7

Solution and Accuracy

The governing equations were solved according to the SIMPLE method in the finite volume formalism with use of a staggered grid (Patankar [15]). The convection and diffusion terms were discretized with the secondorder central differences scheme. For the solution of the uncoupled Eqs. (2)–(4) the successive line under-relaxation (SLUR) solver was adopted together with the well-known tridiagonal matrix algorithm (TDMA). Convergence of the iteration procedure was achieved when the following criterion was satisfied for all nodes:

$$\frac{\|\phi_{ij}^{k+1} - \phi_{ij}^{k}\|_\infty}{\|\phi_{ij}^{k+1}\|_\infty} \leqslant 10^{-5} \tag{10}$$

where ϕ stands for velocities u, v, w, the subscripts i, j represent the x and y coordinates and the superscript k is the kth iteration. It was necessary to use an underrelaxation factor ranging between 0.3 and 0.1 for the momentum and pressure correction equations in order to make the solution converge.

In the computations a grid of 46×46 control volumes was employed for the cross-section. To assure the adequacy of the mesh size, a comparison is made with the data found by Papadopoulos et al. [16] where a curved square duct is examined with an identical method but with different grid sizes. The mean deviations between the present results and the ones obtained with a 60×60 and a 30×30 grid are 0.5 and 0.85%, respectively.

In order to validate our results for the finned duct, computations were conducted for a straight duct with four symmetrical fins by adopting a large value for the radius of curvature ($r=10^9$). These results for the product f Re along with the ones found in Ebadian et al. [17] are shown in Table 1. The maximum deviation that occurs is 4.1%. In Table 2 the Dean numbers of the flow in a curved square duct without fins are presented for various values of the curvature and the pressure gradient. These results are compared with data found by Sakalis et al. [5], which have been obtained by the CVP method and a maximum deviation of 4.4% is observed for the cases of $\kappa=0.1$.

Concerning the curved finned duct, an indirect method of validating our results is by comparing the characteristics of the flow in a channel with two horizontal fins from opposite walls of height $H=1$, with the results for a curved rectangular duct of ratio b/a

Table 2 Dean number results for various curvatures and axial pressure gradients, when $H=0$

κ	dp_a/dz	Re present	De present	De Sakalis [5]	% Divergence
0.01	−19,000	553.6	55.36	55.15	0.4
0.01	−40,000	1033.8	103.38	101.6	1.7
0.01	−70,000	1534.7	153.47	151.4	1.3
0.01	−110,000	2156.6	215.66	211.5	1.9
0.1	−50,000	918.0	290.3	277.46	4.4
0.1	−55,000	987.4	312.23	298.55	4.4
0.25	−25,000	450.7	225.3749	231.15	2.6
0.25	−30,000	516.9	258.442	264.08	2.2

Table 3 Reynolds numbers for a curved square duct with two fins of height $H=1$ (present) and a curved rectangular duct of aspect ratio 0.5 (Cheng [1]), for $\kappa=0.01$

dp_a/dz	Re present	Re Cheng [1]	% Divergence
−5000	143.2	160	10.5
−50,000	1075.4	1126	4.5
−90,000	1721.2	1766	2.5
−110,000	2012.4	2007	0.2

$=0.5$, where b is the height and a the length of the tube. Information about the latter can be found in the work of Cheng et al. [1]. It is however necessary to transform our variables to the nondimensional form for a single duct, as in Cheng et al. [1], by using the relations (9). The corresponding results for the Reynolds number are presented in Table 3, for $\kappa=0.01$ and varying axial pressure gradient and it is seen that a maximum deviation of 10.5% is found for low Re which, however, gradually decreases and good agreement is observed for high Reynolds numbers.

Apart from the results for the Dean and the Reynolds numbers, it is crucial to investigate the validity of our computations regarding the secondary velocities' formations since complex cross-sectional flow patterns are predicted for the finned curved duct. This is done by examining the results for the bifurcation points of the flow in a curved square duct that is due to the balance between the centrifugal forces and the axial pressure gradient. Thus in Table 4 we present the Dean numbers of the original appearance of the four vortices in the cross-sectional plane for various values of the curvature. The present results are compared with others found in the literature.

Results and Discussion

The effects of the Dean number and the fin height on the friction factor for curvatures $\kappa=0.01$, $\kappa=0.1$, and $\kappa=0.25$ can be seen in Figs. 2–4, respectively. It is observed that the friction factor increases for greater fin heights which is expected, for enlargement of the internal surface area of the duct yields to the development of larger shear stresses. It is also observed that, in general, increase of the Dean number results in an increase of the friction factor. However, for fin heights $H=0$ and $H=0.25$, it is seen that discontinuities exist in the curves, which indicate the transition between different cross-sectional flow patterns. For the finless duct ($H=0$) this phenomenon is the well-studied problem of the secondary flow bifurcations and it is observed by the appearance of an additional pair of vortices in the initial two vortices structure after a critical Dean number. A similar behavior is observed in the case of fin height $H=0.25$.

In order to comprehend these results it is necessary to visualize the secondary flow and this is done in Figs. 5–8. Figures 5*a* and 5*b* depict the secondary velocities in vector form for a finless duct before (De=55) and after (De=153) the bifurcation of the solution. The cross-sectional flow patterns for $H=0.25$ are shown in Figs. 6*a* and 6*b* for De=130 and 204, respectively. It is observed

Table 4 Dean numbers of the first bifurcation point of the secondary flow from two to four vortices

Reference	κ	De	De present	Difference %
Shantini [9]	0.01	127	122	5.9
Ghia [3]	0.01	125	122	2.5
Sakalis [5]	0.01	118	122	3.2
Cheng [1]	0.01	202	122	39.6
Winters [8]	0.04	136	125	8.9
Bolinder [13]	0.04	131	125	4.8
Bara [7]	0.066	130	127	2.4
Soh [10]	0.155	130.2	137	4.9
Hille [6]	0.155	150	137	9.5
Bolinder [13]	0.2	142.2	147	4.6

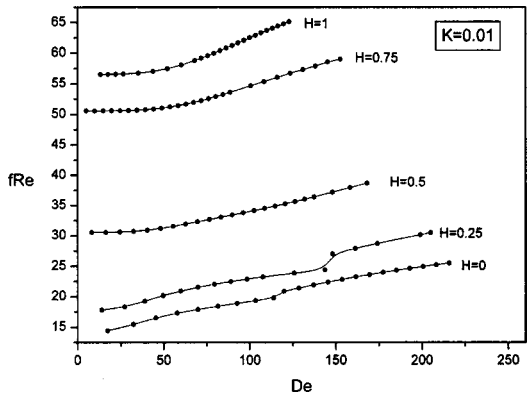

Fig. 2 Friction factor variation with De for curvature $\kappa=0.01$

that due to the limited height of the fins, the flow continues to behave in general like the one in the finless duct by altering between two and four main vortices beyond a certain De. However, it is noted that additional small vortices appear in the inner half of the duct near the inner horizontal and the vertical fins, originating from the backflow created by the fins. Figures 7*a* and 7*b* depict the secondary velocities' vector plots for $H=0.5$ and De=73,150 respectively. Since the fin height has, in this case, increased so as to be comparable to the dimensions of the duct, it is seen that it plays an important role in the formation of the flow behavior. The cross-section of the duct seems to be separated in four minor regions even for low De. Each of them consists of two counterrotating vortices whose magnitude increases with De. This is particularly true for the outer vortex of the flow which, for low De, is confined to the area near the outer horizontal fin, but as De rises it

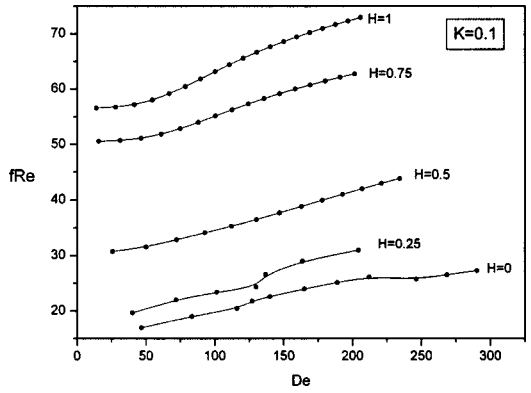

Fig. 3 Friction factor variation with De for curvature $\kappa=0.1$

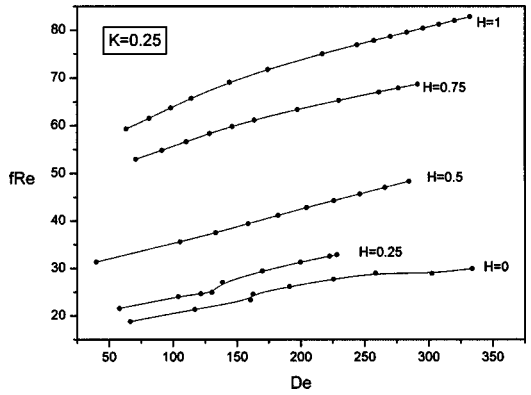

Fig. 4 Friction factor variation with De for curvature $\kappa=0.25$

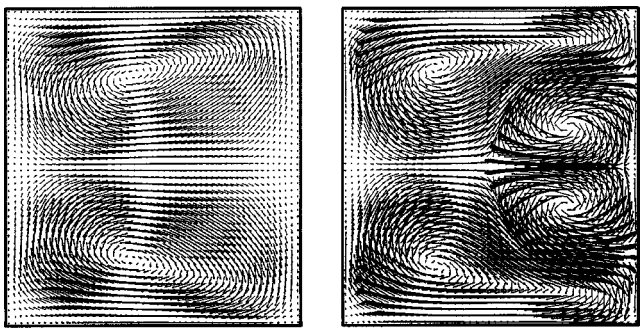

Fig. 5 Secondary velocities' vector plot for (*a*) De=55, H=0 and (*b*) De=153, *H*=0

is enlarged and ends up to occupy half of the quarter of the duct. These regions continue to exist throughout the breadth of Dean numbers that were computed, and, apart from the backflow vortices in the inner side of the upper and lower fins, no other structural changes were detected. In Fig. 8 the case of $H=0.75$ is presented for De=158. The flow behavior here is dominated by the effect of the fins, thus appearing as four separated pairs of counterrotating vortices. The only link among them is the additional pair of vortices that is seen in the middle area of the cross-section.

After this investigation of the various secondary flow patterns, a closer examination of Figs. 2–4 is imminent. First, we consider the case for $H=1$ and observe that the curves for the three values of the curvature are smooth and present no discontinuities. The case of $H=1$ is the one where the duct is separated in four distinguished parts. Although the flow in each part is identical to the flow in a curved finless duct, no bifurcation phenomena were

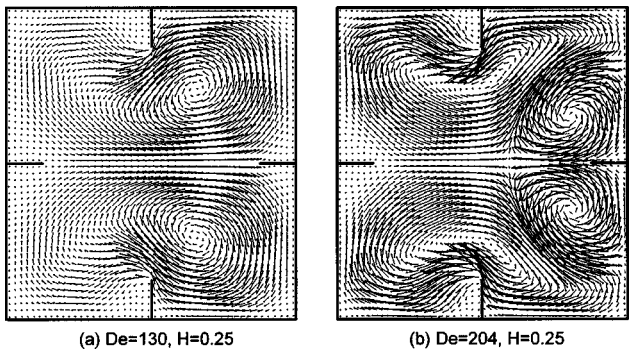

Fig. 6 Secondary velocities' vector plot for (*a*) De=130, *H*=0.25 and (*b*) De=204, *H*=0.25

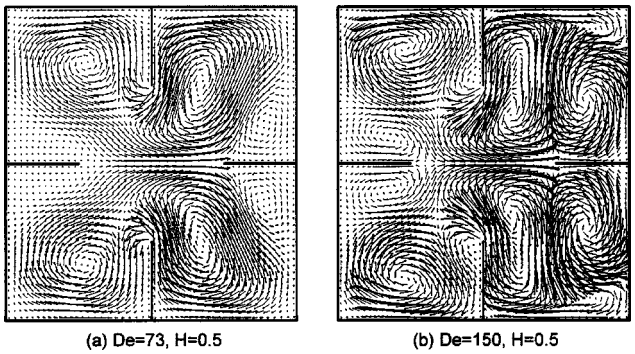

Fig. 7 Secondary velocities' vector plot for (*a*) De=73, *H*=0.5 and (*b*) De=150, *H*=0.5

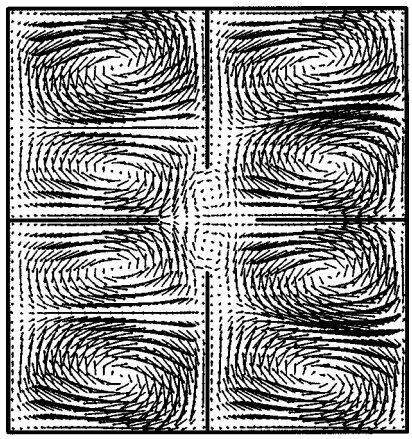

Fig. 8 Secondary velocities' vector plot for De=158, *H*=0.75

detected due to the low De that was reached. According to relation (8), the mean velocity computed in the whole duct is approximately double compared to that of each of the minor ducts and the corresponding curvature is approximately half. It is noted that although relation (8) stands only for straight ducts, for the curved channel the deviation, which is due to the slightly altered curvatures of the inner and outer ducts, is small enough to give indicative results. Therefore, after taking into account that the bifurcation appears near De>122 (Table 4) in the four minor ducts, using Eq. (8), the bifurcation is expected to first appear for De over 350.

The diagrams under consideration also show the effect of the fin height on the friction factor. It is seen that f Re increases by about 19% between the finless duct and the $H=0.25$ case, by about 48% from $H=0.25$ to $H=0.5$, by 58% from $H=0.5$ to $H=0.75$, and by approximately 14% for fins close to $H=1$. These facts can be seen more clearly in Fig. 9 where the friction factor is plotted against the fin height for several Dean numbers. It is observed that the curve remains unchanged and it is just shifted to greater values of f Re for increasing De. The following functional equation is proposed for the product of the friction factor f Re for Dean numbers lower than 350 and for the complete range of fin heights, including $H=0$:

$$f\,\mathrm{Re} = 13.6345 + 44.551 \cdot e^{-4.85\cdot(-0.935+H)^2} - (30 + 82H - 120H^2 + 64H^3)e^A \tag{11}$$

where

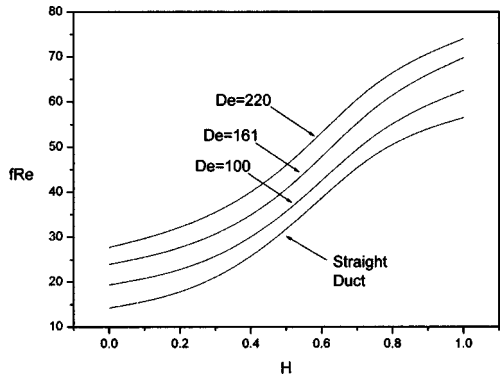

Fig. 9 Friction factor versus fin height for various Dean numbers

Table 5 Numerical results for varying fin height, curvature, and axial pressure gradient

H	κ	dp_a/dz	Re	De	f Re	fc/fs	
0	0.01	−15,000	454.47	45.45	16.5	1.16	
0	0.01	−80,000	1694.6	169.47	23.6	1.66	
0	0.01	−110,000	2156.6	215.66	25.5	1.8	
0.25	0.01	−15,000	389.3	38.93	19.27	1.09	
0.5	0.01	−15,000	245	24.5	30.61	1.01	
0.5	0.01	−80,000	1146.2	114.62	34.9	1.14	
0.5	0.01	−100,000	1372.8	137.28	36.42	1.19	
0.75	0.01	−15,000	148.3	14.83	50.56	1	
0.75	0.01	−95,000	885.9	88.59	53.61	1.06	
1	0.01	−15,000	132.6	13.27	56.54	1	
1	0.01	−110,000	897.9	89.79	61.25	1.08	
1	0.01	−160,000	1228.2	122.83	65.13	1.15	
							fRe increase from κ=0.01
0	0.1	−15,000	366.9	116.02	20.4	1.44	23.6%
0	0.1	−50,000	918	290.3	27.23	1.91	
0.25	0.1	−15,000	321	101.51	23.36	1.33	21.2%
0.5	0.1	−15,000	228.4	72.23	32.83	1.07	6.8%
0.5	0.1	−65,000	740.9	234.26	43.87	1.44	
0.75	0.1	−15,000	146.7	46.4	51.11	1.01	1.1%
0.75	0.1	−80,000	637.7	201.66	62.72	1.24	
1	0.1	−15,000	131.2	41.5	57.15	1.01	
1	0.1	−95,000	651.1	205.9	72.95	1.29	
							fRe increase from κ=0.1
0	0.25	−15,000	320.85	160.43	23.38	1.64	14.6%
0	0.25	−40,000	667.5	333.78	29.96	2.1	
0.25	0.25	−15,000	277.1	138.54	27.07	1.54	15.9%
0.5	0.25	−15,000	210.6	105.3	35.61	1.17	8.5%
0.5	0.25	−55,000	569.1	284.53	48.32	1.58	
0.75	0.25	−15,000	141.5	70.79	52.97	1.05	3.4%
0.75	0.25	−80,000	582.4	291.2	68.68	1.36	
1	0.25	−15,000	126.5	63.26	59.28	1.04	
1	0.25	−110,000	664.2	332.12	82.8	1.46	

$$A = -\frac{231 + 586H - 864H^2 + 416H^3}{35 + 194H - 672H^2 + 544H^3 + \mathrm{De}}$$

The mean deviation of the above equation with the present results is 1.57% and the maximum is 6.59% for the case of De=290, $H=0$. It is noted that although the maximum deviation is over 5%, a closer agreement with the numerical results could not be achieved due to the nature of the problem. The transition between the secondary flow patterns propels a sudden change of the friction factor. A more accurate equation would require knowledge of the exact bifurcation points for the whole range of κ, which is considered unnecessary since the above function is accurate enough to be applicable for most design purposes.

Another interesting aspect of the flow in a curved finned duct is the effect of the curvature alone, on the flow characteristics. Examination of Figs. 2–4 shows that for large fin heights, over $H=0.25$, the curves of f Re for κ=0.01 and varying De are concave pointing downwards. For larger κ this behavior is altered and eventually for κ=0.25 the curves become concave pointing upwards. The dependence of f Re on the curvature, however, cannot be fully understood from the examination of the Dean number alone as this similarity parameter depends on both κ and the axial pressure gradient in an inseparable way. Thus it is considered useful to investigate the friction factor product for constant pressure gradient and varying curvature. In Table 5 results of Re, De, and f Re are presented for various values of the fin height, the curvature, and the axial pressure gradient. The last column presents the increase of the friction factor for constant $dp_a/dz=-15{,}000$, for fin heights $H=0$, 0.25, 0.5, 0.75, and increasing curvature. It is seen that for no fins or low fin heights there is an important increase of f Re of over 20% as the curvature increases from κ=0.01 to κ=0.1. This percentage is reduced to about 15% when the results for κ=0.1 and κ=0.25 are compared. The same behavior is observed for larger fins where the augmentation of f Re from κ=0.01 to κ=0.1 is 6.8% for $H=0.5$ and 1.1% for $H=0.75$. When the two larger curvatures κ=0.25 and κ=0.1 are compared the increase of fRe is 8.5% for $H=0.5$ and 3.4% for $H=0.75$. Thus it is concluded that f Re increases more rapidly for small curvatures in small fin flows. The opposite is true for large fin cases. Furthermore, the dependence of f Re on the curvature is more intense for $H=0$ and it gradually fades for increasing fin height.

In order to examine the relative contribution of the horizontal and vertical fins to the flow, computations where made for a duct with two fins on opposite walls. Table 6 is enlightening on this matter as it shows that the two pairs have almost identical effect on the flow. It is observed that generally the horizontal fins produce a greater friction factor than the vertical, but the maximum difference is of only 5.5% for the case of $H=0.5$. This conclusion is in agreement with the results of Cheng et al. [1] for curved

Table 6 Numerical results for two and four fin flows

			Two horizontal fins		Two vertical fins		Four fins	
H	κ	dp_a/dz	De	f Re	De	f Re	De	f Re
0.25	0.1	−15,000	105.9	22.39	107.72	22.01	101.5	23.01
0.5	0.1	−30,000	150.48	31.52	159.29	29.77	130.11	36.45
0.75	0.1	−20,000	92.63	34.13	95.4	33.14	61	51.83

rectangular ducts, where there are very small differences between the cases of aspect ratios $b/a=0.5$ and $b/a=2$, with b being the height and a the length of the duct. Therefore, if a two-fin duct is to be used in an application, it is of minor importance whether the fins are located in the vertical or the horizontal walls. Finally, it is seen from Table 6 that for low fin heights, the friction factor of the four fins case is only 4% higher than the corresponding one for two fins, whereas for $H=0.75$ the increase is approximately 53%.

Conclusions

The friction factor increases for increasing Dean numbers and fin heights. The secondary flow for ducts with small fins resembles structurally that of the finless duct, but as the height of the fins increases to values of $H=0.5$ and higher, the cross-section is gradually divided to four autonomous regions. Concerning the contributions of the horizontal and vertical fins to the friction factor, they are almost identical, so it is concluded that they influence equally the characteristic quantities of the flow.

Nomenclature

a = half width or height of square channel
A = area of the cross-section $4a^2$
A_e = equivalent area of the cross-section $\pi D_h^2/4$
De = Dean number Re $\sqrt{\kappa}$
D_h = hydraulic diameter $4A/8a=2a$
dp_a/dz = dimensionless axial pressure gradient
f = friction factor
H_f = dimensionfull fin height
H = dimensionless fin height H_f/a
J = the term $1/(\kappa x+1)$ in Eqs. (1)–(4)
P_0 = pressure
p_0 = dimensionless pressure $P_0/(\rho\nu^2/D_h^2)$
p = dimensionless transversal pressure distribution
R = radius of curvature
Re = Reynolds number $(=\overline{w})$
U, V, W = velocity components in X', Y', Z' axes accordingly
u, v, w = dimensionless velocity components in X', Y', Z' axes accordingly $(U,V,W)/(\nu/D_h)$
$\overline{w}$ = average dimensionless axial velocity $\int_A w\,dA/\int_A dA$
X', Y', Z' = toroidal coordinates
x, y, z = dimensionless coordinates $(X',Y',Z')/D_h$

Greek symbols

κ = dimensionless curvature D_h/R
ν = kinematic viscosity
ρ = density

Subscripts

1/4 = reference to each of the four minor ducts in the $H=1$ fin height
1/2 = reference to each of the two minor ducts in the $H=1$ fin height for two fins

References

[1] Cheng, K. C., Lin, R. C., and Ou, J. W., 1976, "Fully Developed Laminar Flow in Curved Rectangular Channels," ASME J. Fluids Eng., **98**, pp. 41–48.
[2] Hwang, G. J., and Chao, C. H., 1991, "Forced Laminar Convection in a Curved Isothermal Duct," ASME J. Heat Transfer, **113**, pp. 48–56.
[3] Ghia, K. N., Ghia, U., and Shih, C. T., 1987, "Study of Fully Developed Incompressible Flow in Curved Ducts Using a Multigrid Technique," ASME J. Fluids Eng., **109**, pp. 226–235.
[4] Thangum, S., and Hur, N., 1990, "Laminar Secondary Flows in Curved Rectangular Ducts," J. Fluid Mech., **217**, pp. 421–440.
[5] Sakalis, V. D., and Hatzikonstantinou, P. M., 2002, "Predictions and Accuracy of the CVP Numerical Method for the Developed Laminar Flow in Curved Ducts," in Proceedings of the 4th GRACM Congress on Computational Mechanics, University of Patras, pp. 1400–1406.
[6] Hille, P., Vehrenkamp, R., and Schulz-Dubois, E. O., 1985, "The Development and Structure of Primary and Secondary Flow in a Curved Square Duct," J. Fluid Mech., **151**, pp. 219–241.
[7] Bara, B., Nandakumar, K., and Masliyah, J. H., 1992, "An Experimental and Numerical Study of the Dean Problem: Flow Development Towards Two-Dimensional Multiple Solutions," J. Fluid Mech., **224**, pp. 339–376.
[8] Winters, K. H., 1987, "A Bifurcation Study of Laminar Flow in a Curved Tube of Rectangular Cross-Section," J. Fluid Mech., **180**, pp. 343–369.
[9] Shantini, W., and Nandakumar, K., 1986, "Bifurcation Phenomena of Generalized Newtonian Fluids in Curved Rectangular Ducts," J. Non-Newtonian Fluid Mech., **22**, pp. 35–59.
[10] Soh, W. Y., 1988, "Developing Fluid Flow in a Curved Duct of Square Cross-Section and Its Fully Developed Dual Solutions," J. Fluid Mech., **188**, pp. 337–361.
[11] Sakalis, V. D., and Hatzikonstantinou, P. M., 2001, "Laminar Heat Transfer in the Entrance Region of Internally Finned Square Ducts," ASME J. Heat Transfer, **123**, pp. 1030–1034.
[12] Aggarwala, B. D., and Gangal, M. K., 1976, "Heat Transfer in Rectangular Ducts With Fins From Opposite Walls," Z. Angew. Math. Mech., **56**, pp. 253–266.
[13] Mori, Y., and Nakayama, W., 1965, "Study on Forced Convective Heat Transfer in Curved Pipes," Int. J. Heat Mass Transfer, **8**, pp. 67–82.
[14] Bolinder, C. J., 1993, "Numerical Visualization if the Flow in a Helical Duct of Rectangular Cross-Section," Exp. Numer. Flow Visual. ASME, **172**, pp. 329–338.
[15] Patankar, S. V., 1980, *Numerical Heat Transfer and Fluid Flow*, McGraw–Hill, New York.
[16] Papadopoulos, P. K., and Hatzikonstantinou, P. M., 2002, "Effects of Various Numerical Methods on the Formation of the Secondary Flow in a Curved Square Duct," in Proceedings of the 4th GRACM Congress on Computational Mechanics, edited by D. T. Tsahalis, University of Patras, pp. 750–758.
[17] Ebadian, M. A., and Dong, Z. F., 1998, "Forced Convection, Internal Flow in Ducts," in *Handbook of Heat Transfer*, W. M. Rohsenow, J. P. Hartnett, and Y. I. Cho, Eds., McGraw–Hill, New York, pp. 5.101–5.105.

A Simplified Model for Determining Interfacial Position in Convergent Microchannel Flows

D. L. Hitt[1]
e-mail: darren.hitt@uvm.edu

University of Vermont,
Department of Mechanical Engineering,
Burlington, VT 05405

N. Macken
Swarthmore College,
Department of Engineering,
Swarthmore, PA 19081

Previous experimental and computational studies have indicated that interfaces formed in steady, converging microchannel flows with similar liquids tend to be planar in nature under a variety of conditions relevant to micro-scale flows, including MEMS/microfluidic devices and even microcirculatory blood flows. Assuming a planar interface, we have developed an analytical framework to predict the fully developed interfacial location downstream of a convergence of identical microchannels. Results have been obtained for microchannels having rectangular, elliptical/circular and triangular cross-sections as a function of the inlet flow ratio. Two-dimensional results have also been obtained for fluids having unequal viscosities. Good agreement is found between this model and 3-D numerical simulations and experimental measurements provided that the flow inertia remains sufficiently small (Re≲10, typically). Where valid, application of this analytical, planar interface method represents a significant decrease in computational effort when compared to using CFD to determine interfacial positions. [DOI: 10.1115/1.1792272]

1 Introduction

Many microfluidic applications involve the control and manipulation of flows through networks of converging and/or diverging junctions. Flow branching is typically used to deliver specific quantities of fluid (or fluids) to various locations in the system whereas converging flows are often associated with mixing processes. An intrinsic quantity that is often used in analyzing converging/diverging flows is the ''separation surface.'' The separation surface can be defined as the collection of streamlines that acts as a division between each inlet component in the downstream flow. For single fluid flows, the separation surface is a virtual one; however, for multicomponent flows the separation surface is a physical interface. The design of microfluidic systems that feature flow branches and/or junctions requires knowledge of the position (and possibly the shape) of the separation surface for various hydrodynamic and geometric parameters. The separation surface can be determined numerically using standard computational fluid dynamics (CFD) packages and with a degree of computational effort.

In this work, we develop a simple analytical framework for predicting the position of a separation surface for convergent flows downstream of a microchannel junction under the assumptions that (1) the flow is fully-developed and steady; (2) the fluids are miscible (i.e., no surface tension); (3) the inlet and outlet branches are of identical cross-section; (4) the flow inertia is ''sufficiently small'' (Re≲10, typically); and (5) the separation surface is planar. Indeed, the key assumption lies in the planar nature of the separation surface whose validity, in turn, hinges on the other assumptions. The consequences of failing to satisfy these constraints are discussed later in the paper (Sec. 6). Assuming that the Reynolds numbers are $\sim O(1)$ the flow rapidly becomes fully-developed downstream of the junction. The solution obtained is therefore valid except for a small region extending a few channel diameters downstream of the junction. The apparently restrictive constraint of a planar interface is shown to yield remarkably good predictions of the interfacial position under hydrodynamic conditions and channel cross-sectional geometries commonly found in micro-scale flows, including MEMS/microfluidic devices [1] and even microcirculatory blood flows [2].

Support for the planar interface assumption can be found in the experimental and computational literature. In macro-scale dye studies, Rong and Carr [3] showed that converging low Reynolds number flows yielded a planar interface for circular channels of equal diameters. Using laser-scanning confocal microscopy, Hitt and co-workers have performed three-dimensional imaging of the separation surface formed between converging flows in microchannels having D-shape [4,5] and rectangular cross-sections [6]. In cases of identical converging fluids and at Reynolds numbers of $\sim$O(1), they reported a nearly planar interface when the inlet cross-sections were equal. Further, it was observed that even when the inlet fluid viscosities differed by as much as 8:1 there was only a minor curvature induced in the separation surface. Reports in the computational literature also indicate that a nearly planar separation surface results provided the inlet diameters are of equal size [7,8]. Clearly the literature indicates that inlet diameter ratios of unity or nearly so are necessary for the validity of the planar assumption. The low Reynolds number assumption is also needed to avoid a significant interfacial curvature from forming when the flows merge.

In this study we present analytic solutions for the planar separation surface position formed between converging flows in microchannels of circular/elliptical, rectangular/square and equilateral triangular cross-sections. For identical inlet fluids the separation surface position is computed as a function of the inlet volumetric flow ratio. Rectangular and triangular geometries were selected owing to their relevance to MEMS/microfabrication techniques and the elliptical/circular channels were chosen as appropriate representations of microcirculatory blood vessels. In all geometries considered, analytical solutions exist for the fully-developed velocity field. As a comparison to the theoretical results, full 3-D numerical simulations of the converging flows have also been performed. We have also obtained analytical solutions for the case of a 2-D channel of infinite depth and with inlet

[1]Corresponding author.

Contributed by the Fluids Engineering Division for publication in the JOURNAL OF FLUIDS ENGINEERING. Manuscript received by the Fluids Engineering Division February 10, 2003, revised manuscript received June 4, 2004. Associate Editor: J. S. Marshall.

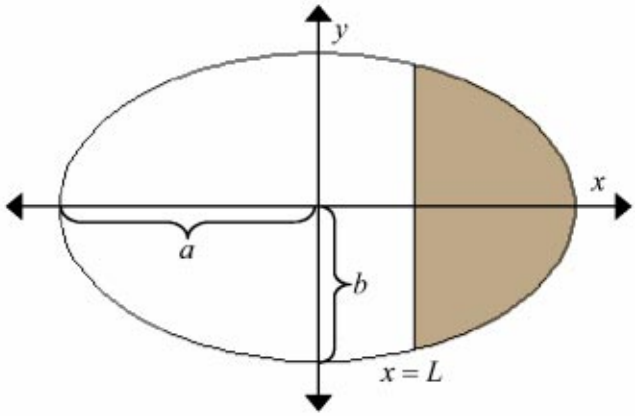

Fig. 1 Schematic diagram showing the geometry for the elliptical circular channel analysis. The view is that of a hypothetical downstream cross-section. The fluid from the side branch inlet is represented by the shaded area and enters the main branch from the right.

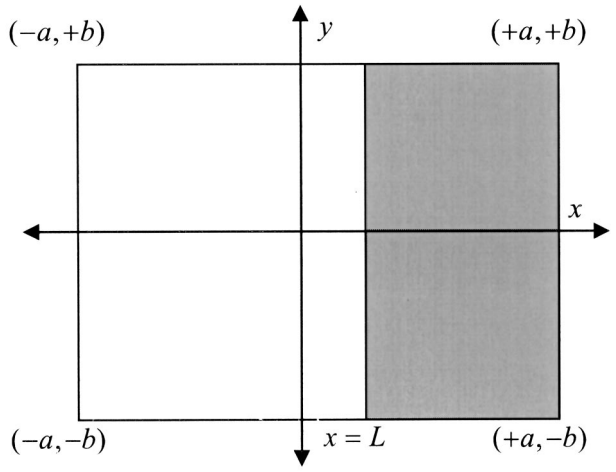

Fig. 2 Schematic diagram showing the geometry for the rectangular channel analysis. The channel has an aspect ratio of *a*/*b*; the square channel corresponds to the special case *a* = *b*. The view is that of a hypothetical downstream cross-section. The fluid from the side branch inlet is represented by the shaded area and enters the main branch from the right.

fluids of different viscosity. Experimental results for square microchannels are also presented where both the volumetric flow ratios and viscosity ratios were varied.

2 Mathematical Model

Here we consider only the case of convergent, miscible flows downstream of a junction under fully-developed, steady, low Reynolds number flow conditions. We further restrict ourselves to channel cross-sections for which analytical solutions for the fully-developed velocity fields exist (e.g., rectangular, circular, triangular). If a planar separation surface in the outlet branch is assumed, its position is dictated by mass conservation of the inlet flows. Mathematically, the interfacial location (L) is determined by the requirement:

$$\frac{\int_{A_{side}} u(x,y,L)\,dA_{side}}{\int_{A_{total}} u(x,y,L)\,dA_{total}} = \frac{Q_{side}}{Q_{total}}, \tag{1}$$

where u is the fully-developed velocity field in the downstream branch, and $Q_{side,total}$ are the side inlet and total volumetric flow rates, respectively. Unless otherwise noted, the converging fluids are taken to be identical. In the sections to follow, we apply the mass conservation statement (1) to different channel cross-sections.

The Elliptical and Circular Channel. We begin with a consideration of the flow in an elliptical channel (Fig. 1) and then recover the circular tube as a special case. From a practical standpoint, elliptical microchannels are likely to be more common owing to the difficulties associated with fabricating perfectly circular geometries. The fully-developed velocity profile in an elliptical tube admits a polynomial solution given by (e.g., [9])

$$u(x,y) = \frac{\nabla P a^2 b^2}{2\mu(a^2+b^2)}\left[1 - \frac{x^2}{a^2} - \frac{y^2}{b^2}\right], \tag{2}$$

where a, b are the semi-major and -minor axes of the elliptical cross-section, ∇P is the pressure gradient, and μ the dynamic viscosity. Without loss of generality, we can define a dimensionless length scale based on the vertical (y) axis such that

$$b_* = 1, \quad a_* = \frac{a}{b}.$$

Doing so and dropping the asterisks for convenience,

$$u(x,y) = \frac{\nabla P a^2}{2\mu(a^2+1)}\left[1 - \frac{x^2}{a^2} - y^2\right],$$

where it is understood that a now represents an aspect ratio of the tube. The total volumetric flow rate in the tube is readily determined as $Q_{total} = \pi a/2$. For an interface located at the arbitrary position $L \in [-a, a]$, the associated flow rate from the side inlet is

$$Q_{side} = 2\int_L^a \left[\int_0^{\sqrt{1-x^2/a^2}} \left(1 - \frac{x^2}{a^2} - y^2\right) dy\right] dx,$$

where the factor of two accounts for the top/bottom symmetry. Evaluation of this integral leads to the following result for the flow ratio:

$$Q^*_{\text{ellipse}} = \frac{Q_{side}}{Q_{total}} = \frac{2}{\pi a}\left[\frac{1}{4}a\pi - \frac{1}{2a}L\sqrt{a^2-L^2} - \frac{1}{2}a\sin^{-1}\frac{L}{a} - \frac{1}{3}\frac{L}{a^3}(a^2-L^2)^{3/2}\right]. \tag{3}$$

The result for a circular cross-section is obtained for the special case of unity aspect ratio ($a = 1$),

$$Q^*_{\text{circle}} = \frac{1}{2} - \frac{\sin^{-1} L}{\pi} + \frac{\sqrt{1-L^2}}{3\pi}(2L^3 - 5L). \tag{4}$$

Referring to the circular channel result, the important cases of Q^* of zero, unity and one-half are readily verified. For the limits $Q^* \to 0$ and $Q^* \to 1$ we find $L \to 1$ and -1, respectively, and the separation surface moves to the channel boundaries. For equal inlet flow rates, $L = 0$ which means the separation surface is in the channel center as expected.

The Rectangular and Square Channel. Next we consider the case of a rectangular cross section of width $2a$ and depth $2b$ (Fig. 2). As in the preceding section, the result for the square microchannel can be obtained as a special case when the aspect ratio is unity. The velocity field for a fully-developed, steady flow through a rectangular duct is given by the infinite series [10]

$$u(x,y)=\frac{\nabla P}{2\mu}\left[b^2+y^2+\frac{32b^2}{\pi^3}\sum_{n=0}^{\infty}R(n)\cosh\left[(2n+1)\frac{\pi x}{2b}\right]\cos\left[(2n+1)\frac{\pi y}{2b}\right]\right], \tag{5}$$

$$R(n)=\frac{(-1)^{n+1}}{(2n+1)^3\cosh[(2n+1)\pi a/2b]}.$$

The total volumetric flow rate through the duct is found by integrating over the entire cross-sectional area,

$$Q_{total}=\frac{4\nabla P b^3}{\mu}\left[\frac{1}{3}a+\frac{-64b}{\pi^5}\sum_{n=0}^{\infty}\frac{[\tanh[(2n+1)]\pi a/2b]}{(2n+1)^5}\right].$$

The volumetric flow rate contributed by the side branch is

$$Q_{side}=\int_{y=-b}^{y=+b}\int_{x=L}^{x=+a}u(x,y)dx\,dy=\frac{\nabla P}{2\mu}\left[\frac{4}{3}b^3(a-L)+\frac{256b^4}{\pi^5}\sum_{n=0}^{\infty}R(n)\left[\sinh\left(n+\frac{1}{2}\right)\frac{\pi a}{b}-\sinh\left(n+\frac{1}{2}\right)\frac{\pi L}{b}\right]\sin\left(n+\frac{1}{2}\right)\pi a\right]. \tag{6}$$

As with the elliptical case we define a new length scale based on the depth of the channel such that

$$b_*=1,\quad a_*=\frac{a}{b}.$$

The volumetric flow rate ratio as a function of interfacial position (L) is found to be, upon dropping the asterisks,

$$Q^*_{\text{rect}}=\frac{\frac{1}{6}(a-L)+(8/\pi^5)\Sigma_{n=0}^{\infty}R(n)\left[\sinh\left(n+\frac{1}{2}\right)\pi a-\sinh\left(n+\frac{1}{2}\right)\pi L\right]\sin\left(n+\frac{1}{2}\right)\pi a}{\frac{1}{3}a+(-64/\pi^5)\Sigma_{n=0}^{\infty}[1/(2n+1)^2]\tanh\left(n+\frac{1}{2}\right)\pi a}. \tag{7}$$

The particular case of a square channel is obtained by setting $a=1$ with the result

$$Q^*_{\text{square}}=\frac{\frac{1}{6}(1-L)+(8/\pi^5)\Sigma_{n=0}^{\infty}R(n)\left[\sinh\left(n+\frac{1}{2}\right)\pi-\sinh\left(n+\frac{1}{2}\right)\pi L\right]\sin\left(n+\frac{1}{2}\right)\pi}{\frac{1}{3}+(-64/\pi^5)\Sigma_{n=0}^{\infty}[1/(2n+1)^2]\tanh\left(n+\frac{1}{2}\right)\pi}. \tag{8}$$

The Equilateral Triangular Channel. The third geometry we consider, and the most difficult, is that of a triangular channel (Fig. 3). While its relevance to MEMS or microfluidic geometries may not be immediately apparent, equilateral triangular channels result naturally in the wet chemical etching of silicon substrates. For example, the etching of the ⟨100⟩ plane of silicon results in planar faces being formed at 54.74° angles with respect to the surface [11]. Put another way, the cross-section is that of an isosceles triangle with a vertex angle of 70.5° which is an excellent approximation to an equilateral triangle examined here. It is important to note, however, that in a wet-etching fabrication of a 90° junction there are likely to be geometric imperfections at the junction corners due to ''over-etching.'' While localized, these imperfections may be considerable. Provided that the Reynolds number of the flow is sufficiently small, it is observed that the interfacial position and shape downstream are insensitive to geometric imperfections at the junction [4]. More discussion on this inertial limitation is given in Sec. 6.

The velocity at a given point within a fully-developed, steady flow in an equilateral triangular duct is [9]

$$u(\mathbf{x})=\frac{2\nabla P}{\sqrt{3a\mu}}h_1h_2h_3, \tag{9}$$

where a is the leg length, and $h_i\,(i=1,2,3)$ are the perpendicular distances to each of the three triangle sides from the location **x**. In order to apply the same technique as described in the previous cases, we must first express the distances h_i in terms of the Cartesian co-ordinates. Each of the legs can be individually represented as a linear equation (see Fig. 3). For a specified point

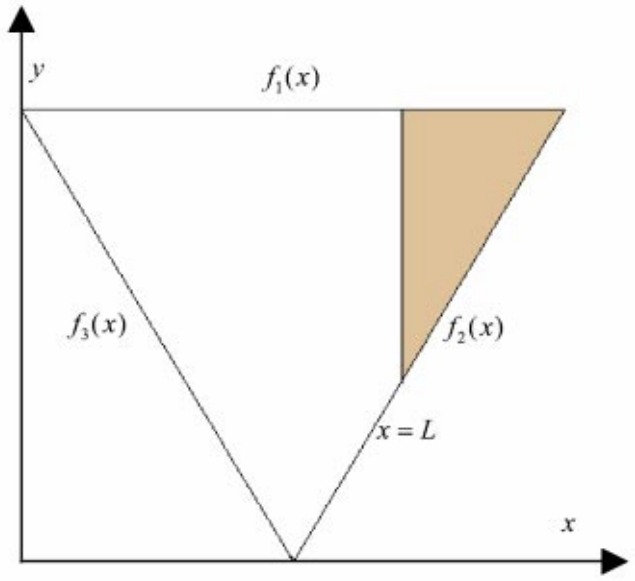

Fig. 3 Schematic diagram showing the geometry for the triangular channel analysis. The view is that of a hypothetical downstream cross-section. The fluid from the side branch inlet is represented by the shaded area and enters the main branch from the right. Each leg of the triangle is represented by a linear equation $f_i(x)$, $i=1, 2, 3$, as dictated by the coordinate system shown.

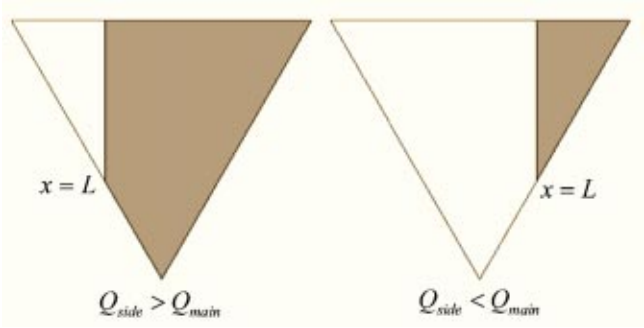

Fig. 4 The piecewise definition of the flow ratio of the triangular duct for the cases $Q^*>0.5$ (left) and $Q^*<0.5$ (right). As before, the shaded are represents the fluid from the side branch and enters the channel from the right.

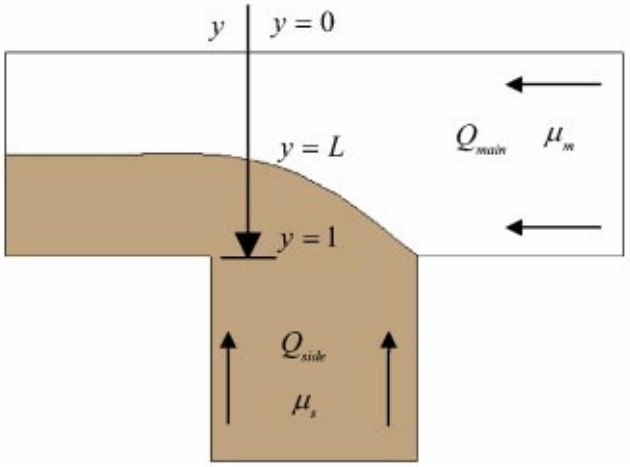

Fig. 5 The problem definition for the 2-D analysis of converging fluids of unequal viscosities

$\mathbf{x}=(x,y)$ the values h_i are found by first finding the equation of the line passing through this point and perpendicular to the respective legs; the distances are then simply the length of the line segment from $\mathbf{x}$ to the points of intersection. It can be shown that the velocity profile then becomes

$$u(x,y)=\frac{2\nabla P}{\sqrt{3a\mu}}\frac{(h-y)(h-(2h/a)x-y)(-h-(2h/a)x-y)}{(2h/a)^2+1}, \tag{10}$$

where now $h(=\sqrt{3}a/2)$ is the height of the duct. From the velocity field, we find the flow fraction of the side branch to the total volumetric flow rate through the duct. Because of the piece-wise definition of the channel walls, there must be a piece-wise definition of the flow rate through a portion of the channel. This problem can be broken into two separate cases: $Q_{side}>Q_{main}$ (case 1) and $Q_{side}<Q_{main}$ (case 2). Here we assume that the side branch enters on the right-hand side (refer to Fig. 4). With this definition, we can now integrate across the duct to find the volumetric flow rate ratio based on the interfacial location. For $Q_{side}>Q_{main}$ integration yields

$$Q^*_{side>main}=\frac{a^5+24L^5-20aL^4}{a^5}, \tag{11}$$

whereas for $Q_{side}<Q_{main}$ one finds

$$Q^*_{side<main}=\frac{(a-L)^4(6L-a)}{(a-L)^4(6L-a)+\left(\frac{5}{4}a^5-6L^5+25aL^4-40a^2L^3+30a^3L^2-10a^4L\right)}. \tag{12}$$

Once again, for the equal flow rate situation $Q^*=0.5$, one finds from either (11) or (12) that the interfacial position lies in the center of the channel.

A 2-D Model for Unequal Viscosities. Up to this point we have assumed the inlet fluids were of equal viscosity. Here we relax this constraint and allow the inlet fluids to possess separate, constant viscosities. We wish to find the interfacial location (L) as a function of the viscosity ratio $\mu^*=\mu_{side}/\mu_{main}$ and the flow ratio Q^* and show that an analytical solution can be obtained for a 2-D channel of infinite depth. Referring to the geometry outlined in Fig. 5, the fully-developed velocity fields in the side branch fluid and the main branch fluid are independently obtained from the direct integration of the Poiseuille equation,

$$u_{side}(y)=\frac{\nabla P}{2\mu_{side}}y^2+C_{side}y+D_{side}, \tag{13}$$

$$u_{main}(y)=\frac{\nabla P}{2\mu_{main}}y^2+C_{main}y+D_{main}.$$

The interfacial location (L) is defined on $L\in[0,1]$. To solve for the coefficients, we apply the no-slip condition at $y=0$, and $y=1$, which gives $u_{main}(0)=0$ and $u_{side}(1)=0$. The second boundary condition that must be satisfied is the continuity of shear stress as the interfacial location L,

$$\mu_{side}\frac{\partial u_{main}(L)}{\partial y}=\mu_{main}\frac{\partial u_{side}(L)}{\partial y}. \tag{14}$$

The third boundary condition that must be satisfied is the continuity of velocity at the interfacial location, $u_{side}(L)=u_{main}(L)$. With these conditions satisfied, we take an approach similar to that of the other analytical solutions to solve for the flow ratio in terms of the interfacial location L and viscosity ratio μ^*:

$$Q^*=\frac{-(L-1)^2[L^2(\mu^*-1)+2L(1-2\mu^*)-1]}{L^4(\mu^*-1)^2+4L^3(\mu^*-1)-6L^2(\mu^*-1)+4L(\mu^*-1)+1}. \tag{15}$$

3 Numerical Simulations

As a comparison to the analytic predictions, full three-dimensional numerical solutions of the flow mixing were also performed. This would provide an assessment of the validity of the foregoing analysis. Three-dimensional branch geometries for circular, rectangular and triangular cases were created and meshed in Gambit® 2.0 grid generation software (Fluent, Inc.). The characteristic dimension of each channel was chosen to be 125 microns, which corresponds with channels that we have used in experimental studies. In the square case, this dimension is the edge length; for the circle, it is the diameter; and in the triangle, it is the side length. The inlet branches and outlet were all chosen to be five characteristic lengths long. In this low Reynolds number regime, these branch lengths are more than adequate to assume a fully-developed flow prior to the junction and also within the downstream branch. In the cases of the square and rectangular cross-section, all elements are quadrilateral. The outlet branch is meshed more finely than the inlet branches. In the triangular cross-section geometry, the elements in the branches are triangular prisms which are created as to minimize the equiangle skewness. In the region of intersection, it is necessary to use pyramidal shaped elements in order to correspond to the shape of the elements in the branches. The meshes for all simulations ranged between 50,000 and 100,000 computational elements. The meshes described here have proven to yield solutions which are insensitive to further refinement.

The full, three-dimensional Navier–Stokes equations were solved in double-precision using the finite-volume FLUENT6® software package (Fluent, Inc.). Inlet velocity boundary conditions were prescribed to achieve the desired flow ratio Q^*; in all cases a Reynolds number of ~ 2 was maintained in the outlet branch. The outlet condition was a constant pressure boundary. The QUICK scheme was used in the discretization of the momentum and volume-of-fluid equations (described below) and the SIMPLE scheme was used for pressure-velocity coupling.

The volume-of-fluid (VOF) multiphase algorithm (e.g., [12]) was used to track the locations of the inlet branch fluids (''Phases 1 and 2'') in the outlet branch. The VOF method was developed for use in multiphase and/or multi-component flows and is based upon tracking the volume fractions of the various fluid components as they move through the flow field. The tracking is accomplished by the solution of the continuity equation for one of the fluid components $\alpha_1(x,y)$; for steady flow the governing equation has the simple form

$$\mathbf{u}\cdot\nabla\alpha_1 = 0, \tag{16}$$

where $\mathbf{u}$ is the velocity field. The volume fraction for the second fluid component is simply $\alpha_2 = 1-\alpha_1$ since mass must be conserved. An implicit VOF scheme was employed for these steady-state calculations. The volume fractions of the two inlet branch fluids are imposed to be 0 and 1, respectively; that is, one fluid is chosen to be the ''primary phase'' whose volume fraction will be tracked (i.e., α_1). The particular assignment of the primary and secondary phases is arbitrary. The separation surface can be extracted from the volume fraction data by creating an iso-surface of volume fraction equal to $\alpha_1 = 0.50$. The basic computational approach represented by (16) for tracking the interface between miscible fluids has been reported by a number of authors for cases of steady flows [4,8,7] and also for unsteady flows [13].

Computations were performed in double-precision mode using a Dell PowerEdge2650 Linux workstation with dual 2.8 GHz Xeon processors and 4 GB of RAM. Convergence was assessed through monitoring residuals and flow quantities at selected locations within the domain. A particularly relevant monitor was the area-weighted average of the volume fraction of the side-branch fluid (α_1) at the outlet.

To compare the separation surface at the outlet with the analytical predictions, it was necessary to compute an equivalent planar separation surface and location. This ''mean position'' was determined based upon a weighted average of the points comprising the curved numerical separation surface. The maximum $\pm$deviations of the numerical separation surface from the mean location were also recorded to provide some quantitative measure of the curvature.

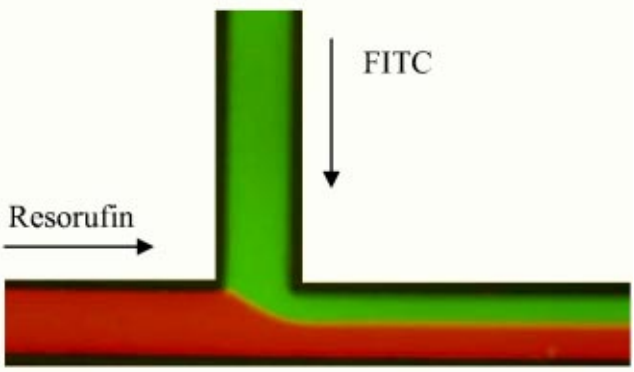

Fig. 6 A sample 2-D experimental image of steady converging flow in a square microchannel with a cross-section of approximately 127×127 microns. Arrows indicate flow direction. The fluids are identical and Reynolds number in the outlet branch is ~2. The image is acquired under fluorescent microscopy with a 10× air objective using FITC (side branch) and resorufin (main branch) as fluorescent labels. For the case shown, the inlet flow rates are identical ($Q^*=0.5$) and the interface is clearly visible in the center of the downstream branch.

4 Experimental Methods

A microfluidic flow system has been developed and constructed at the University of Vermont for studying microchannel flows. The channels are CNC micro-milled into an acrylic substrate and sealed with a glass coverslip that is bonded with ultraviolet curing epoxy. In this study, only 90° ''T-type'' junctions and channels with square cross-sections (127×127 μm) have been used. The flow rates of each inlet are independently controlled using programmable syringe pumps (Harvard Apparatus model PHD2000) with 1 cc Becton-Dickinson plastic syringes. Flow rates were chosen in order to maintain a Reynolds number of $\sim$1–2 (based on the mean velocity in the outlet). Typically, this required flow rates to be on the order of 5–10 μL/min (Q_{total}). Only steady flows were considered and the accuracy of the flow rate delivered by the syringe pumps was $\pm$1% with a repeatability of $\pm$0.1%.

In the case where $\mu^*=1$, both inlet fluids are distilled water, but labeled with different fluorescent dyes for identification under fluorescent microscopy. In one branch we have used FITC/fluorescein and in the other we have used resorufin/Texas-red. When excited the FITC glows a bright green and the resorufin a deep red (see Fig. 6). For cases of $\mu^*\neq1$, an aqueous solution of glycerol and distilled water is used to make fluids of differing viscosities. We have examined cases in the range of $\mu^*\in[1/8,8]$. For 2-D analysis, 24-bit color images are captured on a Zeiss Axioskop 2 fitted with a 10×/0.30 NA air objective though a Zeiss Axiocam using the supplied software. The images are then imported into a commercial graphics package and the interfacial location is measured (in pixels) and then nondimensionalized as a percentage of channel width ($L\in[0,1]$). Referring to the digital image in Fig. 6, there is some uncertainty in the exact location of the interface. This arises due to the combined effects of limited spatial resolution in a digital image and the blurring inherent to the 2-D projection of a slightly curved interface. It was estimated that the uncertainty in the position measurement (in pixels) normalized by the channel width gave an experimental uncertainty of $\pm$2%.

In addition to these 2-D measurements, we have also used dual-channel laser scanning confocal microscopy [4–6] to view the

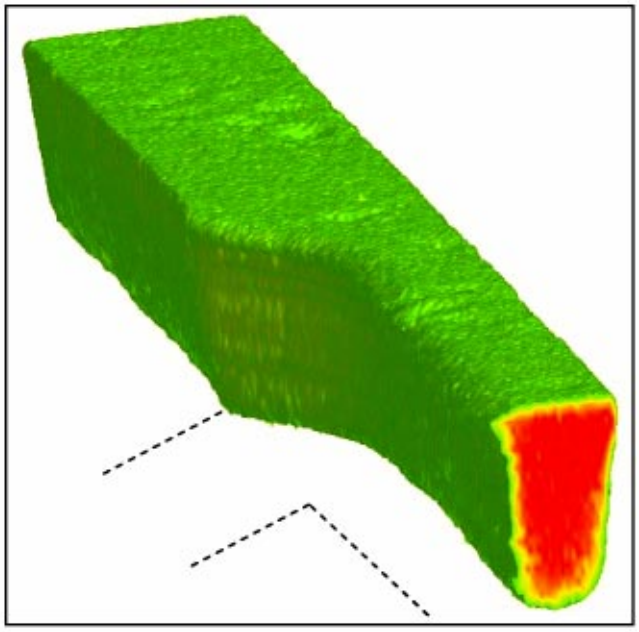

Fig. 7 A sample volumetric reconstruction of the separation surface for converging identical fluids in a square microchannel (127×127 micron cross-section). The flow ratio here is $Q^*=0.5$. This volume was reconstructed from a series of horizontal image slices acquired using single-channel laser-scanning confocal microscopy; details on this experimental methodology are described in Hitt [6]. For improved clarity of the separation surface, only the main branch fluid has been reconstructed. The fully developed separation surface in the downstream branch is located in the middle of the channel as expected and is virtually planar. This provides experimental support for the planar assumption made in this analysis.

3-D curvature of the interface. This is done using a Biorad 1024 ES confocal microscope at the University of Vermont Cell Imaging Facility. Under a 10×/0.30 air objective, horizontal images are acquired at discrete intervals through the depth of the channel and reassembled into a volumetric reconstruction. This enables viewing of the 3-D interface shape and location; further details on this experimental procedure can be found in a recent article by Hitt [6]. A sample reconstruction for converging flows of identical fluids in a square microchannel is shown in Fig. 7. This reconstruction gives support to the assertion that the separation surfaces may be considered planar to a good approximation and thus 2-D imaging is generally adequate for the cases under consideration. As such, we confine our experimental efforts in this paper to the much less demanding 2-D imaging.

5 Results and Discussion

Shown in Fig. 8 are the plots of the planar interfacial location for different cross-sectional duct geometries (circular, rectangular, square, triangular) and $\mu^*=1$ as a function of the flow ratio Q^*. To facilitate this comparison, all of the interfacial locations have been mapped to the interval $L\in[0,1]$ (i.e., $L=0.5$ is the channel center). All of the curves feature a distinct sigmoidal shape and share a common point of intersection at the channel center in the case of equal flow rates. This point of intersection is also an inflection point in the curves owing to the symmetry. The amount of variation in the curves is, overall, surprisingly small with the maximum deviations occurring near the horizontal boundaries. Indeed, with the exception of the triangular case, the curves are nearly linear over the bulk of the parametric range. The triangular

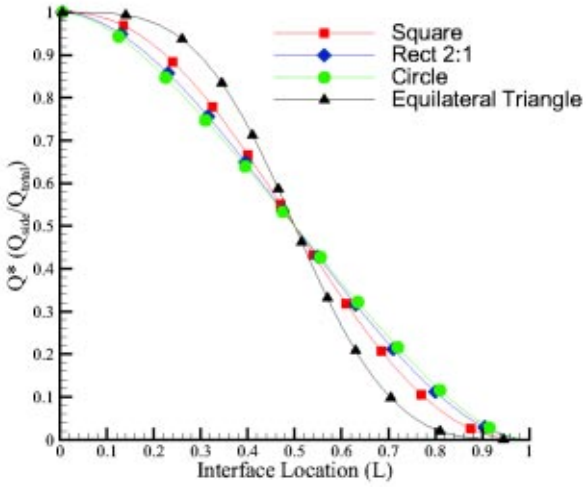

Fig. 8 Plot of the predicted planar interface position as a function of the flow ratio for the various cross sectional geometries. Note the sigmoidal shape common to all of the curves. The maximum discrepancies between the different cases occurs near the walls ($L\rightarrow 0,1$).

case is the most interesting; the relatively rapid variation seen near $L=0$, 1 is linked to the nearly stagnant velocity field in the channel corners.

A comparison of the analytical results with the mean interfacial position obtained from the numerical simulations is shown in Fig. 9. The error bars shown in the figure for the CFD data represent the maximum of the extents of the curved interface. Detailed results from the numerical simulations appear in Fig. 10. Shown are cross-sectional contours of volume fraction in the outlet section for different geometries as a function of Q^*; for orientation, the side branch fluid enters from the right and it is represented by the darker area. For comparison, the arrows in the figure represent interfacial location predicted by the planar model. Referring to this figure, it is seen that there is curvature in the interface in virtually all of the cases, although it is not severe. The case of the

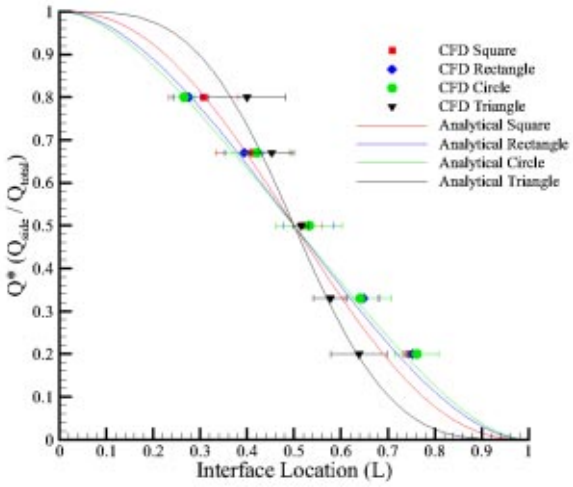

Fig. 9 A comparison of the predicted planar interface positions (solid lines) from Fig. 8 with the weighted-mean interfacial positions as determined by 3-D numerical simulations (symbols). The "error bars" associated with the numerical simulations represent the maximum±lateral extents of the numerical separation surface away from the mean position.

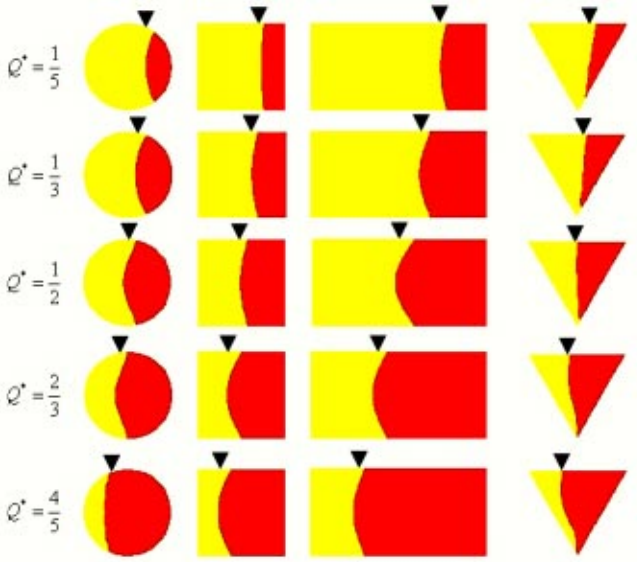

Fig. 10 A table of cross-sectional views of the fully developed separation surface in the outlet branch as obtained from numerical simulations. Shown are the results as a function of flow ratio Q^* and cross-sectional geometry. The side inlet fluid is the darker shade and enters from the right. In all cases the Reynolds number is ~2. Virtually all computed surfaces have some degree of curvature and the triangles show the position of the analytically predicted planar interface. The triangular case offers the most interesting results and features inflection in the curvature.

triangular cross section is again the most interesting with inflection point(s) seen in the interfacial shape for $Q^* \gtrsim 0.5$.

In Fig. 11 the experimental results obtained from 2-D fluorescent imaging for identical converging fluids in a square microchannel are overlaid with the predictions from the analytical model. Overall there is reasonably good agreement between the analytical solution and the experimental results, given the experimental uncertainty. At lower flow ratios ($Q^* \lesssim 0.5$) the experimental data appear to systematically under-predict the portion of the channel occupied by the side fluid; this includes the special case of $Q^* = 0.5$ for which the position should be exactly in the middle of the channel. This trend does not continue for $Q^* > 0.5$ and so it is difficult to attribute the discrepancy to a systematic experimental error.

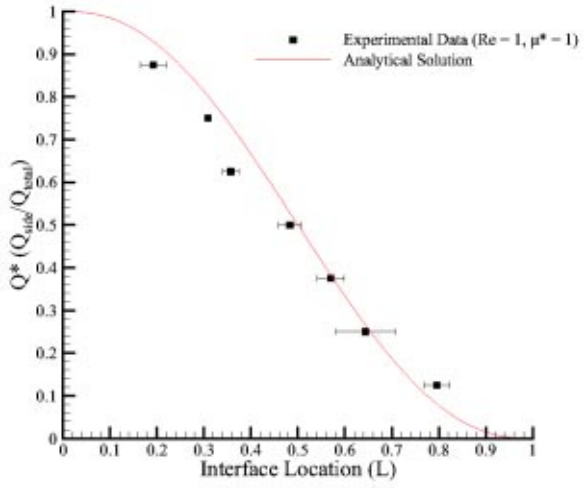

Fig. 11 A comparison of the predicted planar interface positions (solid lines) for a square microchannel (127×127 micron cross-section) with experimental measurements (symbols) obtained from 2-D fluorescence microscopy. The error bars indicate the uncertainty in estimating the interfacial position from the digital images of the flow. Under 2-D imaging one sees a view that is integrated through the channel depth. Surface curvature thus tends to produce a slightly blurred interface.

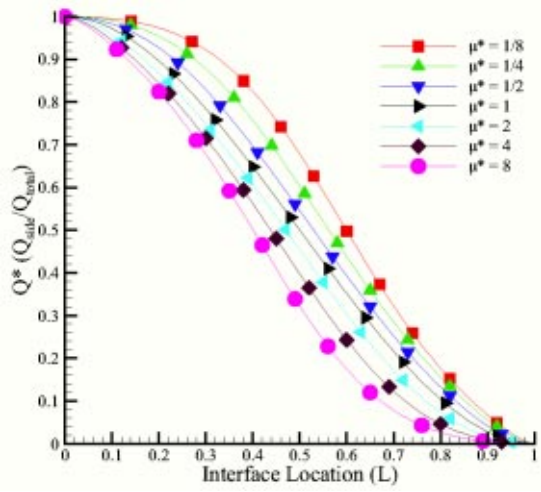

Fig. 12 Plot of the predicted planar interface position as a function of the flow ratio and viscosity ratio for a 2-D channel. For a fixed flow ratio, the more viscous fluid must occupy a larger fraction of the channel to satisfy mass conservation.

The analytical results for the case of unequal inlet viscosities ($\mu^* \neq 1$) are shown in Fig. 12. Although derived for a 2-D channel of infinite depth, these curves share a similar shape as those for the various 3-D channels previously considered. For a given flow ratio, the side branch fluid occupies a greater fraction of the channel as the viscosity ratio increases. This is readily explained in terms of mass conservation. Suppose that the side branch fluid must produce a certain flow rate. The maximum velocity in that fluid is inversely proportional to the viscosity. As the viscosity is increased the region occupied by the side fluid must then increase to maintain the required flow rate. From these results it appears that varying the viscosity ratio μ^* from $\frac{1}{8}$ to 8 produces a more significant change in interfacial location than varying the shape of the channel (see Fig. 8). Figure 13 shows the theoretical predictions overlaid with experimental data from 2-D fluorescent microscopic imaging for flow in a square microchannel and $\mu^* \neq 1$. The approximation of an infinitely deep channel correlates well with experiment which suggests that the impact of the vertical channel boundaries is relatively minor. For the square channel, this can be reasoned by considering the blunted shape of velocity profile; it may be that a poorer comparison would result for other channel cross-sections.

6 Limitations of the Planar Model

The key assumption made in all of the preceding analyses was that the separation surface was planar or at least nearly so. The natural question to be asked is: under what conditions does this planar assumption fail? As the constraints/assumptions cited in the Introduction are relaxed the planar approximation is seen to fail to varying degrees. Here we shall briefly address the consequences.

As indicated earlier, the literature clearly indicates that converging channels of unequal hydraulic diameters will produce nonplanar separation surfaces over a range of Reynolds numbers; moreover, the degree of curvature increases with the size differential. Recent experimental work has confirmed this behavior for low Reynolds numbers (Re~2) in rectangular microchannels [6]. In practical terms, identical channels are favored for simplicity of

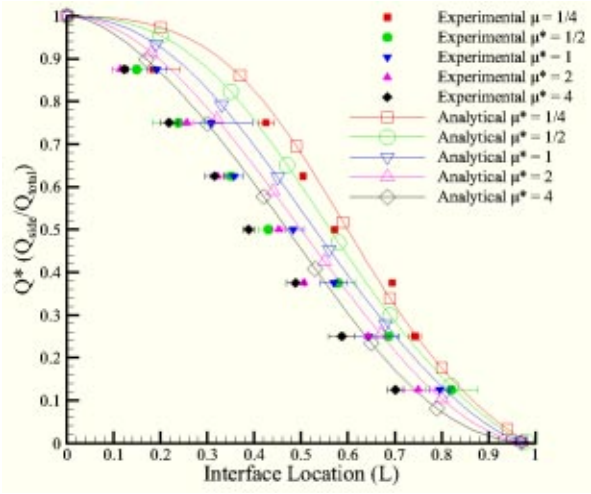

Fig. 13 A comparison of the predicted planar interface positions (solid lines) from Fig. 12 with experimental measurements (symbols) obtained from 2-D fluorescence microscopy in a square microchannel (127×127 micron cross-section). The Reynolds number in all cases is ~2.

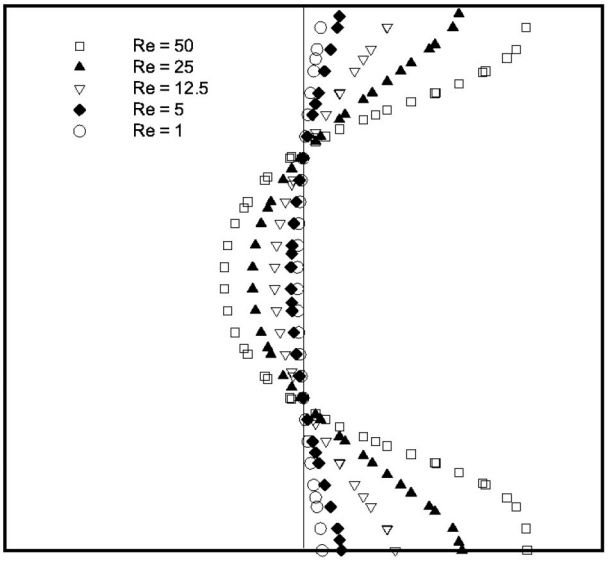

Fig. 14 Fully developed separation surfaces in the downstream branch as a function of Reynolds number as obtained from 3-D numerical simulations. The results are for 90° converging flows of identical liquids in square microchannels with a unity flow ratio ($Q^*=1$). Also shown for comparison is the planar model prediction (solid line). The validity of the planar assumption degrades with increasing Reynolds number and becomes unacceptable for Re≳10.

fabrication in many microfluidic application so this constraint is often satisfied. In microcirculatory flows, however, this is not necessarily the case.

Also stated at the onset of the analyses was the assertion that the flow inertia was required to be ''sufficiently small.'' The best planar approximations are observed for Re→0 and the quality of the approximation degrades as the Reynolds increases. With increased inertia, the side branch flow at the junction ''penetrates'' further into the main branch flow before it is redirected downstream. The inertial effect is most prominent away from the solid boundaries producing a curved separation surface. Further, as alluded to in Sec. 2, imperfections present in the junction geometry also tend to be reflected in the steady-state separation surface as flow inertia is increased. The impact of finite flow inertia is demonstrated in Fig. 14 which shows the separation surfaces obtained from 3-D numerical simulations of converging identical liquids at a 90° square junction for a unity flow ratio and for varying Reynolds numbers. For this particular case the planar approximation remains reasonable for Re≲10 and its validity worsens steadily thereafter. Our experimental and computational work suggests this characterization is a fairly representative of related flows. It is noteworthy to mention that the analysis of a 90° junction provides a conservative estimate for the limiting Reynolds number: as the junction angle is reduced (e.g., 45°) the separation surface becomes less curved for the same value of the Reynolds number [14].

The impact of the inertial effects just discussed are enhanced when the inlet liquids possess different viscosities. For a given Reynolds number it is known that the curvature of the separation surfaces is increased as μ^* moves away from unity (e.g., [8,7]). This is true for all of the geometries considered here. Consequently, the limiting Reynolds number for the approximation to remain acceptable will be less than the value for $\mu^*=1$. A striking alteration in the fluid configuration can occur for unequal viscosities if the Reynolds number is increased to a sufficiently large value. Recently we have experimentally observed the complete transition to a core-annular flow arrangement at Re~50 in square microchannels for miscible fluids with only a modest viscosity ratio of $\mu^*=2$ [15]. A sample 3-D volumetric reconstruction obtained using confocal microscopy is shown in Fig. 15*a*; we believe this to be the first reported observation of this phenomena in microchannels. Note that for this relatively low Reynolds number the transition occurs almost immediately downstream of the microchannel junction. Results from corresponding numerical simulations indicate that the onset to core-annular transition can occur at much smaller Reynolds number but the transition itself requires a greater downstream length to be completed. This phenomenon is currently under active investigation and will be reported in a future article.

In closing this discussion of the model limitations, it is important to address the matter of fluid immiscibility (i.e., surface tension). Recent experimental work in the fluids literature [16–19] has shown that converging immiscible fluids in microchannels at low Reynolds number can produce a range of ''dynamic patterns'' whereby the two fluids are separated from each other. Possible configurations include isolated droplets and slugs as well as more complex configurations. An example of this phenomenon is given in Fig. 15*b* which shows the periodic slug formation between converging flows of aqueous glycerol and octanol at a Reynolds number of ~2. Our ongoing experiments and numerical simulations have indicated that a transition to a core-annular arrangement again occurs at a sufficiently large Reynolds number. *In any case, it is clear that our planar model cannot be applied to cases of immiscible fluids.*

7 Summary

In this paper we have presented an analytical method for determining the position of the steady, fully-developed separation surface formed downstream of a converging microchannel junction. Assuming a planar separation surface and a known velocity field, an analytical determination of the surface position was possible based on mass-conservation principles. The cross-sectional geometries considered are relevant to many important micro-scale flow phenomena. Circular and elliptical channels occur naturally in the microcirculatory system. Rectangular and square channels are most common in MEMS/microfluidic devices given current microfabrication techniques, however elliptical (circular) and triangular channels are also possible. For example, a circular channel can be created by etching semi-circular trenches into two separate substrates and then bonding the pieces together. A slightly elliptical channel is, in fact, more likely given the difficulty in achieving

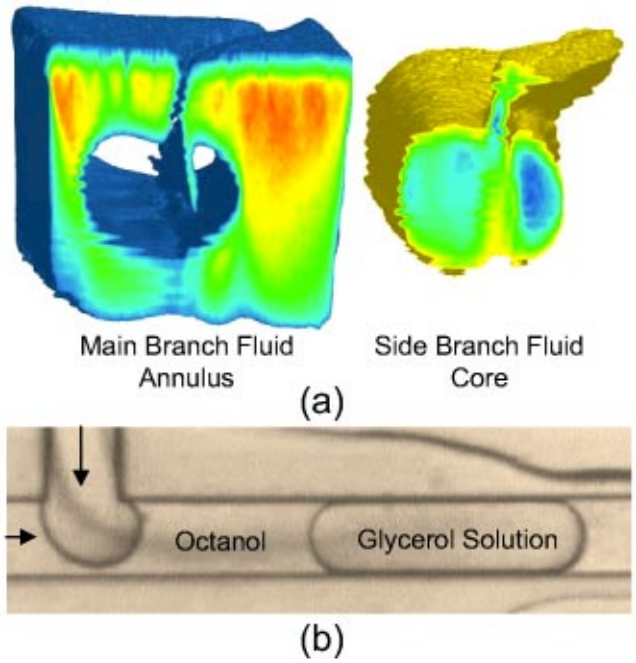

Fig. 15 Experimental demonstrations of possible nonstratified flow configurations that can arise for converging microchannel flows. (a) For miscible fluids with a nonunity viscosity ratio, a core-annular configuration can occur at sufficiently high Reynolds number. Shown is a volumetric reconstruction obtained from confocal microscopy for Re∼50, $Q^*=0.4$, and $\mu^*=2$. (b) For immiscible fluids, periodic slug formation can be observed at low Reynolds numbers. Shown is a high-speed CCD image for converging flows of aqueous glycerol and octanol which have a surface tension $\sigma=0.034$ N/m; here Re∼2, $Q^*=1$, and $\mu^*=1$.

the precision required for a circular section. Although not considered here, a semi-circular channel can also be made by sealing a semi-circular trench with a cover slide. Moreover, an analytical velocity profile exists for such a geometry (e.g., Ref. [20]) and thus our methodology could be applied. Triangular channels, as mentioned earlier, can be created using wet-etching techniques in silicon substrates. The hydrodynamic constraints of the model, discussed at length in Sec. 6, are not terribly restrictive when considering common microfluidic applications.

The theoretical predictions obtained for identical fluids and different channel cross-sections show that the interfacial position varies in a sigmoidal fashion as a function of flow ratio. As expected, there is symmetry through the point corresponding to equal flow rates ($Q^*=0.5$). Varying the cross-sectional geometry produced relatively minor differences among the curves with the greatest differences occurring near the walls (i.e., $Q^*\rightarrow 0$ or 1). This effect can be attributed to the near-stagnation regions that form in the corners of rectangular and triangular sections. Comparisons of these predictions with results from 3-D numerical simulations and 2-D fluorescent microscopic imaging showed good overall agreement. The numerical simulations did, however, reveal clear and significant surface curvature under certain flow conditions which our simplified model cannot capture.

Predictions were also obtained for the case of converging fluids with different viscosities; however, an analytic solution has only been found for a 2-D channel. This is of limited use for practical engineering applications and thus we continue to pursue a theoretical solution for a 3-D channel. Nonetheless, the predictions compare reasonably well with experimental data and show that a nonunity viscosity ratio produces an effect not unlike that seen the different channel cross-section.

In closing, our simplified model yields results with minor errors for a range of hydrodynamic conditions and geometries often found in micro-scale flows (e.g., MEMS devices, microcirculatory blood flow) while offering a substantial decrease in computational effort. For example, a single numerical simulation required ∼2 h of run-time; this saving can be quite significant if a network configuration of microchannels is being considered. Unless 3-D flow details are explicitly required, the accuracy of model should be adequate for many microfluidic engineering and design purposes.

Acknowledgments

Primary funding for this project was provided by the National Science Foundation under CAREER Award CTS-0093767 (DLH); additional support was provided by the University of Vermont SUGRFaME Program (TRH).

Nomenclature

a = ellipse semi-major axis/rectangle half-length
b = ellipse semi-minor axis/rectangle half-width
h = perpendicular distance from point in triangle to duct/height of triangle
u = fully developed velocity field
A = cross-sectional area
L = location of separation surface
∇P = pressure gradient
Q = volumetric flow rate
Q^* = volumetric flow ratio (Q_{side}/Q_{total})
α = volume fraction of phase
μ = dynamic viscosity
μ^* = dynamic viscosity ratio (μ_{side}/μ_{main})

Subscripts

main = refers to main flow/duct
side = refers to side flow/duct
total = refers to combined flow/main duct

References

[1] Ho, C., and Tai, Y., 1998, "Micro-Electro-Mechanical-Systems (MEMS) and Fluid Flows," Annu. Rev. Fluid Mech., **30**, pp. 579–612.
[2] Fung, Y.-C., 1997, *Biomechanics: Circulation*, Springer-Verlag, New York, USA.
[3] Carr, R. T., and Kotha, S. L., 1995, "Separation Surfaces for Laminar Flow in Branching Tubes—Effect of Reynolds Number and Geometry," ASME J. Biomech. Eng., **117**, pp. 442–447.
[4] Hitt, D. L., and Lowe, M. L., 1999, "Confocal Imaging of Flows in Artificial Venular Bifurcations," ASME J. Biomech. Eng., **121**, pp. 170–177.
[5] Peach, J. P., Hitt, D. L., and Dunlap, C. T., 2000, "Three-Dimensional Imaging of Microfluidic Mixing Surfaces Using Dual-Channel Confocal Microscopy," Microelectromechanical Systems (MEMS)—Proceedings of the 2000 ASME International Mechanical Engineering Congress & Exposition, MEMS Vol. 2, pp. 497–504.
[6] Hitt, D. L., 2002, "Confocal Imaging of Fluidic Interfaces in Microchannel Geometries," in *Science, Technology & Education in Microscopy: An Overview*, edited by A. Mendez-Vilas, ed., Vol. 1, 622–9.
[7] Enden, G., and Popel, A. S., 1992, "A Numerical Study of the Shape of the Surface Separating Flow Into Branches in Microvascular Bifurcations," ASME J. Biomech. Eng., **114**, pp. 298–404.
[8] Ong, J., Enden, G., and Popel, A. S., 1994, "Converging Three-Dimensional Stokes Flow of Two Fluids in a T-Type Bifurcation," J. Fluid Mech., **270**, pp. 51–71.
[9] Landau, L. D., and Lifshitz, E. M., 1987, *Course of Theoretical Physics: Volume 6. Fluid Mechanics*, Pergamon Press, New York, USA.
[10] Rosenhead, L., 1963, *Laminar Boundary Layers*, Oxford University Press, New York, USA.
[11] Petersen, K. E., 1982, "Silicon as a Mechanical Material," Proc. IEEE, **2**, pp. 420–457.
[12] Hirt, C. W., and Nichols, B. D., 1981, "Volume of Fluid (VOF) Method for the Dynamics of Free Boundaries," J. Comput. Phys., **39**, pp. 201–225.
[13] Hitt, D. L., and McGarry, M., 2004, "Numerical Simulations of Laminar Mixing Surfaces in Pulsatile Microchannel Flows," in *Mathematics and Computers in Simulation*, Elsevier Mathematics, Elsevier, Amsterdam.
[14] Harris, T. R., 2003, Master's thesis, University of Vermont.
[15] Harris, T. R., and Hitt, D. L., 2003, "Low Reynolds Number Transition to

Core-Annular Flow in Converging Microchannels,'' Bulletin APS—Division of Fluid Dynamics.
[16] Thorsen, T., Roberts, R., Arnold, F., and Quake, S., 2001, ''Dynamic Pattern Formation in a Vesicle-Generating Microfluid Device,'' Phys. Rev. Lett., **86**, No. 18, pp. 4163–4166.
[17] Nisisako, T., Fukudome, K., Torii, T., and Higchi, T., 2001, ''Nanoliter-Sized Droplet Formation in a Microchannel Network,'' Proc. of ISMM2001, pp. 102–103.
[18] Dreyfus, R., Tabeling, P., and Willaime, H., 2003, ''Ordered and Disordered Patterns in Two-Phase Flows in Microchannels,'' Phys. Rev. Lett., **90**, No. 14, pp. 144505-1-4.
[19] Harris, T. R., Hitt, D. L., and Macken, N. A., 2003, ''Periodic Slug Formation in Converging Immiscible Microchannel Flows,'' Bulletin APS—Division of Fluid Dynamics.
[20] Shah, R. K., 1978, *Laminar Flow Forced Convection in Ducts*, Academic Press, New York, USA.

Three-dimensional Hybrid Continuum-Atomistic Simulations For Multiscale Hydrodynamics

H. S. Wijesinghe
Massachusetts Institute of Technology, Cambridge, MA

R. D. Hornung
Lawrence Livermore National Laboratory, Livermore, CA

A. L. Garcia
San Jose State University, San Jose, CA

N. G. Hadjiconstantinou
Massachusetts Institute of Technology, Cambridge, MA

We present an adaptive mesh and algorithmic refinement (AMAR) scheme for modeling multi-scale hydrodynamics. The AMAR approach extends standard conservative adaptive mesh refinement (AMR) algorithms by providing a robust flux-based method for coupling an atomistic fluid representation to a continuum model. The atomistic model is applied locally in regions where the continuum description is invalid or inaccurate, such as near strong flow gradients and at fluid interfaces, or when the continuum grid is refined to the molecular scale. The need for such "hybrid" methods arises from the fact that hydrodynamics modeled by continuum representations are often under-resolved or inaccurate while solutions generated using molecular resolution globally are not feasible. In the implementation described herein, Direct Simulation Monte Carlo (DSMC) provides an atomistic description of the flow and the compressible two-fluid Euler equations serve as our continuum-scale model. The AMR methodology provides local grid refinement while the algorithm refinement feature allows the transition to DSMC where needed. The continuum and atomistic representations are coupled by matching fluxes at the continuum-atomistic interfaces and by proper averaging and interpolation of data between scales. Our AMAR application code is implemented in C++ and is built upon the SAMRAI (Structured Adaptive Mesh Refinement Application Infrastructure) framework developed at Lawrence Livermore National Laboratory. SAMRAI provides the parallel adaptive gridding algorithm and enables the coupling between the continuum and atomistic methods.
[DOI: 10.1115/1.1792275]

1 Introduction and Background

Multiscale simulation of complex physical systems has received increasing attention in recent years. The primary challenge lies in resolving physical phenomena occurring over a broad range of spatial and temporal scales. Often, this challenge cannot be met by conventional, single-method formulations. Efficient multiscale formulations respond to this challenge by limiting the use of an expensive high-resolution model (e.g., atomistic) to the regions in which it is needed, while using a simpler, less expensive method, in the rest of the computational domain. Such a hybrid approach allows effective use of each method in different regions of the problem (e.g., interior and exterior of a shock wave).

Numerous hybrid methods have been proposed and demonstrated for solids [1–3], liquids [4–7], and gases [8–16]. The purpose of this paper is to illustrate one methodology for integrating the concepts of adaptive mesh refinement and hybrid methods. While our continuum-atomistic approach using adaptive mesh refinement uses an unsplit Godunov scheme for the continuum Euler equations (discussed in Section 2), the coupling *methodology* is in no way limited to a particular continuum solution method, provided the latter is a time-explicit conservative formulation [17]. This will be particularly important if the hybrid method needs to be used for the simulation of small-scale flows where Navier-Stokes capabilities are required. In fact, perhaps the most important message from this work is that powerful coupling methods can be developed from already existing continuum-continuum matching techniques [5,18]. This is possible because coupling can only be achieved in regions where both descriptions are equivalent, that is, where the continuum description is valid. This approach is in fact preferred because it typically results in coupling methods that (1) can be rigorously shown to converge and (2) place very few restrictions on the continuum and atomistic constituents other than accommodating the coupling recipe.

In what follows, we will first describe the continuum and atomistic methods and their coupling. Next, the challenging question of choosing reliable grid and algorithm refinement criteria to track fluid interfaces is discussed. Finally, we present numerical results from several test cases and compare them with theory and other simulations to verify our approach.

2 Adaptive Mesh and Algorithmic Refinement

This section describes the Adaptive Mesh and Algorithm Refinement (AMAR) methodology in which a continuum algorithm is replaced by a particle algorithm at the finest grid scale in a hierarchical adaptive grid refinement (AMR) setting. Details of the general AMAR scheme have been presented elsewhere [14]. We will summarize them here for completeness and note differences from previous work.

2.1 AMR Algorithm for Continuum Hydrodynamics. In the AMAR implementation described herein, we employ a structured AMR grid hierarchy on which we solve the compressible, two-species Euler equations on every grid level except the finest. On the finest level, the solution is represented by the Direct Simulation Monte Carlo (DSMC) method. Note that AMAR uses the same adaptive meshing and time integration algorithms developed for continuum modeling of shock hydrodynamics [19,20].

Consider the two-fluid Euler equations in conservative integral form

$$\frac{d}{dt}\int_{\Omega}\mathbf{U}dV+\oint_{\partial\Omega}\mathbf{F}\cdot\hat{n}dS=0, \tag{1}$$

where

Contributed by the Fluids Engineering Division for publication in the JOURNAL OF FLUIDS ENGINEERING. Manuscript received by the Fluids Engineering Division August 21, 2003; revised manuscript received March 29, 2004. Associate Editor: S. Balachandar.

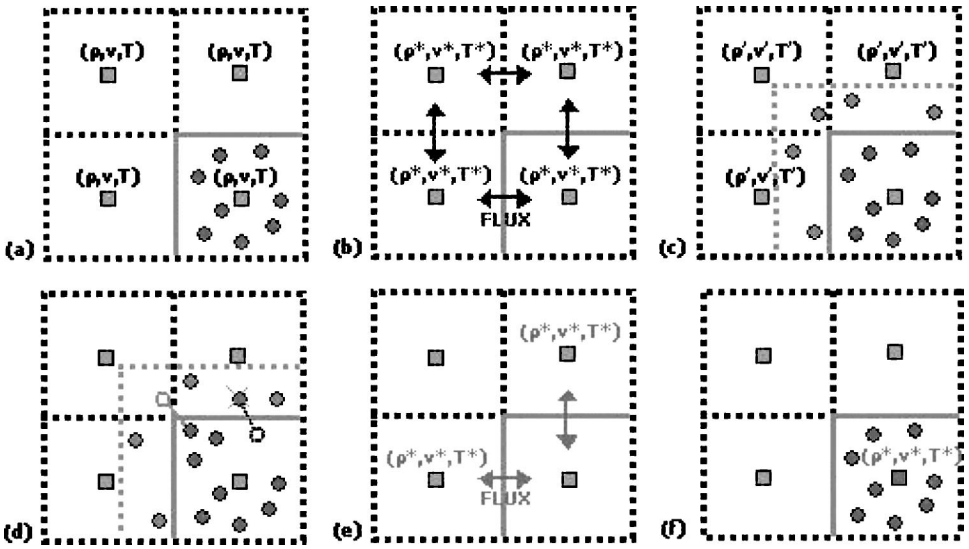

Fig. 1 Outline of AMAR hybrid: (*a*) Beginning of a time step; (*b*) advance the continuum grid; (*c*) create buffer particles; (*d*) advance DSMC particles; (*e*) refluxing; (*f*) reset overlying continuum grid.

$$\mathbf{U}=\begin{pmatrix}\rho\\ p_x\\ p_y\\ p_z\\ e\\ \rho c\end{pmatrix};\quad \mathbf{F}^{\mathbf{x}}=\begin{pmatrix}\rho u_x\\ \rho u_x^2+P\\ \rho u_x u_y\\ \rho u_x u_z\\ (e+P)u_x\\ \rho c u_x\end{pmatrix} \tag{2}$$

Here, we provide only the x-direction component of the flux terms; other directions are similar. We assume a two-species gas with the mass concentrations of the two species being c and $(1-c)$; generalization to more species is straightforward. Discrete time integration is achieved by using a finite volume approximation to Eq. 1. This yields a conservative finite difference expression with $\mathbf{U}_{ijk}^{n}$ appearing as a cell-centered quantity at each time level and $\mathbf{F}_{i+1/2,j,k}^{x,n+1/2}$ located at faces between cells at half-time levels. We use a second-order version of an unsplit Godunov scheme to approximate the fluxes [21–23].

Time stepping on an AMR grid hierarchy involves interleaving time steps on individual levels [20]. Each level has its own spatial grid resolution and timestep (typically constrained by a CFL condition). The key to achieving a conservative AMR algorithm is to define a discretization for Eq. 1 that holds on every region of the grid hierarchy. In particular, the discrete cell volume integrals of **U** and the discrete cell face integrals of **F** must match on the locally-refined AMR grid. Thus, integration of a level involves two steps: solution advance and solution synchronization with other levels. Synchronizing the solution across levels assumes that fine grid values are more accurate than coarse grid values. So, coarse values of **U** are replaced by suitable cell volume averages of finer **U** data where levels overlap, and discrete fine flux integrals replace coarse fluxes at coarse-fine grid boundaries. Although the solution is computed differently in overlapping cells on different levels as each level is advanced initially, the synchronization procedure enforces conservation over the entire AMR grid hierarchy.

2.2 Atomistic Algorithm. Due to our interest in gas flows [24–28], the atomistic algorithm we use is the direct simulation Monte Carlo (DSMC) method [29]. In DSMC, the state of the system is given by positions and velocities of particles, $\{\mathbf{r}_\alpha,\mathbf{v}_\alpha\}$. The system evolves in time using the following two step approach. First, particles are moved without interaction; that is, their positions are updated to $\mathbf{r}_\alpha+\mathbf{v}_\alpha\Delta t_\mathrm{p}$, where Δt_p is a DSMC timestep. Appropriate boundary conditions are applied to particles that reach the boundary of the DSMC domain. Second, after all particles have moved, a given number are randomly selected for collisions. Rather than exactly calculate successive collisions, as in molecular dynamics [30], the DSMC method generates collisions stochastically with scattering rates and post-collision velocity distributions determined from the kinetic theory of a dilute gas. Accuracy of the splitting of streaming and collisions requires the time step Δt_p to be a fraction of the mean collision time τ_m for a particle [31,32]. DSMC has been rigorously shown to provide accurate solutions to the Boltzmann equation in the limit as the number of particles becomes large and the DSMC collision cell size and time step become small [33].

Although DSMC is orders of magnitude faster than molecular dynamics for simulation of gases, it is orders of magnitude slower than continuum algorithms for solving partial differential equations of hydrodynamics in the Navier-Stokes limit. Thus, only flow regions that require molecular resolution are treated by DSMC in the AMAR approach.

2.3 Continuum-Atomistic Coupling. During time integration of continuum grid levels, fluxes computed at each cell face are used to advance the solution **U** (Fig. 1(*b*)). Continuum values are advanced using a time increment Δt_c appropriate for each level, including those that overlay the DSMC region. When the particle level is integrated, it is advanced to the new time on the finest continuum level using a sequence of particle time steps, Δt_p. The relative magnitude of Δt_p to the finest continuum grid Δt_c depends on the finest continuum grid spacing Δx (typically a few λ) and the particle mean collision time.

Euler solution information is passed to the particles via buffer cells surrounding the DSMC region. At the beginning of each DSMC integration step, particles are created in the buffer cells using the continuum hydrodynamic values (ρ, **u**, T) and their gradients (Fig. 1(*c*)). Since the continuum solution is advanced first, these values are time interpolated between continuum time steps for the sequence of DSMC time steps needed to reach the new continuum solution time. DSMC buffer cells are one mean free path wide; thus, the time step Δt_p is constrained so that it is extremely improbable that a particle will travel further than one mean free path in a single time step. The particle velocities are drawn from an appropriate distribution for the continuum solver, such as the Chapman-Enskog distribution [34].

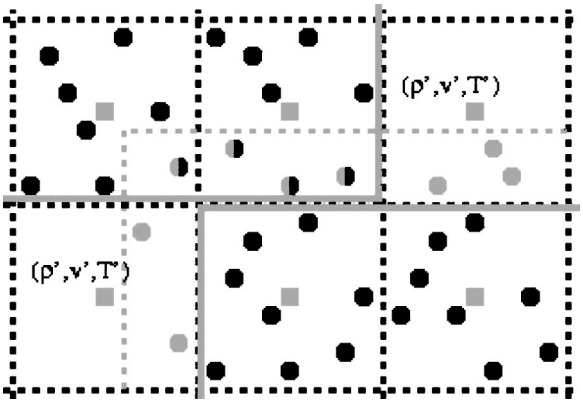

Fig. 2 Multiple DSMC regions are coupled by copying particles from one DSMC region (upper left) to the buffer region of an adjacent DSMC region (lower right). After copying, regions are integrated independently over the same time increment.

During each DSMC time integration step, all particles are moved, including those in the buffer regions (Fig. 1(*d*)). A particle that crosses the interface between continuum and DSMC regions will eventually contribute to the flux at the corresponding continuum cell face during the synchronization of the DSMC level with the finest continuum level. After moving particles, those residing in buffer regions are discarded. Then, collisions among the remaining particles are evaluated and new particle velocities are computed.

After the DSMC region has advanced over an entire continuum grid timestep, the continuum and DSMC solutions are synchronized in a manner analogous to the AMR level synchronization process described earlier. First, the continuum values in each cell overlaying the DSMC region interior are set to the conservative averages of data from the particles within the continuum grid cell region (Fig. 1(*f*)). Second, the continuum solution in cells adjacent to the DSMC region is recomputed using a ''refluxing'' process (Fig. 1(*e*)). That is, a flux correction is computed using a space and time integral of particle flux data,

$$\delta\mathcal{F} = -A\mathbf{F}^{n+1/2} + \sum_{\text{particles}} \mathcal{F}_p . \tag{3}$$

The sum represents the flux of the conserved quantities carried by particles passing through the continuum cell face during the DSMC updates. Finally,

$$\mathbf{U}^{n+1} = \overline{\mathbf{U}^{n+1}} + \frac{\Delta t_c \delta\mathcal{F}}{\Delta x \Delta y \Delta z} \tag{4}$$

is used to update the conserved quantities on the continuum grid where $\overline{\mathbf{U}^{n+1}}$ is the coarse grid solution before computing the flux correction.

In summary, the coupling between the continuum and DSMC methods is performed in three operations. First, continuum solution values are interpolated to create particles in DSMC buffer cells before each DSMC step. Second, conserved quantities in each continuum cell overlaying the DSMC region are replaced by averages over particles in the same region. Third, fluxes recorded when particles cross the DSMC interface are used to correct the continuum solution in cells adjacent to the DSMC region. This coupling procedure makes the DSMC region appear as any other level in the AMR grid hierarchy.

Multiple DSMC parallelepiped regions (i.e., *patches*) are coupled by copying particles from patch interiors to buffer regions of adjacent DSMC patches (see Fig. 2). That is, particles in the interior of one patch supply boundary values (by acting as a reservoir) for adjacent particle patches. After copying particles into buffer regions, each DSMC patch may be integrated *independently*, in the same fashion that different patches in a conventional AMR problems are treated after exchanging boundary data.

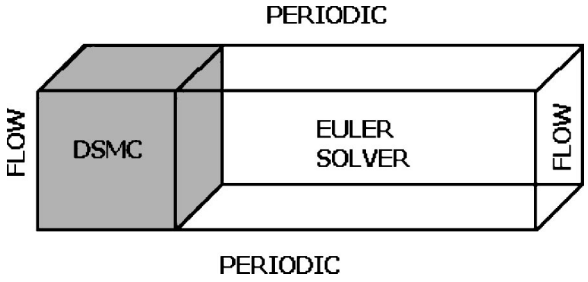

Fig. 3 3D AMAR computational domain for investigation of tolerance parameter variation with number of particles in DSMC cells

2.4 Refinement Criteria. Criteria for refining the mesh and transitioning from continuum to a particle scheme is a significant research topic and is generally problem specific. Standard AMR methods assume that the differential equations of continuum hydrodynamics are valid at all length scales in the computation and grid refinement is often based on ad hoc notions (e.g., refine around steep gradients) or analytical error estimation techniques involving the continuum differential equations (e.g., Richardson extrapolation). In contrast, hybrid methods apply computational models matched to the flow properties at each physical scale. While results presented later demonstrate that we can effectively focus DSMC locally to capture shocks and diffusion fronts, many research issues remain.

The AMAR algorithm can refine the grid and algorithm based on any of a number of possible criteria. However, we have found that for single species flows, refinement based on density gradients is reliable. Tracking concentration gradients or concentration values within some interval is effective for multispecies flows involving concentration interfaces. Parameters for transitioning to DSMC are based on the continuum breakdown parameter method proposed by Bird [35], i.e., refinement is triggered by spatial gradients exceeding continuum tolerances. The gradient detector formula that we use is a variation of a sharp discontinuity detector by Trangenstein and Pember [36].

Due to spontaneous stochastic fluctuations in DSMC computations, it is important to track gradients in a manner that does not allow the fluctuations to trigger unnecessary refinement and excessively large DSMC regions. Let us consider the gas density as an example. Using the fact that for an ideal gas under equilibrium conditions the number of particles in a given volume is Poisson distributed, it can be shown that the standard deviation in the normalized density gradient is [37],

$$\sqrt{\left\langle \left(\frac{d\rho/dx}{\rho} \right)^2 \right\rangle} \approx \sqrt{\left\langle \left(\frac{N_{i+1} - N_i}{\Delta x \langle N_i \rangle} \right)^2 \right\rangle} = \frac{\sqrt{2}}{\Delta x \sqrt{\langle N\text{cell} \rangle}}, \tag{5}$$

where Ncell is the number of particles in a cell where macroscopic properties are defined. The fluid density fluctuation can only be reduced by increasing the number of DSMC simulation particles. This has consequences for the use of density gradient tolerances R_ρ used for AMAR. In general, such tolerances must be based on the number of particles used for the atomistic domain since the spatial gradients of density on the *coarse* grid which is fluctuating (as shown below) are used to decide whether refinement will take place. In particular, in our version of density-gradient-based refinement, refinement occurs in regions where the nondimensionalized density gradients are above the R_ρ threshold, i.e.,

$$R_\rho < \frac{2\lambda}{\rho} \left| \frac{d\rho}{dx} \right| \tag{6}$$

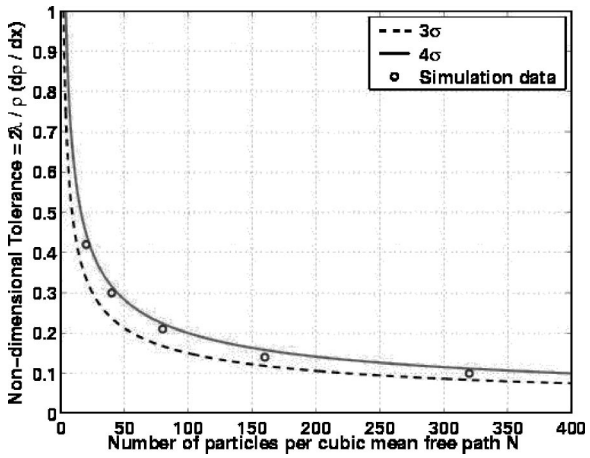

Fig. 4 Variation of density gradient tolerance with number of DSMC particles *N*. Here we use *N* because in our implementation *N*cell=*N*.

Note that the density gradient is calculated in the continuum mesh on a coarser AMR hierarchy level than the DSMC level.

To determine the minimum value of R_ρ required to prevent growth of the atomistic region, simulations were conducted using the domain geometry shown in Fig. 3 for a range of Ncell. Grid refinement occurs during a ''trigger'' event where the density fluctuations exceed R_ρ and the atomistic subdomain grows in the axial direction by a single continuum cell width. The value of R_ρ that yields a 5–10% trigger rate (i.e., between 5–10 trigger events per 100 iterations) is plotted in Fig. 4 as a function of Ncell. In what follows we outline how theoretical predictions bounding these numerical results, shown as solid lines in Fig. 4, can be obtained.

For the geometry considered in this test problem, each continuum cell consists of 8 DSMC cells and hence effectively the contribution of $8\times N$cell particles is averaged to determine the density gradient between continuum cells. If we use Eq. (5) for continuum cells, we obtain

$$\sigma = \sqrt{\left\langle \left(\frac{d\rho/dx}{\rho} \right)^2 \right\rangle_c} \approx \frac{1}{2\Delta x \sqrt{\langle N\text{cell} \rangle}} \tag{7}$$

Note that we are assuming that the fluctuation of the continuum cells across from the atomistic-continuum interface is approximately the same as that in the atomistic region. This was shown to

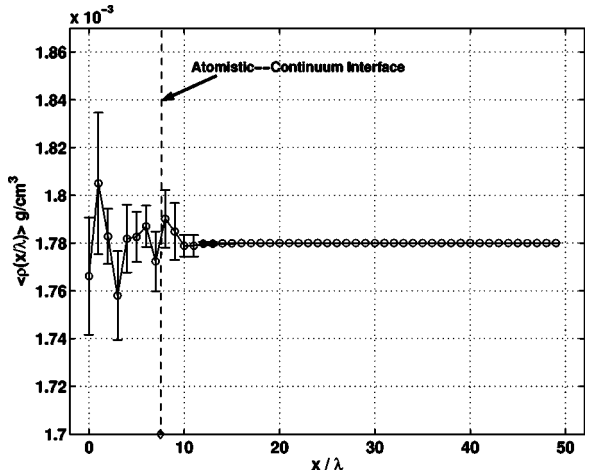

Fig. 5 Average density for stationary fluid Euler-DSMC hybrid simulation with *N*cell=80. Error bars give one standard deviation over 10 samples.

be the case for the diffusion equation and a random walk model in Ref. [38], and is verified here for the Euler-DSMC system as shown in Fig. 5. This allows the use of Eq. (5) that was derived assuming 2 atomistic cells. Note that the observed trigger event is a composite of a large number of probable density gradient fluctuations that could exceed R_ρ; gradients across all possible nearest neighbor cells, next-to-nearest neighbor cells and diagonally-nearest neighbor cells are all individually evaluated by the refinement routines and checked against R_ρ. For a 10% trigger rate (or equivalent probability of trigger) the probability of an individual cell-pair having a density fluctuation exceeding R_ρ can be estimated as $O(0.1/100)$ by observing that,

1. since the trigger event is rare, probabilities can be taken as additive,
2. for the geometry considered, there are $\approx$300 nearest neighbor, next-nearest neighbor and diagonal cells that can trigger refinement and
3. the rapid decay of the Gaussian distribution ensures the decreasing probability ($O(0.1/100) \sim O(0.001)$) of a single event does not significantly alter the corresponding confidence interval and thus an exact enumeration of all possible trigger pairs with correct weighting factors is not necessary.

For example, our probability estimate at $O(0.001)$ suggests that our confidence interval is $3\sigma - 4\sigma$. This is verified in Fig. 4. Larger trigger rates can be achieved by reducing R_ρ. Curves shown in Fig. 4 help prototype tolerance criteria using a small number of particles prior to running larger simulations.

2.5 Euler-DSMC Code Implementation. The Euler-DSMC AMR code discussed here is composed of elements from the SAMRAI object-oriented framework, developed at Lawrence Livermore National Laboratory, and numerical routines specific to the application. SAMRAI provides a general, flexible software toolbox for developing multiphysics AMR applications and supports general parallel data management capabilities, including particle representations, on an AMR grid hierarchy.

The organization of major algorithmic parts in the hybrid Euler-DSMC code is similar to that of an Euler-only AMR code. However, the hybrid code requires a new level integrator that coordinates DSMC and Euler operations on different hierarchy levels. The new integrator, developed for this project, was constructed from elements in SAMRAI. It is interesting to note that all classes appearing in an Euler-only application are used without modification in the hybrid code. Also, the DSMC data structures and numerical routines, developed previous to incorporation in the hybrid application, were introduced without significant modification.

Recall that the Euler continuum model and DSMC particle model are vastly different numerical approaches. The Euler model represents compressible fluid flow as a deterministic system of partial differential equations containing a few grid-based variables. DSMC approximates the Boltzmann equation using a representative, stochastic sampling of a collection of particles whose state and motion are essentially gridless. The DSMC data structures and numerical routines are insulated from SAMRAI abstractions by a ''wrapper'' interface class. This class serves two important functions. First, it acts as a translator between SAMRAI patch data and the DSMC particle structures. Second, it allows the particles to be manipulated on a distributed parallel machine by SAMRAI. More importantly, the *serial* DSMC routines were coupled to the SAMRAI parallel communication framework without changing the particle structures or routines or recompiling SAMRAI library code. Additional details describing how this is done appear in Ref. [17].

3 Code and Algorithm Verification Tests

This section describes a number of test problems used to verify the AMAR hybrid formulation. Tolerance parameters used for grid refinement are also described. The single-species tests use gaseous

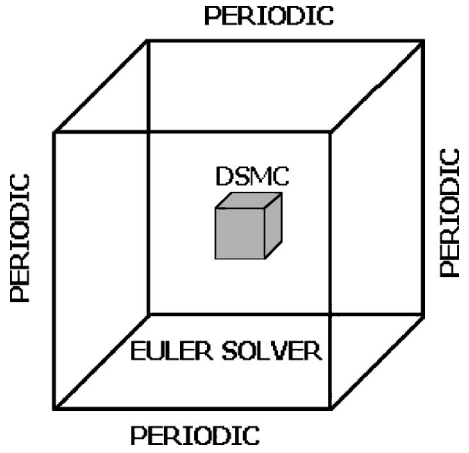

Fig. 6 Computational domain for uniform field test

Argon (molecular mass $m=6.63\times10^{-23}$ g, hard sphere diameter $d=3.66\times10^{-8}$ cm) at atmospheric conditions ($P=1.013\times10^{5}$ Pa and average temperature $\bar{T}=273$ K). This choice is for convenience reasons. The hard sphere diameter for Argon is well-known to reproduce equilibrium and nonequilibrium properties accurately. Argon is also used in a large number of DSMC studies and thus a substantial literature base of simulation and experimental results exist for verification purposes.

3.1 Thermodynamic Equilibrium. We start with the thermodynamic equilibrium test which serves to illustrate that due to the underlying $\mathrm{Re}\to\infty$ ($Pe\to\infty$) assumption associated with our continuum solver, care needs to be taken in not using this model in nonconvectively dominated situations. The computational domain, illustrated in Fig. 6, consists of a cubic DSMC region of size $4\lambda\times4\lambda\times4\lambda$ embedded in the center of an Euler continuum grid of size $32\lambda\times32\lambda\times32\lambda$. The DSMC computation uses 800 particles per λ^3. The continuum cell size is 2λ, while the DSMC grid size is λ. Periodic boundary conditions are applied at each face of the cubic domain. This geometry is the same as in Ref. [14] for comparison purposes. The density and temperature field were initialized at $\rho=1.78\times10^{-3}$ g/cm^3 and $T=273$ K and the initial velocity field was set to zero in all directions. Adaptive refinement (both mesh and algorithmic) was disabled in order to illustrate the following effect. Figure 7 shows that the number of particles in the atomistic subdomain slowly increases in time. This phenomenon can be explained as follows. Although the initial

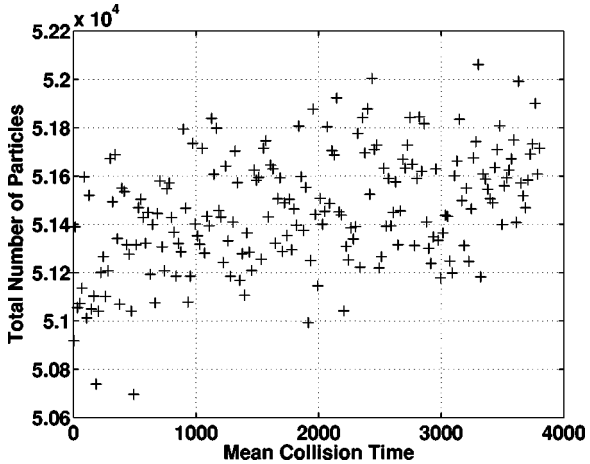

Fig. 7 Particle increase in the DSMC domain resulting from net heat flux transfer from the DSMC to the Euler region

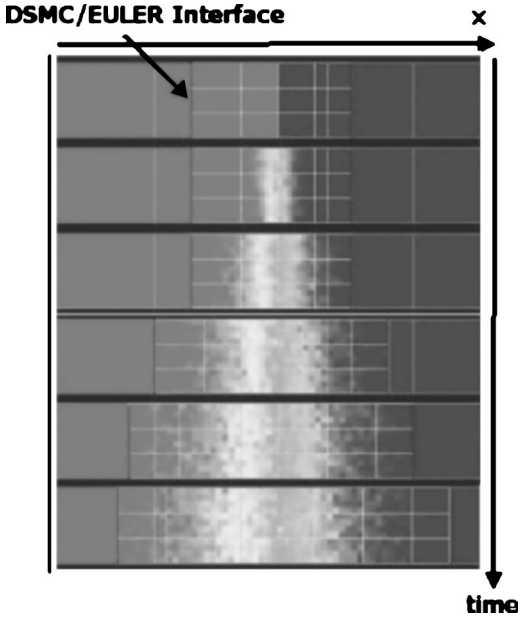

Fig. 8 Computational domain for self-diffusion interface tracked adaptively. The borders of DSMC patches are indicated by the boxes near the middle of the domain. The Euler model is applied in the remainder of the domain.

conditions are uniform, the statistical nature of atomistic solution generates fluctuations that transfer heat to the continuum subdomain. Since the Euler model possesses no mechanism to transfer thermal energy back to the atomistic domain, the result is an energy increase in the continuum subdomain and a corresponding energy decrease in the atomistic subdomain as total energy is conserved. This, in turn, produces an increase in density in the atomistic subdomain so as to maintain mechanical equilibrium (i.e., constant pressure). Hence the total number of particles in the atomistic subdomain increases. This phenomenon has been observed in other Euler/DSMC hybrid schemes [14] and has been shown to be suppressed when diffusive transport (Navier-Stokes terms) are included. Recall, however, that in the $\mathrm{Re}\to\infty$ ($Pe\to\infty$) limit appropriate for Euler calculations, the diffusive timescale associated with molecular transport (the cause of this phenomenon) is much (infinitely) longer than the convective timescale which dominates the flow. As a result, this phenomenon should have no effect in the Euler limit. In some sense, it is a manifestation of the fact that equilibrium is not a convectively dominated situation appropriate to an Euler calculation. This is supported by simple tests we have performed which show that in the presence of a uniform flow this effect is reduced. Additionally, the excellent agreement between our results and benchmark Euler flows presented in the following sections shows that this phenomenon has no effect on solutions in the Euler limit.

3.2 Concentration Diffusion. Concentration diffusion tests were conducted to verify the ability of AMAR to track the spreading of an interface between two gases. The Euler model contains no diffusion terms (except for artificial numerical diffusion) so spreading of the interface is governed by physics modeled by the DSMC routines.

The diffusion coefficient for two gases modeled as hard spheres can be approximated as [39],

$$\mathcal{D}_{12}=\frac{3}{16}\frac{\sqrt{2\pi k^3T^3/\mathcal{M}}}{P\pi d^2}=\frac{3}{8}\frac{1}{nd^2}\sqrt{\frac{kT}{2\pi\mathcal{M}}} \tag{8}$$

where $\mathcal{M}=(1/m_1+1/m_2)^{-1}=m_1m_2/(m_1+m_2)$ is the reduced mass, and $d=(d_1+d_2)/2$ is the average atomic diameter.

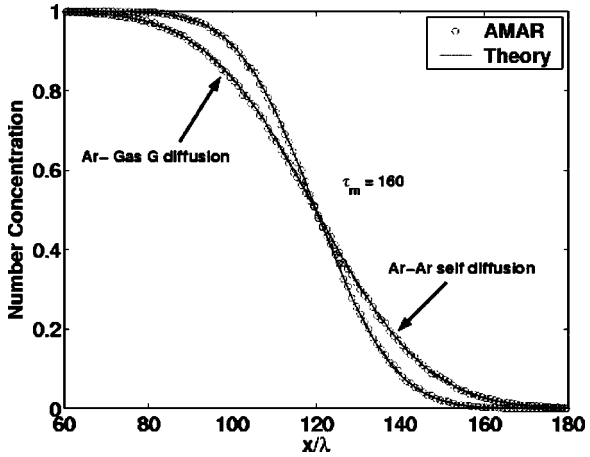

Fig. 9 Comparison of profiles obtained simulating diffusion with AMAR with theoretical diffusion profiles. Both self-diffusion and two-species diffusion are shown. Note λ refers to the Ar-Ar mean free path. The mean collision time τ_m is also associated with the Ar-Ar system.

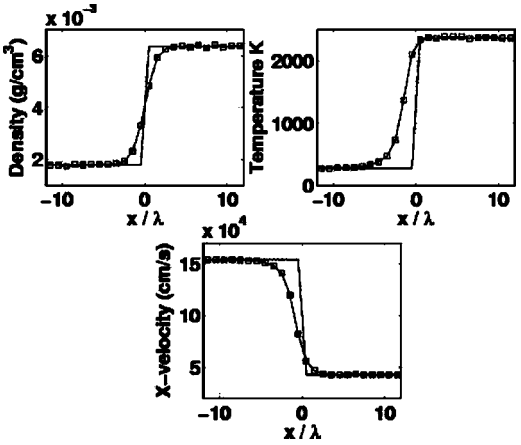

Fig. 11 Equilibrium shock wave profiles for density, temperature and velocity in a stationary Argon shock. The solid line connects the Rankine-Hugoniot jump values through a sharp jump centered on the AMAR shock location as determined by the AMAR density profile. The solid-square line is the AMAR result. Note that the AMAR temperature jump "leads" the AMAR density jump as documented in Ref. [29]. The agreement between AMAR and Rankine-Hugoniot jump values is excellent.

A simple concentration diffusion test involves Argon gas on either side of an interface "colored" differently, i.e., the gases are essentially isotopes with negligible mass differences that undergo self-diffusion. The self-diffusion coefficient for Argon at standard temperature and pressure is $\mathcal{D}_{11}=0.14$ cm^2/s. Figure 8 shows the evolution of the atomistic-continuum computational domain for this self-diffusion test. Initially the gases are separated by a discontinuous interface corresponding to a step function profile for the gas concentration. The gradient of the corresponding mass concentration is used to place the atomistic region at the gas interface at the initial time. Subsequently, the mixing region is tracked using a "mass-concentration-value" refinement criteria which triggers below 0.001 and above 0.999. These values ensure that negligible concentration gradients exist across the atomistic-continuum interface.

The hybrid concentration profiles for the self-diffusion case are compared with theoretical profiles in Fig. 9. Also shown is the concentration profile for a test case using Argon and a fictitious gas G with hard-sphere diameter $d_2=1.516\times10^{-8}$ cm such that the diffusion coefficient is twice the self-diffusion coefficient; that is, $\mathcal{D}_{12}=2\times\mathcal{D}_{11}=0.28$ cm^2/s. The simulation results show excellent agreement with theory in both cases.

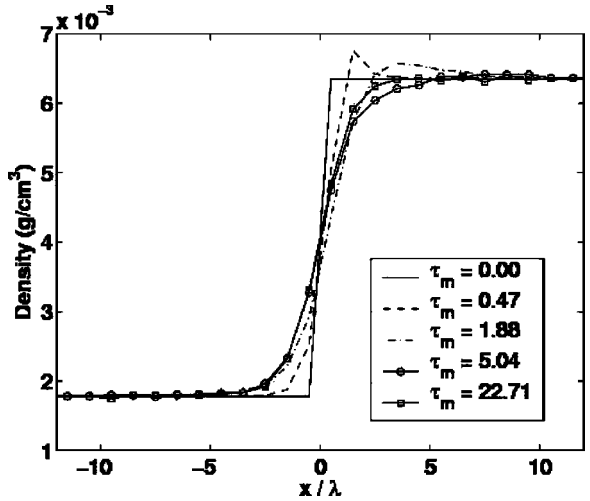

Fig. 10 Argon gas density profile evolution to equilibrium. τ_m is the mean collision time.

3.3 Stationary Shock Waves. Stationary shock simulations were conducted for both a single gas and a binary gas mixture.

3.3.1 Single Gas Stationary Shock Wave. For the single gas case, a shock wave is initialized using the discontinuous step profile given by the Rankine–Hugoniot conditions for Argon gas with an upstream Mach number of 5.0. The shock wave density, temperature and velocity ratios for this Mach number are 3.57, 8.68 and 0.28, respectively. A density gradient tolerance parameter $R_\rho=0.2$ was used to detect and refine the continuum grid across the shock. This value for R_ρ creates a stable $\pm10\lambda$ atomistic region ahead of and behind the shock front.

The time evolution of the density profile is shown in Fig. 10. The initial step profile gradually transitions to a smoother curved profile within 20 mean collision times. The final equilibrium profiles for the pressure, density, velocity and temperature are shown in Fig. 11. The hybrid solution matches the Rankine-Hugoniot jump values in the far field while resolving the flow discontinuity at the shock front. Also note the temperature jump is shown to "lead" the density jump as documented in Ref. [29]. Note that since the initial density gradient in the streamwise direction is essentially infinite, the shock region will be refined for any setting of R_ρ. As the profile becomes smoother however, the value of R_ρ is critical to ensure the shock front remains tagged for refinement while preventing excessive atomistic subdomain growth due to spurious statistical fluctuations. This is achieved successfully with the $R_\rho=0.2$ setting.

3.3.2 Binary Gas Stationary Shock Wave. The binary gas shock simulation was conducted using a mixture of Helium and Xenon gases with number densities of 97% and 3% respectively. The hard sphere mass and diameter chosen to model Helium and Xenon were $m_1=6.65\times10^{-24}$ g, $m_2=2.18\times10^{-22}$ g and $d_1=2.28\times10^{-8}$ cm, $d_2=5.18\times10^{-8}$ cm, respectively. The upstream flow Mach number was set to 3.89 with a temperature of 300 K and reference mass density of 1.07×10^{-7} g/cm^3. These flow conditions were chosen to allow for convenient comparison with literature results. The corresponding Rankine-Hugoniot relations for the shock density, temperature and velocity ratios are 3.34, 5.59, and 0.3, respectively. Tolerance parameters were not

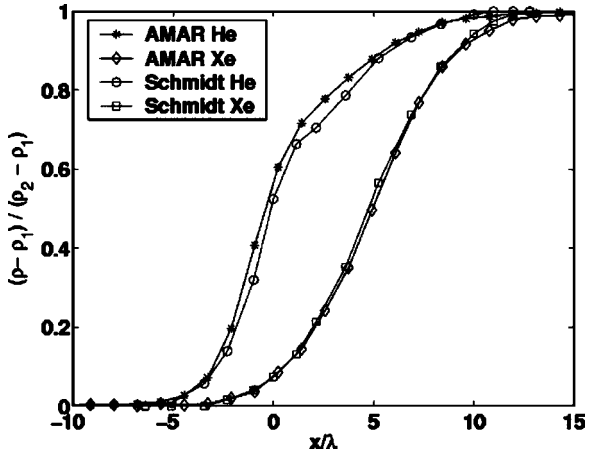

Fig. 12 Comparison of He-Xe binary gas shock wave equilibrium profiles computed with AMAR (blue lines) and with DSMC alone (red lines). The mixture mean free path $\lambda = 0.46$ mm for this test.

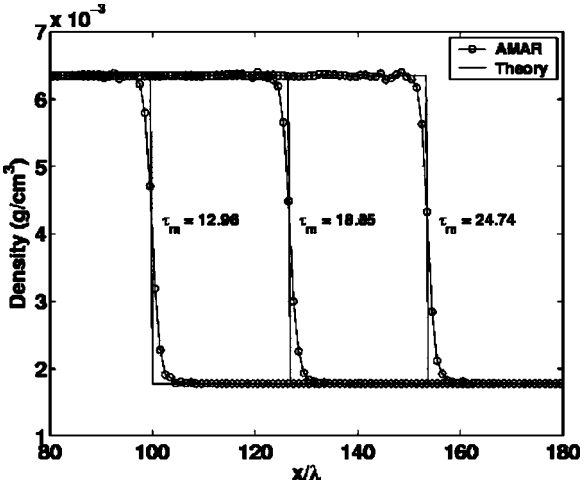

Fig. 14 A moving Mach 5 shock wave though Argon. The AMAR profile (red dots) is compared with the analytical time evolution of the initial discontinuity (blue lines). τ_m is the mean collision time.

used for this test and instead the refinement region was user specified to extend 15λ ahead of and 35λ behind the shock front.

Similar to the single gas shock case, the binary gas shock profile also transitions from an initial discontinuous step profile to a smoother equilibrium profile. A comparison of the equilibrium hybrid density profiles with a fully DSMC simulation performed by Schmidt and Worner [40] are shown in Fig. 12. Good agreement can be seen for both Helium and Xenon density profiles.

3.4 Moving Shock Wave. Adaptive feature-tracking of the AMAR hybrid scheme is further verified using a $M=5$ moving shock passing through a stationary Argon gas. Figure 13 shows the atomistic subdomain dynamically tracking the passage of the shock front. Similar to the case of a stationary $M=5$ shock wave a density gradient tolerance $R_\rho = 0.2$ was found sufficient to extend the atomistic subdomain $\pm 10\lambda$ about the shock front.

The density profile of the moving shock is shown in Fig. 14. Good comparison is seen with the analytical result. Note the hybrid profile does not produce spurious postshock oscillations well-known to plague continuum-only schemes [41,42]. Conventional shock capturing techniques for the Euler equations require artificial viscosity and enhanced smoothing techniques to reduce oscillations that cannot often be eliminated entirely. The AMAR hybrid scheme allows for accurate, adaptive and stable resolution of shock fronts without the need for artificial numerical constructs.

3.5 Richtmyer-Meshkov Instability. The Richtmyer-Meshkov instability (RMI) (Meshkov [43,44], Richtmyer [45]) is generated when the interface between two fluids is impulsively accelerated by a shock wave. The shock impulse causes perturbations on the interface to grow in size which in turn creates a mixing layer between the two gases [46]. In this paper RMI serves as a test problem from which to assess both the adaptive feature tracking and multispecies capability of the AMAR hybrid scheme. For the simulation considered here adaptive mesh refinement is considered only for tracking the shock front, and for computational convenience, only a small system was considered.

The computational domain illustrated in Fig. 15 was used for the RMI simulation. Argon gas and a fictitious gas B with hard sphere mass and diameter $m_B = 1.326 \times 10^{-22}$ g, $d_B = 3.66 \times 10^{-8}$ cm were chosen for the test. In order to reduce diffusion between the gases the cross collision diameter $d = (d_1 + d_2)/2$ was increased by a factor of 4. The density ratio across the gas-gas interface was initialized to $\rho_2/\rho_1 = 1.5$ (which corresponds to an Atwood number $At = ((\rho_2/\rho_1) - 1)/((\rho_2/\rho_1) + 1) = 0.2$). This

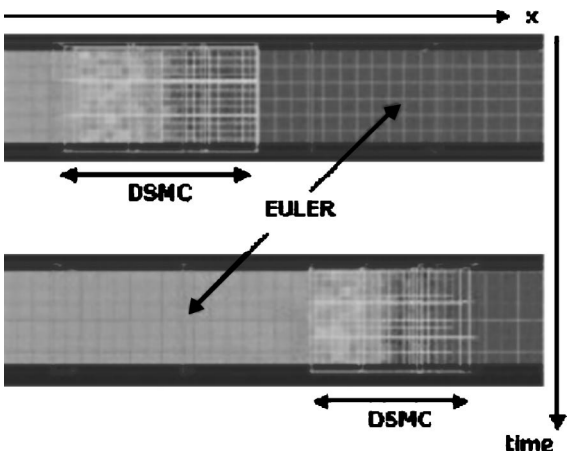

Fig. 13 A moving Mach 5 shock wave though Argon. The AMAR algorithm tracks the shock by adaptively moving the DSMC region with the shock front.

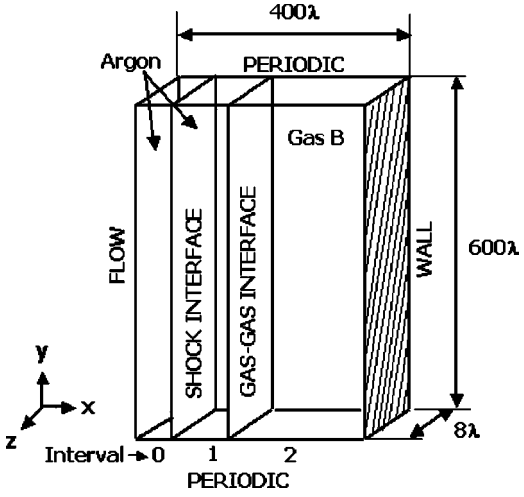

Fig. 15 Computational domain for Richtmyer-Meshkov instability simulation

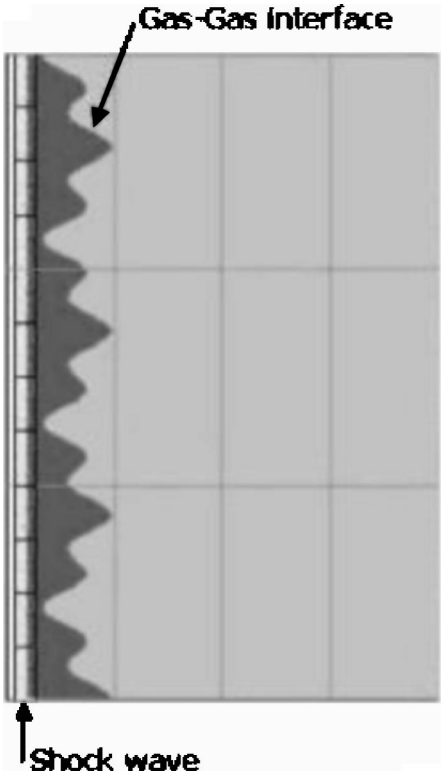

Fig. 16 Richtmyer-Meshkov instability simulation, time $t = 1.3\tau_m$ where τ_m is the Argon-Argon mean collision time. The shock wave is ahead of the gas-gas interface.

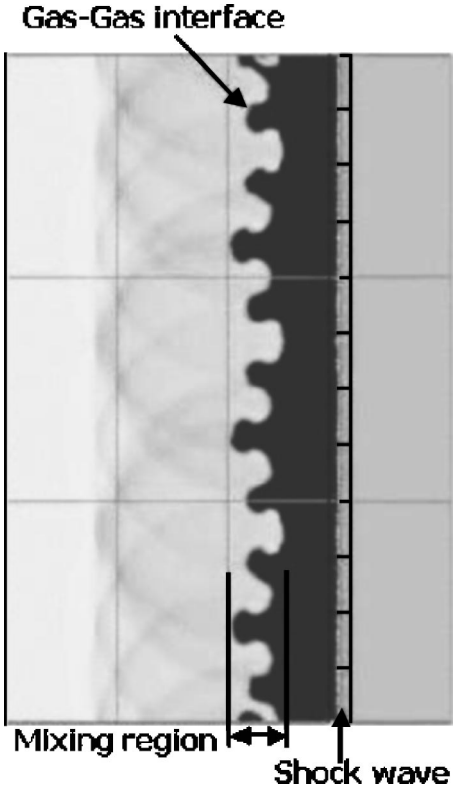

Fig. 18 Richtmyer-Meshkov instability simulation, time $t = 170.1\tau_m$ where τ_m is the Argon-Argon mean collision time. The shock wave has passed the gas-gas interface.

simulation utilizes 20 DSMC particles per cubic mean free path of Argon at the reference density. The lighter Argon gas occupies the left hand side of the interface while the heavier gas B occupies the right hand side. The shock wave is initialized upstream of the gas-gas interface and propagates at Mach number $M = 4.0$ through Argon gas. Classical Navier-Stokes methods have been unable to perform *rigorous* simulation at these Mach numbers [29] which are typical of experimental conditions [47]. The gas-gas interface has an initial sinusoidal profile with wavelengths 171λ and 57λ superimposed. Peak to peak amplitudes vary between 8λ and 32λ. Both the wavelength and disturbance amplitude are typical of real experimental conditions [47].

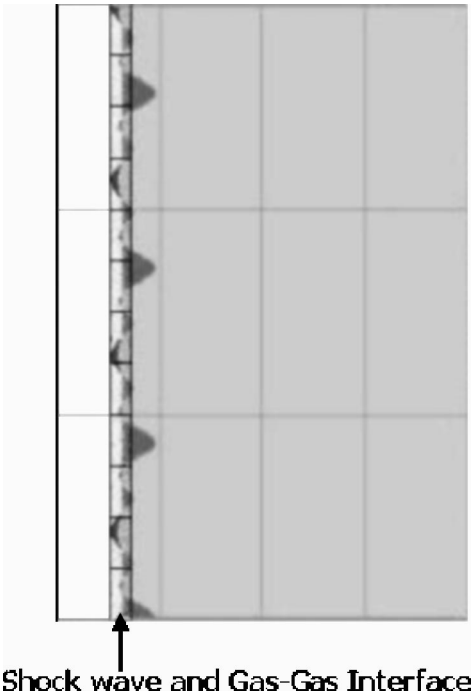

Fig. 17 Richtmyer-Meshkov instability simulation, time $t = 26.0\tau_m$ where τ_m is the Argon-Argon mean collision time. The shock wave intercepts the gas-gas interface.

On interception with the interface, a reflected shock returns upstream and a transmitted shock continues through gas B. On reflection with the right hand wall, the transmitted shock returns past the interface and leaves the domain through the left face. A density gradient tolerance $R_\rho = 0.6$ ensures the atomistic subdomain is localized about the shock wave region only, while the gas-gas interface remains nonrefined. Figures 16, 17 and 18 show the propagation of the shock wave. Note that Fig. 18 also shows a reflected shock wave traveling upstream in addition to the transmitted shock through the gas-gas interface. The choice of R_ρ allows only for the transmitted shock wave to be refined in this case. This hybrid approach achieves a computational savings of $O(10)$ over a fully atomistic solution (assuming that the continuum solution cost is negligible compared to the DSMC solution cost the savings for this problem is more than a factor of 20). Our simulations show that through a judicious choice of refinement criteria and the development of a theory to quantify the effect of fluctuations, reliable fully adaptive mesh and algorithm refinement algorithms are possible. Larger calculations which will allow for comparison with experimental data and other simulation codes (for an example see Ref. [47]) are planned in the future.

4 Concluding Remarks

We have described an adaptive mesh and algorithmic refinement (AMAR) scheme for modeling multiscale, multispecies gas

dynamics and have demonstrated its effectiveness in a hybrid Euler-DSMC code via a series of computational test cases. The atomistic model is applied locally in regions where the continuum description is invalid or inaccurate, such as near strong flow gradients and at fluid interfaces. In particular, accurate and stable solutions for concentration diffusion, single and binary gas stationary shocks waves and moving shock waves have been obtained. These tests suggest that the AMAR code can perform highly-resolved DSMC calculations in a more cost effective manner than a DSMC-only code. An evaluation of code performance and scaling studies to larger problems will be the subject of future work.

While this effort shows the promise of the approach, much work remains to address research issues associated with such hybrid methods. In future work we plan to rigorously address issues related to accuracy and robustness of particle-continuum hybrids, criteria for adaptively switching between models, and effects of statistical fluctuations in particle schemes on the stability of continuum methods to which they may be coupled. In addition, we expect that future adoption of a Navier-Stokes model in the same algorithmic framework will yield a very useful tool for the design of micro and nano scale devices involving *compressible* flow features in which local continuum breakdown occurs.

Finally, the range of scales and dynamic nature of multi-algorithm hybrids that may be applied to a variety of important physical problems emphasizes the need for efficient computational approaches for large-scale parallel computing platforms. The AMR grid hierarchy paradigm offers many advantages to algorithm development and parallel code implementation, including the ability to manage both field data and particles in a single grid system while allowing workload and data for each method to be distributed in parallel independently of one other. We are currently working on more effective dynamic load balancing and data distribution algorithms for our code to increase the scale of the problems we can simulate. These results will be reported in the near future.

Acknowledgments

The authors wish to thank B. Alder, F. Alexander, J. Bell, S. Smith, and A. Wissink for helpful discussions. This work was performed under the auspices of the U.S. Department of Energy by University of California Lawrence Livermore National Laboratory under contract number W-7405-Eng-48.

Nomenclature

A = signed area of a grid cell face
c = mass concentration of reference fluid species
$\mathcal{D}$ = diffusion coefficient
d = atomic diameter
e = total energy density
$\delta\mathcal{F}$ = refluxing correction
$\mathbf{F}$ = flux vector
k = Boltzmann's constant
$\mathcal{M}$ = reduced mass
m = atomic mass
N = number of particles per cubic mean free path
$N\text{cell}$ = number of particles per unit
n = number density
$\hat{n}$ = surface normal
P = pressure
$Pe = \text{Re}\,Pr$ = Peclet number
Pr = gas Prandtl number
$\mathbf{p} = (p_x, p_y, p_z)$ = vector of momentum densities
Re = Reynolds number
$\mathbf{r}$ = particle position vector
S = surface element
T = temperature
Δt = time step
t = time
$\mathbf{U}$ = Euler solution state vector
$\mathbf{u} = (u_x, u_y, u_z)$ = fluid velocity vector
$\mathbf{v}$ = particle velocity vector
$\Delta x, \Delta y, \Delta z$ = grid spacing

Greek

λ = particle mean free path
Ω = fluid volume element
$\partial\Omega$ = boundary of fluid element
ρ = mass density
σ = standard deviation

Subscripts/Superscripts

0 = mean
1,2 = first, second species
α = particle index
c = continuum
i, j, k = coordinate indices
max = maximum
p = particle
n = temporal index
x, y, z = spatial coordinates

References

[1] Abraham, F. F., Broughton, J. Q., Bernstein, N., and Kaxiras, E., 1998, "Spanning the continuum to quantum length scales in a dynamic simulation of brittle fracture," Europhys. Lett., **44**, pp. 783–787.
[2] Rudd, R. E., and Broughton, J. Q., 2000, "Concurrent coupling of length scales in solid state systems," Phys. Status Solidi B, **217**, pp. 251–291.
[3] Shenoy, V. B., Miller, R., Tadmor, E. B., Rodney, D., Phillips, R., and Ortiz, M., 1999, "An Adaptive Finite Element Approach to Atomic-Scale Mechanics—The Quasicontinuum Method," J. Mech. Phys. Solids, **47**, pp. 611–642.
[4] O'Connell, S. T., and Thompson, P. A., 1995, "Molecular dynamics-continuum hybrid computations: A tool for studying complex fluid flows," Phys. Rev. E, **52**, pp. R5792–R5795.
[5] Hadjiconstantinou, N. G., 1999, "Hybrid Atomistic-Continuum Formulations and the Moving Contact-Line Problem," J. Comput. Phys., **154**, pp. 245–265.
[6] Li, J., Liao, D., and Yip, S., 1998, "Coupling continuum to molecular-dynamics simulation: Reflecting particle method and the field estimator," Phys. Rev. E, **57**, pp. 7259–7267.
[7] Flekkoy, E. G., Wagner, G., and Feder, J., 2000, "Hybrid model for combined particle and continuum dynamics," Europhys. Lett., **52**, pp. 271–276.
[8] Wadsworth, D. C., and Erwin, D. A., 1990, "One-Dimensional Hybrid Continuum/Particle Simulation Approach for Rarefied Hypersonic Flows," AIAA Paper 90-1690.
[9] Hash, D., and Hassan, H., 1996, "A Decoupled DSMC/Navier-Stokes Analysis of a Transitional Flow Experiment," AIAA Paper 96-0353.
[10] Bourgat, J., Le Tallec, P., and Tidriri, M., 1996, "Coupling Boltzmann and Navier-Stokes Equations by Friction," J. Comput. Phys., **127**, pp. 227–245.
[11] Alder, B. J., 1997, "Highly discretized dynamics," Physica A, **240**, pp. 193–195.
[12] Le Tallec, P., and Mallinger, F., 1997, "Coupling Boltzmann and Navier-Stokes Equations by Half Fluxes," J. Comput. Phys., **136**, pp. 51–67.
[13] Tiwari, S., and Klar, A., 1998, "Coupling of the Boltzmann and Euler equations with adaptive domain decomposition procedure," J. Comput. Phys., **144**, pp. 710–726.
[14] Garcia, A. L., Bell, J., Crutchfield, W. Y., and Alder, B. J., 1999, "Adaptive Mesh and Algorithm Refinement using Direct Simulation Monte Carlo," J. Comput. Phys., **154**, pp. 134–155.
[15] Aktas, O., and Aluru, N. R., 2002, "A Combined Continuum/DSMC Technique for Multiscale Analysis of Microfluidic Filters," J. Comput. Phys., **178**, pp. 342–372.
[16] Roveda, R., Goldstein, D. B., and Varghese, P. L., 2000, "Hybrid Euler/direct simulation Monte Carlo calculation of unsteady slit flow," J. Spacecr. Rockets, **37**(6), pp. 753–760.
[17] Hornung, R. D., and Kohn, S. R., 2002, "Managing Application Complexity in the SAMRAI Object-Oriented Framework," Concurrency and Computation: Practice and Experience, **14**, pp. 347–368.
[18] Quarteroni, A., 1999, *Domain decomposition methods for partial differential equations*, Oxford, New York; Clarendon Press, Oxford, New York.
[19] Berger, M., and Oliger, J., 1984, "Adaptive Mesh Refinement for Hyperbolic Partial Differential Equations," J. Comput. Phys., **53**, pp. 484–512.
[20] Berger, M., and Colella, P., 1989, "Local Adaptive Mesh Refinement for Shock Hydrodynamics," J. Comput. Phys., **82**, pp. 64–84.
[21] Colella, P., 1985, "A Direct Eulerian MUSCL Scheme for Gas Dynamics," SIAM (Soc. Ind. Appl. Math.) J. Sci. Stat. Comput., **6**, pp. 104–117.

[22] Colella, P., and Glaz, H. M., 1985, ''Efficient Solution Algorithms for the Riemann Problem for Real Gases,'' J. Comput. Phys., **59**, pp. 264–289.
[23] Saltzman, J., 1994, ''An Unsplit 3D Upwind Method for Hyperbolic Conservation Laws,'' J. Comput. Phys., **115**, pp. 153–167.
[24] Hadjiconstantinou, N. G., and Simek, O., 2002, ''Constant-Wall-Temperature Nusselt Number in Micro and Nano-Channels,'' J. Heat Transfer, **124**, pp. 356–364.
[25] Hadjiconstantinou, N. G., 2002, ''Sound wave propagation in transition-regime micro- and nanochannels,'' Phys. Fluids, **14**, pp. 802–809.
[26] Hadjiconstantinou, N. G., 2003, ''Comment on Cercignani's second-order slip coefficient,'' Phys. Fluids, **15**, pp. 2352–2354.
[27] Hadjiconstantinou, N. G., and Simek, O., 2003, ''Sound propagation at small scales under continuum and non-continuum transport,'' J. Fluid Mech., **488**, pp. 399–408.
[28] Zheng, Y., Garcia, A. L., and Alder, B. J., 2002, ''Comparison of kinetic theory and hydrodynamics for Poiseuille Flow,'' J. Stat. Phys., **109**, pp. 495–505.
[29] Bird, G. A., 1994, *Molecular Gas Dynamics and the Direct Simulation of Gas Flows*, Clarendon, Oxford.
[30] Allen, M. P., and Tildesley, D. J., 1987, *Computer Simulation of Liquids*, Clarendon, Oxford.
[31] Garcia, A. L., and Wagner, W., 2000, ''Time step truncation error in direct simulation Monte Carlo,'' Phys. Fluids, **12**, pp. 2621–2633.
[32] Hadjiconstantinou, N. G., 2000, ''Analysis of Discretization in the Direct Simulation Monte Carlo,'' Phys. Fluids, **12**, pp. 2634–2638.
[33] Wagner, W., 1992, ''A Convergence Proof for Bird's Direct Simulation Monte Carlo Method for the Boltzmann Equation,'' J. Stat. Phys., **66**, pp. 1011–1044.
[34] Garcia, A. L., and Alder, B. J., 1998, ''Generation of the Chapman-Enskog Distribution,'' J. Comput. Phys., **140**, pp. 66–70.
[35] Bird, G. A., 1970, ''Breakdown of Translational and Rotational Equilibrium in Gaseous Expansions,'' Am. Inst. Aeronaut. Astronaut. J., **8**, p. 1998.
[36] Trangenstein, J. A., and Pember, R. B., 1992, ''Numerical Algorithms for Strong Discontinuities in Elastic-Plastic Solids,'' J. Comput. Phys., **103**, pp. 63–89.
[37] Hadjiconstantinou, N. G., Garcia, A. L., Bazant, M. Z., and He, G., 2003, ''Statistical error in particle simulations of Hydrodynamic Phenomena,'' J. Comput. Phys., **187**, pp. 274–297.
[38] Alexander, F., Garcia, A. L., and Tartakovsky, D., 2002, ''Algorithm Refinement for Stochastic Partial Diffential Equations: I. Linear Diffusion,'' J. Comput. Phys., **182**(1), pp. 47–66.
[39] Hirschfelder, J. O., Curtiss, C. F., and Bird, B., 1964, *Molecular theory of gases and liquids*, Wiley, New York.
[40] Schmidt, B., and Worner, M., 1983, ''Problems with the Computation of the Shock Structure in Binary Gas Mixtures Using the Direct Simulation Monte Carlo Method,'' Acta Mech., **1–4**, pp. 59–55.
[41] Arora, M., and Roe, P. L., 1997, ''On Postshock Oscillations Due to Shock Capturing Schemes in Unsteady Flows,'' J. Comput. Phys., **130**, pp. 25–40.
[42] Woodward, P. R., and Colella, P., 1984, ''The Numerical Simulation of Two-dimensional Fluid Flow with Strong Shocks,'' J. Comput. Phys., **54**, pp. 115–173.
[43] Meshkov, E. E., 1969, ''Instability of the Interface of two Gases Accelerated by a Shock Wave,'' Fluid Dyn., **43**(5), pp. 101–104.
[44] Meshkov, E. E., 1970, ''Instability of a Shock Wave Accelerated Interface between two Gases,'' NASA Tech. Trans., **F-13074**.
[45] Richtmyer, R. D., 1960, ''Taylor Instability in Shock Acceleration of Compressible Fluids,'' Commun. Pure Appl. Math., **13**, pp. 297–319.
[46] Brouillette, M., 2002, ''The Richtmyer-Meshkov Instability,'' Ann. Rev. Fluid Mech., **34**, pp. 445–468.
[47] Holmes, R. L., Dimonte, G., Fryxell, B., Gittings, M. L., Grove, J. W., Schneider, M., Sharp, D. H., Velikovich, A. L., Weaver, R. P., and Zhang, Q., 1999, ''Richtmyer-Meshkov Instability Growth: Experiment, Simulation and Theory,'' J. Fluid Mech., **389**, pp. 55–79.

Single Grid Error Estimation Using Error Transport Equation

Ismail Celik

Gusheng Hu

Department of Mechanical and Aerospace Engineering,
West Virginia University,
Morgantown, WV 26505-6106
E-mail: Ismail.Celik@mail.wvu.edu

This paper presents an approach to quantify the discretization error as well as other errors related to mesh size using the error transport equation (ETE) technique on a single grid computation. The goal is to develop a generalized algorithm that can be used in conjunction with computational fluid dynamics (CFD) codes to quantify the discretization error in a selected process variable. The focus is on applications where the conservation equations are solved for primitive variables, such as velocity, temperature and concentration, using finite difference and/or finite volume methods. An error transport equation (ETE) is formulated. A generalized source term for the ETE is proposed based on the Taylor series expansion and accessible influence coefficients in the discretized equation. Representative examples, i.e., one-dimensional convection diffusion equation, two-dimensional Poisson equation, two-dimensional convection diffusion equation, and nonlinear one-dimensional Burger's equation are presented to verify this method and elucidate its properties. Discussions are provided to address the significance and possible potential applications of this method to Navier-Stokes solvers.
[DOI: 10.1115/1.1792254]

Keywords: Error Transport Equation, Single Grid Error Estimator, Discretization Error, Numerical Uncertainty, Computational Fluid Dynamics

1 Introduction

As computational fluid dynamics (CFD) is being utilized more and more in research and development in industrial design, the importance of quantifying numerical uncertainty in computer simulations is also being appreciated by the CFD community. Among the many types of errors included in the overall solution, the errors arising from insufficient grid resolution is a major contributor. It is also the type of error that can be controlled by a careful grid convergence study. Thus, it is desired that the quantification of grid convergence error (also called the discretization error) should become an integral part of any CFD application.

Richardson extrapolation (RE), [1,2], is one of the commonly used methods for the purpose of quantifying discretization error. The theory of RE, applications to a wide range of problems, pros and cons can be found in Celik et al. [3], Roache [4,5], Celik and Zhang [6], Celik and Karatekin [7], Stern et al. [8], Cadafalch et al. [9], and Eca and Hoekstra [10] among others. The review of the previous literature shows that although RE is a viable method for quantifying the discretization errors, it has many pitfalls, and in some situations it simply does not work [6,7,10,11]. Theoretically one needs three sets of grids to establish the observed order of accuracy, hence the error; in practice one almost always ends up using as many as four to six different grids to make sure that the three sets of grids used in the final analysis are in the asymptotic range, i.e., in the range where the first few terms in the truncation error series expansion are truly the dominant terms. In some cases a least square approach is necessary [10], which requires more than three sets of grids. Moreover, RE does not work properly when the grid convergence shows an oscillatory behavior, which is often attributed to the common use of mixed order discretization schemes.

Another viable method that can be used for quantification of discretization error is the error transport equation (ETE) method. A brief conceptual review of this method was provided by Roache [4,5]. In this approach a transport equation is derived for the error, which can be solved either simultaneously or as a post processing exercise using the same computer code that solves for a selected field variable. A key issue is the derivation of the error source term in the ETE. Some preliminary work on this topic can be found in Van Straahlen et al. [12], Zhang et al. [13,14], Wilson and Stern [15], Celik and Hu [16], Celik et al. [17], and Qin and Shih [18].

Van Straahlen et al. [12] investigated a similar method specifically for finite volume discretization scheme, and applied it to estimate discretization error of one-dimensional and two-dimensional upwind-based steady convection-diffusion equation. Van Straahlen defines the source term in the error equation as the residual of the original partial differential equation (PDE) when the approximate numerical solution is substituted into the PDE [see Eq. (2.1) in this paper]. For this the numerical solution $\tilde{\phi}_h$ needs to be mapped onto a continuous distribution on the computational domain. To accomplish this, the integral form of the error equation in conjunction with the divergence theorem is used, along with a piecewise linear function that corresponds to centered difference finite volume estimate of the residual. In this regard the method of Van Straahlen does not appear to be general. It differs from the present analysis in many ways, particularly in evaluation of the source term in the error transport equation. The present analysis presents a generalized scheme that is not limited to piecewise linear approximation. It applies to any finite difference/finite volume method.

Zhang et al. [13,14] have proposed an approximate expression for calculating the residual based on the flux difference across the grid cell interfaces within the context of a particular numerical method based on Roe's upwind flux-differencing scheme. Zhang et al. [14] further presented a verification study where they compared various error estimators when applied to one-dimensional Euler equations. Their study is very enlightening in that it elucidates many of the problems posed to the users in quantification of discretization errors.

Wilson and Stern [15] also tried to attack the error estimation problem by using the error equation approach based on classical modified equation concept, but they reported some less favorable comments.

A recent study by Qin and Shih [18] also attempts to utilize the same method to explore the usefulness in the prediction of grid-induced error. They refer to the approximation of the error source

Contributed by the Fluids Engineering Division for publication in the JOURNAL OF FLUIDS ENGINEERING. Manuscript received by the Fluids Engineering Division June 16, 2003; revised manuscript received March 2, 2004. Associate Editor: K. D. Squires.

term as ''modeling'', which is essentially based on the Taylor series expansion for each individual scheme and the corresponding PDE, as in Wilson and Stern [15]. In their approach, a grid-independent solution is needed, which is used as an approximate to the exact solution to evaluate the derivatives in the modeled error source terms. This, of course, is not a practical approach, because if the grid independent solution is already known, error estimation becomes a matter of academics.

So far, most of the work in the literature that is relevant to the derivation of the error source term is problem-specific and scheme-specific; no generalized concept, which is aimed at the integration of this method into a general purpose CFD code, has been proposed. In this context, Celik and Hu [16] proposed a coefficient-based approach to derive the error source term using Taylor series expansion. A number of verification studies can be found in Hu [19], Celik and Hu [16], and Celik et al. [17]. The present authors believe that the potential of the ETE method as an error estimator has not been investigated thoroughly, and it needs to be studied further to expose its full advantages and disadvantages.

As is apparent from the above review, one of the outstanding issues in the application of the ETE method is the calculation of the source term. In the method suggested by Celik and Hu [16], the truncation error is expressed in terms of the coefficient matrix used for the solution of the original dependent field variable. The premise of this approach is such that if the user has access to the coefficient matrix used for the numerical solution of a dependent variable, the same set of coefficients can be used for calculating the source term in the ETE as well as solving for the discretization error in that same variable. A further advantage of this approach is that in most cases the ETE needs no further treatment for boundary conditions while that information is already embodied in the coefficient matrix of the parent equation.

The present paper elucidates the derivation of the error transport equation based on this generalized source term concept, and attempts to demonstrate the feasibility of the ETE and advantages as a viable discretization error estimator.

2 Theory

2.1 Error Transport Equation. In the following derivation we closely follow the notation used by Ferziger [20]. Let ''L'' denote an operator representing a partial differential equation (PDE) constrained by certain boundary conditions. Let ϕ be the exact solution of the given PDE, then we have

$$\mathrm{L}(\phi)=0. \tag{2.1}$$

Also, let ''$\mathrm{L_h}$'' denote a discretized operator for the PDE on a grid size h obtained by applying a certain discretization scheme, say, finite difference or finite volume method. Usually $\mathrm{L_h}(\tilde{\phi})\cong 0$ constitutes a set of linearized algebraic equations, and can be solved using a linear system solver either directly or iteratively. If the iterative convergence error and machine round-off error are negligible during the solution procedure of the linear systems, the numerical solution $\tilde{\phi}$ should satisfy the discretization equation,

$$\mathrm{L_h}(\tilde{\phi})=0. \tag{2.2}$$

If the exact solution ϕ is substituted into Eq. (2.2), a residual term or the so-called truncation error term, which is a function of ϕ, is induced due to the discretization errors, i.e.,

$$\mathrm{L_h}(\phi)=\tau(\phi). \tag{2.3}$$

Subtracting Eq. (2.2) from (2.3), and defining the exact, or the true error as $\varepsilon=\phi-\tilde{\phi}$, yields the desired error transport equation (ETE)

$$\mathrm{L_h}(\varepsilon)=\tau(\phi). \tag{2.4}$$

Usually the left hand side (LHS) of Eq. (2.4) represents the time rate of change, convection and diffusion of the error, a scalar quantity in the present study, and the right hand side (RHS) represents the error source terms, hence the terminology ETE. As long as $\mathrm{L_h}$ and τ are provided, error can be solved for using this equation. It is also possible that instead of substituting ϕ into $\mathrm{L_h}$, one can substitute $\tilde{\phi}$ into L (Eq. (2.1)) and introduce a similar truncation error term [20]. The resulting error equation is then valid in a continuum sense. However, the major conceptual gap in this approach is that the domain of definition of the discrete solution must be extended to the continuum, involving projection. Here the first approach is preferred, and its advantages are discussed in the next section.

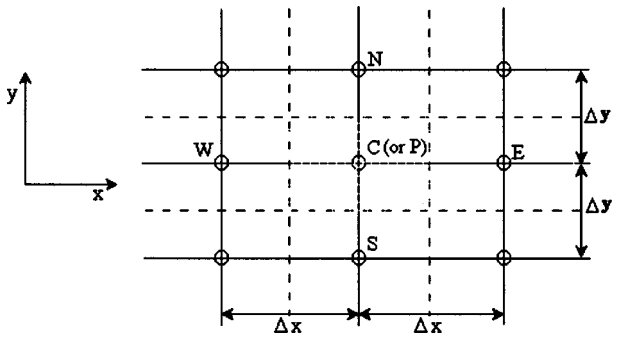

Fig. 1 Typical computational cell arrangement used in finite volume discretization

If iterative convergence error is taken into account, Eq. (2.2) should be modified to

$$\mathrm{L_h}(\tilde{\phi})=R_{iter}. \tag{2.5}$$

Correspondingly, Eq. (2.3) becomes

$$\mathrm{L_h}(\phi)=\tau(\phi)-R_{iter}=\tau_{mod}, \tag{2.6}$$

whereas the resulting error equation retains the same form as Eq. (2.4) but with different contents in τ_{mod}. The iteration error should not be neglected unless the magnitude of the R_{iter} is small compared to τ.

2.2 Generalized Source Term Concept. The main difficulty in solving for error using Eq. (2.4) is the accurate representation and evaluation of the source term τ. The generalized source term concept [16,17,19] relies on a full access to the $\mathrm{L_h}$, i.e., the influence coefficients of the discretized equations. In what follows we present this generalized concept.

It shall be assumed that $\mathrm{L_h}$ already contains the boundary-condition information, and thus $\mathrm{L_h}$ does represent a complete set of equations that are ready to be solved. It is further assumed that $\mathrm{L_h}$ is linearized, thus, the discretized equation for the variable being solved can be arranged into the following form

$$a_P\tilde{\phi}_P-\sum a_{nb}\tilde{\phi}_{nb}=b, \tag{2.7}$$

where a's are the coefficients, the subscript ''P'' denotes the center node in a typical computational cell (see Fig. 1), and ''nb'' denotes the neighboring grid nodes, b usually is a source term, which can be a constant term, or an explicit function of $\tilde{\phi}$ evaluated at previous time step or iteration.

To demonstrate the derivation process, we consider a fully implicit scheme with five-point stencil in two-dimensional space (see Fig. 1) and first order in time. Following the convention shown in Fig. 1, Eq. (2.7) can be written as

$$a_P\tilde{\phi}_P-(a_W\tilde{\phi}_W+a_E\tilde{\phi}_E+a_S\tilde{\phi}_S+a_N\tilde{\phi}_N)=S_C+a_P^o\tilde{\phi}_P^o, \tag{2.8}$$

where S_C denotes the constant part of the source term, $\tilde{\phi}_P^o$ is the numerical value at center grid node and evaluated at the old time

level. Note that how a_p and a_{nb}'s are obtained depends on the particular scheme used and is not our concern. However, their values do need to be known because they carry the information of the discretization error and are responsible for a general expression of τ in the error equation (2.4). According to Eq. (2.3), we rewrite Eq. (2.8) in terms of exact solution ϕ with an extra residual term being introduced:

$$a_P\phi_P-(a_W\phi_W+a_E\phi_E+a_S\phi_S+a_N\phi_N)=S_C+a_P^o\phi_P^o+\tau(\phi). \tag{2.9}$$

Subtracting Eq. (2.8) from Eq. (2.9) side by side yields the transport equation for the true error $\varepsilon=\phi-\tilde{\phi}$,

$$a_P\varepsilon_P-(a_W\varepsilon_W+a_E\varepsilon_E+a_S\varepsilon_S+a_N\varepsilon_N)=a_P^o\varepsilon_P^o+\tau(\phi). \tag{2.10}$$

The expression for $\tau(\phi)$ can be obtained (see Hu, 2002 for more detail) by expanding ϕ_W, ϕ_E, ϕ_S and ϕ_N about the center grid point in Eq. (2.9) using Taylor series. This leads to

$$\begin{aligned}\tau(\phi)=&(a_P-(a_W+a_E+a_S+a_N+a_P^o))\phi\\&+\sum_{m=1}^{\infty}\frac{\Delta t^m}{m!}(-1)^{m+1}a_P^o\phi_{t,(m)}\\&-\sum_{n=1}^{\infty}\frac{\Delta x^n}{n!}((-1)^n a_W+a_E)\phi_{x,(n)}\\&-\sum_{n=1}^{\infty}\frac{\Delta y^n}{n!}((-1)^n a_S+a_N)\phi_{y,(n)}-S_C.\end{aligned} \tag{2.11}$$

In Eq. (2.11), $\phi_{t,(m)}$ is the mth derivative with respect to time, $\phi_{x,(n)}$ is the nth derivative with respect to x, and similarly for y. All the derivative terms as well as ϕ itself should be evaluated at the center node P.

Thus, the derivation of the error equation is completed by Eq. (2.10) with the error source term τ being expressed by (2.11). What needs to be known to solve for error is (i) the coefficients a_P, a_W, a_E, a_S, a_N, a_P^o and the constant source term S_c, (ii) the location of the neighboring nodes (to obtain Δx and Δy) as well as the time step Δt, and (iii) values of ϕ and its derivatives. A key assumption in this coefficient-based concept is that the access to the contents (coefficients and constant source term value) of the discretized equation shall be granted. This can be achieved without much difficulty if the program is properly written by keeping this in mind. Information in part (ii) can be obtained from the same grid that is used to solve for the parent variable ϕ. In the absence of analytical solution of the PDE being solved, obtaining derivatives must rely on discrete evaluations with the help of the numerical solution, $\tilde{\phi}$. Accurate values of those derivative terms become crucial in solving for the error. In Section (2.4), issues regarding numerical evaluation of the derivative terms will be discussed in more detail.

Eq. (2.11) can be simplified for a steady state calculation where a_P^o becomes zero. Further, if the grid size is relatively small the first few terms in Eq. (2.11) will become dominant and it can then be approximated by only including those dominant terms, say up to fourth derivative. This will yield

$$\begin{aligned}\tau(\phi)\cong&(a_P-(a_W+a_E+a_S+a_N))\phi-(-a_W+a_E)\Delta x\phi_x\\&-\tfrac{1}{2}(a_W+a_E)\Delta x^2\phi_{xx}-\tfrac{1}{6}(-a_W+a_E)\Delta x^3\phi_{xxx}\\&-\tfrac{1}{24}(a_W+a_E)\Delta x^4\phi_{xxxx}-(-a_S+a_N)\Delta y\phi_y\\&-\tfrac{1}{2}(a_S+a_N)\Delta y^2\phi_{yy}-\tfrac{1}{6}(-a_S+a_N)\Delta y^3\phi_{yyy}\\&-\tfrac{1}{24}(a_S+a_N)\Delta y^4\phi_{yyyy}-S_C.\end{aligned} \tag{2.12}$$

If iterative convergence error is considered, the modified τ will take the form given in Eq. (2.6) and R_{iter} can be calculated from the known discretization equation

$$R_{iter}=a_P\tilde{\phi}_P-(a_W\tilde{\phi}_W+a_E\tilde{\phi}_E+a_S\tilde{\phi}_S+a_N\tilde{\phi}_N)-(S_C+a_P^o\tilde{\phi}_P^o). \tag{2.13}$$

Formulation of the error equation (Eq. (2.10)) and the τ terms using Eq. (2.11) reveals three major advantages of this coefficient-based approach: (i) by knowing the coefficient matrix in the discretization equation for the parent variable, a generalized truncation error term can be readily calculated, (ii) the same matrix solver that is used to solve for the original variable, ϕ, can be adopted to compute the error field by simply modifying the right hand side of the discretized equation, while the implicit coefficient matrix on the left hand side remains the same as that of the original variable ϕ and need not be recomputed, and (iii) in the error computation no extra grids need to be constructed, all calculations can be performed on a single grid.

2.3 Boundary Condition Issue. Another important advantage this approach brings with it is that there is no need to construct separate boundary conditions for the error equation. All the boundary information that is already contained in the discretized equation for the primitive variable, for example in Eq. (2.8), will be inherited automatically by the error equation. This is due to the fact that different implementations of the boundary conditions for ϕ in the end will be expressed in terms of influence coefficients; the values of those coefficients at the boundaries already implicitly carries the information, such as the order of the differencing scheme and the type of the boundary condition. Therefore, by taking over the values of the coefficients, the error equation recognizes this information and produces the right τ. This point is illustrated in the following example.

Consider a Dirichlet type boundary condition imposed on ϕ at the west boundary. A typical implementation of the discretized equation (Eq. (2.8)) on the first node just adjacent to the west boundary is to replace ϕ_W by the given boundary value, move this term to the right side to be incorporated into the S_c term, then set the coefficient a_W to be zero. The discretized equation on that node then takes the form

$$a_P\tilde{\phi}_P-(a_E\tilde{\phi}_E+a_S\tilde{\phi}_S+a_N\tilde{\phi}_N)=S_C^*+a_P^o\tilde{\phi}_P^o, \tag{2.14}$$

where S_C^* is the modified source term. Correspondingly, Eq. (2.9) becomes

$$a_P\phi_P-(a_E\phi_E+a_S\phi_S+a_N\phi_N)=S_C^*+a_P^o\phi_P^o+\tau(\phi), \tag{2.15}$$

and the discrete error equation becomes

$$a_P\varepsilon_P-(a_E\varepsilon_E+a_S\varepsilon_S+a_N\varepsilon_N)=\tau(\phi). \tag{2.16}$$

We may wish to derive the τ expression by Taylor series expansion directly from the boundary equation (Eq. (2.15)). This will result in the same equation as that derived from the generalized expression for τ (Eq. (2.11)) in which the a_w is set equal to zero, which is a properly treated boundary coefficient.

The same conclusion can be shown to hold for a boundary condition of a Neumann type. In general, if the boundary coefficients are properly treated and modified, i.e., the set of discrete equations for ϕ does cover both the boundary (the node next to the boundary) and the internal nodes, the description of the problem is complete and only one generalized expression for τ (Eq. (2.11)) is needed. Nevertheless, for a much more complex treatment of the boundary conditions of ϕ, where the boundary value

of true error is needed, a separate error equation can be derived from the discretized boundary equation, say, $L_h^B(\tilde{\phi})=0$, to represent the boundary sources for error. An example is presented in the appendix to illustrate this point.

2.4 Evaluation of τ Terms. To elucidate the difficulties in evaluation of the error source term we revisit the error equation (2.10) and the generalized expression for the error source term $\tau(\phi)$. Theoretically, if $\tau(\phi)$ is exact, and no iterative convergence error occurs in solving Eq. (2.10), the obtained error should be exact. However, in most CFD applications the "exact" solution ϕ is not known, what is readily available is the approximate numerical solution $\tilde{\phi}$. For this reason we have no choice but to use the numerical solution $\tilde{\phi}$ to compute the source term $\tau(\phi)$. Consequently, numerical evaluation using certain differencing schemes needs to be considered for evaluating the derivatives that appear in $\tau(\phi)$. Further, evaluating an infinite number of the τ terms is impossible. For schemes of 2nd order or less, the formula expressed in Eq. (2.12) should be sufficient. With the above remarks, the following modified expression for the approximate error, $\tilde{\varepsilon}$, can be obtained:

$$a_P\tilde{\varepsilon}_P-(a_W\tilde{\varepsilon}_W+a_E\tilde{\varepsilon}_E+a_S\tilde{\varepsilon}_S+a_N\tilde{\varepsilon}_N)\cong\tau(\tilde{\phi}), \tag{2.17}$$

with the RHS to be evaluated from

$$\begin{aligned}\tau(\tilde{\phi})\cong&(a_P-(a_W+a_E+a_S+a_N))\tilde{\phi}-(-a_W+a_E)\Delta x\frac{\delta\tilde{\phi}}{\delta x}\\&-\tfrac{1}{2}(a_W+a_E)\Delta x^2\frac{\delta^2\tilde{\phi}}{\delta x^2}-\tfrac{1}{6}(-a_W+a_E)\Delta x^3\frac{\delta^3\tilde{\phi}}{\delta x^3}\\&-\tfrac{1}{24}(a_W+a_E)\Delta x^4\frac{\delta^4\tilde{\phi}}{\delta x^4}-(-a_S+a_N)\Delta y\frac{\delta\tilde{\phi}}{\delta y}\\&-\tfrac{1}{2}(a_S+a_N)\Delta y^2\frac{\delta^2\tilde{\phi}}{\delta y^2}-\tfrac{1}{6}(-a_S+a_N)\Delta y^3\frac{\delta^3\tilde{\phi}}{\delta y^3}\\&-\tfrac{1}{24}(a_S+a_N)\Delta y^4\frac{\delta^4\tilde{\phi}}{\delta y^4}-S_C,\end{aligned} \tag{2.18}$$

where $\tilde{\varepsilon}=\varepsilon-\Delta\varepsilon_{num}$, $\Delta\varepsilon_{num}$ is the error involved in the calculation of the numerical solution of $\tilde{\varepsilon}$, including the approximation used in evaluating $\tau(\phi)$ in Eqs. (2.17) and (2.18). These equations should be viewed as the definition of $\tilde{\varepsilon}$; whether $\tilde{\varepsilon}$ is a good estimate to ε or not will be shown by numerical experiments. Clearly, if the iterative error is large, i.e., $e_{rel}=(\phi-\tilde{\phi})/\phi\sim o(1)$, Eq. (2.18) will not work. Also note, the operator δ represents a differencing operator of the corresponding continuous derivatives. This slight modification by using numerical values and discrete differencing provides us, on the one hand, a practical way for the evaluation of the error source, but, on the other hand, degrades the accuracy of the true τ with its influence on the calculated error to be explored.

It should also be pointed out that the generalized expression for τ usually consists of two parts: one is the original PDE represented by the operator L in Eq. (2.1), and the other is the actual truncation error due to discretization, i.e.,

$$\tau(\phi)=L(\phi)+\tau^*(\phi). \tag{2.19}$$

The two parts are hidden in the generalized τ and cannot be differentiated from each other in general. This point can be made clear by giving an example. Consider the discretized Eq. (3.4): we can obtain τ in Eq. (3.6) by expanding Eq. (3.4) about the center node P using Taylor series. Now, for certain schemes, say 1st order upwind, if we substitute the expressions for the coefficients a_E, a_W etc into the τ expression (Eq. 3.7), we will notice that the τ actually has two parts: one is the original PDE, which should be equal to zero, and the other is the τ^*, which represents the real truncation error:

$$\begin{aligned}\tau(\phi)\cong&(a_P-(a_W+a_E))\phi-(-a_W+a_E)\Delta x\frac{\partial\phi}{\partial x}\\&-\tfrac{1}{2}(a_W+a_E)\Delta x^2\frac{\partial^2\phi}{\partial x^2}-\tfrac{1}{6}(-a_W+a_E)\Delta x^3\frac{\partial^3\phi}{\partial x^3}\\&-\tfrac{1}{24}(a_W+a_E)\Delta x^4\frac{\partial^4\phi}{\partial x^4}\\=&\left(u\frac{\partial\phi}{\partial x}-\Gamma\frac{\partial^2\phi}{\partial x^2}\right)-\tfrac{1}{2}u\Delta x\frac{\partial^2\phi}{\partial x^2}+\tfrac{1}{6}u\Delta x^2\frac{\partial^3\phi}{\partial x^3}\\&-\tfrac{1}{24}(u\Delta x^3+2\Gamma\Delta x^2)\frac{\partial^4\phi}{\partial x^4}\\=&\,\mathrm{PDE}+\tau^*(\phi).\end{aligned} \tag{2.20}$$

Suppose the derivative terms can be evaluated exactly, then the PDE part must be zero, i.e., $L(\phi)=0$ (Eq. (2.1)), with the actual error source being retained. But, if numerical evaluation is applied, the cancellation of $L(\phi)$ usually can not be guaranteed. In order to avoid an extra addition to the error source it may be desirable to subtract that original PDE evaluated using the same set of numerical values and the same differencing schemes as used for the derivative evaluations. For example, if the original PDE has the form of

$$L(\phi)=u\phi_x+v\phi_y-\Gamma(\phi_{xx}+\phi_{yy})=0, \tag{2.21}$$

the accuracy of numerically evaluated τ (Eq. (2.18)) can be further improved by doing the following:

$$\tau^*(\tilde{\phi})\cong\tau(\tilde{\phi})-\mathrm{FDE}, \tag{2.22}$$

where

$$\mathrm{FDE}=u\frac{\delta\tilde{\phi}}{\delta x}+v\frac{\delta\tilde{\phi}}{\delta y}-\Gamma\left(\frac{\delta^2\tilde{\phi}}{\delta x^2}+\frac{\delta^2\tilde{\phi}}{\delta y^2}\right). \tag{2.23}$$

The above formulation of τ or τ's derived in a similar fashion is of greatest importance in practical applications. It should be emphasized that the present formulation uses as examples two-dimensional five-point stencil schemes and a given PDE. In the verification study (Section 3) this approach of formulating τ is adopted for all cases.

The next question is then how to evaluate the derivative terms in τ in a reasonable manner so that a desired accuracy can be attained. At this point, we adopt an approach of consistent evaluation of the derivatives [21], in which it is pointed out that derivative evaluation using a scheme of at least the same formal order as the one used to solve the original dependent variable, ϕ, is desired. Further, if possible, evaluation of τ using the consistent scheme, i.e., not only of the same order but also of the same differencing, will yield better accuracy. In other words, if the original scheme uses first order upwinding to discretize the convection term, we may wish to use 2nd order backward, forward or central differencing to evaluate $\delta\phi/\delta x$ for better accuracy; if the original scheme is 2nd order central differencing, we prefer 2nd order central differencing over other 2nd order methods to evaluate $\delta\phi/\delta x$, i.e., to be consistent. The main advantage of the consistent evaluation is that it enforces the residual of the discretized PDE hidden in the generalized τ to be zero. This means in the above example that we don't have to evaluate FDE (in Eq. (2.22)) and subtract it from the actual τ, since this part should simply be nearly zero. However, consistency is not a necessary condition. If the original scheme is not known, we will not be able to evaluate the derivatives in a consistent way. In this case, we need (i) to

evaluate the derivatives using at least second order method, if the original scheme is first or second order, and (ii) identify the PDE, formulate an equivalent FDE, evaluate it in the same way as evaluating other derivatives, and subtract it from the τ. In this way, the unwanted PDE part of τ will be canceled.

2.5 Extension to More General Schemes. Hu [19] has suggested a feasible extension of this concept from steady-state or fully implicit calculations to a more general transient calculation with arbitrary implicitness and explicitness. The only extra requirement is also to know the influence coefficients on the right hand side of the discretization equation, in addition to those on the left hand side. To differentiate the two types of coefficients, we may call the LHS the implicit coefficients, and the RHS the explicit coefficients. Thus, if an error analysis for a transient calculation is needed, the discretization equation should be properly written in the following form:

$$a_P\tilde{\phi}_P-\sum a_{nb}\tilde{\phi}_{nb}=a_P^o\phi_P^o-\sum a_{nb}^o\tilde{\phi}_{nb}^o+S_c, \qquad (2.24)$$

where the coefficients with the superscript "*o*" are explicit coefficients, while without this are implicit coefficients. Also, the scalar $\tilde{\phi}$ with superscript "*o*" means it is evaluated at a previous time step. Note that both implicit and explicit coefficients are evaluated at the old time level, implicit coefficients can be updated during iterations at the same time level.

In the programming practice, one may not be very concerned about the coefficients on the RHS, since in the end all these would be combined into a single value *b*, which, along with the global matrix A, will be passed to a certain matrix solution routine (that solves a linear system in a form of $Ax=b$). But if a general error analysis were desired, the right hand side of the discretization equation would also need proper care. More precisely, not only the implicit coefficients on the LHS but also the explicit coefficients on the RHS need to be recorded.

The derivation of the error equation as well as the expression for the general source term can proceed in a similar manner. The following provides a brief recapitulation. First, write the discretized equation with induced residual:

$$a_P\phi_P-\sum a_{nb}\phi_{nb}=a_P^o\phi_P^o-\sum a_{nb}^o\phi_{nb}^o+S_c+\tau(\phi). \qquad (2.25)$$

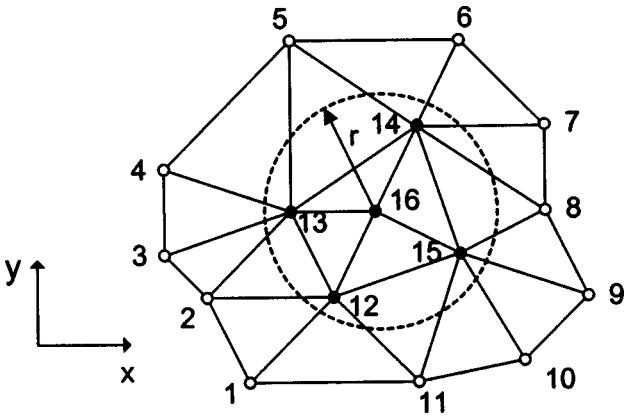

Fig. 2 Influence circle with radius r in unstructured grid. Nodes filled with black color fall into the influence domain of the node 16.

Subtracting Eq. (2.24) from Eq. (2.25) yields the error transport equation

$$a_P\varepsilon_P-\sum a_{nb}\varepsilon_{nb}=a_P^o\varepsilon_P^o-\sum a_{nb}^o\varepsilon_{nb}^o+\tau(\phi). \qquad (2.26)$$

The expression of τ in Eq. (2.26) is obtained from Eq. (2.25) by Taylor series expansion. Note, the expansion base point may be chosen arbitrarily. It is convenient to expand the left hand side about the center node at the new time level, and the right hand side about the center node at the old time level. One major advantage of this choice is that the mixed space-time derivatives that are usually difficult to evaluate would not appear in τ. If again, the five point stencil in two-dimensional space is considered, along with a two time level marching scheme, the source term τ can be written down as

$$\tau(\phi)=\left[\begin{array}{l}(a_P-(a_W+a_E+a_S+a_N))\phi\\ -\sum_{n=1}^{\infty}\frac{\Delta x^n}{n!}((-1)^n a_W+a_E)\phi_{x,(n)}-\sum_{n=1}^{\infty}\frac{\Delta y^n}{n!}((-1)^n a_S+a_N)\phi_{y,(n)}\end{array}\right]$$
$$-\left[\begin{array}{l}(a_P^o-(a_W^o+a_E^o+a_S^o+a_N^o))\phi^o\\ -\sum_{n=1}^{\infty}\frac{\Delta x^n}{n!}((-1)^n a_W^o+a_E^o)\phi_{x,n}^o-\sum_{n=1}^{\infty}\frac{\Delta y^n}{n!}((-1)^n a_S^o+a_N^o)\phi_{y,n}^o+S_C\end{array}\right] \qquad (2.27)$$

For the present study we first limit our work on the verification of the method for steady state problems. The transient calculations using Eq. (2.27) will be verified in a future study; some preliminary applications to transient problems (Celik and Hu, 2002; Hu, 2002) have already yielded fruitful results.

2.6 Generalization to Other Methods. The proposed method should not be only restricted to FVM/FDM with structured mesh. We also propose a possible extension of this method to unstructured grids. The error source term contains the derivatives of the original variable at the center node which are obtained from Taylor series expansion of the neighboring nodal values about the center node. To extend the method to the more general case of FE/FV methods on non-structured grids generalized Taylor series expansion should be used, i.e., $\phi(x,y)=\phi(x_0,y_0)+\phi_x\Delta x+\phi_y\Delta y+\phi_{xy}\Delta x\Delta y$ etc., after selecting an influence domain that signifies the neighboring nodes that influence the center node the most (see Fig. 2).

In the example shown in Fig. 2, the influence coefficients are of those nodes 12, 13, 14 and 15, for the center point 16. Once these influence coefficients are detected by a smart search algorithm, the derivative at those nodes can be evaluated using the same or higher order approximating polynomials that were used in the original scheme.

3 Verification

For simplicity, uniform grids are used in the following numerical computations. However, it should be kept in mind that the entire concept is not only limited to the uniform grids. Also, the iterative convergence error is assumed to be relatively small and therefore not included in the error equation. Special precaution was taken to satisfy this criterion.

3.1 Steady One-Dimensional Convection Diffusion. The steady one-dimensional convection diffusion equation is given by

$$u\phi_x - \Gamma\phi_{xx} = 0. \tag{3.1}$$

In the above equation, u is the velocity, Γ is the diffusivity. For the boundary conditions of

$$\begin{aligned} \phi &= \phi_0 \quad \text{at } x = 0, \\ \phi &= \phi_L \quad \text{at } x = L, \end{aligned} \tag{3.2}$$

the analytical solution is

$$\phi(x) = \left(\frac{\phi_L - \phi_0}{\exp(\mathrm{Pe}) - 1}\right)\left[\exp\left(\mathrm{Pe}\frac{x}{L}\right) - 1\right] + \phi_0, \tag{3.3}$$

where Pe is the Peclet number defined by $\mathrm{Pe} = uL/\Gamma$. In this study we let $L = 1$, $\Gamma = 0.1$, and let u take different positive values to see the effect of Pe on the solution as well as on the calculated error. The grid is arranged in such a way that the first and the last node is located at the west and the east boundary, respectively.

Scheme 1: First Order Upwind. The discretized equation for the above PDE has the general form of

$$a_P\tilde{\phi}_P - (a_W\tilde{\phi}_W + a_E\tilde{\phi}_E) = S_C. \tag{3.4}$$

Applying first order upwind to the convection term and central difference to the diffusion term will yield the following expression for the coefficients:

$$\begin{aligned} a_W &= u/\Delta x + \Gamma/\Delta x^2, \\ a_E &= \Gamma/\Delta x^2, \\ a_P &= u/\Delta x + 2\Gamma/\Delta x^2. \end{aligned} \tag{3.5}$$

Correspondingly, the error equation is then given by

$$a_P\varepsilon_P - (a_W\varepsilon_W + a_E\varepsilon_E) = \tau(\phi). \tag{3.6}$$

The working τ of the error equation for a steady one-dimensional three-point stencil scheme can be simply deduced from Eq. (2.22),

$$\begin{aligned} \tau(\tilde{\phi}) \cong (a_P - (a_W + a_E))\tilde{\phi} - (-a_W + a_E)\Delta x\frac{\delta\tilde{\phi}}{\delta x} \\ - \frac{1}{2}(a_W + a_E)\Delta x^2\frac{\delta^2\tilde{\phi}}{\delta x^2} - \frac{1}{6}(-a_W + a_E)\Delta x^3\frac{\delta^3\tilde{\phi}}{\delta x^3} \\ - \frac{1}{24}(a_W + a_E)\Delta x^4\frac{\delta^4\tilde{\phi}}{\delta x^4} - S_C - \mathrm{FDE}, \end{aligned} \tag{3.7}$$

where

$$\mathrm{FDE} = u\frac{\delta\tilde{\phi}}{\delta x} - \Gamma\frac{\delta^2\tilde{\phi}}{\delta x^2}. \tag{3.8}$$

It should be noted that the coefficients listed above are valid for all the internal nodes, but will be subject to proper modification on boundary nodes depending on the boundary conditions and the order of implementation at the boundary; however, this will not change the general expression of τ. This statement applies for all of the following examples.

Scheme 2: Central Difference. The grid Peclet number is defined by

$$\mathrm{Pe}_\Delta = u\Delta x/\Gamma. \tag{3.9}$$

If the Pe_Δ is less than two, the central difference scheme can be used. Coefficients in Eq. (3.4) will then become

$$\begin{aligned} a_W &= u/(2\Delta x) + \Gamma/\Delta x^2, \\ a_E &= -u/(2\Delta x) + \Gamma/\Delta x^2, \\ a_P &= 2\Gamma/\Delta x^2. \end{aligned} \tag{3.10}$$

According to the discussion in the previous section, the general expression for τ given in Eq. (3.8) is independent of the discretization scheme, as long as the scheme is based on a three-point stencil.

Results for the first order upwind scheme are presented in Figs. 3(*a*) through (*d*) for various Peclet (or grid Peclet) numbers. It can be observed that the calculated error agrees well with the exact error even at high Peclet numbers. Figures 4(*a*) and (*b*) shows the results for the central differencing scheme. As expected, the discretization error for the second order central differencing is much smaller than that for first order upwind scheme, and the present method captures both the magnitude and the sign of the error very well.

It is also observed in Figs. 3(*a*) through (*d*) that even though the exact error is significantly large near $x = 1.0$, it is still predicted well by the method.

Time Marching Scheme. It is worthwhile to mention that the steady solution for both ϕ and its error can be obtained by a time advancing scheme as well. In this case a slight modification is needed by including an extra term in the τ expression with the corresponding coefficient denoted by a_P^o, as already stated in the derivation of the previous section. Thus, Eq. (3.4) becomes

$$a_P\tilde{\phi}_P - (a_W\tilde{\phi}_W + a_E\tilde{\phi}_E) = S_C + a_P^o\tilde{\phi}_P^o. \tag{3.11}$$

If a first order backward time differencing is used, the coefficients a_W and a_E are still given by Eq. (3.5) and a_P changes to

$$\begin{aligned} a_P &= u/\Delta x + 2\Gamma/\Delta x^2 + a_P^o, \\ a_P^o &= 1/\Delta t, \end{aligned} \tag{3.12}$$

and the τ changes to

$$\begin{aligned} \tau(\tilde{\phi}) \cong (a_P - (a_W + a_E + a_P^o))\tilde{\phi} + a_P^o\Delta t\frac{\delta\tilde{\phi}}{\delta t} - (-a_W + a_E)\Delta x\frac{\delta\tilde{\phi}}{\delta x} \\ - \frac{1}{2}(a_W + a_E)\Delta x^2\frac{\delta^2\tilde{\phi}}{\delta x^2} - \frac{1}{6}(-a_W + a_E)\Delta x^3\frac{\delta^3\tilde{\phi}}{\delta x^3} \\ - \frac{1}{24}(a_W + a_E)\Delta x^4\frac{\delta^4\tilde{\phi}}{\delta x^4} - S_C - \mathrm{FDE}, \end{aligned} \tag{3.13}$$

where the FDE is already given in Eq. (3.8). Using this alternative approach the same results are obtained as those shown in Figs. 3–6.

3.2 Two-Dimensional Poisson Equation. The two-dimensional Poisson equation considered here is given by

$$\phi_{xx} + \phi_{yy} = \phi + g(x,y). \tag{3.14}$$

A manufactured solution on a rectangular domain of size $a \times b$ is constructed as

$$\phi(x,y) = \exp(-y/b)\cos(\pi x/a). \tag{3.15}$$

The function g and boundary conditions can then be deduced from Eq. (3.15),

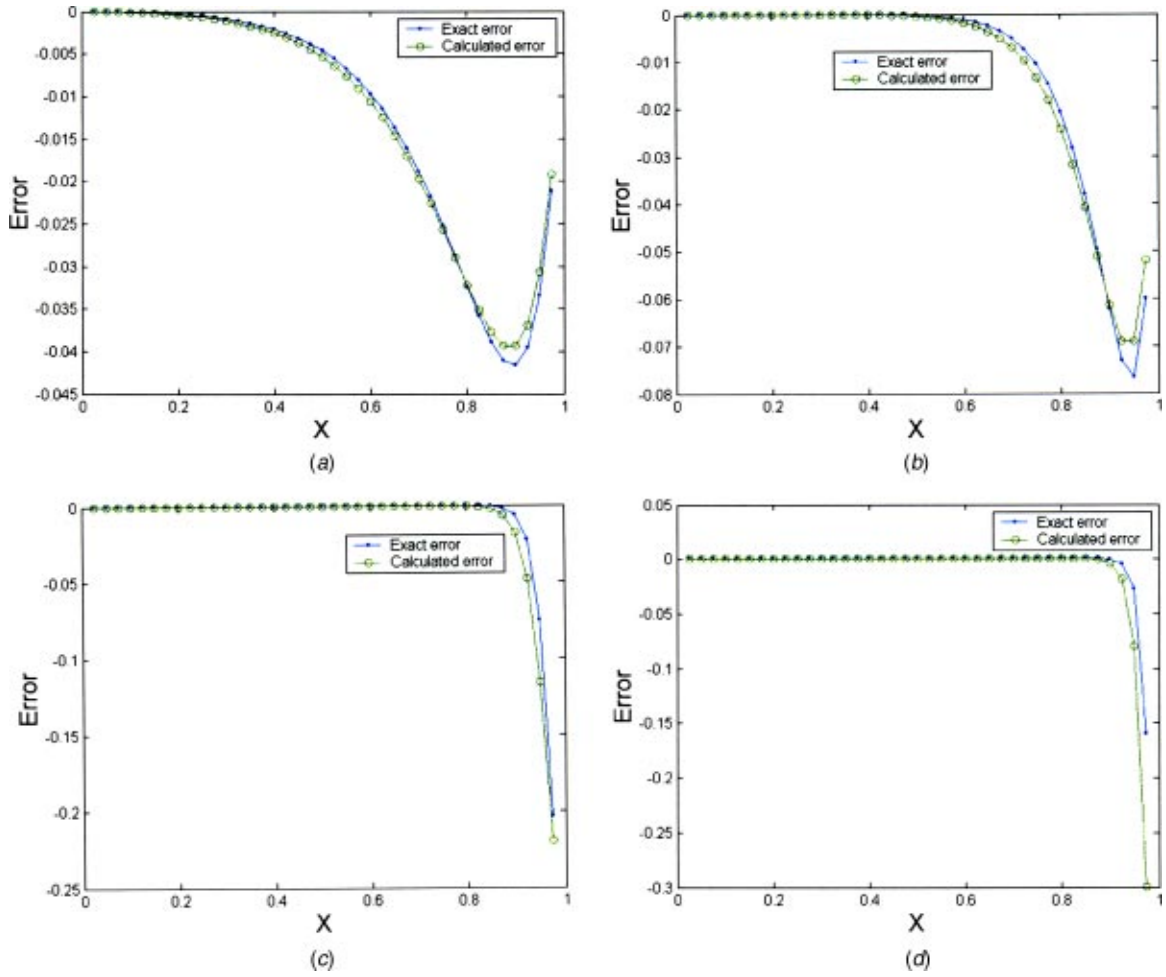

Fig. 3 Exact versus calculated error for steady 1D convection diffusion equation, first order upwind scheme, 41 nodes, velocity varies to obtain different Peclet numbers, (*a*) Pe=10, Pe_Δ=0.25, (*b*) Pe=20, Pe_Δ=0.5, (*c*) Pe=100, Pe_Δ=2.5, (*d*) Pe=200, Pe_Δ=5.0

$$g(x,y)=(-(\pi/a)^2+1/b^2+1)(\exp(-y/b)\cos(\pi x/a)), \tag{3.16}$$

and

$$\begin{aligned} \phi_x&=0 \quad \text{at } x=0,\\ \phi_x&=0 \quad \text{at } x=a,\\ \phi&=\cos(\pi x/a) \quad \text{at } y=0,\\ \phi&=\exp(-1)\cos(\pi x/a) \quad \text{at } y=b. \end{aligned} \tag{3.17}$$

In the examples given below, a and b are set equal to one. Also, the first and the last grid nodes in each direction are located exactly on the corresponding boundaries.

Using the central differencing scheme the discretization error equation for two-dimensional Poisson equation (3.14) on five-point stencil can be written as

$$a_P\varepsilon_P-(a_W\varepsilon_W+a_E\varepsilon_E+a_S\varepsilon_S+a_N\varepsilon_N)=\tau(\phi) \tag{3.18}$$

with the coefficients given by

$$\begin{aligned} a_W&=a_E=1/\Delta x^2,\\ a_S&=a_N=1/\Delta y^2,\\ a_P&=a_W+a_E+a_S+a_N+1, \end{aligned} \tag{3.19}$$

and τ given by Eq. (2.18) minus FDE, where

$$\text{FDE}=\frac{\delta^2\phi}{\delta x^2}+\frac{\delta^2\phi}{\delta y^2}-\phi-g(x,y). \tag{3.20}$$

Note, in this problem the Neumann boundary conditions (for ϕ not for $\tilde{\varepsilon}$!) are involved at south and north boundaries. Although the central differencing is second order, this is only valid on the internal nodes. The actual order of the entire scheme is also dependent on the implementation of the boundary conditions. One way of modifying the boundary coefficients is, for example for the west boundary, to let $\phi_W=\phi_P$ and set $a_P=a_P+a_W$ and $a_W=0$. This is a first order implementation of the Neumann boundary condition, therefore, the observed order of the scheme will be between one and two.

Figure 5 shows the contours of the predicted error in comparison to the exact error. Figures 6(*a*) and (*b*) show the profiles of error along a line at $y=0.5$, the midsection of the computational domain. A quick check of the convergence rate confirms the formal order of the scheme to be approximately first order. Again, a very good agreement is obtained between exact and predicted error. It is apparent from these figures that not only the magnitude but also its sign is predicted well.

3.3 Steady Two-Dimensional Convection Diffusion. The steady two-dimensional convection diffusion equation is given by

$$u\phi_x+v\phi_y-\Gamma(\phi_{xx}+\phi_{yy})=0, \tag{3.21}$$

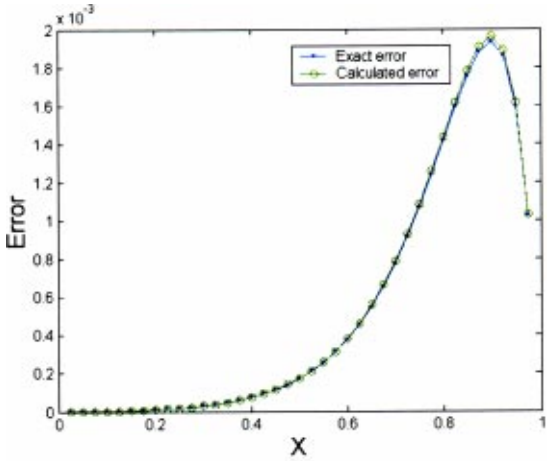

Fig. 4 Exact versus calculated error for steady 1D convection diffusion equation, central difference scheme, 41 nodes, velocity varies to obtain different Peclet numbers, (*a*) Pe=10, Pe_Δ =0.25, (*b*) Pe=20, Pe_Δ=0.5

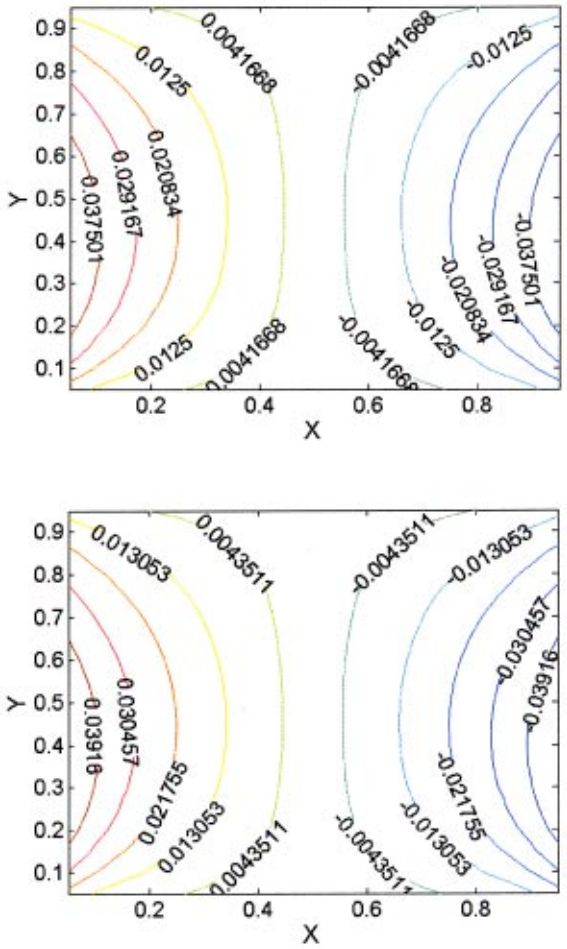

Fig. 5 Exact versus calculated error for 2D Poisson equation, central difference scheme, 21*21 grid; (*a*) exact error, (*b*) calculated error

where u and v are convective velocities in x and y direction respectively; Γ is again the diffusivity. If a steady line source is introduced into a point on an infinitely large xy-plane, the analytical solution can be derived by transformation of coordinate systems,

$$\phi(x,y)=\frac{\dot{m}}{2\pi\Gamma}\exp\left(\frac{Vx'}{2\Gamma}\right)\mathrm{K}_0\left(\frac{r}{2\Gamma}\right), \tag{3.22}$$

where $\dot{m}$ is the constant mass flow rate of the line source, V is the velocity magnitude in the x'-direction of the transformed coordinate system, K_0 is the modified Bessel function of second kind, r is the distance from the line source.

For the numerical computation, Γ is set equal to 0.1, V is 1. Also, a square computational domain of $x\in[0,1]$ and $y\in[0,1]$ is chosen with the line source located at $x=-1$, $y=-1$ being kept outside the computational domain. Dirichlet conditions are imposed at all boundary nodes using the analytical solution.

Consider a five-point stencil method. As in the example of the previous section the discretized equation for $\underline{\phi}$ and error can be written as

$$a_P\tilde{\phi}_P-(a_W\tilde{\phi}_W+a_E\tilde{\phi}_E+a_S\tilde{\phi}_S+a_N\tilde{\phi}_N)=S_C, \tag{3.23}$$

$$a_P\phi_P-(a_W\phi_W+a_E\phi_E+a_S\phi_S+a_N\phi_N)=S_C+\tau(\phi), \tag{3.24}$$

$$a_P\varepsilon_P-(a_W\varepsilon_W+a_E\varepsilon_E+a_S\varepsilon_S+a_N\varepsilon_N)=\tau(\phi), \tag{3.25}$$

where the expression for τ is given by Eqs. (2.22) and (2.23).

Scheme 1: First Order Upwind. When the first order upwind scheme is applied to the convective terms and central differencing is applied to viscous terms, the coefficients for the internal nodes can be expressed as

$$\begin{aligned} a_W&=u/\Delta x+\Gamma/\Delta x^2,\\ a_E&=\Gamma/\Delta x^2,\\ a_S&=v/\Delta y+\Gamma/\Delta y^2,\\ a_N&=\Gamma/\Delta y^2,\\ a_P&=a_W+a_E+a_S+a_N\,. \end{aligned} \tag{3.26}$$

The predicted error trends for this scheme are presented in Fig. 7 for a grid of 41*41 and in Figs. 8(*a*) and (*b*) for a grid of 41*41 and 81*81, respectively. From a comparison of the maximum error on the two grids it is seen that the error only decreases by one half with grid doubling, that is, the observed order of the scheme is first order, which is also predicted by the calculated error.

Scheme 2: Central Difference. If central difference is used for all the terms in Eq. (3.21), the coefficients are

$$\begin{aligned} a_W&=u/(2\Delta x)+\Gamma/\Delta x^2,\\ a_E&=-u/(2\Delta x)+\Gamma/\Delta x^2, \end{aligned}$$

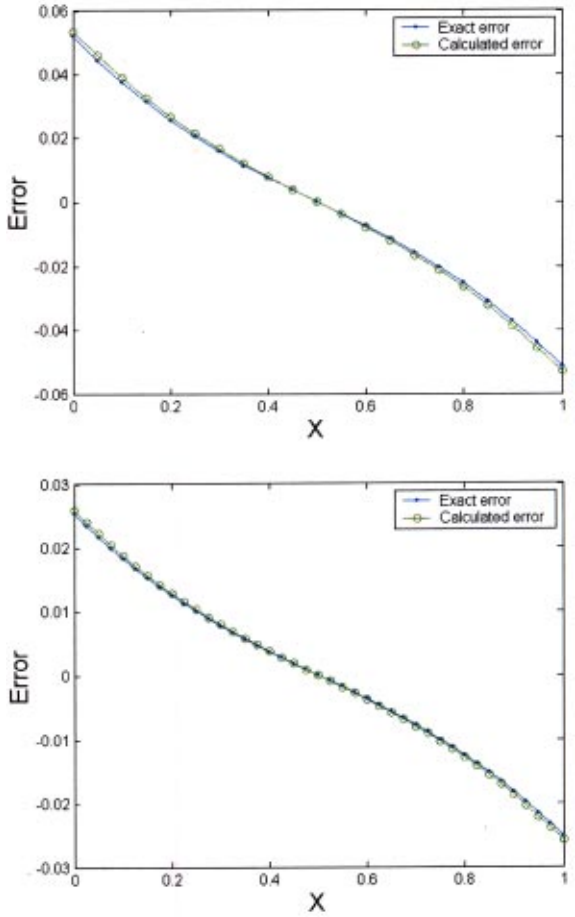

Fig. 6 Exact versus calculated error for 2D Poisson equation along the line of y=0.5, central difference scheme, (*a*) 21*21 grid, (*b*) 41*41 grid

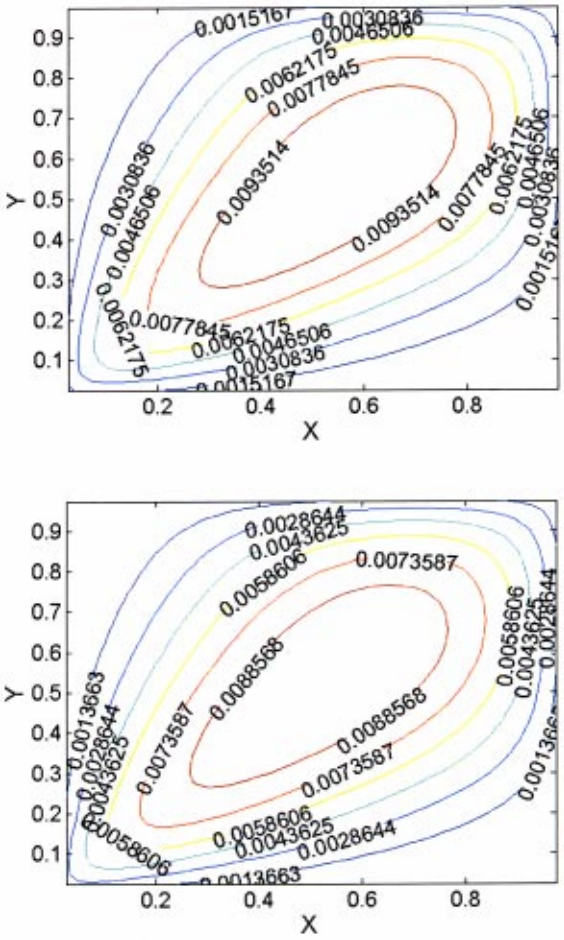

Fig. 7 Exact versus calculated error for 2D convection diffusion equation, 1st order upwind scheme, 41*41 grid; (*a*) exact error, (*b*) calculated error

$$a_S = v/(2\Delta y) + \Gamma/\Delta y^2, \tag{3.27}$$

$$a_N = -v/(2\Delta y) + \Gamma/\Delta y^2,$$

$$a_P = a_W + a_E + a_S + a_N .$$

Figures 9 and 10 show the exact error versus predicted error on the same two grids as the ones with the upwind scheme. Comparison of Figs. 7 and 9 shows that the error in the case of center differencing is much smaller, as expected. Figures 10(*a*) and (*b*) indicate that the error decreases approximately four times as the number of grids doubled; that is, the observed order in this case is second order, as expected.

It can be seen from Figs. 8(*a*) and (*b*) that the sign and the magnitude of the discretization error are predicted accurately for the case of upwind convective scheme where the errors are large. In the case of central differencing (see Figs. 10(*a*) and (*b*)) the overall trend of the error distribution is still captured well. However, the whole profile of the calculated error is shifted downwards away from the exact error. The difference between both becomes large especially near the origin ($x=0$ and $y=0$); this also leads to an incorrect sign of the predicted error at nodes in the vicinity of the origin. Generally, this behavior is due to the relatively large difference between the exact τ and the numerically evaluated τ. To be specific, it is due to the limitation in the accuracy of the numerical evaluation of the derivatives in the τ-expression. With increased order of the original scheme, the calculated error will tend to be more sensitive to the accuracy of the evaluated derivatives. Especially, if the derivative evaluation at, or close to the boundaries is not accurate enough, large error around the boundaries may occur for a boundary value problem.

3.4 Steady One-dimensional Non-linear Burger's Equation In the above examples the differential operator was linear. Here the proposed method is tested for a well-known nonlinear Burger's equation. The time marching is used as a means of iteration to account for the non-linear convection term. The Burger's equation is

$$\phi_t + \phi\phi_x = \nu\phi_{xx} . \tag{3.28}$$

For the boundary conditions

$$\begin{aligned} \phi &= \phi_0 \quad \text{at } x=0, \\ \phi &= 0 \quad \text{at } x=L, \end{aligned} \tag{3.29}$$

the steady-state analytical solution can be written as

$$\phi = \phi_0 \bar{\phi} \frac{1-\exp(\bar{\phi}\,\mathrm{Re}(x/L-1))}{1+\exp(\bar{\phi}\,\mathrm{Re}(x/L-1))}, \tag{3.30}$$

where $\mathrm{Re}=\phi_0 L/\nu$ is the Reynolds number and $\bar{\phi}$ is implicitly given by

$$\frac{\bar{\phi}-1}{\bar{\phi}+1} = \exp(-\bar{\phi}\,\mathrm{Re}). \tag{3.31}$$

For the present numerical study the domain length $L=1$ and the viscosity $\nu=0.1$. As has been already mentioned in Section 3.1, a

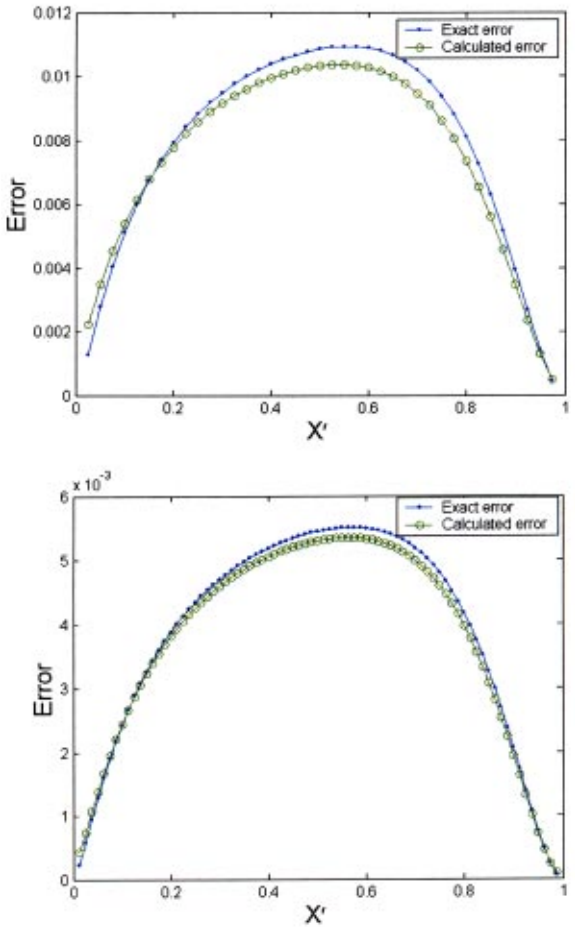

Fig. 8 Exact versus calculated error for 2D convection diffusion equation along the diagonal of the square domain, 1st order upwind scheme, x′=distance from the origin along the diagonal line, (*a*) 41*41 grid, (*b*) 81*81 grid

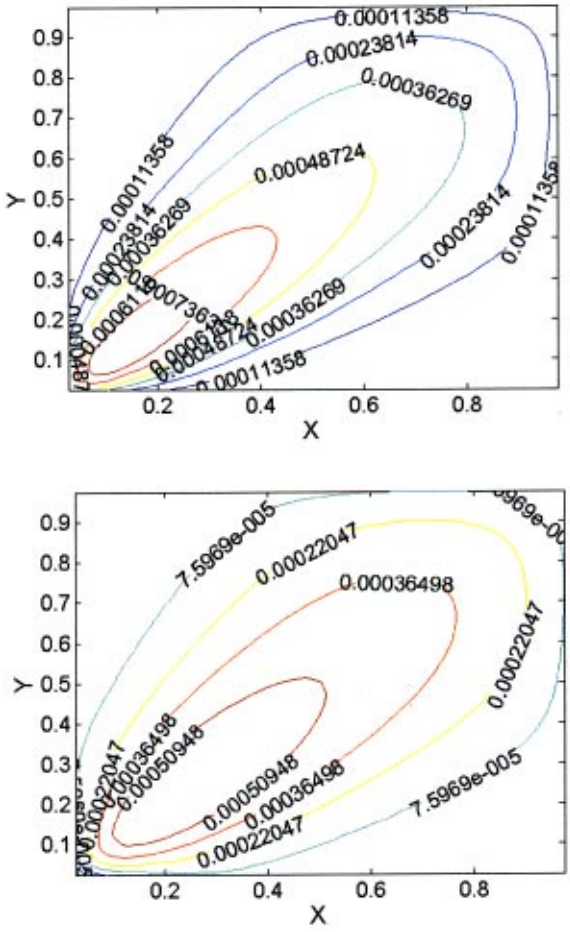

Fig. 9 Exact versus calculated error for 2D convection diffusion equation, central difference scheme, 41*41 grid; (*a*) exact error, (*b*) calculated error

steady-state solution may also be achieved by marching in time until a converged solution is attained. For that, the time derivative term is retained in Eq. (3.28). The linearized system of equations for this non-linear problem has the same form as the discretization equation, Eq. (3.11), but some coefficients may contain the variable ϕ that is evaluated at old time step or iteration. Similar to the first example, two schemes for the convective term, mainly, the first order upwind and the central difference, will be explored.

Scheme 1: First Order Upwind. When the first order upwind scheme is applied to the convective term and central differencing is applied to the viscous terms, the influence coefficients are given by

$$\begin{aligned} a_W &= \tilde{\phi}^o/\Delta x + \nu/\Delta x^2, \\ a_E &= \nu/\Delta x^2, \\ a_P^o &= 1/\Delta t, \\ a_P &= a_W + a_E + a_P^o . \end{aligned} \tag{3.32}$$

Computation is performed on a 41-nodes grid. The results for Re=10 and 200 (or Re_Δ=0.25 and 5.0) are plotted in Figs. 11(*a*) and (*b*) respectively; note, $\mathrm{Re}_\Delta=\phi_0 \Delta x/\nu$. On 41 grid nodes the exact error is large for a higher Reynolds number; in spite of this, the ETE captures the trend and the sign of the discretization error. The magnitude of the error is somewhat underestimated at those locations where the largest error occurs. The under-prediction of error is most probably due to the iterative solution procedure of a non-linear problem, in which zero error is assumed for the coefficients that are functions of the parent variable ϕ. In fact, perturbation of the coefficients as follows,

$$a_P(\phi) = a_P(\tilde{\phi}) + \frac{\partial a_P}{\partial \phi}\varepsilon_P , \tag{3.33}$$

reveals that we may have neglected higher order terms of $o(\varepsilon_P^2)$ in our calculations. It may also be thought that the time marching method might have an influence, but this is not the case; the same results were obtained with significantly different time steps.

Scheme 1: Central Difference. The coefficients when the central differencing is applied have the following form:

$$\begin{aligned} a_W &= \tilde{\phi}^o/(2\Delta x) + \nu/\Delta x^2, \\ a_E &= -\tilde{\phi}^o/(2\Delta x) + \nu/\Delta x^2, \\ a_P^o &= 1/\Delta t, \\ a_P &= a_W + a_E + a_P^o . \end{aligned} \tag{3.34}$$

Figures 12(*a*) and (*b*) show the predicted error at Re=10 and 60 (or Re_Δ=0.25 and 1.5) on the same set of grids used for the upwind difference. The discretization errors in this case are much smaller due to the use of central differencing. The predicted error

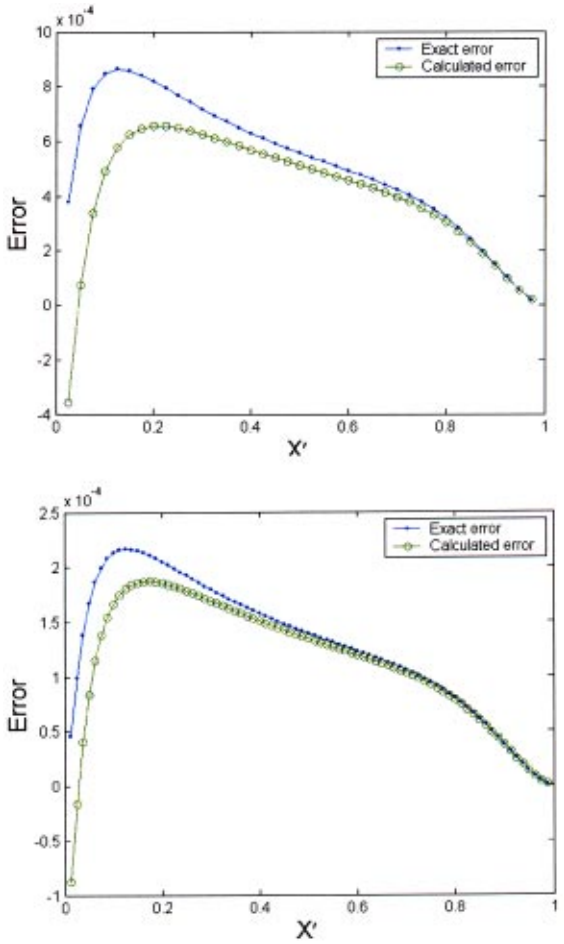

Fig. 10 Exact versus calculated error for 2D convection diffusion equation, central difference scheme, (*a*) 41*41 grid, (*b*) 81*81 grid

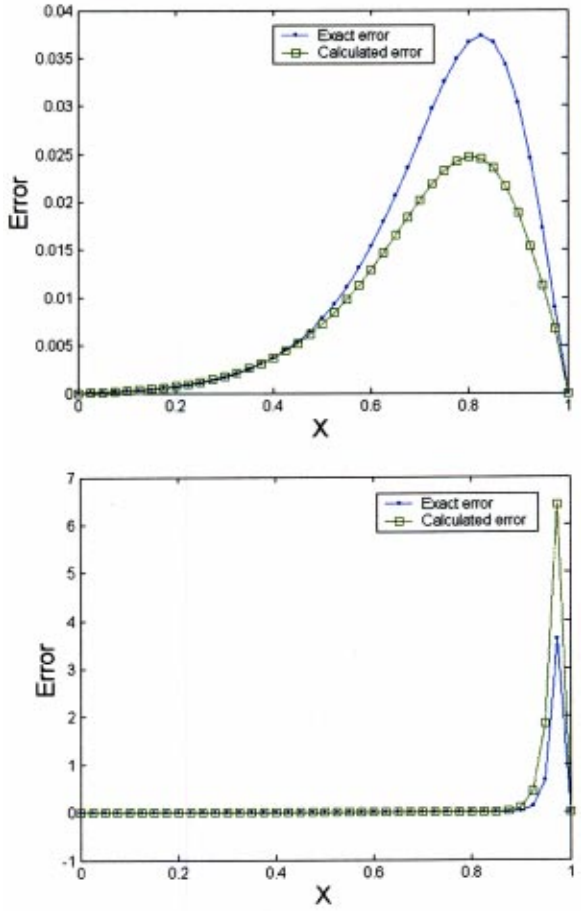

Fig. 11 Exact versus calculated error for steady 1D Burger's equation, first order upwind scheme, 41 nodes, inlet velocity varies to obtain different Reynolds numbers, (*a*) Re=10, Re_Δ =0.25, (*b*) Re=200, Re_Δ=5

trends are again satisfactory for this case with regards to the magnitude. Similar comments apply as in the case of first order upwind scheme.

4 Conclusions and Perspective

The method of error transport equation (ETE) for quantifying discretization error is studied further to demonstrate the capability and potential of this method for CFD applications. A fairly general methodology has been suggested for calculating the source term in the error equation based on the formalism of the finite difference/finite volume approach. It is conjectured that the only information needed to carry out the error analysis are (i) the single grid geometry, (ii) the original partial differential equation being solved, and (iii) the access to the influence coefficients of the discretized equation for the dependent variable being considered. It has been demonstrated that the discretization error can be predicted on the same grid used to solve for the original PDE. Both sign and magnitude of the discretization error can be captured in a satisfactory manner. The examples given in the present study involve one- and two-dimensional steady problems discretized over three- or five-point stencils in space. It should be emphasized that all of the cases presented in this paper used the same expression for the error source term $\tau(\phi)$ (for three- or five-stencil discretization schemes); the only difference is that the influence coefficients are different for each scheme and/or equation considered. Further, no boundary conditions beyond those provided by those hosted equations need to be applied for the discretized error equation. Extension of the method to three-dimensions seems straightforward, and extension to a transient problem will also be possible, as long as the numerical solution for the primitive variable is not seriously polluted by the numerical diffusion and its accuracy still kept in an acceptable range. Moreover, the ETE method would also be a strong candidate for two important applications, i.e., the error analysis for Navier-Stokes solvers, and for adaptive grid control. In applications for adaptive grids only the error source term may be considered to focus on the regions where error is generated, thus avoiding the false indication due to the transport of error from one region to another. Work is underway by the present authors to verify this method for a typical Navier-Stokes solver.

Appendix: Error Equation for Boundary Nodes

Generalized (mixed) boundary condition on a boundary can be written as

$$\left(\Gamma\frac{\partial\phi}{\partial y}+\gamma\phi\right)_{sb}=q_{sb}. \tag{A.1}$$

The discretized form of Eq. (*A*.1) is

$$L_h^{(sb)}(\tilde{\phi})=Q_{sb}, \tag{A.2}$$

or

$$L_h^{(sb)}(\phi)=Q_{sb}+\tau^{(sb)}(\phi), \tag{A.3}$$

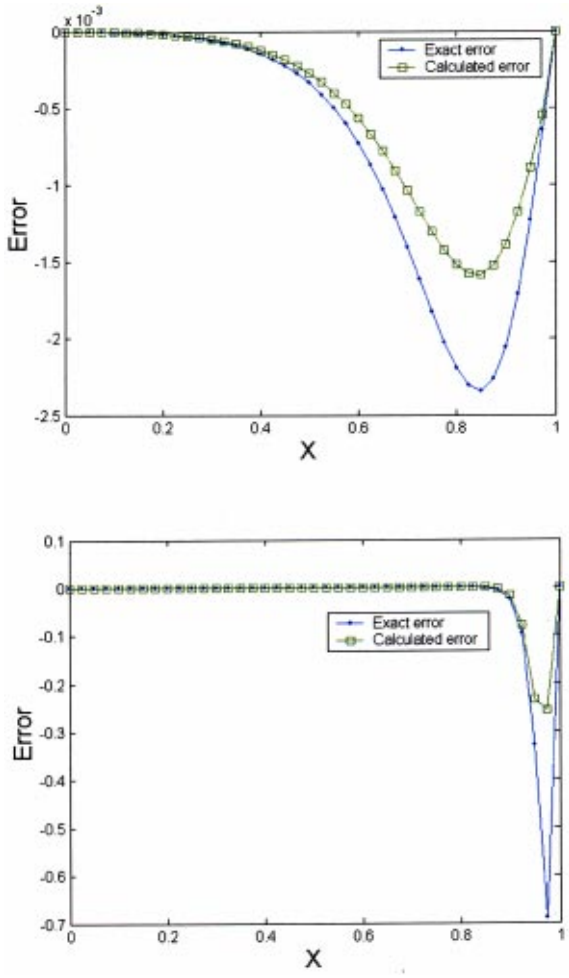

Fig. 12 Exact versus calculated error for steady 1D Burger's equation, central difference scheme, 41 nodes, inlet velocity varies to obtain different Peclet numbers, (*a*) Re=10, Re_Δ =0.25, (*b*) Re=60, Re_Δ=1.5

where ϕ and $\tilde{\phi}$ denote the exact and the numerical solutions, respectively. Subtracting Eq. (*A*.2) from (*A*.3) yields

$$L^{(sb)}(\varepsilon) = \tau^{(sb)}(\phi). \tag{A.4}$$

Equation (*A*.2) can be written using the notation given in Fig. A1 as

$$a_P\phi_P - a_N\phi_N - a_{NN}\phi_{NN} = Q_{sb}\,. \tag{A.5}$$

Using Taylor series expansion about the point "*P*", Eq. (*A*.3) can be written explicitly as

$$a_P\phi_P - a_N\phi_N - a_{NN}\phi_{NN} = \phi_{sb} + \tau^{(sb)}(\phi), \tag{A.6}$$

where

$$\tau^{(sb)}(\phi) = \sum_{k=1}^{\infty} (a_N + 2^k a_{NN}) \frac{\Delta y^k}{k!} \phi_{y,(k)}\,. \tag{A.7}$$

Here $\phi_{y,(k)}$ is the *k*th derivative of ϕ with respect to *y*.

Example:

Let $\Gamma=1$, $\gamma=0$ in Eq. (*A*.1) to have a Neumann condition

$$\frac{\partial\phi}{\partial y} = 0. \tag{A.8}$$

Applying second order forward differencing for the grid shown in Fig. A1(*a*) yields

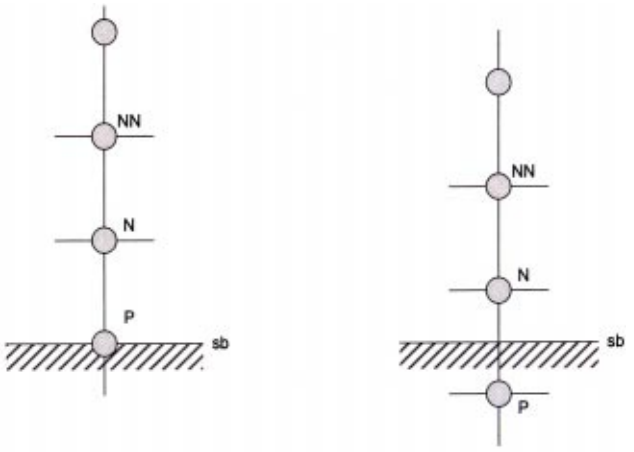

Fig. A1 Illustration of three-point stencil for implementation of boundary condition on a typical boundary, here denoted as the south boundary. (*a*) First grid node at the boundary, (*b*) first grid node outside the boundary.

$$a_P = \frac{3}{2\Delta y}, \quad a_N = \frac{4}{2\Delta y}, \quad a_{NN} = -\frac{1}{2\Delta y}. \tag{A.9}$$

Substitute these values into (*A*.7) and noting that $\phi_y = 0$ yields

$$\tau^{(sb)}(\phi) \cong -\frac{1}{3}\Delta y^2 \phi_{yyy} - \Delta y^3 \phi_{yyyy}\,. \tag{A.10}$$

That is,

$$L_h^{sb}(\varepsilon) \cong -\frac{1}{3}\Delta y^2 \frac{\delta^3\phi}{\delta y^3} - \Delta y^3 \frac{\delta^4\phi}{\delta y^4}. \tag{A.11}$$

Implementation of the boundary condition using second order central differencing on two grid nodes for the grid of Fig. A1(*b*) yields

$$a_P\phi_P - a_N\phi_N = \tau^{(sb)}(\phi). \tag{A.12}$$

For this case we expand ϕ_N and ϕ_P about the point $y=0$ (i.e., the south boundary) to obtain

$$\tau^{(sb)}(\phi) = (a_P - a_N)\phi_{sb} - \frac{a_P + a_N}{2}\Delta y\,\phi_y + \sum_{k=2}^{\infty}\left(\frac{a_P + (-1)^{k+1}a_N}{2^k}\right)\frac{\Delta y^k}{k!}\phi_{y,(k)}\,. \tag{A.13}$$

The derivatives in (*A*.13) are to be evaluated at the south boundary, i.e., $y=0$. Analogous to Eq. (*A*.11) we write

$$a_P\varepsilon_P - a_N\varepsilon_N \cong (a_P - a_N)\phi_{sb} - \left(\frac{a_P + a_N}{2}\right)\Delta y\,\phi_y + \frac{a_P - a_N}{4}\frac{\Delta y^2}{2!}\phi_{yy} - \frac{a_P + a_N}{8}\frac{\Delta y^3}{3}\phi_{yyy} + \frac{a_P - a_N}{16}\frac{\Delta y^4}{4!}\phi_{yyyy}\,. \tag{A.14}$$

Discretization of Eq. (*A*.8) using second order central differencing yields

$$a_P = 1/\Delta y, \quad a_N = 1/\Delta y. \tag{A.15}$$

Substituting the above into Eq. (*A*.14) and also noting that $\phi_y = 0$ yields

$$L_h^{(sb)}(\varepsilon) \cong -\frac{1}{24}\Delta y^2 \frac{\delta^3 \phi}{\delta y^3}. \qquad (A.16)$$

Both (*A*.11) and (*A*.16) contain second order leading terms which are consistent with the order of approximation of the Neumann condition at the south boundary for this example.

If additional equations are derived for calculating the error on the boundary using the discretized boundary equation for the parent variable, the coefficient used in the error transport equation must be saved before the coefficients for the interior points are modified. Then the additional equation derived above can be used to calculate the boundary values of ϕ as well as the error source term on the boundary, hence leading to the calculation of the error at the boundary.

References

[1] Richardson, L. F., 1910, ''The Approximate Arithmetical Solution by Finite Differences of Physical Problems Involving Differential Equations, With an Application to the Stresses in a Masonary Dam,'' Philos. Trans. R. Soc. London, Ser. A, **210**, pp. 307–357.

[2] Richardson, L. F., and Gaunt, J. A., 1927, ''The Deferred Approach to the Limit,'' Philos. Trans. R. Soc. London, Ser. A, **226**, pp. 299–361.

[3] Celik, I., Chen, C. J., Roache, P. J., and Scheurer, G., eds., 1993, *Quantification of Uncertainty in Computational Fluid Dynamics*, ASME Publ. No. FED-Vol. 158, ASME Fluids Engineering Division Summer Meeting, Washington, DC, 20–24 June.

[4] Roache, P. J., 1993, ''A Method for Uniform Reporting of Grid Refinement Studies,'' Proc. of Quantification of Uncertainty in Computation Fluid Dynamics, I. Celik et al., eds., ASME Fluids Engineering Division Spring Meeting, Washington, D.C., June 230–240, ASME Publ. No. FED-Vol. 158.

[5] Roache, P. J., 1998, *Verification and Validation in Computational Science and Engineering*, Hermosa Publishers, Albuquerque.

[6] Celik, I., and Zhang, W.-M., 1993, ''Application of Richardson Extrapolation to Some Simple Turbulent Flow Calculations,'' Proceedings of the Symposium on *Quantification of Uncertainty in Computational Fluid Dynamics*, I. Celik et al., eds., ASME Fluids Engineering Division Spring Meeting, Washington, C.C., June 20–24, pp. 29–38.

[7] Celik, I., and Karatekin, O., 1997, ''Numerical Experiments on Application of Richardson Extrapolation With Nonuniform Grids,'' ASME J. Fluids Eng., **119**, pp. 584–590.

[8] Stern, F., Wilson, R. V., Coleman, H. W., and Paterson, E. G., 2001, ''Comprehensive Approach to Verification and Validation of CFD Simulations—Part 1: Methodology and Procedures,'' ASME J. Fluids Eng., **123**, pp. 793–802, December.

[9] Cadafalch, J., Perez-Segarra, C. C., Consul, R., and Oliva, A., 2002, ''Verification of Finite Volume Computations on Steady State Fluid Flow and Heat Transfer,'' ASME J. Fluids Eng., **124**, pp. 11–21.

[10] Eca, L., and Hoekstra, M., 2002, ''An Evaluation of Verification Procedures for CFD Applications,'' 24th Symposium on Naval Hydrodynamics, Fukuoka, Japan, July 8–13.

[11] Coleman, H. W., Stern, F., Di Mascio, A., and Campana, E., 2001, ''The Problem With Oscillatory Behavior in Grid Convergence Studies,'' ASME J. Fluids Eng., **123**, pp. 438–439.

[12] Van Straalen, B. P., Simpson, R. B., and Stubley, G. D., 1995, ''A Posteriori Error Estimation for Finite Volume Simulations of Fluid Flow Transport,'' Proceedings of the Third Annual Conference of the CFD Society of Canada, Vol. I, Banff, Alberta, 25–27 June, P. A. Thibault and D. M. Bergeron, eds.

[13] Zhang, Z., Trepanier, J. Y., and Camarero, R., 1997, ''A Posteriori Error Estimation Method Based on an Error Equation,'' Proceedings of the AIAA 13th Computational Fluid, pp. 383–397.

[14] Zhang, Z., Pelletier, D., Trepanier, J. Y., and Camarero, R., 2000, ''Verification of Error Estimators for the Euler Equations,'' 38th AIAA Aerospace Sciences Meeting and Exhibit, AIAA-2000-1001.

[15] Wilson, R. V., and Stern, F., 2002, ''Verification and Validation for RANS Simulation of a Naval Surface Combatant,'' American Institute of Aeronautics & Astronautics (AIAA) 2000-0904, 40th Aerospace Sciences Meeting & Exhibit, January 14–17.

[16] Celik, I., and Hu, G., 2002, ''Discretization Error Estimation Using Error Transport Equation,'' Proceedings of ASME FEDSM '02, paper No. 31372, Montreal, Canada, July 14–18.

[17] Celik, I., Hu, G., and Badeau, A., 2003, ''Further Refinement and Benchmarking of a Single-Grid Error Estimation Technique,'' Paper No. AIAA-2003-0628, 41st Aerospace Sciences Meeting & Exhibit, Reno, Nevada, January 6–9.

[18] Qin, Y., and Shih, T. I.-P., 2003, ''A Method for Estimating Grid-Induced Errors in Finite-Difference and Finite-Volume Methods,'' Paper No. AIAA-2003-0845, 41st Aerospace Sciences Meeting & Exhibit, Reno, Nevada, January 6–9.

[19] Hu, G., 2002, ''Uncertainty Assessment for CFD Using Error Transport Equation,'' Master Thesis, Mechanical & Aerospace Engineering Department, West Virginia University, May.

[20] Ferziger, J. H., 1993, ''Estimation and Reduction of Numerical Error,'' ASME transaction on the *Quantification of Uncertainty in Computational Fluid Dynamics*, I. Celik et al., eds., FED-Vol. 158.

[21] Hu, G., and Celik, I., 2004, ''On Consistency in Evaluating the Residuals and Derivatives for Finite Difference/Volume Methods,'' submitted to *Communications in Numerical Methods in Engineering*.

Factorial Design Applied to CFD

Michel J. Cervantes
Michel.Cervantes@ltu.se

T. Fredrik Engström
Fredrik.Engstrom@ltu.se

Division of Fluid Mechanics, Luleå University of Technology, SE-97187 Luleå, Sweden

Factorial design, a statistical method widely used for experiments, and its application to CFD are discussed. The aim is to propose a systematic, objective, and quantitative method for engineers to design a set of simulations in order to evaluate main and joint effects of input parameters on the numerical solution. The input parameters may be experimental uncertainty on boundary conditions, unknown boundary conditions, grid, differencing schemes, and turbulence models. The complex flow of the Turbine-99 test case, a hydropower draft tube flow, is used to illustrate the method, where four factors are chosen to perform a 2^4 factorial design. The radial velocity at the inlet (not measured) is shown to have an important influence on the pressure recovery (7%) and the energy loss factor (49%). [DOI: 10.1115/1.1792277]

1 Introduction

The use of computer simulations to predict turbulent flows in complex geometries instead of model, or full scale, experiments can substantially decrease the cost of a project and still increase the knowledge of the flow problem. It makes such an approach attractive to the industry. Even if widely used, computational fluid dynamics (CFD) is not fully trusted by industry due to difficulties of obtaining reliable results. Until now, most academic work has been directed towards the validation of particular codes and turbulence models in simplified geometries [1]. Recently, more effort has been dedicated to compile the knowledge of all parts of CFD and its application in order to guide the usage of CFD as an engineering tool and thus improve the quality of the simulations. Members from both industry and the academic world work in this direction in the QNET-CFD network [1] and the ERCOFTAC Special Interest Group Quality and Trust for the Industrial Application of CFD [2]. The latter recently published the *Best Practice Guidelines* for industrial CFD users, edited by Casey and Wintergerste [3].

The lack of reliability of CFD in industrial applications is due to the discrepancy between simulated and experimental results and the difficulty to identify the sources of error. Turbulence models and grid errors are often discussed. It is true that ''simple turbulence models'' often are used for industrial simulations, which have difficulties in reproducing complex industrial flows. Also, the actual computational power makes grid-independent solutions difficult to achieve. Furthermore, the fluid engineers using CFD face a difficult task with a multitude of inputs and assumptions necessary to simulate a problem. These difficulties also contribute to making the results uncertain, which may force the engineer to stop at a qualitative instead of a quantitative assessment of the results. However, with the computational power now available, several test cases can be investigated, thus allowing a sensitivity analysis of the input parameters as recommended by the *Best Practice Guidelines* [3]. Several authors have already used such an approach, but there seems not to have been a systematic approach to plan and quantify the results. A complicating factor in such studies is that interaction between several factors may not be detected by varying one parameter at a time. Therefore, a systematic method to evaluate the simultaneous effects of several parameters on the numerical solution is necessary for engineers to get a quantitative ground for flow design.

The input parameters in CFD are numerous. They may be divided into three main groups: *flow modeling*, *numerics*, and *implementation*. The *flow modeling* embraces the mathematical modeling of the flow as well as the boundary conditions. The mathematical modeling involves several approximations that differ from one model to another, e.g. two-equation and second-moment closure turbulence models have different levels of approximation. Large eddy simulations (LES) begin to appear in commercial codes and represent yet another level. The boundary conditions may be experimental data such as velocity profiles, flow rates, pressures, wall roughness, etc. However, some or all boundary conditions must often be estimated, due to the technical difficulties and/or financial cost to measure them. Also, even in cases where experimental data are available, it has to be adapted for the computations, which often calls for further processing such as smoothing and extrapolation. The *numerics* involves the grid, the discretization method, the numerical scheme(s), the solver, and the convergence criteria. Important issues are grid independence, discretization, and iterative errors. There are methods to estimate these errors. For instance, Bergström and Gebart [4] used Richardson extrapolation with curve fitting to investigate the discretization error. The *implementation* is concerned with the generation of the CFD code. The user cannot always influence this issue since the code is normally developed by others. However, comparison between different codes may be performed as done by Iaccarino [5], who pointed out the different implementations of the same turbulence model in three commercial codes.

The complexity of CFD may be compared to industrial processes, such as the chemical industry, which contain many parameters whose influence and interaction are seldom clearly understood. A standard approach to analyze such complex processes is *factorial design*, a statistical method that quantifies the influence of the parameters. The present work presents the application of factorial design to CFD and a complex engineering flow, the Turbine-99 draft tube test case, is used to illustrate the method. The influence of four input parameters are evaluated on engineering quantities such as pressure recovery and energy loss factor. The results and a discussion are followed by the conclusions.

2 Factorial Design

Factorial design is a statistical method for experimental design. The main areas of use are process troubleshooting, development and optimization. A short description of the method is presented. Further information may be found in the book by Box, Hunter, and Hunter [6].

In this method, the factors influencing a process are varied in a certain pattern leading to a set of experimental runs. The influence of one factor (main effect) and the interaction of different factors (joint effect) on one or more representative quantities of the process are evaluated. Such a quantity may be the yield in a production process or an objective function in an optimization. It is important to note that interaction between several factors may not be detected by varying only one factor at a time. Potentially, all input parameters may be subject for investigation. A successful factorial design depends on the choice of the key factors, e.g., the most

Contributed by the Fluids Engineering Division for publication in the JOURNAL OF FLUIDS ENGINEERING. Manuscript received by the Fluids Engineering Division August 21, 2002; revised manuscript received May 12, 2004. Associate Editor: W. W. Copenhaver.

influencing factors for an optimization. If k factors are chosen, and each factor is tested at n levels (values), the design is called a n^k factorial design, since each experimental trial has n^k runs. Therefore, n^k statistics can be calculated; one average, k main effects, $\binom{k}{2}$ 2-factor interactions, . . . , and one k-factor interaction. The interpretation of a variable's main effect is made individually only if there is no evidence of interaction with other variables. Generally, for a large number of factors, the higher-order interactions may be neglected, since they are mainly due to experimental noise. Instead, they may be used to estimate the error level of an effect and thereby the significance of that effect. Replicated runs may also be performed for error analysis.

A two-level design is generally used as a first step in the analysis of a process where each parameter is assigned either a ''low'' or a ''high'' value. The main and joint effects are calculated as the difference between the mean of the high levels and the mean of the low levels. For joint effects, an even number of low levels for the interacting factors contribute to the high level value of the effect and an odd number of low levels contribute to the low level value. Further investigation of the process may be done by the introduction of a new factor or by the addition of new levels for one or more factors to detect nonlinear effects, as they are not detected by a two-level design.

In order to avoid redundance when several factors are chosen, *fractional factorial design* may be used to reduce the number of runs by a factor two. For instance, in a 2^5 factorial design, interactions between three factors or more may not be considered important, thus reducing the number of runs by two, from 2^5 to 2^4. By choosing the reduced number of runs after a certain pattern, an optimum resolution for the interactions may be found. Reducing the number of runs confounds disregarded higher-order interactions with assumed significant effects and interactions. For the reduced 2^5 design, main effects are confounded with fourth-order interactions, second-order interactions are confounded with third-order interactions and the mean value is confounded with the fifth-order interaction. The reduced number of runs of fractional factorial designs is advantageous in CFD, since complex industrial turbulent flow simulations may require several hours or days to converge and generally have several unknown input parameters.

The application of factorial design to CFD differs from its application to industrial processes since a simulation will yield exactly the same result over and over again, if the same residual is reached and machine precision error can be neglected. Therefore, a *standard error analysis* based on replicated runs is not possible in CFD. Furthermore, higher-order interactions are significant for fully converged solutions, since there is no random variation in the inputs of CFD, i.e., no noise. However, if a simulation is not fully converged, the quantity under evaluation may contain an iterative error. It sets a threshold in the significance of the different effects.

The identification of the key factors and their levels represents the main task for success with factorial design applied to CFD. The levels may be specified by experimental uncertainties in the case of a measured boundary condition. For unknown parameter values, a preliminary study may be necessary or assumptions for the appropriate upper and lower levels may be made. Compared to a single value, two levels give both an average and an indication of the sensitivity. Since the factors in factorial design may also be categorical variables, any input in CFD such as the turbulence model, differencing scheme, and computational grid may also be investigated with this approach.

The simulation of the complex flow encountered in a hydropower draft tube is treated to illustrate the method. The case is of great interest since two workshops on this flow have been organized and results are available. Therefore, comparison can be made between the result of the workshops and the result of the factorial design.

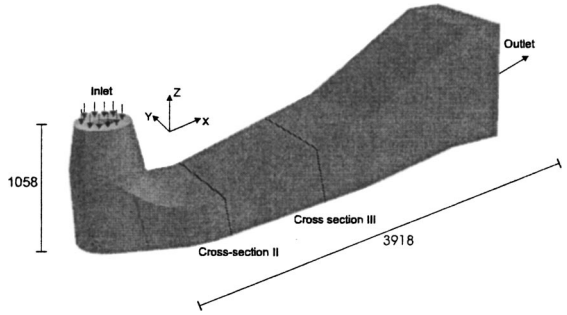

Fig. 1 CAD drawing of the Höllefors draft tube, dimensions in millimeters

3 The Turbine-99 Benchmark

Luleå University of Technology and Vattenfall Utveckling AB, Sweden, jointly organized the two Turbine-99 IAHR/ERCOFTAC Workshops in 1999 [7] and 2001 [8]. The aim was to determine the state of the art in CFD simulations of hydropower draft tube flows.

The draft tube follows immediately after the runner. The function of the draft tube is to convert the kinetic energy of the fluid leaving the runner into pressure energy with a minimum of losses. Modern draft tubes are composed from the inlet to the outlet of a conical diffuser, an elbow, and a straight asymmetric diffuser. A cone is attached below the runner to avoid a large separation region, which gives an annular inlet. Figure 1 shows the Höllefors draft tube model (1:11) used for the workshop; the inlet outer diameter is 472 mm and the inner diameter is 196 mm.

Draft tube flows are challenging for the CFD community due to the different phenomena that appear: swirling flow in straight and curved diffusers, separation, unsteadiness, impingement, and turbulence. It also presents an interesting engineering challenge since major hydropower installations in Sweden were built in the 1950s and will soon be refurbished [9]. In low head power plants, the draft tube is responsible for up to 50% of the total losses at high loads. Although hydropower plants are already highly efficient, up to 95%, a small increase in efficiency would correspond to a great value for the hydropower companies.

For the first workshop, the organizers provided the geometry of the draft tube model, as well as an extensive set of experimental data for the inlet boundary conditions measured in a 1:11 draft tube model at Vattenfall Utveckling AB [7] (Fig. 1). Some data at the inlet could not be measured, such as the radial velocity, some of the Reynolds stresses, and the turbulence (dissipation) length scale. The periodic fluctuations arising from the blade passages and the turbulent fluctuations in the measurements were chosen by the organizers to contribute to the steady turbulent intensities. The grid and the turbulence model were not disclosed to the participants.

The results of the pressure recovery obtained by the different participants at the first workshop presented a significant scatter, $\pm 45\%$ (see Fig. 2). The results of the second workshop will be commented on later in the discussion. The scatter is explained by the different assumptions for the boundary conditions as well as the different codes, grids, and turbulence models used by the participants. Several participants undertook a sensitivity analysis for some boundary conditions. For instance, Page and Giroux [7] investigated the inlet radial velocity and Bergström [7] the grid. This kind of analysis will be systemized here with factorial design.

3.1 Choice of Factors. The choice of the factors focused on the lack of information about the boundary conditions. Therefore, the radial velocity and the turbulence length scale at the inlet and also the surface roughness on the walls were chosen. The Reynolds stress could also have been a factor. However, the difficulty

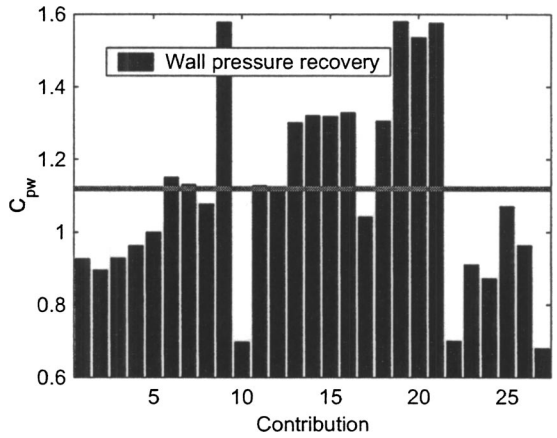

Fig. 2 Pressure recovery obtained at the first Turbine-99 Workshop. The line represents the experimental value 1.12.

to assign relevant levels is far from trivial in such a flow. The variety of grids present at the Turbine-99 workshop and the difficulty to obtain grid-independent solutions makes the grid an interesting factor.

A full factorial design at two levels was used. Thus, $2^4=16$ runs were performed. The different runs are presented in Table 1, where TLS, RV, and SR stand, respectively, for turbulence length scale, radial velocity, and surface roughness. The high and low levels are represented by + and a −, respectively.

3.1.1 Turbulence Length Scale. There are no experimental data on the turbulence length scale. According to Casey and Wintergerste [3], the turbulence length scale should be 1–10 % of the hydraulic diameter for internal flows. The hydraulic diameter at the inlet of the draft tube is defined as

$$D_H=\frac{4A}{P}=\frac{4\pi(R_{\text{wall}}^2-R_{\text{cone}}^2)}{2\pi(R_{\text{wall}}+R_{\text{cone}})}=2(R_{\text{wall}}-R_{\text{cone}}),$$

where A is the area of the cross section and P the wetted perimeter. The hydraulic diameter here is $D_H=0.28$ m and the corresponding turbulence length scale l ranges from 2.8 to 28 mm. The values 5 and 100 mm have been used as test values. The value of 100 mm was given by the organizers of the second Turbine-99 workshop.

The turbulence or dissipation length scale defines the inlet boundary condition for the dissipation rate ϵ of the turbulent kinetic energy k. The inlet boundary condition for k is estimated from the measured rms velocities. The dissipation rate is set to

$$\epsilon=\frac{k_{\text{inlet}}^{3/2}}{l}$$

where k_{inlet} is the turbulent kinetic energy at the inlet. A low value of the turbulence length scale corresponds to a high level of dissipation and vice versa.

3.1.2 Radial Velocity Profile. The radial velocity profile at the inlet was not measured. For the second workshop, the organizers assigned a velocity profile based on the assumption that the flow is attached to the walls at the inlet. The inlet has an annular cross section with the diffuser cone of the draft tube on the outside and the runner cone on the inside. The assumption of attached flow was used by Bergström and Gebart [4] at the first workshop and further confirmed by Nilsson [8] at the second workshop by a numerical investigation of the corresponding runner flow. In this case, the radial velocity is determined by the following relation:

$$u_{\text{radial}}=u_{\text{axial}}\tan(\theta),$$
$$\theta=\theta_{\text{cone}}+\frac{\theta_{\text{wall}}-\theta_{\text{cone}}}{R_{\text{wall}}-R_{\text{cone}}}(r-R_{\text{cone}}), \tag{1}$$

where u_{axial} is the measured axial inlet velocity, θ is the flow angle in the axial-radial direction, and θ_{cone} and θ_{wall} are the angles of the runner cone and the diffuser cone wall, respectively. r is the radial coordinate from the runner axis and R_{cone} is the runner cone radius. Equation (1) represents the low level of the radial velocity. The high level of the radial velocity is set to zero, an assumption used by many participants of the first workshop:

$$u_{\text{radial}}=0. \tag{2}$$

3.1.3 Surface Roughness. The organizers prescribed a surface roughness $k_s=10\ \mu$m (equivalent sand roughness height) for the entire draft tube. For the factorial design, a surface roughness of 0 and 200 μm were chosen. The upper limit corresponds to the roughness of cast iron [10].

Since wall functions are used to model the near-wall region, the surface roughness modifies the constant B in the assumed logarithmic velocity profile [11]:

$$\frac{U}{u_\tau}=\frac{1}{\kappa}\ln\left(\frac{yu_\tau}{\nu}\right)+B_{\text{smooth}}-\Delta B, \tag{3}$$

where $u_\tau=\sqrt{\tau_w/\rho}$, y, and ν represent, respectively, the friction velocity, the distance from the wall, and the kinematic viscosity. τ_w is the wall shear stress and ρ the density. The extra constant ΔB is added to account for the surface roughness effect. The CFD code used to perform the simulations, CFX 4.4 from AEA Technology, uses $\kappa=0.42$, $B_{\text{smooth}}=5.45$, and the correlation suggested by White for ΔB [11]:

$$\Delta B=\frac{1}{\kappa}\ln(1+0.3k_s^+),$$
$$k_s^+=\frac{k_s u_\tau}{\nu}. \tag{4}$$

The curve fit of Eq. (4) represents experimental data approximately for the smooth, transitional and fully rough regimes. In the limit of fully rough conditions, where viscous effects are negligible, Eq. (3) becomes

$$\frac{U}{u_\tau}=\frac{1}{\kappa}\ln\left(\frac{y}{k_s}\right)+8.3, \tag{5}$$

where Eq. (4) has been used.

3.1.4 Grid. The two grids used in the calculations have been produced by Bergström [7] using the program ICEM CFD. The coarse grid, shown in Fig. 3, is composed of 326,536 cells. It has a minimum angle of 37.6 deg and 284 cells have an angle lower

Table 1 Factorial design of the Turbine-99 test case

Run	1	2	3	4	5	6	7	8	9	10	11	12	13	14	15	16
TLS	−	+	−	+	−	+	−	+	−	+	−	+	−	+	−	+
RV	−	−	+	+	−	−	+	+	−	−	+	+	−	−	+	+
SR	−	−	−	−	+	+	+	+	−	−	−	−	+	+	+	+
Grid	−	−	−	−	−	−	−	−	+	+	+	+	+	+	+	+

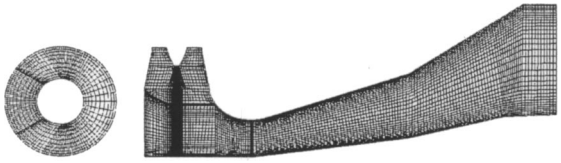

Fig. 3 Inlet and XZ midplane of the draft tube with the coarse grid

than 40 deg. The fine grid, shown in Fig. 4, has 668,166 cells. The minimum angle is 37.9 deg and 16 cells have an angle lower than 40 deg.

The grids have the same topology, and the refinement is general. The region below the cone is dense in order to resolve the separation zone. The near-wall cell size is determined by the requirement for the y^+ value at the cell center to be valid for the wall function method. The large and complex computational domain makes the requirement for the y^+ value at the cell center difficult to reach. The average value of y^+ for the 16 runs is 254 and the average standard deviation 231. A summary of the levels used for the different factors is presented in Table 2.

3.2 Other Computational Input. Several other input parameters were also required for the simulations.

3.2.1 Numerics. The code CFX 4.4 from AEA Technology was used for the simulations. The code is based on the finite-volume method and uses a colocated multiblock grid. More details concerning the code may be found in Ref. [12].

The standard k-ϵ model with the standard wall function was chosen to perform the isothermal, incompressible, and steady calculations. The choice of the turbulence model is motivated by the results of the first workshop, which showed no significant difference between different models. The standard k-ϵ model uses the eddy viscosity hypothesis for the Reynolds stresses, which relates them linearly to the mean velocity gradient:

$$-\overline{u_i u_j} = 2\nu_T S_{ij} - \tfrac{2}{3}k\delta_{ij}, \tag{6}$$

where ν_T is the eddy viscosity and S_{ij} is the mean strain rate tensor. The turbulent kinetic energy and its dissipation rate are used to get the velocity and length scales for the eddy viscosity, which is

$$\nu_T = C_\mu \frac{k^2}{\epsilon}. \tag{7}$$

The steady and incompressible equations for k and ϵ are

$$U_j \frac{\partial k}{\partial x_j} = -\overline{u_i u_j}\frac{\partial U_i}{\partial x_j} - \epsilon + \frac{\partial}{\partial x_j}\left[(\nu + \nu_T/\sigma_k)\frac{\partial k}{\partial x_j}\right], \tag{8}$$

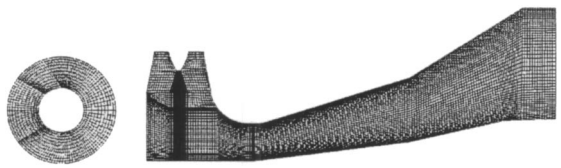

Fig. 4 Inlet and XZ midplane of the draft tube with the fine grid

Table 2 High and low levels of the factors

Factor/Level	−	+
Dissipation length scale (mm)	5	100
Radial velocity	Eq. (1)	Eq. (2)
Surface roughness (μm)	0	200
Grid	Coarse	Fine

Table 3 Differencing schemes [HUW, higher-order upwind differencing (2nd order); CENTRAL, central differencing (2nd order); HYBRID, hybrid differencing (1st order)], under-relaxation factors and solvers (BLST, Block Stone's method; ICCG, preconditioned conjugate gradients) used in the simulations

Equation	Differencing scheme	Under-relaxation factor	Linear solver
u velocity	HUW	0.65	BLST
v velocity	HUW	0.65	BLST
w velocity	HUW	0.65	BLST
pressure	CENTRAL	1	ICCG
k	HYBRID	0.70	LINE SOLVER
ϵ	HYBRID	0.70	BLST

$$U_j \frac{\partial \epsilon}{\partial x_j} = -C_{\epsilon 1}\frac{\epsilon}{k}\overline{u_i u_j}\frac{\partial U_i}{\partial x_j} - C_{\epsilon 2}\frac{\epsilon^2}{k} + \frac{\partial}{\partial x_j}\left[(\nu + \nu_T/\sigma_\epsilon)\frac{\partial \epsilon}{\partial x_j}\right], \tag{9}$$

where the summation convention is assumed and the model constants are: $C_\mu = 0.09$, $C_{\epsilon 1} = 1.44$, $C_{\epsilon 2} = 1.92$, $\sigma_k = 1$, and $\sigma_\epsilon = 1.3$.

The differencing schemes, under-relaxation factors, and solver methods for the linearized equations used for the computations are reported in Table 3. The choice of a first-order accurate scheme for the k and ϵ equations is motivated by the industrial nature of the flow.

3.2.2 Boundary Conditions. The experimental boundary conditions at the inlet of the draft tube provided by the organizers for the T mode, i.e. the top of the propeller curve, were used. The axial and tangential velocity mean components (u,w) were measured along a radial line. The radial velocity was specified as described above. The periodic fluctuations arising from the blade passages and the turbulent fluctuations in the measurements were both chosen by the organizers to contribute to the steady turbulent quantities ($\overline{u'^2}$, $\overline{v'^2}$ and $\overline{u'v'}$). The following assumptions at the inlet of the draft tube were made to perform the calculations as specified by the organizers:

$$\overline{v'^2} = \overline{w'^2},$$

$$\overline{u'v'} = \overline{v'w'} = \overline{u'w'},$$

where u', v', and w' represent the axial, radial, and tangential velocity fluctuations, respectively. The inlet conditions are assumed to be axisymmetric. At the outlet, the Neumann boundary conditions are imposed on all transport variables. Their gradient is set to zero except for the velocity gradient, which is modified to ensure mass conservation. Such an assumption is disputable, since the outlet is close to the straight diffuser where the flow still develops. Such a geometry was provided by the organizers of the first workshop. The pressure is extrapolated from upstream.

4 Results and Discussion

The engineering quantities used at the Turbine-99 workshops were used to evaluate the influence of the four input parameters:

- Wall pressure recovery:

$$C_{pw} = \frac{p_{\text{outlet wall}} - p_{\text{inlet wall}}}{\frac{1}{2}\rho(Q/A_{\text{inlet}})^2}.$$

- Mean pressure recovery:

$$C_{pm} = \frac{(1/A_{\text{outlet}})\int_{A_{\text{outlet}}} p\, dA - (1/A_{\text{inlet}})\int_{A_{\text{inlet}}} p\, dA}{(1/A_{\text{inlet}})\int_{A_{\text{inlet}}} \frac{1}{2}\rho(u^2+u^2+w^2)dA}.$$

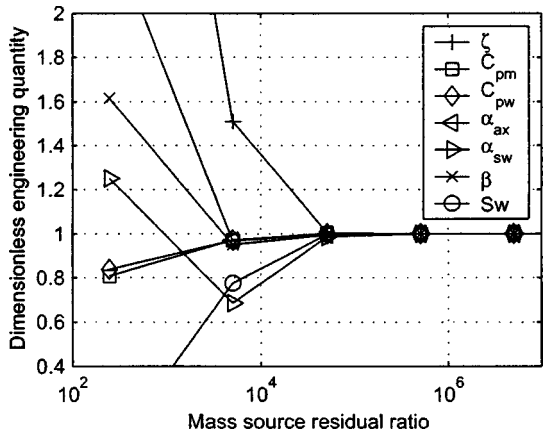

Fig. 5 Normalized engineering quantity function of the ratio of the mass source residual of the second iteration and the last iteration for run 2

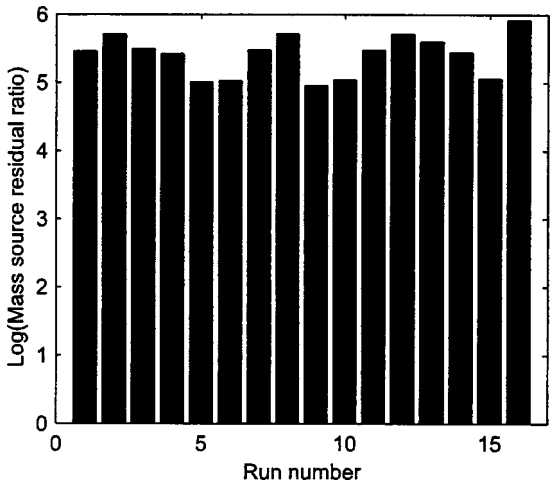

Fig. 6 Ratio of the mass source residual of the second iteration and the last iteration for the different runs

- Energy loss factor:

$$\zeta=\frac{\int_{A_{\text{inlet}}}E\vec{u}\cdot\vec{n}dA+\int_{A_{\text{outlet}}}E\vec{u}\cdot\vec{n}dA}{\int_{A_{\text{inlet}}}[\frac{1}{2}\rho(u^2+v^2+w^2)]\vec{u}\cdot\vec{n}dA},$$

where E represents the mechanical energy:

$$E=p+\tfrac{1}{2}\rho(u^2+v^2+w^2).$$

- Kinetic energy correction factor:

$$\alpha_{\text{axial}}=\frac{1}{A\overline{u^3}}\int_A u^3dA.$$

- Kinetic energy correction factor:

$$\alpha_{\text{swirl}}=\frac{1}{A\overline{u^3}}\int_A w^2udA.$$

- Momentum correction factor:

$$\beta=\frac{1}{A\overline{u^2}}\int_A u^2dA.$$

- Swirl intensity:

$$\text{Sw}=\frac{1}{R}\frac{\int_A ruw\,dA}{\int_A u^2dA},$$

where $\vec{u}$ is the velocity vector with the axial, radial, and tangential components u, v, and w, respectively. Q is the volume flow rate, p is the static pressure, ρ is the density, and A is the cross-section area with the outward normal vector $\vec{n}$. α_{axial}, α_{swirl}, β, and Sw are evaluated at cross section III, which is midway between the end of the elbow and the outlet of the draft tube (see Fig. 1). The center of the cross section is used as the origin for the calculation of α_{sw}, Sw, and r.

4.1 Convergence Criteria and Iterative Error. In order to reduce the computational time without losing accuracy, an investigation of the iterative error as a function of the mass source residual was undertaken on runs 2, 4 and 8. Figure 5 represents the engineering quantities as a function of the ratio of the mass source residual obtained at the second and the last iteration for run 2. The values are normalized with the value obtained at the highest ratio of the mass source residual, i.e., 7.1×10^8. The solution is assumed fully converged for this residual. The iterative error for the engineering quantities becomes lower than 2% for a mass source residual of 10^5. The result is similar for runs 4 and 8 (see Table 4). Therefore, the convergence criterium was set to 10^5 for all runs, assuming the iterative error is independent of the run. Convergence was easily achieved independently of the levels of the input parameters. The ratio of the mass source residual of the second to the last iteration for the different runs is represented in Fig. 6. The average residual reduction for the u, v, and w equations was above four decades, while for the k and ϵ equations above five decades.

The convergence criterion induces an iterative error on the statistics. A confidence interval for each statistic is necessary to determine whether an effect is significant. The iterative errors evaluated for runs 2, 4, and 8 are used to calculate the dimensionless sample standard deviation s for each engineering quantity:

$$s^2=\frac{\Sigma_{i=2,4,8}e_i^2}{2}, \tag{10}$$

where e_i is the iterative error of the ith run. The standard normal deviate

$$t=\frac{y_0-\eta}{s} \tag{11}$$

is considered, where y_0 is the dimensionless limit of the confidence interval and η the dimensionless mean value of the differ-

Table 4 Iterative error in percent for runs 2, 4, and 8 with a mass source residual of 10^5. Sample standard deviations and limits for a 95% confidence interval.

	C_{pw}	C_{pm}	ζ	α_{ax}	α_{sw}	β	Sw
Run 2	0.01	0.06	0.15	0.34	1.32	0.57	0.30
Run 4	0.04	0.05	0.11	0.58	0.29	0.23	0.16
Run 8	0.22	0.32	1.08	0.44	1.86	0.35	0.60
s	0.02	0.06	0.60	0.32	2.65	0.25	0.24
y_0	0.68	1.01	3.35	2.45	7.00	2.17	2.10

Table 5 Mean value of the engineering quantities for runs 1 to 16

Run	1	2	3	4	5	6	7	8
C_{pw}	1.084	1.089	0.994	1.013	1.047	1.058	0.965	0.985
C_{pm}	0.948	0.943	0.810	0.828	0.916	0.920	0.782	0.799
ζ	0.054	0.050	0.190	0.163	0.080	0.072	0.215	0.195
α_{ax}	1.144	1.219	0.876	1.352	1.186	1.232	1.044	1.408
α_{sw}	0.234	0.090	0.057	0.062	0.206	0.086	0.070	0.066
β	1.372	1.215	0.987	1.240	1.331	1.207	1.111	1.281
Sw	0.268	0.160	0.149	0.082	0.240	0.157	0.152	0.081
Run	9	10	11	12	13	14	15	16
C_{pw}	1.089	1.088	0.991	1.016	1.032	1.062	0.969	0.983
C_{pm}	0.950	0.945	0.809	0.828	0.903	0.917	0.786	0.799
ζ	0.046	0.050	0.189	0.165	0.096	0.071	0.218	0.194
α_{ax}	1.170	1.160	0.968	1.380	1.081	1.371	1.071	1.350
α_{sw}	0.194	0.083	0.058	0.065	0.246	0.103	0.093	0.062
β	1.324	1.170	1.051	1.257	1.323	1.300	1.157	1.248
Sw	0.239	0.159	0.133	0.082	0.270	0.163	0.174	0.083

ences between the fully converged solution and the solution with a mass source residual of 10^5 for the different runs. The differences between the fully converged and partially converged solution are expected to be normally distributed around zero; thus $\eta=0$. The quantity t is assumed to have a Student's t distribution [6]. For a confidence interval of 95% with two degrees of freedom $t=2.920$. The limits are reported in Table 4.

4.2 Results of Factorial Design. The engineering quantities were calculated for the 16 runs. The results are reported in Table 5. The results of the main and joint effects are reported in percent of the mean value in Table 6. For instance, the main effect of the turbulence length scale on the energy loss factor ζ is calculated as

$$\zeta_{\mathrm{TLS}}=\frac{\zeta_2+\zeta_4+\zeta_6+\zeta_8+\zeta_{10}+\zeta_{12}+\zeta_{14}+\zeta_{16}}{8}-\frac{\zeta_1+\zeta_3+\zeta_5+\zeta_7+\zeta_9+\zeta_{11}+\zeta_{13}+\zeta_{15}}{8}.$$

The joint effect of the turbulence length scale and the radial velocity on ζ is

$$\zeta_{\mathrm{TLS}\times\mathrm{RV}}=\frac{\zeta_1+\zeta_4+\zeta_5+\zeta_8+\zeta_9+\zeta_{12}+\zeta_{13}+\zeta_{16}}{8}-\frac{\zeta_2+\zeta_3+\zeta_6+\zeta_7+\zeta_{10}+\zeta_{11}+\zeta_{14}+\zeta_{15}}{8}.$$

Some effects are disregarded due to the iterative error. These effects are outside the confidence interval of 95%. Significant effects deviate from the normal distribution on a normal probability plot. See Fig. 7 for the effects on the energy loss factor.

The function of a draft tube is to recover the kinetic energy leaving the runner into pressure with a minimum of losses. Therefore, the pressure recovery coefficients are of major interest. Pressure recovery (C_{pw}) based on wall pressure is used for comparison with the experimental value. The mean value of the 16 runs is 1.029 and this should be compared with the experimental value of 1.12. Pressure recovery (C_{pm}) based on the mean values of the pressure over the inlet and outlet areas may be, however, more relevant when evaluating the performance of the draft tube, since it is less sensible to local variations. Both pressure recovery factors are mostly influenced by the radial velocity, a parameter not measured for the workshop. A small separation zone is present below the runner cone at the low level of the radial velocity. The high level of the radial velocity induces a large separation zone from the runner cone to the elbow. It strongly alters the flow structure and increases the energy loss factor. Both pressure recovery factors decrease with a zero radial velocity. This result is confirmed with the approximate analytical relation between C_{pm} and ζ found using the energy equation:

$$\zeta\approx\left(1-\frac{C_{pm}}{\alpha_{\mathrm{inlet}}}\right)-\frac{\alpha_{\mathrm{outlet}}}{\alpha_{\mathrm{inlet}}}\left(\frac{A_{\mathrm{inlet}}}{A_{\mathrm{outlet}}}\right)^2,$$

where α_{outlet} and α_{inlet} represent the total kinetic energy correction factors. Both terms in parentheses are of the same order, around 0.1. As $C_{pm}\approx 1$, a small variation in the pressure recovery induces a large variation of the loss factor. It explains the effect of 49% on ζ as the radial velocity profile moves from its low level, attached flow, to its high level, zero radial velocity.

The surface roughness has a lower influence on the loss factor than expected, 11%. From pipe flow, it is known that an increase in surface roughness from 0 to 200 μm corresponds to an increase of the friction factor by 56% at the inlet and 16% at the outlet, at the corresponding Reynolds numbers. The effects of surface roughness do not influence the flow as it does in fully developed pipe flow. More surprising is the small influence of the turbulence length scale on ζ, around 6% despite a factor 20 between the high and low levels.

The difference between the two grids does not have a striking influence on the engineering quantities relative to the other factors. This shows that the present grid refinement is not significant enough to improve the accuracy of the engineering quantities.

Table 6 Mean value of the engineering quantities for the 16 runs. Main and joint effects (E=ABC, F=ABD, G=BCD and H=ABCD) in percent of the factors (A=TLS, B=RV, C=SR and D=grid) on the engineering quantities, significant values are in bold. Joint effects BCD and ABCD are negligible and not presented.

	Mean	A	B	C	D	AB	AC	AD	BC	BD	CD	E	F	G	H
C_{pw}	1.029	**1**	**−4**	**−2**	0	0	0	0	0	0	0	0	0	0	0
C_{pm}	0.868	1	**−7**	**−2**	0	0	0	0	0	0	0	0	0	0	0
ζ	0.128	**−6**	**49**	**11**	1	−3	−1	−1	0	−2	0	2	1	−1	0
α_{ax}	1.188	**10**	−1	2	−2	**6**	0	−1	1	2	−2	**−3**	0	0	0
α_{sw}	0.111	**−30**	**−40**	5	2	**28**	−3	−5	1	−5	−2	−2	**7**	−1	2
β	1.223	1	**−5**	2	−1	**6**	0	−1	1	0	−1	−2	1	0	0
Sw	0.162	**−25**	**−28**	2	1	**4**	−2	−1	2	**−3**	0	−2	**4**	0	1

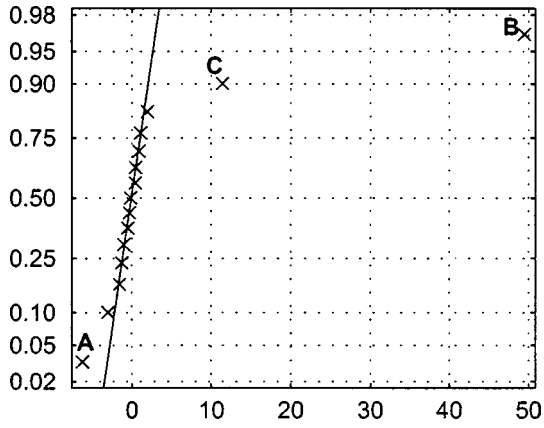

Fig. 7 Normal probability plot for the effects on ζ. Significant effects deviate from the normal distribution represented by the straight line.

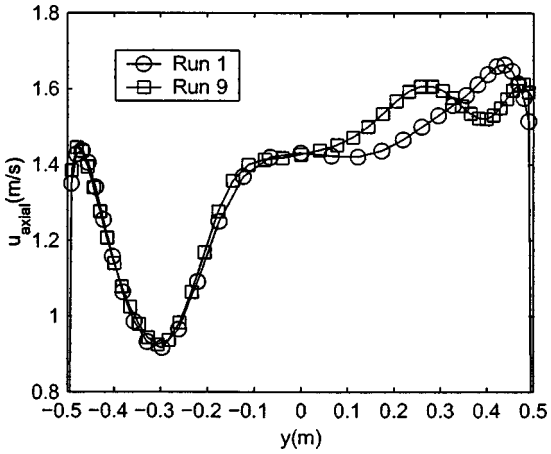

Fig. 8 Horizontal velocity profiles at the center of cross section II for runs 1 and 9

Such a result does not mean that the solution is grid independent as seen in Fig. 8, where the axial velocity profiles of runs 1 and 9 at cross section II show some differences. The weak sensitivity of the engineering quantities to the grid is due to their integral form, which suppresses local deviations. A Richardson extrapolation may be performed to estimate the error due to the space discretization. Bergström and Gebart [4] estimated the grid error to 3–7% for the wall pressure recovery and a grid with 3.9×10^6 to 222 $\times10^6$ cells to lower the grid error to 1% for C_{pw}, using a Reynolds stress model. Such a topology extends beyond our computational power and had to be disregarded. Thus, future efforts should focus on a better estimate of the radial velocity rather than a further grid refinement, because the radial velocity has a much stronger influence on the engineering quantities.

Several joint effects appear, for instance, the interaction between the turbulence length scale and the radial velocity for α_{swirl}, which is the contribution to the kinetic energy flux from the tangential velocity. The flow field in cross section III is shown in Fig. 9 for runs 1–4. These are the runs calculated with the coarse grid and represent the four different combinations of the turbulence length scale and radial velocity levels. The streamwise velocity field is indicated with contours and the secondary motion is described by vectors. It is obvious that both parameters have a significant influence on the flow. The large vortex to the left moves further to the left when the turbulence length scale is increased from 5 to 100 mm (top row to bottom row). Less energy is dissipated with a high turbulence length scale between the inlet and the beginning of the elbow than with a low turbulence length scale. Thus, the swirl intensity is higher, and the gyroscopic effect displaces the vortex further to the left. When the radial velocity is changed from the low level [Eq. (1)] to the high level ($u_{\text{radial}}=0$), a new counterrotating vortex appears to the right (left column to right column). For the high level of the radial velocity, a large separation zone from the runner cone to the elbow appears. The separation zone splits into two vortices, one due to the gyroscopic effect and one due to the fluid impinging on the bottom of the draft tube. These effects are confirmed in Table 6, where α_{swirl} decreases when either the turbulence length scale or the radial velocity changes from low to high level. However, there is also a strong interaction effect (28%). The interpretation is that the effect

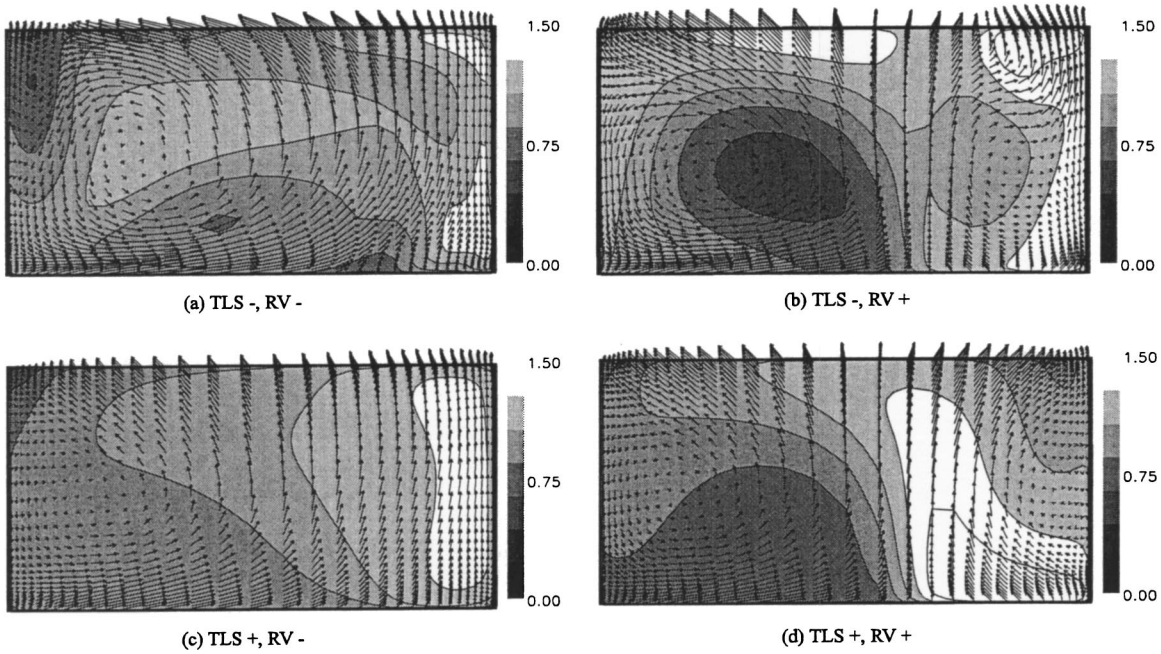

Fig. 9 Streamwise velocity (contours) and secondary motion (vectors) in cross section III. View is upstream: (a) run 1, (b) run 3 (c) run 2, (d) run 4.

of increasing the turbulence length scale is different, depending on the level of the radial velocity. Since the joint effect is positive, α_{swirl} increases more when the turbulence length scale is increased at a high level of radial velocity, than it does at a low level.

Assuming a Student's t distribution for the 16 runs, a 95% confidence interval for the wall pressure recovery was calculated, $C_{pw}=1.029\pm0.096$. The present confidence interval does not include the grid error (3–7%) and the iterative error (<2%). Therefore, the input parameters analyzed here, the iterative error and grid error explain partially the scatter in the results of the first Turbine-99 workshop (see Fig. 2). The rest of the explanation may be found in the results of the second workshop, where a reference simulation was performed by all participants with the boundary conditions, the grid, and the turbulence model specified. The purpose was to resolve the differences in implementation and postprocessing between different contributors. The results still show a large scatter for the wall pressure recovery, $0.86\leqslant C_{pw}/C_{pw}^{\text{mean}}\leqslant1.38$. When submitted data were recalculated with the same method, the scatter decreased, $0.87\leqslant C_{pw}/C_{pw}^{\text{mean}}\leqslant1.28$. Obviously, postprocessing is an important issue for workshops and engineers. The mean pressure (C_{pm}) recovery was also calculated by the organizers with the data from the participants, $0.95\leqslant C_{pm}/C_{pm}^{\text{mean}}\leqslant1.06$. Unfortunately, this factor was not requested for the workshops. Nevertheless, it points out the difficulty to calculate C_{pw} correctly.

4.3 Discussion. Factorial design applied to CFD yields a confidence interval for any engineering quantity, where the effects of all input parameters under investigation are included. This interval, together with the iterative and grid errors, gives a measure of the uncertainty of the numerical simulation. The method also shows which parameter has the largest influence and which parameters interact significantly. Therefore, a deeper understanding of the flow and valuable insight for further investigations may be reached. An important benefit of the method is the possibility to choose both variable parameters, as in the Turbine-99 example, and categorical parameters such as the turbulence model or discretization scheme. For instance, an interaction effect could be the response of different turbulence models to different levels of dissipation at the inlet.

The major challenge is the choice of parameters and their high and low levels. Procedures to find parameters and appropriate levels were shown in the Turbine-99 example. Another challenge, specific to the application to CFD, is the significance level for an effect. Experimental runs are always associated with a random error, which defines a significance threshold for each effect. If the effect is below the threshold, it is assumed to be noise. There are no natural, significant random errors in CFD. The iterative error was used here to define a threshold and therefore some effects were assumed to be insignificant. By allowing a non-negligable iterative error, simulation time was decreased substantially.

With factorial design the engineer has a systematic, objective, and quantitative method to evaluate the sensitivity to different input parameters. A large main effect will identify, e.g., an important boundary condition for which further analysis or experiments have to be considered. Therefore, the results form a reliable foundation for crucial decisions. The increased computational time resulting from the larger number of simulations may be warranted for large investments or safety critical projects.

Factorial design may also be used to organize workshops where several scientists with different affiliations contribute with one or more runs. However, the results of both Turbine-99 workshops show that workshops are a difficult exercise, as discussed by Apsley and Leschziner [13]. Even if most of the inputs are defined by the organizers, there are still some degrees of freedom leading to discrepancies between the results due to preprocessing, codes, and postprocessing.

As the computational power increases, factorial design may be automated and implemented in commercial codes, where the engineer will select the levels for the desired inputs. The program will perform the different simulations and present the different engineering quantities with a confidence interval as well as the main and joint effects.

5 Conclusion

The application of factorial design to CFD has been discussed. It is a systematic, objective, and quantitative method to investigate the influence of input parameters, such as unknown boundary conditions, turbulence models, and computational grids. The main task is the choice of parameters and their levels.

The illustration of the method with the Turbine-99 test case, a hydropower draft tube flow, clearly illustrates the advantages. Engineering quantities are given within a confidence interval based on the influence of all parameters. Main and joints effects of input parameters are evaluated and permit a better understanding of the flow. For instance, the radial velocity is shown to be a fundamental factor for obtaining accurate results of the pressure recovery and especially the energy loss factor of a draft tube. The use of factorial design in engineering applications may improve the quality of the results and increase the trust in CFD in the industry.

References

[1] Hirsh, C., 2001, "The QNET-CFD Project," QNET-CFD Network Newsletter, **1**, January, pp. 4–5.

[2] Hutton, A. G., and Casey, M. V., 2001, "Quality and Trust in Industrial CFD—A European Initiative," 39th Aerospace Sciences Meeting and Exhibit, Reno, NV, Jan. 8–11.

[3] Casey, M., and Wintergerste, T., eds., 2000, *Best Practice Guidelines*, ERCOFTAC Special Interest Group on Quality and Trust in industrial CFD.

[4] Bergström, J., and Gebart, B. R., 1999, "Estimation of the Numerical Accuarcy for the Flow Field in a Draft Tube," Int. J. Numer. Methods Heat Fluid Flow, **9**, pp. 472–486.

[5] Iaccarino, G., 2000, "Prediction of the Turbulent Flow in a Diffuser With Commercial CFD Codes," Center for Turbulence Research, Annual Research Briefs, pp. 271–278.

[6] Box, E. P., Hunter, W. G., and Hunter, J. S., 1978, *Statistics for Experimenters*, Wiley, New York.

[7] Gebart, B. R., Gustavsson, L. H., and Karlsson, R. I., 1999, Proceedings of Turbine-99 Workshop on Draft Tube Flow, Porjus, Sweden, June 20–23.

[8] Karlsson, R. I., and Gustavsson, L. H., 2001, The Second ERCOFTAC Workshop on Draft Tube Flow, Älvekarleby, Sweden, June 18–20, published at http://www.luth.se/depts/mt/strl/turbine99/.

[9] Dahlbäck, N., 1996, "Redesign of Sharp Heel Draft Tube—Results From Tests in Model and Prototype," Proc. of the XVIIIth IAHR Symp. on Hydraulic Machinery and Cavitation, Vol. 2, pp. 985–993.

[10] Roberson, J. A., and Crowe, C. T., 1997, *Engineering Fluid Mechanics*, Wiley, New York, p. 368.

[11] White, F. M., 1991, *Viscous Fluid Flow*, McGraw-Hill, New York, pp. 426–428.

[12] AEA Technology, "CFX4.4 Solver," Fluid Dynamics Services, Building 8.19, Harwell Laboratory, Oxfordshire, United Kingdom.

[13] Apsley, D. D., and Leschziner, M. A., 1999, "Advanced Turbulence Modelling of Separated Flow in a Difffuser," Flow, Turbul. Combust., **63**, pp. 81–112.

Inverse Design and Optimization of a Return Channel for a Multistage Centrifugal Compressor

Árpád Veress
Department of Aircraft and Ships,
Budapest University of Technology and Economics,
H-1111 Budapest, Sztoczek u. 6 J ép. 4.em. 426,
Hungary

René Van den Braembussche[1]
Turbomachinery and Propulsion Department,
von Kármán Institute for Fluid Dynamics,
Waterloose steenweg, 72,
B-1640 Sint-Genesius-Rode,
Belgium

The design and optimization of a multistage radial compressor vaneless diffuser, cross-over and return channel is presented. An analytical design procedure for 3D blades with prescribed load distribution is first described and illustrated by the design of a 3D return channel vane with leading edge upstream of the cross-over. The analysis by means of a 3D Navier–Stokes solver shows a substantial improvement of the return channel performance in comparison with a classical 2D channel. Most of the flow separation inside and downstream of the cross-over could be avoided in this new design. The geometry is further improved by means of a 3D inverse design method to smooth the Mach number distribution along the vanes at hub and shroud. The Navier–Stokes analysis shows a rather modest impact on performance but the calculated velocity distribution indicates a more uniform flow and hence a larger operating range can be expected. The impact of vane lean on secondary flows is investigated and further performance improvements have been obtained with negative lean.
[DOI: 10.1115/1.1792258]

Introduction

Impellers of multistage compressors are linked by a diffuser, cross-over, and return channel (Figs. 1 and 2). The main task of the vaneless or vaned diffuser is to transform as much as possible kinetic energy, available at the impeller exit, into static pressure rise. The main purpose of the return channel, containing highly curved vanes, is to take out the swirl while guiding the flow to the inlet of the next impeller.

The diffuser and return channel are normally connected by a vaneless 180°. cross-over bend. Big losses may occur in this part because of the flow separation resulting from the strong meridional curvature and because of the long flow paths corresponding to the swirl velocity. The flow distortion at the exit of the cross-over bend and the large circumferential turning, that is required in the return channel, often result in large losses, including areas of separated flow, and limit the pressure that can be achieved in the return channel.

There are not many ways to increase the efficiency or pressure recovery of the diffuser and return channel. The use of vaned diffusers allows an increased pressure rise but unfavorably affects the operating range. As the vaneless diffuser pressure ratio depends on the outlet over inlet radius ratio, an increase of diffuser pressure recovery would require an increase of the overall dimensions. This is not desirable because compactness of these nonrotating parts is very important, especially in the case of compressors operating at high pressure (Fig. 1) where the cost of the barrel increases with the diameter to the power 3.

Thygesen [1] has shown that higher efficiencies are possible by extending the deswirl vanes upstream of the return bend. Similar experience is reported in [2]. It provides a way to increase the overall compressor performance without increasing the dimensions.

The traditional design approach for 2D return channels is not suited to generate high performance vanes for a complex 3D flow with high inlet swirl in a strongly curved meridional contour. The present paper describes an analytical method to design a vaned cross-over duct in combination with the return channel and further improvements by means of a 3D inverse design method. Results are compared to the ones of a classical 2D return channel geometry to quantify the improvements that are achieved with the advanced designs. It is further evaluated what additional improvements can be realized by leaning the blades.

All geometries are analyzed by means of the commercial solver CFX-TASCflow. This Navier–Stokes solver is now routinely used in many industry and research establishments to predict perfor-

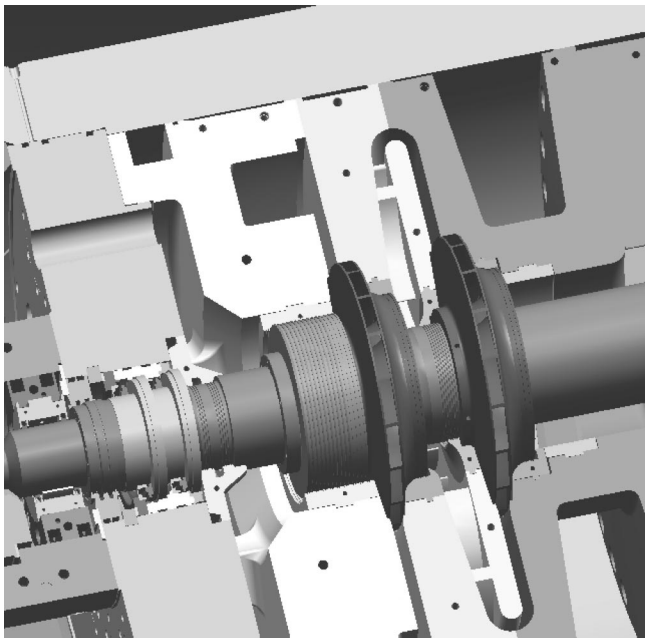

Fig. 1 Typical multistage barrel compressor cross section (courtesy MAN-Turbo)

[1]Corresponding author.

Contributed by the Fluids Engineering Division for publication in the JOURNAL OF FLUIDS ENGINEERING. Manuscript received by the Fluids Engineering Division October 14, 2002; revised manuscript received April 29, 2004. Associate Editor: B. Schiavello.

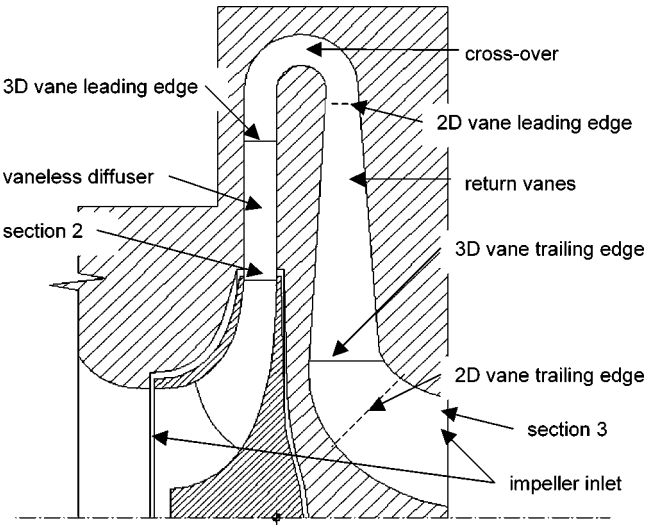

Fig. 2 Schematic view of meridional cross section of the compressor stage with geometry definitions.

mance. CFX-TurboGrid is used to generate a 3D grid with 128 points in the streamwise direction, 24 points in the pitchwise directions, and 26 points in the spanwise direction. Calculations have been made according to the "Best Practice Guidelines" [3]. Grid dependence has not been studied again in this project because calculations [4–6] using the same solver on similar grid density have shown good agreement with experimental results. Anyway care has been taken to have a $y+$ value less than 1.0 at the first point near the wall. All Navier–Stokes calculations have been evaluated using the $k-\varepsilon$ turbulence model with wall function. The dependence of the solution on the turbulence model has not been evaluated in this study, but a comprehensive assessment on the computation of turbomachinery flows using the $k-\varepsilon$ model has been made by Lakhsminarayana [7]. This is supported by [4–6] showing a satisfactory agreement with experimental results for diffusers and cross-over bends with flow separation. The detailed study of Lenke and Simon [6] indicates that calculations with a standard $k-\varepsilon$ model underestimate the separation length at lower Reynolds and that a modification of the turbulence model may be needed when comparing with laboratory testing at low pressure or compressors with extremely low flow coefficients. However, the Reynolds number of the present high pressure compressor flow is sufficiently high to avoid this problem. A residual RMS value less than 10^{-6} is used as convergence criterion. This corresponds to a maximum residual of 10^{-4} to 10^{-5}.

The designs are made for a typical compressor stage with nondimensional specific speed 0.52 operating in air. The inlet boundary conditions (total pressure, total temperature, and flow angle) are the ones predicted by the VKI 1D design and off-design analysis program CCOD [8]. The average static pressure at the next stage inlet is adjusted to obtain the prescribed mass flow. Inlet and outlet boundary conditions are listed in Table 1.

Table 1 Comparison of overall performance

Design	Non-extended	CBL	CBL+ Inverse design
β_2	67.7°	67.7°	67.7°
P_2^o [Pa]	299,700.	299,700.	299,700.
P_2^s [Pa]	158,760.	182,298.	174,800.
P_3^o [Pa]	231,601.	262,248.	262,854.
P_3^s [Pa]	225,713.	257,524.	256,594.
β_3	9.22°	4.25°	−5.37°
ω	0.483	0.319	0.295
C_p	0.475	0.641	0.655
$\dot{m}$ [kg/s]	4.71	4.00	4.49

A schematic view of the meridional cross section and the position of the 2D and 3D vane leading and trailing edge are shown on Fig. 2. The inlet section is defined by the impeller exit width and the outlet is defined by the next stage inlet section. The meridional contour remains unchanged during the design process.

Reference Geometry

Reference geometry is a vaneless diffuser and cross-over followed by a vaned return channel of which the leading and trailing edge positions are shown on Fig. 2. The quasi 2D vanes are defined by the method described by Rothstein [9,10]. This method starts from a central streamline that is tangent to the incoming flow at the leading edge and radial/axial at the outlet. The blade suction and pressure side are defined by specifying a channel of constant or slightly diverging width around this central streamline (Fig. 3). The purpose is to create a channel that turns the flow to radial while controlling the deceleration of the average velocity. A nonzero outlet swirl may have a favourable effect on the flow in the next stage but this option was out of the scope of present study.

The intersection between the different flow channels results in a sharp leading and trailing edge. Only the leading edge is rounded off.

The shortcomings of this geometry are best illustrated by the radial component of the velocity vectors, calculated by the Navier–Stokes solver, on a grid surface near the vane suction side (Fig. 4). One observes a first zone of separated flow on the shroud side near the inlet of the cross-over. It is mainly due to the large deceleration of the meridional velocity as a consequence of the strong meridional curvature. A second zone of separated flow is observed on the vane suction side. This one starts at the suction side hub corner and extends over a large part of the blade suction side. It is caused by the nonoptimum incidence, resulting from the large flow variation from hub to shroud, in combination with the local deceleration of the meridional velocity at the end of the cross-over. The return channel exit average flow conditions are calculated by conservation of mass, momentum, and energy. They correspond to fully mixed-out flow and are listed in Table 1. The

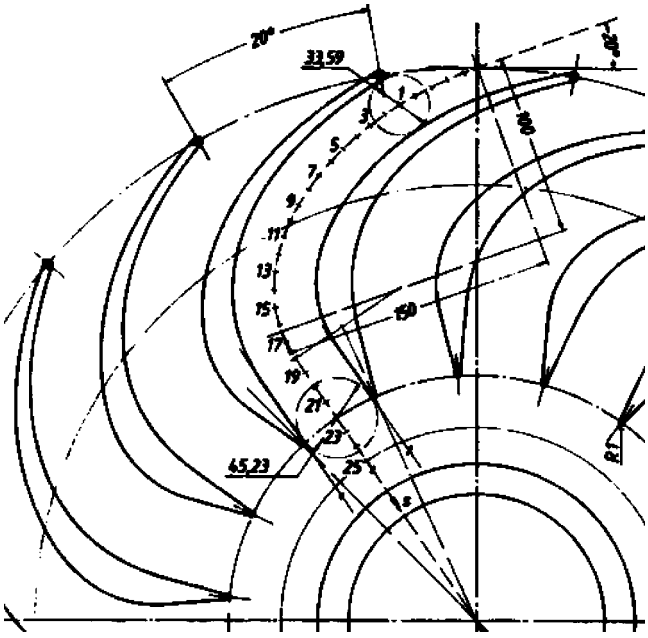

Fig. 3 Return vane design by the method of Rothstein

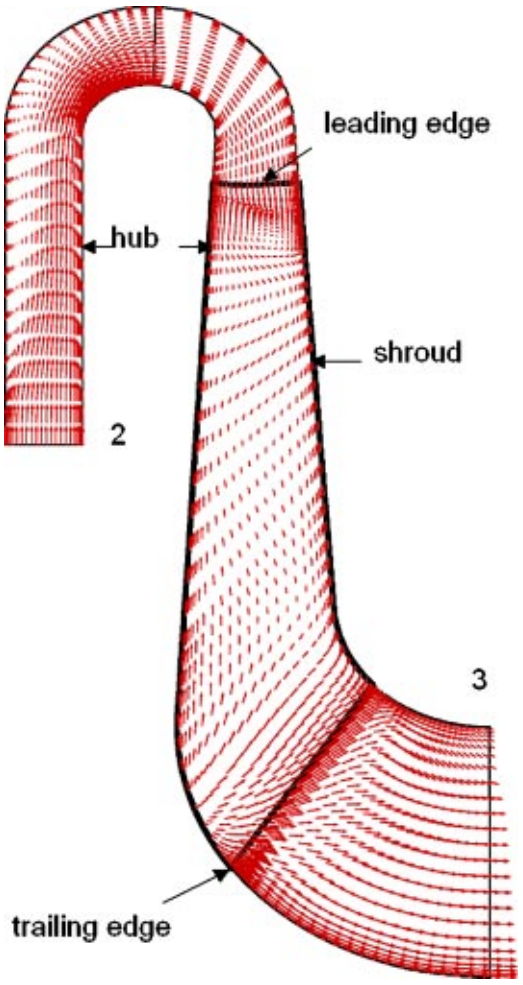

Fig. 4 Radial velocity component on a grid surface near the suction side of the return vanes (reference geometry)

calculated overall performance, defined in Eqs. (7) and (8), is very close to the best performance point measured in [9] for a similar return channel and confirms the validity of present Navier–Stokes calculations.

3D Vane Design

In an attempt to avoid the massive flow separation observed in the reference return channel, it has been decided to extend the vanes upstream of the cross-over duct up to the vaneless diffuser exit (Fig. 2). The vane leading edge is located sufficiently away from the impeller exit not to cause any reduction in operating range. The number of vanes is kept unchanged at 18 with the trailing edge positioned at constant radius.

It is not obvious how a good 3D vane should look like in terms of blade camber and normal thickness distribution. This is particularly difficult in radial geometries where the blade loading depends as well on camber as on radius change and meridional curvature. An analytical design procedure, called BLADECONTOUR, in which the blade loading can be prescribed, has been developed for this purpose.

The vanes are defined by the camber line position (R,θ) and thickness (δ_{th}) distribution at hub and shroud. The method starts by defining the mid-span β distribution corresponding to an irrotational flow $(\nabla\times\vec{W}=0)$ with **C**ontrolled **B**lade **L**oading (CBL) from leading to trailing edge.

Imposing zero circulation on the closed contours, defined by part of the suction and pressure side of two adjacent vanes and

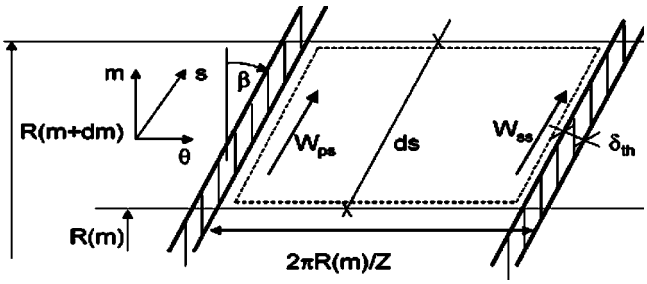

Fig. 5 Control surface for the analytical vane design method

two lines at constant radius (Fig. 5), provides the following relation between vane loading and the change in flow angle β [8]:

$$W_{ss}-W_{ps}=\cos\beta_{bl}\frac{d}{dm}\left(\left(\frac{2\pi R}{z}-\frac{\delta_{\text{th}}}{\cos\beta_{\text{bl}}}\right)W_m.tg\beta_{\text{fl}}\right). \quad (1)$$

Replacing the local meridional velocity by the pitchwise averaged value

$$\overline{W}_m=\frac{\dot{m}}{\rho zb\left(\frac{2\pi R}{z}-\frac{\delta_{\text{th}}}{\cos\beta_{\text{bl}}}\right)} \quad (2)$$

and assuming that the average flow angle equals the blade camber angle $(\beta_{\text{fl}}=\beta_{\text{bl}})$, one obtains following relation between blade angle variation and loading

$$W_{ss}-W_{ps}=\left(\frac{\dot{m}}{\rho zb}\right)\frac{1}{\cos\beta_{\text{bl}}}\frac{d\beta_{\text{bl}}}{dm} \quad (3)$$

Imposing

$$(W_{\text{ss}}-W_{\text{ps}})\rho zb/\dot{m}=C^t \quad (4)$$

corresponds to constant blade loading $(W_{\text{ss}}-W_{\text{ps}}=C)$ only in the case of constant density and channel width. The eventual increase/decrease of ρ and b along the channel length will result in a proportional decrease/increase of the loading towards the trailing edge. Substituting (4) into (3) results in

$$\beta_{\text{bl}}=C^t\int_{\text{LE}}\cos\beta_{\text{bl}}\,dm \quad (5)$$

It allows the calculation of the vane camber angle at any position between leading edge and trailing edge by integrating (5) from leading edge up to that position. The leading edge blade angle $\beta_{\text{bl-LE}}$ is set equal to the local flow angle, which corresponds to zero incidence operation. The C^t is adjusted until the trailing edge angle $\beta_{\text{bl-TE}}$ is zero. Considering the small pitch to chord ratio (many long blades) one can assume that the difference between flow and blade angle will be small and that also the exit flow angle will be close to zero. This is confirmed by the deviation angles evaluated by the Navier–Stokes solver and listed in Table 1.

The blade angle distribution at hub and shroud requires a modification of the calculated midspan distribution as indicated on Fig. 6. The meridional length is adjusted to account for the difference in contour length of the cross-over at hub and shroud. In order to avoid that this difference on contour length results in an excessive lean of the vanes at the exit of the cross-over one must increase the blade angle on the hub contour and decrease it at the shroud. An elliptic variation of the flow angle is added in the cross-over area. The decrease of blade angle in combination with the decrease of meridional velocity on the concave shroud contour results in an extra loading at the shroud wall. The increase of blade angle in combination with an increase of the meridional velocity on the convex hub contour results in a decreased loading at the hub wall. Both phenomena are confirmed by the results of the

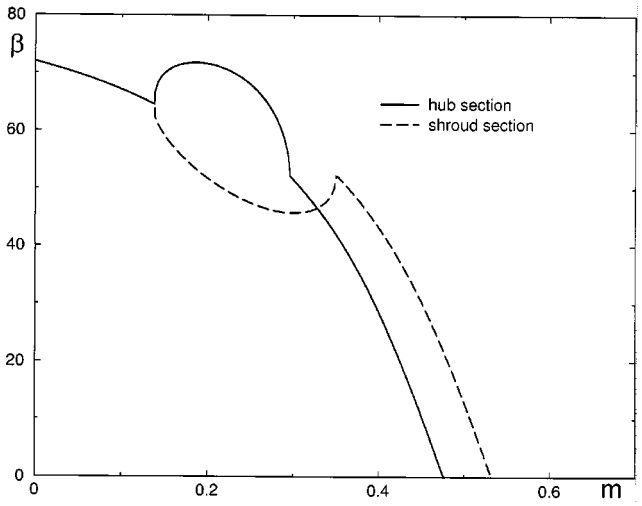

Fig. 6 Flow angle distribution imposed at hub and shroud

Euler calculations (Fig. 8). This difference in loading is not desired but necessary if one wants to avoid excessive lean.

The vane camber line circumferential position $\theta(R)$ is then defined at any location between LE and TE by integrating the vane angle along the meridional length at hub and shroud up to that point.

$$\theta(R) = \int_{LE} \frac{\tan(\beta_{bl})}{R} dm \tag{6}$$

Imposing $\theta_{\text{hub-LE}} = \theta_{\text{shroud-LE}}$ corresponds to zero lean at leading edge. The amplitude of the elliptic angle variation at the cross-over is adjusted until $\theta_{\text{hub-TE}} = \theta_{\text{shroud-TE}}$, corresponding to zero lean at trailing edge.

The blade design is completed by adding a thickness distribution to the camberline. The thickness is defined by an ellipse in the first 25% of the blade length at midspan. The short axis is 10% of the longitudinal one which results in a 2.5% maximum blade thickness relative to the total midspan vane length. A linear variation is imposed in the second part of the blade between the point of maximum thickness and the prescribed trailing edge thickness.

The results of the 3D Navier–Stokes analysis of the new geometry are shown on Fig. 7. The separation at the inlet of the cross-over has disappeared but the flow is still close to separated at the hub side downstream of the cross-over. As will be explained in the next section, this is mainly due to a local variation in blade loading resulting from the sudden change in meridional velocity.

Inverse Design of Vanes

In an attempt to further improve the flow in this complex geometry, it has been decided to redesign the blades by means of the inverse design method "INVERSE-H," developed by Demeulenaere et al. [11,12]. This is an iterative procedure in which an initial geometry is modified until the desired/prescribed velocity or pressure distribution on the blade contour is obtained. It makes use of a 3D Euler solver with modified boundary conditions to calculate the velocity V_n normal to the blade contour, that goes with the required velocity on the present blade contour. This V_n distribution is then input for a transpiration technique to define the new blade geometry by the streamlines of previous Euler solution. It is a full 3D method in which the designer can decide in how many sections along the blade span he wants to specify the Mach number distribution on suction and pressure side. In the present design the Mach number distribution is specified only at hub and shroud. The Mach number distribution imposed at every grid point on the blade is obtained by a linear interpolation between these two sections. The numerical accuracy and convergence of the procedure

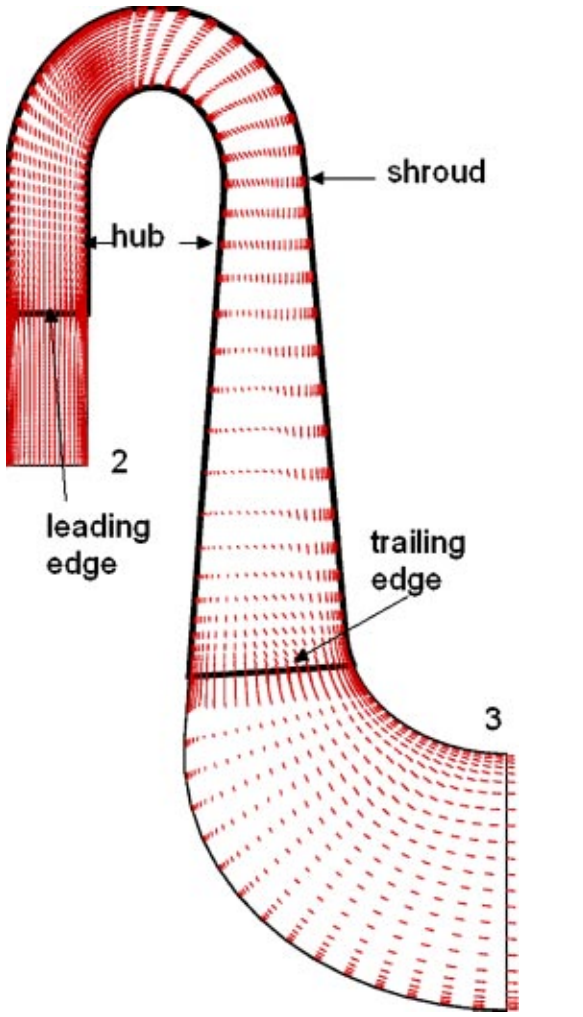

Fig. 7 Meridional velocity component on a grid surface near the suction surface of the controlled blade loading vanes

have been extensively verified in [11,12]. The accuracy, however, is limited to what one can expect from an inviscid Euler solver. The performance of the redesigned geometries are therefore verified by the 3D Navier–Stokes solver of which the accuracy is discussed in the Introduction.

The main problem when making an inverse design is to define a Mach number or pressure distribution that is not only optimum in terms of losses and pressure rise but that corresponds to a vane that satisfies the constraints related to vane thickness, flow angle, and maximum lean or any other geometrical constraint one may want to impose on the blade shape. This is particularly difficult in the present case because the vanes are very long and of small height, so that small variations from hub to shroud may lead to excessive lean angles. Experience has shown that the easiest way to define a realistic Mach number distribution is by deriving it from the one calculated on an initial vane taking into account some basic flow relations. This is not a requirement but it helps to speed up the convergence to a blade that satisfies the constraints.

Present inverse design starts from the previously defined 3D geometry and the imposed Mach number distribution is derived from the one obtained by a 3D Euler analysis and indicated by $+++$ on Fig. 8. The abscissa s/c corresponds to the blade contour length along suction and pressure side, nondimensionalized by the meridional length "c" between the leading edge and trailing edge.

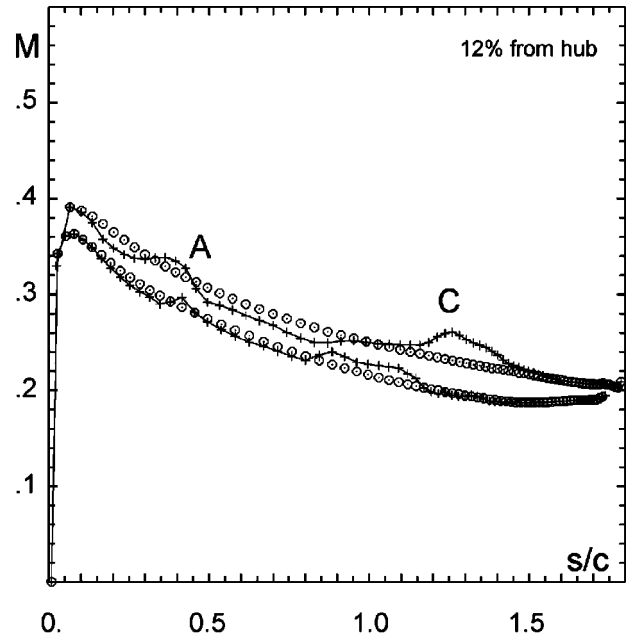

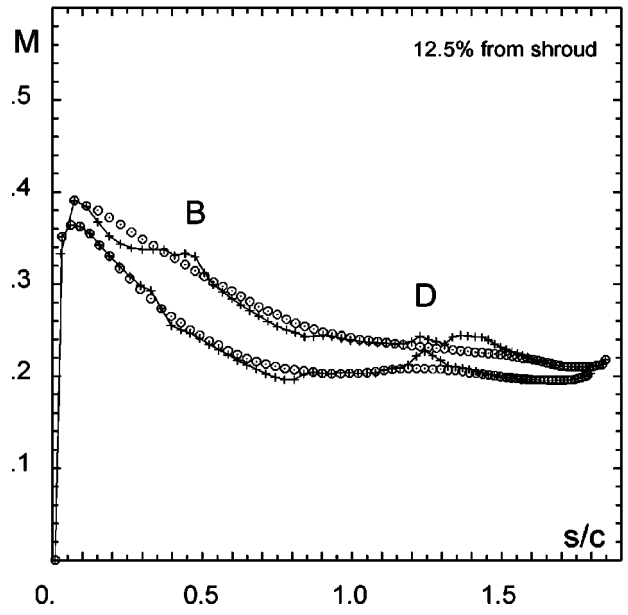

Fig. 8 Mach number distribution on the initial blade at 12% blade height from hub and shroud

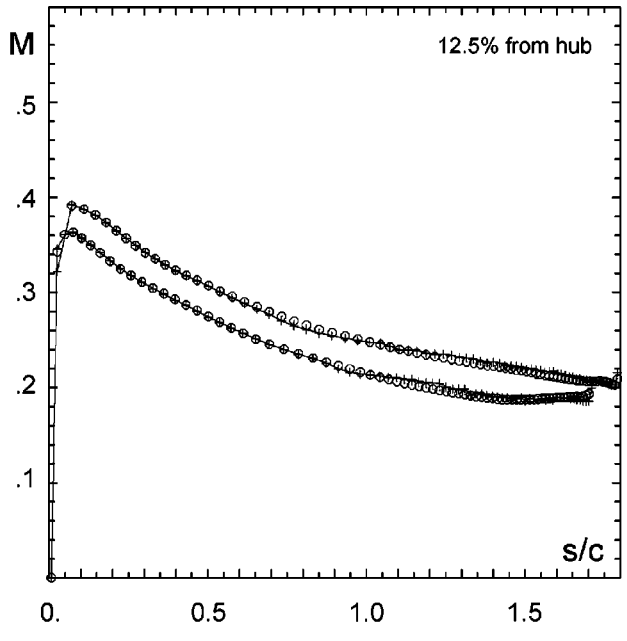

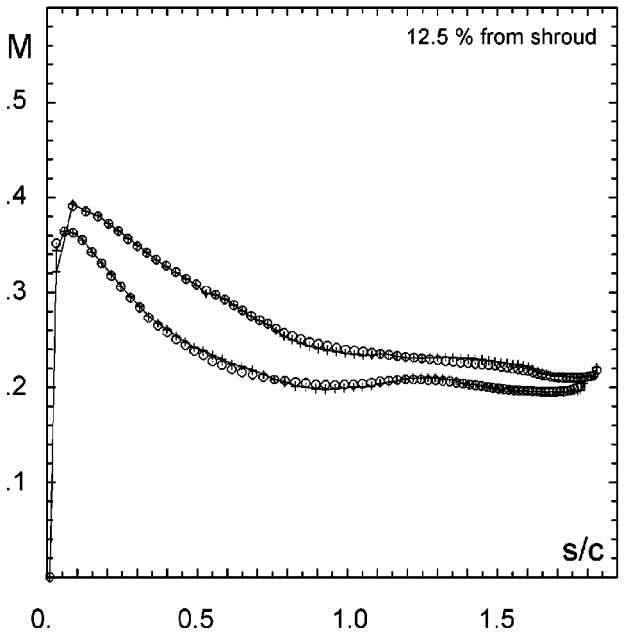

Fig. 9 Imposed (o) and calculated (+) Mach number distribution on the redesigned vane at 12% blade height from hub and shroud.

Two critical areas, where improvements are possible, are easily distinguished in these initial Mach number distributions. The first one is at the start of the cross-over bend where the meridional velocity increases near the hub because of the convex curvature. As the tangential velocity remains unchanged, the flow turns to more axial (lower β_{fl}) and the blade loading locally reduces to almost zero (A). The opposite occurs near the shroud wall (B) where the meridional velocity decreases under the influence of the concave wall. This results in an increased blade loading to keep the flow tangent to the blade.

The second critical zone is at the end of the cross-over where the impact of the curvature disappears and the meridional velocity becomes again uniform over the passage width. The meridional velocity component suddenly decreases on the hub contour (end of convex wall) and the flow turns to more tangential. This results in a local increase of the blade loading (C). A sudden decrease of the blade loading is observed in point (D) on the shroud wall where the flow suddenly accelerates when going from the concave to the straight wall.

The main purpose of the vane redesign by means of the inverse design method is to eliminate these local flow accelerations and decelerations and as such to reduce the risk of flow separation and consequent losses in the cross-over and return channel.

The smoothed Mach number distribution imposed on the suction and pressure side at hub and shroud during the inverse design is shown by circles on Fig. 8 and 9. As the meridional contour is unchanged during this design process, one does not expect big changes of the average velocity, which is conserved. The irregular blade loading, however, is replaced by a more constant one. Attention is given to keep the integral of the blade loading

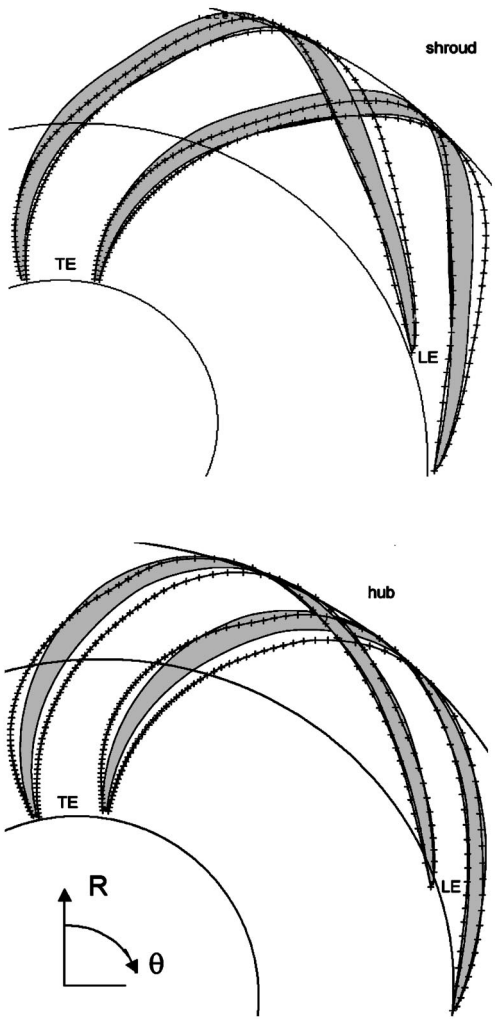

Fig. 10 Comparison between original (gray) and redesigned (+++) vanes

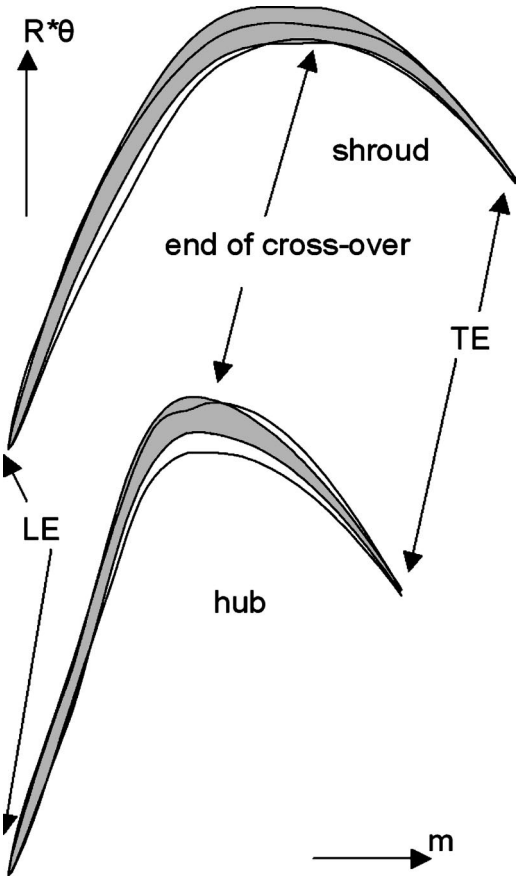

Fig. 11 Comparison between original (gray) and redesigned (line) vanes in the $m, R^*\theta$ plane.

$\int_{LE}^{TE}(W_{ss}-W_{ps})\,ds$ unchanged in order to limit the change in outlet flow angle. For reasons explained in the previous section the same loading cannot be imposed at hub and shroud.

The inverse solver was fully converged after 550 time steps and the imposed and calculated Mach number distributions agree very well as shown in Fig. 9.

The original (gray) and redesigned vanes (+++ lines) are compared in Fig. 10. The main modifications of the blades are at the cross-over and downstream of it. They are more clearly visible on the $(m,R^*\theta)$ plots on Fig. 11. The vane thickness near the shroud increases at the start of the cross-over and remains constant until the end of the cross-over. This increased blockage compensates for the deceleration that normally takes place at the start of the concave side of the cross-over and pushes the flow towards the hub side. The sudden decrease at the end of the cross-over (near maximum value of $R^*\theta$) tries to compensate for the acceleration that takes place at the end of the concave shroud contour.

The blade thickness at the hub remains unchanged up to the end of the cross-over. A decrease of the thickness would be desirable to compensate for the meridional velocity increase at the start of the convex wall of the cross-over. However, it is not allowed from the point of view of minimum blade thickness. The increase of the vane thickness, near the outlet of the cross-over (near maximum value of $R^*\theta$), compensates for the meridional velocity deceleration that takes place when going from a convex surface towards a straight one. The blade sections shown on Fig. 11 have a $-45°$. slope at the trailing edge but correspond to a radial outlet with constant θ. dR being equal to $-dm$ in the radial part of the return channel, means that $d(R\vartheta)/dm=-1$ if θ is constant and the arctangent of it corresponds to the $-45°$. blade trailing edge angle observed in Fig. 11.

Overall Performance

The main parameters to characterize the performance are the inlet to outlet static pressure recovery and total pressure loss coefficient defined by

$$C_p=\frac{\overline{P}_3^s-P_2^s}{P_2^o-P_2^s} \tag{7}$$

$$\omega=\frac{P_2^o-\overline{P}_3^o}{P_2^o-P_2^s} \tag{8}$$

The latter one is of less importance in diffusers and return channels but, as shown by the following relation,

$$C_p+\omega=1-\frac{\overline{P}_3^o-\overline{P}_3^s}{P_2^o-P_2^s}\approx 1-\frac{\overline{P}_2^o-\overline{P}_{3is}^s}{P_2^o-P_2^s}\approx C_{p_{is}} \tag{9}$$

quantifies for a given geometry how much of the possible static pressure rise is not achieved because of total pressure losses. Input data are the results of the Navier–Stokes calculations presented in previous sections. The averaging is based on the conservation of mass, momentum, and energy and the values shown in Table 1 correspond to fully mixed-out conditions.

An attempt was made to perform all the Navier–Stokes calculations at the same mass flow. However, as one imposes the outlet

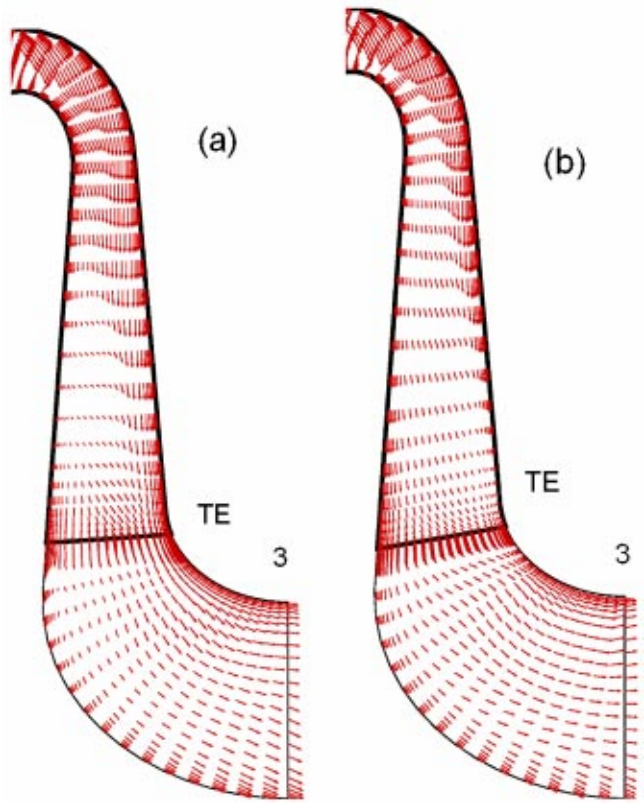

Fig. 12 Velocity vectors on the second grid surface near the suction side of the CBL blade (*a*) and inverse designed blade (*b*)

static pressure, the mass flow will be influenced by the total pressure losses. One has therefore iteratively adjusted the outlet static pressure until the mass flow was within some tolerances around the target value. Anyway the absolute inlet flow angle is kept constant at 67.6° so that a change in mass flow will not modify the vane incidence angle. Mach numbers are also rather low so that one can assume that the small changes in mass flow will not significantly influence the nondimensional coefficients C_p and ω. The performance coefficients, mass flow, values of the exit pressures, and exit swirl angle are listed in Table 1.

The results show a large increase of the static pressure rise for the longer CBL (controlled blade loading) blade.

The inverse design of the blade resulted in a rather limited performance improvement. However, this improvement takes place in addition to an almost 10°. increase of turning (the outlet flow angle has changed from 4.25° to −5.37°). A more detailed look at the Navier–Stokes results shows that the sudden deceleration to nearly separated flow downstream of the cross-over (Fig. 12*a*) has been replaced by a higher and more uniform velocity on the suction side. As a consequence one can expect a more stable flow and a larger off-design operation range for the inverse designed blade.

Influence of Lean

It can be expected that these long flow channels of small height will generate large secondary flows. A common way to control secondary flows is by introducing lean and sweep. Only lean has been investigated because it is unlikely that sweep may have a significant impact on the flow in these long channels of small height. As the inverse design is based on the inviscid Euler equations it can not be used to reduce secondary flows and the following evaluation about the impact of lean on performance has been made with the Navier–Stokes solver.

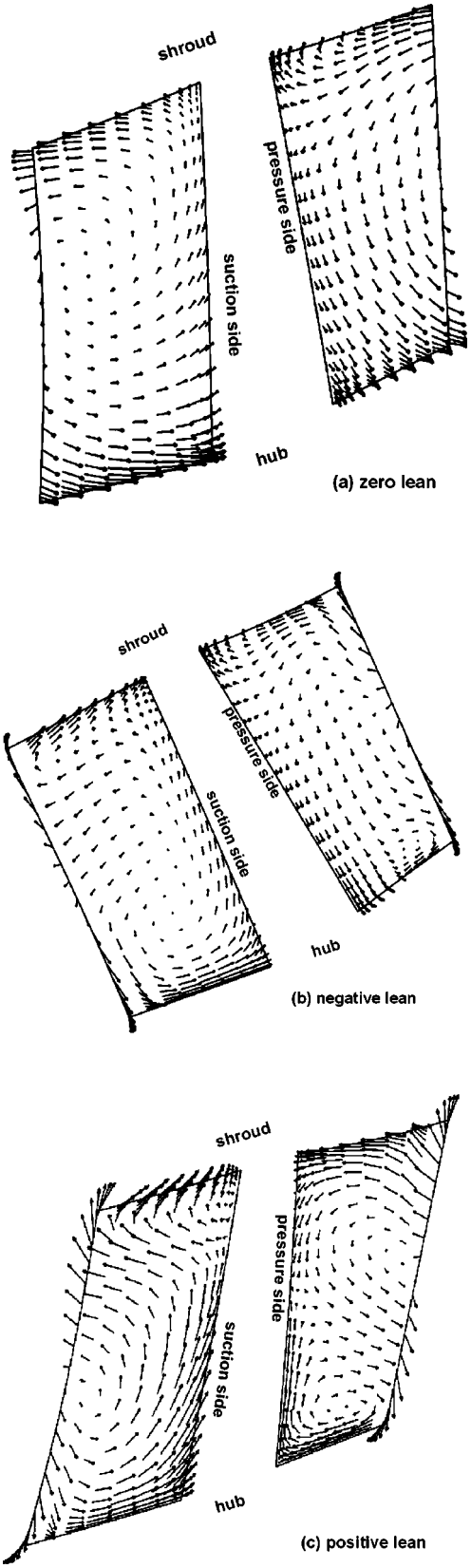

Fig. 13 Velocity vectors projected on a cross section near the vane trailing edge

Lean is introduced by rotating the shroud blade over $\Delta\theta = 4.0°$ around the symmetry axis into the direction of the suction side (negative lean) and towards the pressure side (positive lean). The hub section is unchanged and the vanes are reconstructed by

Table 2 Impact of lean on return vane performance

	CBL	No lean	Negative lean	Positive lean
ω	0.319	0.295	0.280	0.312
C_p	0.641	0.655	0.671	0.632
β_3'	4.25°	−5.37°	−2.99°	10.75°

straight lines from hub to shroud. This circumferential shift of the shroud results in a maximum vane lean of 27.0° inside the cross-over (at the point of maximum radius).

The impact of lean on performance is listed in Table 2. One observes an additional increase of the pressure rise and a small decrease of prerotation with negative lean. Positive lean results in larger losses and a substantial decrease of the turning.

The way lean influences secondary flows and vane outflow conditions is illustrated by the projection of the velocity vectors in a grid surface shortly upstream of the vane trailing edge (Fig. 13). Shown is the flow in one half pitch on each side of the vane. The left part of each figure should be placed next to the right one to obtain an idea of the complete passage vortex. The non-negligible counter-clockwise vortex at 0.0° lean (Fig. 13*a*) does not only become weaker but is even locally inverted when introducing negative lean (Fig. 13*b*). The higher losses at positive lean are due to the much stronger counter-clockwise vortex near the shroud surface and an additional clockwise vortex near the hub pressure side corner (Fig. 13*c*).

Conclusions

Large separation bubbles are likely to occur on the shroud side at the cross-over inlet and in the hub vane suction side corner of classical 2D return channels. The first event is caused by a sudden deceleration at the inlet of the cross-over. The latter situation is caused by the sudden deceleration of the flow at the exit of the cross-over in combination with incidence problems resulting from the strong flow variation from hub to shroud.

It has been shown that an extension of the vanes upstream of the cross-over may result in a considerable improvement of the performance. However, this requires a careful design of the blades to control the blade loading. The upstream vane extension provides the potential to improve the performance at given dimensions or to reduce the overall dimension and hence cost without loss in performance.

Avoiding flow separation on the vane suction side by redesigning the 3D vanes by means of an inverse method provides some additional gain in performance and permits a larger operating range.

Optimum vane leaning further contributes to a performance increase by reducing the vorticity resulting from secondary flows.

The impact of the cross-over curvature radius and the divergence of the return channel may allow further improvement of the performance but has not been investigated.

Nomenclature

b = hub to shroud channel width
c = reference length
C_p = pressure recovery factor
m = meridional coordinate
$\dot{m}$ = mass flow
P = pressure
R = radius
s = curvilinear coordinate along streamline and blade surface
W = velocity
z = number of vanes
β = flow or blade angle (measured from radial)
δ_{th} = blade normal thickness
θ = angular coordinate
ρ = density
ω = loss coefficient

Subscripts

bl = blade
fl = flow
LE = leading edge
TE = trailing edge
th = thickness
ps = pressure side
ss = suction side
2 = impeller exit—vaneless diffuser inlet
3 = return channel exit—next impeller inlet
is = isentropic

Superscripts

-- = averaged value
o = total conditions
s = static conditions

References

[1] Thygesen, R., 2000, "Optimization of Return Channel Blades for Radial Compressors," von Karman Institute PR 2000–21, Sint-Genesius-Rode, Belgium.
[2] Meng, S. Y., and Jackson, E. D., 1983, "The continuous Diffusion Crossover System Design," ASME FED-Vol. 3, Return Passages of Multistage Turbomachinery.
[3] Casey M., and Wintergerste T., 2000, "Best Practice Guidelines," Ercoftac Special Interest Group on "Quality and Trust in Industrial CFD," Ercoftac.
[4] Sorokes, J., and Kopko, J., 2001, "Analytical and Test Experiences Using a Rib Diffuser in a High Flow Centrifugal Compressor Stage," ASME 2001-GT-0320.
[5] Ardizzon, G., and Pavesi, G., 2003, "Influence of the Stator/Rotor Interaction on Reverse Flow at Off-design Operation," Proceedings of 5th European Conference on "Turbomachinery Fluid Dynamics and Thermodynamics," Prague, pp. 619–628.
[6] Lenke, L. J., and Simon, H., 1998, "Numerical simulation of the flow through the return channel of Mutltistage Centrifugal Compressors," ASME 98-GT-255.
[7] Lakhsminayarana, B., 1996, "Fluid Dynamics and Heat Transfer of Turbomachinery," Wiley, New York.
[8] Van den Braembussche, R. A., 1990, "Design and Optimization of Centrifugal Compressor," von Karman Institute CN 141, Sint-Genesius-Rode, Belgium.
[9] Rothstein, E., 1984, "Experimentelle und Theoretische Untersuchung der Strömungsvorgänge in Rückfürkanälen von Radialverdichterstufen insbesondere solchen mit geringen Kanalbreite," Ph.D. thesis, RWTH Aachen, Germany.
[10] Simon, H., and Rothstein, E., 1983, "On the Development of Return Passages of Multistage Centrifugal Compressors," ASME FED-Vol. 3, Return Passages of Multistage Turbomachinery.
[11] Demeulenaere, A., 1997, "Conception et development d'une methode inverse pour la generation d'aubes de turbomachines," von Karman Institute, Ph.D thesis, Sint-Genesius-Rode, Belgium.
[12] Demeulenaere, A., and Van den Braembussche, R. A., 1998, "Three-dimensional Inverse Method for Turbomachinery Blading Design," ASME J. Turbomach., **120**, pp. 247–255.
[13] Veress, A., 2001, "Inverse Design on Return Flow Channel for Multistage Radial Compressor," von Karman Institute PR 2001–27, Sint-Genesius-Rode, Belgium.

Characteristics of the Liquid Film and Pressure Drop in Horizontal, Annular, Two-phase Flow Through Round, Square and Triangular Tubes

Timothy A. Shedd[1]
Multiphase Flow Visualization and Analysis Laboratory,
Department of Mechanical Engineering,
University of Wisconsin–Madison,
Madison, WI 53706
e-mail: shedd@engr.wisc.edu

Ty A. Newell
Department of Mechanical and Industrial Engineering,
University of Illinois at Urbana–Champaign,
Urbana, IL 61801
e-mail: t-newell@uiuc.edu

A unique set of liquid film thickness and pressure drop data has been obtained for horizontal, annular flow of air and water through round, square and triangular tube using a noninvasive, optical liquid film thickness measurement system. In the square and triangular tubes, the liquid film was thinned in the corners, indicating an effect of turbulent secondary flows in these geometries. In addition, when the film thickness is nondimensionalized using a friction velocity based on the total pressure drop, it is found that virtually all the data lie below $h^+=35$ *and that dryout occurs at approximately* $h^+=5$. *The two-phase friction factor for the annular flows examined in all the tubes can be correlated using the Lockhart–Martinelli parameter,* X_{tt}, *when adjustments are made for the hydraulic diameters of the nonround tubes.* [DOI: 10.1115/1.1792261]

Introduction

Flow through noncircular passages is quite common, and it has been known for nearly a century that the behavior of these flows is somewhat different from those in circular passages. Pressure losses are typically greater, and heat and mass transfer are not uniform along the walls. While a large number of studies have been made of turbulent single-phase flow in square and triangular geometries, very little has been done with two-phase flow.

The lack of work in this area is somewhat surprising, given the large number of noncircular flow passages in the nuclear power generation industry and the growing number of heat exchangers constructed with square, rectangular, and triangular channels [1,2]. In addition, Zietlow and Pedersen [3] have found that heat transfer and pressure loss predictions for relatively large channels scale well to the microchannel regime. Microchannel heat exchangers are now quite widely used. An understanding of annular flow through channels with corners may also help improve the state of knowledge of flow through internally finned tubes and plate-fin exchangers [4].

Annular flow is a common two-phase regime for flow inside of tubes in which a gas or vapor flows through the center of the tube shearing a liquid layer along the wall. Although it is not yet entirely clear how the liquid becomes distributed about the circumference of the tube, general characteristics can be identified. In a horizontal tube, a low flow of gas may flow concurrently with a stratified layer of liquid flowing along the bottom of the tube. As the velocity of the gas increases, waves are generated at the interface, leading to a thinner liquid layer between waves and the intermittent wetting of the upper tube wall as waves pass. Higher gas velocities increase the frequency of these waves until a stable level of wall wetting is achieved. In smaller tubes this flow will wet the entire circumference, and is designated wavy-annular flow by [5]; fully annular flow may not be observed larger tubes (greater than 25.4 mm in diameter) at this point. At gas velocities of approximately 30 m/s, significant entrainment of droplets from the peaks of waves commences [6], and this process completes the wetting of the wall circumference in larger tubes. It is also about this point that ringlike turbulent waves appear that are generally referred to as disturbance waves to distinguish them from other interfacial structures. The flows measured in this study were observed to be in annular flow, with some near the transition to disturbance wave flow. Further details of annular flow behavior may be found in [7] and [8].

Fukano et al. [9] obtained information about two-phase horizontal flow in square and rectangular channels, focusing primarily on the film flow along the bottom wall. They obtained mean film thickness measurements and used a unique method to obtain film flow information in eight zones across the bottom wall. Although visual observations were used to generate a flow-regime map, no detailed film thickness measurements were obtained in this study. Fukano et al. also studied two-phase stratified annular flow in square and rectangular channels, but their publications were concerned primarily with the gross behavior of the liquid film and did not report two-phase pressure gradient or detailed film distribution information [10,11]. A flow regime map has been generated for horizontal and vertical flows through rectangular channels by Troniewski and Ulbrich [12] as well.

This work presents a survey of horizontal annular air-water flow through various geometries. Specifically, the effect of corners on the liquid distribution was investigated using square and triangular tubes with comparison to round tubes. Two different sizes of both the square and round tubes were tested to determine behaviors associated with tube size. In addition, two different orientations of both the square and triangular tubes were examined to delineate the effect of gravity on the flows. The results of these experiments will be discussed with respect to the effects of geometry and orientation on liquid film profiles, dryout, and pressure drop.

Experimental Apparatus

A schematic of the flow loop used in this work is shown in Fig. 1. A large wet-vacuum was used to generate suction on one end of the test section. Air entered the apparatus through a long, smooth, round pipe with a valve at its opening to control air flow.

[1]Corresponding author

Contributed by the Fluids Engineering Division for publication in the JOURNAL OF FLUIDS ENGINEERING. Manuscript received by the Fluids Engineering Division September 18, 2001; revised manuscript received April 20, 2004. Associate Editor: L. Mondy.

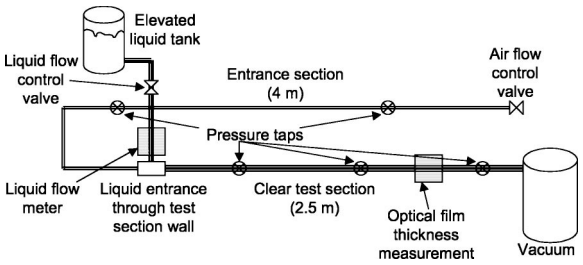

Fig. 1 Schematic of the two-phase flow loop used in this set of experiments

The test sections were all constructed of acrylic. Two round test sections, one 12.7 mm i.d. and one 25.4 mm i.d., were of cast acrylic with manufacturer's listed tolerances of ± 0.08 mm. Each had 3.1 mm thick walls and were 6.5 m long. The square sections were of extruded acrylic with inner sidewalls measuring 15.2 and 22.7 mm, respectively. The walls were 1.5 mm thick and these test sections were also 6.5 m in length. The manufacturer gives a tolerance of ± 0.025 mm for the dimensions of these tubes. To achieve the long test section, the ends of shorter tube lengths were sanded plane with a final polishing of 1500 grit sandpaper. The tube section ends were secured in PVC flanges. For the square test sections, alignment tabs were affixed to two sides of each end so that two test section ends would mate and self-align. The sections were then bolted together and leak tested. While seamless joints were not achieved, very little flow disturbance was observed at the joints as confirmed by pressure drop measurements.

The triangular test sections were formed from three 2.5 m long, 40 mm wide sheets of cast acrylic, each 3 mm thick. These were held together with a circular form at each end while the corners were sealed with silicon sealant. Once dried, a layer of tape was applied externally to protect the sealant. The triangular section was coupled to round entrance and exit sections via round rubber adapter fittings and silicon sealant. In this case only, liquid was injected through the wall of a round section preceding the test section, rather than directly through the test section walls.

Abbreviations are frequently used for the different tubes and orientations studied in this work: LR, 25.4 mm i.d. round; SR, 12.7 mm round; LS, 22.1 mm square; and SS, 15.2 mm square. The square tubes were tested at 45° rotation as well to obtain the ''diamond'' sets, LD and SD. The triangle was examined with its apex upward (TU) and downward (TD).

Following [13], the air flow rate was determined by measuring the pressure drop across a 3 m length of the entrance tube. An inclined manometer was used for this pressure difference because the pressure drops were often quite small. The manometer was mounted to give ten times the sensitivity of the vertical position. The Colebrook relation for turbulent friction factor [14], together with the definitions of the friction factor, Reynolds number, and mass flow rate, were then solved simultaneously to provide the mass flow rate of air in the loop. This process was simplified and automated by using an equation solver software package. A propagation of error analysis performed for this experiment according to [15] gives a total worst-case uncertainty of 3.5% in the air mass flow measurement. Comparison with an in-line spring-loaded volumetric flow meter using a compressed air source gave agreement to within the uncertainty of the flow meter.

Liquid was introduced from a large gravity-fed tank, through a bank of flow meters, and into the test section via several holes drilled around the circumference of the test section wall. A pump controlled by a liquid level switch in the receiving tank at the end of the loop pumped liquid back to the raised tank. During the course of a measurement, the liquid level in the tank never changed more than 2% of the total head, providing a nearly constant head liquid source. Liquid flow rates were determined both by timing the dropping liquid level in the raised tank and by variable-area volume flow meters. Measurements of the liquid flow had uncertainties of ± 0.00025 kg/s, or about 10% of the lowest flows. Repeatability of flow conditions was within 10% from run to run.

The flow conditions tested are listed in Table 1. The velocities listed in this table are superficial velocities defined by

$$U_{sg} = \frac{\dot{m}_g}{\rho_g A_{Dh}} \tag{1}$$

$$U_{sl} = \frac{\dot{m}_l}{\rho_l A_{Dh}} \tag{2}$$

where A_{Dh} is the cross-sectional area of the test section calculated using the hydraulic diameter of the tube.

All pressure drops were measured using U-tube water manometers. Vertical manometers could be read to a precision of 1 mm (9.8 Pa) at low liquid flow rates. At higher liquid flows, pressure fluctuations in the test section caused significant variation in the manometer levels. An average of these fluctuating levels was recorded for each of the 16 to 20 runs of a flow condition, resulting in estimated uncertainties in the pressure measurements for the lower three flow rates (flows A–C) of 60 Pa and 130 Pa for the higher three flow rates (flows D–F).

Local liquid film thicknesses were obtained using an optical measurement system described in [16] and [17]. The time-averaged liquid film thicknesses presented here were measured to within ± 0.003 mm ($\pm$ one standard error). Briefly, a point light source is placed on a transparent test section wall which has a translucent, diffusing coating on it. The light travels through the wall and liquid layer, but when it reaches the gas/liquid interface, any light arriving at an angle greater than or equal to the critical angle for the substances will be reflected back from the interface, creating a ring of light around the light source. The diameter of this light ring is directly proportional to the vertical distance travelled by the light. An image of this light ring is sampled at regular intervals and the mean liquid film thickness is determined from several hundred samples. If the surface is highly disturbed, the light will be significantly scattered and no measurement will be possible. As has been verified by [18], the experimental results presented here exclude large liquid waves from the calculated average thickness; the thicknesses reported reflect only the thin base film that exists between the large liquid waves. This is an important consideration, as several of the correlations for pressure drop and film distribution in the literature assume time-averaged values obtained with electrical impedance methods that include the waves. Example images of the base film and wave structure, obtained through planar laser induced fluorescence [19], are shown in Fig. 2.

Film thicknesses were measured at 16 equally spaced circumferential locations on the round tubes. Four equally spaced points were used on each of the four sides of the 15.2 mm square and five equally spaced points were used on each side of the 22.1 mm square. Four equally spaced points were used on each side of the triangle. Thus, film thickness from 16 points for each flow condition comprise the LR, SR, SS and SD data sets; 20 points the LS and LD sets; and 12 points the TU and TD sets. Complete tables of these film thickness data sets may be found in [20].

Results

Ensemble-averaged two-phase measurements for all of the flows and geometries are presented in Table 2. The quality, x, is

Table 1 Flow conditions for the data obtained in all geometries

Flow conditions									
	Round					Triangle			
Flow	$\dot{m}_g$ (kg/s)	$\dot{m}_l$ (kg/s)	U_{sg} (m/s)	U_{sl} (m/s)	Flow	$\dot{m}_g$ (kg/s)	$\dot{m}_l$ (kg/s)	U_{sg} (m/s)	U_{sl} (m/s)
LR-A	0.0248	0.0048	49	0.0095	TD-A	0.0251	0.0042	36	0.0061
LR-B	0.0219	0.0138	43	0.027	TD-B	0.0231	0.0126	33	0.018
LR-C	0.0174	0.0340	34	0.067	TD-C	0.0221	0.0210	32	0.030
LR-D	0.0141	0.0498	28	0.098	TD-D	0.0206	0.0314	30	0.045
LR-E	0.0156	0.0229	31	0.045	TD-E	0.0174	0.0314	25	0.045
					TD-F	0.0183	0.0210	26	0.030
SR-A	0.0052	0.0021	41	0.017	TU-A	0.0256	0.0042	37	0.006
SR-B	0.0045	0.0042	35	0.033	TU-B	0.0237	0.0126	34	0.018
SR-C	0.0036	0.0084	29	0.066	TU-C	0.0219	0.0210	32	0.030
SR-D	0.0032	0.0074	25	0.058	TU-D	0.0205	0.0314	30	0.045
SR-E	0.0035	0.0063	27	0.050	TU-E	0.0177	0.0314	26	0.045
SR-F	0.0038	0.0037	30	0.029	TU-F	0.0190	0.0210	27	0.030
	Square					Diamond			
LS-A	0.0231	0.0044	49	0.0093	LD-A	0.0232	0.0053	49	0.0111
LS-B	0.0217	0.0084	46	0.018	LD-B	0.0224	0.0080	47	0.017
LS-C	0.0196	0.0168	41	0.035	LD-C	0.0199	0.0178	42	0.038
LS-D	0.0173	0.0282	36	0.059	LD-D	0.0177	0.0289	37	0.061
LS-E	0.0135	0.0356	28	0.075	LD-E	0.0151	0.0320	32	0.067
LS-F	0.0153	0.0164	32	0.035	LD-F	0.0168	0.0126	35	0.027
LS-G	0.0161	0.0072	34	0.015	LD-G	0.0181	0.0059	38	0.012
SS-A	0.0102	0.0032	44	0.014	SD-A	0.0103	0.0032	44	0.014
SS-B	0.0082	0.0095	35	0.041	SD-B	0.0081	0.0095	35	0.041
SS-C	0.0076	0.0126	33	0.054	SD-C	0.0075	0.0126	32	0.054
SS-D	0.0064	0.0211	27	0.091	SD-D	0.0064	0.0210	27	0.091
SS-E	0.0059	0.0211	25	0.091	SD-E	0.0056	0.0210	24	0.091
SS-F	0.0067	0.0126	29	0.0543	SD-F	0.0064	0.0126	27	0.054

the flowing mass quality, defined by

$$x = \frac{\dot{m}_g}{\dot{m}_g + \dot{m}_l}. \tag{3}$$

The Lockhart–Martinelli parameter for turbulent-turbulent flow is calculated using the correlation developed by [21],

$$X_{tt} = \left(\frac{1-x}{x}\right)^{0.9}\left(\frac{\rho_g}{\rho_l}\right)^{0.5}\left(\frac{\mu_l}{\mu_g}\right)^{0.1}. \tag{4}$$

Another important parameter is the percent of the tube perimeter that is wetted by the liquid film, Wet%. The h_{avg} columns list the average liquid film thickness over the wetted perimeter (not the average film thickness over the entire perimeter).

Round. Film profiles for the round tube flows may be found in Figs. 3 and 4. These represent the average of the measurements taken for each of the 16 runs required to obtain the full set of film thickness data. Note that the film thicknesses have been magnified several times for clarity. Tabulated film thickness values may be found in [20].

The liquid in both LR-A and SR-A only partially wets the tube. However, inspection of the plots indicates that the film is very uniform, not like the asymmetrical profiles associated with the stratified and stratified annular flow regimes in the sense normally discussed in the literature. In addition, highly symmetrical film flow is expected in a smooth round tube at these flow conditions based on the correlation of previously reported data developed by [22]. Thus, this appears to be a profile of what is termed high-quality dryout in the heat transfer literature. An appropriate designation might be shear-driven dryout, as it appears that a film has been sheared into a uniform film that lacks sufficient liquid to completely coat the tube wall. Further, it is interesting to note that the mean film thickness values for the film are within 0.010 mm of each other for both the 12.7 and 25.4 mm tubes. This indicates, perhaps, that some physical limit of film thickness is being approached.

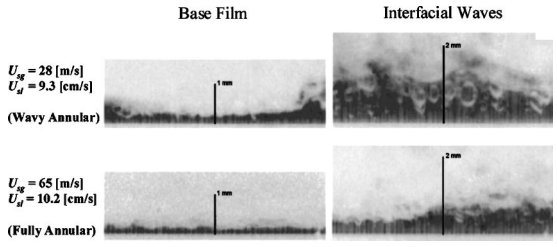

Fig. 2 A comparison of the base liquid film and interfacial waves in annular flow. The optical film thickness measurement reports only the thickness of the base film. These images were obtained using planar laser induced fluorescence.

Square. Data for flow in the large and small square test sections are presented in Figs. 5 and 6. Flow through the square tubes exhibited several unique behaviors. For example, a definite threshold was qualitatively observed in flow quantities before the top side of the tube would fully wet. For a given air flow rate below that required for significant atomization, as liquid flow increased, the film would climb the wall until the upper corners were approached. Then, although rivulets might exist along the top, the liquid flow could be increased some amount further without a visible change in film behavior. At some level, however, the top would suddenly wet and fully annular flow would persist. This transition can be visualized with plots LS-A, LS-B, and LS-C in Fig. 5. In the reverse direction, as liquid flow decreased, first the upper corners would dry and a rivulet would form down the center of the tube, thinning rapidly with reduction in flow rate. No hys-

Table 2 Measured two-phase quantities for the specified flow conditions in all the tubes

Two-phase flow measurements											
	Round						Triangle				
Flow	x	X_{tt}	Wet%	dP/dx (N/m^2)	h_{avg} (mm)	Flow	x	X_{tt}	Wet%	dP/dx (N/m^2)	h_{avg} (mm)
LR-A	0.84	0.011	63	1188	0.161	TD-A	0.86	0.009	50	976	0.150
LR-B	0.61	0.031	100	1343	0.191	TD-B	0.65	0.027	92	1057	0.150
LR-C	0.34	0.086	100	1530	0.273	TD-C	0.51	0.045	100	1171	0.174
LR-D	0.22	0.147	100	1169	0.310	TD-D	0.40	0.068	100	1220	0.205
LR-E	0.40	0.067	100	944	0.253	TD-E	0.36	0.079	100	878	0.202
						TD-F	0.47	0.053	83	789	0.199
SR-A	0.71	0.021	75	1991	0.152	TU-A	0.86	0.009	33	975	0.191
SR-B	0.51	0.045	100	2010	0.133	TU-B	0.65	0.026	67	1137	0.182
SR-C	0.30	0.101	100	2048	0.182	TU-C	0.51	0.045	83	1251	0.185
SR-D	0.30	0.101	100	1902	0.173	TU-D	0.39	0.068	100	1284	0.193
SR-E	0.36	0.081	100	1913	0.156	TU-E	0.36	0.078	75	975	0.245
SR-F	0.50	0.047	100	1876	0.127	TU-F	0.48	0.051	67	845	0.228
	Square						Diamond				
LS-A	0.84	0.011	50	1337	0.141	LD-A	0.81	0.012	55	1329	0.151
LS-B	0.72	0.020	75	1398	0.158	LD-B	0.74	0.019	75	1385	0.155
LS-C	0.54	0.041	100	1472	0.173	LD-C	0.53	0.043	95	1480	0.183
LS-D	0.38	0.073	100	1496	0.197	LD-D	0.38	0.073	100	1576	0.213
LS-E	0.27	0.113	100	1177	0.219	LD-E	0.32	0.093	95	1150	0.245
LS-F	0.48	0.050	85	1014	0.181	LD-F	0.57	0.036	65	978	0.197
LS-G	0.69	0.023	55	887	0.175	LD-G	0.75	0.017	35	827	0.186
SS-A	0.76	0.017	50	1719	0.127	SD-A	0.76	0.016	44	1723	0.098
SS-B	0.46	0.054	94	1922	0.137	SD-B	0.46	0.055	94	1906	0.141
SS-C	0.38	0.075	100	1968	0.146	SD-C	0.37	0.076	94	1944	0.156
SS-D	0.23	0.140	100	2021	0.168	SD-D	0.23	0.139	94	1989	0.198
SS-E	0.22	0.150	100	1748	0.174	SD-E	0.21	0.156	94	1643	0.212
SS-F	0.35	0.085	100	1601	0.149	SD-F	0.33	0.088	94	1472	0.170

teresis was observed in the steady-state liquid film profiles, however; i.e., the steady-state liquid film profile at a given flow condition was identical regardless of whether that flow condition was achieved by increasing or decreasing the liquid flow rate.

Like the round tube flows, the highest quality flows have relatively uniform, partially wetting films. As liquid flow increases, a very noticeable thinning of the film in the corners of the tube with respect to the wall center locations becomes evident. The difference in thickness between the bottom center point of the LS data and the bottom corner points is generally between 0.05 and 0.1 mm, much greater than the average standard error of 0.005 mm. In addition, the measurements were very repeatable.

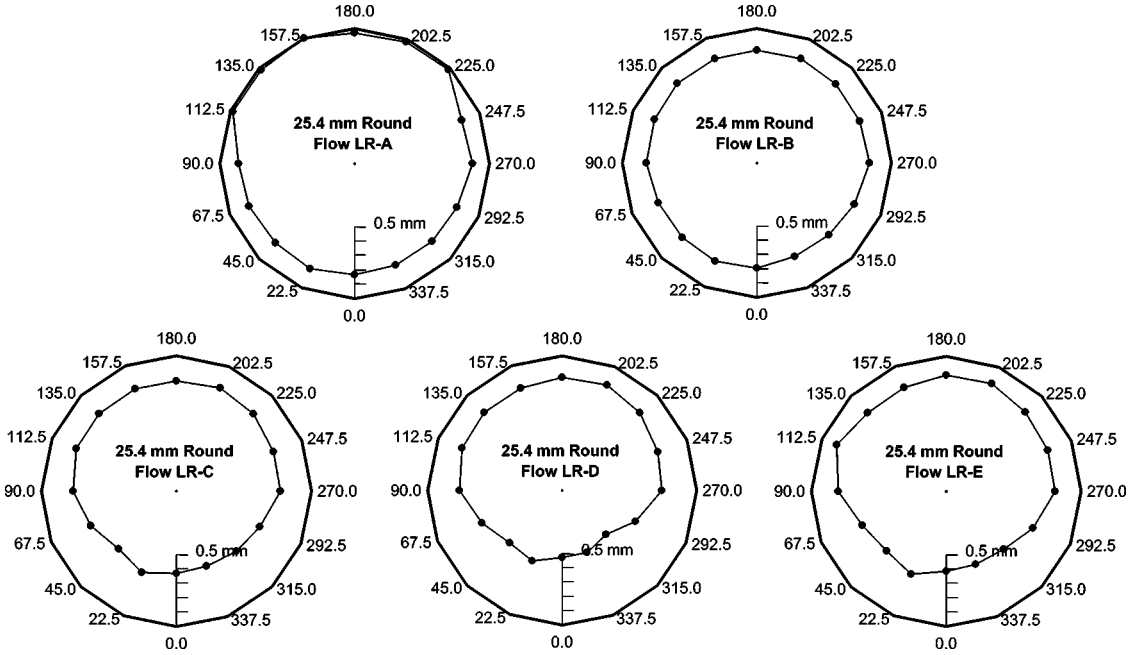

Fig. 3 Film thickness profiles in a 25.4 mm round tube

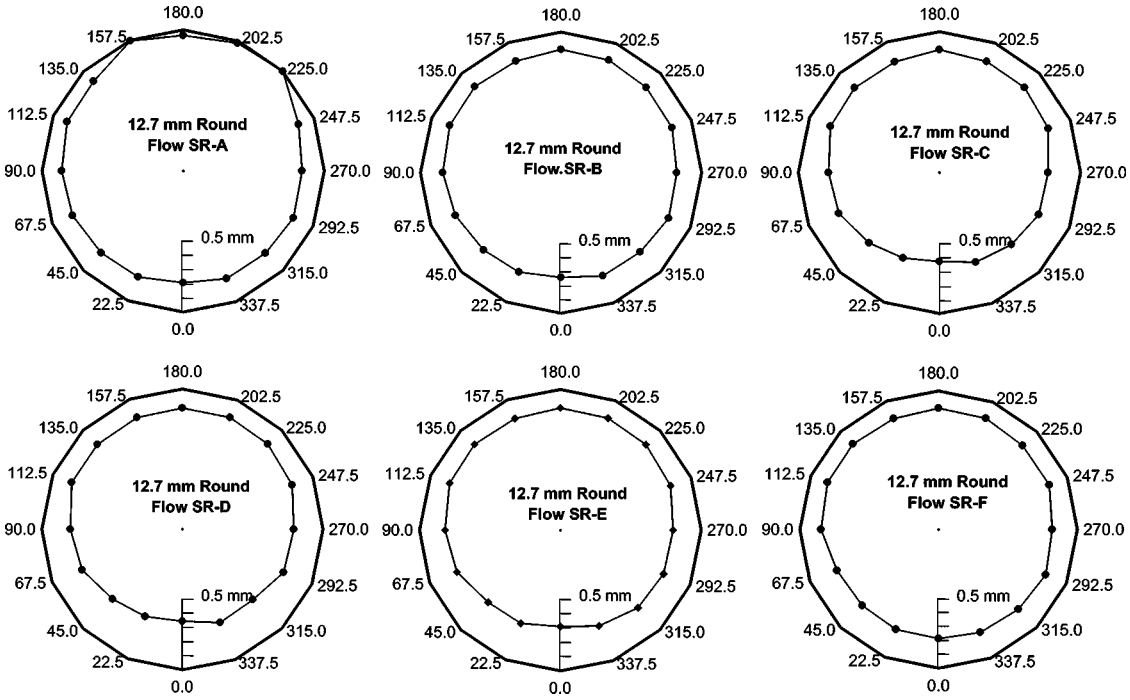

Fig. 4 Film thickness profiles in a 12.7 mm round tube

Diamond. The rotated square, or ''diamond,'' results are presented in Figs. 7 and 8. The high quality uniformity is again generally apparent, as well as the thinning in the corners—even the bottom corner to which liquid tended to drain. The change in orientation did appear to have a noticeable impact on the uniformity of the film as liquid drained into the bottom corner. Interestingly, the overall dryout characteristics, as quantified by the ''Wet%'' column of the data tables, appear to be little affected by the rotation. Also unaffected, within experimental error, was the pressure gradient.

Comparing the film profiles, especially for LD-A, B and LS-A, B, it would appear that there exists an equilibrium base film flow which distributes itself to cover the same perimeter regardless of orientation.

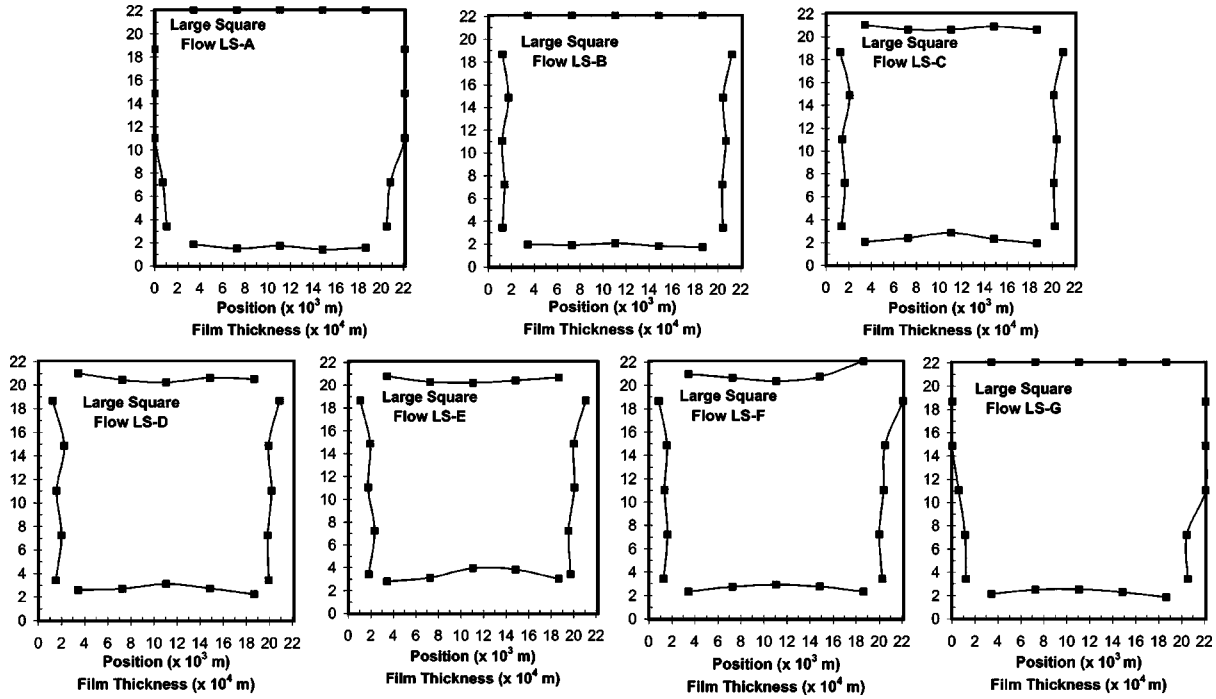

Fig. 5 Film thickness profiles in a 22.1 mm square tube

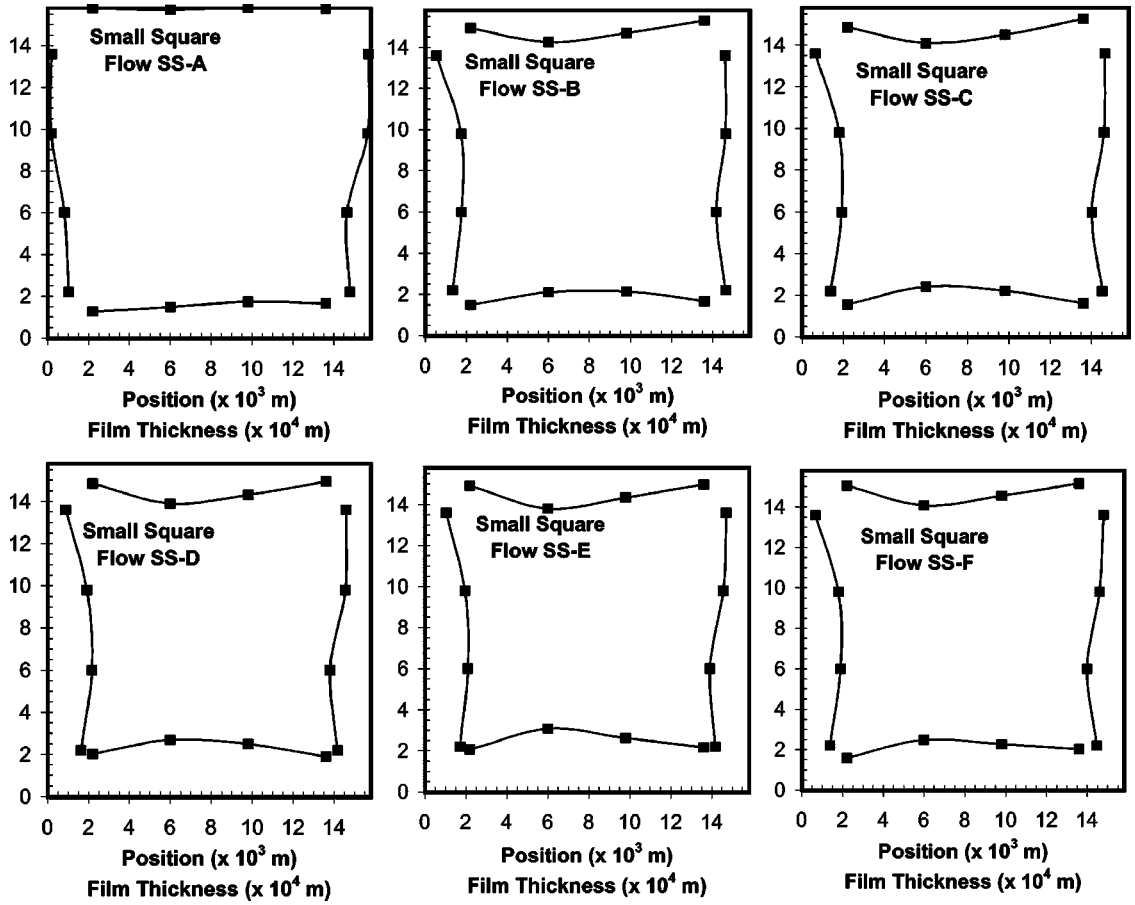

Fig. 6 Film thickness profiles in a 15.8 mm square tube

Triangle. Figures 9 and 10 give the results of the measurements for triangle tube flow. Although the flows were carefully matched for both the apex-up and apex-down trials, several significant differences in flow behavior are apparent. For example, it was much easier to wet the walls of the tube in the apex-down configuration. Though flow TU-D indicates 100% wet walls, in reality, the walls near the apex of the upward pointing triangle never appeared to maintain a steady film. Thus, dryout is significantly affected by the tube orientation. In addition, because the liquid was distributed around less of the tube perimeter, the mean

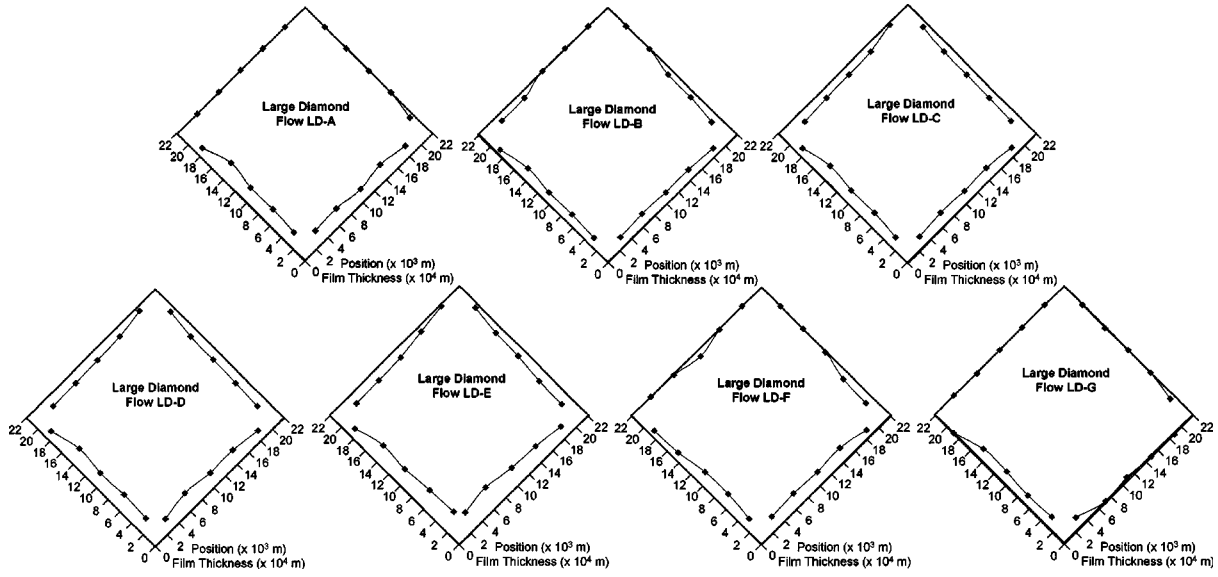

Fig. 7 First set of film thickness profiles in the 22.1 mm square tube rotated 45 deg. Note that the labeled flow conditions, A–F, correspond closely with the A–F flow conditions for the unrotated 22.1 mm square results presented above.

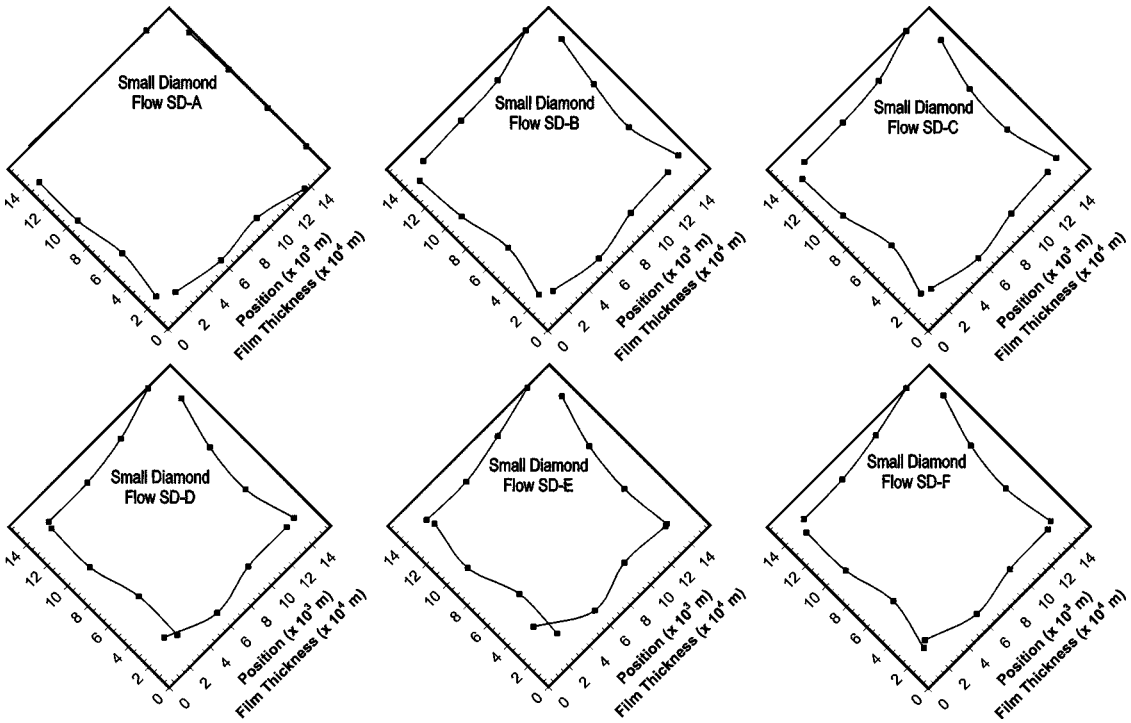

Fig. 8 Film thickness profiles in the 15.8 mm square tube rotated 45 deg. Note that the labeled flow conditions, A–F, correspond closely with the A–F flow conditions for the unrotated 15.8 mm square results presented above.

wetted film thickness measurements are generally greater in the apex-up configuration.

Apparently because liquid was more likely to drain to the downward-pointing apex, the apex-up data show consistently higher film uniformities. Flow TU-A with a film only along the bottom of the tube achieved the highest uniformity of any profile measured in this work, being very nearly constant at 0.190 mm. The fairly uniform film that forms on the top wall of the apex-down flows is interesting as well. The mean thickness of this film ranges from about 0.100 to 0.160 mm.

In spite of these differences, pressure drop is not significantly affected by orientation, as was noted with the square tube flows. The apex-up data are consistently higher, but these differences fall within the error in the pressure measurement. This is somewhat

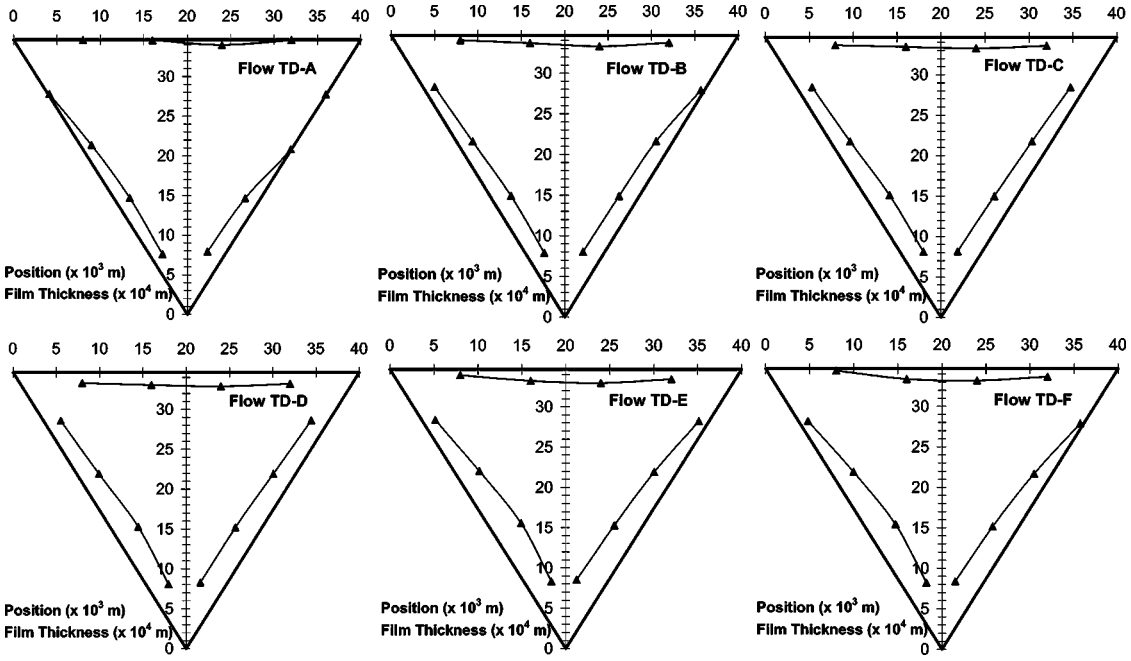

Fig. 9 Film thickness profiles in an equilateral triangular tube with 40 mm sides and the apex up

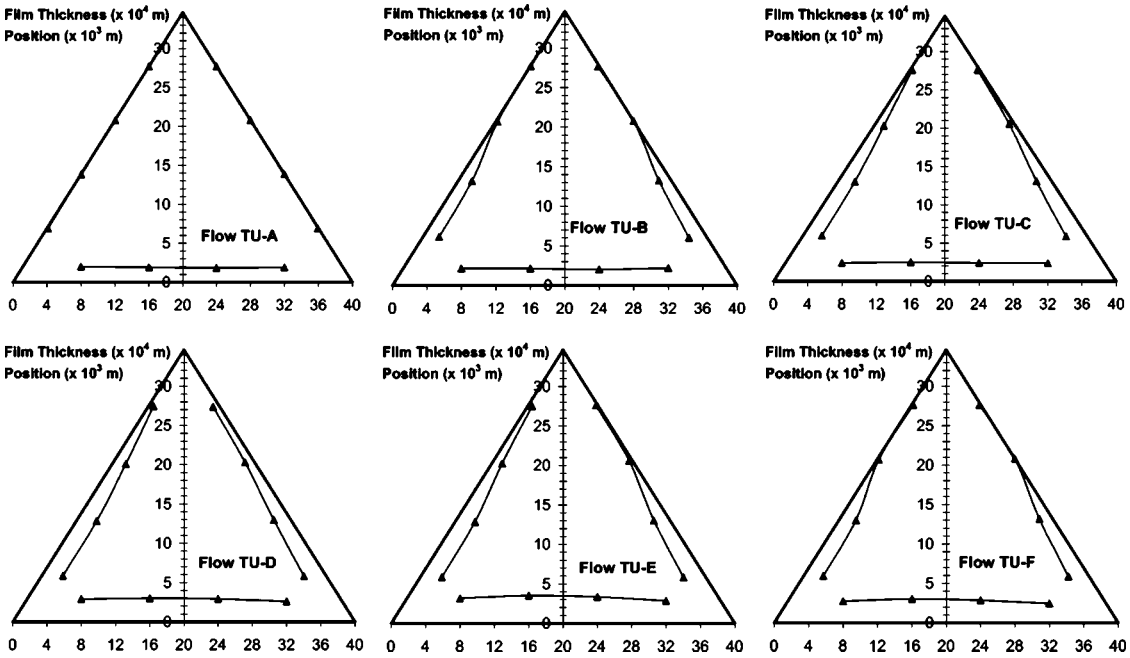

Fig. 10 Film thickness profiles in an equilateral triangular tube with 40 mm sides and the apex down

surprising as it could be expected that pressure losses would be lower in a tube with less of its wall wetted at the same gas flow condition; the smooth wall should present significantly less resistance than the liquid film. Perhaps this increase in smooth wall area is compensated for by the presence of the thicker films which many have associated with greater interfacial shear.

Pressure Drop. Pressure drop data are reported in Table 2 for all the flow conditions and geometries. These data were nondimensionalized in the form of a two-phase friction factor defined as

$$f = \frac{\Delta p}{(L/D_h)(\rho_g U_{sg}^2)/2}, \tag{5}$$

where U_{sg} is the superficial gas velocity and D_H is the hydraulic diameter, $4A/P$. As is the case with single-phase flow, pressure drop through triangular channels could not be correlated in exactly the same manner as the round and square data. The superficial velocity used in calculating the triangle tube friction factor is defined as

$$U_{sg} = \frac{\dot{m}_g}{\rho_g A_{Dh}}, \tag{6}$$

where

$$A_{Dh} = \frac{\pi D_h^2}{4} \tag{7}$$

is the area of the circle defined by the hydraulic diameter. This has the effect of significantly increasing the gas velocity in the calculations for the noncircular tubes, bringing these friction factors in line with the round tube data.

As shown in Fig. 11, the pressure drop data for all geometries are well-correlated by the Lockhart–Martinelli parameter, X_{tt}, using the relation

$$f = 0.215 X_{tt} + 0.01. \tag{8}$$

Discussion

The purpose of this investigation was to obtain a broad set of film thickness data for annular flow through round, square and triangle tubes and observe influences on flow behavior due to tube size, shape and orientation. Tube size had very little impact overall. Pressure gradients increased with smaller cross section, as expected.

Rotating the square tubes had surprisingly little impact on the flow behavior. Dryout behavior was essentially unaffected as was the mean film thickness. The film did become less uniform, however. Unlike the square, the triangular channel was significantly affected by orientation.

General Characteristics of the Liquid Film. The film thicknesses measured can be nondimensionalized following a procedure commonly used with the wall-normal coordinate in wall-bounded turbulent shear flows:

$$h^+ = \frac{h u_i^*}{\nu_l}. \tag{9}$$

In this case, the friction velocity,

$$u_i^* = \left(\frac{\tau_i}{\rho_l}\right)^{0.5}, \tag{10}$$

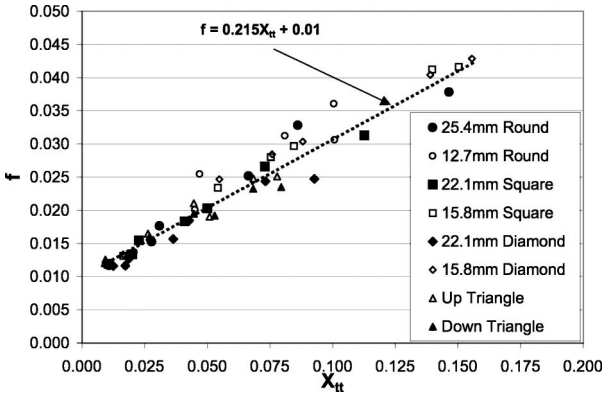

Fig. 11 Friction factor versus the Lockhart–Martinelli parameter, X_{tt}, compiled from the two-phase pressure gradients measured for all of the geometries and flow conditions.

is based on the mean interfacial shear between the liquid and the gas. Since the interfacial shear and the shear between the liquid and the wall must, on average, balance each other in a steady flow, τ_i is determined experimentally from the measured pressure drop by a force balance for flow through a round tube,

$$\tau_i = \frac{\Delta p}{L}\frac{D_n}{4}, \tag{11}$$

where L is the length between pressure taps and D_n is the hydraulic diameter of the tube.

When this nondimensionalization was carried out for all of the data collected in this study, virtually all of the nondimensional film thickness values fell between 5 and 35. It seems that perhaps the film flow follows the same general behavior as wall-bounded single-phase flow, i.e.,

$$\text{viscous region:} \quad h^+ < 5,$$

$$\text{transition region:} \quad 5 < h^+ < 30,$$

$$\text{log region:} \quad h^+ > 30.$$

Below $h^+ = 5$, the film broke down, leaving a dry wall or just rivulets and droplets. It appears that a continuous film cannot be sustained in annular flow when it reaches a thickness where viscous forces dominate. This agrees with the extensive data set compiled by Hewitt and Lacey [23] who examined the minimum liquid flow required to rewet an artificially-induced dry spot in annular vertical upflow. The limiting liquid thickness at this minimum flow lay consistently between $h^+ = 4.75$ and $h^+ = 6.5$.

Recalling that the optical film thickness measurement system used in this study reports the thickness of the base film between large waves [18], the fact that the majority of the data tend to fall within $5 < h^+ < 35$ could be interpreted to mean that the liquid film in annular flow is comprised of a fluctuating base film with properties similar to the buffer region in wall-bounded turbulent shear flow. Additional liquid beyond that needed to fill out this buffer layer then tends to go into highly turbulent waves which move over the base film. This interpretation agrees with previous findings of Schadel [24] and Andreussi et al. [25], who noted a critical film flow rate in vertical annular flow at which disturbance waves would begin to form.

This turbulent wall-bounded profile is a popular assumption made in modeling the liquid film, but Dobran [26,27] has shown that a model modifying this profile by reducing the turbulent mixing somewhat as the gas-liquid interface is approached gives much better agreement to physical behavior. This was noted independently by Leuthner et al. [28] as well. In agreement with these modelers' observations, the present results suggest that the turbulent velocity profile cannot be extended into the logarithmic region without taking the intermittency of the waves into account.

Thinning of the Film in Corners. As noted above, one of the most interesting features of the flow in the square and triangular channels is the thinning of the liquid film in the corners. Other researchers have noticed similar effects when studying turbulent flow through rectangular and square channels. An experimental study of the liquid film in horizontal two-phase annular flow through a 4 cm square and 1 cm by 8 cm rectangular duct was carried out by [9]. To understand the liquid distribution, Fukano et al. measured mean liquid film thickness using a conductance method at the center of the bottom wall and then divided the bottom wall at the outlet into eight channels using very thin copper dividers, recording the flow rate collected in each of these sections. In interpreting this data, the fact that liquid is pushed up the side walls and across the top must be taken into account. For instance, it appears from the presentation of flow results in the 1 cm by 8 cm channel that a very thick film appears in the corners when, in reality, this is an indication of flow along the side walls, not flow in the corners themselves. Unfortunately, these authors chose not to present their data for the 4 cm by 4 cm channel, so direct comparison of their work with the current is not possible. However, the 1 cm by 8 cm results do show the same trends that are found in Figs. 5 and 6 with a higher mass flow of liquid in the center, diminishing toward the corners, then peaking in the corners due to the flow on the side walls.

The liquid film profiles in the square tubes are remarkably similar to the profiles of isotachs (lines of equal velocity) found in single phase turbulent flow through these geometries in [29–32] and others. The results of [9] in two-phase flow, discussed above, as well as mass transfer studies in [33] further verify this unique behavior. No known attempts have been made to accurately model the liquid film of annular flow in noncircular tubes, either horizontal or vertical. However, the experimental results just presented appear to suggest that forces act upon the film in such a way that the film tends to follow curves of constant velocity in the gas. Secondary flows are responsible for the distorted isotachs, so it is possible that secondary flows play an important role in two-phase flow as well. As well, it is likely that the additional roughness and asymmetry of the liquid film act to enhance secondary flows in the gas.

Experimental work of [34,35] and [36] has shown that secondary flows exist in turbulent two-phase flow in straight, horizontal round pipes even though this has not been documented in round pipe single-phase flow. Hence, it has long been speculated that the secondary flows may act directly at the interface with the liquid film to drag it up the wall against the action of gravity [36–40]. However, order of magnitude analysis by [41] and numerical simulations by [42] show that the magnitudes of the velocities involved (about 1 to 4 percent of the axial flow) are not large enough to produce a dramatic effect.

Another possible mechanism for the thinning in the corners is the action of redistributed axial shear on the film. Secondary flow in the gas carries axial momentum from the center of the tube into the corners. This increased momentum will contribute to increased interfacial shear in the corner regions versus central regions at the same distance from the wall, which could act to thin the liquid film in the corners. As the film thins in the corner with respect to the center, the interfacial shear will tend to approach a constant value across the side. This agrees with the single-phase work of Leutheusser [43] who found that the secondary flows acted to equalize the axial wall shear in turbulent flow.

Pressure Drop. It is somewhat surprising that such a simple relation as that given by Eq. (8) could fit data across such a range of geometries and flows. However, if annular flow is considered to be essentially a turbulent flow of gas over a fully roughened surface created by the liquid layer, we should expect a friction factor that is essentially constant with increasing gas Reynolds number and that can account for the different geometries through the hydraulic diameter concept. However, as noted by Wallis [44], the roughness presented by the liquid film is variable according to flow rate. The Lockhart–Martinelli parameter, which is theoretically a ratio of the liquid only to gas only pressure drops in the pipe, appears to correlate this variable roughness effect by incorporating a ratio of liquid to gas flows. A similar ratio proposed by Henstock and Hanratty [45] was found to correlate data for annular flow through different diameter round pipes.

It is expected that this correlation will work with any arbitrary orientation of the horizontal square and triangular tubes. However, caution should be used in applying this to flows with larger X_{tt} values or in rectangles with aspect ratios greater than 1. In addition, the validity of this correlation cannot be assured outside the quality range between 0.2 and 0.85. The dependence of the Lockhart–Martinelli parameter on mass quality limits its applicability at very low and very high quality conditions as well.

Many other two-phase pressure drop correlations exist in the literature; the reader is referred to [46] and [47] for current, detailed reviews.

Conclusion

Detailed liquid film thickness measurements have been presented for horizontal air/water annular flow through round, square and triangular tubes. A summary of the significant observations is as follows:

1. For the flow rates considered, relatively uniform, symmetrical film profiles were observed.
2. Most of the nondimensional film thickness data fell between $5<h^+<35$, suggesting that the film may comprise a layer similar to the transition layer in wall-bounded turbulent single-phase flow. Waves tend to flow outside of this region.
3. The liquid film appears to dry out for $h^+<5$.
4. Orientation of the square tubes had little effect on flow behavior, but greater effect on the triangular tube.
5. The liquid film in the square and triangular tubes was thinned in the corners, possibly indicating the effect of secondary gas flows on the liquid film distribution.
6. The pressure drop data could be correlated by X_{tt} when plotted as a two-phase friction factor.

Acknowledgments

The authors gratefully acknowledge the financial support of the Air Conditioning and Refrigeration Center at the University of Illinois at Urbana–Champaign (an NSF-sponsored university-industry collaborative research center). Assistance with film thickness data was provided by Cyndra Lattimore. Daniel Rodríguez provided the PLIF images.

Nomenclature

Symbols

A = Cross sectional area of tube (m^2)
D = Diameter of the tube (m)
D_h = Hydraulic diameter of tube (m)
f = Friction factor
h = Film thickness (m)
h^+ = Nondimensional film thickness
L = Pipe length between pressure taps (m)
$\dot{m}_g$ = Mass flow rate of gas (kg/s)
$\dot{m}_l$ = Mass flow rate of liquid (kg/s)
p = Pressure (N/m^2)
P = Tube perimeter (m)
u^* = Friction velocity (m/s)
U = Superficial velocity (m/s)
x = Mass quality
X_{tt} = Lockhart–Martinelli parameter

Greek symbols

μ = Dynamic viscosity (Ns/m^2)
ν = Kinematic viscosity (m^2/s)
ρ = Density (kg/m^3)
τ = Shear stress (N/m^2)
Δ = Change in a value

Subscripts

Dh = Based on hydraulic diameter
g = Gas
i = Interfacial quantity
l = Liquid
sg = Superficial gas quantity
sl = Superficial liquid quantity

References

[1] Leung, C. W., and Probert, S. D., 1997, ''Forced-convective turbulent-flows through horizontal ducts with isosceles-triangular internal cross-sections,'' Appl. Energy, **57**, No. 1, pp. 13–24.
[2] Mayinger, F., and Klas, J., 1992, ''Compact heat exchangers.'' In *Heat Transfer; 3rd UK National Conference*, Vol. 1. Institute of Chemical Engineers, Warwickshire, UK, pp. 35–49.
[3] Zietlow, D. C., and Pedersen, C. O., 1995, ''Heat transfer and flow characteristics of condensing refrigerants in small-channel cross-flow heat exchangers,'' Tech. Rep. TR-73, Air Conditioning and Refrigeration Center, University of Illinois at Urbana-Champaign, Urbana, IL.
[4] Webb, R. L., 1990, *Principles of Enhanced Heat Transfer*, Wiley, New York.
[5] Barnea, D., and Taitel, Y., 1986, *Encyclopedia of Fluid Mechanics*, Vol. 3, Gulf Publishing Company, Houston, TX, pp. 403–474.
[6] Dallman, J. C., 1978, ''Investigation of Separated Flow Model in Annular Gas-Liquid Two-Phase Flows,'' Ph.D. thesis, University of Illinois at Urbana–Champaign, Urbana, IL.
[7] Hewitt, G. F., and Hall-Taylor, N. S., 1970, *Annular Two-Phase Flow*, Pergamon, Oxford, England.
[8] Hetsroni, G., Ed., 1982, *Handbook of Multiphase Systems*, Hemisphere, Washington, DC.
[9] Fukano, T., Akenaga, H., Ikeda, M., Itoh, A., Kuriwaki, T., and Takamatsu, Y., 1984, ''Liquid film flowing concurrently with air in horizontal duct (4th report, effect of the geometry of duct cross-section on liquid film flow),'' Bull. JSME, **27**, No. 230, pp. 1644–1651.
[10] Fukano, T., Sakamoto, T., Tominaga, A., and Katoh, E., 1987, ''Experimental study on the flow mechanism of a thin liquid film flowing concurrently with a high speed gas flow in a horizontal rectangular duct,'' *Proceedings of the 1987 ASME-JSME Thermal Engineering Joint Conference*, Vol. 5, pp. 351–357.
[11] Fukano, T., Nakagawa, H., Mori, Y., and Watanabe, M., 1997, ''Liquid film formation on the inner surface of the horizontal channel,'' Nucl. Eng. Des., **175**, pp. 3–13.
[12] Troniewski, L., and Ulbrich, R., 1984, ''Flow regime maps and pressure drop in two-phase gas-liquid flow in a rectangular channel,'' in *Multi-Phase Flow and Heat Transfer III. Part A: Fundamentals*, T. N. Veziroğlu and A. E. Bergles, Eds., Elsevier Science, Amsterdam, pp. 155–166.
[13] Rush, T. A., Newell, T. A., and Jacobi, A. M., 1999, ''An experimental study of flow and heat transfer in sinusoidal wavy passages,'' Int. J. Heat Mass Transfer, **42**, pp. 1541–1553.
[14] Colebrook, C. F., 1938–39, ''Turbulent flow in pipes, with particular reference to the transistion region between smooth and rough pipe laws,'' J. Instit. Civil Eng., **11**, pp. 133–156.
[15] Taylor, B. N., and Kuyatt, C. E., 1994, ''Guidelines for evaluating and expressing uncertainty of NIST measurement results,'' Tech. Rep. 1297, National Institute of Standards and Technology, Bethesda, MD.
[16] Hurlburt, E. T., and Newell, T. A., 1996, ''Optical measurement of liquid film thickness and wave velocity in liquid film flows,'' Exp. Fluids, **21**, No. 5, pp. 357–362.
[17] Shedd, T. A., and Newell, T. A., 1998, ''Automated optical liquid film thickness measurement method,'' Rev. Sci. Instrum., **69**, No. 12, pp. 4205–4213.
[18] Rodriguez, D. J., 2004, ''Characterization of bubble entrainment, interfacial roughness, and the sliding bubble mechanism in horizontal annular flow,'' Ph.D. thesis, University of Wisconsin-Madison, Madison, Wisconsin, USA.
[19] Rodíguez, D. J., and Shedd, T. A., 2004, ''Cross-sectional imaging of the liquid film in horizontal two-phase annular flow,'' in 2004 ASME Heat Transfer/Fluids Engineering Summer Conference, Paper 56445.
[20] Shedd, T. A., 2001, ''Characteristics of the Liquid Film in Horizontal Two-Phase Annular Flow,'' Ph.D. thesis, University of Illinois at Urbana–Champaign, Urbana, IL.
[21] Martinelli, R. C., and Nelson, D. B., 1948, ''Prediction of pressure drop during forced-circulation boiling of water,'' Trans. ASME, **70**, pp. 695–702.
[22] Hurlburt, E. T., and Newell, T. A., 2000, ''Prediction of the circumferential film thickness distribution in horizontal annular gas-liquid flow,'' ASME J. Fluids Eng., **122**, pp. 1–7.
[23] Hewitt, G. F., and Lacey, P. M. C., 1965, ''The breakdown of the liquid film in annular two-phase flow,'' Int. J. Heat Mass Transfer, **8**, pp. 781–791.
[24] Schadel, S. A., 1988, ''Rate of atomization and drop size in annular two-phase flow,'' Ph.D. thesis, University of Illinois at Urbana–Champaign, Urbana, Illinois.
[25] Andreussi, P., Asali, J. C., and Hanratty, T. J., 1985, ''Initiation of roll waves in gas-liquid flows,'' AIChE J., **31**, pp. 119–126.
[26] Dobran, F., 1983, ''Hydrodynamic and heat transfer analysis of two-phase annular flow with a new liquid film model of turbulence,'' Int. J. Heat Mass Transfer, **26**, No. 8, pp. 1159–1171.
[27] Dobran, F., 1985, ''Heat transfer in an annular two-phase flow,'' ASME J. Heat Transfer, **107**, pp. 472–476.
[28] Leuthner, S., Maun, A. H., and Auracher, H., 1999, ''Influence of waves on heat transfer to falling films of a binary mixture,'' in *Two-Phase Flow Modelling and Experimentation 1999*, G. P. Celata, P. D. Marco, and R. K. Shah, Eds., Vol. 2, Edizioni ETS, Pisa, pp. 1241–1247.
[29] Nikuradse, J., 1930, ''Untersuchungen über turbulente strömungen in nicht kreisförmigen rohren,'' Ingenieur-Archiv, **1**, pp. 306–332.
[30] Gessner, F. B., and Jones, J. B., 1965, ''On some aspects of fully-developed turbulent flow in rectangular channels,'' J. Fluid Mech., **23**, No. 4, pp. 689–713.
[31] Gessner, F. B., 1973, ''The origin of secondary flow in turbulent flow along a corner,'' J. Fluid Mech., **58**, No. 1, pp. 1–25.
[32] Melling, A., and Whitelaw, J. H., 1976, ''Turbulent flow in a rectangular duct,'' J. Fluid Mech., **78**, No. 2, pp. 289–315.
[33] Goldstein, R. J., Jabbari, M. Y., and Brekke, J. P., 1992, ''The near-corner mass

transfer associated with turbulent flow in a square duct,'' Wärme-und Stoffübertragung, **27**, pp. 265–272.
[34] Darling, R. S., and McManus, H. N., 1968, ''Flow patterns in circular ducts with circumferential variation of roughness: a two-phase flow analog,'' Proceedings of the 11th Mid-Western Mechanics Conference (Developments in Mechanics), Vol. 5, pp. 153–170.
[35] Dykhno, L. A., Williams, L. R., and Hanratty, T. J., 1994, ''Maps of mean gas velocity for stratified flows with and without atomization,'' Int. J. Multiphase Flow, **20**, No. 4, pp. 691–702.
[36] Flores, A. G., Crowe, K. E., and Griffith, P., 1995, ''Gas-phase secondary flow in horizontal, stratified and annular two-phase flow,'' Int. J. Multiphase Flow, **21**, No. 2, pp. 207–221.
[37] Pletcher, R. H., and McManus, Jr., H. N., 1965, ''The fluid dynamics of three dimensional liquid films with free surface shear: A finite difference approach,'' Proceedings of the 9th Mid-Western Conference on Mechanics (Developments in Mechanics), Vol. 3, pp. 305–318.
[38] Butterworth, D., 1972, ''Air-water annular flow in a horizontal tube,'' Prog. Heat Mass Transfer, **6**, pp. 235–251.
[39] Laurinat, J. E., Hanratty, T. J., and Jepson, W. P., 1985, ''Film thickness distribution for gas-liquid annular flow in a horizontal pipe,'' PCH, PhysicoChem. Hydrodyn., **6**, No. 1, 2, pp. 179–195.
[40] Lin, T. F., Jones, O. C., Lahey, R. T., Block, R. C., and Murase, M., 1985, ''Film thickness measurements and modelling in horizontal annular flows,'' PCH, PhysicoChem. Hydrodyn., **6**, No. 1/2, pp. 197–206.
[41] James, P. W., Wilkes, N. S., Conkie, W., and Burns, A., 1987, ''Developments in the modelling of horizontal annular two-phase flow,'' Int. J. Multiphase Flow, **13**, No. 2, pp. 173–198.
[42] Jayanti, S., Wilkes, N. S., Clarke, D. S., and Hewitt, G. F., 1990, ''The prediction of turbulent flows over roughened surfaces and its application to interpretation of mechanisms of horizontal annular flow,'' Proc. R. Soc. London, Ser. A, **431**, pp. 71–88.
[43] Leutheusser, H. J., 1963, ''Turbulent flow in rectangular ducts,'' J. Hydraul. Div., Am. Soc. Civ. Eng., **HY3**, pp. 1–19.
[44] Wallis, G. B., 1969, *One-dimensional Two-phase Flow*, McGraw-Hill, New York.
[45] Henstock, W. H., and Hanratty, T. J., 1976, ''The interfacial drag and the height of the wall layer in annular flows,'' AIChE J., **22**, No. 6, pp. 990–1000.
[46] Collier, J. G., and Thome, J. R., 1994, *Convective Boiling and Condensation*, 3rd ed., Oxford U.P. Oxford.
[47] Wilson, M. J., 2001, ''Two-phase flow through flattened tubes,'' Ph.D. thesis, University of Illinois at Urbana–Champaign, Urbana, IL.

Oscillatory Free Surface Displacement of Finite Amplitude in a Small Orifice

Brian J. Daniels

James A. Liburdy

Department of Mechanical Engineering,
Oregon State University,
Corvallis, OR 97331

The oscillatory free-surface displacement in an orifice periodically driven at the inlet is studied. The predictions based on a potential flow analysis are investigated in light of viscous and large curvature effects. Viscous effects near the wall are estimated, as are surface viscous energy loss rates. The curvature effect on the modal frequency is shown to become large at the higher modal surface shapes. Experimental results are obtained using water for two orifice diameters, 794 and 1180 μm. Results of surface shapes and modal frequencies are compared to the predictions. Although modal shapes seem to be well predicted by the theory, the experimental results show a significant shift of the associated modal frequencies. A higher-order approximation of the surface curvature is presented, which shows that the modal frequency should, in fact, be reduced from potential flow predictions as is consistent with the large curvature effect. To account for the effect of finite surface displacements an empirical correlation for the modal frequencies is presented. [DOI: 10.1115/1.1789525]

Introduction

Precise droplet formation is an important process in a number of applications such as atomization of fuels for combustion, mixing of liquids, ink-jet printing, and manufacturing of fine powders or granules. Control of droplet size is becoming an increasing concern in microfluidic applications. Adjusting droplet size without changes to hardware can potentially save cost, time, and provide a more robust device.

This paper examines surface deformation as a precursor to droplet formation, which may prove useful in controlling droplet sizes from a fixed diameter orifice. Such a method has been proposed by Burr, Tence, and Berger [1,2] and Berger et al. [3]. This method consists of exciting resonance modes on the free surface of an orifice with a periodic forcing function at the inlet of the orifice. The resulting oscillating surface, as predicted using inviscid flow theory, results in a radial dependence of the interfacial shape at discrete resonance modes expressed in terms of a Bessel function.

The situation of surface modes in an orifice driven by a periodic inlet condition is similar in some respects to standing waves in vertically vibrated containers. This case has been examined extensively in the literature beginning with Faraday, Matthiessen, and Rayleigh who performed linearized analyses prior to 1900 [4]. Benjamin and Ursell [4] subsequently looked at the subject and examined the special case of a liquid in a vibrating right circular cylinder. Their linearized analysis predicted the shapes of the free-surface modes to be based on Bessel functions. Their results were limited in that they were not able to predict the height of the free-surface oscillations.

There have been several nonlinear analyses of the free-surface shapes generated in rectangular vibrating containers. From these analyses, predictions of the surface height were made. Examples include Penny and Price [5], Taylor [6], and Tadjbakhsh and Keller [7]. Experimental validations of these analyses have been performed by Fultz [8] and Edge and Waters [9]. The first nonlinear analysis of the surface shapes in a vertically vibrated circular cylinder was performed by Mack [10]. This analysis predicted the height of the surface shapes as a function of input amplitude. Mack's analysis results in Bessel functions as the basis for the free-surface shapes, which was validated by their own experiments as well as those by Fultz and Murty [11].

Dodge, Kana, and Abramson [12] also used a nonlinear analysis for the free surface shapes in a vertically vibrated circular cylinder. Their results show that the resulting surface shapes are Bessel function dependent. Their experimental work agrees well with the predictions. All the analyses to date, both linear and nonlinear, employ a potential flow solution with an impermeable wall boundary condition, thereby allowing the axial velocity to be nonzero. This inviscid condition has been shown to be a reasonable assumption for the large-scale flows where edge effects play a minor role on the surface modal shape. However, there is a region near the solid boundary where viscous effects become important. The influence of this region will depend on the extent of the flow domain and oscillation frequency.

A potentially important and interesting aspect of the orifice surface oscillation is the dynamic condition at the surface–edge interface. The oscillatory nature of the surface requires either a time-dependent contact angle, or a constant contact angle with an otherwise complicated time-dependent surface shape. Dynamic contact angles have been usually studied with regard to a moving interface for flow along a surface or inside a duct; oscillatory conditions at an edge are poorly understood. Vanden-Broeck and Tuck [13] show how the contact angle varies for steady flow from an orifice with an angle dependent on the flow rate. Marsh, Garoff, and Dussan [14] indicate the strong dependence of contact angle on the surface shape near the contact line. Dussan V. and Davis [15] found that a steadily moving contact line has a different contact angle depending on whether the flow is advancing or receding. For the surface oscillation under study it is assumed that the complex dynamic nature of the edge contact angle does not significantly influence the surface shape in the majority of the center of the orifice, which is the region of concern for potential droplet formation. This is supported by the experimental results given in this paper.

This study examines the modal surface shapes at a free surface formed in a small diameter orifice. Due to the small size, the analysis provides a means to account for the viscous region near the orifice edge. The fluid is driven by a periodic forcing function at the inlet while the orifice is stationary. The nature of the predicted modal shapes are compared to predicted characteristics from potential flow solutions with and without modifications for

Contributed by the Fluids Engineering Division for publication in the JOURNAL OF FLUIDS ENGINEERING. Manuscript received by the Fluids Engineering Division February 8, 2003; revised manuscript received March 23, 2004. Associate Editor: J. S. Marshall.

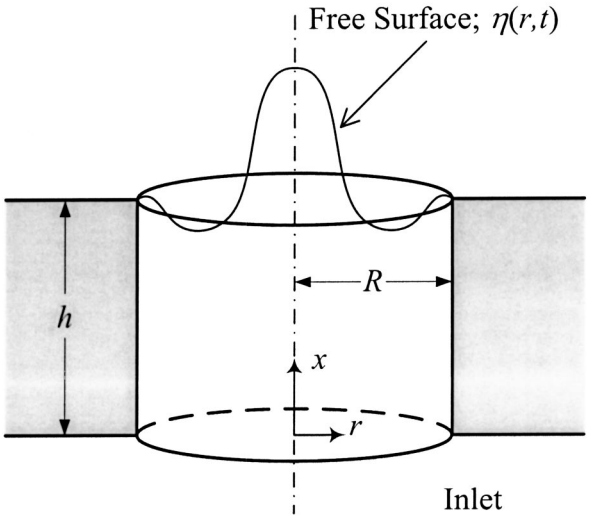

Fig. 1 Flow analysis geometry

the viscous effects at the wall of the orifice. The surface displacement amplitudes in the experiments are lower than those required for droplet formation, but are shown to be too large for infinitesimal displacement approximations. Large displacements lead to two additional effects on the surface modal shapes: (1) significant surface curvature, which increases the local surface tension forces, and (2) increased viscous dissipation at the surface. An exact finite-amplitude solution to this problem is not available. However, an approximate analysis is used to indicate the occurrence of these effects and the resultant consequence to the modal frequencies. Experimental data for two orifice diameters, using water, are presented to substantiate these trends and to determine the functional relationship between the modal parameter and the resultant free-surface modal frequencies.

Mathematical Model

A potential flow solution for the oscillatory surface flow in the orifice is presented, which is modified to account for edge viscous effects. This solution includes the effects of surface tension at the free surface whose oscillation amplitudes are below those necessary to form droplets. The geometry for this problem is shown in Fig. 1. Based on the velocity potential, Φ, the conservation of mass for an axisymmetric flow of an incompressible fluid in cylindrical coordinates is

$$\frac{1}{r}\frac{\partial}{\partial r}\left(r\frac{\partial\Phi}{\partial r}\right)+\frac{\partial^2\Phi}{\partial x^2}=0. \tag{1}$$

The boundary conditions for this problem are defined at the orifice inlet, free surface, orifice wall or edge, and centerline. At the inlet, the potential is set to a reference value of zero. Since the flow is assumed axisymmetric, the radial velocity across the centerline is zero. And, since the orifice walls are impermeable, the radial velocity at the wall is also zero. These conditions result in the following boundary conditions:

$$\begin{aligned} x=0:&\quad \Phi=0\\ r=0:&\quad \frac{\partial\Phi}{\partial r}=0\\ r=R:&\quad \frac{\partial\Phi}{\partial r}=0. \end{aligned} \tag{2}$$

The boundary condition at the free surface is discussed later.

In order to account for edge viscous effects an analysis of oscillating flow in a cylinder provides a measure of the extent of the viscous region away from the wall. The thickness of a layer of fluid near the wall where the viscous forces are important, δ, is determined based on the fluid properties, oscillating frequency, and radius of the cylinder. An effective wall location, $R'=R-\delta$, is defined where the inviscid flow wall boundary condition is then applied. The value of δ is determined from the velocity profile, the solution for this flow is provided by Schlichting and Gersten [16],

$$\frac{u}{U_\infty}=ie^{i\omega t}\left[\frac{I_0\left(\sqrt{i}\lambda\frac{r}{R}\right)}{I_0(\sqrt{i}\lambda)}\right], \tag{3}$$

where U_∞ is the centerline fluid velocity, and λ is the nondimensional parameter ratio of the actual radius to the viscous diffusion length:

$$\lambda=R\sqrt{\frac{\omega}{\nu}}, \tag{4}$$

where ω is the oscillation frequency and ν is the kinematic viscosity. If the thickness of the viscous layer, δ, is defined based on the position where the velocity is 99% of the free stream velocity, then the effective wall location for inviscid flow, R', from Eq. (3) is obtained from

$$I_0\left(\sqrt{\frac{i\omega}{\nu}}R'\right)=0.01I_0\left(\sqrt{\frac{i\omega}{\nu}}R\right). \tag{5}$$

As the oscillating frequency increases the viscous layer decreases rapidly towards zero. The effect of the reduction of the effective orifice radius from R to R' is to add stiffness to the free surface, which increases the resultant modal frequency of the surface, as will be shown later.

The free-surface boundary condition is determined by the relationship between the acceleration of the free surface and the pressure difference across the surface generated by surface tension. This can be expressed as the linear equation:

$$x=\eta(r,t)+h:\quad \frac{\partial^2\Phi}{\partial t^2}+\frac{\sigma}{\rho}\frac{\partial\kappa}{\partial t}=0, \tag{6}$$

where η describes the position of the free surface relative to the top of the orifice, h is the height of the orifice, and κ is the curvature of the free surface. Gravity is neglected from this force balance since it is shown by Probstein [17] that gravitational forces are small if the wavelength of the surface waves is much less than $2\pi\sqrt{\sigma/\rho g}$. When evaluated for water this wavelength upper limit is about 17 mm, which is much greater that the 1 mm or less orifice size being considered in this study.

The curvature κ is defined in terms of η as

$$\kappa=\frac{\frac{\partial^2\eta}{\partial r^2}}{\left[1+\left(\frac{\partial\eta}{\partial r}\right)^2\right]^{3/2}}=\frac{\nabla^2\eta-\frac{1}{r}\frac{\partial\eta}{\partial r}}{\left[1+\left(\frac{\partial\eta}{\partial r}\right)^2\right]^{3/2}}. \tag{7}$$

In this expression, the surface slope $\partial\eta/\partial r$ is, in general, a function of r and t. Defining

$$\varepsilon=\frac{\partial\eta}{\partial r} \tag{8}$$

allows the curvature to be rewritten as

$$\kappa=\frac{1}{(1+\varepsilon^2)^{3/2}}\left(\nabla^2\eta-\frac{\varepsilon}{r}\right)=\frac{\nabla^2\eta}{(1+\varepsilon^2)^{3/2}}-\frac{\varepsilon}{r(1+\varepsilon^2)^{3/2}}. \tag{9}$$

Table 1 Theoretical modal frequencies, effective orifice radii for viscous modified potential theory, and ratio of viscous to modal time scales

	1180-μm diameter orifice				794-μm diameter orifice			
	Potential theory	Viscous modified potential theory			Potential theory	Viscous modified potential theory		
Mode Number	ω_n (rad/s)	ω_n (rad/s)	R' (μm)	τ_ν/τ_n	ω_n (rad/s)	ω_n (rad/s)	R' (μm)	τ_ν/τ_n
2	4,470	5,696	502.0	33.60	8,098	10,576	332.3	27.56
3	11,074	12,936	532.0	24.83	20,063	23,812	354.2	20.37
4	19,338	21,761	545.4	20.62	35,036	39,906	346.0	16.92
5	28,984	31,924	553.2	18.02	52,511	58,415	369.8	14.78
6	39,837	43,263	558.4	16.21	72,174	79,052	373.6	13.29
7	51,777	55,667	562.2	14.85	93,805	101,611	376.4	12.18

In the limit of small-amplitude oscillations, $\varepsilon \approx 0$, the curvature simplifies to $\kappa = \nabla^2 \eta$, which is the condition assumed for small surface waves and used by Burr, Tence, and Berger [1–3]. This approximation is referred to here as the zeroth-order approximation of curvature.

For any given shape of the free surface, as the amplitude of the oscillation increases, the value of the slope of the free surface also increases. However, for a given driving amplitude as the mode number increases, the wavelength decreases and the local surface curvature increases. Retaining only the first term in Eq. (9) results in a decreasing value of κ with increasing amplitude, and is defined as the first-order approximation to the curvature. Inclusion of the second term modifies the first-order approximation by either decreasing or increasing the curvature depending on the sign of ε and is referred to as the second-order approximation.

Substituting the expression of the zeroth-order curvature into the surface boundary condition and expressing it in terms of the potential function result in

$$x = \eta + h: \quad \frac{\partial^2 \Phi}{\partial t^2} + \frac{\sigma}{\rho} \frac{\partial^3 \Phi}{\partial r^2 \partial x} = 0, \quad \text{zeroth order.} \tag{10}$$

For the higher-order expressions of curvature an analytical solution is not available. A measure of the relative impact of increasing surface slope can be obtained by assuming ε to be a single-valued function of mode number. Consequently, the surface condition can be written as

$$x = \eta + h: \quad \frac{\partial^2 \Phi}{\partial t^2} + \frac{\sigma}{\rho} \frac{1}{(1+\varepsilon^2)^{3/2}} \frac{\partial^3 \Phi}{\partial r^2 \partial x} = 0,$$

$$\text{first and second order.} \tag{11}$$

Solving Eq. (1) with the boundary conditions of Eq. (2) but replacing R with R' to account for the viscous effects near the wall, and assuming that Φ can be expressed as a periodic function in time, the following form for the velocity potential results:

$$\Phi = A_n J_0\left(\gamma_n \frac{r}{R'}\right) \sinh\left(\gamma_n \frac{x}{R'}\right) \sin(\omega_n t), \tag{12}$$

where A_n is the amplitude, ω_n is the modal frequency of the free surface, and γ_n is the nth eigenvalue of the solution, which are roots of the zeroth-order Bessel function of the first kind, $J_0(\gamma_n) = 0$. Evaluating the free-surface boundary conditions of Eqs. (10) and (11) results in the following expressions for the modal frequencies:

$$\omega_n = \sqrt{\frac{\sigma}{\rho}\left(\frac{\gamma_n}{R'}\right)^3 \coth\left(\frac{\gamma_n}{R'}(\eta + h)\right)}, \quad \text{zeroth order,} \tag{13}$$

$$\omega_n = \sqrt{\frac{\sigma}{\rho} \frac{1}{(1+\varepsilon^2)^{3/2}} \left(\frac{\gamma_n}{R'}\right)^3 \coth\left(\frac{\gamma_n}{R'}(\eta + h)\right)},$$

$$\text{first and second order.} \tag{14}$$

If the argument for the hyperbolic cotangent is greater than 2, which is true for an orifice height h on the order of R', these expressions simplify to

$$\omega_n = \sqrt{\frac{\sigma}{\rho}\left(\frac{\gamma_n}{R'}\right)^3} = \sqrt{\frac{\sigma}{\rho}}\left(\frac{\gamma_n}{R'}\right)^{3/2}, \quad \text{zeroth order} \tag{15}$$

$$\omega_n = \sqrt{\frac{\sigma}{\rho} \frac{1}{(1+\varepsilon^2)^{3/2}} \left(\frac{\gamma_n}{R'}\right)^3}$$

$$= \sqrt{\frac{\sigma}{\rho} \frac{1}{(1+\varepsilon^2)^{3/2}}}\left(\frac{\gamma_n}{R'}\right)^{3/2}, \quad \text{first and second order.} \tag{16}$$

Note that R' has a dependence on γ_n such that R' approaches R as the mode number increases. Also, ε is mode-number dependent, with ε increasing as the mode number increases. Because of this, finite values of ε result in decreased modal frequencies compared to those predicted for very small surface displacements.

Obtaining modal frequencies based on the zeroth-order approximation of curvature is a straightforward iteration between Eqs. (15) and (5) to solve for both ω_n and R'. The results of this iteration for two orifice sizes are shown in Table 1 along with results for the nonviscous potential flow analysis. As mentioned previously, the modal frequencies for the viscous modified potential solution are higher than those for the potential solution. This is a result of the reduction in the inviscid region of the flow and the associated increase in stiffness due to the reduced radius. Since the modal frequency increases with mode number, the length ratio λ also increases with mode number, indicating that the viscous region near the wall becomes thinner with increasing mode number. This effect is shown in Table 1, as the effective radius R' approaches R at high mode number.

In addition to the near-wall viscous effects on the flow, the surface viscous forces also influence the dynamic response of the surface. A full solution of the governing equations would be required to incorporate this effect into the surface response. However, the magnitude of this effect in relationship to the modal frequency can be evaluated based on the time scales associated with the viscous dissipation. Lamb [18] illustrates the determination of the time scale associated with capillary wave dissipation for small-amplitude waves by relating the dissipation rate to the work rate done at the free surface by viscous forces. This same approach was applied to the circular geometry of the orifice surface that accounts for a wavelength dependence on modal number that appears through the eigenvalue, γ_n. The resulting dissipation time scale is

Table 2 Annular peak locations for potential theory and viscous modified potential theory solutions nondimensionalized by the orifice radius

Mode number	Potential theory		Viscous modified potential theory			
			1180 μm		794 μm	
	Second	Third	Second	Third	Second	Third
3	1	—	0.9016	—	0.8921	—
4	0.6896	—	0.6374	—	0.6323	—
5	0.5266	1	0.4937	0.9376	0.4904	0.9314
6	0.4259	0.8089	0.4031	0.7656	0.4009	0.7613

$$\tau_\nu = \frac{2R^2}{\nu \gamma_n^2}. \tag{17}$$

Consequently for high mode numbers and small orifice size, relatively small dissipation time scales occur. By comparing this time scale to the modal time scale, τ_n (period of one cycle), the relative impact of viscous dissipation can be evaluated. Results of τ_ν/τ_n are given in Table 1 for both orifice sizes. Since the dissipation time scale is large compared to the cycle time scale it is concluded that viscous dissipation has only a minor effect on the observed modal frequencies.

Evaluation of modal frequencies for the first- and second-order approximations of the curvature requires information about the surface slope parameter ε. A measure of this effect would be based on the surface displacement that is determined from the velocity potential solution [see Eq. (24) below] and then evaluating a representative value for the slope of the free surface. The slope will be a continuous function of radial location and time. Representative values for the surface slope parameter ε can be obtained using the assumed solution form of Eq. (12) to identify such parameters as the maximum surface slope, the average surface slope, or the rms value of the surface slope, which are expressed as

$$\varepsilon_{\max} = \max\left(\left|\frac{\partial \eta}{\partial r}\right|\right) = \frac{A_n}{\omega_n}\left(\frac{\gamma_n}{R'}\right)^2 \max\left(\left|J_0\left(\gamma_n \frac{r}{R'}\right)\right|\right)\cosh\left(\gamma_n \frac{\eta+h}{R'}\right), \tag{18}$$

$$\varepsilon_{\text{av}} = \frac{1}{R'}\int_0^{R'} \frac{\partial \eta}{\partial r}\, dr = \frac{A_n}{\omega_n}\left(\frac{\gamma_n}{R'}\right)^2 \frac{1}{\gamma_n}[1 - J_0(\gamma_n)]\cosh\left(\gamma_n \frac{\eta+h}{R'}\right), \tag{19}$$

$$\varepsilon_{\text{rms}} = \sqrt{\frac{1}{R'}\int_0^{R'}\left(\frac{\partial \eta}{\partial r}\right)^2 dr} = \frac{A_n}{\omega_n}\left(\frac{\gamma_n}{R'}\right)^2 \sqrt{\frac{1}{\gamma_n}\int_0^{\gamma_n} J_1^2(z)\, dz}\cosh\left(\gamma_n \frac{\eta+h}{R'}\right). \tag{20}$$

Each of these expressions for the measure of the surface slope have a general form, in terms of the eigenvalues, γ_n, which could be written as

$$\varepsilon = C f\left(\frac{\gamma_n}{R}\right), \tag{21}$$

where C contains the fluid properties, amplitude, and orifice size. The form of $f(\gamma_n/R)$ depends on the selected measure of ε and is based on Bessel function and hyperbolic cosine distributions. Since the hyperbolic cosine increases rapidly as the mode number increases, the appropriate measure of the surface slope should also increase rapidly with mode number. The form of $f(\gamma_n/R)$ is assumed to be approximated with a power law, and, referring to Eq. (16), which contains the term $1+\varepsilon^2$, the following is used:

$$1 + \varepsilon^2 = K^2\left(\frac{\gamma_n}{R}\right)^{2m}, \tag{22}$$

where K absorbs the value of C in Eq. (21). Substituting this into Eq. (16) yields

$$\omega_n = \sqrt{\frac{\sigma}{\rho}\frac{1}{[K^2(\gamma_n/R)^{2m}]^{3/2}}\left(\frac{\gamma_n}{R}\right)^3} = \sqrt{\frac{\sigma}{\rho}\frac{1}{K^3}\left(\frac{\gamma_n}{R}\right)^{(3/2)(1-m)}}. \tag{23}$$

When $m=0$ and $K=1$, the potential flow solution for predicting the modal frequencies, Eq. (15), is retrieved.

In addition to modal frequencies the surface shape is of interest. The surface function η is related to the potential function Φ through the following relationship:

$$\eta = \int_0^t \frac{\partial \Phi}{\partial x}\, d\tau. \tag{24}$$

From this relationship, the normalized radial dependence of the surface function defined as η_r is determined to be of the form

$$\eta_r = J_0\left(\gamma_n \frac{r}{R}\right). \tag{25}$$

The locations of the annular peaks can be determined from this expression using both the potential flow theory, as well as the viscous modified theory by replacing R with R'. The locations for the first two annular peaks, labeled second and third, respectively, for two orifice sizes are shown in Table 2, where they are nondimensionalized by the orifice radius R. Annular peaks only occur for mode numbers 3 and higher; therefore only these modes are included in Table 2. The peaks predicted from the viscous modified potential theory are located closer to the centerline than those based on the potential theory solution. This is due to the smaller effective radius of the viscous modified potential theory solution. The data in the table also show a small effect related to the orifice size for the viscous modified case. As the orifice diameter decreases, the relative location of the annular peaks shift inward, and the corresponding modal frequencies shown in Table 1 increase.

The goals of the experimental portion of this study are to (i) verify the modal surface shapes as predicted by the Bessel function dependence and (ii) determine if the modal frequencies are accurately modeled based on the modifications to the potential theory contained in Eq. (23).

Experimental Set-up

The test device, shown in Fig. 2, was used to generate the free-surface oscillations being studied. This test device consisted of a sharp-edged orifice, pressure reservoir, refill reservoir, and a piezoelectrically driven diaphragm. The liquid free surface is formed at the top surface of the orifice. The pressure reservoir is acted upon by the diaphragm motion, which serves to establish the inlet condition to the orifice. The lower refill reservoir provides a constant-pressure source for the refilling of the pressure reservoir through three small holes ($\sim$50 μm diameter) located around the

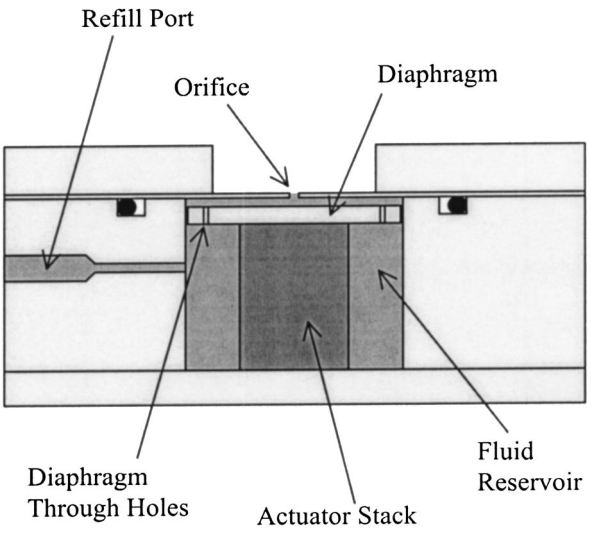

Fig. 2 Schematic of the test device

circumference of the diaphragm. These holes were sized such that the flow resistance from the pressure reservoir to the refill reservoir is much larger than the flow resistance through the orifice. The diaphragm motion is provided by an actuator stack consisting of a top insulator, an APC #856 piezoelectric disk (supplied by American Piezo Ceramics), a bottom insulator, and a spacer, all cemented together.

A schematic of the complete experimental setup is shown in Fig. 3. The test device was mounted on an optical table along with a 1300×1030 pixel cooled charge-coupled device (CCD) camera fitted with a long-distance microscopic lens. The fluid surface in the test device was illuminated with a frequency-doubled Nd:YAG (yttrium aluminum garnet) pulsed laser-emitting light at a wavelength of 532 nm, mounted on a separate optical table. The working fluid in the test device was a 10^{-3} M solution of rhodamine 6G chloride in water. Since the concentration of rhodamine 6G chloride is very small, the properties of the solution were taken to be those of water. Rhodamine 6G chloride is a fluorescent dye

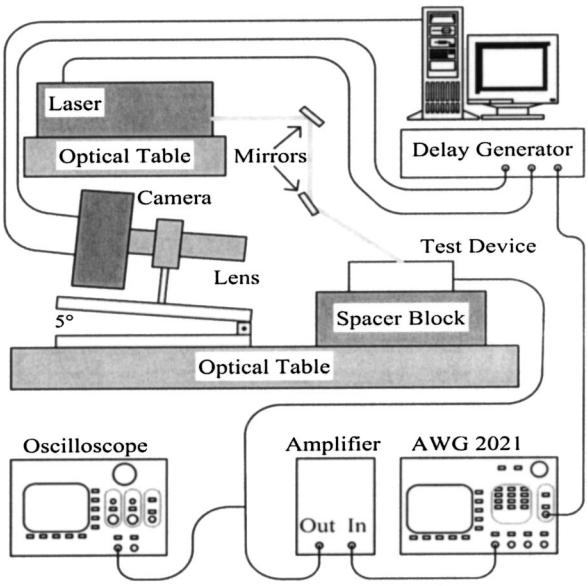

Fig. 3 Schematic of the experiment setup

with a primary emission of light at a wavelength of 551 nm when excited at 532 nm. The power of the laser was adjusted to provide sufficient fluorescence for imaging. The fluorescence was recorded with the CCD camera using a 5-nm bandpass filter centered at 550 nm to eliminate any reflections of the laser light from the fluid surface. The pixel resolution for this setup was about 1 μm per pixel.

The piezoelectric crystal was driven by the amplified signal from an arbitrary waveform generator; the frequency and amplitude of this signal were verified with an oscilloscope. The sequential timing of the onset of the piezoelectric driving signal, the laser light pulse, and the image acquisition were controlled by a digital delay generator to within 2.5×10^{-5}% of a typical time delay.

Data were collected for a range of driving frequencies at 100-Hz intervals to capture at least five modal shapes using two different orifice sizes. For each of the frequencies and for both the orifice sizes, a series of 20 images was taken at different phases of one cycle. Images were also captured for each of these frequencies when the center peak was at its highest amplitude.

The data collected were gray-scale images of the surface shape. Along with the image of the free surface, a reflection of the fluorescence from the orifice plate surface also appears. This is a result of the shallow viewing angle of the camera (approximately 5° from the orifice plate surface), and the polished surface of the orifice plate. Also, since the images were obtained at a slight angle, reliable data of the surface shape could only be obtained in the center region of the surface. However, it was possible to identify the locations of the annular peaks associated with the higher mode oscillations. Surface profiles of the central peak were generated after creating a binary image and performing an edge detection of the surface. Annular peak locations were measured radially outward from the central peak location.

Results

Results of surface oscillations are presented for orifice diameters of 794 and 1180 μm for frequencies through those predicted for mode 6. Data gathered at the predicted modal frequencies are compared to theory in two ways. First, the surface profiles of the highest amplitude of the central peak are compared with theory when oscillated at the predicted modal frequencies. Second, the annular peak locations are compared to those predicted in Table 2. In addition, experimental frequencies are identified that correspond to specific modal shapes based on the radial location of secondary peaks. That is, the associated driving frequency is noted when the modal shapes match those predicted based on the radial location of the second annular peak.

Figure 4 compares the shape of the central peak to the predicted shapes using both the potential flow analysis and the viscous modified analysis. Mode numbers 2 through 5 are shown for both orifice diameters. Note the change of radial scale for each mode number; this is due to the fact that higher mode numbers have smaller radial extent of the central peak. Only the central peak surface shape could be obtained experimentally because of the angle of the camera, which caused the axisymmetric secondary rings to interfere with the valleys beyond the central peak. This is obvious in Fig. 5, which shows a series of images and is discussed later. The potential flow solution for the surface elevation is always slightly above the viscous modified solution due to the reduced effective radius of the latter. The measured surface, for the lower mode numbers, is in very good agreement with the predicted shape. At the highest mode number of five the measured values are higher, but this is likely a result of higher relative experimental uncertainty for the smaller peaks as well as the greater interference of the secondary annular peaks.

To obtain a better measure of the surface shape the location of the higher-order annular peaks were determined. Table 3 shows the difference between the measured annular peak locations and those predicted by the potential flow and viscous modified solutions. These data are normalized by both the orifice radius and by

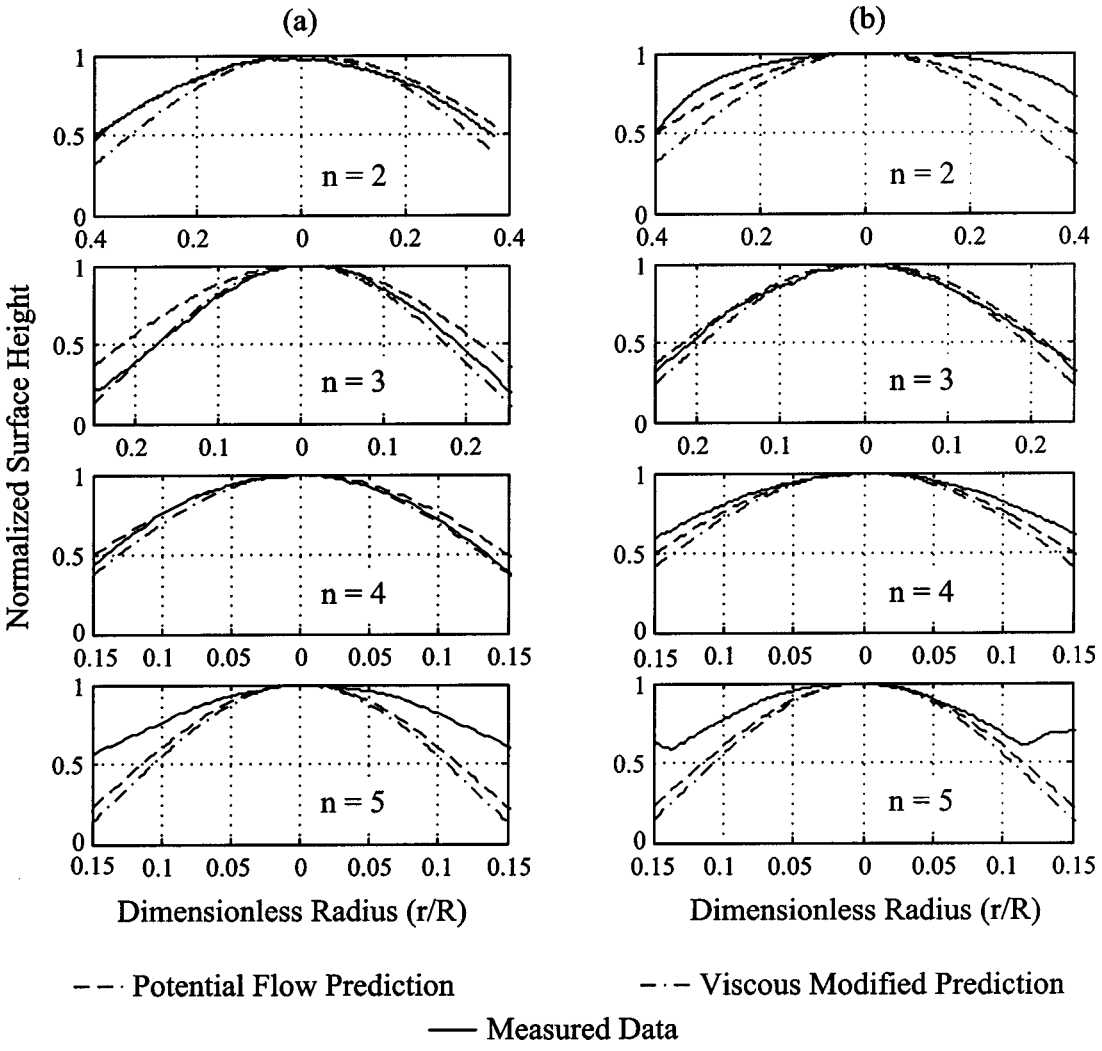

Fig. 4 Measured and predicted surface profiles using the potential theory and viscous modified theory of the central peak for modes 2 through 5 for (*a*) the 794-μm and (*b*) the 1180-μm diameter orifices

the predicted peak location. Figure 5 shows graphically this comparison between the viscous modified prediction and the measured annular peak locations. The measured peak locations (in gray) are consistently inside of the predicted locations (in white), indicating that the surface shape is contracted in the radial direction. As indicated in Table 3 these differences are as much as 30% for the

Table 3 Difference between annular peak locations and measured peak location, normalized by both the orifice radius and the predicted peak location. Upper numbers use potential theory; lower numbers use viscous modified theory.

Mode Number	1180 μm Diameter				794 μm Diameter			
	Normalized by Orifice Radius		Normalized by Peak Location		Normalized by Orifice Radius		Normalized by Peak Location	
	2nd	3rd	2nd	3rd	2nd	3rd	2nd	3rd
3	0.335 / 0.236	- / -	0.335 / 0.262	- / -	0.310 / 0.203	- / -	0.310 / 0.227	- / -
4	0.129 / 0.077	- / -	0.187 / 0.121	- / -	0.201 / 0.144	- / -	0.291 / 0.227	- / -
5	0.116 / 0.083	0.246 / 0.184	0.219 / 0.167	0.246 / 0.196	0.129 / 0.093	0.249 / 0.181	0.246 / 0.190	0.249 / 0.194
6	0.109 / 0.086	0.195 / 0.151	0.256 / 0.167	0.241 / 0.198	0.014 / 0.088	0.085 / 0.124	0.033 / 0.219	0.105 / 0.163

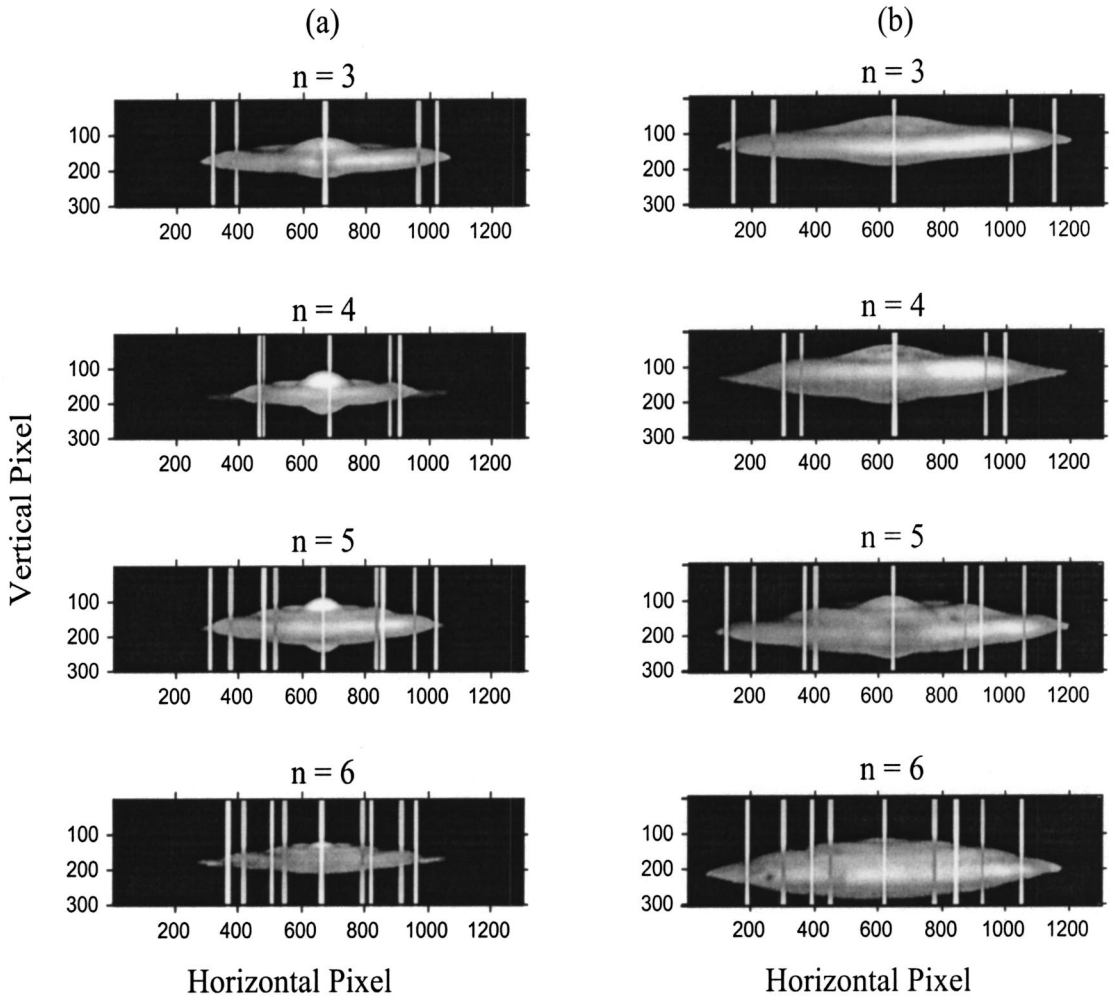

Fig. 5 Comparison of predicted (white) and measured (gray) annular peak locations for mode numbers 3 through 6 using the viscous modified solutions for (*a*) the 794-μm- and (*b*) the 1180-μm-diameter orifices

low mode numbers. At higher mode numbers for the smaller-diameter orifice these differences are on the order of 10% or less.

It was determined experimentally that the locations of the higher-order annular peaks shift gradually with changing driving frequency. Increased frequencies result in annular peak shifting to smaller radial positions. New annular peaks form at the orifice periphery when the frequency is sufficiently high, resulting in a shift towards the next highest mode. To observe how the surface shape changes with frequency, the location of the annular peaks were measured over a range of frequencies. Figure 6(*a*) shows the secondary peak location versus frequency for the 794-μm-diameter orifice. Also shown are predictions for the potential flow and the viscous modified analyses. The secondary peak locations gradually shift inward as the frequency increases. A measured modal frequency can be defined from these data by the frequency at which the secondary peak location agrees with the prediction. This process is shown in Fig. 6(*a*), where, for example, the secondary peak location for mode number 6 is predicted to occur at $r/R' = 0.4$ using the viscous modified results, and this occurs at a measured frequency of 6650 Hz. Since there is scatter in the data, a 10-μm interval around the predicted peak location was selected, and an average of the frequencies within this interval was used as the measured modal frequency. Figure 6(*b*) shows similar data for the 1180-μm-diameter orifice. The measured modal frequencies in this case were determined by interpolation between the data shown. There is a significant reduction of the measured modal frequencies compared to the predicted values for both orifice radii. These results show a consistent decrease of modal frequency for each mode number. Or, this implies that to achieve a specified mode shape, the required driving frequency is significantly lower than that predicted by either the potential flow or viscous modified theories.

To further explore this modal frequency reduction, modal frequency data and predictions were plotted versus either γ_n/R or γ_n/R' as shown in Fig. 7. This is a log–log plot and clearly indicates the power-law dependence of frequency on modal eigenvalue. It should be noted that γ_n takes on discrete values and is not a continuous function. Per Eq. (15) the exponent of the modal parameter is 1.5 for both the potential flow (using R) and the viscous modified predictions (using R'). This same exponential dependence fits the experimental data quite well, with a slight shift in the constant depending if R or R' is used to normalize γ_n. Comparing this result to Eq. (23), which includes the γ_n^{2m} dependence on the modal frequency that arises from the surface curvature, indicates that $m=0$, $K=1.270$ (using R), and $K=1.374$ (using R'). The modal frequency can then be written as

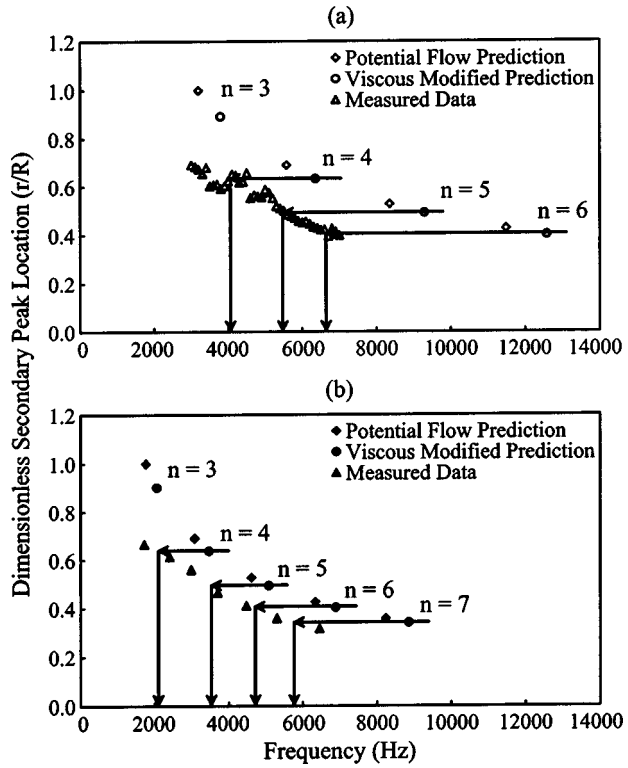

Fig. 6 Predicted secondary peak locations versus frequency for potential theory and viscous modified potential theory, as well as measured data for (*a*) the 794-μm- and (*b*) the 1180-μm-diameter orifices

$$\omega_n = \sqrt{\frac{\sigma}{\rho}\frac{1}{K^3}}\left(\frac{\gamma_n}{R}\right)^{(3/2)(1-m)} = \sqrt{\frac{\sigma}{\rho}\frac{1}{(1.270)^3}}\left(\frac{\gamma_n}{R}\right)^{3/2} = \sqrt{\frac{\sigma}{\rho}\frac{1}{(1.374)^3}}\left(\frac{\gamma_n}{R'}\right)^{3/2}. \tag{26}$$

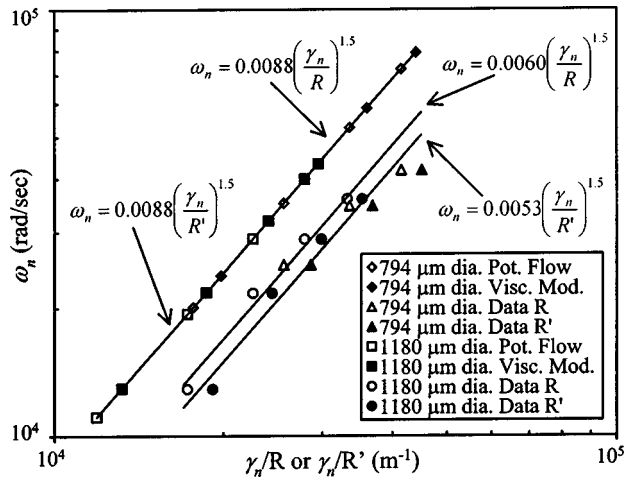

Fig. 7 Potential theory modal frequency predictions versus γ_n/R and viscous modified potential theory frequency predictions versus γ_n/R'; as well as measured modal frequencies versus γ_n/R and γ_n/R' for both the 794- and 1180-μm orifices

The higher-mode-number data may indicate a somewhat reduced slope but more data would be needed to confirm this. The existing data indicate that, since $m=0$, ε is not a significant function of γ_n (or mode number). Since the higher-mode-number data indicates a reduced slope it may be that $m>0$ at higher modes (greater than six). If this is the case then the higher modes would yield an even larger reduction of the predicted modal frequencies.

A possible interpretation of this reduced modal frequency is put forward as follows. The analysis leading to Eq. (16), the higher-order expression for ω_n, assumes a measure of the surface slope ε, to be independent of position and time as is the parameter K. In so doing, as ε increases the modal frequency decreases. This is consistent with the data. Higher-modal shapes have smaller wavelengths, implying greater surface curvature if the surface amplitudes are comparable, see Fig. 5. From the surface boundary condition, Eq. (6), a greater pressure difference and therefore curvature across the interface are required to sustain the higher local accelerations associated with higher mode numbers. By including a measure of increased slope (increasing ε) the curvature actually decreases [see Eq. (9)]. Therefore the higher-order analysis shows decreased curvature with increased mode number. This would imply that the pressure difference across the interface is reduced, resulting in a lower-mode shape at a particular frequency, not a higher-mode shape as shown by the data. This inconsistency is argued to be the result of assuming ε to be constant for any given mode. The Bessel function modal shapes are such that there is a high curvature locally at the peaks and valleys, and relatively low curvature. As the mode number increases the spatial extent of regions of high curvature is reduced, but the peak curvature magnitude is increased. A proper measure of ε that accounts for both effects may be very complex. In fact a higher-order moment, in contrast to those given in Eqs. (18)–(20), may provide a better representation. A fourth-order moment may be a means to assess the spatially concentrated curvature. Consequently, the higher-order analysis, with increased ε, predicts a lower curvature that would be expected to be associated with lower mode numbers, but in fact higher mode numbers have spatial concentrations of high curvature with large regions of low curvature. These regions of high curvature drive the oscillations with large pressure differences across the interface. Therefore, lower frequencies are capable of sustaining higher-mode shapes. It should be noted that once the driving amplitude is increased, and the spatial distribution of ε becomes dominant, it is not assured that a Bessel function shape is appropriate and the results presented may not be valid.

Conclusions

A potential flow analysis of the surface shapes in an orifice driven by a periodic forcing function at the inlet was examined. The analysis accounts for edge viscous effects and finite amplitude surface oscillations. The predicted surface shapes were compared with experimental data for two orifice sizes. The shape of the central peak was found to be in agreement with the shape predicted by the Bessel function although there is some disagreement at high mode numbers due to inaccuracies in the data collection technique. The locations of the annular peaks at the predicted modal frequencies were found to be shifted inward towards the centerline from their predicted locations. When finite surface displacements are modeled, it is shown that the modal frequency is reduced by the parameter ε, which represents the slope of the free surface. A power law representation in terms of the eigenvalues γ_n is incorporated into the predicting equation for the modal frequencies. The result is fitted to the measured modal frequency data, providing an empirical function for the modal frequency in terms of the eigenvalues. Interestingly, the power law exponent is not affected by the finite-amplitude oscillations; however this may not be valid if the driving amplitude is significantly increased. These data indicate that much lower frequencies are sufficient to obtain higher-order modal surface conditions. Further study of the effects of driving amplitude on surface curvature will further the understanding of modal surface shapes, particularly at high mode numbers.

Nomenclature

A_n = Arbitrary coefficient (m^2/s)
f = Frequency (Hz)$=\omega/2\pi$
h = Height of orifice (m)
n = Mode-number index
r = Radial coordinate (m)
R = Orifice radius (m)
R' = Effective orifice radius (m)
t = Time (s)
u = Axial velocity (m/s)
U_∞ = Centerline axis velocity (m/s)
x = Axial coordinate (m)

Greek Symbols

γ_n = Eigenvalue
δ = Thickness of viscous effected region at orifice wall (m)
ε = Representative of free surface slope
η = Free surface function (m)
η_r = Dimensionless free surface, function of r only
κ = Free surface curvature (l/m)
λ = Dimensionless parameter
ν = Kinematic viscosity (m^2/s)
ρ = Density (kg/m^3)
σ = Surface tension (N/m)
Φ = Potential function (m^2/s)
ω_n = Modal frequency (rad/s)

References

[1] Burr, R. F., Tence, D. A., and Berger, S. S., 1996, ''Multiple Dot Size Fluidics for Phase Change Piezoelectric Ink Jets,'' Proc. IS&T's *International Conference on Digital Printing Technologies*, Vol. 12, pp. 12–18.

[2] Burr, R. F., Berger, S. S., and Tence, D. A., 1996, ''Overview of Phase Change Piezoelectric Ink Jet Fluids Modeling and Design,'' Proc. ASME Fluids Division Sumer Meeting, Vol. 4, pp. 94–99.

[3] Berger, S. S., Burr, R. F., Padgett, J. D., and Tence, D. A., 1997, ''Ink Manifold Design of Phase Change Piezoelectric Ink Jets,'' Proc. IS&T's *International Conference on Digital Printing Technologies*, Vol. 13, pp. 703–708.

[4] Benjamin, T. B., and Ursell, F., 1954, ''The Stability of the Plane Free Surface of a Liquid in Vertical Periodic Motion,'' Proc. R. Soc. London, Ser. A, **225**, pp. 505–515.

[5] Penny, W. G., and Price, T. R., 1952, ''Part II Finite Periodic Stationary Gravity Waves in a Perfect Liquid,'' Philos. Trans. R. Soc. London, Ser. A, **244**, pp. 254–284.

[6] Taylor, G. I., 1953, ''An Experimental Study of Standing Waves,'' Proc. R. Soc. London, Ser. A, **218**, pp. 44–59.

[7] Tadjbakhsh, I., and Keller, J. B., 1960, ''Standing Surface Waves of Finite Amplitude,'' J. Fluid Mech., **8**, pp. 442–451.

[8] Fultz, D., 1962, ''An Experimental Note on Finite-Amplitude Standing Gravity Waves,'' J. Fluid Mech., **13**, pp. 193–212.

[9] Edge, R. D., and Walters, G., 1964, ''The Period of Standing Gravity Waves of Largest Amplitude on Water,'' J. Geophys. Res., **69**, pp. 1674–1675.

[10] Mack, L. R., 1962, ''Periodic, Finite-Amplitude, Axisymmetric Gravity Waves,'' J. Geophys. Res., **67**, pp. 829–843.

[11] Fultz, D., and Murty, T. S., 1963, ''Experiments on the Frequency of Finite-Amplitude Axisymmetric Gravity Waves in a Circular Cylinder,'' J. Geophys. Res., **68**, pp. 1457–1462.

[12] Dodge, F. T., Kana, D. D., and Abramson, H. N., 1965, ''Liquid Surface Oscillations in Longitudinally Excited Rigid Cylindrical Containers,'' AIAA J., **3**, pp. 685–695.

[13] Vanden-Broek, J.-M., and Tuck, E. O., 1994, ''Flow Near the Intersection of a Free Surface With a Vertical Wall,'' SIAM (Soc. Ind. Appl. Math.) J. Appl. Math., **54**, pp. 1–13.

[14] Marsh, J. A., Garoff, and S., Dussan, V., 1993, ''Dynamic Contact Angles and Hydrodynamics Near a Moving Contact Line,'' Phys. Rev. Lett., **70**, pp. 2778–2781.

[15] Dussan, V. E.B., and Davis, S. H., 1986, ''Stability in Systems With Moving Contact Lines,'' J. Fluid Mech., **173**, pp. 115–130.

[16] Schlicting, H., and Gersten, K., 2000, *Boundary-Layer Theory*, 8th ed., Springer-Verlag, Berlin.

[17] Probstein, R. F., 1989, *Physicochemical Hydrodynamics an Introduction*, Butterworth, Stoneham MA, pp. 289–300.

[18] Lamb, H., 1932, *Hydrodynamics*, 6th ed., Dover, New York.

Similarity Analysis for Nonequilibrium Turbulent Boundary Layers*

Luciano Castillo

Xia Wang

Rensselaer Polytechnic Institute, Department of Mechanical, Aerospace and Nuclear Engineering, Troy, NY 12180

In his now classical paper on pressure gradient turbulent boundary layers, Clauser concluded that equilibrium flows were very special flows difficult to achieve experimentally and that few flows were actually in equilibrium [1]. However, using similarity analysis of the Navier–Stokes equations, Castillo and George [2] defined an equilibrium flow as one where the pressure parameter, $\Lambda=[\delta/(\rho U_\infty^2 d\delta/dx)](dP_\infty/dx)$, was a constant. They further showed that most flows were in equilibrium and the exceptions were nonequilibrium flows where $\Lambda\neq$constant. Using the equations of motion and similarity analysis, it will be shown that even nonequilibrium flows, as those over airfoils or with sudden changes on the external pressure gradient, are in equilibrium state, but only locally. Moreover, in the case of airfoils where the external pressure gradient changes from favorable to zero then to adverse, three distinctive regions are identified. Each region is given by a constant value of Λ_θ, and each region remains in equilibrium with Λ_θ =constant, respectively. [DOI: 10.1115/1.1789527]

1 Introduction

Clauser [1] defined an equilibrium boundary layer with pressure gradient (PG) as one where the pressure parameter given as,

$$\beta=-\frac{\delta_*}{\rho u_*^2}\frac{dP_\infty}{dx}, \tag{1}$$

was a constant and the velocity deficit profile normalized with the friction velocity, u_*, was independent of the streamwise direction. Thus, the profiles should collapse into a single curve. However, most flows did not satisfy these conditions, especially flows near separation or separated, where the friction velocity, u_*, was approaching zero. Clauser [1] further concluded that these equilibrium flows were a special type of flows which were difficult to generate and maintain in equilibrium, and therefore most flows were recognized as nonequilibrium flows.

Bradshaw [3] showed that a necessary condition for a turbulent boundary layer to maintain equilibrium was that the contribution of the pressure gradient to the growth of the momentum deficit should be a constant multiple of the contribution from the surface shear stress, which was shown to be the same as Clauser's pressure parameter, β.

Townsend [4] developed a self-preserving theory which was more rigorous than the analysis by Clauser [1]. Unfortunately, Townsend [4] overconstrained the problem by assuming the existence of a single velocity scale. Rotta [5] studied the adverse pressure gradient (APG) flow and showed that the length scale and the velocity scale were given as, $\delta_* U_\infty/u_*$ and u_*, respectively. Obviously, these scalings also failed for flows with strong APG or near separation. Later on, a criterion given as $U_\infty=\alpha(x-x_0)^m$ with $m<0$ was used very often to predict the equilibrium adverse pressure gradient boundary layer by Townsend [6], East and Sawyer [7] and Skåre and Krogstad [8]. However, there have been a lot of disagreements on the range of m in which the equilibrium boundary layer should exist. Kader and Yaglom [9] carried out a similarity analysis on moving-equilibrium turbulent boundary layers with APG. Their so-called moving-equilibrium turbulent boundary layers were restricted to exclude the effects of the upstream conditions, even though many equilibrium flows and near-equilibrium flows fell into this group.

As stated earlier, most of the previous definitions about equilibrium boundary layers were proposed assuming that a single velocity scale existed. However, the classical log-law based on this single velocity scale assumption (i.e., the friction velocity) did not work for all flows, especially for those with strong APG. Furthermore, Coles and Hirst [10] mentioned that the classical scaling laws failed for turbulent boundary layers experiencing strong pressure gradient and for relaxing flow where there was a sudden change in the external pressure gradient or boundary conditions.

Recent results using similarity analysis of the RANS equations by Castillo and George [2] showed that the proper velocity scale for the outer part of the boundary layer was the free stream velocity instead of the friction velocity. Subsequently, an equilibrium boundary layer was found to exist only when the pressure parameter Λ, defined as

$$\Lambda=\frac{\delta}{\rho U_\infty^2 d\delta/dx}\frac{dP_\infty}{dx}, \tag{2}$$

was a constant. Integrating the above equation, a power law relation can be obtained between the boundary layer thickness, δ, and the free stream velocity, U_∞. Furthermore, it was shown that the power coefficient was given by the pressure parameter as $-1/\Lambda$, i.e., $\delta\sim U_\infty^{-1/\Lambda}$. Moreover, if the experimental data after the taken logarithm was plotted, this power law must show a linear relationship if an equilibrium flow existed at all. Surprisingly enough, Castillo and George [2] showed that this was the case for most pressure gradient (PG) flows, and the exceptions were nonequilibrium flows where the pressure parameter was not a constant. In addition, it seemed that only three values of the pressure parameter were needed to characterize all equilibrium boundary layers. One was for the adverse pressure gradient (APG) flow with $\Lambda\cong 0.22$, one for the favorable pressure gradient (FPG) flow with $\Lambda\cong -1.92$, and one for the zero pressure gradient (ZPG) flow with $\Lambda=0$. This simple definition makes it easier to study the behavior of boundary layers. Most recently, Castillo et al. [11] showed that even flows approaching separation or at separation obeyed this simple relation, and hence remained in equilibrium.

*This paper has been presented in the 32th AIAA Fluid Dynamics Conference and Exhibit June 24–26, 2002, St. Louis, Missouri.

Contributed by the Fluids Engineering Division for publication in the JOURNAL OF FLUIDS ENGINEERING. Manuscript received by the Fluids Engineering Division October 18, 2002; revised manuscript received March 15, 2004. Associate Editor: T. B. Gatski.

There is still another type of flow where $\Lambda \neq$ constant, i.e., the "nonequilibrium flow," which needs further investigation. This nonequilibrium flow occurs very often in the case of airfoils where the external pressure gradient usually undergoes from favorable to zero and then to adverse. Another possible case is the relaxed flows as defined by Bradshaw [12], where sudden changes in the external conditions lead to a flow history dependence in the downstream flow. Consequently, they exhibit a very different behavior from those expected in the classical log-law. Therefore, the primary goal of this paper is to study the behavior of nonequilibrium boundary layers using similarity analysis of the equations of motion. In addition, it will be shown that although this type of flow cannot be considered to be in equilibrium since $\log(U_\infty)$ vs $\log(\delta)$ is nonlinear, it is still in equilibrium, but only locally.

2 Similarity Analysis

The outer scales of the turbulent boundary layer must be determined from the equilibrium similarity analysis of the governing equations, and not chosen *a priori*. Castillo and George [2] applied this concept to the outer boundary layer equations in order to determine the mean velocity and Reynolds stresses scales. The present analysis is restricted to a 2D, incompressible turbulent boundary layer, and steady state on the mean. The continuity equation is given as,

$$\frac{\partial U}{\partial x}+\frac{\partial V}{\partial y}=0. \tag{3}$$

The boundary layer equation for the outer flow ($y/\delta > 0.1$ typically) reduces to

$$U\frac{\partial U}{\partial x}+V\frac{\partial U}{\partial y}=-\frac{1}{\rho}\frac{dP_\infty}{dx}+\frac{\partial}{\partial y}[-\langle uv\rangle]+\frac{\partial}{\partial x}[\langle v^2\rangle-\langle u^2\rangle], \tag{4}$$

where $U\to U_\infty$, $\langle uv\rangle \to 0$ as $y\to\infty$, $\langle u^2\rangle$ and $\langle v^2\rangle \to 0$ as $y\to\infty$ as well according to Tennekes and Lumley [13]. This equation, along with the continuity equation, describes the outer flow exactly in the limit as the Reynolds number approaches to infinity. The Reynolds normal stresses gradients, $\partial/\partial x[\langle v^2\rangle-\langle u^2\rangle]$ are of the second order compared to the other terms and are usually neglected. However, they will be retained in the present similarity analysis because in flows approaching separation, the contribution of the Reynolds normal stresses gradients is about 30%. (Simpson et al. [14–16], Alving and Fernholz [17], Elsberry et al. [18]). Notice that Eq. (4) does not take into account the case of the large surface curvature where the free stream pressure and the static pressure on the wall are not necessarily the same. On the flat surface, $\partial p/\partial y$ is of the order of δ while on the curvature surface, $\partial p/\partial y$ is of the order one, Goldstein [19].

2.1 Similarity Solutions. In order to determine the scales of the mean flow and the turbulent quantities, similarity solution forms shown below are sought. The basic assumption is that it is possible to express any dependent variable, in this case the outer deficit velocity, $U-U_\infty$, the outer Reynolds shear stress, $\langle uv\rangle$, and outer Reynolds normal stresses, $\langle u^2\rangle$, $\langle v^2\rangle$ as a product of two functions, i.e.,

$$U-U_\infty = U_{so}(x) f_{op}(\overline{y},\delta^+;\Lambda;*), \tag{5}$$

$$-\langle uv\rangle = R_{so}(x) r_{op}(\overline{y},\delta^+;\Lambda;*), \tag{6}$$

$$\langle u^2\rangle = R_{sou}(x) r_{opu}(\overline{y},\delta^+;\Lambda;*), \tag{7}$$

$$\langle v^2\rangle = R_{sov}(x) r_{opv}(\overline{y},\delta^+;\Lambda;*), \tag{8}$$

where U_{so} and R_{so} are the outer velocity scale and the outer Reynolds shear stress scale, respectively, which depend on x only; R_{sou} and R_{sov} are the Reynolds normal stresses scales corresponding to the $\langle u^2\rangle$ and $\langle v^2\rangle$ components, and depend only on x as well. Note that the outer velocity scale, U_{so}, the outer Reynolds shear stress scale, R_{so}, and the outer Reynolds normal stresses scales, R_{sou} and R_{sov} *must* be determined from the boundary layer equations. The arguments inside the similarity functions (f_{op}, r_{op}, r_{opu}, and r_{opv}) represent the outer similarity coordinate, $\overline{y}=y/\delta_{99}$, the Reynolds number dependence, $\delta^+=\delta u_*/\nu$, the pressure parameter, Λ, and any possible dependence on the upstream conditions,*, respectively.

2.2 Asymptotic Invariance Principle: AIP. This principle means that in the limit as $\mathrm{Re}\to\infty$ the boundary layer equations become independent of the Reynolds number; therefore, any function or scaling must also be independent of δ^+ as well. Thus, in this limit Eqs. (5) and (6) must also become independent of the local Reynolds number, i.e.,

$$f_{op}(\overline{y},\delta^+;\Lambda;*)\to f_{op\infty}(\overline{y},\Lambda,*), \tag{9}$$

$$r_{op}(\overline{y},\delta^+;\Lambda;*)\to r_{op\infty}(\overline{y},\Lambda,*), \tag{10}$$

$$r_{opu}(\overline{y},\delta^+;\Lambda;*)\to r_{opu\infty}(\overline{y},\Lambda,*), \tag{11}$$

$$r_{opv}(\overline{y},\delta^+;\Lambda;*)\to r_{opv\infty}(\overline{y},\Lambda,*), \tag{12}$$

as $\delta^+\to\infty$. The subscript $_\infty$ is used to distinguish these infinite Reynolds number solutions from the finite Reynolds number profiles used in Eqs. (5)–(8).

2.3 Transformed Equations. Using the asymptotic functions of Eqs. (9)–(12), it is possible to get a new outer scale for velocity deficit profiles and Reynolds stresses profiles, respectively. Substituting Eqs. (9)–(12) into Eq. (4) and clearing terms yield:

$$\begin{aligned}&\left[\frac{\delta}{U_{so}}\frac{dU_\infty}{dx}+\left(\frac{U_\infty}{U_{so}}\right)\frac{\delta}{U_{so}}\frac{dU_{so}}{dx}\right]f_{op\infty}+\left[\frac{\delta}{U_{so}}\frac{dU_{so}}{dx}\right]f_{op\infty}^2-\left[\frac{U_\infty}{U_{so}}\frac{d\delta}{dx}\right.\\&\left.+\frac{\delta}{U_{so}}\frac{dU_\infty}{dx}\right]\overline{y}f'_{op\infty}-\left[\frac{d\delta}{dx}+\frac{\delta}{U_{so}}\frac{dU_{so}}{dx}\right]f'_{op\infty}\int_0^{\overline{y}}f_{op\infty}(\tilde{y})d\tilde{y}\\&=\left[\frac{R_{so}}{U_{so}^2}\right]r'_{op\infty}-\left[\frac{R_{sov}}{U_{so}^2}\frac{d\delta}{dx}\right]r'_{opv\infty}+\left[\frac{R_{sou}}{U_{so}^2}\frac{d\delta}{dx}\right]r'_{opu\infty},\end{aligned} \tag{13}$$

where the term involving $-dP_\infty/dx$ has been cancelled by the $\rho U_\infty dU_\infty/dx$ term from Euler's equation for the external flow, and the V component is obtained by the integration of the continuity equation.

2.4 Equilibrium Similarity Conditions. For the particular type of "equilibrium" similarity solutions suggested by George [20], all the terms in the governing equations must maintain the same relative balance as the flow develops. These *equilibrium similarity* solutions exist only if all the square bracketed terms have the same x dependence and are independent of the similarity coordinate, $\overline{y}$. Thus, the bracketed terms must remain proportional to each other as the flow develops, i.e.,

$$\begin{aligned}&\frac{\delta}{U_{so}}\frac{dU_{so}}{dx}\sim\frac{\delta}{U_{so}}\frac{dU_\infty}{dx}\sim\left(\frac{U_\infty}{U_{so}}\right)\frac{\delta}{U_{so}}\frac{dU_{so}}{dx}\sim\frac{d\delta}{dx}\sim\left(\frac{U_\infty}{U_{so}}\right)\frac{d\delta}{dx}\\&\sim\frac{R_{so}}{U_{so}^2}\sim\frac{R_{sov}}{U_{so}^2}\frac{d\delta}{dx}\sim\frac{R_{sou}}{U_{so}^2}\frac{d\delta}{dx},\end{aligned} \tag{14}$$

where "$\sim$" means "has the same x dependence as." It is clear that full similarity of the "equilibrium-type" is possible only if,

$$U_{so}\sim U_\infty, \tag{15}$$

$$R_{so}\sim U_{so}^2\frac{d\delta}{dx}\sim U_\infty^2\frac{d\delta}{dx}, \tag{16}$$

and

$$R_{sou}\sim R_{sov}\sim U_{so}^2\sim U_\infty^2. \tag{17}$$

Thus, the outer equations do admit to full similarity solutions in the limit of infinite Reynolds number, *and these solutions determine outer scales*. No other choice of scales can produce profiles (of the assumed form), which are asymptotically independent of the Reynolds number, at least unless they reduce to these scales in the limit, George and Castillo [21].

2.5 Pressure Gradient Parameter. Besides the similarity conditions for the mean velocity and Reynolds stresses, other constraint for the pressure gradient can be obtained as well from the analysis such as,

$$\frac{d\delta}{dx} \sim \frac{\delta}{U_\infty}\frac{dU_\infty}{dx} \sim \frac{\delta}{\rho U_\infty^2}\frac{dP_\infty}{dx}. \tag{18}$$

Note, that the pressure gradient controls the growth rate of the boundary layer. A surprising consequence of this condition is that it is satisfied by a power law relation between the free stream velocity and the boundary layer thickness, i.e.,

$$\delta \sim U_\infty^n, \tag{19}$$

where n can, to this point at least, be any nonzero constant. This is the familiar Falker–Skan solutions of laminar boundary layers with pressure gradient discussed by Batchelor [22], but with δ as the variable instead of x. The pressure gradient parameter Λ can be defined as,

$$\Lambda \equiv \frac{\delta}{\rho U_\infty^2 d\delta/dx}\frac{dP_\infty}{dx} = \text{constant} \tag{20}$$

or equivalently

$$\Lambda \equiv -\frac{\delta}{U_\infty d\delta/dx}\frac{dU_\infty}{dx} = \text{constant}. \tag{21}$$

Because equilibrium flows require Λ=constant for similarity, Eq. (21) can be integrated (for nonzero values of Λ) to obtain

$$\delta \sim U_\infty^{-1/\Lambda}. \tag{22}$$

Thus, not only is there a power law relation between the boundary layer thickness and the imposed *free stream* velocity, but the exponent is determined uniquely by the pressure gradient parameter; i.e.,

$$n = -\frac{1}{\Lambda}. \tag{23}$$

Therefore, an ''equilibrium'' boundary layer *in the present approach* is one where Λ=constant and $\delta \sim U_\infty^{-1/\Lambda}$.

2.6 Relations Between the Length Scales and Λ. The goal in this section is to show that the pressure gradient parameter, Λ, can be expressed in terms of the displacement thickness, δ_*, or the momentum thickness, θ. Using the definitions of the momentum thickness, θ, and the displacement thickness, δ_*, it is possible to show that $\theta \sim \delta \sim \delta_*$ according to Castillo [23]. Therefore, the pressure parameter in terms of the momentum thickness is given as,

$$\Lambda_\theta \equiv \frac{\theta}{\rho U_\infty^2 d\theta/dx}\frac{dP_\infty}{dx} = -\frac{\theta}{U_\infty d\theta/dx}\frac{dU_\infty}{dx} = \text{constant}, \tag{24}$$

and in term of the displacement thickness as,

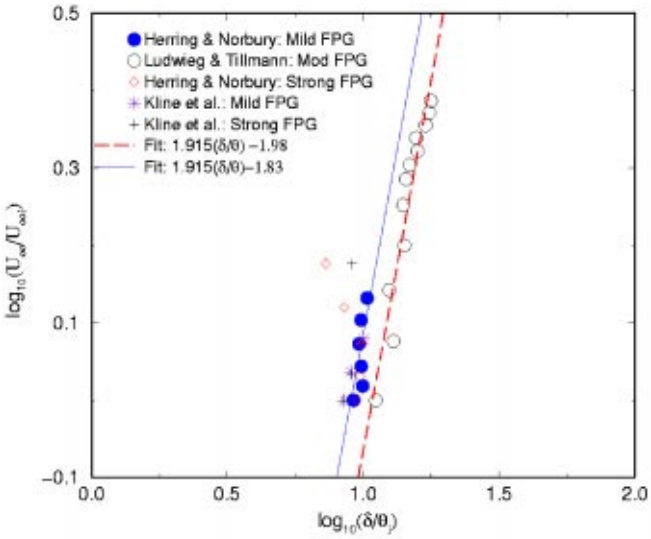

(a) Equilibrium FPG Flow: $\Lambda = -1.92$

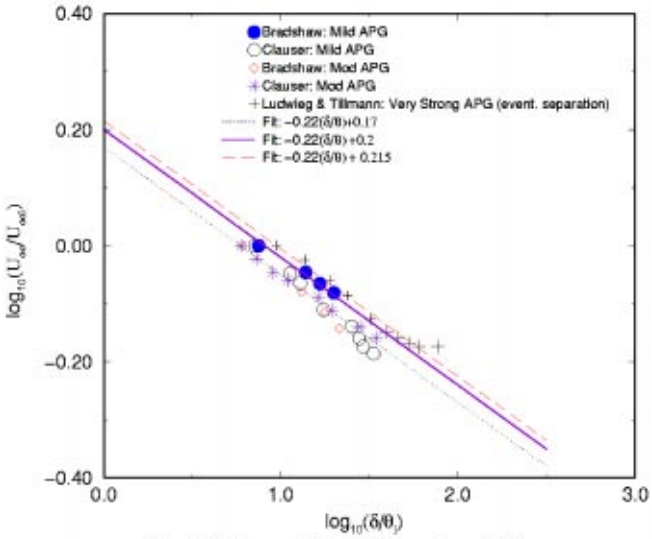

(b) Equilibrium APG Flow: $\Lambda = 0.22$

Fig. 1 Plots of log(U_∞) vs log(δ_{99}) for FPG and APG data. The plot is normalized with $U_{\infty i}$ and θ_i for the first measured location Castillo and George [2].

$$\Lambda_{\delta^*} \equiv \frac{\delta_*}{\rho U_\infty^2 d\delta_*/dx}\frac{dP_\infty}{dx} = -\frac{\delta_*}{U_\infty d\delta_*/dx}\frac{dU_\infty}{dx} = \text{constant}. \tag{25}$$

Since $\theta \sim \delta \sim \delta_*$ exists at least in the limit of Re$\to\infty$, it is easily to obtain

$$\Lambda_\theta \sim \Lambda_{\delta_*} \sim \Lambda. \tag{26}$$

Thus, asymptotically at least, the following relationship

$$U_\infty \sim \delta^{-\Lambda} \sim \delta_*^{-\Lambda_{\delta_*}} \sim \theta^{-\Lambda_\theta} \tag{27}$$

exists.

But what is the relation between these pressure parameters at the finite Reynolds number of experiments? Castillo [24] and Castillo et al. [25] were able to show from experiments that all velocity profiles for nonseparating adverse pressure gradient boundary layers could be collapsed onto a single curve using the scaling proposed by Zagarola/Smits [26], $U_\infty \delta_*/\delta$. They also

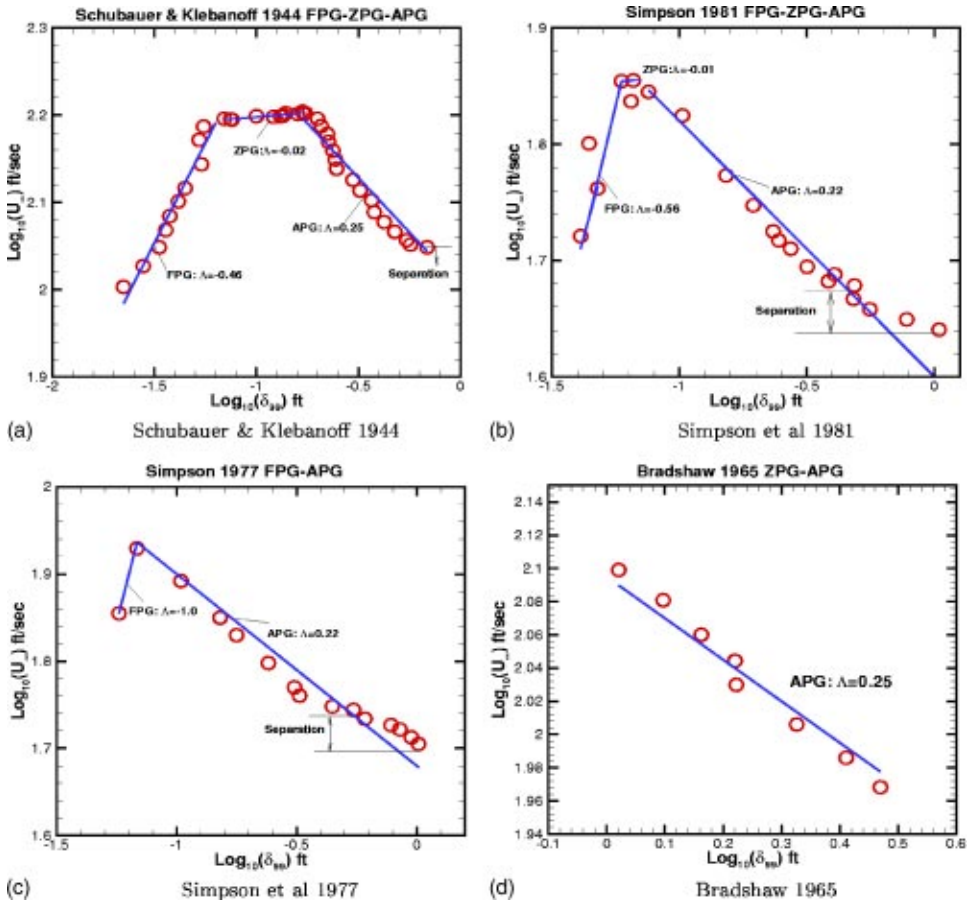

Fig. 2 Nonequilibrium boundary layers: Plots of log(U_∞) vs log(δ_{99})

showed that the same profiles collapsed to a single curve using U_∞ only if the upstream conditions were fixed as shown by Walker and Castillo [27] and Castillo and Walker [28]. Thus all of the variation among different sets of data could be attributed to the upstream conditions. They showed that the ratio δ_*/δ was approximately constant for fixed upstream conditions. Wosnik [29] argued that for ZPG flow, a necessary consequence of the observed success of the Zagarola/Smits scaling was that the ratio $\tilde{\delta}_*/\delta$ be exactly a constant, but the constant differed for different upstream conditions. The length scale $\tilde{\delta}_*$ was calculated like the displacement thickness, but only using data *outside* $y/\delta > 0.1$.

Clearly, an equilibrium flow exists only if the data show a linear relation between the logarithmic length scales and the logarithmic free stream velocity. Also, the slope should correspond to the value of each pressure parameter (i.e., Λ, Λ_θ, and Λ_{δ_*}). Previous investigation by Castillo and George [2] suggested that the pressure parameter is given by $\Lambda \cong 0.22$ for APG equilibrium flow and $\Lambda \cong -1.92$ for FPG equilibrium flow as shown in Fig. 1. Figure 1(a) shows various FPG experimental data of $\log(U_\infty/U_{\infty i})$ versus $\log(\delta/\theta_i)$. In order to compare the results from different experiments, the free stream velocity, U_∞, and the boundary layer thickness, δ, were normalized by $U_{\infty i}$ and θ_i, where the subscript i means the first downstream location. Since all the data (at least away from the entrance and exit) have approximately the same slope, it is clear that $\Lambda \cong -1.92$ is a suitable description of these data even though the strength of the pressure gradient varies from mild, moderate to strong FPG. A similar behavior occurs for APG flows with different strengths of pressure gradient shown in Fig. 1(b). Clearly, $\Lambda \cong 0.22$ describes properly most of equilibrium APG flows. But, can the APG region of a nonequilibrium flow be described by the same value of the pressure parameter, $\Lambda \cong 0.22$? Also, what are the values of the pressure parameter for the FPG region or ZPG region of a nonequilibrium flow?

3 Nonequilibrium Flows

Figures 2 and 3 show some cases of nonequilibrium turbulent boundary layers. Figure 2 displays a nonlinear relationship between $\log(U_\infty)$ vs $\log(\delta)$ corresponding to each experiment described below. Figure 3 shows the same experimental data using the momentum thickness, θ, as the length scale. Consequently, the pressure parameter Λ and Λ_θ are obtained. Notice that θ is an integral value over the whole profile, whereas δ is just a local value at a certain position (i.e., δ_{95} or δ_{99}). Therefore, there are less errors associated with the calculation of θ than δ_{99} or δ_{95}. Notice that Fig. 3 shows a better linear relation between $\log(U_\infty)$ vs $\log(\theta)$ than $\log(U_\infty)$ vs $\log(\delta)$ in Fig. 2.

For the nonequilibrium data from Schubauer and Klebanoff [30] ($1420 < \mathrm{Re}_\theta < 76\,700$), and Simpson et al. [15] ($1380 < \mathrm{Re}_\theta < 18\,700$), the external PG changes from FPG to ZPG and then from ZPG to APG with eventual separation. It is obvious that these flows are not in equilibrium since globally the pressure parameter is not a constant. However, they remain in equilibrium locally. Another interesting fact is that there are three distinctive regions: one for FPG with $\Lambda_\theta = -0.44$ (for Schubauer and Klebanoff [30]), $\Lambda_\theta = -0.8$ (for Simpson et al. [15]); one for ZPG with $\Lambda_\theta = -0.03$ (for Schubauer and Klebanoff [30]), $\Lambda_\theta = 0$ (for Simpson et al. [15]); and one for the APG region with $\Lambda_\theta = 0.22$ for both cases.

A similar behavior occurs for the experimental data from Simpson et al. [31] ($2240 < \mathrm{Re}_\theta < 38\,000$) as shown in Figs. 2(c) and

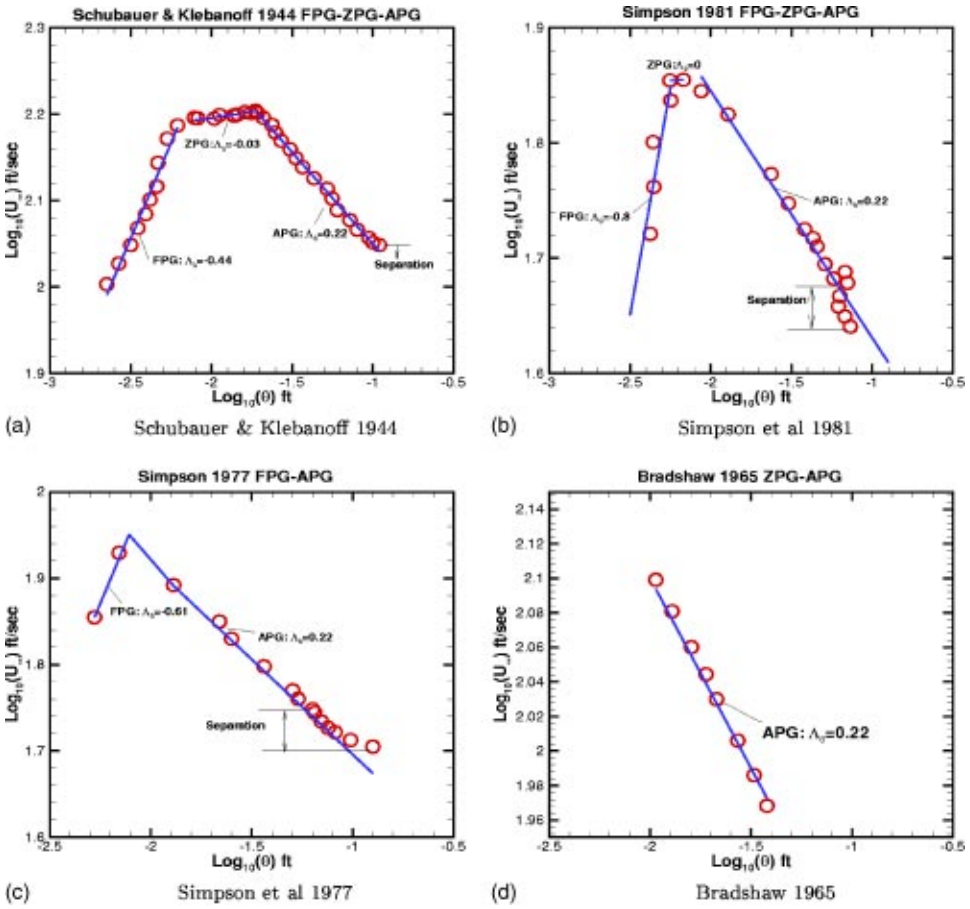

Fig. 3 Nonequilibrium boundary layers: Plots of log(U_∞) vs log(θ)

3(c). For this experimental data, there are two distinctive regions: one for the FPG and one for the APG region. Each region is locally in equilibrium, and is characterized by a constant pressure parameter $\Lambda_\theta = -0.61$ for the FPG region and $\Lambda_\theta = 0.22$ for the APG region, respectively. Meanwhile, for the measurements of relax flow from Bradshaw [12] ($8593 < \mathrm{Re}_\theta < 22\,582$) shown in Figs. 2(d) and 3(d), the flow still remains in equilibrium with $\Lambda_\theta = 0.22$ even when it undergoes a sudden change in pressure gradient from ZPG to APG.

In addition, notice that for the experimental data from Schubauer and Klebanoff [30] and Simpson et al. [15,31], the flow eventually separates and it is indicated in Figs. 2 and 3. Moreover, the experimental data by Simpson et al. [15,31] show a long range of separation.

Clearly, $\Lambda_\theta \cong 0.22$ exists for the APG region of nonequilibrium flows, which is same as the pressure parameter Λ for equilibrium boundary layers as reported by Castillo and George [2]. In addition, Castillo et al. [11] showed that the pressure parameter Λ_θ for separated flows was close to 0.21. Table 1 summarized all results from the equilibrium flows of Castillo and George [2] and Wang [32], the results from separated flows in the analysis of Castillo et al. [11], and the results from the present investigation.

4 Zagarola/Smits Scaling Using Similarity Analysis

Most recently, Castillo and Walker [28] showed that using the Zagarola/Smits scaling [26] for all APG flows, velocity deficit profiles collapse into a single curve, which is an indication that all APG flows (at least equilibrium flows) could be characterized by a single profile. Since the pressure parameter is a constant with $\Lambda_\theta \cong 0.21$ or 0.22 for all equilibrium and nonequilibrium boundary layers with APG, it means that it is possible to represent APG flows for equilibrium boundary layers with one profile and for nonequilibrium flows with the similar approaches.

Table 1 Pressure parameter for equilibrium and nonequilibrium flows

	Experiments	APG
Equilibrium flows Λ_θ: Castillo and George [2], Wang [32]	Bradshaw Mild and Mod APG, Clauser Mild and Mod APG, Ludwig and Tillman strong APG and Mod APG; Skåre and Krogstad APG, Marusic APG, and Elsberry et al. Strong APG.	0.21 ± 0.04
Separation flows Λ_θ: Castillo, Wang and George [11]	Newman strong APG, Alving and Fernholz, Ludwig and Tillman, Simpson et al. 1977, Simpson et al. 1981	0.21 ± 0.01
Nonequilibrium flows Λ_θ:	Schubauer and Klebanoff FPG-ZPG-APG 1944, Bradshaw ZPG-APG 1965, Simpson et al. FPG-APG 1977, Simpson et al. FPG-ZPG-APG 1981	0.22

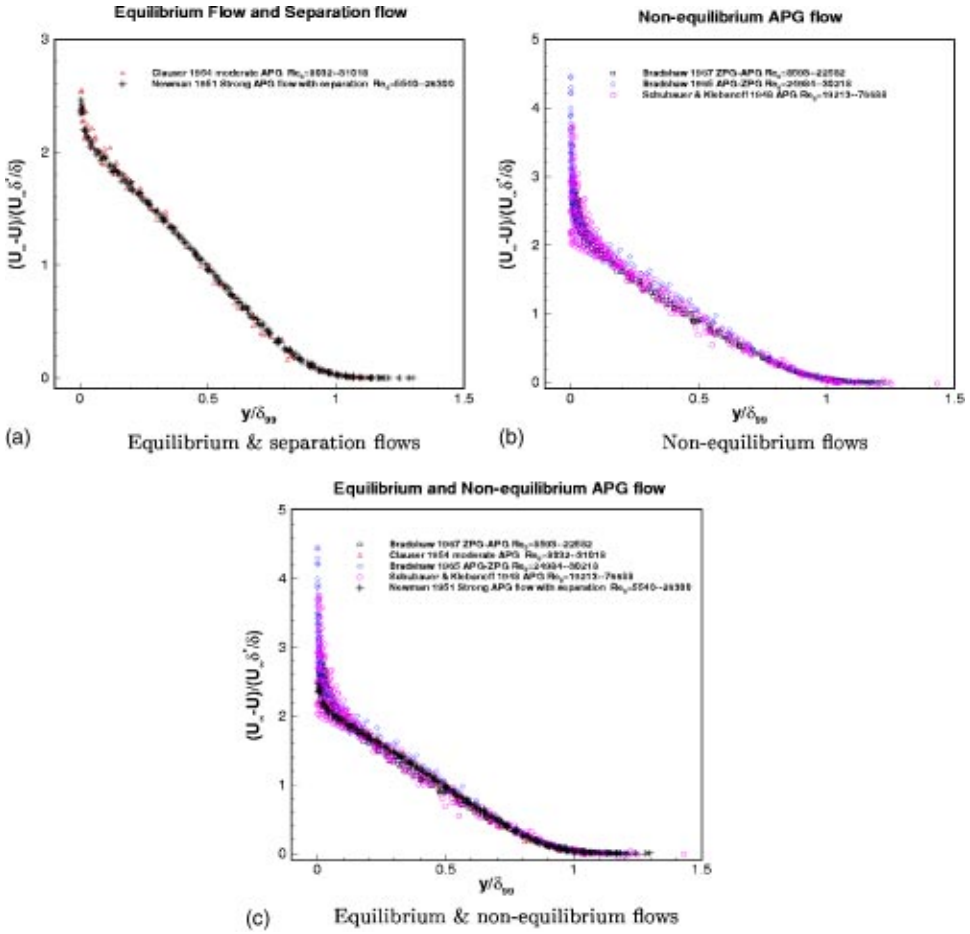

Fig. 4 APG velocity profiles using Zagarola/Smits scaling: nonequilibrium flows and equilibrium flows

Using the similarity ideas outlined in the previous sections, the empirical velocity scaling of Zagarola/Smits [26], $U_{so}=U_\infty(\delta_*/\delta)$, will be derived in this section. It is assumed that the function f_{op} can be expressed as a product of two functions, i.e.,

$$f_{op}(\overline{y},\delta^+;\Lambda;*)=G(\delta^+;*)F_{op\infty}(\overline{y};\Lambda). \tag{28}$$

The first term $G(\delta^+;*)$ contains the dependence on the Reynolds number, δ^+, and the upstream conditions,*, while the second term $F_{op\infty}(\overline{y};\Lambda)$ contains the normalized dependence on the distance from the wall, $\overline{y}$, and the pressure parameter, Λ. This profile, $F_{op\infty}$, represents the asymptotic velocity profile in the limit as $\mathrm{Re}\to\infty$. It is this profile that must reduce to a similarity solution of the RANS equations as required by the asymptotic invariance principle. Hence, this asymptotic profile must be independent of Reynolds number, but its shape may be different for ZPG, FPG, and APG turbulent flows depending on the values of the pressure parameter, Λ. Note, that a similar decomposition of the profile was used by Wosnik and George [33] for ZPG boundary layers.

For the incompressible flow, the displacement thickness is given by

$$U_\infty\delta_*=\int_0^\infty(U_\infty-U)dy. \tag{29}$$

The function, $G(\delta^+,*)$, can be determined by substituting Eq. (28) into the definition for the displacement thickness Eq. (29):

$$[\delta_*]\approx[\delta G]\int_0^\infty F_{op\infty}(\overline{y},\Lambda)d\overline{y}, \tag{30}$$

where a small contribution from the inner layer has been neglected. It is easy to show that Eq. (30) is exact in the limit of the infinite Reynolds number. Now, since Eq. (30) is in similarity variables, the integral part depend on Λ at most, which itself must be independent of x. Therefore, δ and δ_* must have the same x dependence. It follows immediately that,

$$G\propto(\delta_*/\delta). \tag{31}$$

The function G can be combined with Eqs. (4) and (28) to yield the outer velocity scale of Zagarola/Smits, $U_{so}=U_\infty(\delta_*/\delta)$. Note the fact that the Zagarola/Smits scaling contains the Reynolds number dependence term, δ_*/δ, which means that the boundary layer is indeed Reynolds number dependent, exactly as argued by Castillo and George [2] and George and Castillo [21].

Castillo and Walker [28] showed that $\delta_*/\delta\to$constant in the limit of the infinite *local* Reynolds number, but argued that the constant might depend on the upstream conditions. This result obeys the Asymptotic Invariance Principle, which requires that any properly scaled similarity function must be asymptotically independent of Reynolds number. Thus, in the limit as $\delta^+\to\infty$, $G\to G_\infty(*)$ only. Therefore, if the proposed separation of f_{op} is valid, all of the effects of upstream conditions should be removed by the Zagarola/Smits scaling. Or conversely, if the Zagarola/

Smits scaling proves successful, then the separation of solution must be at least approximately valid in the limit as $\delta^+ \to \infty$.

It is important to note that since $\delta_* / \delta \to$ constant as $\delta^+ \to \infty$, the Zagarola/Smits scaling, $U_\infty(\delta_* / \delta)$, reduces to the GC scaling, U_∞, in the same limit. Thus, both the U_∞ and $U_\infty \delta_* / \delta$ scalings are consistent with the equilibrium similarity analysis. The latter, of course, also removes the upstream and local Reynolds number effects, if the hypothesis of Eq. (28) is correct. This can be contrasted with the analysis of Clauser [1] which requires that $U_\infty \delta_* / \delta \sim u_*$. Obviously, if this classical result is correct, there should be no difference between the ZS-scaled profiles and those using u_*, contrary to the finding of Zagarola and Smits [26].

Figure 4 shows the velocity profiles normalized by the Zagarola/Smits scaling for the APG experimental data of Bradshaw [34] initially at ZPG developing into a sudden moderate APG, the Bradshaw [12] data for relaxed flow, the Clauser [1] data for moderate APG, the Newman [35] experimental data with eventual separation and finally the Schubauer and Klebanoff [30] data for nonequilibrium flow. Notice that the experimental data from Clauser [1] and Newman [35] are in equilibrium. However, the other three measurements are nonequilibrium flows because the pressure parameter is not a constant. Also, for the measurement by Schubauer and Klebanoff [30], the flow eventually separates. In spite of all the differences, the APG velocity profiles collapse into nearly one single curve. Figure 4(a) shows some of the profiles from equilibrium boundary layers as given by Castillo and George [2]. Clearly, there is a single velocity profile for the equilibrium APG flow while normalized by the Zagarola/Smits scaling. The nonequilibrium deficit profiles are shown in Fig. 4(b). Notice that there is nearly a single profile for these nonequilibrium flows as described by the single pressure parameter Λ_θ. Figure 4(c) includes the equilibrium and nonequilibrium APG flows and the profiles follow nearly only one curve too.

5 Summary and Conclusions

Using similarity analysis for nonequilibrium flows, the main results of the present investigation can be summarized as:

1. Nonequilibrium boundary layers, defined as $\Lambda_\theta \neq$ constant, remain in equilibrium, but only locally with a pressure parameter, $\Lambda_\theta =$ constant, for each region.

2. Each local region is characterized by a constant pressure parameter. For the FPG region of a nonequilibrium flow, the pressure parameter varies from -0.44 up to -0.8. For the ZPG region of a nonequilibrium flow, the pressure parameter is nearly zero. The APG region of the current nonequilibrium flow has the value of about $\Lambda_\theta \cong 0.22$, which is the same as the pressure parameter for the equilibrium flow in terms of Λ.

3. It has been found that nearly a single velocity profile exists for all APG flows including equilibrium and nonequilibrium flows when scaled by the Zagarola/Smits scaling.

In conclusion, flows that are exposed to sudden external changes in pressure gradient (PG) still remain in a local equilibrium. Moreover, the similarity theory proves to be a powerful tool to understand PG flows and their tendency to remain in equilibrium state.

Acknowledgment

The authors are very grateful to the reviewers for their insightful comments and suggestions which result in an improved paper.

Nomenclature

R_{so} = outer Reynolds stress scale for $\langle uv \rangle$
R_{sou} = outer Reynolds stress scale for $\langle u^2 \rangle$
R_{sov} = outer Reynolds stress scale for $\langle v^2 \rangle$
U_{so} = outer velocity scale
U_∞ = free stream velocity
$U_\infty - U$ = mean velocity deficit
$U_\infty \delta_* / \delta$ = Zagarola/Smits scaling
u_* = friction velocity, $u_* = \sqrt{\tau_w / \rho}$
δ = boundary layer thickness, e.g., δ_{99}
δ_* = displacement thickness, $\int_0^\infty (1 - U/U_\infty) dy$
δ^+ = local Reynolds number dependence, $\delta u_* / v$
Λ = pressure parameter, $(\delta / \rho U_\infty^2 d\delta / dx)(dP_\infty / dx)$
Λ_{δ_*} = pressure parameter, $(\delta_* / \rho U_\infty^2 d\delta_* / dx)(dP_\infty / dx)$
Λ_θ = pressure parameter, $(\theta / \rho U_\infty^2 d\theta / dx)(dP_\infty / dx)$
θ = momentum thickness, $\int_0^\infty (U/U_\infty)(1 - U/U_\infty) dy$
$*$ = unknown upstream conditions
PG = pressure gradient
ZPG = zero pressure gradient
FPG = favorable pressure gradient
APG = adverse pressure gradient

References

[1] Clauser, F. H., 1956, "The Turbulent Boundary Layer," Adv. Appl. Mech., **4**, pp. 1–54.
[2] Castillo, L., and George, W. K., 2001, "Similarity Analysis for Turbulent Boundary Layer With Pressure Gradient: Outer Flow," AIAA J., **39**, pp. 41–47.
[3] Bradshaw, P., 1967, "The Turbulent Structure of Equilibrium Boundary Layers," J. Fluid Mech., **29**, pp. 624–645.
[4] Townsend, A. A., 1956, The Structure of Turbulent Shear Flow, Cambridge University Press, London.
[5] Rotta, J. C., 1962, "Turbulent Boundary Layers in Incompressible Flow," *Progr. Aeronautical Sci.*, Vol. 2., Pergamon, New York.
[6] Townsend, A. A., 1976, *The Structure of Turbulent Shear Flow*, 2nd ed., Cambridge, London.
[7] East, L. F., and Sawyer, W. G., 1979, "An Investigation of the Equilibrium Turbulent Boundary Layers," Turbulent Boundary Layers: Experiment Theory and Modelling, AGARD, CP-271, 6.1–6.19.
[8] Skåre, P. E., and Krogstad, P., 1994, "A Turbulent Equilibrium Boundary Layer Near Separation," J. Fluid Mech., **272**, pp. 319–348.
[9] Kader, B. A., and Yaglom, A. M., 1977, "Similarity Treatment of Moving-Equilibrium Turbulent Boundary Layers in Adverse Pressure Gradients," J. Fluid Mech., **89**, pp. 305–342.
[10] Coles, D. E., and Hirst, E. A., 1968, Computational of Turbulent Boundary Layers-1968 AFOSR-IFP-Stanford Conference, Vol. II.
[11] Castillo, L., Wang, X., and George, W., 2003, "Separation Criterion for Turbulent Boundary Layers via Similarity Analysis," J. Fluid Eng. **126**, pp. 297–304.
[12] Bradshaw, P., and Ferriss, D., 1965, "The Response of a Retarded Equilibrium Turbulent Boundary Layer to the Sudden Removal of Pressure Gradient," NPL Aero. Rep., 1145.
[13] Tennekes, H., and Lumley, J. L., 1972, *A First Course in Turbulence*, MIT, Cambridge, MA.
[14] Simpson, R. L., 1989, "Turbulent Boundary-Layer Separation," Annu. Rev. Fluid Mech., **21**, pp. 205–234.
[15] Simpson, R. L., and Chew, Y. T., 1981, "The Structure of a Separating Turbulent Boundary Layer. Part 1. Mean Flow and Reynolds Stresses," J. Fluid Mech., **113**, pp. 23–51.
[16] Simpson, R. L., and Chew, Y. T., 1981, "The Structure of a Separating Turbulent Boundary Layer. Part 2. Higher-Order Turbulence Results," J. Fluid Mech., **113**, pp. 53–73.
[17] Alving, A. E., and Fernholz, H. H., 1995, "Turbulence Measurements Around a Mild Separation Bubble and Down-Stream of Reattachment," J. Fluid Mech., **322**, pp. 279–328.
[18] Elsberry, K., Loeffler, J., Zhou, M. D., and Wygnanski, I., 2000, "An Experimental Study of a Boundary Layer That is Maintained on the Verge of Separation," J. Fluid Mech., **423**, pp. 227–262.
[19] Goldstein, S., "*Modern Developments in Fluids Dynamics*," 1965, Dover, New York.
[20] George, W. K., 1995, "Some New Ideas for Similarity of Turbulent Shear Flows," *Turbulence, Heat and Mass Transfer*, edited by K. Hanjalic and J. C. F. Pereira, Begell House, New York.
[21] George, W. K., and Castillo, L., 1997, "Zero-Pressure-Gradient Turbulent Boundary Layer," Appl. Mech. Rev., **50**, pp. 689–729.
[22] Batchelor, G. K., 1966, *An Introduction to Fluid Dynamics*, Cambridge Univeristy Press, London.
[23] Castillo, L., 1997, "Similarity Analysis of Turbulent Boundary Layers," Ph.D. dissertation, SUNY Buffalo, Buffalo, NY.
[24] Castillo, L., 2000, "Application of Zagarola/Smits Scaling in Turbulent Boundary Layers With Pressure Gradient," Advances in Fluids Mechanics 3, Montreal, Canada, May 24–26, 2000, edited by M. Rahman and C. A. Brebbia, pp. 275–288.
[25] Castillo, L., Walker, D. J., and Wosnik, M., 2000, "The Effect of the Upstream Conditions on the Mean Velocity Deficit of Turbulent Boundary Layers," Fluids 2000 Conference and Exhibit paper #AIAA2000–2309. Denver, Colorado, June 19–22.
[26] Zagarola, M. V., and Smits, A. J., 1998, "Mean-Flow Scaling of Turbulent Pipe Flow," J. Fluid Mech., **373**, pp. 33–79.
[27] Walker, D., and Castillo, L., 2002, "Effect of the Upstream Conditions on

Turbulent Boudnary Layers,'' AIAA J., **40**, pp. 2540–2542.
[28] Castillo, L., and Walker, D., 2002, ''The Effect of the Upstream Conditions on the Outer Flow of Turbulent Boundary Layers,'' AIAA J., **40**, pp. 1292–1299.
[29] Wosnik, M., 2000, ''On Wall-Bounded Turbulent Flows,'' Ph.D. thesis, SUNY Buffalo, Buffalo, NY.
[30] Schubauer, G. B., and Klebanoff, P. S., 1951, ''Investigation of Separation of the Turbulent Boundary Layer,'' NACA Report 1030, NACA Technical Note 2133.
[31] Simpson, R. L., and Strickland, J. H., 1977, ''Features of a Separating Turbulent Boundary Layer in the Vicinity of Separation,'' J. Fluid Mech., **79**, pp. 553–594.
[32] Wang, X., ''Similarity Analysis for Turubulent Boundary Layers Subject to Pressure Gradient and Heat Transfer,'' 2003, Ph.D. dissertation, Rensslaer Polytechnic Institute, Troy, NY.
[33] Wosnik, M., and George, W. K., 2000, ''Reconciling the Zagarola/Smits Scaling With the George/Castillo Theory for the Zero Pressure Gradient Turbulent Boundary Layer,'' 38th AIAA Ann. Atg. Reno, NV, Jan 10–13.
[34] Bradshaw, P., 1967, ''The Response of a Constant-Pressure Turbulent Boundary Layer to the Sudden Application of an Adverse Pressure Gradient,'' NPL Aero. Rept. 1219.
[35] Newman, B. G., 1951, ''Some Contributions to the Study of the Turbulent Boundary Near Separation,'' Austr. Dept. Supply Rep. ACA-53.

Very Large-Scale Structures and Their Effects on the Wall Shear-Stress Fluctuations in a Turbulent Channel Flow up to $Re_\tau = 640$

Hiroyuki Abe[1]

Hiroshi Kawamura[†]

Department of Mechanical Engineering
Tokyo University of Science,
Noda-shi, Chiba 278-8510, Japan

Haecheon Choi
School of Mechanical and Aerospace
Engineering, Seoul National University,
Seoul 151-744, Korea

Direct numerical simulation of a fully developed turbulent channel flow has been carried out at three Reynolds numbers, 180, 395, and 640, based on the friction velocity and the channel half width, in order to investigate very large-scale structures and their effects on the wall shear-stress fluctuations. It is shown that very large-scale structures exist in the outer layer and that they certainly contribute to inner layer structures at high Reynolds number. Moreover, it is revealed that very large-scale structures exist even in the wall shear-stress fluctuations at high Reynolds number, which are essentially associated with the very large-scale structures in the outer layer. [DOI: 10.1115/1.1789528]

1 Introduction

The behavior of fluctuations of the wall flow variables in a turbulent boundary layer flow or in a turbulent channel flow is of fundamental interest in many applications involving drag, noise, and heat transfer. Among these, the wall pressure fluctuations have been intensively investigated by many researchers. The scaling law in the wall pressure power spectrum and the functional dependence of $p_{w_{\mathrm{rms}}}/\tau_w$ on the Reynolds number have been fairly well established as discussed by Choi and Moin [1] and Farabee and Casarella [2], where p_w is the wall pressure fluctuations, τ_w is the mean shear stress at the wall, and the subscript rms denotes the root-mean-square value.

Unlike the wall pressure fluctuations, however, only limited information about the wall shear-stress fluctuations has been available, mainly because of measurement difficulties associated with the spatial resolution and frequency response of the probe and also with heat conduction to the wall. Therefore, in the experiment, a lot of difficulties have been encountered in determining the scaling law in the wall shear-stress (τ_1 and τ_3) power spectra and the functional dependence of $\tau_{1_{\mathrm{rms}}}/\tau_w$ or $\tau_{3_{\mathrm{rms}}}/\tau_w$ on the Reynolds number (see Jeon et al. [3]), where $\tau_1 = \mu\partial u'/\partial y|_w$ and $\tau_3 = \mu\partial w'/\partial y|_w$ are the two components of the wall shear-stress fluctuations, u' and w' are the streamwise and spanwise velocity fluctuations, respectively, y is the distance from the wall, and μ the dynamic viscosity. Moreover, the studies focusing on the wall flow variables from direct numerical simulation (DNS) have been limited mostly to $Re_\tau = u_\tau\delta/\nu = 180$ [1,3,4], where u_τ is the friction velocity, δ the channel half width, and ν the kinematic viscosity.

The importance of the contribution from the outer layer to the inner layer has been indicated by several experimental studies in wall-bounded turbulence at high Reynolds numbers [5–10]. These studies revealed that large-scale or very large-scale motions in the outer layer affect the near-wall region and that this effect increases with increasing Reynolds number. For example, Bullock et al. [5] performed an experiment in a turbulent pipe flow at $Re_\tau = 2600$ and found from the premultiplied frequency spectra of streamwise velocity fluctuations that large scale (low frequency) turbulence fluctuations extend over the majority of the radial region. Naguib and Wark [6] also found that the contribution of the outerlayer-structures to the streamwise velocity fluctuations increases with increasing Reynolds number. Hites [7] conducted an experiment in a turbulent boundary layer at $Re_\tau \approx 1500-6000$ and indicated that the premultiplied frequency spectra of streamwise velocity fluctuations show a bimodal distribution in the range of $38 < y^+ < 100$. Kim and Adrian [8] measured the streamwise velocity in a turbulent pipe flow at $Re_\tau = 1058$, 1984, and 3175 and obtained the premultiplied wave number spectrum of the streamwise velocity fluctuations derived from the frequency spectrum using Taylor's hypothesis. They showed that the premultiplied wave number spectra have a bimodal distribution and the characteristic wavelength of the large-scale mode increases through the logarithmic layer. Moreover, they found that very large-scale motions corresponding to approximately 12–14 times the pipe radius exist in that region. Österlund [9] observed the effect from the outer layer even in the wall flow variables such as the wall shear stress by investigating the two-point correlation. Metzger and Klewicki [10] investigated the near-wall turbulence quantities such as the streamwise velocity and its gradient for a turbulent boundary layer. They found that the influence of the low frequency components, i.e., large-scale structures, on the turbulence statistics increases with increasing Reynolds number.

Owing to the recent rapid increase in computer power, DNSs of turbulent channel flow have been performed for relatively high Reynolds numbers (see, for example, Antonia and Kim [11], Moser et al. [12], and Abe et al. [13]), where the Reynolds-number effect on the root-mean-square velocity and vorticity fluctuations inside the channel was carefully studied. However, since these studies were performed with relatively small computational boxes, the effects of very large-scale structures in the outer layer on turbulence quantities were not clearly examined.

More recently, with the aid of huge computer memory, DNSs with large computational boxes have been carried out by del Álamo and Jiménez [14,15] and Abe and Kawamura [16]. del Álamo and Jiménez [14,15] indicated that very large-scale structures of streamwise velocity fluctuations span most of the channel height and penetrate into the buffer region. Also, Jiménez et al. [17] showed that, when the flow in the outer layer is artificially

[1]Present Affiliation: Japan Aerospace Exploration Agency, Chofu, Tokyo 182-8522, Japan.

[†]Electronic mail: kawa@rs.noda.tus.ac.jp

Contributed by the Fluids Engineering Division for publication in the JOURNAL OF FLUIDS ENGINEERING. Manuscript received by the Fluids Engineering Division April 14, 2003; revised manuscript received February 15, 2004. Associate Editor: T. B. Gatski.

Table 1 Computational box size, grid points, spatial resolution, and sampling time period

Re_τ	180	395	640
$L_x \times L_y \times L_z$	$12.8\delta \times 2\delta \times 6.4\delta$	$12.8\delta \times 2\delta \times 6.4\delta$	$12.8\delta \times 2\delta \times 6.4\delta$
$L_x^+ \times L_y^+ \times L_z^+$	$2304 \times 360 \times 1152$	$5056 \times 790 \times 2528$	$8192 \times 1280 \times 4096$
$N_x \times N_y \times N_z$	$256 \times 128 \times 256$	$512 \times 192 \times 512$	$1024 \times 256 \times 1024$
$\Delta x^+, \Delta y^+, \Delta z^+$	$9.00, 0.20 \sim 5.90, 4.50$	$9.88, 0.15 \sim 6.52, 4.94$	$8.00, 0.15 \sim 8.02, 4.00$
Tu_m/L_x	49	50	14

removed, the near-wall turbulence structures become infinitely long, but the averaged turbulence quantities do not noticeably change in the near-wall region.

In the present study, we have performed DNS of turbulent channel flow at three Reynolds numbers, Re_τ=180, 395, and 640, with a large computational box ($L_x \times L_z = 12.8\delta \times 6.4\delta$) in order to include very large-scale structures existing in the outer layer. The computational box size of our previous study [13] for Re_τ=640 was $L_x \times L_z = 6.4\delta \times 2\delta$ [$4096 \times 1280(\nu/u_\tau)^2$], which contained sufficient numbers of near-wall (more than ten) streaky structures in the spanwise direction, but was not large enough to include sufficient numbers of very large-scale structures in the outer layer. Accordingly, the difference between the results from the present and previous computations should be attributed to the effects of the very large-scale structures existing in the outer layer. Hence, the purpose of the present paper is to investigate the very large-scale structures and their effects on the turbulence quantities, especially on the wall shear-stress fluctuations, from root-mean-square values, power spectra and instantaneous flow fields.

2 Numerical Procedure

The flow in the present study is a fully developed turbulent channel flow driven by a streamwise mean pressure gradient. In the present computation, a fractional step method proposed by Dukowics and Dvinsky [18] is adopted, and a semi-implicit time advancement is taken (the Crank–Nicolson method for the viscous terms with wall-normal derivatives and the second-order Adams–Bashforth method for the other terms). For the spatial discretization, a fourth-order central difference scheme proposed by Morinishi et al. [19] is adopted in the streamwise and spanwise directions, and the second-order central difference scheme is used in the wall-normal direction. Further details of the present numerical method can be found in Abe et al. [13].

As pointed out by Jiménez [20], very large-scale structures existing near the center of the channel have a spanwise size of 2δ. Recently, del Alamo and Jiménez [14,15] reported that very large-scale structures of $2–5\delta$ in length in the streamwise direction exist in the outer layer at a relatively high Reynolds number of Re_τ =550. They also indicated that at least ten washout times are needed to obtain stationary statistics related to large scales. Therefore, irrespective of the Reynolds number, the size of the present computational box ($L_x \times L_y \times L_z$) was chosen to be $12.8\delta \times 2\delta \times 6.4\delta$ in the streamwise (x), wall-normal (y), and spanwise (z) directions, respectively, in order to include quite a few very large-scale structures in our computational box. The integration time for statistical sampling was set to be more than ten washout times for all the cases. The computational box size, number of grid points (N_x, N_y, N_z), spatial resolution ($\Delta x, \Delta y, \Delta z$) and sampling time period (Tu_m/L_x) are given in Table 1, where u_m denotes the bulk mean velocity. Accuracy at the present spatial resolution has already been confirmed by Kawamura et al. [21], Abe et al. [13], and Abe and Kawamura [16].

3 Results and Discussion

3.1 Very Large-Scale Structures

3.1.1 Effects of Very Large-Scale Structures on Mean Flow Variables and Turbulence Quantities. Before we discuss the behavior of very large-scale structures in the outer layer, we examine their effects on the mean flow variables and the root-mean-square velocity fluctuations for Re_τ=640 by comparing the present results with those from our previous study [13], in which a smaller computational box was used for the same Reynolds number. In wall-bounded turbulence, one of the most important quantities is the friction coefficient. It is defined as

$$C_f = \frac{\tau_w}{\frac{1}{2}\rho u_m^2}. \tag{1}$$

The friction coefficient in the present study for Re_τ=640 is $C_f = 5.47 \times 10^{-3}$, whereas the one in the previous study [13] for Re_τ=640 was $C_f = 5.42 \times 10^{-3}$. The difference is less than 1%.

The mean velocity distribution has also been investigated and is shown in Fig. 1. The experimental result of Hussain and Reynolds [22] and the DNS results of Moser et al. [12] in a turbulent channel flow at Re_τ=590 and of Spalart [23] in a turbulent boundary layer at $\mathrm{Re}_\tau \approx 650$ are also included for comparison. Note that a superscript+denotes a variable normalized by wall units. It can be seen from Fig. 1 that agreement between the present and previous results is excellent. Other mean quantities were also compared, but their differences were also very small.

The root-mean-square values of the streamwise, wall-normal and spanwise velocity fluctuations, u'_{rms}, v'_{rms}, and w'_{rms}, for Re_τ=640 are compared with those of the previous studies [12,13,15,22] and are shown in Fig. 2. Again, agreement with the data at the same Reynolds number [13,22] is excellent except for

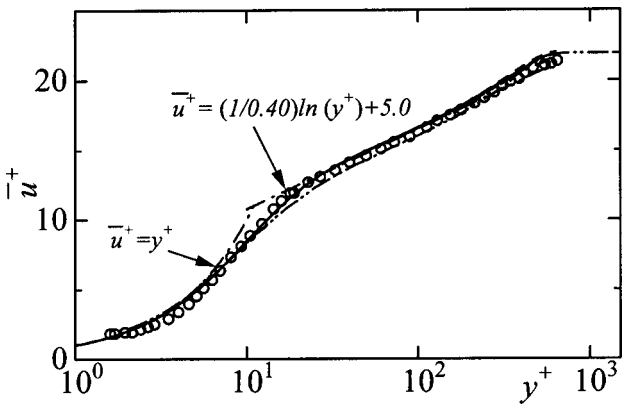

Fig. 1 Mean velocity distribution for Re_τ=640. (——), present; (— — —), Abe et al. [13]; (- - -); Moser et al. [12] for Re_τ=590; (–···–), Spalart [23] for $\mathrm{Re}_\tau \approx 650$; (○) Hussain and Reynolds [22] for Re_τ=640.

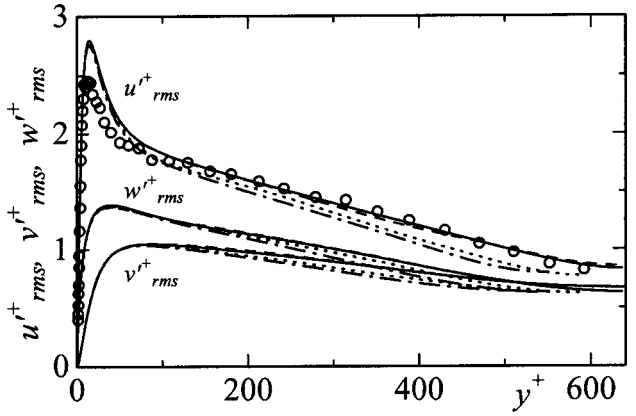

Fig. 2 Root-mean-square velocity fluctuations for Re_τ=640. (—), present; (— — —), Abe et al. [13]; (- - -), Moser et al. [12] for Re_τ=590; (–·–), del Alamo and Jiménez [15] for Re_τ=550; (○), Hussain and Reynolds [22] for Re_τ=640.

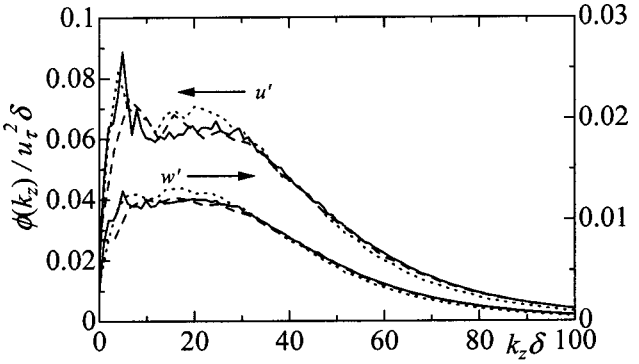

Fig. 4 One-dimensional spanwise wave number power spectra of u' and w' for Re_τ=640 at y^+=5.38 normalized by u_τ and δ in linear scales. (——), present; (— — —), Abe et al. [13]; (- - -), Moser et al. [12] for Re_τ=590 y^+=5.34.

the near-wall streamwise velocity fluctuations, where the measurement with a hot wire is very difficult. Moreover, the present result agrees well with those of the other previous DNS studies at slightly different Reynolds numbers [12,15] in the near-wall region, although a small difference is found in the outer layer because of the difference in Re_τ.

Thus, one can conclude that the effect of the computational box size, in other words, very large-scale structures, is negligibly small for the mean flow variables and the second-order turbulence statistics within the limit of the Reynolds numbers investigated here.

We further investigate the effect of very large-scale structures on energy spectra in the inner and outer layers. The energy spectra of u', v', and w' are defined as

$$\int_0^\infty \phi(k_x)dk_x = \int_0^\infty \phi(k_z)dk_z = u'^2_{\rm rms}, v'^2_{\rm rms} \text{ or } w'^2_{\rm rms}, \qquad (2)$$

where $\phi(k_x)$ and $\phi(k_z)$ are the energy spectra, and k_x and k_z are the wave numbers in the x and z directions, respectively. Figure 3 shows the energy spectra of the velocity fluctuations for Re_τ =640 at $y^+\approx 5$ together with those from the previous studies [12,13]. Excellent agreement with the previous results is observed at intermediate and high wave numbers, whereas a small but noticeable difference is found at low wave numbers, especially for the spanwise energy spectra of u' and w'. The low-wave number behavior of the spanwise energy spectra of u' and w' is shown in Fig. 4, which is scaled with u_τ and δ and is drawn in linear scales. In Fig. 4, a large local peak is clearly observed in the spanwise spectra at a low wave number from the present data, whereas a less prominent peak is observed in the previous studies [12,13]. This difference is closely associated with very large-scale structures in the outer layer. Also, we see a number of small local peaks at low wave numbers, which could be due to statistical noise, as will be discussed later. The present comparison suggests that the computational box size used in this study should be required to capture the effect of the outer layer structures on the near-wall flow behavior. Nevertheless, when the energy spectra are integrated for the whole range of wave numbers, the differences in the mean-square values are ~3%. In summary, within the Reynolds number range investigated, the very large-scale structures in the outer layer have little effect on the time-averaged near-wall turbulence quantities, but they clearly exist even in the near-wall region and contribute to the energy at low wave numbers.

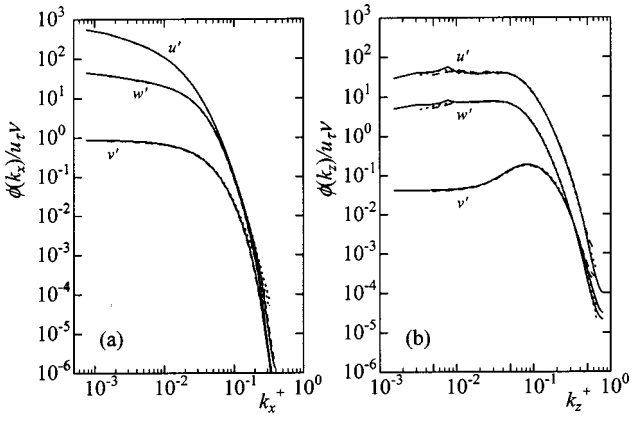

Fig. 3 One-dimensional wave number energy spectra of velocity fluctuations for Re_τ=640 at y^+=5.38 in wall units: (a) streamwise wave number; (b) spanwise wave number. (——), present; (— — —), Abe et al. [13]; (- - -), Moser et al. [12] for Re_τ=590 at y^+=5.34.

An examination of very large-scale structures in the outer layer using DNS requires a large computational box. In this region, the longest and widest structures are expected for the streamwise and spanwise velocities, respectively. This is because streamwise and spanwise directions are not constrained in the present configuration. Although the present computational box was chosen to be as large as possible, the box size at Re_τ=640 ($L_x \times L_z = 12.8\delta \times 6.4\delta$) is half in the streamwise and spanwise directions of that of del Alamo and Jiménez [14,15] at Re_τ=550 ($L_x \times L_z = 8\pi\delta \times 4\pi\delta$). Therefore, the validity of the present computational box size for Re_τ=640 must be investigated. Figure 5 shows the streamwise premultiplied spectrum of u' and spanwise premultiplied spectrum of w' in the outer layer for Re_τ=640, together with those of del Alamo and Jiménez [14] for Re_τ=550. Here, the premultiplied spectra are defined as

$$\int_0^\infty k_x\phi(k_x)d(\log\lambda_x) = \int_0^\infty k_z\phi(k_z)d(\log\lambda_z) = u'^2_{\rm rms} \text{ or } w'^2_{\rm rms}, \qquad (3)$$

where $\lambda_x(=2\pi/k_x)$ and $\lambda_z(=2\pi/k_z)$ are the streamwise and spanwise wavelengths, respectively. In spite of the slight differences in the wall-normal locations where the spectra are obtained and the Reynolds numbers adopted, agreement between the present study and that of del Alamo and Jiménez [14] is very good, i.e., the peak values of the premultiplied spectra and the

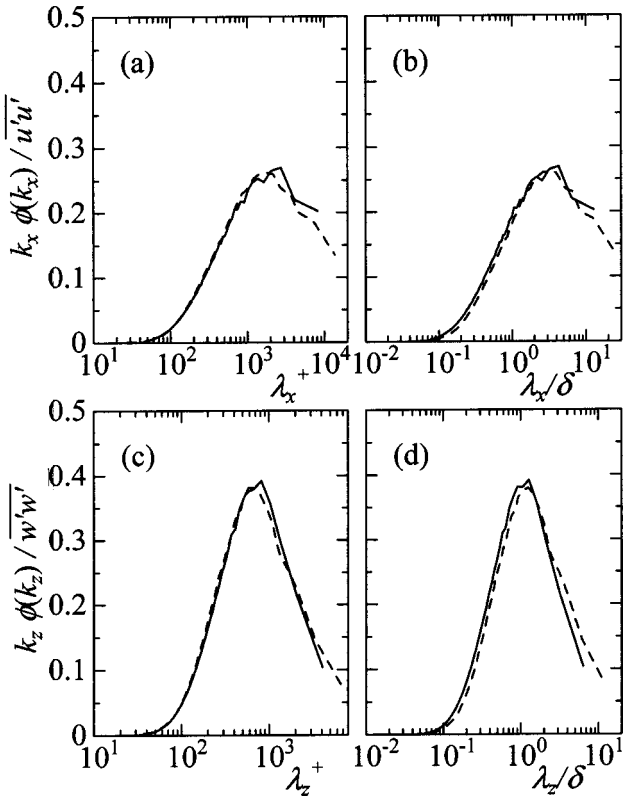

Fig. 5 Streamwise and spanwise premultiplied spectra of u' and w', $k_x\phi(k_x)/\overline{u'u'}$ and $k_z\phi(k_z)/\overline{w'w'}$, in the outer layer: (a), (b) $k_x\phi(k_x)/\overline{u'u'}$; (c), (d) $k_z\phi(k_z)/\overline{w'w'}$. (——), present for $Re_\tau=640$ at $y/\delta=0.47$ ($y^+=298.2$); (– – –), del Alamo and Jiménez [14] for $Re_\tau=550$ at $y/\delta=0.5$ ($y^+=275$).

energy at short wavelengths agree well with those of del Álamo and Jiménez [14]. Moreover, no artificial energy contamination is observed at long wavelengths.

Considering that the area under the premultiplied spectrum represents the mean-square velocity fluctuations as shown by Eq. (3), the present streamwise box size is not still enough to contain all the large-scale contributions [Figs. 5(a) and 5(b)], whereas the present spanwise box size seems to be quite sufficient [Figs. 5(c) and 5(d)]. It can be roughly estimated from Figs. 5(a) and 5(b) that one needs at least 100δ as a proper streamwise box size in order to obtain zero energy at the longest streamwise wavelength, at which point the simulation becomes very expensive.

3.1.2 Spanwise Very Large Scales. The large-scale structures are often referred to as the large-scale motions (LSMs) existing in the outer layer of the flow (see, for example, Falco [24]; Brown and Thomas [25]), and many experimental studies on the LSMs have been conducted for turbulent pipe, boundary layer and channel flows (see, for example, Kim and Adrian [8]; Adrian et al. [26]; Liu et al. [27]). Moreover, Kim and Adrian [8] found that very large-scale motions (VLSMs), which are much longer than the LSMs exist in the outer layer in a turbulent pipe flow. These studies mainly focused on the behavior of the LSMs or the VLSMs in the streamwise direction. On the other hand, some experimental studies have been performed on the spanwise organization of near-wall turbulence (see, for example, Smith and Metzler [28]), but little information is available for the spanwise behavior of large- or very large-scale structures in the outer layer from experiments (see, for example, Nakagawa and Nezu [29]). Therefore, we investigate here the behavior of the VLSMs in the spanwise direction with the aid of DNS.

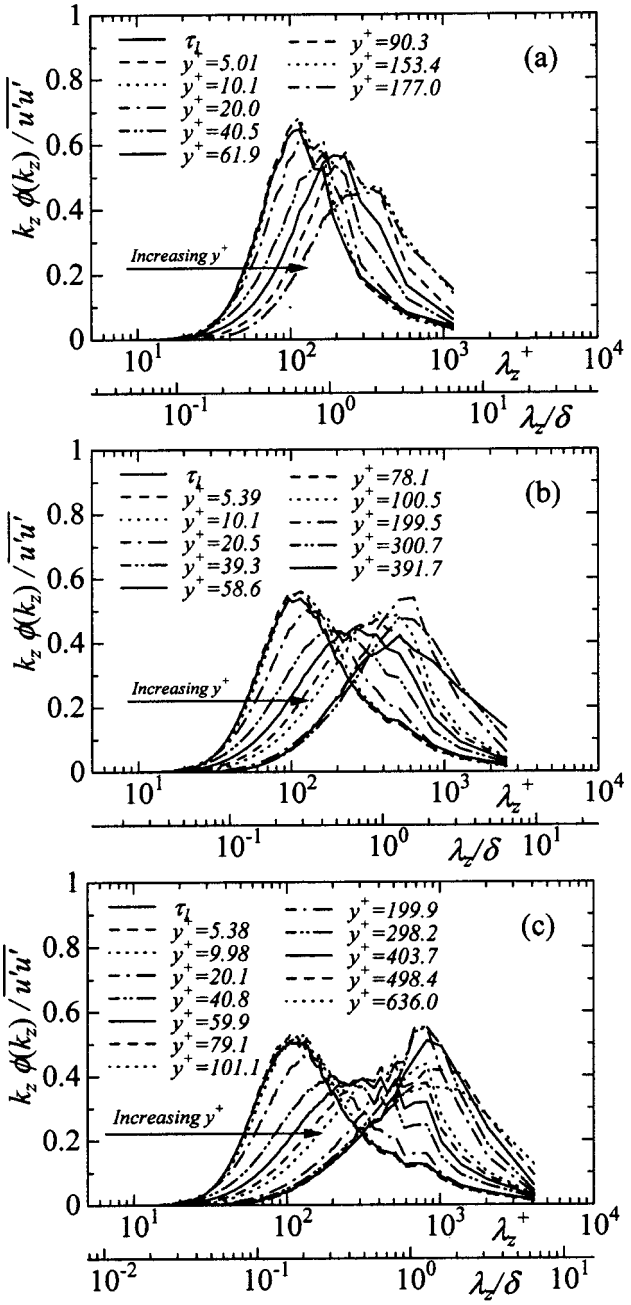

Fig. 6 Spanwise premultiplied energy spectra of the streamwise velocity fluctuations $k_z\phi(k_z)/\overline{u'u'}$: (a) $Re_\tau=180$; (b) $Re_\tau=395$; (c) $Re_\tau=640$

Figure 6 shows the spanwise pre-multiplied energy spectra of the streamwise velocity fluctuations for $Re_\tau=180$, 395, and 640. The spanwise premultiplied spectra of τ_1 are also included in this figure. Note that the peak location in the premultiplied spectrum corresponds to the wavelength of the energy-containing eddy (Perry et al. [30]). In the near-wall region (up to $y^+=10$), the premultiplied spectra of u' are nearly identical to that of τ_1 for each Reynolds number and their peaks are found at $\lambda_z^+\approx100$. Moving away from the wall, the peak position in the spectra of u' shifts to a longer wavelength. With increasing Reynolds number, the small and large scales corresponding to the energy-containing eddies in the near-wall and outer layer regions, respectively, are more clearly separated, and broad peaks appear between these two regions (e.g., at $y^+=60-100$ for $Re_\tau=640$). Jiménez [20] pointed out that a very large-scale structure with a spanwise wavelength of

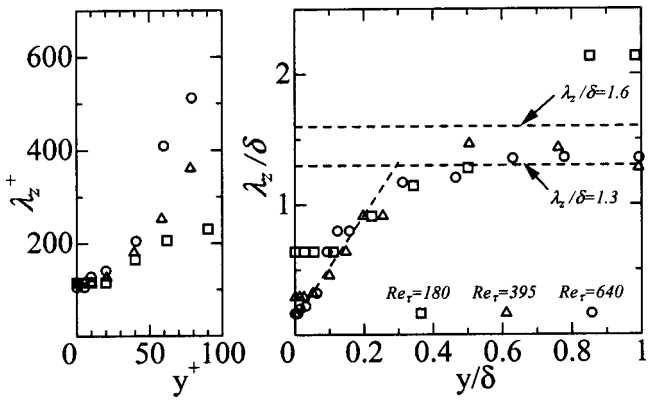

Fig. 7 Spanwise wavelengths of the most energetic eddies obtained from the premultiplied energy spectra of u' for Re_τ =180, 395, and 640

around 2δ exists at the midheight to the channel center. The present result indicates the same trend with a more definite determination of its wavelength as $1.3–1.6\delta$ (see the peak location for $y/\delta=0.5$). It is interesting to notice that the near-wall premultiplied spectra show a local peak at the wavelength corresponding to the very large-scale structures for $Re_\tau=640$ but not for $Re_\tau=180$, indicating that the VLSMs in the outer layer contribute more to the inner layer structures with increasing Reynolds number.

The spanwise wavelengths of the most energetic eddies (MEW), for all three Reynolds numbers ($Re_\tau=180$, 395, and 640) are obtained from Fig. 6 and are presented in Fig. 7. Note that when the premultiplied spanwise spectrum shows a clear peak we have taken the most energetic wavelength, while when the spectrum shows a broad peak we have computed a least-square interpolating polynomial in the region where the spectrum shows the most energetic power. The behavior of the wavelength of the most energetic eddy can be divided into three regions from Fig. 7. In the central region ($0.3<y/\delta<1$), the MEW stays essentially at a constant value of $1.3–1.6\delta$. From $y^+=20$ to $y/\delta\simeq0.3$, the MEW is linearly proportional to the wall-normal distance from the wall, agreeing well with the experimental result of Nakagawa and Nezu [29] and the DNS result of del Álamo and Jiménez [15]. This lower bound ($y^+=20$) seems to be scaled well with wall units, while the upper bound ($y/\delta\approx0.3$) may be scaled with the outer variable δ. Finally, in the wall vicinity ($y^+<20$), the MEW remains constant at $\lambda_z^+\approx100$ that is the well-known spanwise separation distance of the near-wall streaky structures [28].

3.1.3 Visualization of Very Large-Scale Structures. To visualize the VLSMs in the outer layer, iso-surfaces of the instantaneous streamwise velocity fluctuations normalized by their own rms value at each y^+ for $Re_\tau=180$ and 640 are shown in Fig. 8. This normalization is done because when the streamwise velocity fluctuations are normalized by the friction velocity, the structures emerge only in the wall vicinity due to the strong intensity there, and thus no structure can be captured in the outer region. It is seen from Fig. 8 that the VLSMs appear in the outer layer for both Reynolds numbers and as expected the high Reynolds number case shows a wider range of scales. The high- and low-speed regions appear with a spanwise spacing of about $1.3–1.6\delta$ and with a streamwise extent larger than 3δ. This streamwise structure corresponds to those obtained from the measurements in pipe and channel flows (Kim and Adrian [8]; Liu et al. [27]) and from the DNS of a channel flow (del Álamo and Jiménez [14,15]).

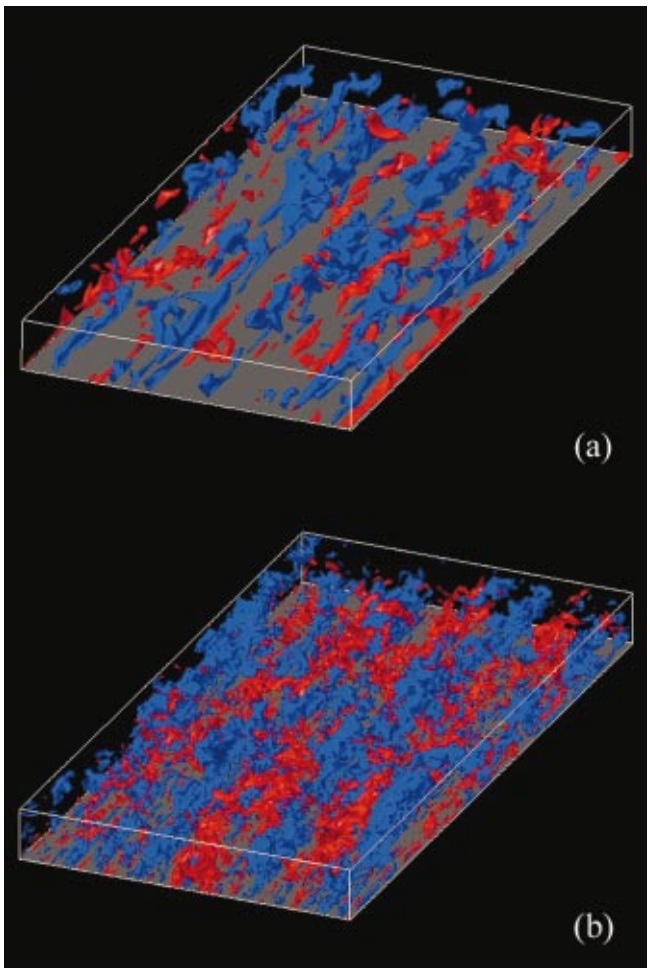

Fig. 8 Iso-surfaces of the instantaneous streamwise velocity fluctuations normalized by their own rms value at each y^+ for $Re_\tau=180$ and 640: (a) $Re_\tau=180$; (b) $Re_\tau=640$ (red), $u'/u'_{rms}>1.75$; (blue), $u'/u'_{rms}<-1.75$. The boxes visualized here are $12.8\delta\times\delta\times6.4\delta$ in the streamwise, wall-normal and spanwise directions, corresponding to those of $2304\times180\times1152(\nu/u_\tau)^3$ and $8192\times640\times4096(\nu/u_\tau)^3$ for $Re_\tau=180$ and 640, respectively.

4 Wall Shear-Stress Fluctuations

4.1 Root-Mean-Square Values. The rms values of the wall shear-stress fluctuations (τ_1 and τ_3) normalized by τ_w for $Re_\tau=180$, 395, and 640 are given in Fig. 9, together with those obtained from DNS [3,11,31–34] and experiment [35] for the channel flow. The present result agrees very well with those of other DNS and experiment. The increase in $\tau_{1_{rms}}$ from $Re_\tau=180-640$ is smaller (~11%) than that of $\tau_{3_{rms}}$ (~31%), which agrees well with the finding by Moser et al. [12] that w_{rms} shows a larger variation than u_{rms} as Re_τ increases. Especially, the value of $\tau_{1_{rms}}$ seems to be nearly saturated at around $0.4\tau_w$ at $Re_\tau=640$. This can also be observed from the literature. That is, Alfredsson et al. [36] carried out an experiment using a hot-film probe and specially designed sensors for the channel and boundary layer flows and reported that $\tau_{1_{rms}}=0.40\tau_w$. Recently, Fischer et al. [35] conducted an experiment using a laser Doppler anemometry and reported that the limiting value of $\tau_{1_{rms}}$ tends to approach $0.40\tau_w$ at relatively high Reynolds number. More recently, Metzger and Klewicki [10] performed an experiment using a hot-wire probe in a turbulent boundary layer at high Reynolds numbers and indicated that the wall value of the spanwise vorticity fluctuations, i.e., $\tau_{1_{rms}}$, does

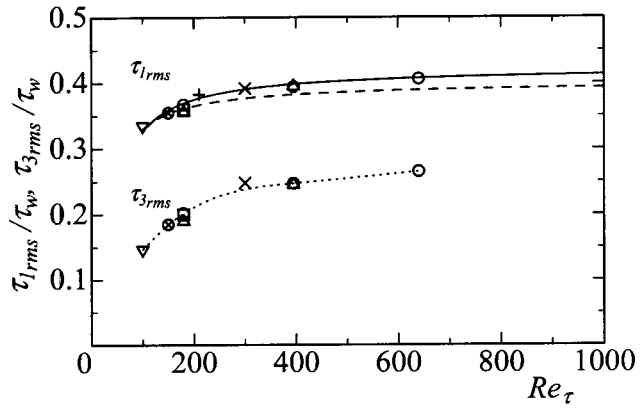

Fig. 9 Variations of the rms wall shear-stress fluctuations as a function of the Reynolds number. (○) present study; (▽), Kuroda et al. [31]; (+), Gilbert and Kleiser [32]; (⊗), Kuroda et al. [33]; (△), Antonia and Kim [11]; (×), Günther et al. [34]; (□), Jeon et al. [3]; (——), fitting for $\tau_{1_{rms}}/\tau_w$ by Fischer et al. [35] from DNS; (— — —), fitting for $\tau_{1_{rms}}/\tau_w$ by Fischer et al. [35] from experiments; (- - -), fitting for $\tau_{3_{rms}}/\tau_w$.

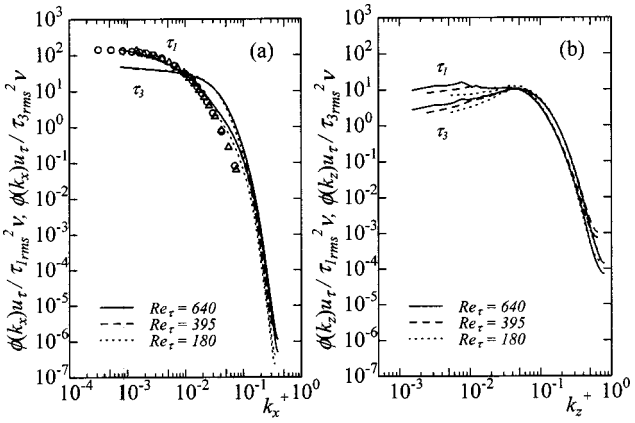

Fig. 10 One-dimensional wave number power spectra of τ_1 and τ_3 normalized by the mean-square values: (a) streamwise wave number; (b) spanwise wave number. (○), Wietrzak and Lueptow [37] (Re_τ=896); (△), Nepomuceno and Lueptow [38] (Re_τ=751).

not vary with the Reynolds number when the Reynolds number is sufficiently high, although they showed a logarithmic increase in the peak value of u'. Also, recent DNSs of turbulent channel flow indicated that $\tau_{1_{rms}}=0.405\tau_w$ at $Re_\tau=590$ [12] and $0.409\tau_w$ at $Re_\tau=640$ [13]. From the past and present results, therefore, it may be concluded that $\tau_{1_{rms}}$ is about $0.4\tau_w$ at sufficiently high Reynolds numbers.

Conducting another investigation on the Reynolds-number dependence of the wall shear-stress fluctuations as the mean-square values, i.e., $\tau^2_{1_{rms}}$ and $\tau^2_{3_{rms}}$, the increase in $\tau^2_{1_{rms}}$ and $\tau^2_{3_{rms}}$ from $Re_\tau=180$ to 640 is 0.030 and 0.029, respectively. Interestingly, almost the same increase is obtained in the streamwise and spanwise directions.

4.1.1 Power Spectra. The power spectra of τ_1 and τ_3 are defined as

$$\int_0^\infty \phi(k_x)dk_x = \int_0^\infty \phi(k_z)dk_z = \tau^2_{1_{rms}} \text{ or } \tau^2_{3_{rms}}, \qquad (4)$$

where $\phi(k_x)$ and $\phi(k_z)$ are the power spectra. As was shown in Fig. 9, the mean-square values, i.e., integrations of the spectra over the wave number, increase with increasing Reynolds number. Accordingly, the streamwise- and spanwise-wave number spectra of τ_1 and τ_3 are normalized by their own mean-square values and are shown in Fig. 10. The frequency spectra measured by Wietrzak and Lueptow [37] (Re_τ=896) and Nepomuceno and Lueptow [38] (Re_τ=751) are also plotted for comparison, using Taylor's hypothesis with a convection velocity of $0.53U_o$ [3], where U_o is the freestream velocity or channel centerline velocity. Agreement between the present result and the measurement results [37,38] is satisfactory, although there exists a discernible difference at high wave numbers. This difference may be caused by the fact that the convection velocity associated with the energy containing eddy (i.e., low wave number) is used for all wavenumbers.

In Fig. 10(a), the streamwise wave number power spectra of τ_1 and τ_3 show good collapse at the whole range of wave numbers for the three Reynolds numbers, meaning that the contributions from small, intermediate, and large scales in the streamwise direction to the rms values are essentially the same, at least for the Reynolds number range investigated. In contrast, the spanwise wave number power spectra of τ_1 and τ_3 show collapse at small scales (i.e., at large wave numbers) only, whereas they exhibit an increase in power at large scales (i.e., at small wave numbers) with increasing Reynolds number [Fig. 10(b)]. This indicates that the contribution from large scales in the spanwise direction to the rms values increases with increasing Reynolds number. Moreover, it is interesting to note that local peaks are observed at low wave numbers for Re_τ=395 and 640 and the corresponding wave numbers in walls units become smaller with increasing Reynolds number, indicating that very large-scale structures should exist in τ_1 and τ_3 for high Reynolds numbers.

In order to examine the behavior of these local peaks, the spanwise spectra of τ_1 and τ_3 normalized with τ_w and δ are redrawn for all three Reynolds numbers at $k_z\delta<100$ in linear scales and are shown in Fig. 11. In this figure, there appears a clear local peak at $k_z\delta\simeq5$ in the spectra of τ_1 at Re_τ=395 and 640, where the wavelength corresponding to this wave number is 1.3δ. Moreover, this local peak is identical with that of the near-wall spanwise premultiplied spectra of u', which is closely associated with the most energetic peak in the outer layer [see Figs. 6(b) and 6(c)]. These results indicate that the VLSMs in the outer layer maintain a certain influence even upon the wall flow variables such as the wall shear stresses at high Reynolds number cases. Moreover, it can be seen in Fig. 11 that the local peak in the spanwise spectra of τ_1 becomes more prominent with increasing Reynolds number. At Re_τ=640, an excess of the power at the local peak over the averaged power in the nearly constant range, $k_z\delta=10-30$, is about 3% of the total power. In contrast, integrating the spectra over the range of wave numbers, $k_z\delta=0-10$, in which the spectra

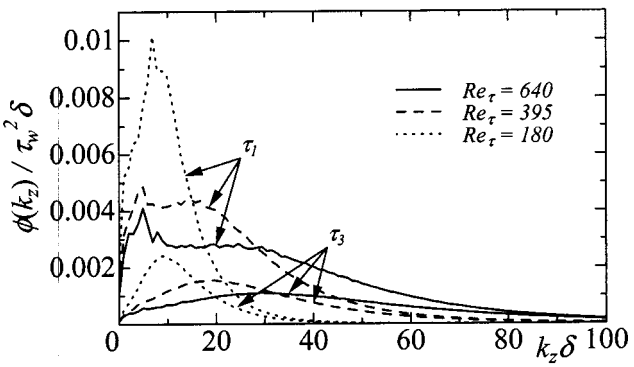

Fig. 11 One-dimensional spanwise wave number power spectra of τ_1 and τ_3 normalized by τ_w and δ in linear scales

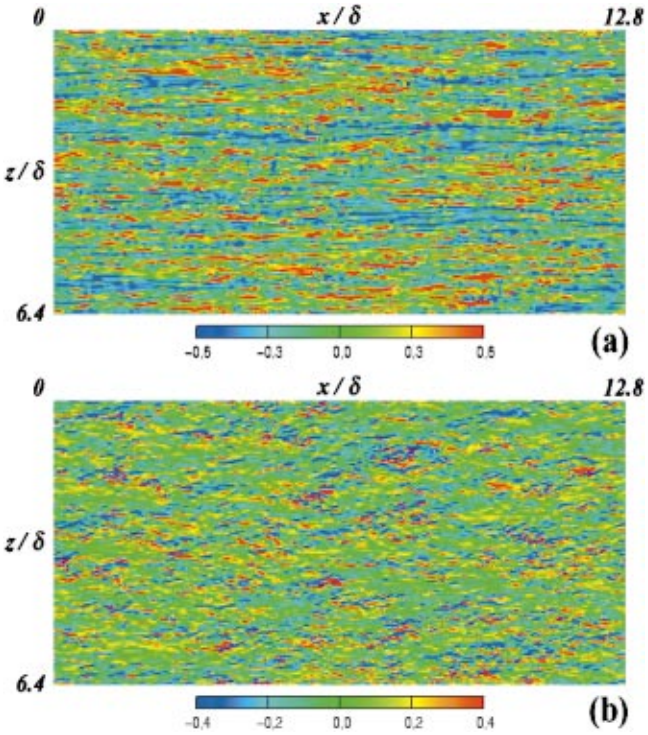

Fig. 12 Contours of the instantaneous wall shear-stress fluctuations for Re_τ=640; (a) τ_1; (b) τ_3

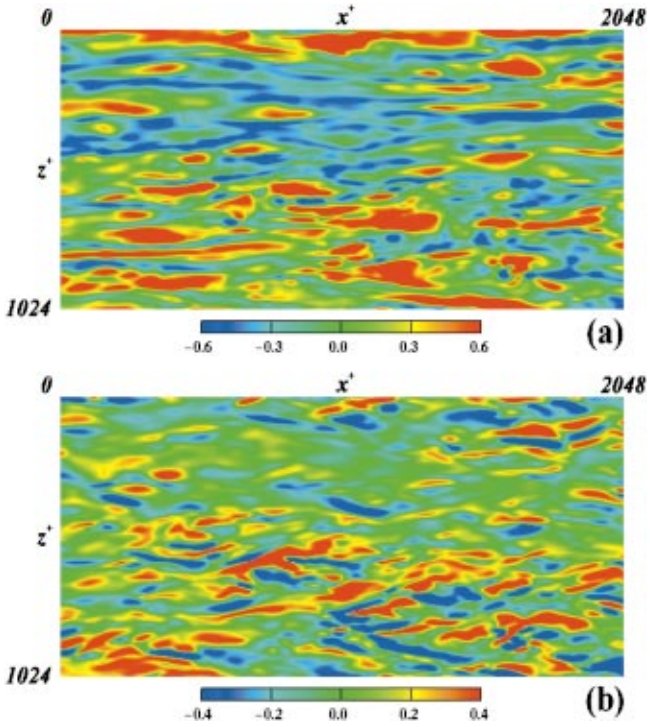

Fig. 13 Enlarged view of Fig. 12: (a) τ_1; (b) τ_3

show the local peak, the power contained in the range of the wave numbers is about 20% of the total power, suggesting that the importance of the low wave numbers in the spanwise direction increases with increasing Reynolds number. At the low Reynolds number of Re_τ=180, we see local peaks at $k_z\delta \simeq 7$ and 9, which correspond to $\lambda_z/\delta \simeq 0.9$ and 0.7, respectively. The latter wavelength is very close to the streak spacing at this Reynolds number. It is not so clear why we have the first peak at $k_z\delta \simeq 7$ rather than at $k_z\delta \simeq 5$ for Re_τ=180. We consider the first peak at $k_z\delta \simeq 7$ to be the result of a low Reynolds-number effect because the separation of two scales (streaky structure near the wall and very large-scale structure in the outer layer) is not so evident at Re_τ=180 as shown in Fig. 6(a). On the other hand, a clear local peak is not observed at $k_z\delta \simeq 5$ either in the spectra of τ_3 in Fig. 11, because the power at this spanwise wave number is much smaller than the maximum power at $k_z^+ = 0.06$ corresponding to the streak spacing unlike the case of τ_1 at high Reynolds number [see Fig. 10(b)].

One may wonder if these local peaks in Figs. 10 and 11 come from insufficient time averaging, and they could be due to the statistical noise. In order to investigate this issue, we performed a long time integration for the case of Re_τ=395, where the sampling period is $50L_x/u_m$. Indeed, with longer time averaging, the spectra become smoother but the large local peak still exists.

4.1.2 Instantaneous Flow Fields. In this section, we show from instantaneous flow fields that there exist very large-scale patterns in the wall shear-stress fluctuations and the corresponding length scales are closely associated with the peaks at low wave numbers in the spanwise spectra in Fig. 10(b).

Figure 12 shows the contours of the instantaneous wall shear-stress fluctuations for Re_τ=640 in the full computational domain. In the case of τ_1, a few (or several) streaks of negative τ_1's (blue color) are packed together and make a group in space (called a "negative dominant" region, hereafter). Moreover, this dense clustering of negative τ_1's clearly exhibits a very large-scale pattern.

In the case of τ_3 [Fig. 12(b)], there exist two substantially different regions: one of them consists of dense clustering of strong positive and negative τ_3's (called an "active" region, hereafter) and the other is a region of weak τ_3's (called an "inactive" region, hereafter). A careful inspection of the instantaneous flow fields indicates that the active region of τ_3 is closely associated with the group of positive τ_1's and the inactive one occurs where the group of negative τ_1's exists (see Fig. 13 for the enlarged view).

To inspect the very large-scale pattern of τ_1 in more detail, a filtering procedure is applied to the instantaneous field shown in Fig. 12(a). A top-hat filter defined as

$$\tilde{\tau}_1(x,z) = \frac{1}{4\ell_x\ell_z}\int_{-\ell_x}^{\ell_x}\int_{-\ell_z}^{\ell_z}\tau_1(x+\xi,z+\zeta)\,d\zeta\,d\xi \qquad (5)$$

is employed, where a tilde denotes a filtered value. Referring to Komminaho et al. [40], the streamwise filter length ℓ_x is chosen as the integral scale and the spanwise filter length ℓ_z is roughly the same length as the first zero-crossing point of the spanwise two-point correlation. The filtered instantaneous field with $\ell_x^+ = 232$ and $\ell_z^+ = 44$ is shown in Fig. 14(a), where very large-scale patterns with a spanwise spacing of about $1.3–1.6\delta$ (about 1000 in wall units for Re_τ=640) are more clearly illustrated. This spanwise spacing corresponds to the spanwise wave number of $k_z\delta = 4–5$ (or $k_z^+ = 0.006–0.008$) at which the spectrum of τ_1 shows a local peak at Re_τ=640 (see Fig. 11). In order to examine the interaction between the inner and outer layers, the top view of the instantaneous low-speed regions in the outer layer ($u'/u'_{rms} < -1.75$) shown in Fig. 8(b) is superimposed on the filtered τ_1 shown in Fig. 14(a). The resultant figure is given in Fig. 14(b). It is clear from this figure that the negative dominant regions of τ_1 are mostly overshadowed by the low-speed regions in the VLSMs.

To examine this point more quantitatively, we introduce a function called an overlap ratio (OLR). In the OLR, variables ϕ and ψ are binarized to be either 0 or 1 based on a certain threshold, and the binarized ones are represented by $\hat{\phi}$ and $\hat{\psi}$. Then, the OLR is defined as the ratio of the overlapping area between $\hat{\phi}$ and $\hat{\psi}$ to the area of either $\hat{\phi}$ or $\hat{\psi}$:

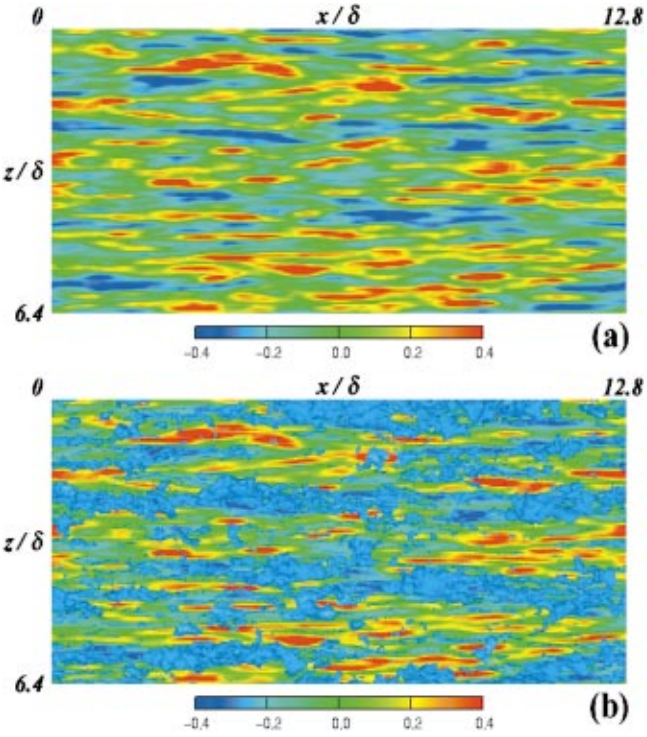

Fig. 14 Contours of the filtered τ_1 and top view of the low-speed regions in the VLSMs for Re_τ=640: (a) filtered τ_1; (b) top view of the low-speed regions in the outer layer ($u'/u'_{rms} < -1.75$ denoted as blue iso-surfaces) shown in Fig. 8(b), which is superimposed on the filtered τ_1 shown in Fig. 14(a)

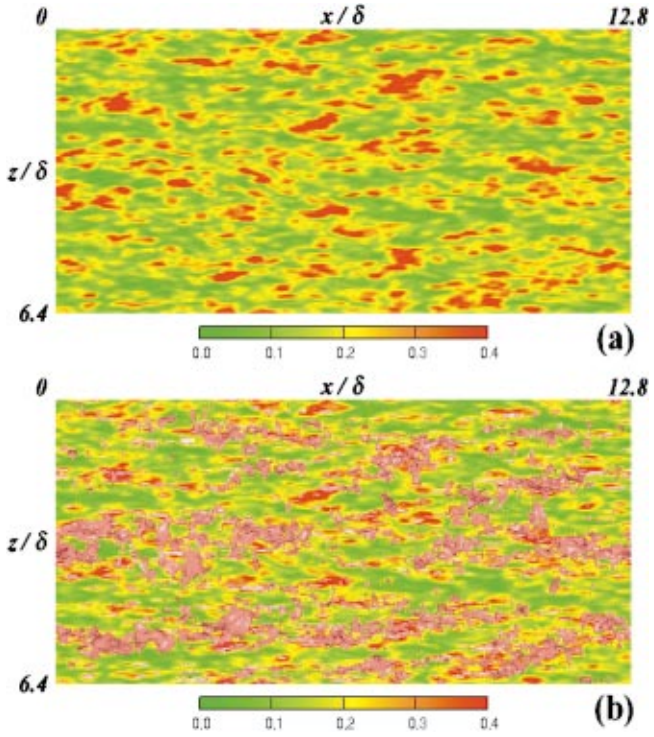

Fig. 15 Contours of the filtered τ_3 and top view of the high-speed regions in the VLSMs for Re_τ=640: (a) filtered τ_3; (b) top view of the high-speed regions in the outer layer ($u'/u'_{rms} > 1.75$ denoted as red iso-surfaces) shown in Fig. 8(b), which is superimposed on the filtered τ_3 shown in Fig. 15(a)

$$\mathrm{OLR}(\phi<\phi_0 \text{ or } \phi>\phi_0 | \psi<\psi_0 \text{ or } \psi>\psi_0) = \sum \hat{\phi}\hat{\psi} / \sum \hat{\psi}^2, \tag{6}$$

where ϕ_0 and ψ_0 are the threshold values. We obtain the OLR between the filtered τ_1 (i.e., $\tilde{\tau}_1$) and the projected area of high- or low-speed regions in the VLSMs. First, $\tilde{\tau}_1$ is binarized with a threshold of $\tilde{\tau}_{1_0}/\tilde{\tau}_{1_{rms}} = \pm 1.5$. Next, the projected and binarized high- and low-speed regions are obtained through the following operations: (i) u' is binarized with respect to $u'_0/u'_{rms} = \pm 1.75$, (ii) the binarized values $\hat{u}'$ are integrated along the wall-normal direction up to the channel center, and (iii) the integrated values are rebinarized to be either 0 or 1 with a threshold of 1. This procedure reveals that the OLR between the low-speed region in the VLSMs and the negative region of τ_1 is $\mathrm{OLR}(u' < -1.75u'_{rms} | \tilde{\tau}_1 < -1.5\tilde{\tau}_{1_{rms}}) = 0.76$, whereas the OLR between the low-speed region in VLSMs and the positive region of τ_1 is $\mathrm{OLR}(u' < -1.75u'_{rms} | \tilde{\tau}_1 > 1.5\tilde{\tau}_{1_{rms}}) = 0.20$. Moreover, it is found that the OLR between the high-speed region in the VLSMs and the positive region of τ_1 is $\mathrm{OLR}(u' > 1.75u'_{rms} | \tilde{\tau}_1 > 1.5\tilde{\tau}_{1_{rms}}) = 0.65$, whereas the OLR between the high-speed region in VLSMs and the negative region of τ_1 is $\mathrm{OLR}(u' > 1.75u'_{rms} | \tilde{\tau}_1 < -1.5\tilde{\tau}_{1_{rms}}) = 0.19$. These results clearly indicate that the very large-scale structure observed in τ_1 is essentially associated with the VLSMs existing in the outer layer of the flow.

Now we will examine the active and inactive regions of τ_3 in detail. To emphasize the difference between these two regions, the filtering procedure is again applied to τ_3. In the filtering of τ_3, its absolute value is filtered to avoid possible cancellation of τ_3 because its positive and negative values lie quite close to each other. The filtered instantaneous field with $\ell_x^+ = 80$ and $\ell_z^+ = 28$ is shown in Fig. 15(a), where the active (red color) and inactive (green color) regions are more clearly seen for τ_3. From Figs. 14(a) and 15(a), one can easily notice that the active region of τ_3 corresponds much more often to the positive dominant region of τ_1 than the negative one of τ_1. The OLR between the positive region of τ_1 and the active region of τ_3 is $\mathrm{OLR}(\tilde{\tau}_1 > 1.0\tilde{\tau}_{1_{rms}} | |\tilde{\tau}_3| > 1.5\tilde{\tau}_{3_{rms}}) = 0.43$, whereas the OLR between the negative region of τ_1 and the active region of τ_3 is $\mathrm{OLR}(\tilde{\tau}_1 < -1.0\tilde{\tau}_{1_{rms}} | |\tilde{\tau}_3| > 1.5\tilde{\tau}_{3_{rms}}) = 0.02$, which clearly supports the visual impression mentioned above.

To examine the relation between τ_3 and the VLSMs, the top view of the high-speed regions in the outer layer ($u'/u'_{rms} > 1.75$) shown in Fig. 8(b) is superimposed on the filtered τ_3 shown in Fig. 15(a), and the result is given in Fig. 15(b). The OLR between the high-speed region in the VLSMs and the active region of τ_3 is $\mathrm{OLR}(u' > 1.75u'_{rms} | |\tilde{\tau}_3| > 1.5\tilde{\tau}_{3_{rms}}) = 0.55$, whereas the OLR between the high-speed region in VLSMs and the inactive region of τ_3 is $\mathrm{OLR}(u' > 1.75u'_{rms} | |\tilde{\tau}_3| < 0.3\tilde{\tau}_{3_{rms}}) = 0.16$. Thus, the active region of τ_3 mostly corresponds to the high-speed region in the VLSMs.

5 Summary and Conclusions

In this study, we obtained the mean flow variables, root-mean-square (rms) values, power spectra, and two-point correlations from direct numerical simulation of turbulent channel flow at Re_τ=180, 395, and 640, and examined the very large-scale structures and their effects on the wall shear-stress fluctuations.

It was shown that very large-scale structures with a spanwise spacing of 1.3–1.6δ exist in the outer layer and that they certainly contribute to the inner layer structures for high Reynolds number. Moreover, it was found that the effects of the very large-scale structures in the outer layer on the mean flow variables and the turbulence quantities are negligibly small for the Reynolds num-

ber range investigated, whereas those of the very large-scale structures on the spanwise premultiplied spectra at long wavelengths are significant.

The effects of the very large-scale structures were also found even in the wall shear-stress fluctuations. That is, the local peaks appeared in the spanwise wave number power spectra of τ_1 and τ_3 at low wave numbers for $\mathrm{Re}_\tau=395$ and 640 and they became more prominent with increasing Reynolds number, indicating that very large-scale structures exist even in τ_1 and τ_3 for high Reynolds number.

The instantaneous flow field showed that the very large-scale structures appear not only in the outer layer but also at the wall for high Reynolds number. That is, the very large-scale motions with a streamwise extent of more than 3δ and a spanwise spacing of $1.3-1.6\delta$ existed in the outer layer, and very large-scale structures with dense clustering flow patterns appeared in the wall shear-stress fluctuations. The filtering procedure disclosed the very large-scale structures in τ_1 and τ_3 more clearly. Notably, it was indeed found in τ_1 that the very large-scale structures with a spanwise spacing of about $1.3-1.6\delta$ exist. This spanwise spacing corresponds to the spanwise wave number of $k_z\delta=4-5$ at which the spectrum of τ_1 shows a local peak at $\mathrm{Re}_\tau=395$ and 640.

Inspection of the interaction between the inner and outer layers revealed that the positive and negative dominant regions in τ_1 correspond, respectively, to the high- and low-speed regions in the very large-scale motions in the outer layer, whereas the active region in τ_3 corresponds to the high-speed region in the very large-scale motions. These results indicate that the very large-scale structures existing in τ_1 and τ_3 for $\mathrm{Re}_\tau=640$ are essentially phenomena associated with the very large-scale motions existing in the outer layer of the flow.

The database is posted at http://murasun.me.noda.tus.ac.jp.

Acknowledgments

The authors are grateful to Dr. Y. Matsuo of the Japan Aerospace Exploration Agency for his help in the early stage of this computation. Computations were made with the VPP5000 at the Tokyo University of Science and also those at the Computer Centers of Nagoya and Kyushu Universities. H.C. acknowledges support from the National Creative Research Initiatives of the Korean Ministry of Science and Technology.

References

[1] Choi, H., and Moin, P., 1990, "On the Space-Time Characteristics of Wall Pressure Fluctuations," Phys. Fluids A, **2**, pp. 1450–1460.
[2] Farabee, T. M., and Casarella, M. J., 1991, "Spectral Features of Wall Pressure Fluctuations Beneath Turbulent Boundary Layers," Phys. Fluids A, **3**, pp. 2410–2420.
[3] Jeon, S., Choi, H., Yoo, J. Y., and Moin, P., 1999, "Space-Time Characteristics of the Wall Shear-Stress Fluctuations in a Low-Reynolds-Number Channel Flow," Phys. Fluids, **11**, pp. 3084–3094.
[4] Kim, J., 1989, "On the Structure of Pressure Fluctuations in Simulated Turbulent Channel Flow," J. Fluid Mech., **205**, pp. 421–451.
[5] Bullock, K. J., Cooper, R. E., and Abernathy, F. H., 1978, "Structural Similarity in Radial Correlations and Spectra of Longitudinal Velocity Fluctuations in Pipe Flow," J. Fluid Mech., **88**, pp. 585–608.
[6] Naguib, A. M., and Wark, C. E., 1992, "An Investigation of Wall-Layer Dynamics Using a Combined Temporal Filtering and Correlation Technique," J. Fluid Mech., **243**, pp. 541–560.
[7] Hites, M. H., 1997, "Scaling of High-Reynolds Number Turbulent Boundary Layers in the National Diagnostic Facility," Ph.D. thesis, Illinois Institute of Technology.
[8] Kim, K. C., and Adrian, R. J., 1999, "Very Large-Scale Motion in the Outer Layer," Phys. Fluids, **11**, pp. 417–422.
[9] Österlund, J. M., 1999, "Experimental Studies of Zero Pressure-Gradient Turbulent Boundary Layer Flow," Ph.D. thesis, Department of Mechanics, Royal Institute of Technology, Stockholm.
[10] Metzger, M. M., and Klewicki, J. C., 2001, "A Comparative Study of Near-Wall Turbulence in High and Low Reynolds Number Boundary Layers," Phys. Fluids, **13**, pp. 692–701.
[11] Antonia, R. A., and Kim, J., 1994, "Low-Reynolds-Number Effects on Near-Wall Turbulence," J. Fluid Mech., **276**, pp. 61–80.
[12] Moser, R. D., Kim, J., and Mansour, N. N., 1999, "Direct Numerical Simulation of Turbulent Channel Flow up to $\mathrm{Re}_\tau=590$," Phys. Fluids, **11**, pp. 943–945.
[13] Abe, H., Kawamura, H., and Matsuo, Y., 2001, "Direct Numerical Simulation of a Fully Developed Turbulent Channel Flow With Respect to the Reynolds Number Dependence," ASME J. Fluids Eng., **123**, pp. 382–393.
[14] del Álamo, J. C., and Jiménez, J., 2001, "Direct Numerical Simulation of the Very Anisotropic Scales in a Turbulent Channel," Center for Turbulence Research Annual Research Briefs, pp. 329–341.
[15] del Álamo, J. C., and Jiménez, J., 2003, "Spectra of the Very Large Anisotropic Scales in Turbulent Channels," Phys. Fluids, **15**, pp. L41–L44.
[16] Abe, H., and Kawamura, H., 2002, "A Study of Turbulence Thermal Structure in a Channel Flow Through DNS up to $\mathrm{Re}_\tau=640$ With $\mathrm{Pr}=0.025$ and 0.71," Proceedings of 9th European Turbulence Conference, pp. 399–402.
[17] Jiménez, J., Flores, O., and García-Villalba, M., 2001, "The Large-Scale Organization of Autonomous Turbulent Wall Regions," Center for Turbulence Research Annual Research Briefs, pp. 317–327.
[18] Dukowics, J. K., and Dvinsky, A. S., 1992, "Approximate Factorization as a High Order Splitting for the Implicit Incompressible Flow Equations," J. Comp. Physiol., **102**, pp. 336–347.
[19] Morinishi, Y., Lund, T. S., Vasilyev, O. V., and Moin, P., 1998, "Fully Conservative Higher Order Finite Difference Schemes for Incompressible Flow," J. Comp. Physiol., **143**, pp. 90–124.
[20] Jiménez, J., 1998, "The Largest Scales of Turbulent Wall Flows," Center for Turbulence Research Annual Research Briefs, pp. 137–154.
[21] Kawamura, H., Abe, H., and Shingai, K., 2000, "DNS of Turbulence and Heat Transport in a Channel Flow With Different Reynolds and Prandtl Numbers and Boundary Conditions," Proceedings of 3rd International Symposium Turbulence, Heat and Mass Transfer, pp. 15–32.
[22] Hussain, A. K. M. F., and Reynolds, W. C., 1975, "Measurements in Fully Developed Turbulent Channel Flow," J. Fluids Eng., **97**, pp. 568–580.
[23] Spalart, P. R., 1988, "Direct Simulation of a Turbulent Boundary Layer up to $R_\theta=1410$," J. Fluid Mech., **187**, pp. 61–98.
[24] Falco, R. E., 1977, "Coherent Motions in the Outer Region of Turbulent Boundary Layers," Phys. Fluids, **20**, pp. S124–SS132.
[25] Brown, G. L., and Thomas, A. S. W., 1977, "Large Structure in a Turbulent Boundary Layer," Phys. Fluids, **20**, pp. S243–S252.
[26] Adrian, R. J., Meinhart, C. D., and Tomkins, C. D., 2000, "Vortex Organization in the Outer Layer Region of the Turbulent Boundary Layer," J. Fluid Mech., **422**, pp. 1–54.
[27] Liu, Z., Adrian, R. J., and Hanratty, T. J., 2001, "Large-Scale Modes of Turbulent Channel Flow: Transport and Structure," J. Fluid Mech., **448**, pp. 53–80.
[28] Smith, C. R., and Metzler, S. P., 1983, "The Characteristics of Low-Speed Streaks in the Near-Wall Region of a Turbulent Boundary Layer," J. Fluid Mech., **129**, pp. 27–54.
[29] Nakagawa, H., and Nezu, I., 1981, "Structure of Space-Time Correlations of Bursting Phenomena in an Open-Channel Flow," J. Fluid Mech., **104**, pp. 1–43.
[30] Perry, A. E., Henbest, S., and Chong, M. S., 1986, "A Theoretical and Experimental Study of Wall Turbulence," J. Fluid Mech., **165**, pp. 163–199.
[31] Kuroda, A., Kasagi, N., and Hirata, M., 1989, "A Direct Numerical Simulation of the Fully Developed Turbulent Channel Flow at a Very Low Reynolds Number," Proceedings of the International Symposium on Computational Fluid Dynamics, Nagoya, pp. 1174–1179.
[32] Gilbert, N., and Kleiser, L., 1991, "Turbulence Model Testing With the Aid of Direct Numerical Simulation Results," Proceedings of the Eighth Symposium on Turbulent Shear Flows, TU of Münich, pp. 26.1.1–26.1.6.
[33] Kuroda, A., Kasagi, N., and Hirata, M., 1993, "Direct Numerical Simulation of the Turbulent Plane Couette-Poiseuille Flows: Effect of Mean Shear on the Near Wall Turbulence Structures," Proceedings of the Ninth Symposium on Turbulent Shear Flows, Kyoto, pp. 8.4.1–8.4.6.
[34] Günther, A., Papavassiliou, D. V., Warholic, M. D., and Hanratty, T. J., 1998, "Turbulent Flow in a Channel at a Low Reynolds Number," Exp. Fluids, **25**, pp. 503–511.
[35] Fischer, M., Jovanović, J., and Durst, F., 2001, "Reynolds Number Effects in the Near-Wall Region of Turbulent Channel Flows," Phys. Fluids, **13**, pp. 1755–1767.
[36] Alfredsson, P. H., Johansson, A. V., Haritonidis, J. H., and Eckelmann, H., 1988, "The Fluctuating Wall-Shear Stress and the Velocity Field in the Viscous Sublayer," Phys. Fluids, **31**, pp. 1026–1033.
[37] Wietrzak, A., and Lueptow, R. M., 1994, "Wall Shear Stress and Velocity in a Turbulent Axisymmetric Boundary Layer," J. Fluid Mech., **259**, pp. 191–218.
[38] Nepomuceno, H. G., and Lueptow, R. M., 1997, "Pressure and Shear Stress Measurements at the Wall in a Turbulent Boundary Layer on a Cylinder," Phys. Fluids, **9**, pp. 2732–2739.
[39] Robinson, S. K., 1991, "The Kinematics of Turbulent Boundary Layer Structure," NASA TM, 103859.
[40] Komminaho, J., Lundbladh, A., and Johansson, A. V., 1996, "Very Large Structures in Plane Turbulent Couette Flow," J. Fluid Mech., **320**, pp. 259–285.

Khaled S. Abdol-Hamid

S. Paul Pao

Configuration Aerodynamics Branch, MS 499,
NASA Langley Research Center,
Hampton, VA 23681

Steven J. Massey
Eagle Aeronautics, Inc.,
13 West Mercury Blvd.,
Hampton, VA 23669

Alaa Elmiligui
Analytical Services & Materials, Inc.,
107 Research Dr.,
Hampton, VA 23660

Temperature Corrected Turbulence Model for High Temperature Jet Flow

It is well known that the two-equation turbulence models under-predict mixing in the shear layer for high temperature jet flows. These turbulence models were developed and calibrated for room temperature, low Mach number, and plane mixing layer flows. In the present study, four existing modifications to the two-equation turbulence model are implemented in PAB3D and their effect is assessed for high temperature jet flows. In addition, a new temperature gradient correction to the eddy viscosity term is tested and calibrated. The new model was found to be in the best agreement with experimental data for subsonic and supersonic jet flows at both low and high temperatures. [DOI: 10.1115/1.1792266]

Introduction

Computational fluid dynamics (CFD) codes have become an attractive option for the analysis of aerospace systems due to advances in flow solvers and computer hardware technologies. With the re-emergence of jet noise as a significant contributor to total airplane noise, the accurate prediction of three-dimensional 3-D jet flows has again become an important research goal [1–3]. In recent years, sophisticated techniques such as Large Eddy Simulation (LES) have been used to simulate jet flow. However, the routine use of LES methods to calculate nozzle and jet flows to a high degree of accuracy is not yet possible. This is due to the requirement of large computational grids and very long computer run time to analyze even a simple nozzle configuration at low Reynolds numbers [4–5].

Solving the Reynolds-averaged Navier-Stokes (RANS) equations is considered to be the practical approach for calculating steady state nozzle and jet flows, and it is necessary to enhance the capabilities of currently available RANS methods. Advanced turbulence models are needed to predict propulsion aerodynamic effects in transonic and supersonic free-stream conditions. In the present paper, we used the two-equation k-ϵ turbulence model, which can be applied to the near-wall region as well as far away regions from wall boundaries. For flow regions far away from solid boundaries, the high Reynolds number form of the model can be used [6].

For transonic and supersonic jet flow applications, the local density variation in standard incompressible turbulence models does not adequately duplicate the experimentally observed reduction in growth rate of the mixing layer with increasing convective Mach number. However, substantial progress has been made in the development of appropriate compressibility corrections to the transport equation turbulence models, [7–8]. These corrections resulted from the direct numerical simulation of homogeneous compressible turbulence. Notably, Sarkar et al. [7] recognized the importance of including compressible dissipation in the two-equation turbulence model when computing high-speed flows. A simple correction was proposed for compressible dissipation that can be included easily in the existing two-equation turbulence models. The standard model is recovered as the coefficient of the correction vanish in the absent of these complicated factors.

Large temperature fluctuations have a profound effect on turbulence, much like large pressure fluctuations. While several models have been developed to account for the effect of pressure fluctuations (compressibility correction models), very little has been done to account for large temperature fluctuations. This has led to the poor CFD prediction of nonisothermal flows. It is therefore very important to develop thermal correction models that can account for the effect of temperature fluctuations on turbulence.

For high-temperature jet flow, the standard turbulence models lack the ability to predict the observed increase in growth rate of mixing layer [2–3]. Several researchers [9–14] have modified one or more terms of the transport equations to obtain better agreement in high temperature flows. All these modifications affect directly or indirectly the closure terms of the turbulent heat flux ($\rho\overline{u_i\theta}$) and stresses ($\rho\overline{u_iu_j}$). Theis and Tam [9] changed several coefficients in the turbulent transport equations. However such extensive modifications of model coefficients completely changes the characteristics of the equations and it may cause a deficiency in the flow prediction accuracy for other problems. Other attempts to sensitize the turbulence model to temperature fluctuations involve a more sophisticated closure for the turbulent heat flux term appearing in the average energy equation [12–14]. Explicit algebraic nonlinear heat flux models have also been tested for this purpose. These models had been successful in some fully developed high temperature turbulent flows. In this paper, we will test the capabilities of such models in predicting high speed shear flows. This includes all the stages of jet flow development regions namely, core, mixing, and fully developed stages.

Our objective in the present work is to test simple modifications to the Boussinesq's closure model coefficient turbulence model for better predicting the mean flow feature of high temperature jet flows. Experimental studies by Seiner et al. [2] and Thomas et al. [3] showed that the high total temperature gradient led to faster mixing and spreading of jet flow. Based on these observations, a simple modification to the k-ϵ turbulence model is proposed. The empirical ideas behind the simplified turbulence model modification started with the observation that density gradient in a turbulent flow would add to instability due to local accelerations in the turbulent velocity field. A layered fluid medium is statically unstable when the dot product of the density gradient vector and the acceleration vector is negative. This criterion is met perhaps half the time in a turbulent flow with a density gradient created by a temperature gradient. Instead of using directly the density gradient, we have chosen to use the total temperature gradient as an approximation. This choice is driven by two other considerations. First, the modified k-ϵ should reduce to the standard model for constant temperature flow in the boundary layer. Second, the modification should be insensitive to density and temperature gradients due to Mach wave expansion and the embedded shocks in

Contributed by the Fluids Engineering Division for publication in the JOURNAL OF FLUIDS ENGINEERING. Manuscript received by the Fluids Engineering Division July 18, 2003; revised manuscript received May 12, 2004. Associate Editor: W. W. Copenhaver.

supersonic jet. It was observed in (Seiner's measurements and Hamid's computation) (do we have a reference for the Mach 2 jet comparison?) that the embedded shocks merely modulate the axial and transverse components of the turbulence intensity as the turbulence passes through the shock, but no addition to the overall turbulent kinetic energy. By choosing the total temperature gradient to represent the concept of additional mixing instability, we are able to satisfy these important compatibility requirements. The modification is intended to produce enhanced mixing only for high total temperature gradient jet flows. The modification will also take into account the commonly accepted compressibility effect corrections on mixing.

New modifications are implemented in PAB3D [1], which is a three-dimensional structured grid flow analysis computer code based on solving the Reynolds Averaged Navier-Stokes (RANS) equations. The PAB3D flow solver has several robust (production quality) two-equation turbulence models, which include anisotropic algebraic Reynolds stress models. This code has been used to simulate complex aerodynamic flow configurations, such as mixer-ejector nozzles, thrust vectoring, jet mixing, and propulsion installation, and is currently being used in several national programs. The PAB3D code is part of the CFD Resource at NASA Langley. In the present study we use the benchmark experiments performed at the NASA Langley Research Center (LaRC) Jet Noise Laboratory [2] and multi-stream subsonic jet flows [3] to test and calibrate the present modifications.

Approach

The governing equations of the RANS formulation include the conservation equations for mass, momentum, energy, and the equation of state. In the present study, we choose the perfect gas law to represent the air properties, and use the eddy viscosity concept to model the Reynolds stresses. Previous studies had found that even using a more sophisticated algebraic stress model does not have much influence on mixing.

The mass, momentum, and energy conservation equations of the RANS equations can be written in a conservative form as follows:

$$\frac{\partial \rho}{\partial t}+\frac{\partial \rho u_i}{\partial x_i}=0$$

$$\frac{\partial \rho u_i}{\partial t}+\frac{\partial(\rho u_i u_j+p\,\delta_{ij})}{\partial x_j}=\frac{\partial(\tau_{ij}-\rho\overline{u_i u_j})}{\partial x_j}$$

$$\frac{\partial \rho e_0}{\partial t}+\frac{\partial(\rho e_0 u_i+p u_i)}{\partial x_i}=\frac{\partial(\tau_{ij}u_j-\rho\overline{u_i u_j}u_j)}{\partial x_i}-\frac{\partial(q_i+C_P\rho\overline{u_i\theta})}{\partial x_i}+\frac{\partial}{\partial x_i}\left[\mu_l+\frac{\mu_t}{\sigma_k}\frac{\partial k}{\partial x_i}\right]$$

To close the RANS equations, we will use the two-equation (k-ϵ) turbulence model [6] as follows:

$$\frac{\partial \rho k}{\partial t}+\frac{\partial \rho u_j k}{\partial x_j}=-\rho\overline{u_j u_i}\frac{\partial u_i}{\partial x_j}+\frac{\partial}{\partial x_j}\left[\mu_l+\frac{\mu_t}{\sigma_k}\frac{\partial k}{\partial x_j}\right]-\rho\epsilon(1+M_\tau^2) \tag{1}$$

$$\frac{\partial \rho \epsilon}{\partial t}+\frac{\partial \rho u_j \epsilon}{\partial x_j}=-C_{\epsilon 1}\rho\overline{u_j u_i}\frac{\partial u_i}{\partial x_j}\frac{\epsilon}{k}+\frac{\partial}{\partial x_j}\left[\mu_l+\frac{\mu_t}{\sigma_\epsilon}\frac{\partial \epsilon}{\partial x_j}\right]-C_{\epsilon 2}\rho\frac{\epsilon^2}{k} \tag{2}$$

$\mu_t=\rho C_\mu(k^2/\epsilon)$, $C_\mu=.09$, $C_{\epsilon 1}=1.44$, *and* $C_{\epsilon 2}=1.92$.

In this paper, we will examine five different modifications to the standard two-equation turbulence model. The first four are directly related to the modeling of the turbulence heat flux terms ($\rho\overline{u_i\theta}$). The fifth modification is based on simple temperature gradient and compressibility corrections to the eddy viscosity (μ_t). The modifications are as follows:

(1) The Simple Eddy Diffusivity (SED) is based on the Boussinesq viscosity model. This approach is used to model all the scalar diffusion terms appearing in the RANS and standard k-ϵ equations. For the heat flux term, the SED is written as follows:

$$\rho\overline{u_i\theta}=-\frac{\mu_\tau}{\sigma_\tau}\frac{\partial T}{\partial x_i}$$
$$\mu_\tau=\rho C_\mu k^2/\epsilon,\quad C_\mu=0.09,\quad \sigma_\tau=0.9 \tag{3}$$

This is the simplest and most commonly used formulation in CFD codes to calculate the heat flux term.

(2) So and Sommer [12] (hereinafter referred to as the Sommer-So model) proposed the following algebraic heat-flux model including the effect of the mean-velocity gradient:

$$\rho\overline{u_i\theta}=-\rho k\tau_m C_{ji}\frac{\partial T}{\partial x_i}$$

$$C_{ji}=-C_\lambda\delta_{ji}+\frac{1}{C_{1\theta}}\{(2C_\mu\tau_u+C_{2\lambda}\tau_m)S_{ji}+C_2\tau_m\Omega_{ji}\} \tag{4}$$

$$C_2=C_\lambda[1-C_{2\theta}]$$

$C_\lambda=0.095$, $C_{1\theta}=3.28$, $C_{2\theta}=0.4$, $\tau_u=k/\epsilon$, $\tau_m=0.83\tau_u$.

(3) The Generalized Gradient Diffusion Hypothesis (GGDH) adds the stress effect into the heat flux term. A complete description of this model is discussed by Ronki and Gatski [13]

$$\rho\overline{u_i\theta}=-C_\tau\rho\overline{u_j u_i}\frac{k}{\epsilon}\frac{\partial T}{\partial x_i}$$

$$\rho\overline{u_j u_i}=2\mu_\tau S_{ji}-\frac{2}{3}\delta_{ji}\rho k, \tag{5}$$

$$C_\tau=0.3$$

(4) This model adds more complexity to the GGDH model by changing the constant C_τ to include the effect of the mean-velocity gradient (Abe et al. [14]). The model is as follows:

$$\rho\overline{u_i\theta}=-C_{jl}\rho\overline{u_l u_i}\frac{k}{\epsilon}\frac{\partial T}{\partial x_i}$$

$$C_{jl}=C_\Delta\{-\delta_{jl}+\tau_m[C_{T32}S_{jl}+C_{T23}\Omega_{jl}]\}$$

$$C_\Delta=\frac{C_{T1}\tau_m}{1+0.5\tau_m^2[C_{T23}^2\Omega^2-C_{T32}^2S^2]}$$

$$C_{T1}=C_{T2}=0.18,\quad C_{T3}=0.02,$$

$$C_{T23}=C_{T2}-C_{T3},\quad C_{T32}=C_{T2}+C_{T3} \tag{6}$$

$$\tau_m=0.75\frac{k}{\epsilon}$$

$$S_{jl}=\frac{1}{2}\left[\frac{\partial u_j}{\partial x_l}+\frac{\partial u_l}{\partial x_j}\right]-\frac{1}{3}\delta_{jl}\frac{\partial u_j}{\partial x_l}$$

$$\Omega_{jl}=\frac{1}{2}\left[\frac{\partial u_j}{\partial x_l}-\frac{\partial u_l}{\partial x_j}\right]$$

(5) Temperature Corrected Turbulence Model: Large fluctuations in either thermodynamic variable (pressure or temperature) leads to variations in density and consequently nonzero dilatation. Nonzero dilatation then affects turbulence evolution. It is clear then that the source of dilatation be it pressure or temperature fluctuations, must be accounted for in turbulence modeling. At the RANS level of closure modeling, dilatation has two important effects on turbulent statistics.

Effect on Turbulent Kinetic Energy. The presence of an extra dissipation term (the so-called dilatational dissipation) in the kinetic energy transport equation has long been known and adequately modeled in high turbulent-Mach number flows. The very same logic dictates that large temperature-fluctuations must also contribute to the very same dilatational dissipation. The modeling challenge would then be to derive a closure model for the thermal

dilatational-dissipation in terms of known temperature-field statistics—temperature variance, mean-temperature gradients, etc.

Effect on Pressure-Strain Correlation. Nonzero dilatation also has an important effect on the pressure-strain redistribution of turbulent kinetic energy among various components. Dilatation makes the redistribution from high-energy components to low-energy components less efficient. The trace of the pressure-strain correlation is nonzero in the presence of dilatation. This directly affects the Reynolds stress anisotropy and hence the constitutive relation. The consequence of this change in the character of the pressure-strain correlation on two-equation models can be inferred by deriving the algebraic Reynolds stress model by making the standard weak-equilibrium assumption. The dilatation effects manifest in the standard k-ϵ equation as a modification of C_μ. The presence of the extra dissipation term also would modify the C_μ.

In the present work, we propose to modify C_μ to account for the effect of high temperature fluctuations. As a first step, rather than deriving the modification analytically, we will use experimental data to determine the modification. The functional relationship was determined by the best match to total temperature experimental data from case (3) of the supersonic flow nozzle and the axisymmetric multistream subsonic round nozzle.

We introduce in this study a temperature correction in the form of a variable C_μ which is a function of the local total temperature gradient normalized by the local turbulence length scale:

$$T_g = \nabla(T_t)(k^{3/2}/\epsilon)/T_t$$

$$\nabla(T_t) = \sqrt{\left(\frac{\partial T_t}{\partial x_i}\right)^2}$$

To extend the model for high speed flow, we require the model to be also a function of turbulence Mach number:

$$M_\tau = \frac{\sqrt{2k}}{a}$$

where a is the local acoustic speed and k is the turbulence kinetic energy. It is found that the functional form of C_μ (in terms of T_g and M_τ) produces the required effects:

$$C_\mu = 0.09 C_T$$
$$C_T = \left[1 + \frac{T_g^3}{0.041 + f(M_\tau)}\right] \tag{7}$$

where,

$$f(M_\tau) = (M_\tau^2 - M_{\tau 0}^2) H(M_\tau - M_{\tau 0}),$$

$H(x)$ is the Heaviside step function; and $f(M_\tau) = 0$ for no compressibility correction. We have selected $M_{\tau 0} = 0.1$ for the present model.

We have chosen to use the total temperature gradient for a number of empirical reasons.

i. The temperature correction is not coupled to Mach number effects because the total temperature is not Mach number dependent. Hence, flow features that are not related to shear layer mixing, such as flow expansion, compression, and internal shocks, will not influence the turbulence model.
ii. The total temperature gradient locates itself automatically in the shear layer where corrections are intended to occur.
iii. The proposed turbulence model reverts back to the standard k-ϵ model in the boundary layer where the total temperature is constant. In general, the correction vanishes everywhere the total temperature gradient is absent in the flow. This is particularly important for flow simulation in the boundary layer.
iv. This correction is well behaved over a very large temperature range in a shear flow. The smooth functional form of the correction allows for the unrestricted application to shear flows with simple as well as complex configurations.

In Ref. [18], Birch et al. used a zonal modification of the turbulence Prandtl number, σ_τ, to compute high temperature axisymmetric and chevron nozzle jet flows. The range of his modification is over a factor of approximately 2.0 between 0.4 and 0.7 to distinguish between shear mixing layer and developed jet flow regions to correct for the temperature effect. The predictive accuracy of the zonal method as shown in Ref. [18] was excellent. In our computations, C_μ is modified through the value of C_T in Eq. (7). The maximum value of C_T for jet simulation rarely exceeded 3.0, with an average of less than 2.0. While the effective turbulence Prandtl number appears in Eq. (3) as σ_τ / C_μ, our modification is very similar to the zonal modification of the Prandtl number by Birch with a constant value of $C_T = 1.0$.

Test Cases and Comparisons

Two test cases were selected to evaluate the present modifications. The first test case is a supersonic axisymmetric jet operated at total design pressure condition. We selected this case to compare the present modification with the four other approaches in modeling the turbulence heat flux terms. This case covers a wide range of temperatures and the numerical solution will help in verifying the predicted effect of temperature on jet mixing. The second test case is a multistream subsonic jet configuration. This case provides the calibration of the present model in the subsonic flow and it also addresses the complexity of modeling multistream flows.

Supersonic Jet Flow. In the present study we use the benchmark experiments performed by Seiner [2] at the NASA LaRC Jet Noise Laboratory. These experiments investigated an axisymmetric water-cooled Mach 2 nozzle with an exit diameter $D = 3.60$ in. (91.44 mm). The simple geometry made it practical to run a larger number of numerical calculations and to a more complete evaluation of different temperature corrected turbulence models proposed by others in the literature. Three sets of data were selected from the reported test results, with the nozzle plenum stagnation temperature ($T_{t,c}$) varied, as indicated in Table 1. The nozzle operated at fully expanded conditions for this series of cases. The Reynolds number, based on D, varied from 1.3×10^6 to 8.3×10^6.

The computational grid used for these nozzle calculations is generated by Dembowski and Georgiadis [15] as shown in Fig. 1. The computational mesh is an axisymmetric wedge shaped grid with one cell in the circumferential direction. The computational domain is divided into three blocks where block one is the nozzle, and the remaining two blocks represent the free stream. The mesh has a total of 66 640 cells. Grid points are clustered near the solid surfaces and around the shear layer. The value of y^+ for the first cell off the surface varied between 0.2 and 2.

Five PAB3D solutions were obtained for each of the three operating conditions as listed in Table 1, with the first using the SED, the second using Sommer-So [12], the third using the GGDH [3] model, the fourth using the Abe et al. [14] model, and the fifth using the present temperature corrected model. All the flow simulation cases used the Sarkar [7] compressibility correction to compensate for the Mach number effect. All of these cases were run using a free stream Mach number of 0.01.

Table 1 Experimental nozzle flow conditions

Case	$T_{t,c}$ (°R)	$P_{t,c}$ (psi)	$T_{t,0}$ (°R)	$P_{t,0}$ (psi)	M_0
1	563	115	563	14.7	static
2	1359	115	563	14.7	static
3	2009	115	563	14.7	static

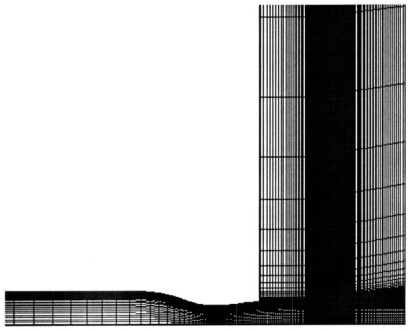

Fig. 1 Computational grid for the supersonic jet flow

Figures 2–4 compare centerline profiles of stagnation pressure, Mach number, and stagnation temperature for the five PAB3D solutions and the experimental data of Seiner [2]. The stagnation temperature is not shown for the unheated case with nozzle plenum temperature set to 563°R. In Fig. 2, all the five modifications give a good prediction of the stagnation pressure and Mach number as compared with experimental data for $T_t = 563°$R. The difference in the prediction between the cases is insignificant. This establishes that all the modifications reduced to the standard k-ϵ turbulence model. For flow conditions (2) and (3), the nozzle operated at stagnation temperatures of 1359°R and 2009°R, respectively. All the models that had changes to the heat flux term significantly overpredicted the stagnation pressure. Even though the present temperature corrected model was calibrated with respect to only the total temperature of case (3), it more accurately predicted the stagnation pressure data for both cases (2) and (3). In general, the present model gives the best comparison with experimental data for the stagnation pressure, the Mach number, and the stagnation temperature distributions for all three cases. GGDH [13] also produces good predictions for the stagnation temperature profile shown in Figs. 3(c) and 4(c) but fails to accurately predict the stagnation pressure and Mach number.

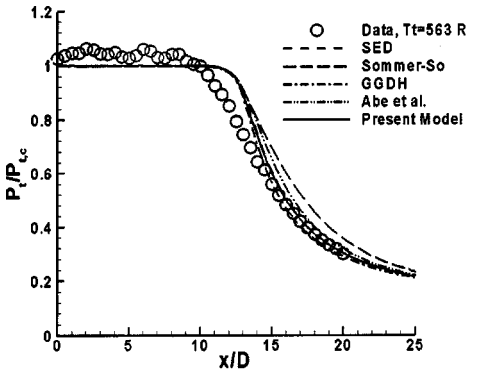

a) Centerline Stagnation Pressure

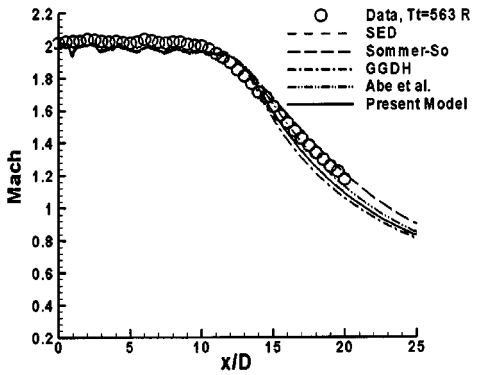

b) Centerline Mach Number

Fig. 2 A comparison of solutions at $T_t = 563.67$ R using different turbulence models with data [2]

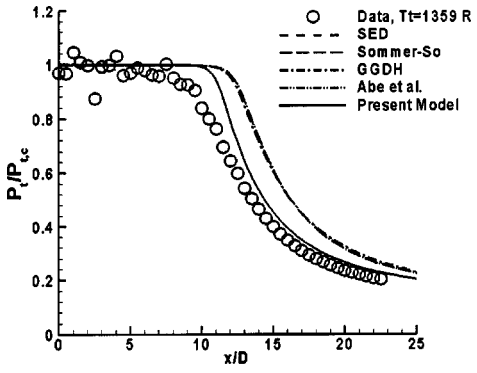

a) Centerline Stagnation Pressure

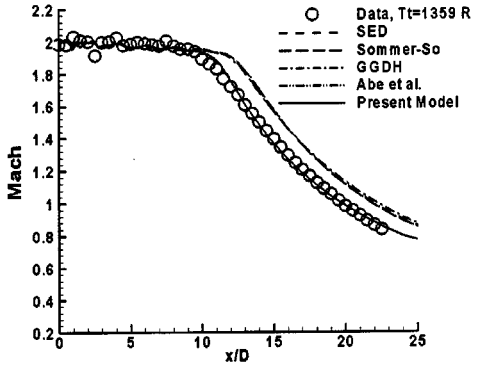

b) Centerline Mach Number

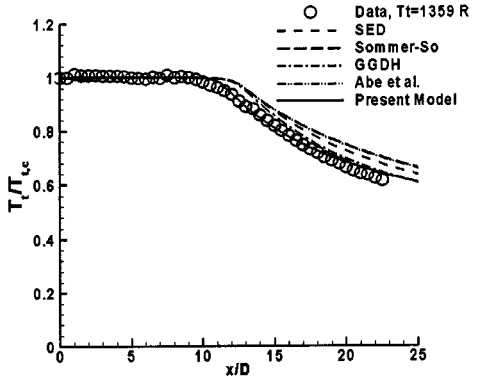

c) Centerline Stagnation Temperature

Fig. 3 A comparison of solutions at $T_t = 1359.67$ R using different turbulence models with data [2]

Multistream Subsonic Jet Flow. The second test configuration includes a separate fan and core nozzle flows at a bypass ratio of five with an external plug. One set of data was selected from the reported test results [16], with the flow condition as indicated in Table 2 for core, fan and free stream. This test configuration is part of a comprehensive investigation for jet exhaust noise due to the pylon-chevron-jet interaction similar to the configuration shown in Fig. 5, which was tested at NASA. As previously discussed, the present model was tuned on the axisymmetric grid to the round nozzle experimental results. Particular attention was

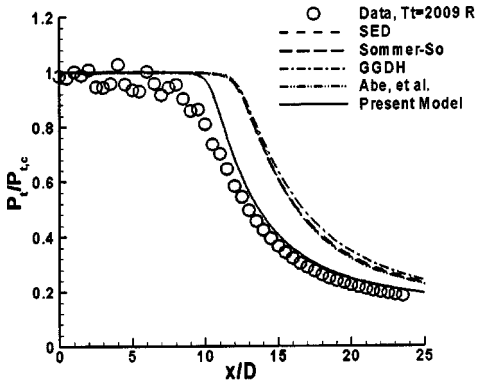

a) Centerline Stagnation Pressure

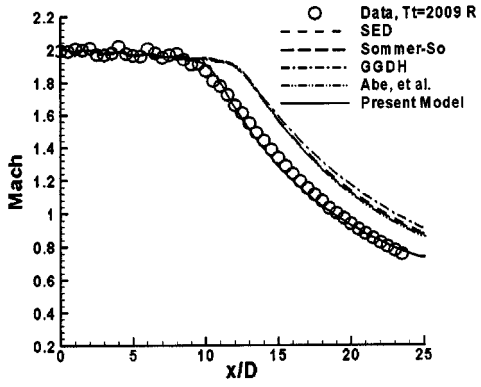

b) Centerline Mach Number

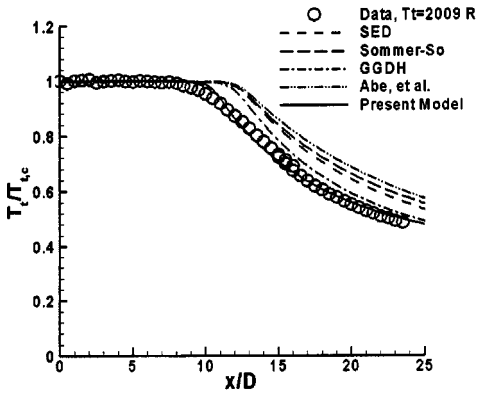

c) Centerline Stagnation Temperature

Fig. 4 A comparison of solutions at $T_t = 2009.67$ R using different turbulence models with data [2]

paid to matching the centerline total temperature at $x/D_c = 5$ and 10. The model was then frozen for the other cases [16–17]. References [16] and [17] give an extensive comparison with the present temperature correction turbulence model as compared with aerodynamic and acoustic data, respectively. For the limited

Table 2 Experimental Subsonic Condition

	T_t (°R)	P_t (psi)	M
Core	1498	21.72	···
Fan	647	24.36	···
Free stream	530	14.7	0.28

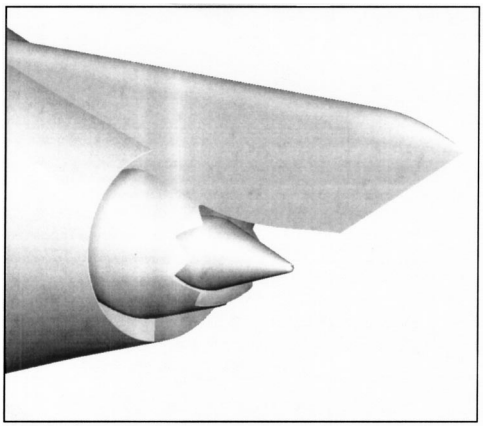

Fig. 5 Configuration 4, 8-chevron core nozzle with round fan nozzle and pylon

space and scope of this paper, we will discuss the comparison with only the axisymmetric configuration shown in Fig. 6.

The computational domain for the solution extended from $x/D_c = -6.3$ to $x/D_c = 31.6$ in the axial direction and $6.3D_c$ in the radial direction, where D_c is the diameter of the baseline core nozzle, 12.80 cm. The origin, $x/D_c = 0.0$ was set at the exit of the fan nozzle so that the exit of the core nozzle is at about $x/D_c = 0.5$. The computational grid used in the present study is shown in Fig. 7. The computational mesh is an axisymmetric wedge-shaped grid with two cells in the circumferential direction, each cell being 3°. The computational domain is divided into 12 blocks, where block one is the core nozzle, block two is the fan nozzle, and the remaining ten blocks representing the free stream. The mesh has a total of 296 928 cells. Grid points are clustered near the solid surfaces and around the shear layer. The value of y^+ for the first cell off the surface varied between 0.16 and 1.8.

Computational solutions were obtained for standard k-ϵ model using SED, and the temperature corrected model. The simulated conditions were set to coordinate with the data presented in Ref. [3]. The computational results were conducted for a free stream Mach number of 0.28.

A comparison between computed stagnation temperature, using SED and the present model, and experimental data is shown in Fig. 8. As shown in Fig. 8, the present model was able to more accurately predict the temperature flow field and match the experimental data while the SED approach overpredicted the temperature in the core region. A comparison between the computed cen-

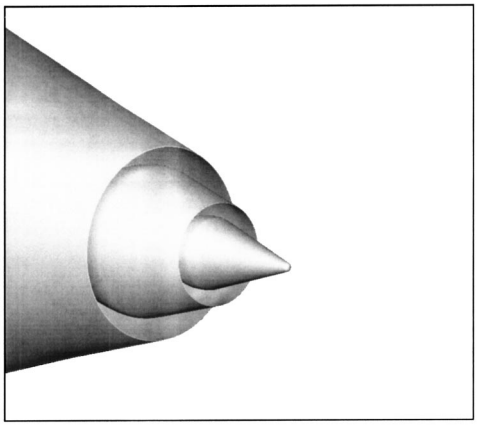

Fig. 6 Configuration 1, baseline round core nozzle with round fan nozzle

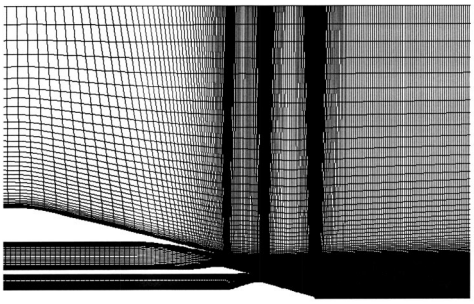

Fig. 7 Computational domain for the mutistream jet flow

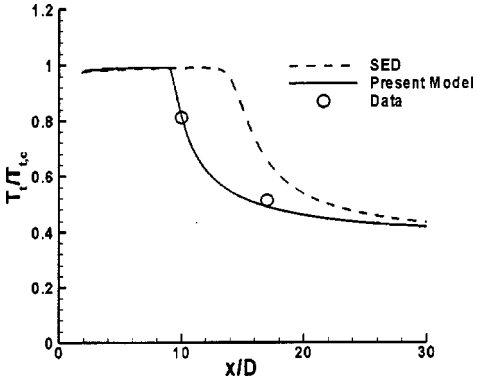

Fig. 9 Comparison of computed center line stagnation temperature and data [16]

terline stagnation temperature and the experimental data is shown in Fig. 9. The SED approach was not able to match the experimental data accurately while the present model was within 1% of the experimental value for the first point and 4% for the second experimental point.

A grid sensitivity study was conducted to determine the effect of grid resolution on the accuracy of the present model solution. The flow field for the dual subsonic jet flow was computed for three grid levels: coarse (1/4 grid resolution), medium (1/2 grid resolution), and fine grid. The computing strategy was to first run the problem on a coarse grid and once convergence is achieved to interpolate the solution to the next grid level and run the solution on the next finer grid level. The centerline stagnation temperature profiles for all grid levels are shown in Fig. 10. The temperature profiles essentially do not vary between grid levels and compare well with experimental. Further grid sensitivity analyses were not conducted since the solution was not sensitive to the grid level. A comprehensive investigation of the dual subsonic jet flow is presented by the authors in Refs. [16–18].

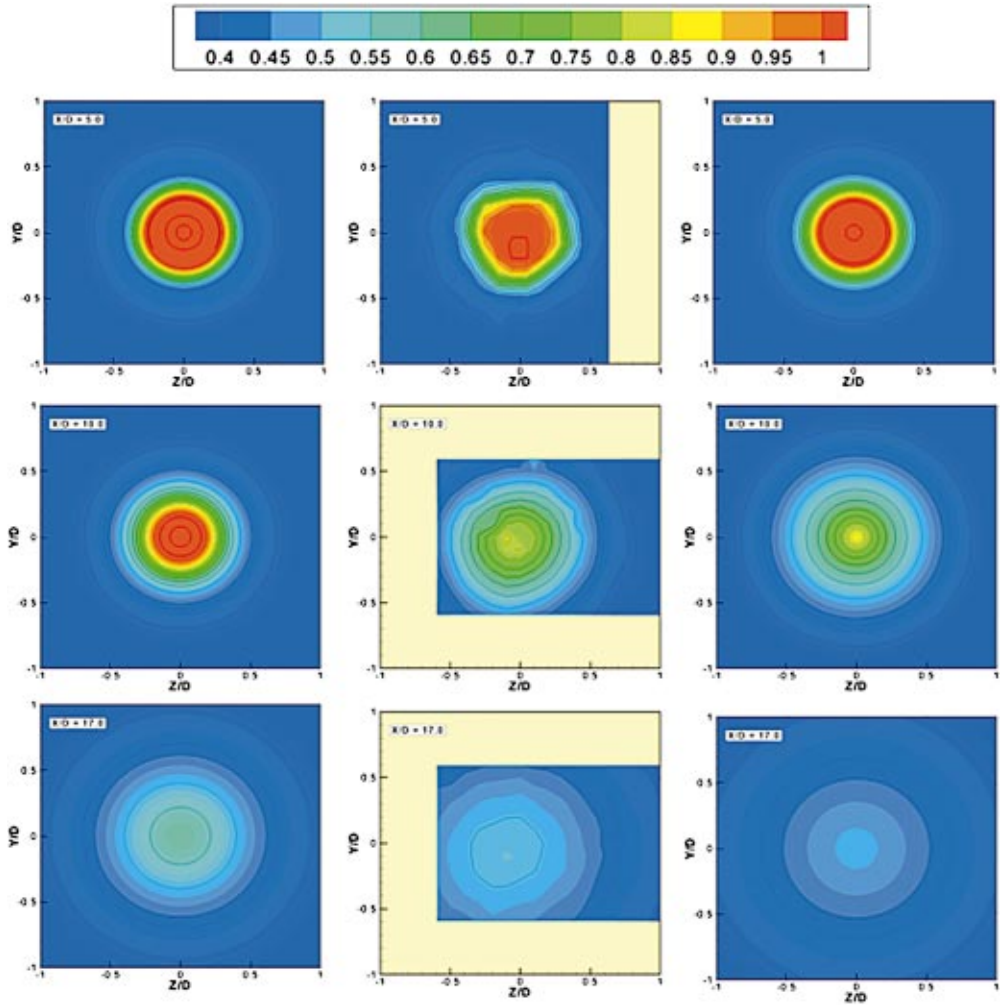

Fig. 8 A comparison of the stagnation temperature prediction with data [16]

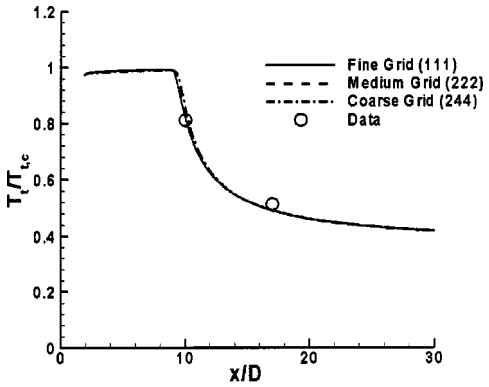

Fig. 10 A comparison of computed results for coarse, medium and fine grid level and data [16]

Concluding Remarks

Our objective in this paper is to explore the various modifications to the standard Boussinesq's closure to effect better predictions of flows with large temperature fluctuations. This knowledge can be very useful for more formal theoretical turbulence model development. The resulting model leads to more accurate aerodynamic and aeroacoustic predictions for 3-D jet flows. In this paper, computations using different modifications to the k-ϵ model for the simulation of high speed high temperature jet flows are presented and compared with experimental data. The present modification to the turbulent viscosity holds great promise in predicting high temperature jet flows while showing good predictions for the low or constant temperature jet flows. The present model accurately simulated different jet flow conditions which confirm the accuracy and robustness of the model.

Acknowledgment

This work is part of a larger ongoing study of complex nozzle configurations. A jet noise prediction method based on the computational information is also being pursued together with the computational results and the experiments. The third and fourth authors would like to acknowledge the support of the NASA Langley Research Center for providing the funding needed to carry out this work.

Nomenclature

a = speed of sound, m/sec

$C_2\, C_j\, C_\lambda$ $C_{2\lambda} C_{1\theta} C_{2\theta}$ = coefficients in heat flux model Eq. (4)

C_p = specific heat at constant pressure, J/°K

C_{T1}, C_{T2}, C_{T3}, $C_{,T32}, C_\Delta$ = coefficients in heat flux model Eq. (6)

C_T = coefficient in temperature corrected model Eq. (7)

$C_{\epsilon 1}$, $C_{\epsilon 2}$ = coefficients in ϵ—Eq. (2)

C_μ = turbulent viscosity coefficient

C_τ = coefficients in heat flux model Eq. (5)

D = Nozzle diameter

e_0 = total energy

H = Heaviside function

k = turbulent kinetic energy

M = Mach number

M_τ = turbulence Mach number

$M_{\tau 0}$ = lower limit of turbulence Mach number

P = static pressure

q_i = heat flux vector

R = absolute temperature

S_{ij} = strain rate tensor

t = time

T_g = temperature correction function

T_t = total temperature

u_i = velocity vector

x = axial distance from the jet exit

x_i = position vector

y^+ = wall distance, $u_\tau y/\nu$

δ_{ij} = Kronecker delta

ϵ = dissipation per unit mass

θ = fluctuating component of temperature

μ = molecular dynamic viscosity

μ_t = turbulent eddy viscosity

ρ = density

σ_k, σ_ϵ = turbulent Prandtl number for k and ϵ

σ_τ = turbulent Prandtl number for e_0

τ_m = time scale for Eq. (4)

τ_u = time scale for Eqs. (4) and (5)

τ_{ij} = Reynolds stress tensor

Ω_{ij} = vorticity tensor

Subscripts

c = nozzle core

o = free stream conditions

t = stagnation condition

References

[1] PAB3D Code Manual Originally developed by the Propulsion Aerodynamics Branch, now under cooperative program between the Configuration Aerodynamics Branch, NASA Langley Research Center and Analytical Services & Materials, Inc. Hampton, VA. See http://www.asm-usa.com/software/pab3d.html.

[2] Seiner, J. M., Ponton, M. K., Jansen, B. J., and Lagen, N. T., 1992, "The Effects of Temperature on Supersonic Jet Noise Emission," DGLR/AIAA 14th Aeroacoustics Conference, Aachen, Germany, AIAA Paper No. 92-02-046, May 1992.

[3] Thomas, R. H., Kinzie, K. W., and Pao, S. Paul, 2001, "Computational Analysis of a Pylon-Chevron Core Nozzle Interaction," AIAA Paper 2001-2185, May 2001.

[4] DeBonis, J. R., and Scott, J. N., 2001, "A Large-Eddy Simulation of a Turbulent Compressible Round Jet," AIAA Paper 2001-2254, May 2001.

[5] Georgiadis, N. J., Alexander, J. I. D., and Reshotko, E., 2001, "Development of a Hybrid RANS/LES Method for Compressible Mixing Layer Simulations," AIAA Paper 2001-0289, Jan. 2001.

[6] Jones, W. P., and Launder, B. E., 1972, "The Prediction of Laminarization With a Two-Equation Model of Turbulence," Int. J. Heat Mass Transfer, **15**, pp. 301–314.

[7] Sarkar, S., Erlebacher, G., Hussaini, M. Y., and Kreiss, H. O., 1991, "The Analysis and Modeling of Dilatational Terms in Compressible Turbulence," J. Fluid Mech., **227**, pp. 473–495.

[8] Wilcox, David C., 1987, "Progress in Hypersonic Turbulence Modeling," AIAA 91-1785, June 1991; Vol. 109, June 1987, pp. 156–160.

[9] Theis, A. T., and Tam, C. K. W., 1996, "Computation of Turbulent Axisymmetric and Non-Axisymmetric Jet Flows Using the k-ϵ Model," AIAA J., **34**, pp. 309–316.

[10] Tam, C. K. W., and Ganesan, A., 2003, "A Modified k-ϵ Model for Calculating the Mean Flow and Noise of Hot Jets," AIAA 2003-1064, January 2003.

[11] Lebedev, A. B., Lyubimov, A. D., Maslov, V. P., Mineev, B. I., Secundov, A. N., and Birch, Stanley F., 2002, "The Prediction of Three-Dimensional Jet Flows for Noise Applications," AIAA 2002–2422, 2002.

[12] So, R. M. C., and Sommer, T. P., 1995, "An Explicit Algebraic Heat-Flux Model for the Temperature Field," Int. J. Heat Fluid Flow, **7**, pp. 455–465.

[13] Ronki, M., and Gatski, Thomas B., 2001, "Predicting Turbulent Convective Heat Transfer in Fully Developed Duct Flows," Int. J. Heat Fluid Flow, **22**, pp. 381–392.

[14] Abe, K., Kondoh, T., and Nagano, Y., 1996, "A Two-Equation Heat Transfer Model Reflecting Second-Moment Closures for Wall and Free Turbulent Flows," Int. J. Heat Fluid Flow, **17**, pp. 228–237.

[15] Dembowski, M. A., and Georgiadis, N. J., 2002, "An Evaluation of Parameters Influencing Jet Mixing Using the WIND Navier-Stokes Code," NASA TM 2002-211727, 2002.

[16] Massey, S. J., Thomas, R. H., Abdol-Hamid, K. S., and Elmiligui, A., 2003, "Computational and Experimental Flowfield Analyses of Separate Flow Chevron Nozzles and Pylon Interaction," AIAA-2003-3212.

[17] Hunter, C., Pao, S., and Thomas, R., 2003, "Development of a Jet Noise Prediction Method for Installed Jet Configurations," AIAA 2003-3169.

[18] Birch, Stanley F., Lyubimov, D. A., Secundov, A. N., and Yakubovsky, K. Ya., 2003, "Numerical Modeling Requirements for Coaxial and Chevron Nozzle Flows," AIAA Paper 2003-3287.

Large-Scale Disturbances and Their Mitigation Downstream of Shallow Cavities Covered by a Perforated Lid

Stephen A. Jordan
Naval Undersea Warfare Center,
Newport, RI 02841
e-mail: jordansa@npt.nuwc.navy.mil

Flow past cavities covered by perforated lids pose a challenging problem for design engineers. Kelvin–Helmholtz waves appear early in the separated shear layers above the perforations that quickly mature into large-scale coherent structures far downstream. This evolution is sustained by a hydrodynamic feedback mechanism within the cavity even when its aft wall is far removed from the lid. Herein, the results from large-eddy simulations show analogous fundamental characteristics between open and perforated-cover cavities. Both adequately scale the fundamental frequency of the large-scale disturbance using the freestream velocity and the cavity width (or lid length). Moreover, the dimensionless frequencies jump to higher modes at equivalent length scales. Unlike the open cavity, one can invoke certain conditions that instigate the instability above the perforations but not a simultaneous long-term feedback mechanism necessary to fully sustain the periodic oscillation. The lid itself offers options for mitigating (or even eliminating) the instability. Results (for laminar separation) show the perforation spacing as the key factor. While maintaining the same fundamental frequency, one can easily dampen its spectral peak to complete disappearance by extending the perforation spacing.
[DOI: 10.1115/1.1792270]

Introduction

Incompressible flow past open cavities can generate a large-scale instability that remains coherent for many cavity lengths downstream. This instability originates early within the separated upstream shear layer that has destabilized due to a feedback mechanism from a hydrodynamic event occurring within the cavity itself. Given certain geometric and kinematic conditions, this process can be self-sustaining whether upstream separation is laminar or turbulent. In many applications, engineers desire to eliminate or at the very least attenuate these intense oscillations to an acceptable level. Good distinct examples are automobile sunroofs, bomb bays of low-speed aircraft, and submarine weapon launch inlets. But a more recent problem of the latter application deals with sizeable oscillations detected downstream of a closed cavity that is configured with a perforated cover (or cantilevered door). The perforations are necessary to relax the pressure gradient across the door such that a minimal actuation load is required to expose the cavity when the submarine is underway. Herein, we will examine the well-understood physics of the self-sustaining open cavity flow to aid our investigation of the large-scale periodic oscillations found downstream of a cavity covered with a perforated lid.

Knowing that the open cavity can sustain periodic oscillations regardless of the upstream conditions, we will restrict our attention to the case involving upstream laminar separation. Additionally, the cavities are considered shallow which rules out oscillations attributed to resonant transverse acoustic waves as the destabilizing forcing function. One of the earliest investigations characterizing this cavity flow problem stems from the laboratory experiments by Sarohia [1,2] who tested three axisymmetric models. His experiments lead to certain quantitative criteria necessary to suppress an oscillatory state. For cavity depths $d/\delta_o > 2.5$, a maximum cavity width $b\sqrt{\mathrm{Re}_{\delta_o}}/\delta_o \sim 300$ will inhibit amplified disturbances in the shear-layer while traversing the cavity opening. Beyond this width, the cavity will instigate growth into large-scale instabilities of the first mode ($f_1 b/U$). If the cavity is widened, the initial value $f_1 b/U$ modestly rises until a sudden jump to the next mode. This second mode is synonymous with an abrupt shortening of the instability wavelength. With further widening, higher modes are possible until the cavity reaches wake mode [3] where the separated flow is suddenly visualized as a bluff-body wake. Under a fixed Reynolds number, Sarohia [2] developed an empirical relationship between the disturbance wavelength and the cavity width; $b/\lambda = N + \frac{1}{2}$ where N is the mode integer.

Our understanding of the physical mechanism responsible for sustaining an oscillating cavity flow is largely attributed to the extensive efforts of Rockwell et al. [4–8]. The essential feedback mechanism is actually present in a much wider class of geometries including planar (or axisymmetric) jets and mixing layers impinging on a downstream structure. In the case of the open cavity configuration, the flow impinges onto the downstream wall. This act instigates an instantaneous upstream propagation that subsequently destabilizes the separated shear layer. Kelvin–Helmholtz instabilities form within the shear layer that amplified into large-scale coherent structures prior to their impingement onto the downstream wall. Rockwell and Naudascher [6] categorized this vortex evolution as ''fluid-dynamic'' whose process is devoid of an acoustic delay. Recently, Rowley et al. [9] successfully applied this physical perception to exposed cavities where the flow was compressible and separation was laminar.

Contrary to the open geometry, the perforated-cover cavity has received little attention outside of isolating the ''fluid-resonant'' feedback mechanisms [6]. King et al. [10] observed amplified instabilities within longitudinal slots that were in line with the streamwise flow direction of a cylindrical duct. Recently, Celik and Rockwell [11] reported self-sustaining instabilities over a deep cavity when covered by a specific perforated lid and approached by a laminar boundary layer. Besides demonstrating a frequency reduction of the salient spectral peaks and modal jumps

Contributed by the Fluids Engineering Division for publication in the JOURNAL OF FLUIDS ENGINEERING. Manuscript received by the Fluids Engineering Division September 17, 2003; revised manuscript received May 30, 2004. Associate Editor: F. F. Grinstein.

with increased impingement length, they also found that the instability wavelength scales with the streamwise extent of the perforations rather than the circular perforations themselves. Ozalp et al. [12] subsequently extended their experiments to investigate the same phenomena, but approached by a turbulent boundary layer. For hole diameters $D/\theta<4$, Ozalp et al. reaffirmed the prior conclusion [11] that the dimensionless frequency of the large-scale disturbance remains consistent for a specific mode of oscillation. Another important conclusion of their work deals with the spanwise coherency of the instabilities. Unlike the free shear layer spanning the open cavity, they noted little correlation of the spanwise structure directly adjacent to the perforated lid.

In contrast to the above investigations, the present study aims to broaden our current physical understanding of a self-sustained oscillatory flow over an elongated shallow cavity covered by a perforated lid. The impetus for considering this specific configuration stems from the present need to ascertain detectable far-field noise emanating from complex cavities recessed within Naval surface and undersea vessels. The downstream wall of the elongated cavity is far removed from the perforated lid. Thus, impact of a ''rolled-up'' vortex (or a portion thereof) onto this structure is not the vital element leading to an instantaneous feedback that sustains the oscillations. Furthermore, the depth criteria $d/\delta_o<10$ and $d/b<1.0$ of the present geometry clearly identifies a shallow cavity, which is nearly an order-of-magnitude less than previously studied deep configurations. The lid perforations of the full-scale cavity appear as a series of closely packed staggered holes whose center spacings are a diameter apart in both the streamwise and spanwise directions.

Knowledge about the large-scale instability downstream of this particular geometry and the restoring hydrodynamic perturbations is gained herein by examining the flow physics resolved through large-eddy simulations (LES). Although initial separation is laminar, this methodology is needed to resolve transition and the subsequent turbulent physics evolving in the traversing shear layer. Jordan and Ragab [13] among others [14,15] have clearly demonstrated the capability of the LES strategy for resolving the fine-scale physics within separated shear layers including final roll-up of a large-scale Karman-type structure. In view of the previous experimental observations [12], the spanwise hole spacing is sufficiently tight to model them as slots. Thus, the streamwise length scale is defined by the leading and trailing edge of the first and last slot, respectively. Relevant full-scale pressure data was measured on-board a US Navy submarine at several locations throughout an elongated recessed inlet. However, some of these pressure measurements may be conflicting due to poor correlation, and consequently unusable for quantifying the respective large-scale oscillation. Thus, the present investigation includes examination of the direct communication between the external oscillation and the internal cavity to aid processing the full-scale pressure data.

Governing Equations for the Resolved Field

Resolving growth of the shear-layer instabilities along the perforated cavity lid demands stretch grids to ensure the proper spatial resolution. Stretched grid topologies typically require reformulating the governing equations into a curvilinear coordinate system (ξ,η,ζ). The corresponding LES equations can be derived according to the procedure suggested by Jordan [16] where the first spatial operation is formal transformation of Navier–Stokes equations to the curvilinear system. The resultant system is a set of direct numerical simulation equations that are solved in the computational domain. Instituting a formal filter operation derives the respective LES formulation. For the present application, we will assume that the filter width and local grid spacing are equal. Thus, the resolved and filtered turbulent fields are mathematically the same. The differentiation and filtering commute similar to the filter operation applied to the Navier–Stokes equations in Cartesian coordinates. The resultant grid-filtered equations in curvilinear coordinates become

$$\text{Continuity:}\quad \frac{\partial \overline{U}^k}{\partial \xi^k}=0 \tag{1a}$$

$$\text{Momentum:}\quad \frac{\partial \sqrt{\tilde{g}}\overline{u_i}}{\partial t}+\frac{\partial \overline{U}^k\overline{u_i}}{\partial \xi^k}=\frac{\partial \sqrt{\tilde{g}}\tilde{\xi}^k_{x_j}\overline{p}}{\partial \xi^k}+\frac{\partial \sigma_i^k}{\partial \xi^k}+\frac{1}{\mathrm{Re}}\frac{\partial}{\partial \xi^k}\left[\sqrt{\tilde{g}}\tilde{g}^{k\ell}\frac{\partial \overline{u_i}}{\partial \xi^\ell}\right] \tag{1b}$$

where the transformation operation redefines the real SGS stress (σ_i^k) in terms of the resolved Cartesian $(\overline{u},\overline{v},\overline{w})$ and contravariant $(\overline{U},\overline{V},\overline{W})$ velocity components; specifically, $(\sigma_i^k=\overline{U^k u_i}-\overline{U^k}\,\overline{u_i})$. During the computation, each contravariant velocity component is evaluated in terms of their resolved counterparts using the definition $\overline{U^k}=\sqrt{\tilde{g}}\tilde{\xi}^k_{x_j}\overline{u_j}$. The overbar in this definition denotes the filter variable whereas the tilde symbolizes implicit filtering of the metric coefficients $(\tilde{\xi}^k_{x_j})$ and Jacobian $(\sqrt{\tilde{g}})$ through their numerical approximation [16].

The above LES equation system for the resolved field was numerically approximated and time-advanced according to a procedure outlined by Jordan [17]. His solution strategy has demonstrated acceptable numerical accuracy for many engineering problems dealing with both internal and external flows. However, resolution of the large-scale instability in the present computations differs slightly by the higher-order treatment of the convective derivative. Specifically, compact fourth-, fifth-, and sixth-order stencils approximated this derivative in the streamwise, normal, and spanwise directions, respectively.

Dynamic Subgrid Scale Model

Turbulence scales beneath the grid's spatial resolution are termed the subgrid-scales (SGS) of the LES computation. To model these scales, we used an eddy viscosity relationship that has been modified for dynamic computation of the model coefficient [18–20]. The dynamic improvement [19] promotes the correct asymptotic behavior of the modeled turbulent stresses when approaching no-slip walls. Besides this feature, numerous applications show that the dynamic version will correctly contribute little in the low to zero turbulence regions of the flow domain. The model in the transformed space is expressed as

$$\sigma_i^k+1/3\tilde{\varsigma}_i^k\tau_{\ell\ell}=2C\overline{\Delta}^2|\overline{S}|\overline{S_i^k} \tag{2}$$

where C is evaluated dynamically based on the resolved scales and $\tilde{\varsigma}_i^k$ is a filtered metric term defined as $\tilde{\varsigma}_i^k=\sqrt{\tilde{g}}\tilde{\xi}^k_{x_j}\delta_{ij}=\tilde{\xi}^k_{x_i}$. The turbulent eddy viscosity (ν_T) is defined by $\nu_T=C\overline{\Delta}^2|\overline{S}|$ where $|\overline{S}|=\sqrt{2\overline{S_{ij}}\overline{S_{ij}}}$ and $\overline{\Delta}$ is the grid-filter width. The resolvable strain-rate field $(\overline{S_i^k})$ is expressed as $\overline{S_i^k}=\sqrt{\tilde{g}}\tilde{\xi}^k_{x_j}\overline{S}_{ij}$.

Evaluating the model coefficient dynamically in the computation involves a unique derivation that starts with explicitly filtering the grid-scale LES equations [Eq. (1)] a second time by a test filter [19]. This derivation leads to an algebraic expression that determines the coefficient over a local narrow band of finest resolved scales as given by the test filter kernel and width $(\bar{\bar{\Delta}}_t)$. The test filter employed herein is actually a form of volume averaging [21] where the filter width is twice the local grid spacing; $\bar{\bar{\Delta}}_t=2\Delta_g$. The user has the choice of test filtering along the curvilinear lines in either the physical domain or computational space that depends on whether the SGS term is implemented in a non-conservative or conservative form [20]. However, the user must

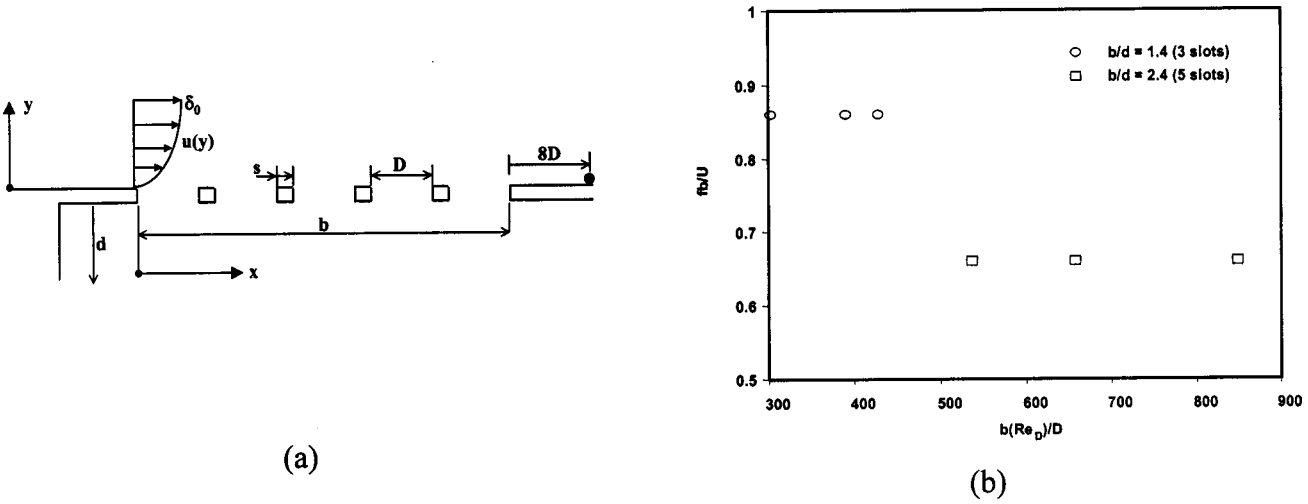

Fig. 1 Example slot geometry (five slots) and the initial frequency spectra of the large-scale instability (*a*) Slot geometry. (*b*) Oscillation frequency.

avoid the associated second-order error produced in the physical domain by numerically evaluating each contributing first-order derivative prior to the explicit filter operation. The modified Leonard term (L_i^k) of the test-filter equations has the cognate form

$$L_i^k = T_i^k - \overline{\sigma_i^k} \tag{3}$$

in the computational space where the bar over the Reynolds stress denotes the test filter operator. In this identity, the modified Reynolds stress (T_i^k) is defined by

$$T_i^k - \tfrac{1}{3}\tilde{\varsigma}_{x_j}^k T_{\ell\ell} = 2C\bar{\bar{\Delta}}^2 |\bar{\bar{S}}| \bar{\bar{S}}_i^k \tag{4}$$

Substituting this definition and the test-filter SGS stress $\overline{\sigma_i^k}$ into the identity [Eq. (3)] gives a second form of the transformed Leonard term from which we determine C;

$$L_i^k - \tfrac{1}{3}\tilde{\varsigma}_{x_j}^k L_{\ell\ell} = 2C\overline{\Delta}^2 M_i^k \tag{5}$$

The model stress (M_i^k) is defined in terms of resolvable tensors as $M_i^k = \alpha^2 |\bar{\bar{S}}| \bar{\bar{S}}_i^k - \overline{|S| S_i^k}$ where the filter width ratio $\alpha = 2$.

Contracting L_i^k in Eq. (5) gives a unique expression for the model coefficient C. The derivation must yield rotational invariance of the coefficient in both the physical domain and transformed space. The proper procedure requires writing the error function in the physical domain before minimizing its square. Along the curvilinear lines in the physical domain, the contravariant error tensor (E_i^k) becomes

$$E_i^k = \sqrt{\bar{\bar{g}}}\,\bar{\bar{\xi}}_{x_j}^k L_{ij} - \tfrac{1}{3}\bar{\bar{\varsigma}}_{x_j}^k L_{\ell\ell} - 2C\overline{\Delta}^2 \sqrt{\tilde{\bar{g}}}\,\tilde{\bar{\xi}}_{x_j}^k M_{ij} \tag{6}$$

where matrices L_{ij} and M_{ij} are not summed independently. Minimizing this error gives the expression

$$C = \frac{L_i^k \cdot M_i^k}{2\overline{\Delta}^2 M_m^k \cdot M_m^k} \tag{7}$$

for the model coefficient that operates on the inner product of the Cartesian tensor components of L_i^k and M_i^k in the computational space.

Inasmuch as the model coefficient is dependent on the local instantaneous strain-rates of the resolved field, either positive or negative values are possible in its evaluation. While the positive coefficients denote forward scatter in the turbulent energy spectrum, the negative values symbolize backscatter, or the reverse of energy from the SGS scales to the finest scales of the resolved field. Experience has demonstrated that the backscatter physics correlate well over long execution times, which quickly demand ''ad hoc'' measures to guarantee stability. However, in most simulations the statistical contribution of the SGS model is usually small compared to the resolved fields. Thus, the best choice for maintaining a stable computation at the instantaneous level is to truncate all negative contributions from the dynamic model to yield a net zero effect.

Results and Discussion

The following investigation seeks to characterize the large-scale instability downstream of a rectangular cavity covered by a perforated lid. Moreover, we desire a simple correction to the perforations that tend toward mitigating (or possibly eliminating) the instability. The cavity itself is classified here as one that is shallow, where the streamwise length (b) of the lid perforations exceeds the cavity depth (d). Additionally, the cavity is elongated meaning that its aft wall boundary is far removed from the last perforation such that impingement is not the governing mechanism for self-sustaining the periodic oscillation. As noted earlier, the spanwise spacings of the perforations are sufficiently tight to model the lid geometry as a streamwise series of slots. This modification is justified in view of the analogous results seen by Rockwell [22] for both staggered holes and slots perforating the lid of his deep cavity configuration ($b/d \leqslant 0.5$).

Geometric and Flow Conditions. The final slot size and streamwise distribution selected for the LES computations mimics the staggered hole pattern of a scaled inlet cavity recessed within a US submarine. This configuration is sketched in Fig. 1*a* where the slot gap width (D) to spacing (s) is $s/D = 0.25$. We note that this ratio remained constant in the simulations because varying D (fixed s) by as much as 30% revealed no discernible differences in the dimensionless oscillation frequency fb/U. Figure 1*b* illustrates this fact for six LES computations involving both three-slotted and five-slotted lids where fb/U denotes the dimensionless frequency of the peak spectral amplitude taken $8D$ lengths downstream of the lid. Besides s/D the cavity depth (d) also remained fixed in the simulations with the lid length (b/d) ranging as $1.4 \leqslant b/d \leqslant 5.4$ which depicts lids perforated by 3 to 11 slots. Inside the cavity the fore and aft walls were modeled $2D$ and $12D$ beyond the slots. Externally, the inflow and outflow boundaries were placed $8D$ upstream and $12D$ downstream from the lid's leading and trailing edges, respectively. The respective upper boundary limit was situated at least ten boundary layer thicknesses ($10\delta_o$) above the cavity lid's leading edge.

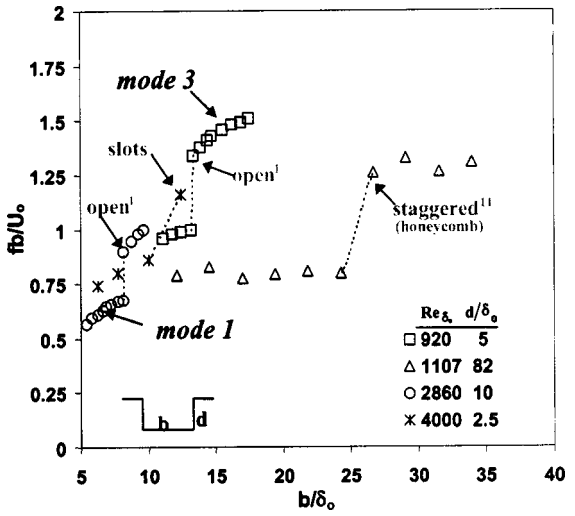

Fig. 2 Scaled frequency of the large-scale instability as a function of the streamwise cavity width for three geometric configurations (open, staggered and slotted)

Various structured grids were generated that obviously depended on the number of lid slots. The largest grid (11 slots) housed $565\times131\times17$ points in the streamwise (ξ), transverse (η), and spanwise (z) directions, respectively. We found a spanwise spacing of $\Delta z=0.03\pi$ coupled with the sixth-order compact stencil and periodic boundary conditions to be satisfactory for resolving transition in the separated shear layers as well as the energy scales of the subsequent turbulent field. As shown in the following comparisons, this spatial resolution and boundary conditions gave acceptable agreement with the experimental evidence in terms of quantifying the instability's fundamental character for a variety of geometric configurations. Inasmuch as upstream separation was laminar as well as the large-scale instability and its self-sustaining feedback mechanism being largely two-dimensional [12], fine grid spacing over a wider span was found not necessary for this particular application. This observation agrees with the conclusion reached by Ozalp et al. [12] where their experimental measurements indicated low spanwise correlation when the dominant behavior was well-organized and self-sustaining.

Using an exponential distribution function, the ξ grid lines were cluster towards the lid boundary such that the first field point above the wall near the exit remained as $\langle y^+\rangle\leqslant5$. At this outlet boundary, the transformed form of the Euler equations was found satisfactory to exit the instability with little distortion, which is similar to the outflow condition tested by Pauley et al. [24]. Conversely, the Blasius boundary layer equations for laminar flow were applied to fix the inflow condition during each LES computation. At separation the shape factor (H) ranged as $2.56\leqslant H\leqslant2.61$. Finally, a fixed streamwise velocity was upheld along the upper boundary with the two-dimensional continuity equation used to determine the respective vertical component given the spanwise component set to zero.

Characterizing the Instability. We can begin quantifying the large-scale disturbance downstream of a perforated lid by attempting analogies to the well-understood physics of the open cavity. Comparisons of the previous experimental measurements and the present computational results of the instability dimensionless frequency fb/U as generated for laminar flow separation over both open and covered cavities are shown in Fig. 2. Two sets of hot-wire anemometry measurements [1] are included for the open cavity geometry at Reynolds numbers $\mathrm{Re}_\delta=920$ and 2860, which are based on the boundary layer thickness at separation (δ_o). Conversely, the third experimental dataset [11] depicts pressure measurements taken just downstream of a deep cavity ($d/\delta_o=82$) that is covered by a staggered hole pattern. Each hole was offset streamwise by one hole diameter ($D=6.4$ mm) and drilled through a 5.5 mm thick plate ($t/D=0.86$). Collectively, these data adequately depict the large-scale instability in terms of the downstream predominant frequency, which is properly scaled by the length (b) and the freestream velocity (U). In each case, the initial separated shear-layer was laminar.

Although the Reynolds numbers and cavity geometries differ significantly in these four datasets, each shares several analogous hydrodynamic characteristics. Clearly, the characteristic length scale for the large-scale instability in each case is the streamwise length b. This fact is demonstrated in Fig. 3 for test cases involving three- and five-slotted lids where strong correlation exists between the downstream instability (indicated by the dot 8D from the last slot) and the trailing edge of the first slot. Interestingly, this cross-correlation reduced slightly when the instability oscillation entered into its second mode ($fb/U=0.86$, Fig. 3*a*). High correlation is equally displayed between the lid slots and an inside point on the cavity floor adjacent to the aft-end wall (Fig. 3*b*). This observation is further emphasized in Fig. 4 where the correlation is highest between the cavity aft volume and the adjacent region encompassing the periodic structure ($C_r\geqslant0.67$). These results suggest that the hydrodynamic feedback mechanism is present within the cavity itself, which destabilizes the initial shear layer and maintains the self-excited oscillations. However, the

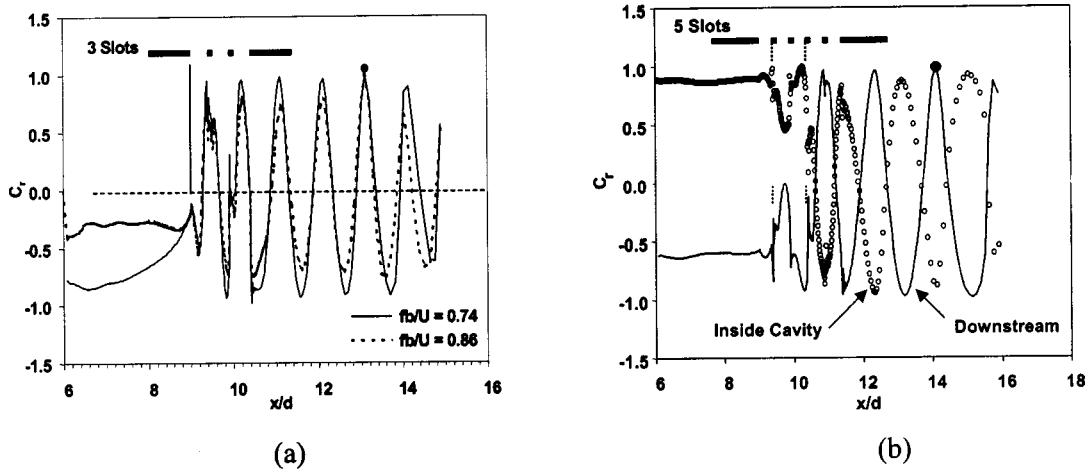

Fig. 3 Cross correlation coefficient (averaged over ten instability cycles); three slots (Re_d=4210, 6210) and five slots (Re_d=8680). (*a*) Three slots. (*b*) Five slots.

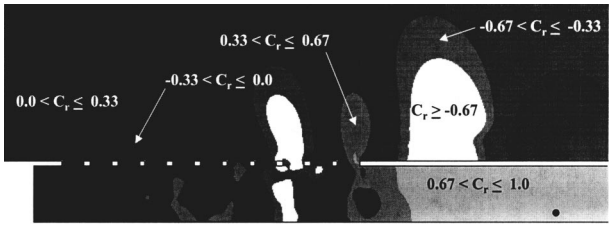

Fig. 4 Cross correlation coefficient between the Aft Cavity Pressure (indicated by the dot) and the resolved pressures (11 slots)

specific source of this feedback is apparently different between the open and covered cavities. Ostensibly, the perforated-cover cavity cannot support periodic impingement of rolled-up vortices on its downstream edge whose impact attributes to an upstream feedback system. Likewise, Celik and Rockwell [11] concluded that the large-scale periodic instability over their deep cavity ($d/\delta_o = 82$) is not sustained by an acoustic resonance state. This latter conclusion is equally applicable to the present shallow cavity ($d/\delta_o = 2.5$) where the aft wall is far removed from the lid's trailing edge.

Referring back to Fig. 2, a second self-similar characteristic is clearly discernible among the four datasets. Each geometry supports jumps to higher modes of the large-scale disturbance when subjected to a lengthened cavity width or lid cover (b/δ_o). Furthermore, while under a particular mode of oscillation, all three configurations indicate a moderate increase in fb/U by expanding b/δ_o. Like the open cavity, computations of the instability for the slotted-lid cavity will switch between modes simply by adding or reducing the respective number of slots. For laminar flow at separation, $b/\delta_o > 12$ caused a jump to the higher mode. However, at $b/\delta_o \sim 14$ (11 slots) we note that the previous mode oscillation had not fully disappeared from the frequency spectrum. Celik and Rockwell [11] also detected jumps between modes in their perforated lids, but as depicted in Fig. 2 they occurred at lengths (b/δ_o) much higher than the open or slotted-cover cavities. As noted earlier, Sarohia [1] first recognized this important characteristic by expressing a direct integral connection between the disturbance wavelength (λ) and length b; $b/\lambda \sim N + \frac{1}{2}$. For the present geometry, $\lambda/b = 0.64$ just before the frequency jump which indicates its first state of oscillation ($N \sim 1$).

Better agreement between the present LES computations and the experimental evidence can be reached by expanding the cavity length scale (b/δ_o) in terms of the boundary layer properties at separation. By replotting the dimensionless frequency versus the length scale $b\sqrt{\mathrm{Re}_{\delta_o}}/\delta_o$, Fig. 5 illustrates remarkable analogy in the disturbance character even though significant differences exist among the cavities geometric scales. For example, although the cavity depth d/δ_o of the staggered-hole cover [11] and present slotted lid differ by a large factor, both configurations show modal jumps at the same length scale. Sarahia [2] measured a first to second modal jump in his open axisymmetric cavity at length scale $b\sqrt{\mathrm{Re}_{\delta_o}}/\delta_o = 433$, which surprisingly agrees with the same jump computed herein for the slotted lid. Moreover, each modal stage indicates a similar modest rise in the dimensionless frequency fb/U when subjected to an increased length $b\sqrt{\mathrm{Re}_{\delta_o}}/\delta_o$. Figure 5*b* gives the dimensionless length $b\sqrt{\mathrm{Re}_{\delta_o}}/\delta_o$ that is required to instigate the large-scale instability for either an open [1] or slotted-lid cavity. Note that these lengths depict generation of the disturbance very early inside the separated shear layer after laminar separation. The circles and squares denote the present LES results with the open symbols specifying no oscillations sustained in the long-term. The notations δ, ν, U_o, and d adjacent to each solid symbol note the specific parameter that was increased to destabilize the initial shear layer using the nonoscillatory results as the initial flow condition. In one instance, the three parameters δ, ν, U_o were slightly amplified to instigate the disturbance. Of special interest is the oscillation/no-oscillation boundary for $d/\delta_o < 5$. At first glance, a slightly longer length $b\sqrt{\mathrm{Re}_{\delta_o}}/\delta_o$ is necessary to sustain the large-scale instability in the slotted-cover case compared to the open cavity for the same depth scale d/δ_o. This result is indicated for both the three- and five-slotted configurations. Not shown are the measured dimensionless frequencies downstream of the staggered-hole cover [11] because $b\sqrt{\mathrm{Re}_{\delta_o}}/\delta_o > 400$ in each experiment, which is well above the lower boundary limit denoting an oscillatory state.

Sustaining the Instability. Besides revealing analogous characteristics of the salient disturbance between the slotted-lid and open cavities, their agreement lends credibility to the LES computations including the generated spatial resolution. Given this similarity, we can now use the LES results to explore a few noteworthy differences. Unlike the open cavity configuration, destabilizing the initial shear-layer of the slotted-cover cavity does not guarantee an established long-term feedback mechanism sufficient

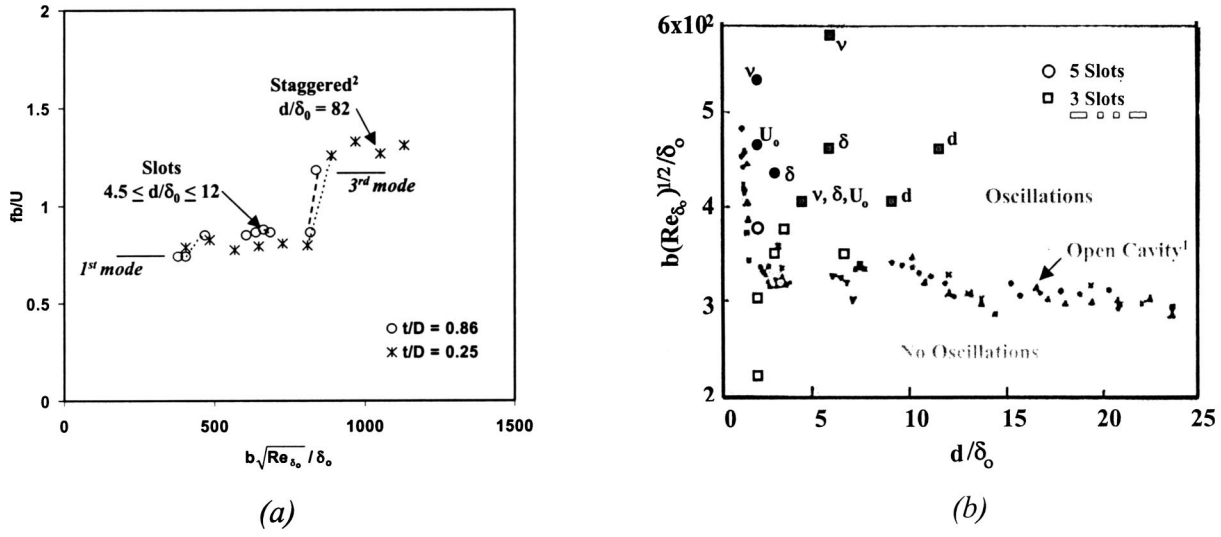

Fig. 5 Staggered-hole [11], open [1] and slotted-cover cavity results indicating the dimensionless frequency and minimum streamwise length of an oscillatory flow for a specific cavity depth. (*a*) Dimensionless frequency. (*b*) Minimum streamwise length.

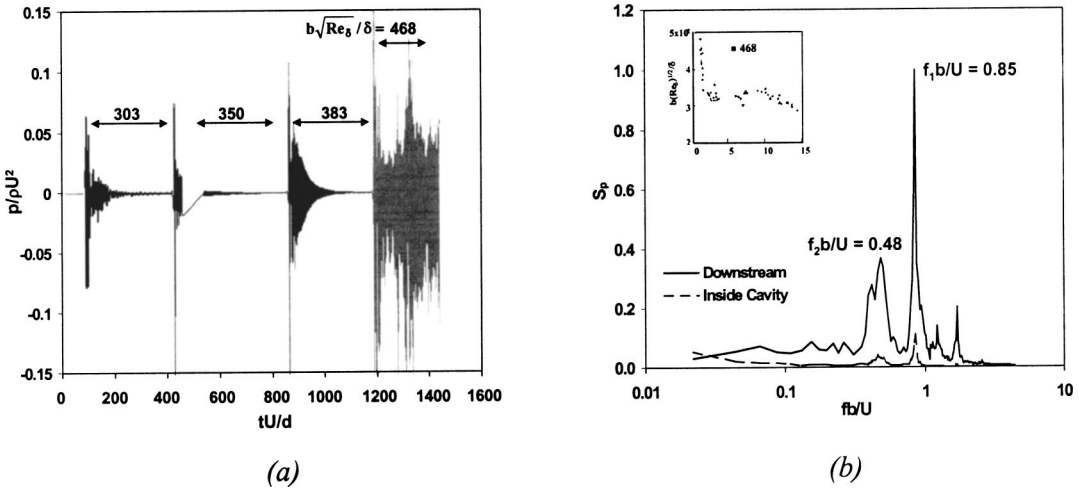

Fig. 6 Time series and frequency spectrum of the large-scale oscillation for a three slotted-lid cavity. (*a*) Time series. (*b*) Frequency spectrum: $b\sqrt{\mathrm{Re}_{\delta_o}}/\delta_o = 468$.

enough to uphold the oscillation. Lid lengths $b\sqrt{\mathrm{Re}_{\delta_o}}/\delta_o$ well below the minimum can temporarily support a large-scale oscillation by pulsing the flow using any one of the scale parameters that defines this streamwise length. For example, Fig. 6*a* illustrates temporary occurrence of the large-scale instability starting with the length $b\sqrt{\mathrm{Re}_{\delta_o}}/\delta_o = 303$. The cover geometry holds three slots and the cavity itself houses depth $d/\delta_o = 2.25$. In this first case, reducing the kinematic viscosity ν sparked the instability. After approximately 100 time units, the instability quasi-exponentially decayed to an insignificant level. The length $b\sqrt{\mathrm{Re}_{\delta_o}}/\delta_o = 350$ represents a sudden reduction of the upstream boundary layer thickness (δ_o) where the scaled depth was consequently raised to $d/\delta_o = 2.84$. Notice that the sudden amplification of the disturbance exceeds that of the previous case and approximately 50% more time was necessary to adequately dampen the peak levels.

Further reductions of the upstream boundary layer thickness constitute the remaining lengths $b\sqrt{\mathrm{Re}_{\delta_o}}/\delta_o$ in Fig. 6*a* until the cavity provided sufficient feedback to sustain growth of the large-scale oscillation ($b\sqrt{\mathrm{Re}_{\delta_o}}/\delta_o = 468$ and $d/\delta_o = 5.81$). The frequency spectrum of this disturbance taken at length 8D downstream of the cavity is shown in Fig. 6*b*. Clearly, the oscillation at length scale $b\sqrt{\mathrm{Re}_{\delta_o}}/\delta_o = 468$ is transitioning from the first mode ($f_1 b/U = 0.48$) to the second ($f_2 b/U = 0.85$). A discernible drop in magnitude and frequency of the former mode oscillation was computed as the large-scale disturbance completed its transition phase. Gharib and Roshko [8] also observed this reduction in their experiments of laminar flow past an open axisymmetric cavity. We note that the length $b\sqrt{\mathrm{Re}_{\delta_o}}/\delta_o = 468$ falls within the range of hysteresis where the oscillations can switch between modes by manipulating the length scale. Evidence of hysteresis is also discernible near the cavity's aft end (see dot in Fig. 4) where the higher mode holds the peak amplitude. This latter amplitude is an order-of-magnitude lower than the oscillation peak due to the limited exposure of the cavity volume to the traversing large-scale disturbance (only three slots). In Fig. 6*b* the last spike in the spectrum denotes the first harmonic of the second mode, whereas the smallest amplitude is a mix of the first and second modes ($mf_2 \pm nf_1$). Specifically, this mixed mode is defined by $f_2 - f_1$.

Inside the no-oscillation zone any excited disturbances will eventual decay exponentially regardless of the number of slots in the cover. Conversely, the oscillation zone defines growth of the initial disturbance into a large-scale instability that is clearly detectable far downstream of the cavity. However, transition across their shared boundary is not distinct. This fact is illustrated in Fig.

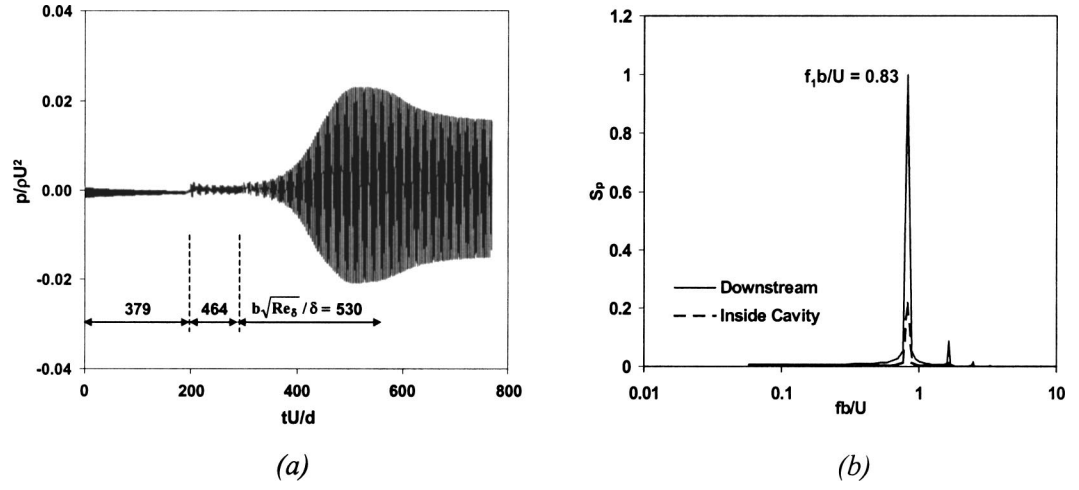

Fig. 7 Time series and frequency spectrum of the large-scale oscillation for a five slotted-cover cavity. (*a*) Time series. (*b*) Frequency spectrum: $b\sqrt{\mathrm{Re}_{\delta_o}}/\delta_o = 530$.

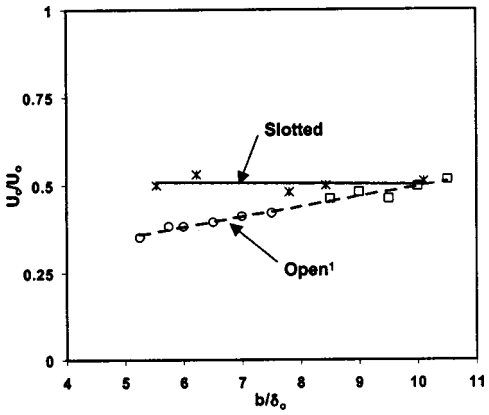

Fig. 8 Comparison of the disturbance phase velocities over an open [2] and slotted-lid cavity; circle and square symbols signify the first and second modes of the open cavity, respectively

7 where three separate time series of the large-scale instability downstream of a five-slotted lid are plotted along with the frequency spectrum of the final oscillation. Beginning with a damped field ($b\sqrt{\mathrm{Re}_{\delta_o}}/\delta_o=379$), low intensity disturbances were sustained by raising the freestream velocity such that the length scales $b\sqrt{\mathrm{Re}_{\delta_o}}/\delta_o=464$ and $d/\delta_o=2.3$ concurrently lie very near the lower limit defining an oscillatory flow. Further increase in the former parameter ($b\sqrt{\mathrm{Re}_{\delta_o}}/\delta_o=530$), by lowering ν, amplified these disturbances to produce the first oscillatory mode. The corresponding frequency spectrum shows the aft end of the cavity reverberating at an intensity that is approximately 20% of the fundamental oscillation and twice the level of the three-slotted cover. A small amplitude harmonic of the first mode is also detectable in the spectrum.

Final comparison of the present results to the open cavity configuration deals with the phase velocity (U_c) of the disturbance as it traverses the slots; $U_c=\lambda f$. Sarohia [1] found an increase in the scaled wave speed (U_c/U_o) simply by lengthening the cavity opening. But as illustrated in Fig. 8, the scaled phase velocity of the large-scale disturbance remains constant regardless of the number of slots. This result was consistent in all the LES simulations of lids housing 3 to 11 slots given a constant value for the scaled depth d/δ_o.

Given sufficient time, the aft cavity volume of the present simulated geometry will reverberate at the same fundamental frequency as the large-scale disturbance. This conclusion can be reach by observing Figs. 4 and 9 where the latter figure (nine slots) denotes scaled inside cavity spectra (S_p) that includes time records taken adjacent to the cavity aft wall (see dot located in Fig. 4). Apparently, a solid aft cavity wall in close proximity to the last slot is not necessary to instill a hydrodynamic feedback mechanism for destabilizing the initial shear layer and sustaining the large-scale oscillation. For the pressure spectra shown in Fig. 9*a* of the nine-slotted lid ($b\sqrt{\mathrm{Re}_{\delta_o}}/\delta_o=686$), cross-correlation between this reverberation region and the downstream disturbance was typically better than 60%. Reducing the number of slots improved this correlation by shortening their communication length. Conversely, the shorter lids lead to larger disparities between the two respective pressure spectra as indicated by the ratio of their peak spectral amplitudes plotted in Fig. 9*b*. For example, simulation of only three slots in the cavity cover ($b/d=1.4$) reduced the peak spectral level near the cavity aft end to approximately an order-of-magnitude lower than that of the instability itself. Lastly, we note that varying the extent over which the instability traverses the cavity lid had no definable trend on its absolute peak spectral magnitude. The peak values were in fact highly dependent on the boundary layer properties at separation.

Mitigating the Instability: Understanding these analogies between the open and slotted-lid cavities lends us options for mitigating or possibly eliminating the streamwise growth of the large-scale disturbance. More specifically, we desire to passively control the disturbance amplitude and frequency downstream of the cavity by manipulating its growth inside the separated shear layer. External spoilers are certainly an option of choice, but herein we choose to focus on the lid perforations themselves and their streamwise distribution. Knowing that the level of shear layer growth across an open cavity is similar to that of a turbulent mixing layer [2,25], the ratio s/D becomes an important length scale for attenuating the Reynolds stresses within that layer. Small values tend toward the open cavity configuration while longer lengths approach flat plate flow.

Results from several test cases are shown in Fig. 10 where the slot spacing was incrementally increased to $s/D=1.5$ (fixed D) along the cavity lid. In particular, the notation s/Dn in the figure denotes the n number of slot spaces increased beyond the first. Notation $s/D5$ indicates conversion of the nine-slotted lid to five-slots, but with the same cover length (b). Each test used the LES resolved field for a nine-slotted lid ($s/D=0.25$) as the initial oscillating flow state. Clearly, lengthening the slot spacing attenuated the large-scale instability. The $s/D1$ modification reduced the peak amplitude by 40% and the $s/D2$ configuration by 66%. A pressure spectrum is not plotted in Fig. 10*a* for the $s/D5$ test case because the initial oscillations eventually damped to an insignifi-

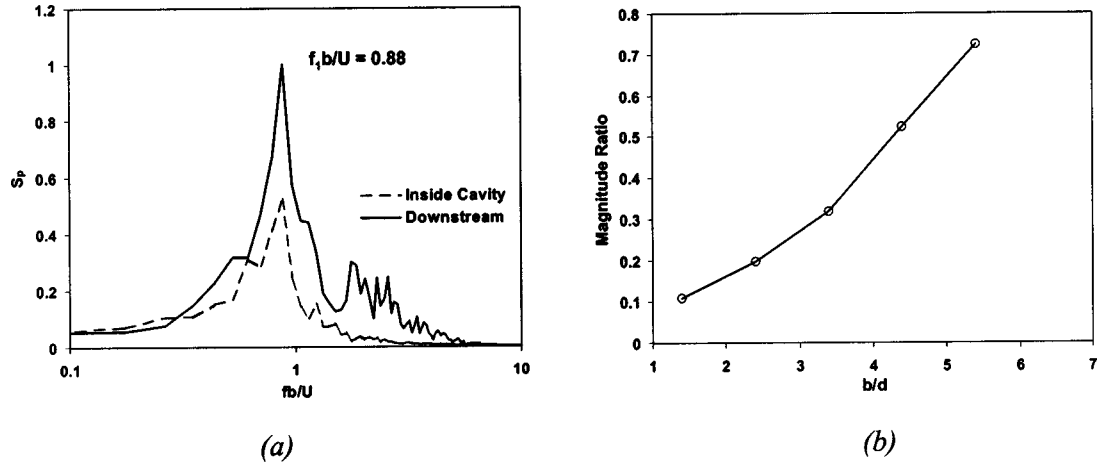

Fig. 9 Scaled pressure spectrum (9 slots, $b/d=4.5$) and ratio of the spectral peaks inside and downstream of the slotted-covered cavity (3–11 slots). (*a*) Pressure spectrum. (*b*) Peak *Sp* ratio.

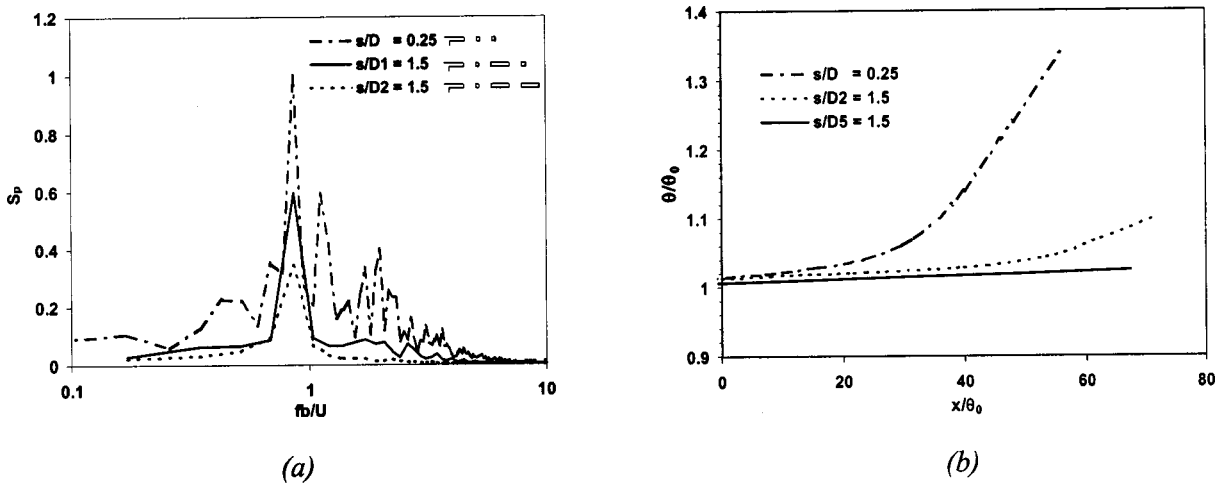

Fig. 10 Comparison of the phase velocities of the large-scale instability over an open and slotted-cover cavity; circle and square symbols signify the first and second modes, respectively. (*a*) Pressure spectra. (*b*) Momentum thickness.

cant level. Interestingly, the fundamental frequency of the disturbance is unaffected by the ratio s/D which suggests that the length scale of the feedback mechanism remained intact within the cavity volume.

Examining growth of the momentum thickness (θ) within the separated shear layer is a leading indicator of the instability's streamwise evolution. In the original nine-slotted configuration ($s/D=0.25$), Fig. 10*b* suggests that the disturbance completed transition to a turbulent state after traversing approximately 60% over the lid's length. The streamwise turbulent intensity contours in Fig. 11*a* support this observation by signifying the highest levels over the last three slot gaps. However, this figure also indicates that the transition process actually began much earlier by showing over 2% levels just after the second slot. Growth of the momentum thickness within the turbulent shear layer is $d\theta/dx=0.0123\,(b\sqrt{\mathrm{Re}_{\theta_o}}/\theta_o=1850)$ which is substantially lower than $d\theta/dx=0.022$ for the open cavity $(b\sqrt{\mathrm{Re}_{\theta_o}}/\theta_o=1635)^2$ and $d\theta/dx=0.035$ for the turbulent mixing layer [25]. Extending the second and third slot spacing (case s/D2) not only delayed transition, but also lowered the instability growth rate as reflected by its reduced peak in the pressure spectra. The streamwise turbulent intensity is comparatively lower and much more broadband within the turbulent shear layer as suggested by its contours in Fig. 11*b*.

Besides lowering the turbulent intensity, delaying transition to turbulence also has a profound effect on the downstream coherency of the periodic structures. This fact is illustrated in Fig. 12 where the phased-averaged contours of the streamwise turbulent intensity over the nonuniform lid clearly demonstrates a strong organized pattern. Ostensibly, the K-H waves have matured into large-scale structures sufficient enough to withstand breakdown by the Reynolds stresses developed further downstream. This suggestion reconciles the distinct differences observed by invoking this passive control option. Moreover, permitting maturity of the K-H wave while delaying transition distinguishes theses physics from the well-understood transition process in the shear layers of the open cavity. Finally, we note that although less obvious in Fig. 12, delaying transition did not change the average instability wavelength.

Simulating a five-slotted lid $(b\sqrt{\mathrm{Re}_{\theta_o}}/\theta_o=2296)$ with $s/D=1.5$ for all the slots inhibited long-term growth of the disturbance altogether. Observations showed that even the separated shear layers in the latter slot gaps reattached to the lid. Moreover, the free shear layers and bounded layers remained laminar across the lid. However, the slot gaps did cause jumps in the growth rate such that the averaged value $d\theta/dx=0.0003$ exceeds that of a fully attached laminar boundary layer $(d\theta/dx=0.0002)$ under equivalent upstream conditions.

Final Remarks

Controlling the streamwise growth of the large-scale instability downstream of a recess cavity that is covered by a series of perforations is an important attribute in design engineering. At the very least, we desire to mitigate the instability because its growth matures into large-scale periodic structures that remain coherent

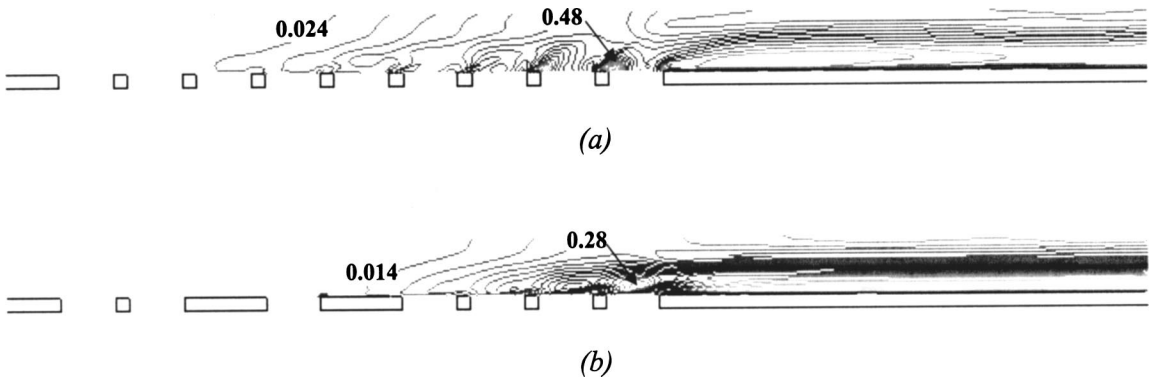

Fig. 11 Comparison of time-averaged streamwise turbulence intensity $\langle u'\rangle/U$ for uniform and variable slot spacing. (*a*) Contours Max. 0.48, Min. 0.0, Incr. 0.024. (*b*) Contours Max. 0.28, Min. 0.0, Incr. 0.014.

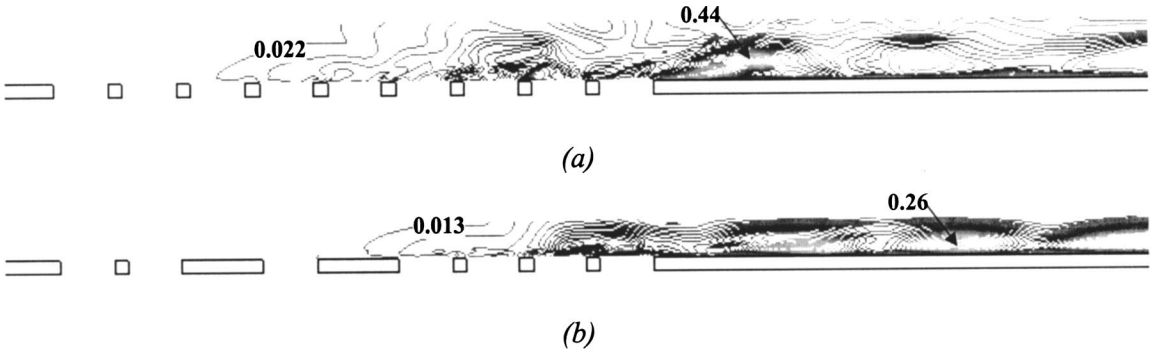

Fig. 12 Comparison of phase-averaged streamwise turbulence intensity $\langle u' \rangle / U$ (ten averages at the fundamental frequency) for uniform and variable slot spacing (*a*) Contours Max. 0.44, Min. 0.0, Incr. 0.022. (*b*) Contours Max. 0.26, Min. 0.0, Incr. 0.013.

far downstream as well as noisy in the remote field. For laminar upstream boundary layers, the present investigation showed that open and covered cavities (by either a staggered-hole pattern or a series of streamwise slots) all instigate the same disturbance. Proper scaling of its fundamental frequency into a dimensionless form requires the same large-scale length and velocity scales as the open cavity. Moreover, the instability will jump to higher modes in each configuration given the same dimensionless length scale in terms of the cavity width and boundary layer parameters (laminar flow) at separation. Sustaining the self-oscillation is achieved in each case by destabilizing the initial separated shear layer through a hydrodynamic feedback mechanism that exits whether the cavity is open or covered and deep or shallow, even if the aft inside wall is far removed from the perforations as illustrated in the present study.

Starting with a steady flow state, one can easily adjust certain geometric and/or boundary layer parameters such that the instability sustains full cycle. Previously unexplored, however, is the response of the flow if pulsed by one or more of these conditions while experiencing a no oscillation state. The present computations show that we can instigate the large-scale disturbance quite easily, but not the feedback mechanism to sustain the oscillation. The periodicity decays quasi-exponentially back to statistical steady state. This result suggests that the oscillation/no-oscillation zones as defined by Sarohia [1] to identify presence of a large-scale disturbance downstream of an open cavity, which is quantitatively applicable to the present slotted-lid cavities, actually represent existence of the feedback/no-feedback mechanism sufficient for self-sustaining the oscillation.

Options for passively mitigating the oscillation become obvious when dealing with perforated-cover cavities. Although the present computations showed negligible influence by varying the slot gap, successively lengthening their streamwise distribution ultimately extinguished the disturbance. Specifically, one can fully damp growth of a young K-H wave while it crosses between slots separated uniformly by a large margin. Alternatively, we can mitigate the oscillation to any level simply by invoking nonuniform spacing, but this control must take place near the leading edge of the lid before the wave reaches maturity. Notably, the dimensionless frequency of the large-scale instability appeared unaffected by the slot streamwise distribution. One question regarding passive control over the instability by varying the slot spacing is its success given a turbulent boundary layer at separation.

Finally, the present investigation also sheds light on the proper instrumentation strategy for measuring the fundamental frequency of the large-scale disturbance passed shallow cavities, such as those recessed within the hull of Navy vessels. Inasmuch as high correlation exits between the aft cavity volume and the disturbance itself for all lid lengths, installing sensors along the hull surface downstream of the cavity appears unnecessary to obtain a direct measurement. Moreover, analyzing the relative magnitudes of the peak spectra within the aft cavity volume is a simple and inexpensive metric for determining the feasibility of specific options for mitigating the periodic oscillation.

Acknowledgments

The author wishes to thank R. D. Joslin (program officer, Office of Naval Research, Code 333) and R. B. Philips (NUWC, Code 10) for their support of LES research related to flow over covered cavities. The computational work was supported in part by a grant of HPCMP resources from the Arctic Region Supercomputing Center (ARSC) and the Naval Oceanographic Office Major Shared Resource Center (NAVO MRSC).

Nomenclature

C = model coefficient
C_r = cross-correlation coefficient
D = slot gap width
E = model error tensor
H = shape factor
L_{ij} = modified Leonard term
M_{ij} = model stress tensor
N = oscillation mode
Re = Reynolds number
S_{ij} = strain rate tensor
S_p = pressure spectra
T_{ij} = modified Reynolds stress tensor
U, V, W = contravariant velocity components
U_o = freestream velocity
U_c = instability velocity
b = cavity streamwise length
d = cavity depth
f = frequency
$\sqrt{\tilde{g}}$ = filtered transformation Jacobian
g^{ij} = metric coefficients
m, n = mixed mode integers
p = pressure
s = slot spacing
t = lid thickness
u, v, w = Cartesian velocity components
u' = streamwise turbulent intensity
x, y, z = Cartesian coordinates
α = filter width ratio
$\bar{\bar{\Delta}}_t$ = test filter width
Δ_g = grid filter width
δ_o = boundary layer thickness at separation
θ = momentum thickness
ν_T = turbulent eddy viscosity
λ = wavelength
ρ = fluid density

τ = Reynolds stress
σ = Contravariant Reynolds stress
ξ, η, ζ = curvilinear coordinates
$\tilde{\varsigma}$ = filtered metric coefficient

References

[1] Sarohia, V., 1975, ''Experimental and Analytical Investigation of Oscillations in Flows Over Cavities,'' Ph.D. thesis, California Institute of Technology.
[2] Sarohia, V., 1977, ''Experimental Investigation of Oscillations in Flows Over Shallow Cavities,'' AIAA J., **15**, No. 7, pp. 984–991.
[3] Gharib, M., and Roshko, A., 1987, ''The Effect of Flow Oscillations on Cavity Drag,'' J. Fluid Mech., **177**, pp. 504–530.
[4] Rockwell, D., 1977, ''Vortex Stretching due to Shear Layer Instability,'' ASME J. Fluids Eng., **99**, pp. 240–244.
[5] Rockwell, D., 1977, ''Prediction of Oscillation Frequencies for Unstable Flow Past Cavities,'' ASME J. Fluids Eng., **99**, pp. 294–300.
[6] Rockwell, D., and Naudascher, E., 1979, ''Self-Sustained Oscillations of Impinging Free Shear Layers,'' Annu. Rev. Fluid Mech., **11**, pp. 67–94.
[7] Rockwell, D., and Knisely, C., 1980, ''Observations of the Three-Dimensional Nature of Unstable Flow Past a Cavity,'' Phys. Fluids, **23**, No. 3, pp. 425–431.
[8] Knisely, C., and Rockwell, D., 1982, ''Self-Sustained Low-Frequency Components in an Impinging Shear Layer,'' J. Fluid Mech., **116**, pp. 157–186.
[9] Rowley, C. W., Colonius, T., and Basu, A. J., 2002, ''On Self-Sustained Oscillations in Two-Dimensional Compressible Flow Over Rectangular Cavities,'' J. Fluid Mech., **455**, pp. 315–346.
[10] King, J. L., Boyle, P., and Ogle, J. B., 1958, ''Instability in Slotted Wall Tunnels,'' J. Fluid Mech., **4**, pp. 283–305.
[11] Celik, E., and Rockwell, D., 2002, ''Shear Layer Oscillation Along a Perforated Surface: A Self-Excited Large-Scale Instability,'' Phys. Fluids, **14**, No. 12, pp. 4444–4447.
[12] Ozalp, C., Pinarbasi, A., and Rockwell, D., 2003, ''Self-Excited Oscillations of Turbulent Inflow Along a Perforated Plate,'' J. Fluids Struct., **17**, pp. 995–970.
[13] Jordan, S. A., and Ragab, S., 1998, ''A Large-Eddy Simulation of the Near Wake of a Circular Cylinder,'' ASME J. Fluids Eng., **120**, pp. 243–252.
[14] Kravchenko, A. G., and Moin, P., 2000, ''Numerical Studies of Flow Over a Circular Cylinder at $Re_D = 3900$,'' Phys. Fluids, **12**, No. 2, pp. 403–417.
[15] Breuer, M., 1998, ''Numerical and Modeling Influences on Large-Eddy Simulations for the Flow Past a Circular Cylinder,'' Int. J. Heat Fluid Flow, **19**, pp. 512–521.
[16] Jordan, S. A., 1999, ''A Large-Eddy Simulation Methodology in Generalized Curvilinear Coordinates,'' J. Comput. Phys., **148**, pp. 322–340.
[17] Jordan, S. A., 2003, ''Resolving Turbulent Wakes,'' ASME J. Fluids Eng., **125** pp. 823–834.
[18] Smagorinsky, J., 1963, ''General Circulation Experiments With the Primitive Equations, I. The Basic Experiment,'' Mon. Weather Rev., **91**, pp. 99–164.
[19] Germano, M., Piomelli, U., Moin, P., and Cabot, W. H., 1991, ''A Dynamic Subgrid-Scale Eddy Viscosity Model,'' Phys. Fluids, **3**, pp. 1760–1765.
[20] Jordan, S. A., 2001, ''Dynamic Subgrid-Scale Modeling for Large-Eddy Simulations in Complex Topologies,'' ASME J. Fluids Eng., **123**, pp. 1–10.
[21] Schumann, U., 1975, ''Subgrid-Scale Model for Finite Difference Simulation of Turbulent Flows in Plane Channel and Annuli,'' J. Comput. Phys., **18**, pp. 376–404.
[22] Rockwell, D., 2003, personal communication.
[23] Mansy, H., Yang, P., and Williams, D. R., 1990, ''Quantitative Measurements of Three-Dimensional Structures in the Wake of a Circular Cylinder,'' J. Fluid Mech., **270**, pp. 277–296.
[24] Pauley, L. L., Moin, P., and Reynolds, W. C., 1990, ''The Structure of Two-Dimensional Separation,'' J. Fluid Mech., **220**, pp. 397–411.
[25] Liepmann, H. W., and Lufer, J., 1947, ''Investigation of Free Turbulent Mixing,'' NACA Technical Note No. 1257.

Wake Flow of Single and Multiple Yawed Cylinders

A. Thakur
Graduate Research Assistant

X. Liu
Graduate Research Assistant

J. S. Marshall
Professor and Chair,
jeffrey-marshall@uiowa.edu
Department of Mechanical and Industrial Engineering
and IIHR—Hydroscience and Engineering,
The University of Iowa, Iowa City, IA 52242
Phone: (319) 335-5817, Fax: (319) 335-5669

An experimental and computational study is performed of the wake flow behind a single yawed cylinder and a pair of parallel yawed cylinders placed in tandem. The experiments are performed for a yawed cylinder and a pair of yawed cylinders towed in a tank. Laser-induced fluorescence is used for flow visualization and particle-image velocimetry is used for quantitative velocity and vorticity measurement. Computations are performed using a second-order accurate block-structured finite-volume method with periodic boundary conditions along the cylinder axis. Results are applied to assess the applicability of a quasi-two-dimensional approximation, which assumes that the flow field is the same for any slice of the flow over the cylinder cross section. For a single cylinder, it is found that the cylinder wake vortices approach a quasi-two-dimensional state away from the cylinder upstream end for all cases examined (in which the cylinder yaw angle covers the range $0 \leqslant \phi \leqslant 60°$*). Within the upstream region, the vortex orientation is found to be influenced by the tank side-wall boundary condition relative to the cylinder. For the case of two parallel yawed cylinders, vortices shed from the upstream cylinder are found to remain nearly quasi-two-dimensional as they are advected back and reach within about a cylinder diameter from the face of the downstream cylinder. As the vortices advect closer to the cylinder, the vortex cores become highly deformed and wrap around the downstream cylinder face. Three-dimensional perturbations of the upstream vortices are amplified as the vortices impact upon the downstream cylinder, such that during the final stages of vortex impact the quasi-two-dimensional nature of the flow breaks down and the vorticity field for the impacting vortices acquire significant three-dimensional perturbations. Quasi-two-dimensional and fully three-dimensional computational results are compared to assess the accuracy of the quasi-two-dimensional approximation in prediction of drag and lift coefficients of the cylinders.* [DOI: 10.1115/1.1792276]

1 Introduction

Cable flow problems often involve flow oriented both normal and parallel to the cable axis. In cases such as towed cables behind ships and airplanes, the axial translation of the cable can be much larger than the cross-flow velocity. In other cases, such as cables used to tether structures or the probes used in multi-wire hot-wire anemometers, the axial and cross-flow velocity components may be of a similar magnitude. The vortical wake of a yawed cable is important because the wake vortices induce forces on the cable and on other downstream structures. For instance, in naval towed array systems, cable cross-flow occurs due to ship maneuvering or heaving in moderate to heavy sea states. Vortices shed by cross-flow to towed array cables induce a fluctuating pressure which interferes with noise reception of hydrophones embedded in the cable. Recent designs for naval towed array systems utilize an array of parallel cables, introducing the further possibility of cable interference with wake vortices of other cables.

In laboratory studies, a cable exposed to a combination of axial and cross-stream flow is most easily represented by a yawed cylinder. Previous laboratory studies of yawed cylinder flow have been conducted by numerous investigators [1–9] for cases with a fixed cylinder mounted in a wind tunnel or water flume with yaw angle ranging from 0 to 75°. The cylinder yaw angle ϕ is defined [Fig. 1(*b*)] as the angle that the cylinder axis makes with the plane normal to the free-stream flow, so that the yaw angle is 0° for the pure cross-flow case and 90° for the pure axial flow case. Experimental data from these studies indicate that cylinder base pressure and the wake vortex shedding frequency for a yawed cylinder are approximately the same as for a cylinder in cross-flow with the same normal component of the free-stream velocity. This observation is often referred to as the *Independence Principle* in the literature (or the Cosine Rule in the early literature), since the cross-plane forces and flow field appear to be independent of the axial flow. Several experimental studies [2,4,8] describe deviations from the Independence Principle for large yaw angles. However, we note that large cylinder yaw angle also introduces numerous experimental difficulties, such as cylinder vibration and extensive regions of the flow influenced by upstream effects, and it is not clear if these deviations would occur for rigid cylinders of infinite length (which might more accurately describe a cable under tension).

Flow visualization studies indicate that the wake vortices of a yawed cylinder are aligned parallel to the cylinder sufficiently far from the upstream cylinder end. A typical flow visualization result for a fixed cylinder in a wind tunnel (from Ramberg [6]) is shown in Fig. 2. Near the upstream end of the cylinder the wake vortices are approximately parallel to each other, but they are aligned at a yaw angle greater than the cylinder yaw angle. A transition then occurs at a specific location along the cylinder, such that beyond this point the wake vortices are aligned at approximately the same yaw angle as the cylinder. This latter state in which the wake vortices are parallel to the cylinder is referred to as the quasi-two-dimensional limit since the velocity field is approximately the same at any cylinder cross-sectional plane. Theoretical and computational studies of quasi-two-dimensional yawed cylinder flows are given by Moore [10] and Marshall [11]. Marshall [11] examines the vorticity dynamics of the yawed cylinder flow and shows that the vorticity component in the cross-stream plane (a plane whose normal is parallel to the cylinder axis) rolls up around the Karman wake vortices, leading to a deficit of the axial velocity within the wake vortex cores. He argues based on stability theory [12,13] that the axial velocity deficit could destabilize the wake vortices at sufficiently high yaw angles. A three-dimensional computational study of flow past a yawed cylinder with infinite length is given by Lucor and Karniadakis [14], which shows that at high yaw angle the vortices shed from the cylinder are oriented at a

Contributed by the Fluids Engineering Division for publication in the JOURNAL OF FLUIDS ENGINEERING. Manuscript received by the Fluids Engineering Division July 22, 2003; revised manuscript received April 12, 2004. Associate Editor: K. D. Squires.

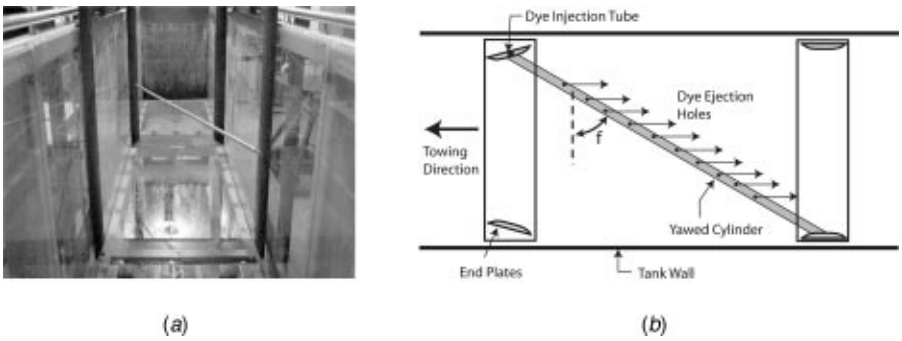

Fig. 1 Photograph and schematic showing the experimental apparatus mounted in the tow tank at 60° yaw

yaw angle somewhat less than the cylinder yaw angle (e.g., for a vortex yaw angle of 70°, the wake vortices are observed to shed at 58°).

The first objective of the current paper is to provide quantitative validation of the predictions of the quasi-two-dimensional theory for yawed cylinder wakes. Previous experimental work on yawed cylinder wakes have reported flow visualization of dye emitted from the cylinder boundary layer and pressure measurements on the cylinder surface, but no quantitative measurements of the wake flow field have been reported. The second objective of the current study is to examine the effect of wall boundary condition on the vortex orientation near the upstream cylinder end. In particular, whereas all previous experiments were performed with the cylinder fixed in a wind tunnel or flume, the current experiments are performed for a cylinder towed in a water tank, so that the walls move relative to the cylinder. Finally, although many applications involve an array of parallel yawed cylinders, there seems not have been any previous work done for interaction of multiple yawed cylinders. The third objective of the current paper is to examine interaction of two parallel yawed cylinders, focusing particularly on the extent to which the quasi-two-dimensional nature of the flow is preserved as the vortices of the upstream cylinder impact on the downstream cylinder.

2 Methods of Investigation

The research reported in this paper utilizes a combination of experiments performed in a tow tank and three-dimensional and quasi-two-dimensional computations. The present section describes these experimental and computational approaches.

2.1 Experiments. The experiments are carried out in a towing tank measuring 3.66 m long, 0.61 m wide, and 0.76 m deep. A photograph and schematic of the single cylinder model mounted in the tank are given in Fig. 1. Experiments are performed for cylinder yaw angles of 0° (cross flow), 30°, and 60°. The cylinders used in the experiments are smooth, steel cylinders, with 1.27 cm diameter. The cylinder is supported at its ends by streamlined aluminum plates, which are angled inwards by 10° to minimize the end effects on the wake structure [6]. In multi-cylinder experiments, a second parallel cylinder is mounted downstream of the main cylinder. The supports of the downstream cylinder are designed such that the distance between the two cylinder axes can be adjusted both in the horizontal and vertical directions.

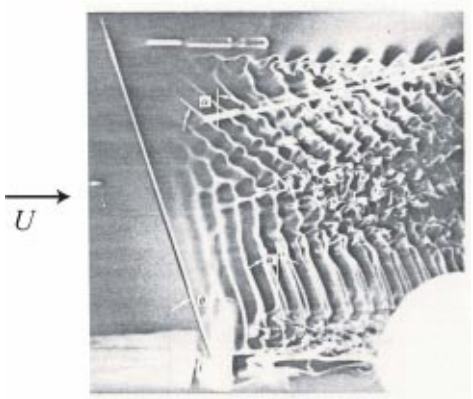

Fig. 2 Flow visualization image showing wake vortices of a yawed cylinder mounted in a wind tunnel (from Ramberg [6])

The cylinder supports are attached to a carriage that tows the apparatus along the tank at speeds ranging from 0 to 5 cm/s. The carriage is driven by a computer-controlled screw drive to provide steady translation with prescribed ramp-up acceleration and steady-state velocity. The experiments are carried out for a cross-flow Reynolds number (based on the component of flow normal to the cylinder axis) of 296 for the 0° and 60° yaw cases and 513 for 30° yaw case for both single and multi-cylinder experiments. All quantitative wake data are reported for the single cylinder 60° yaw case.

Flow visualization is performed using the laser-induced fluorescence (LIF) method, with Sulforhodamine Chloride 640 dye, which fluoresces red when excited by laser light with wavelength in range of 500–600 nm. The dye is stored in a reservoir and gravity-fed into the hollow annulus of the cylinder through a tube that runs through the supporting plate. The dye is fed into the boundary layer through two rows of holes drilled along the cylinder length, with the two rows spaced 0.64 cm apart. Consecutive holes are spaced more closely near the center of the cylinder span (0.33 cm) and are farther apart over the rest of the span (1.25 cm). The flow rate of the dye is controlled with a petcock valve and is maintained at a rate such that when the model is towed, the dye flows along the cylinder surface without disturbing its boundary layer. The dye is excited using a 200 mJ, pulsed Nd:YAG laser with wavelength of 532 nm. We examine both laser sheets and laser volumes, created using one or two cylindrical lenses, respectively. Photographs are taken using a digital video camera mounted on the tow carriage. The laser light is filtered out, so that only the light emitted by the dye fluorescence is captured on the film.

The velocity field in the wake of a single cylinder is measured using a cross-correlation particle-image velocimetry (PIV) system. The PIV system employs a double-pulsed Nd:YAG laser (Continuum) synchronized with a cross-correlation camera (Cooke SensiCam) with 1280×1024 pixel resolution. The images are acquired with the camera held fixed in the laboratory frame. The images are analyzed using a cross-correlation PIV method [15]. The flow is seeded using neutrally buoyant particles (Optimage) with nominal diameter of 10 μm. Only a section of the tank is seeded for PIV imaging prior to each run. A beaker of heavily seeded water is poured into the fresh water in the tank, and the

tank water is then stirred to distribute the seeding particles within a selected region of the tank. After stirring, the water is allowed to settle until no motion of the particles is observed prior to each experimental run. Planar images in the cylinder wake are taken in both vertical and horizontal planes. The size of the images captured is 150×80 mm in the vertical planes and 150×170 mm in the horizontal planes. The resolution of the images is 4–6 pixels per mm. Each interrogation area measures 40×40 pixels (8×8 mm) with a search radius of 4–5 pixels (about 1 mm). The velocity vectors in a given plane are obtained by averaging the results of four pairs of images taken over a time period of 1.0 s.

The uncertainty in the instantaneous velocity vectors measured by PIV has several sources [16]: camera resolution, noise introduced due to aberration of camera lens or electronic noise in circuits, error in locating the centroid and edge of individual particle images, density of particle images available in an interrogation area, size of the interrogation area, and out-of-plane displacement of seeding particles. PIV measurement errors are minimized by carefully selecting the seeding density, the time separation between images, and the laser sheet thickness to satisfy the guidelines of Keane and Adrian [17] (see also Thakur [18]). The precision of the PIV measurements is evaluated using a uniform-flow test, in which the camera is mounted on the carriage and moved at a uniform speed along the tank containing still water, thus creating an illusion of uniform flow as seen by the camera. Two images of an acquired pair are analyzed using different sizes of interrogation area to test the sensitivity of results to the interrogation window size. As would be expected, the measured standard deviation of the mean flow velocity decreases as the size of the interrogation window is increased. The interrogation window size for the cylinder wake experiments is selected to be as small as possible such that the velocity standard deviation in the uniform flow test is less than 5%.

2.2 Computations. Computations of the three-dimensional yawed cylinder wake are performed using a finite-volume method with a block-structured grid [19]. The control volumes (cells) have a quadrilatural cross section in the *x-y* (cross-stream) plane and uniform spacing in the axial (z) direction. The numerical method stores all dependent variables at the cell centers, and it uses a novel interpolation method to yield second-order accurate approximation of the diffusive and convective fluxes on the cell boundaries for arbitrary meshes (even for unstructured meshes). In order to provide additional numerical stability, the time derivative is weighted between a second-order time derivative approximation and a first-order upwind approximation, with characteristically about an 80-20 weighting ratio.

The free-stream velocity has a component U_N normal to the cylinder and a component U_T tangent to the cylinder axis. A cylinder-based coordinate system is used in which z is oriented along the cylinder axis, x is parallel to the normal component U_N of the free-stream velocity, and y is normal to both the cylinder axis and the free-stream velocity. For computations with a single cylinder, the computational grid has 31,542 points in the cylinder cross-plane and 45 points in the axial direction, for a total of 1,419,390 points in a region defined by $0\leqslant x/d\leqslant30$, $0\leqslant y/d\leqslant10$ and $0\leqslant z/d\leqslant4$. For computations with two parallel cylinders, the grid has 36,166 points in the cylinder cross-plane and 45 points in the axial direction, for a total of 1,627,470 points in a region defined by $-4.0\leqslant x/d\leqslant8.0$, $0\leqslant y/d\leqslant5.2$ and $0.0\leqslant z/d\leqslant5.0$. Periodic boundary conditions are used along the cylinder axis in order to approximate vortex shedding from a long cable. Symmetry boundary conditions are used in the y direction, and inflow and outflow boundary conditions are used in the x direction. An axial perturbation of the normal component of the inflow velocity is introduced as

$$u_{\text{inflow}}=U_N[1+\varepsilon\cos(2\pi z/L)], \tag{1}$$

where $L=5$ is the grid dimension in the axial direction and ε is the perturbation amplitude. We experimented with different values of ε, but for the computations presented in the paper we set $\varepsilon=0.05$. The computations are performed first using a steady-state code for a cylinder in constant cross-flow velocity. The steady-flow computational result is used as an initial condition for the unsteady-flow computation, in which we introduce both an axial velocity and a perturbation of the inflow cross-flow velocity.

Table 1 Effect of cross-sectional mesh refinement on computed drag and lift coefficients and Strouhal number for a single cylinder in cross-flow using the quasi-two-dimensional approximation. Experimental values are from Fleischmann and Sallet [20].

Flow measurement	Mesh1	Mesh2	Mesh3	Experiment
C_D (mean value)	1.48 ± 0.04	1.45 ± 0.04	1.44 ± 0.06	1.4 ± 0.1
$C_{L,\text{amp}}$ (mean value)	0.61 ± 0.20	0.65 ± 0.22	0.60 ± 0.28	0.6 ± 0.25
St (mean value)	0.199 ± 0.002	0.199 ± 0.001	0.199 ± 0.006	0.21 ± 0.01

Independence of the computational results to choice of cross-sectional grid is examined by repeating a two-dimensional flow computation with three different meshes—*mesh 1* (10,514 grid points), *mesh 2* (15,771 grid points), *mesh 3* (31,542 grid points). Results for computed mean drag coefficient, amplitude of lift coefficient variation, and Strouhal number are given in Table 1, in comparison to experimental values [20]. Results are close to the experimental values for all three grids. The sensitivity of the flow to spanwise grid resolution was evaluated by comparing three-dimensional computations for flow past a single cylinder at a 60° yaw angle with 25 points and with 45 points in the spanwise direction. The drag and lift coefficients and Strouhal number for this lower resolution case differ from the values obtained for the higher resolution case by only about 3% for the lift coefficient and about 2% for the drag coefficient and Strouhal number (see Table 2). Additional grid independence results for vorticity values in the cylinder wake are presented in Sec. 3.

3 Single Yawed Cylinder

Laser-induced fluorescence is used in both volumetric and vertical planar sheets to examine the qualitative structure of the cylinder wake vortices at different yaw angles. Of particular interest is determination of the wake vortex orientation relative to the cylinder yaw angle. Volumetric LIF pictures of the cylinder wake at yaw angles of 0°, 30°, and 60° are shown in Fig. 3 in a region immediately behind the cylinder, as indicated in the sketches below each picture. In the zero degree yaw case, the wake vortices are approximately parallel to the cylinder, but exhibit some waviness. In the 30° yaw case, the vortices are also approximately parallel to the cylinder, although near the upstream end of the cylinder the vortex yaw angle is slightly less than the cylinder yaw angle. For the 60° yaw case, the vortices are observed to curve significantly across the tank width. Near the side of the tank corresponding to the cylinder upstream end, the vortices are ori-

Table 2 Effect of spanwise mesh refinement on computed drag and lift coefficients and Strouhal number for a single cylinder in cross-flow using three-dimensional computations with 25 spanwise points (lower resolution) and 45 spanwise points (higher resolution). Experimental values are from Fleischmann and Sallet [20].

Flow measurement	Lower resolution $N_s=25$	Higher resolution $N_s=45$	Experiment
C_D (mean value)	1.44 ± 0.06	1.41 ± 0.08	1.4 ± 0.1
$C_{L,\text{amp}}$ (mean value)	0.60 ± 0.28	0.62 ± 0.16	0.6 ± 0.25
St (mean value)	0.199 ± 0.006	0.202 ± 0.011	0.21 ± 0.01

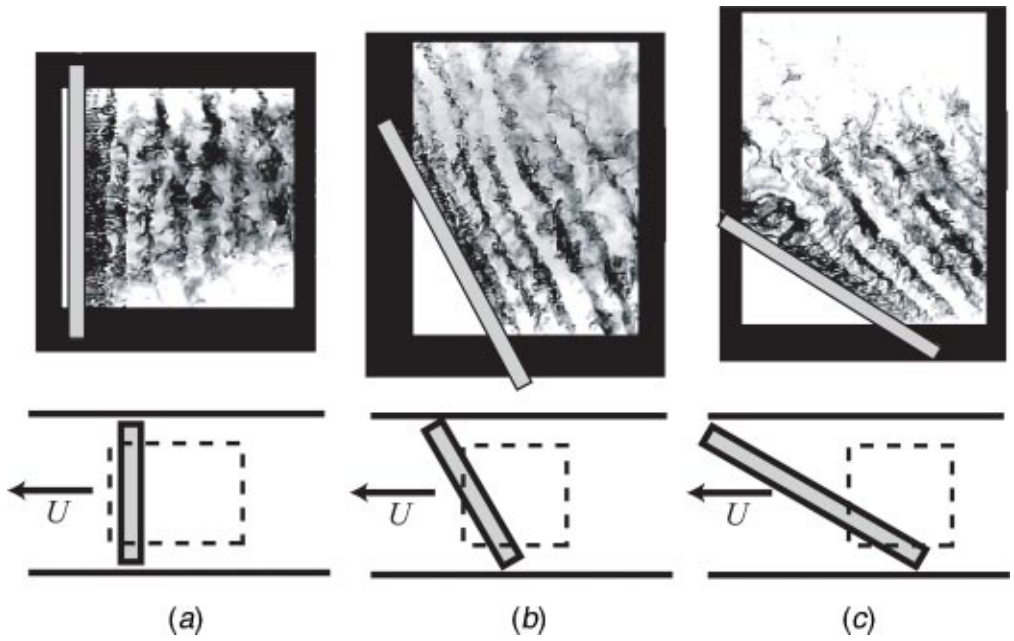

Fig. 3 Volumetric LIF images showing orientation of wake vortices of cylinders at yaw angles (*a*) 0°, (*b*) 30° and (*c*) 60°. The imaging region is indicated in the sketches below each image, and the towing direction is indicated by an arrow.

ented at an angle that is significantly less than the cylinder yaw angle. The vortices gradually bend with distance across the tank, such that near the opposite side of the tank they are oriented nearly parallel to the cylinder.

It is of note that the vortex orientation near the upstream end of the cylinder for the current study, involving a cylinder towed in a tank, is significantly different than observed in previous studies involving flow past a stationary cylinder in a water flume or wind tunnel. In particular, whereas we observe the vortices near the upstream end to have a *lesser* yaw angle than the cylinder, studies with flow past a fixed cylinder have observed the vortices near the upstream end to have a *greater* yaw angle than the cylinder (see, for instance, Fig. 2). The difference between the two cases appears to be due to the wall velocity relative to the wake vortices. When a cylinder is towed relative to a fixed wall, the downstream tank wall velocity (relative to the cylinder) is slightly greater than the mean vortex advection speed within the central part of the channel. The wake vortices (which end on the side walls) consequently appear to be dragged forward by the relative wall motion, giving rise to a decreased yaw angle near the cylinder upstream end. When the cylinder is fixed in a flowing stream, the wall appears to be moving backward relative to the mean wake vortex advection velocity, such that the wall drags the vortices backwards and gives rise to a substantially increased vortex yaw angle near the cylinder upstream end. Further understanding of this phenomenon might be gained by a detailed study of the side wall—vortex interaction region; however, as we are primarily interested in long cables this issue is outside the scope of the current study.

The Strouhal number for the three yaw angles examined, based on the component of the towing velocity normal to the cylinder, is observed to be 0.22, 0.24, and 0.28 for the cases with 0°, 30°, and 60° yaw, respectively. The Strouhal number for 0° yaw is consistent with the standard literature value of 0.20 ± 0.01 for this Reynolds number [20]. The observed increase in Strouhal number with increase in yaw angle is consistent with the experiments of van Atta [9], who cites Strouhal numbers of 0.20, 0.21, and 0.28 for the three yaw angles examined, respectively. A similar increase in Strouhal number is predicted in the computational study of Lucor and Karniadakis [14].

PIV measurements were obtained for a variety of vertical and horizontal planar slices of the flow field for the 60° yaw angle case. The PIV measurements are obtained after the cylinder has traveled a distance of at least 50 cylinder diameters, so as to avoid startup effects. For ease of image acquisition, the imaging plane for vertical slices is oriented parallel to the towing direction, as shown in the sketch in Fig. 4, rather than in the cross-sectional plane of the cylinder. We define the normal and tangential components of the towing velocity to the cylinder axis as $U_N = U \cos \phi$ and $U_T = U \sin \phi$, respectively, where U is the carriage tow speed and ϕ is the cylinder yaw angle. The velocity components in this coordinate system (u,v,w) and the vorticity components $(\omega_x, \omega_y, \omega_z)$ are nondimensionalized as

$$x^* = x/d, \quad y^* = y/d,$$
$$u^* = u/U_N, \quad v^* = v/U_N, \quad w^* = w/U_T, \tag{2}$$
$$\omega_x^* = \omega_x d/U_T, \quad \omega_y^* = \omega_y d/U_T, \quad \omega_z^* = \omega_z d/U_N,$$

where d is the cylinder diameter. Marshall [11] showed that within the context of the quasi-two-dimensional approximation, the dimensionless quantities (2) are independent of the cylinder yaw angle and depend only on the cross-stream Reynolds number $\mathrm{Re}_C \equiv dU_N/\nu$.

Experimental results for vorticity field ω_M in the vertical plane are plotted in Fig. 4(*b*) for the $\phi = 60°$ case. These measurements are taken in a plane with upstream end at a distance $7.5d$ and downstream end at a distance $18.5d$ behind the cylinder along the PIV measurement plane. The measured vorticity field is compared to quasi-two-dimensional computational results [Fig. 4(*a*)], where the computed vorticity field is projected from the cylinder cross-stream plane to obtain the vorticity component ω_M normal to the PIV measurement plane using

$$s = x/\cos \phi, \quad \frac{\omega_M d}{U_N} = \omega_z^* \cos \phi - \omega_x^* \tan \phi \sin \phi \tag{3}$$

The $\tan \phi$ term in Eq. (3) is equal to the ratio U_T/U_N, which arises due to the different expressions used to nondimensionalize ω_x^* and ω_z^*. The region in Fig. 4 that is common for the experimental and computational results is indicated by a dashed rect-

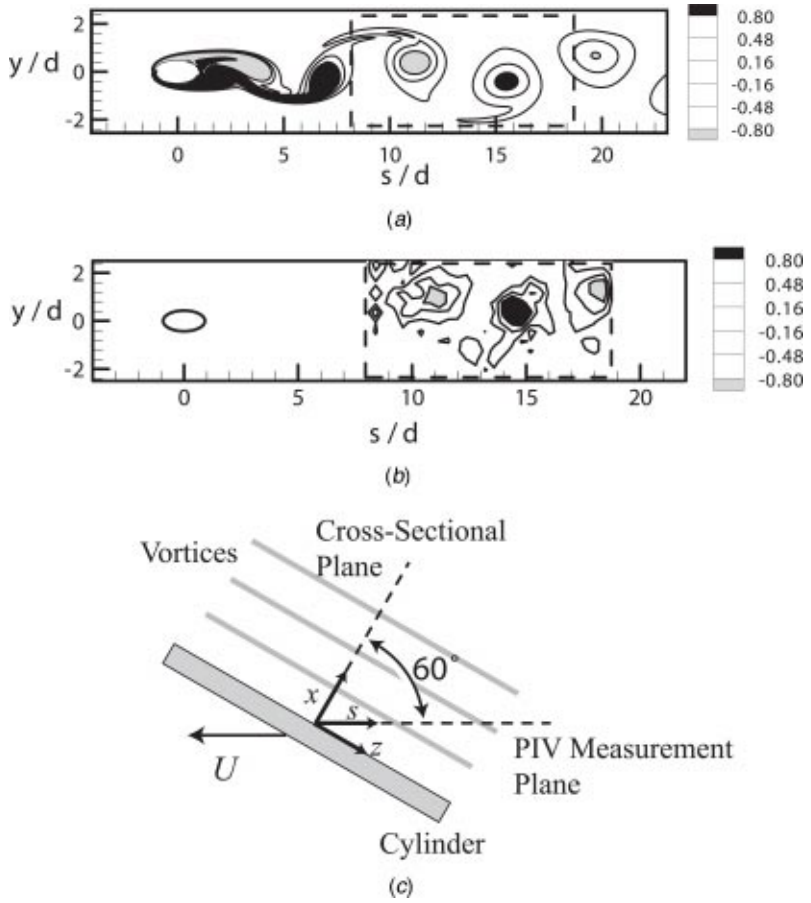

Fig. 4 Dimensionless vorticity component $\omega_M d/U_N$ in a vertical section of the flow oriented parallel to the towing direction for a cylinder at 60° yaw: (*a*) quasi-two-dimensional computational results and (*b*) experimental data measured using PIV. The computational results obtained in the cross-sectional plane are projected into the PIV measurement plane, as indicated in the sketch (*c*). The location of the experimental data is indicated by a dashed rectangle in both (*a*) and (*b*).

angle. The spacing between the vortices is somewhat smaller in the experimental results, corresponding to the experimental observation noted previously that the Strouhal number is about 40% higher than predicted by the Independence Principle, but otherwise the experimental and computational data exhibit similar flow features.

A comparison is given in Fig. 5 between the maximum vorticity ω_M within the vortex cores as a function of distance s for the experimental and quasi-two-dimensional computational results. The uncertainty in experimental vorticity values in this plot is estimated to be about 10%, based on the 5% velocity uncertainty and the grid increment size $\Delta s/d=\Delta y/d=0.4$. The quasi-two-dimensional computational results are given both for a computation with the medium-refined mesh 2 (dashed curve) and a computation with the more highly refined mesh 3 (solid curve). The quasi-two-dimensional computational predictions for wake vorticity appear to agree well with experimental values even for cylinder yaw angles as large as 60°.

Results from a quasi-two-dimensional computation in the cylinder cross-stream plane are plotted in Fig. 6, which shows contours of the axial vorticity ω_z^*, the cross-stream vorticity magnitude $\omega_C^2 \equiv [(\omega_x^*)^2+(\omega_y^*)^2]^{1/2}$, and the axial velocity w^*. The cross-stream vorticity is shed from the cylinder and wraps around

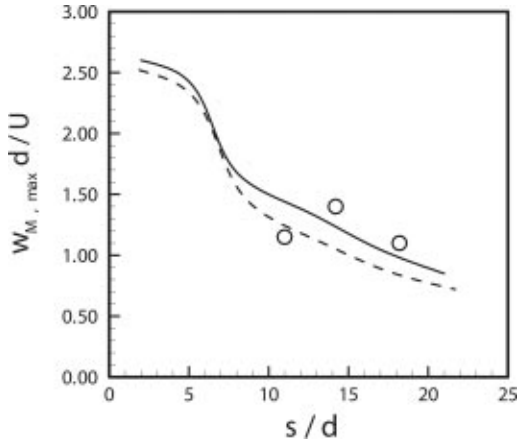

Fig. 5 Comparison of experimental data (circles) and quasi-two-dimensional computational results, with mesh 2 (dashed curve) and mesh 3 (solid curve), for vorticity magnitude ω_M at the center of the Karman vortices projected into the PIV measurement plane

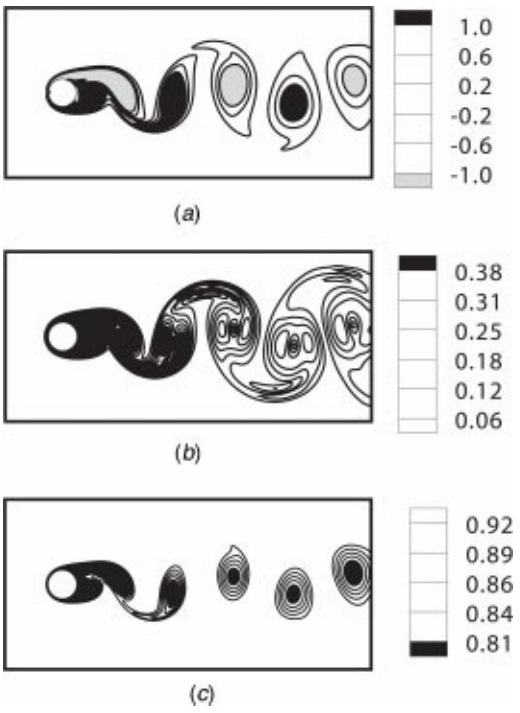

Fig. 6 Computed contours of (*a*) axial vorticity ω_z^*, (*b*) cross-stream vorticity magnitude ω_C, and (*c*) axial velocity *w for quasi-two-dimensional flow at $Re_C=300$**

the wake vortices, giving rise to an axial velocity deficit within the vortex cores. For $Re_C=300$, the velocity deficit within the vortex cores measures about 10%–15% of the free-stream axial velocity U_T in this region of the flow. Similar results were obtained by Marshall [11] using a vortex method.

PIV velocity measurements are obtained in horizontal planes slicing through the wake vortices, located at $y/d=\pm 0.4$ (which pass nearly through the vortex cores) and $y/d=\pm 1.2$ (which pass above and below the vortex cores, respectively). Contour plots of the cross-stream and axial velocity components, u^* and w^*, in the horizontal plane at $y/d=0.4$ are shown in Fig. 7. The contour plot of u^* in Fig. 7(*a*) shows the imprint of the Karman vortex street, where vortices rotating in opposite directions yield values of u^* of opposite sign, directed either toward or away from the cylinder. These streaks in the cross-stream velocity contours are somewhat intermittent due to the wavy nature of the Karman wake vortices. The projections of the mean vortex centerlines are plotted in Fig. 7 as solid and dashed lines, corresponding to vortices with positive and negative circulation, oriented at an average yaw angle of about 48°, which is consistent with the vortex orientation in the LIF images in this region of the tank. The magnitude of the fluctuation in cross-flow velocity component u ranges between 40% and 60% of the free-stream cross-flow velocity U_N.

Experimental contours of axial velocity component w^* obtained from PIV in the $y/d=0.4$ plane are shown in Fig. 7(*b*). Since the cylinder is towed in still water and the camera is fixed, the figure shows only the axial velocity deficit. This figure exhibits intermittent regions of axial flow located generally along the vortex cores. We note that the solid lines in Fig. 7(*b*) are not the vortex centerlines themselves but rather *projections* of the vortex centerlines, where the imaging plane is positioned to pass approximately through the mean vortex core centers for the vortices corresponding to the dashed lines in the figure. The measured maximum axial velocity deficit ranges between about 10% and 15% of U_T, which is consistent with the range of values cited above for the computational predictions for axial velocity. Since the PIV velocity measurements are subject to an uncertainty of about 5% of the free-stream velocity (see Sec. 2), the experimental uncertainty in the axial velocity deficit measurements is roughly 50% of its maximum value, which no doubt is responsible for some of the noise apparent in Fig. 7(*b*).

The validity of the quasi-two-dimensional approximation for the cylinder wake vortices is also examined using fully three-dimensional numerical simulations, with periodic axial boundary conditions (in order to consider flow past a long cable with negligible upstream end effect) and perturbation of the form (1) with $\varepsilon=0.05$. Computations are presented in Fig. 8 for a case with yaw angle $\phi=60°$. Figure 8 shows a perspective view of iso-vorticity magnitude contours with $\omega^*=1.0$. In agreement with our experimental flow visualization, the three-dimensional computational results indicate that the flow remains nearly quasi-two-dimensional, with wake vortices approximately parallel to the cylinder, although vortex bending perturbations are observed to gradually grow in amplitude with distance downstream of the cylinder.

4 Interaction of Two Parallel Yawed Cylinders

The flow past two parallel yawed cylinders of equal diameter, positioned one behind the other, is examined experimentally using LIF for cases with yaw angles of 0°, 30°, and 60°. The experimental apparatus is designed such that the distance ℓ between the cylinders in the x direction and the vertical offset distance h in the y direction (Fig. 9) can be adjusted independently. The experiments are conducted with $h/d=0.5$, such that wake vortices of one sign from the upstream cylinder impact at the center of the

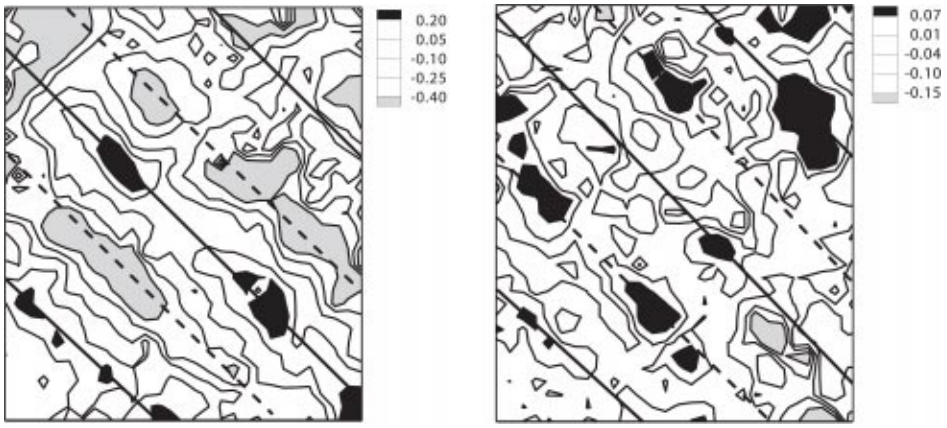

Fig. 7 PIV data in a horizontal plane at $y/d=0.4$ for (*a*) cross-stream velocity component u^* and (*b*) axial velocity component *w*

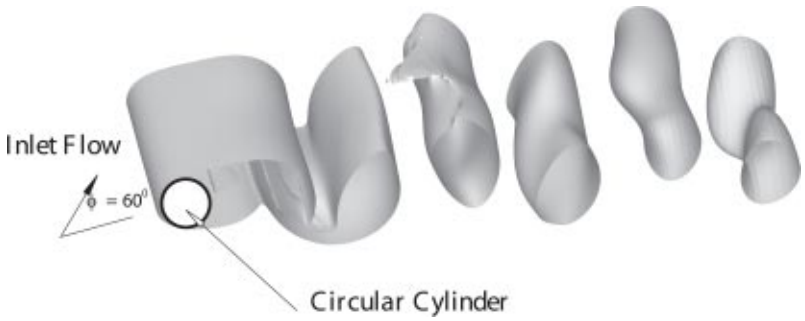

Fig. 8 Iso-surface of vorticity magnitude $\omega^* = 1.0$ obtained from a three-dimensional computation of flow past a single cylinder with 60° yaw angle

second cylinder. The distance between the cylinders is set at $\ell/d = 11$, 10, and 9 for cases with yaw angles 0°, 30°, and 60°, respectively. Both experimental and computational studies of two parallel cylinders in pure cross-flow [21–24] indicate that the vortex shedding from the upstream cylinder is suppressed if the cylinder spacing ℓ is less than $3-4d$, for which case the two cylinders seem to act as a single body and the vortices are shed directly from the downstream cylinder. For the cases considered in the current paper the cylinder spacing distance is sufficiently large that the vortex shedding from the upstream cylinder is nearly the same as for single-cylinder flow.

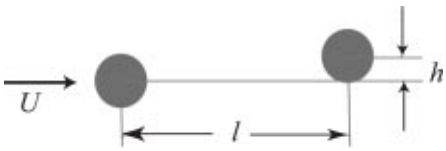

Fig. 9 Cylinder horizontal and vertical separation distances for experiments with two cylinders

The vortex orientation in the region just upstream of the downstream cylinder is shown in volumetric LIF images in Fig. 10, where the imaging region is indicated in the sketch below each picture. For each of the three yaw angles considered the vortex orientation is parallel to the cylinder up until the vortex has advected to about a cylinder diameter from the face of the downstream cylinder. After this point the vortex core cross-sectional shape becomes increasingly deformed and it is difficult to accurately detect the vortex orientation as it impinges on the downstream cylinder.

The vortex core deformation is observed more clearly in the vertical LIF slices taken in a plane normal to the downstream cylinder axis, as shown in Fig. 11 for a case with 30° yaw angle. The shape of the vortex core remains approximately unchanged by the presence of the downstream cylinder until the vortex approaches within a distance of about one cylinder diameter from the downstream cylinder face. The core then begins to increasingly deform in shape as it gets closer to the downstream cylinder, and finally wraps around the upstream face of the downstream cylinder. This vortex core deformation results from the cross-stream flow field, and the results for core deformation are not sensitive to the cylinder yaw angle.

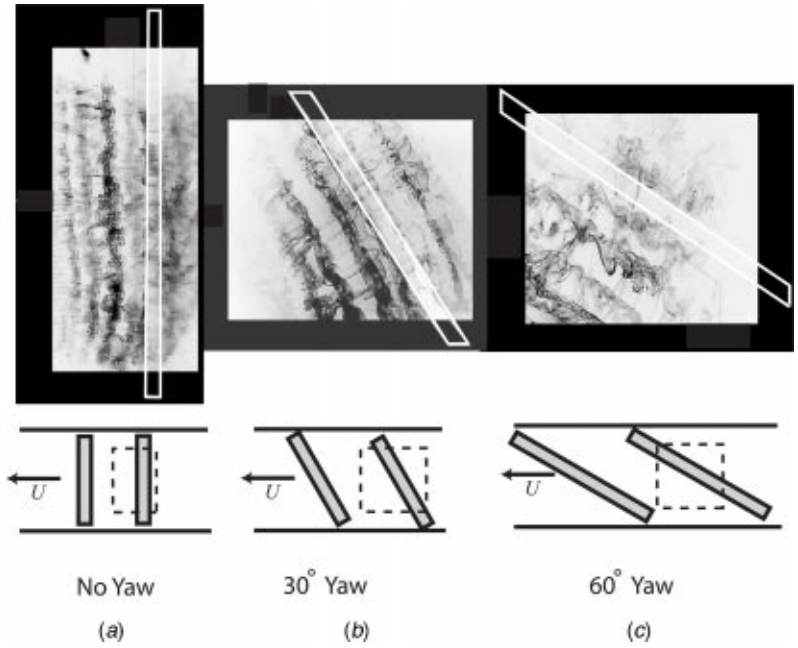

Fig. 10 Volumetric LIF images showing vortices shed from the upstream cylinder impinging upon the downstream cylinder at (*a*) 0°, (*b*) 30°, and (*c*) 60° yaw angle. The imaging regions are shown in the sketches below the pictures and the towing direction is indicated by an arrow

Fig. 11 Planar LIF image showing core deformation of a wake vortex from the upstream cylinder as it impinges on the downstream cylinder for a case with yaw angle of 30°. The imaging plane is indicated by a dashed line in the figure on the right.

The vortex core deformation is dominated by inviscid effects and can therefore be characterized by the dimensionless parameter $\Gamma/U_N d$. To examine the vortex core deformation in more detail, simulations are performed for two-dimensional flows in which a vortex patch with initial diameter d and circulation Γ is advected into a cylinder of diameter d by a uniform flow with speed U. Cases are examined with values of the parameter Γ/Ud of 1.0, 8.8, and 31, and with cross-stream Reynolds number $\mathrm{Re}_C=300$ for all cases. The case with $\Gamma/Ud=8.8$ corresponds to the experimental value observed in Fig. 11, and cases with $\Gamma/Ud=1.0$ and 31 are typical of flows with low and high values of this parameter, respectively. It is apparent from the computational results for these three cases shown in Fig. 12 that for low values of the circulation parameter (e.g., $\Gamma/Ud=1$), the vortex core is weak in strength and the vorticity region deforms as a passive marker and merges with the cylinder boundary layer as it wraps around the cylinder front surface. For the experimental value of this parameter ($\Gamma/Ud=8.8$), the vortex core is comparatively stronger and tends to drift upward (due to the image vorticity), but still flattens into a thin sheet and eventually merges with the cylinder boundary layer. For the strong-vortex case ($\Gamma/Ud=31$), the vortex core remains intact and is deflected around the cylinder, although it still deforms into an oblong shape under the straining induced by the image vortex. For this case, the flow induced by the vortex dramatically alters the cylinder wake and leads to shedding of strong secondary vortices from the cylinder that interact with the initial vortex.

The three-dimensional computational method is used to examine flow behavior when the upstream cylinder wake vortices advect close to and impinge upon the downstream cylinder face. In particular, we are interested in assessing the extent to which the high straining rate involved in the vortex-cylinder impact will amplify small perturbations of the upstream cylinder wake vortices, leading to a breakdown of the quasi-two-dimensional nature of the flow just upstream of the downstream cylinder. The flow features in this region are unclear in the experimental flow visualization because of the large amount of vortex core deformation. The computations are performed for two parallel cylinders at 30° yaw and cross-flow Reynolds number of $\mathrm{Re}_C=300$, with the downstream cylinder axis at a distance of $\ell=5d$ behind the upstream cylinder axis and displaced vertically a distance $h=0.2d$. The perturbation of the uniform flow at the inlet is selected in the form (1) with amplitude $\varepsilon=0.05$.

Iso-surfaces are of the dimensionless vorticity magnitude and axial velocity field for the three-dimensional flow are shown in Fig. 13 at two times. In the two figures at the top in Fig. 13 ($t=20$), a wake vortex shed from the first cylinder is about one vortex core diameter upstream of the second cylinder. The bending perturbations on the vortex core grow to give the vortex a wavy shape, even as the deformation induced by the downstream cylinder causes the vortex core cross section to flatten into an oblong shape. The iso-surface of axial velocity shown in Fig. 13(*b*) exhibits strong deviations from the quasi-two-dimensional form upstream of the second cylinder. In the two figures at the bottom of Fig. 13 ($t=21$), the vortex has now impinged on the boundary layer along the upstream face of the second cylinder and is observed to form a wavy pattern on the vorticity iso-surface within the boundary layer.

Since the vorticity field exhibits significant three-dimensional

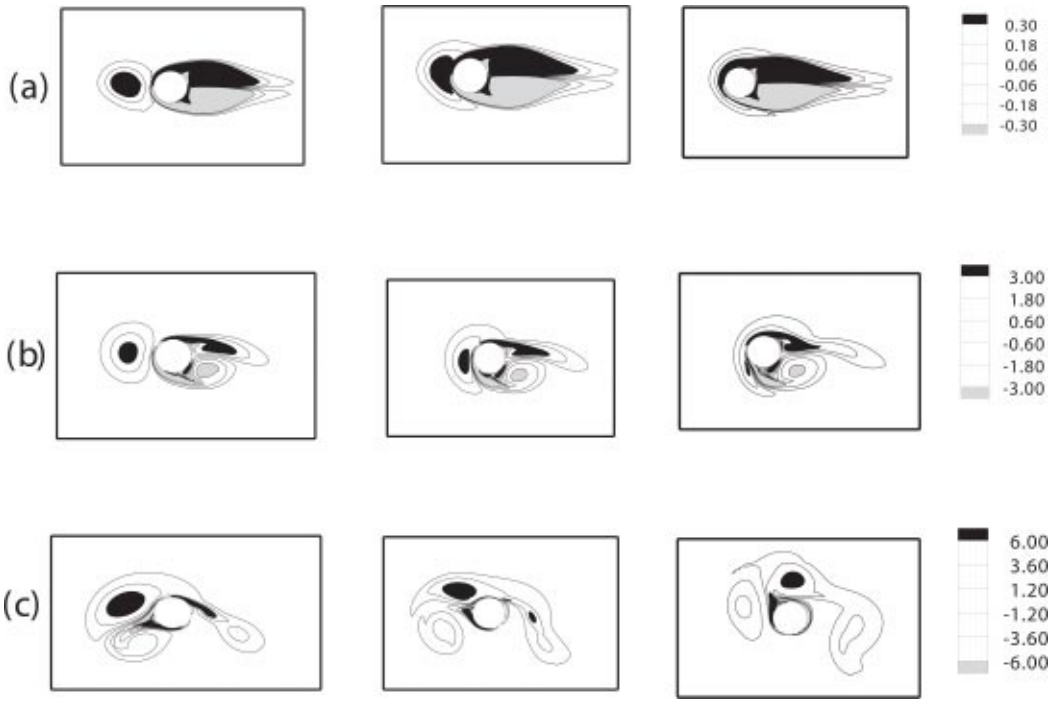

Fig. 12 Time series of vorticity contours for two-dimensional computations of a vortex impinging upon a cylinder with (*a*) $\Gamma/Ud=1.0$, (*b*) 8.8 (experimental value), and (*c*) 31

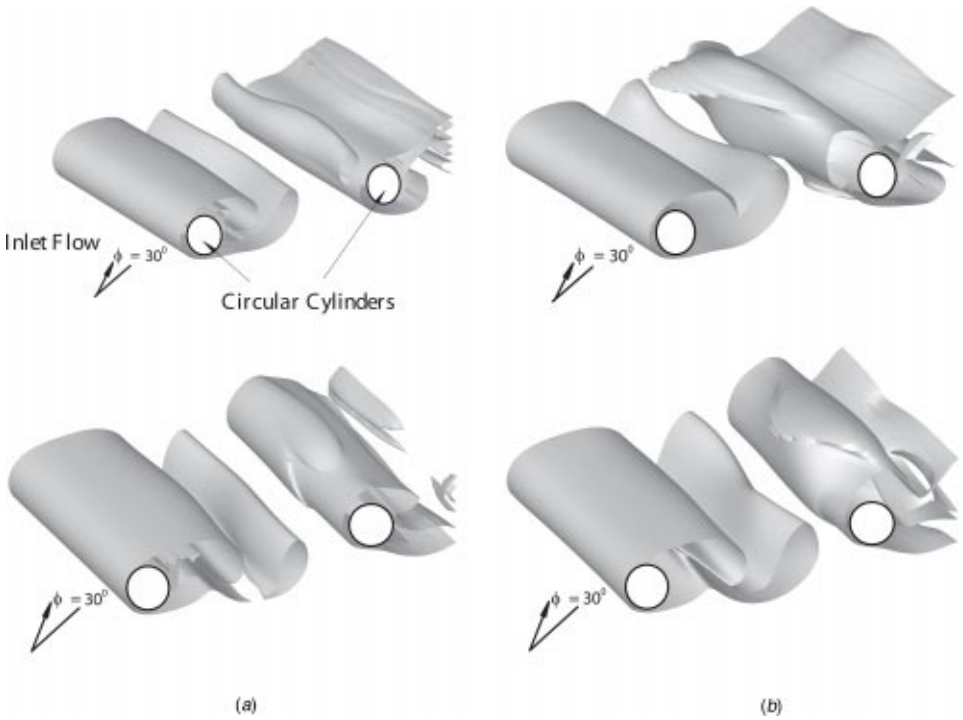

Fig. 13 Iso-surface of (*a*) vorticity magnitude $\omega^*=2$ and (*b*) axial velocity $w^*=0.87$ at times $t^*=20$ (top) and $t^*=21$ (bottom) showing amplification of vortex perturbations when vortices shed from the upstream cylinder impinge on the front face of the downstream cylinder

perturbations for the two-cylinder computations (the extent of which depends in part on the value of the upstream perturbation amplitude ε), it is of interest to examine the differences in the drag and lift coefficients predicted by a quasi-two-dimensional computation and by an equivalent fully three-dimensional computation. A comparison showing predictions for mean drag coefficient, amplitude of lift coefficient, and Strouhal number for both the upstream (first) and downstream (second) cylinders for quasi-two-dimensional and fully three-dimensional flows is given in Table 3. The Strouhal number is found to be nearly identical for the two cylinders, and the drag coefficient for the downstream cylinder is about 70% of that for the upstream cylinder. The fluctuation amplitude for the drag on the second cylinder is considerably larger than that of the first cylinder due to impact of the upstream cylinder wake vortices on the downstream cylinder. The amplitude of the fluctuating lift coefficient is also significantly larger for the downstream cylinder than it is for the upstream cylinder, by a factor of about 3. This difference is indicative of the effect of the impinging upstream vortices in increasing the fluctuating lift magnitude of the downstream cylinder. Although there is a fairly large deviation in value of lift amplitude, the computed lift coefficient is observed to be lower for the first cylinder and higher for the second cylinder in the three-dimensional computations than in the quasi-two-dimensional computations. The lift coefficient might be expected to be sensitive to waves on the shed vortex cores, which lead to phase differences in the induced lift force along the cylinder axis.

Table 3 The drag and lift coefficients and Strouhal number for two parallel cylinders at 30° yaw angle for both the quasi-two-dimensional computations and the fully three-dimensional computations.

		C_D	$C_{L,\text{amp}}$	St
Q2D	First cylinder	1.29 ± 0.04	0.63 ± 0.12	0.21 ± 0.02
	Second cylinder	0.89 ± 0.17	1.80 ± 0.14	0.22 ± 0.02
3D	First cylinder	1.32 ± 0.04	0.45 ± 0.05	0.22 ± 0.02
	Second cylinder	0.90 ± 0.17	2.11 ± 0.14	0.22 ± 0.02

5 Conclusions

An experimental and computational investigation is reported for flow past a single cylinder and two parallel cylinders inclined at a yaw angle to the free-stream flow. The experimental study uses LIF for flow visualization and PIV for velocity and vorticity field measurement for a finite-length rod towed in a tank. Computations are performed using a three-dimensional finite-volume method with periodic boundary conditions along the cylinder axis. Results are compared to quasi-two-dimensional computations, in which derivatives vanish in the axial direction, in order to assess the applicability of the quasi-two-dimensional approximation.

In experiments with a single yawed cylinder, the wake vortices are observed to approach the cylinder yaw angle (in agreement with the quasi-two-dimensional approximation) sufficiently far from the cylinder upstream end. Near the cylinder upstream end the wake vortices have a lesser yaw angle than the cylinder, which is in contrast to other experimental results that observe a higher vortex yaw angle in this upstream region. We attribute the difference to the fact that the cylinder moves relative to the tank walls in the current study, whereas in previous studies the cylinder was fixed relative to the tank or tunnel walls.

The Strouhal number for vortex shedding is consistent with previous experimental results for yawed cylinders, exhibiting an increase in Strouhal number for cylinders with high yaw angle compared to predictions of the Independence Principle. Measurements of maximum axial vorticity within the wake vortices yield values that agree closely with quasi-two-dimensional computations. The wake vortices also exhibit an axial velocity deficit with magnitude on the order of that predicted by the quasi-two-dimensional theory, although the small value of the vortex axial velocity and the wavy nature of the wake vortices makes it difficult to measure with high accuracy in the experiments.

For cases with two parallel yawed cylinders, the vortices shed from the upstream cylinder are observed in both experiments and computations to remain nearly parallel to the cylinders until they approach to within less than one cylinder diameter to the downstream cylinder face. The degree of deformation of the wake vortex cores as they approach the downstream cylinder depends on the dimensionless circulation parameter $\Gamma/U_N d$, such that vortices with large values of this parameter exhibit modest core deformation and deflect around the cylinder and vortices with small values of this parameter flatten out into a vortex sheet that wraps around the cylinder front face. For cases considered in the current experiments, the vortex core deformation was sufficiently large that it was difficult to clearly identify the vortex structure once it moved very close to the cylinder. Three-dimensional computations indicate that small perturbations of the upstream wake vortices are amplified during the final stages of the vortex-cylinder impact, such that the impacting vortices wrap around the downstream cylinder face with large three-dimensional variation. Comparison of computational results for fully three-dimensional flows and for quasi-two-dimensional flows indicates that the drag coefficient and Strouhal number are well predicted by the quasi-two-dimensional approximation, for both the single-cylinder and cylinder-pair cases, but that the amplitude of the fluctuating lift coefficient is somewhat different for the three-dimensional computations due to the phase difference in the lift force caused by waves on the wake vortex cores.

Acknowledgments

We thank Lichuan Gui for permission to use the EDPIV software for PIV analysis and Yong Lai for assistance with the U2RANS finite-volume code. This project was supported by the Office of Naval Research under Grant No. N00014-01-1-0015. Dr. Thomas Swean is the program manager.

References

[1] Bursnall, W. J., and Loftin, L. K., 1951, ''Experimental Investigation of the Pressure Distribution About a Yawed Circular Cylinder in the Critical Reynolds Number Range,'' NACA TN 2463.
[2] Friehe, C., and Schwarz, W. H., 1960, ''Deviations from the Cosine Law for Yawed Cylindrical Anemometer Sensors,'' J. Appl. Mech., **35**, 655–662.
[3] Gatto, A., Ahmed, N. A., and Archer, R. D., 2000, ''Investigation of Upstream End Effect on the Flow Characteristics of a Yawed Circular Cylinders,'' Aeronaut. J., **104**, 125–128.
[4] Hanson, A. R., 1966, ''Vortex Shedding from Yawed Cylinders,'' AIAA J., **4**, 738–740.
[5] King, R., 1977, ''Vortex Excited Oscillations of Yawed Circular Cylinders,'' J. Fluids Eng., **99**, 495–502.
[6] Ramberg, S., 1983, ''The Effects of Yaw and Finite Length Upon the Vortex Wakes of Stationary and Vibrating Circular Cylinders,'' J. Fluid Mech., **128**, 81–107.
[7] Relf, E. F., and Powell, C. H., 1917, ''Tests on Smooth and Stranded Wires Inclined to the Wind Direction and a Comparison of the Results on Stranded Wires in Air and Water,'' British A.R.C. R+M Report 307.
[8] Snarski, S. R., and Jordan, S. A., 2001, ''Fluctuating Wall Pressure on a Circular Cylinder in Cross-Flow and the Effect of Angle of Incidence,'' 2001 ASME Fluids Engineering Division Summer Meeting, New Orleans, LA, May 29–June 1, 2001.
[9] Van Atta, C. W., 1968, ''Experiments in Vortex Shedding from Yawed Circular Cylinders,'' AIAA J., **6**, 931–933.
[10] Moore, F. K., 1956, ''Yawed Infinite Cylinders and Related Problems—Independence Principle Solutions,'' Adv. Appl. Mech., **4**, 181–187.
[11] Marshall, J. S., 2003, ''Wake Dynamics of a Yawed Cylinder,'' J. Fluids Eng., **125**, 97–103.
[12] Lessen, M., Singh, P. J., and Paillet, F., 1974, ''The Instability of a Trailing Line Vortex. Part 1. Inviscid Theory,'' J. Fluid Mech., **63**, 753–763.
[13] Mayer, E. W., and Powell, K. G., 1992, ''Viscous and Inviscid Instabilities of a Trailing Vortex,'' J. Fluid Mech., **245**, 91–114.
[14] Lucor, D., and Karniadakis, G. E., 2003, ''Effects of Oblique Inflow in Vortex-Induced Vibrations,'' Flow, Turbul. Combust., **71**, 375–389.
[15] Fei, R., Gui, L., and Merzkirch, W., 1999, ''Comparative Study of Correlation-Based PIV Evaluation Methods,'' Mach. Graphics Vision, **8**, 571–578.
[16] Megerle, M., Sick, V., and Reuss, D. L., 2002, ''Measurement of Digital Particle Image Velocimetry Precision using Electro-Optically Created Particle-Image Displacements,'' Meas. Sci. Technol., **13**, 997–1005.
[17] Keane, R. D., and Adrian, R. J., 1990, ''Optimization of Particle Image Velocimeters. I. Double Pulsed Systems,'' Meas. Sci. Technol., **1**, 1202–1215.
[18] Thakur, A., 2003, *An Experimental Investigation of Flow Past a Single Cylinder and Two Parallel Cylinders at an Angle of Yaw*, M.S. thesis, University of Iowa, Iowa City.
[19] Lai, Y. G., 2000, ''Unstructured Grid Arbitrarily Shaped Element Method for Fluid Flow Simulation,'' AIAA J., **38**, 2246–2252.
[20] Fleischmann, S. T., and Sallet, D. W., 1981, ''Vortex Shedding from Cylinders and the Resulting Unsteady Forces and Flow Phenomenon. I,'' Shock Vib. Dig., **13**, 9–22.
[21] Zdravkovich, M. M., 1977, ''Review of Flow Interference between Two Circular Cylinders in Various Arrangements,'' J. Fluids Eng., **99**, 618–633.
[22] Kiya, M., Arie, M., Tamura, H., and Mori, H., 1980, ''Vortex Shedding from Two Circular Cylinders in Staggered Arrangement,'' J. Fluids Eng., **102**, 166–173.
[23] Li, J., Chambarel, A., Donneaud, M., and Martin, R., 1991, ''Numerical Study of Laminar Flow Past One and Two Circular Cylinders,'' Comput. Fluids, **19**, 155–170.
[24] Mittal, S., Kumar, V., and Raghuvanshi, A., 1997, ''Unsteady Incompressible Flows Past Two Cylinders in Tandem and Staggered Arrangements,'' Int. J. Numer. Methods Fluids, **25**, 1315–1344.

Entrainment by a Refrigerated Air Curtain Down a Wall

Pratik Bhattacharjee

Eric Loth[1]
e-mail: e-loth@uiuc.edu

Department of Aeronautical and Astronautical Engineering,
University of Illinois Urbana Champaign,
104 S Wright St., Urbana, IL 61801

Thermal entrainment is important as it adversely affects energy consumption and evaporator humidity levels of refrigerated air curtain display cases, often at transitional Reynolds numbers. In order to get a more fundamental understanding of the mean and unsteady thermal entrainment processes, the shelf structure of a display case has been idealized to that of a plane, adiabatic wall subjected to refrigerated wall jets at laminar and transitional flow conditions. The wall jets are studied at different inflow profiles, Reynolds numbers, and Richardson numbers to investigate the effect on thermal entrainment rates. The primary simulation technique was direct numerical simulation of the Navier–Stokes equations in two dimensions for the low and moderate Reynolds numbers (though three-dimensional simulations were also conducted). At higher Reynolds numbers, a conventional Reynolds averaged Navier–Stokes approach was employed, which was found to give reasonable agreement with the above approach at a wall jet (early-transitional) Reynolds number of 2000. In general, the results yielded a significant variation in entrainment as a function of Reynolds number, with a minimum occurring at flow speeds immediately prior to transition. The entrainment rates were also sensitive to the initial velocity distribution, whereby a constant gradient profile (where any local velocity-gradient peaks were minimized) provided the least entrainment. Entrainment was also found to decrease with increasing Richardson number. [DOI: 10.1115/1.1792263]

1 Introduction

Background of Refrigerated Air Curtains. To maintain the interior at a low temperature while allowing open access, refrigerated display-cases rely on an air curtain to contain and deliver cold air to the product within the case, e.g., see Fig. 1. The overall fluid dynamics of the air curtain are quite complex and not well understood, but are important because they control the entrainment. Entrainment of ambient air into the air curtain increases the heat flux across the curtain and thus the load on the refrigeration unit in the case which, in turn, is directly related to the overall thermal efficiency of the unit. In addition, measured ambient air entrainment causes humidity levels in the case to rise, leading to an increase in the required frequency of defrost cycles. As such, the entrainment should be ideally minimized to reduce the energy and defrost requirements.

The air curtain for refrigerated display cases is achieved by blowing downward along the vertical opening to prevent ambient hot and humid air from entering the case. Upstream of this jet injection, a deflector and a honeycomb are used to turn the horizontal flow downward. Detailed measurement of the mean velocity profile for a typical display case indicates that this exit profile tends to vary nonuniformly, i.e., is neither constant or linear in variation (Field [1]). However, the ideal velocity profile for minimum entrainment is suspected (based on internal qualitative studies by manufacturers) to have higher velocities near the inner portion. But, as discussed by Field and Loth [2], there have been no studies in the open literature which have quantitatively examined the sensitivity of thermal entrainment to various velocity profiles. In addition, the influence of Reynolds number, inlet velocity profile, co-flow, and air curtain buoyancy effects is not well understood, especially at transitional Reynolds numbers.

Since the fundamental fluid physics that cause thermal entrainment for an air curtain have not been previously investigated in detail, the present study seeks to simplify the flow to it's basic and critical elements. For the computational model of the air curtain, the complex geometry is simplified to that of a wall jet with no initial turbulence. This is also consistent with the type of changes which may help reduce turbulent entrainment. In addition, recent experimental work by Field [1] has shown that the wall jet is a close qualitative approximation of the air curtain in a fully stocked display-case.

Figure 2 shows a sketch of a wall jet with its important parameters. The inlet width is represented as H, and typically the spanwise length is ten or more times the inlet width such that the flow is approximately two-dimensional (in the mean) along most of it's span. The effects of side-wall boundaries can be important near the end-walls but are not considered in the present study. The average velocity, density, and temperature of the jet at its inlet are represented by V_{jet}, ρ_{jet}, and T_{jet}, respectively. The temperature and density of the ambient room air are represented as T_{amb} and ρ_{amb}, and a Cartesian coordinate system is placed at the intersection of the wall and the jet inlet with x in the streamwise direction and y in the transverse direction. At the bottom of the jet is a capture area, given by y_{capture}. This represents capture of a net mass flow rate equal to that of the initial jet, i.e., the captured airflow that is returned to the refrigeration cycle but contains a fraction (α) of the ambient air through the process of entrainment. To obtain the dimensionless entrainment (assuming constant density, a reasonable approximation) we may write

$$\int_0^H V_{\text{jet}}\,dy = \int_0^{y_{\text{capture}}} V(y)\,dy$$

By taking an average temperature of the flow being entrained in this domain, we define a T_{capture} by

$$T_{\text{capture}} = \frac{\int_0^{y_{\text{capture}}} T(y)\,dy}{y_{\text{capture}}}$$

We can then define an entrainment parameter,

$$\alpha = (T_{\text{capture}} - T_{\text{jet}})/(T_{\text{amb}} - T_{\text{jet}})$$

where T_{capture} is the average temperature across the capture area at the bottom of the curtain and T_{jet} is the temperature of the jet at the inlet of the curtain. As the entrainment of ambient air into the

[1]Corresponding author.

Contributed by the Fluids Engineering Division for publication in the JOURNAL OF FLUIDS ENGINEERING. Manuscript received by the Fluids Engineering Division March 4, 2003; revised manuscript received March 2, 2004. Associate Editor: K. O. Squires.

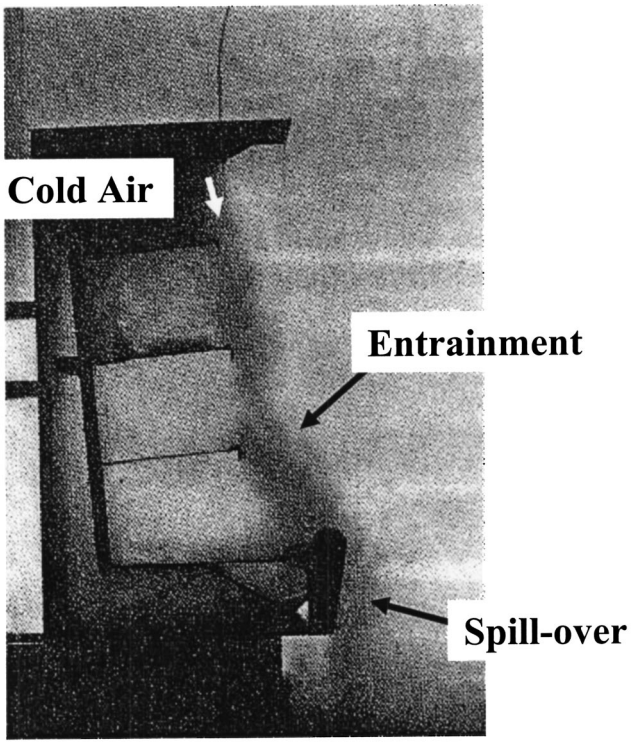

Fig. 1 Smoke injection visualization of the air-curtain for a refrigerated display-case where the smoke is injected at the cold-air jet at the top of the curtain. The diffusion of the jet shows the ambient air entrainment into the air curtain and at the bottom the spillover of injected air can be seen [6].

curtain increases, α approaches a value of 1. In the ideal air curtain, the entrainment would be zero, yielding $\alpha=0$.

In order to properly nondimensionalize these wall-jet characteristics, one must consider the dominating fluid dynamics forces. There are three primary fluid forces for a refrigerated wall jet, the momentum forces, the viscous forces, and the buoyancy forces. Thus, along with geometry, there are two primary parameters than can be used to define a wall jet: the Reynolds number and the Richardson number. For the air curtain, we define the Reynolds number (the ratio of the momentum forces to the viscous forces) by the width of the curtain inlet; i.e., $\mathrm{Re}=(V_{\mathrm{jet}}\rho_{\mathrm{jet}}H)/\mu_{\mathrm{jet}}$ where μ_{jet} is the viscosity of the curtain air. The other primary dimensionless number of interest is the Richardson number $\mathrm{Ri}=[(\rho_{\mathrm{amb}}-\rho_{\mathrm{jet}})gH]/\rho_{\mathrm{amb}}V_{\mathrm{jet}}^2$, which is the ratio of the gravitational forces to the momentum forces, where g is the acceleration due to gravity. The geometrical effect can be related by x/H.

For typical air curtains, the jet Reynolds numbers are about 4000 [1], which is often in the transitional regime of a wall jet, i.e., the flow is highly unsteady but may not be fully turbulent. Moreover, there is qualitative evidence that reducing the Reynolds number and inflow turbulence may reduce thermal entrainment [1]. With respect to geometry, a typical curtain length is 150 cm and the width is 75 cm, indicating that the regime of interest is from $x/H=0$ to about $x/H=20$, as will be considered herein. The typical Richardson number for a refrigerated air curtain is 0.25, which means that the curtain is generally dominated by momentum effects from the jet exhaust rather than gravitational effects which pull the cold air down by buoyancy. However, even this modest value of Ri may significantly modify the wall-jet dynamics based on experimental results [2].

Previous Studies

Initial contributors to the analysis of heat transfer through simple vertical air curtains include Stribling et al. [3], Hayes [4], and Hetsroni et al. [5]. However, their models were for uniform inflow velocity profile, high Reynolds numbers (e.g., 20,000 or more) and the robustness of these models is not as strong for $L/H<10$.

In recent years, computational studies have been conducted to model particular refrigeration case configurations and analyze the respective curtain dynamics. For example, Baleo et al. [6] studied time-averaged air flow distribution in a refrigerated display-case which imposed minimum air temperatures at the three levels. In this work, the k-ε model closure model was used to solve the Reynolds-averaged Navier–Stokes (RANS) equations for the air curtain flow. The computational grid was modeled based on the two-dimensional cross-section of an unloaded case configuration. Introduction of radiative heat transfer in the computations was found to affect only the temperature in the solids, but not affect the air flow, so this aspect was ignored in the simulations. Five different flow conditions were studied, and an experimental co-study was conducted using hot wire anemometry and thermocouple probes at these flow conditions. Comparisons with the experimental results for the intermediate portion of the air curtain indicated that the numerical simulations provide significantly larger velocities in the inner portion of the flow and there were also dissimilarities in the angular positions of the air jet. The authors indicated that a possible factor in the reported differences was the turbulence model. Specifically the k-ε model was reputed to overestimate the air entrainment at the edge of the jet and that leads to an overestimation of the external vortex dimensions and the velocity magnitude at the left-hand side of the air curtain.

Similarly, RANS approaches have also been used by George and Buttsworth [7] for an empty refrigerated display-cases. They also found that these numerical approaches were only qualitatively correct for typical air curtains. The authors attributed this to the transitional nature of these flows, i.e., they are neither laminar nor fully developed. Howell [8] did a study of another air curtain configuration, but at a low Reynolds number and the simulation was compared with an experimental study. Once again the curtain thickness was under-predicted by the numerical results. There additional examples of attempted predictions of the air curtains using RANS (Reynolds-averaged Navier–Stokes) techniques, for which only qualitative success was achieved [9].

In cases where RANS results (which employs empiricism to model the turbulent mixing) have not been sufficient in prediction fidelity, some researchers have turned to direct numerical simulation (DNS), whereby all length and times scales of the flow are fully resolved. This technique avoids the empiricism of RANS turbulence models and is thus a powerful technique to predict the fluid dynamics without estimations. However, it requires substantial CPU usage such that while there have been some 2-D and 3-D studies of backward facing steps [10] and isothermal jets [11], DNS has not been used for thermal entrainment of air curtains or wall-jets.

Based on the above it is known that significant (unwanted) entrainment occurs for refrigerated open display-cases. However, there have been no numerical or experimental studies which have quantified thermal or momentum entrainment as a function of Re, Ri, x/H, co-flow velocity, or jet velocity profile. Furthermore, it has been shown that RANS predictions tend to overestimate momentum distribution when air curtains are modeled for full display-cases. This may be due to the empiricism of the turbulence models employed. However, the lack of fidelity may also be attributed to complex geometries or insufficient detail of initial conditions. Finally, the previous studies have each focused on the configurations of display cases which were specific to a manufacturer, such that a general understanding of the air curtain fluid dynamics was not obtained.

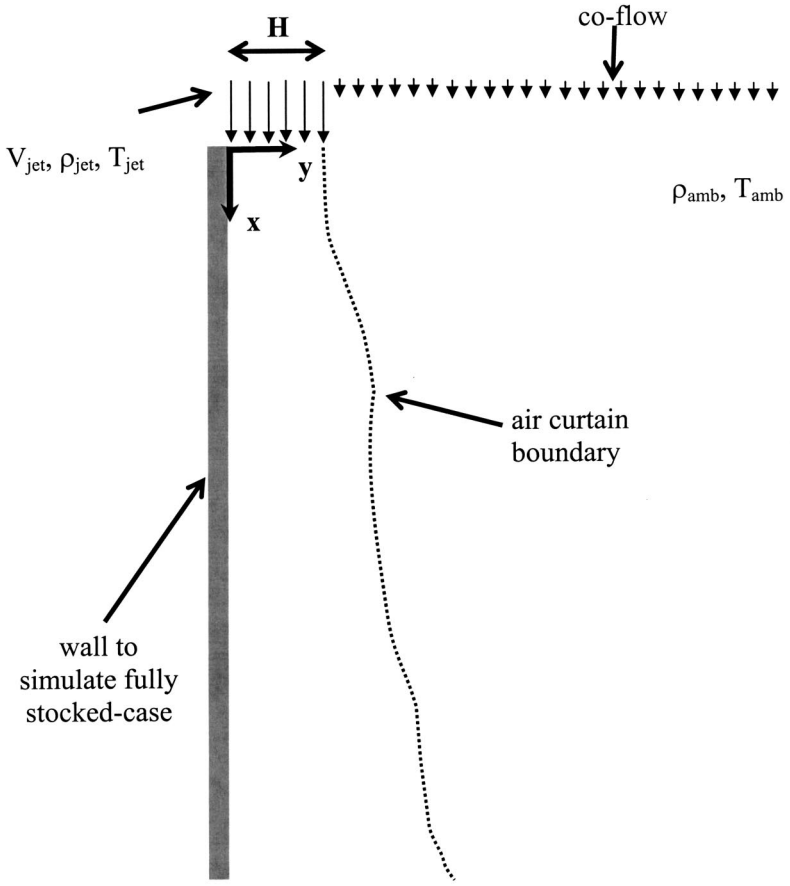

Fig. 2 Air curtain idealized as a wall jet with a uniform inflow profile and a uniform co-flowing stream

Study Objectives

The purpose of this study was to increase the understanding of the fundamental air curtain fluid physics and quantify the resulting flow entrainment. In particular, this study focused on effects of Reynolds number, velocity profile, and Richardson number on unsteady and time-averaged entrainment of an idealized air curtain. The present study therefore focused on these issues by employing a systematic computational study of the thermal entrainment characteristics for an idealized wall jet. The effect of Reynolds number on the entrainment was be primarily studied at various streamwise variations of $x/H=10$, 15, and 20. To investigate the effects of the initial velocity distribution, three profiles were tested: parabolic (as found in laminar flow through parallel plates), uniform (i.e., plug flow at the exit), and a ramp profile (where the maximum velocity is at the wall and a constant linear decrease in velocity to zero occurs till the outside edge of the jet, and beyond this edge there is a constant co-flow velocity. The influence of buoyancy (through Richardson number) and co-flow velocity was also studied. Finally, the comparison of DNS with the RANS approaches was investigated, in order to assess the reasonableness of the latter in well-defined conditions. This type of information may be helpful to reduce the entrainment in refrigeration systems design, as no previous numerical studies have focused on transitional wall jets with finite Richardson number or have examined effects of Reynolds number or velocity profile or entrainment of such flows.

Methodology

The code employed in the present study is ''WIND,'' which can provide time-accurate viscous 2-D and 3-D simulations for variable density, non-isothermal flows. WIND is a structured, multizone, compressible flow and a detailed description of this code is discussed in [10]. The code is used in both DNS and RANS modes in the present study.

Since the flow-field of a wall jet involves both free shear and boundary layer features, the SST (shear stress transport) model was used for the RANS simulations in this study. The SST is a hybrid of two successful two-equation models: the k-e and k-ω model and was first proposed by Menter [11]. In this hybrid model, a blending function is introduced, which is set to 1 near the free-stream (yielding the κ-ϵ model solution) and 0 near the wall (yielding the κ-ω model solution). Cazalbou et al. [12] have shown an improved prediction of the flowfield at the free stream boundaries. In addition, Yoder et al. [13] did a study of the ''WIND'' code performance using the Menter SST model and its near wall accuracy for flow over a turbulent flat plate. The model was shown to give accurate results of the boundary layer thickness.

Direct numerical simulation involves solving the full Navier–Stokes equations, resolving all scales of motion for a given set of initial and boundary conditions. Unlike the steady-state RANS models which solves only mean values using modeling of the turbulence, the DNS approach is without any empirical modeling and each solution at a time-step determines the instantaneous flowfield for that realization of the flow. However, the requirements for the spatial and temporal discretization require relatively fine grid sizes and timesteps. As such, DNS computations are only currently possible at moderate Reynolds numbers.

While generally a full three-dimensional description is required for the simulation of fully-turbulent flows with DNS, a two-

Table 1 Two-dimensional inflow test conditions, where flow in all cases is at a Richardson number=0 and a co-flow of 6.7% of mean inflow velocity

Inflow	DNS Steady				DNS Unsteady			RANS	
Parabolic	100	200	300	550	700	1000	2000	4000	10,000
Uniform	100	200	300	550	700	1000	2000	4000	10,000
Ramp	100	200	300	550	700	1000	2000	4000	10,000

dimensional DNS approach may be employed for flows which are early-transitional in nature and which are dominated by two-dimensional structures and instabilities, e.g., computations by Kaiktis et al. [14] as well as Loth and Matthys [15]. However, such flows are typically relegated to low Reynolds numbers, with laminar inflows. The ''WIND'' codes were validated in this mode for a flow over a backward facing step (with laminar inflow). The results are discussed in detail by Bhattacharjee [15] and showed good agreement for a range of Reynolds numbers from 50 to 1150, where 700 corresponds to the transition from steady to unsteady flow.

In the proposed set of simulations, the Reynolds numbers at which the DNS approach is conducted are in the early transitional range, i.e., limited to wall jet Reynolds numbers of 700 to 2000. For these conditions, the flows are primarily governed by two-dimensional characteristics. As such, a 2-D DNS approach is primarily employed. However, 3-D DNS simulations were also conducted at the highest wall jet Reynolds number to ensure that the two-dimensional results were reasonable at these conditions. At higher Reynolds numbers (Re$>$2000), the RANS approach is used; and at lower Reynolds number (Re$<$700), a steady laminar solution was found since no significant instabilities developed. The parameter ranges investigated for the simulations are given in Tables 1 and 2. The baseline conditions, unless specified, for the results to be presented in the following section are for a parabolic velocity profile for the jet with a co-flow velocity of 6.6% and a Richardson number of zero.

The air-curtain grid for all the simulations (RANS and DNS) is shown in Fig. 3 and is a clustered grid of 451$\times$139, packed toward the flow inlet (with $\Delta x/\mathrm{H}=0.025$ in the range of $0<x<12\mathrm{H}$), after which it is stretched. In the y direction, the grid is clustered near the wall and expanded using a hyperbolic tangent function, the smallest grid distance being $0.0008H$. For the 3-D DNS simulations, additional resolution of 16 nodes was applied in the span-wise direction over a range of $3H$. These grid were found to provide grid-independent results for the DNS case at Re=2000 and the RANS case at Re=10,000, respectively the highest Reynolds numbers (and those most demanding) for the two numerical approaches. Similarly, a time-step resolution of $\Delta t=0.00125$ (normalized by V_{jet}/H) was determined to give sufficient temporal resolution (to within 1% of entrainment rates) for the DNS case, while the RANS results were obtained once sufficient convergence (to within 1% of entrainment rates) was achieved. Details of the spatial and temporal resolution studies are given by Bhattacharjee [15].

Results

The two- and three-dimensional DNS simulations were found to be unsteady for Re greater than around 700, a result which was similar to that found for the backward facing step. Sample instantaneous contours of the temperature field for Re=700, 1000, and 2000 for the two-dimensional case are shown in Fig. 4 for parabolic inflow velocity and a Richardson number of zero. It is apparent that instabilities of the wall jet become more pronounced as the ratio of convective to viscous forces increases, yielding successively more pronounced Kelvin–Helmholtz-type vortex structures (due to the shear flow instabilities). In general, the intensity and size of the vortex structures increase with Reynolds number.

Table 2 Test condition matrix for investigating Richardson number and co-flow velocity effects, where flow in all cases is treated with DNS at a Re=2000 for a parabolic inflow velocity

Co-flow	6.6%	3.3%	13.2%	6.6%				6.6%
Richardson no.		0.0		0.25	0.5	1.0	1.5	0.0
Dimensionality		2-D		2-D				3-D

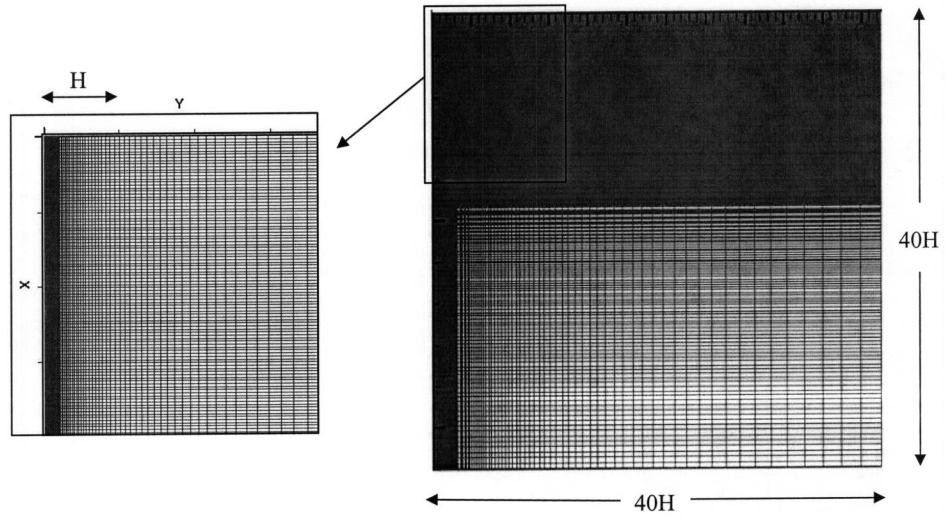

Fig. 3 Wall jet grid showing (a) close-up near inflow and (b) overall domain

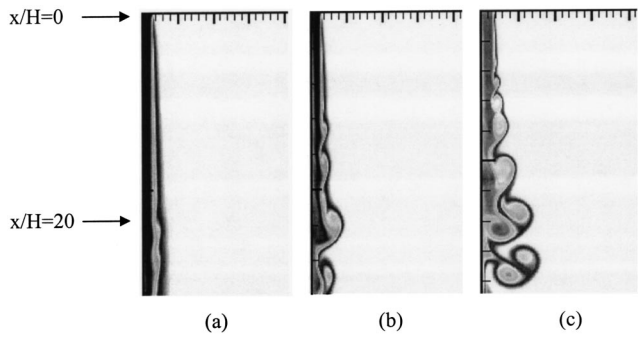

Fig. 4 Instantaneous temperature contours with parabolic inflow for (a) Re=700, (b) Re=1000, and (c) Re=2000

This will be shown to be consistent with increasing mean thermal entrainment and unsteadiness, as one might expect. At Re of 700, the transition to unsteadiness is seen to just begin at a downstream position of $x/H=20$ onwards. For 1000 and 2000, this point of onset of unsteadiness moves closer to the inlet, e.g., the point of onset is about $x/H\sim5$ for Re=2000 and where even mushroom-shaped vortex structures begin to develop downstream (at x/H of 20 and on). Such structures are a result of the wall presence coupled with the above shear-layer instabilities and have been noted in experiments of acoustically forced wall jets at similar Reynolds numbers [16].

The degree of unsteadiness as a function of Reynolds number is also illustrated in Fig. 5 by examining the time-dependent variation of the thermal entrainment (integrated from the instantaneous temperature contours such as given in Fig. 4). The time-scale is normalized by the mean jet inlet velocity and the initial jet thickness ($\mathbf{t^*=tV_{jet}/H}$). At the lowest Reynolds number shown (Re =700), the variation is approximately periodic for all three of the velocity inflow profiles. At the larger Reynolds numbers, the periodicity is reduced and the fluctuations peaks have varying amplitudes, and the amplitudes are seen to generally increase with Reynolds number. The frequency also increases; for example, for the uniform profile at Re=700 the nondimensional period is about 35, while at Re=1000 this time-scale is about 18 and by Re =2000 the time-scale is reduced to about 10 (though it's definition becomes less clear due to aperiodic aspects of the time variation). This decrease in time-scale (i.e., increase in frequency) is consistent with the decreased distances between vortex structures as the Reynolds number increases (Fig. 4). These results indicate significant time-wise variations of the entrainment values, where the frequency, irregularity, and amplitude of the variations increase with the Reynolds numbers. This is consistent with increasing flow instabilities and level of complexity caused as the flow changes from laminar flow to early transitional flow.

However, even at the highest DNS Reynolds number of 2000, the flow was found to be reasonably approximated with a two-dimensional description if span-wise end-wall effects are not considered. This is evidenced by the comparison between the temporal development of thermal entrainment for 2-D DNS vs. 3-D DNS cases (where the 3-D simulations included periodic span-wise boundary conditions to eliminate fixed-wall boundary effects) as shown in Fig. 6 for a sample time period at $x/H=10$ (along the center-plane). Although some three-dimensional structures appeared in the flow-field, the frequencies as well as the magnitude of the variations are very similar for the 2-D and 3-D cases. In addition, as shown in Table 3, the variation in the time-averaged thermal entrainment is minor (a few percent) between the two cases, although it was more significant as $x/H=20$ then at $x/H=10$ due to additional mixing caused by the downstream development of some streamwise vorticity effects [15]. However, the CPU usage of the 3-D cases was nearly 20-fold larger as compared to the 2-D cases. As such, the majority of the simulations were conducted two-dimensionally in order to allow a comprehensive study.

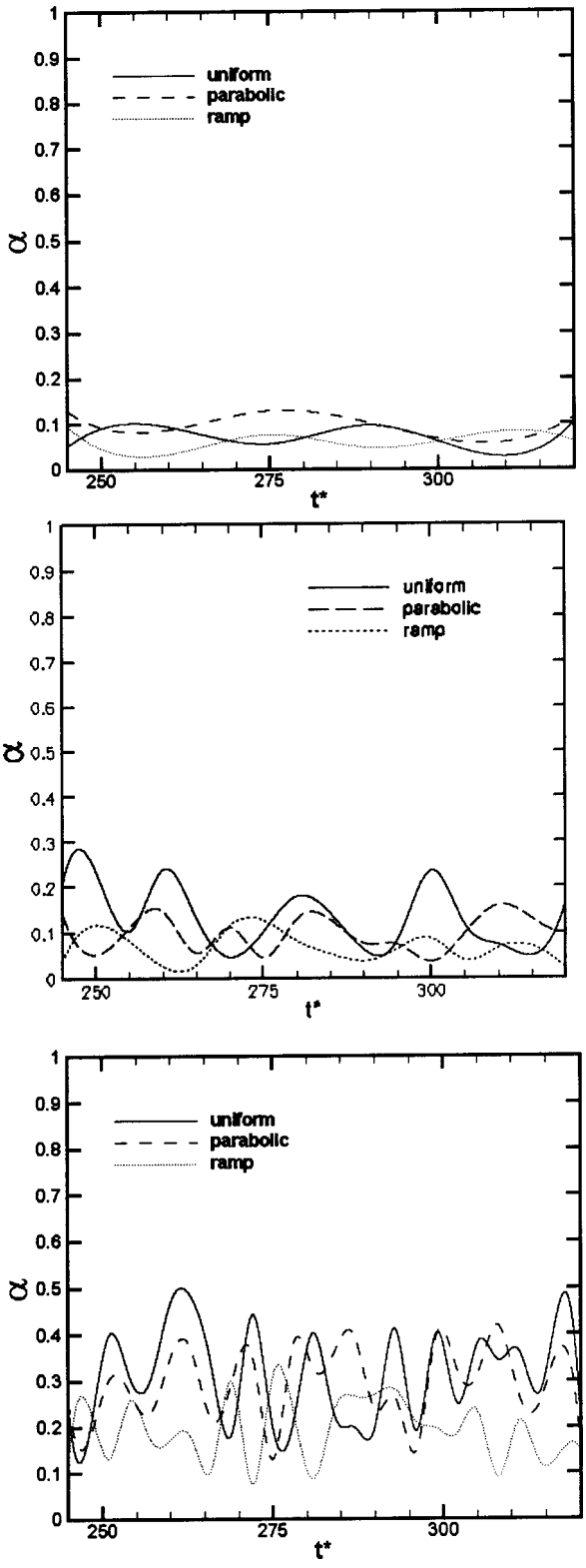

Fig. 5 Instantaneous thermal entrainment at $x/H=10$ with uniform, parabolic, and ramp inflow for (a) Re=700, (b) Re=1000, and (c) Re=2000

The DNS results of the thermal entrainment are given as a function of time in Fig. 7 for the parabolic, uniform, and ramp

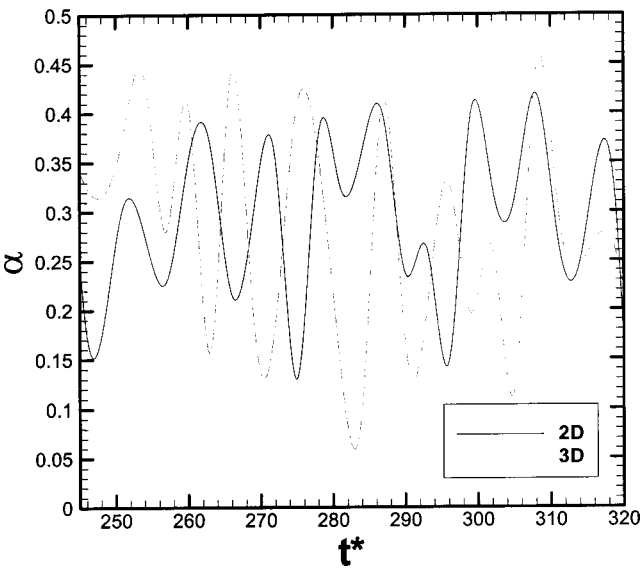

Fig. 6 The instantaneous thermal entrainment at $x/H=10$ at Re=2000: 3-D versus 2-D

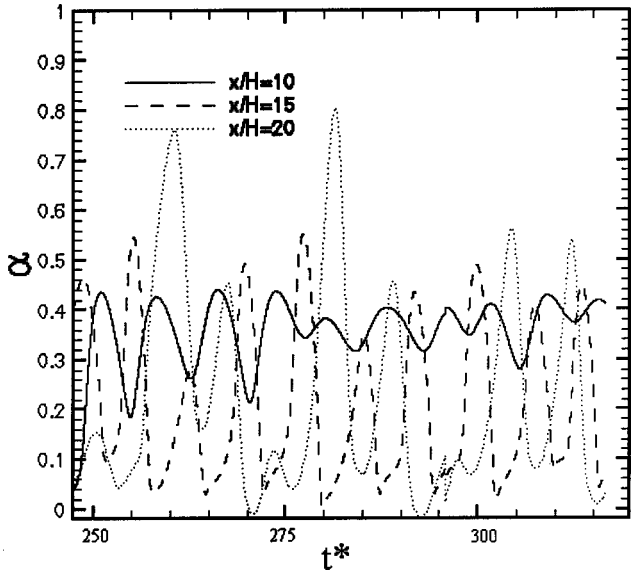

Fig. 8 Time variation of thermal entrainment for Reynolds number of 2000 at three various streamwise stations

profiles. These results indicate significant time-wise variations of the entrainment values in, where the amplitude of the variations tends to increase as the flow goes from ramp to parabolic to uniform inflow conditions. This is consistent with increasing flow instabilities and level of complexity caused by an increase in the peak velocity gradient, i.e., the peak velocity gradient (away from the wall) is minimized for the ramp profile (since the velocity gradient is effectively constant throughout the profile) while it is maximized for the uniform velocity profile (due to the velocity discontinuity at the jet edge). However, these changes are not as substantial as the changes due to Reynolds number as seen in Fig. 5.

Table 3 Comparison of 2-D and 3-D time-average thermal entrainment (α)

Approach	$x/H=10$	$x/H=20$
2-D DNS	0.267	0.254
3-D DNS	0.273	0.268

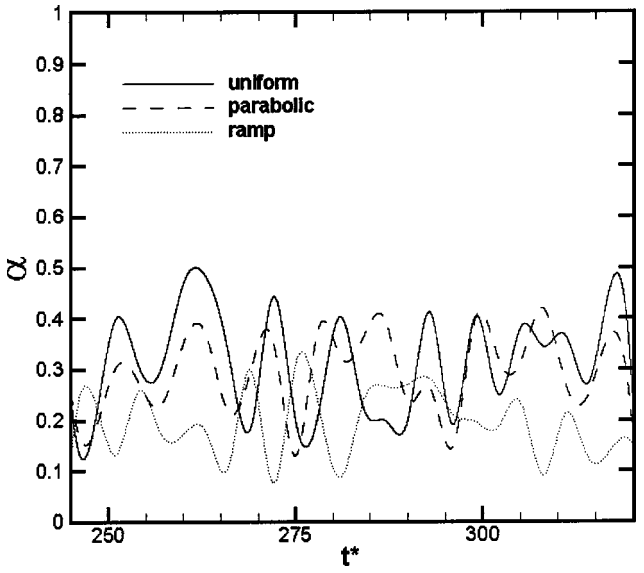

Fig. 7 Instantaneous thermal entrainment versus time for various velocity profiles $x/H=10$ and for Re=2000

The degree of unsteadiness was also investigated as a function of streamwise distance in Fig. 8 for the parabolic inflow profile at Re=2000. As expected, further downstream the amplitude increases, indicating larger and more energetic eddies. However, the degree of periodicity and the time-scale of the variations does not show the large degree of variation noted in Fig. 5 for different flow speeds, indicating that the stream-wise development is *not* equivalent to the Reynolds number development. Interestingly, there was a minor decrease in the average thermal entrainment from x/H of 10 to 15 and then an increase from 15 to 20. This is a result of the definition of the thermal entrainment since the y_{capture} is a function of the velocity profile. Between $x/H=10$ and $x/H=15$, the velocity profile development was such that y_{capture} actually decreased such that the α decreased as well [16]. Therefore, the diffusion of the momentum and the temperature did not always change is a consistent fashion, at least at this transitional Reynolds number

Figure 9 shows the variation of the entrainment with Re at the streamwise stations of $x/H=10$ and 20, for different profiles. The trends at either station are very smiliar, indicating that streamwise development did not substantially affect thermal entrainment. In the lower Reynolds numbers (100–550), the flow is in the laminar diffusion regime, and this leads to a larger spread in the flow as viscous effects increase (as Re reduces), and hence larger thermal entrainment. In the range from 700 to 2000, transitional effects are seen to cause a marked shift in the Reynolds number effect. Recalling from the flow visualization in Fig. 4 at Re=700 the flow begins to show the production of eddies, and by Re=2000, there is a regular production of eddies and the flow is clearly transitional. Correspondingly, the entrainment values were found to be least at about Re of 700 and increased significantly as the Reynolds number increased. It was postulated for this study that the entrainment would always be least at the point when the flow just begins to change from the steady laminar regime into the early transitional regime, and the present results are consistent with this hypothesis.

Interestingly, the thermal entrainment sees a marked increase from Re=1000 to 2000, an effect attributed to the large vortex structures observed at the higher Reynolds number. At the higher Reynolds numbers of 4000 and 10,000, RANS was the only meth-

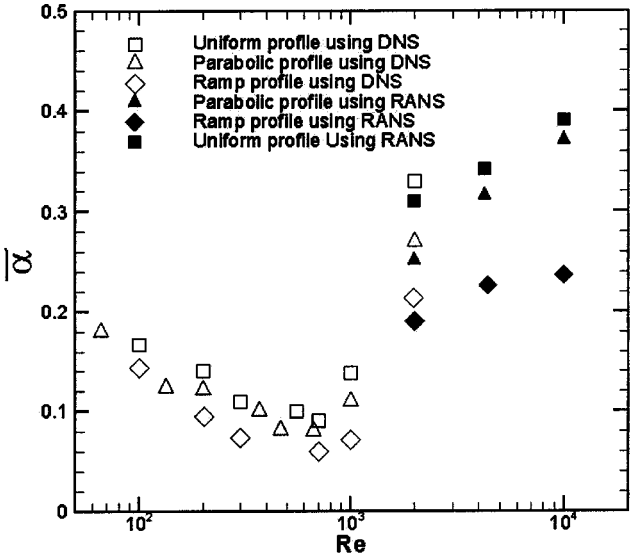

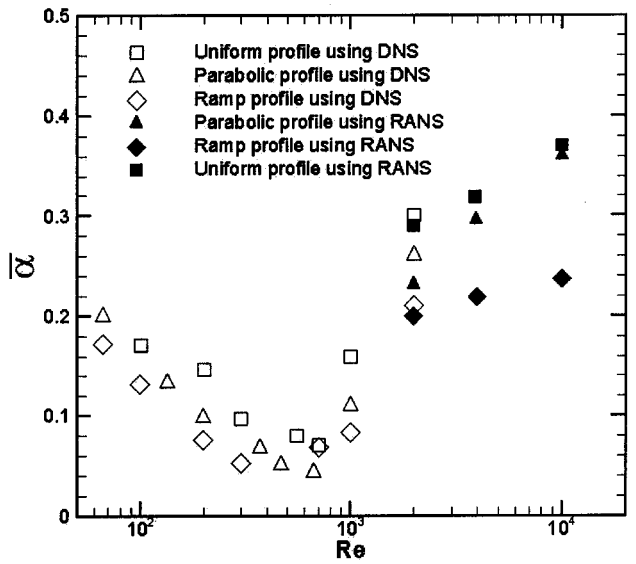

Fig. 9 Thermal entrainment as a function of Reynolds number at $x/H=10$ and 20

odology which was employed (as the CPU usage required for DNS became prohibitive, since it would require higher grid and time-step resolutions as well as 3-D development for discretizational and dimensional independence at such conditions). The RANS thermal entrainment was found to increase continually from Re=2000 to 10,000. This is attributed to the increase of turbulence viscosity (as compared to laminar viscosity) with the higher Reynolds number such that the momentum and mass mixing is enhanced. It is also interesting to compare the DNS results and the RANS results at Re=2000. While it was found that the RANS consistently underpredicted thermal entrainment, the discrepancy in values was rather moderate, e.g., 11%. This moderate difference was somewhat surprising considering that the flow at this Reynolds number is far from being fully developed turbulence. This suggests that RANS results may be at least qualitatively reasonable at values of Re=2000 and higher, at least for these simple wall-jet conditions.

The influence of the inflow velocity profile had an effect on the entrainment behavior, though the variation is smaller than that seen for changes in Reynolds number. In general it was found that the ramp profile consistently gave the lowest entrainment for both

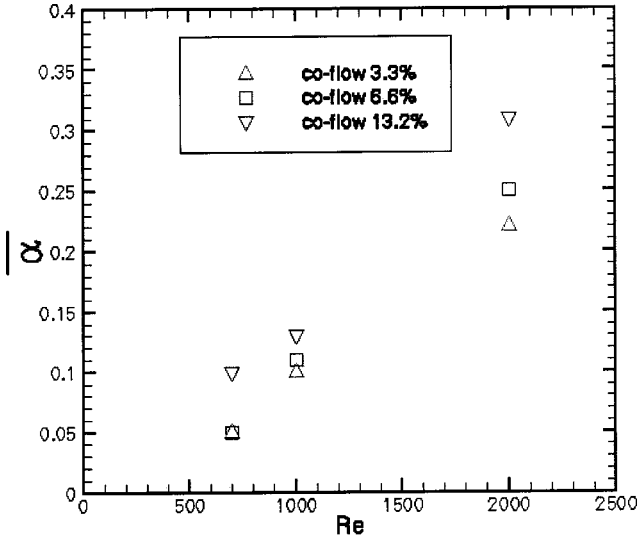

Fig. 10 Co-flow effects: thermal entrainment variation with Reynolds number

laminar and transitional flow conditions, while the uniform profile gave the consistently highest entrainment. In contrast, the uniform velocity profile cases (which contains a velocity discontinuity at the edge) yielded the highest entrainment at all Reynolds numbers. As such, the results indicate that avoiding a local peak of the velocity gradient in the inflow profile yields a reduction in entrainment. This is because a peak in the velocity gradient (and shear stresses) in turn increases momentum and scalar diffusion rates for laminar, transitional and nearly turbulent conditions (for the transitional conditions, the increase in flow instabilities plays the key role). Related to this result, refrigerated display-case companies have empirically noted that a flow profile roughly corresponding to the ramp profile (i.e., highest speeds on the interior of the jet and lowest speeds near the exterior of the jet) gave the lowest entrainment results and base overall performance, which further corroborates the hypothesis that minimization of the velocity gradient throughout the jet profile is beneficial.

It was also desired to examine the effect of co-flow on the entrainment parameters, and it is shown in Fig. 10. The thermal entrainment was found to be increasing with higher co-flow, showing more sensitivity at higher Reynolds numbers. For Re =2000, the mean thermal entrainment was 0.22 at a co-flow velocity of 3.3% while 0.32 at a co-flow velocity of 13.2%. This result is attributed to the prescribed step discontinuity between the jet inflow and the co-flow which was included in these simulations in an effort to better mimic the velocity deficit which would occur due to the finite separation distance and no-slip condition between a co-flow and the jet flow. Since the amplitude of this discontinuity increases with the co-flow (as does the peak velocity gradient at this location), this gives rise to local diffusion which in turn increases the thermal entrainment. This result can be of some practical significance, since the introduction of co-flow should be done with care at transitional Reynolds numbers in order to avoid significant velocity discontinuities.

The effect of buoyancy was next examined, whereby the Richardson number is varied from 0 (i.e., no gravity) to 1.5 for the case of Re=2000 with a parabolic inflow profile. There was a consistent trend of a decrease in the thermal entrainment with the increasing Richardson number as shown in Fig. 11. The almost threefold decrease is attributed to the tendency for the heavier cold jet flow to be more insensitive to flow instabilities since the negative-buoyancy effect pulls the air curtain in the same direction as the forced convection. This result is also qualitatively consistent with the flow for typical display case configurations in that

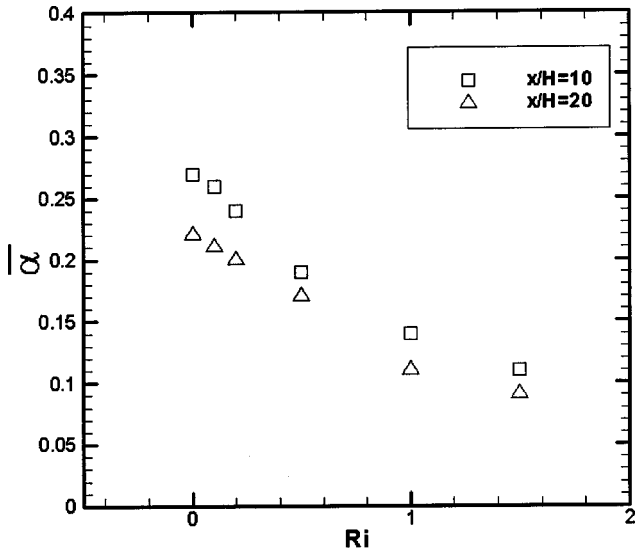

Fig. 11 Variation of the thermal entrainment with Richardson number for parabolic flow at Re=2000 for two different streamwise locations

the air curtain remains more closely attached to the products when the air curtain is refrigerated (and can even separate from the products or a solid wall for the isothermal condition at low enough speeds [1]).

Finally, the net thermal energy loss of the wall jet was investigated for various Reynolds numbers. The variation is of interest because the thermal paper losses of a refrigerator display-case are strongly dependent on this parameter for the air curtain. The net thermal energy rate per unit span of the curtain can be defined by

$$E = \dot{m} C_p \Delta T$$

If written in terms of the dimensionless thermal entrainment and Reynolds number, this becomes

$$E = \mathrm{Re}\, \mu C_p \alpha (T_{\mathrm{amb}} - T_{\mathrm{jet}})$$

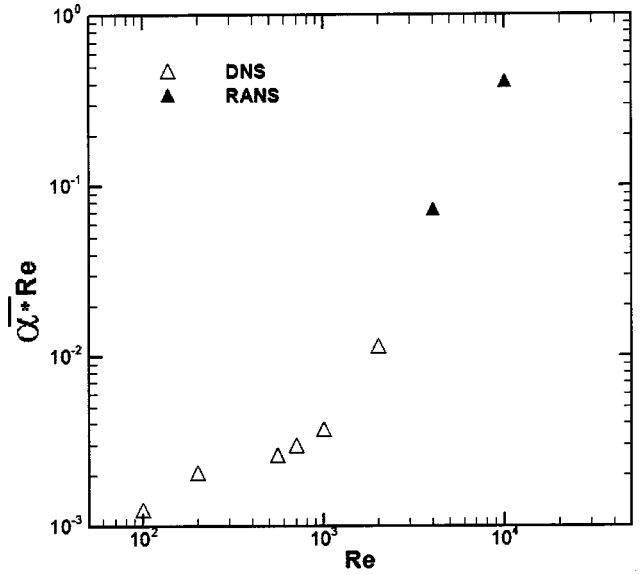

Fig. 12 Variation of the convective thermal energy loss with the Reynolds number for a jet with parabolic inflow at $x/H = 20$

If normalized by $\mu C_p(T_{\mathrm{amb}} - T_{\mathrm{jet}})$, we have, a dimensionless thermal energy loss due to convection (E^*) which can be simply related to the thermal entrainment and the Reynolds number as

$$E^* = \mathrm{Re}\, \alpha$$

It should be noted that in a typical design of a display-case the product $\mu C_p(T_{\mathrm{amb}} - T_{\mathrm{jet}})$ is approximately constant, such that minimizing E^* would be the goal for minimzing convective thermal entrainment. The dimensionless energy loss is plotted in Fig. 12 as a function of the Reynolds number for the parabolic profile. The variation shows that energy loss increases dramatically with the Reynolds number, within the range of Reynolds numbers investigated. This suggests that lower Re values may be of value for refrigerated air curtains if low inflow turbulence could be experimentally incorporated. However, the effect of a more realistic geometry and the requirement for convective cooling of radiant and translucent loading may require higher flow rates and Reynolds numbers in conventional display cases.

Conclusions

This study has documented the properties of the air curtain of a refrigerated display-case idealized as a wall jet. The numerical simulations were done using the DNS and RANS techniques (primarily with a 2-D computational domain). From the velocity profiles and the temperature profiles at any given station, the thermal entrainment was obtained for a variety of test cases and different configurations.

The thermal entrainment showed a definite sensitivity to the Reynolds number (defined by jet thickness and jet mean velocity), with a minimum at around Re of 700, which is consistent with the hypothesis that the mixing is minimized just at the onset of unsteadiness due to flow instabilities. The unsteady variations of the thermal entrainment were found to indicate significant increases in terms of amplitude, frequency, and spectral broadening as the Reynolds number increased. Furthermore, the increase in Reynolds numbers yielded more complex flow structures, beginning with the appearance of Kelvin–Helmholtz-type vortices at Re =700 and 1000, and additionally yielding mushroom vortices for the Re=2000 case.

The ramp profile in general was found to yield the least thermal entrainment, followed by the parabolic and uniform profiles (which gave the highest entrainment). This was consistent with the hypothesis that the thermal entrainment was degraded by the introduction of successively larger peaks of the velocity gradient within the jet profile. The RANS results indicated only modest over-prediction compared to the DNS results, indicating that the transition to turbulent conditions may be rapid for these flows. In addition, the differences between the 2-D and 3-D DNS results were modest in terms of unsteady and time-averaged thermal entrainment up to a Re of 2000. The Richardson number also had a significant impact on the entrainment (e.g., yielded a twofold decrease at a Re of 2000), due to the stabilizing effect associated with the negative buoyancy acting in the direction of the forced convection. Finally, it was noted that the net convective thermal energy losses for a fixed temperature difference are minimized with decreasing Reynolds number.

Acknowledgments

This study was funded by the Air Conditioning and Refrigeration Center at the University of Illinois at Urbana–Champaign (UIUC), and the simulations were completed using the resources of the National Center for Supercomputing Applications (NCSA).

References

[1] Field, B., 2001, "Entrainment in Refrigerated Air Curtains," M.S thesis, Department of Mechanical Engineering, University of Illinois at Urbana–Champaign.

[2] Field, B., and Loth, E., 2001, "Understanding and Reducing Air Curtain Entrainment: an Experimental Study," in Proceedings of ASME: Fluids Engineer-

ing Division Summer Meeting 29 May–1 June, 2001, New Orleans, LA.
[3] Stribling, D., Tassou, S., and Marriott, D., 1995, ''A Two-Dimensional CFD Model of a Refrigerated Display Case,'' ASHRAE Transactions, Research 4018.
[4] Hayes, F. C., 1968, ''Heat Transfer Characteristics of the Air Curtain: a Plane Jet Subjected to Transverse Pressure and Temperature Gradients,'' Dissertation.
[5] Hetsroni, G., Hall, C. W., and Dhanak, A. M., 1963, ''Heat Transfer Properties of an Air Curtain,'' Trans. ASAE, **6**, pp. 328–334.
[6] Baleo, J. N., Guyonnaud, L., and Solliec, C., 1995, ''Numerical Simulation of Air Flow Distribution in a Refrigerated Display Case Curtain,'' National Congress of Refrigeration Proceedings.
[7] George, B., and Buttsworth, D. R., 2000, ''Investigation of an Open Refrigeration Cabinet Using Computational Simulations With Supporting Equipment,'' IMECE, Orlando, FL.
[8] Howell, R. H., 1993, ''Effects of Store Relative Humidity on Refrigerated Display Case Performance,'' ASHRAE Transactions, Research: 3686.
[9] Navaz, H. K., Faramarzi, R., Gharib, M., Dabiri, D., and Modarress, D., 2002, ''The Application of Advanced Methods in Analyzing the Performance of the Air Curtain in a Refrigerated Display Case,'' ASME J. Fluids Eng., **124**, pp. 756–764.
[10] Bush, R. H., Power, G. D., and Towne, C. E., 1998, ''WIND: The Production Flow Solver of the NPARC Alliance,'' AIAA 98-0935.
[11] Menter, F., 1994, ''Two-Equation Eddy Viscosity Turbulence Models for Engineering Applications,'' AIAA J., **32**, pp. 1598–1605.
[12] Cazalbou, J. B., Spalart, P. R., and Bradshaw, P., 1994, ''On the Behavior of Two-Equation Models at the Edge of a Turbulent Region,'' Phys. Fluids, **6**, pp. 1797–1804.
[13] Yoder, D. A., Georgiadis, N., and Nicholas, J., 1999, ''Implementation and Validation of the Chien k-Epsilon Turbulence Model in the WIND Navier-Stokes Code,'' AIAA Paper 99-0745.
[14] Nichols, R. H., and Tramel, R. W., 1997, ''Application of a Highly Efficient Numerical Method for Overset-Mesh Moving Body Problems,'' AIAA Paper 97-2255.
[15] Bhattacharjee, P., 2002, ''Simulation of Wall Jet Entrainment,'' M.S thesis, Aeronautical and Astronautical Engineering, University of Illinois at Urbana–Champaign.
[16] Gogineni, S., and Shih, C., 1997, ''Experimental Investigation of the Unsteady Structure of a Transitional Wall Jet,'' Exp. Fluids, **23**, pp. 121–129.
[17] Gogineni, S., Visbal, M., and Shih, C., 1998, ''Phase-Resolved PIV Measurements in a Transitional Plane Wall Jet: a Numerical Study,'' Exp. Fluids, **27**, pp. 126–136.
[18] Kim, J., Moin, P., and Moser, R., 1987, ''Turbulence Statistics in Fully Developed Channel Flow at Low Reynolds Number,'' J. Fluid Mech., **177**, pp. 133–166.
[19] Wilcox, D. C., 1993, ''Turbulence Modeling for CFD,'' La Canada, CA, DCW Industries.

Effect of Wall Roughness on Laminar Flow of Bingham Plastic Fluids through Microtubes

Tahsin Engin,[1] Umit Dogruer, Cahit Evrensel, Scott Heavin, and Faramarz Gordaninejad
Department of Mechanical Engineering, University of Nevada, Reno, Nevada 89557
e-mail: egint@sakarya.edu.tr

[DOI: 10.1115/1.1792252]

1 Introduction

Miniaturization of traditional devices is in high demand for micro-electro-mechanical systems (MEMS). Examples include but are not limited to optics, communication and information systems, fluidics, biotechnology, medicine, automotive, and aerospace. An area of interest in several engineering fields is the control of fluid flow within microchannels and microtubes. The applications include, but are not limited to, fields such as vibration control of structures and systems using small devices, reactors for modification and separation of biological cells, energy systems as a mobile power supply, heat exchangers for micro and macro devices, and propulsion engines [1–3].

In recent years, there has been growing attention given to the liquid flow in microchannels in parallel with the development of miniaturized devices and systems. The understanding of flow characteristics, such as velocity distribution and pressure loss is necessary in design and process control of microfluidic devices. Peng, Peterson, and Wang [4] experimentally studied the flow characteristics of water flowing through rectangular microchannels having hydraulic diameters of 0.133 to 0.367 mm and height to width ratios of 0.333 to 1. Their results indicated that the laminar flow transition occurred for the range of the Re number between 200 and 700. They also claimed that friction behavior for both laminar and turbulent flow depart from classical thermofluid correlations, and the friction factor is proportional to $\mathrm{Re}^{-1.98}$ rather than Re^{-1}. Mala and Li [5] investigated the water flow through the microtubes with diameters ranging from 50 to 254 μm. In terms of flow friction, they observed significant departure from the conventional laminar flow theory. They also proposed a roughness-viscosity model to interpret the data. Weilin, Mala, and Li [6] conducted experiments to investigate the flow characteristics of water through silicon microchannels with hydraulic diameters ranging from 51 to 169 μm. They also reported considerable deviations from conventional theory. They concluded that the measured higher-pressure gradient and flow friction could be due to the effect of surface roughness of the microchannels. Judy, Maynes, and Webb [7] carried out experiments for pressure-driven liquid flow through round and square microchannels fabricated from fused silica and stainless steel. They argued that there was no distinguishable deviation from the conventional laminar flow theory for microchannels they tested. Papautsky [8] experimentally investigated the flow of water through microchannels with widths ranging from 150 to 600 μm, heights from 22.7 to 26.35 μm, and with a surface roughness of about 3.3×10^{-4} μm. Their results show a friction factor increase of about 20% above macroscale theoretical values within $0.001<\mathrm{Re}<10$. A recent literature review of microchannel flows has been done by Garimella and Sobhan [9].

A class of materials exhibits little or no deformation up to a certain level of stress, called the yield stress. These materials are often known as Bingham plastics. Paints, slurries, pastes, and some food substances such as margarine, mayonnaise, and ketchup are good examples of Bingham plastics. Although there are numerous studies on Bingham plastic flow in macrosized channels, there is no comprehensive study dealing with the behavior of fluids that exhibit Bingham plastic properties.

The present work is a preliminary study of the flow behavior of non-Newtonian fluid through microtubes using Bingham plastic constitutive model. This study focuses on the effects of the wall roughness and yield stress on the flow behavior. The analytical solution of the laminar Bingham plastic fluid is introduced, and a roughness-viscosity model proposed by Mala [10] is adapted to account for variation of dynamic viscosity of Bingham fluid across a microtube. The governing differential equation describing the flow in the microtubes is solved numerically using a finite difference method (FDM).

2 Roughness-Viscosity Model for Bingham Plastic Fluid Flow

The effect of tube wall roughness on the laminar flow in macroscale circular tubes has been ignored and for a Newtonian fluid the friction factor is assumed to be a function of only the Reynolds number. However, the presence of surface roughness affects the laminar velocity profile when the fluid is flowing through microscale tubes or channels. This phenomenon has been illustrated by a number of experiments and a comprehensive review can be found in the literature [10–12]. In order to consider the effects of surface roughness on laminar flow in microtubes, Mala [10] proposed a roughness-viscosity function based on the Merkle-Kubota-Ko [11] modified viscosity model as follows:

$$\frac{\mu_R}{\mu_0}=A\,\mathrm{Re}_\varepsilon\frac{r}{\varepsilon}\left[1-\exp\left(-\frac{\mathrm{Re}_\varepsilon}{\mathrm{Re}}\frac{r}{\varepsilon}\right)\right]^2, \tag{1}$$

where μ_R is the roughness viscosity, ε is the wall roughness, and the roughness Reynolds number is given by $\mathrm{Re}_\varepsilon=(\varepsilon^2/v)\times(du/dr)_{r=R}$ and the coefficient A is defined as

$$A=0.1306\left(\frac{R}{\varepsilon}\right)^{0.3693}\exp\left[\mathrm{Re}\left(6\times10^{-5}\frac{R}{\varepsilon}-0.0029\right)\right]. \tag{2}$$

The analytical model of Merkle, Kubota, and Ko [11] describes the manner in which distributed surface roughness affects transition from laminar to turbulent regime, and pictures an additional momentum transport near the wall that augments the transfer of momentum by molecular viscosity. This additional momentum transfer was taken into account by means of an effective viscosity that was large near the wall and diminishes to the molecular viscosity far from the wall.

By adding the roughness viscosity in the momentum equation in a manner similar to the eddy viscosity in turbulent flow, the momentum equation becomes

$$-\tau_y+(\mu_0+\mu_R)\frac{du}{dr}=-\frac{1}{2}r\frac{dp}{dz}. \tag{3}$$

By dividing both sides of Eq. (3) by μ_0 and combining with Eq. (1) one can obtain

$$\left\{1+A\,\mathrm{Re}_\varepsilon\frac{r}{\varepsilon}\left[1-\exp\left(-\frac{\mathrm{Re}_\varepsilon}{\mathrm{Re}}\frac{r}{\varepsilon}\right)\right]^2\right\}\frac{du}{dr}-\frac{1}{2\mu_0}\frac{dp}{dz}r-\frac{\tau_y}{\mu_0}=0. \tag{4}$$

[1]Author to whom correspondence should be addressed. Present address: University of Sakarya, Faculty of Engineering, Dept. of Mechanical Engineering, Esentepe Campus, 54187 Sakarya, Turkey.

Contributed by the Fluids Engineering Division for publication in the JOURNAL OF FLUIDS ENGINEERING. Manuscript received by the Fluids Engineering Division June 6, 2003; revised manuscript received March 4, 2004. Associate Editor: P. Signier.

Equation (4) can be expressed in terms of nondimensional parameters. By multiplying both sides of Eq. (4) by $D^2\rho/\mu_0$, and after some manipulations one obtains

$$8\left\{1+A\,\mathrm{Re}\bar{\varepsilon}\bar{r}\left.\frac{d\bar{u}}{d\bar{r}}\right|_{\bar{r}=1}\frac{\bar{r}}{\bar{\varepsilon}}\left[1-\exp\left(-\bar{\varepsilon}\bar{r}\left.\frac{d\bar{u}}{d\bar{r}}\right|_{\bar{r}=1}\right)\right]^2\right\}\frac{d\bar{u}}{d\bar{r}}-\mathrm{Re}\frac{d\bar{p}}{d\bar{z}}\bar{r}-4\frac{\mathrm{He}}{\mathrm{Re}}=0, \tag{5}$$

where the Reynolds number is

$$\mathrm{Re}=\frac{\rho U_m D}{\mu_0},$$

the Hedsrom number is

$$\mathrm{He}=\frac{D^2\rho\tau_y}{\mu_0^2},$$

and

$$\bar{u}=\frac{u}{U_m},\quad \bar{r}=\frac{r}{D/2},\quad \bar{\varepsilon}=\frac{\varepsilon}{D},\quad \bar{p}=\frac{p}{\frac{1}{2}\rho U_m^2}.$$

As can be seen from the selected dimensionless parameters, Re represents the Newtonian behavior of the fluid and tube geometry, and He represents the effect of yield stress. Equation (5) is a modified momentum equation that includes the effect of tube wall roughness in a laminar flow of non-Newtonian fluids exhibiting Bingham plastic behavior. It is also a first-order nonlinear differential equation, which does not have a closed-form solution. It can be solved using the FDM. The dimensionless velocity gradient in Eq. (5) is written in backward difference form for the shear flow region, and the resulting nonlinear system of equations is solved by using the Newton-Raphson method.

3 Results and Discussion

It is generally accepted that the surface roughness has an effect on laminar flow characteristics and results in a reduction in Reynolds number [11,12]. Based on the Merkle-Kubota-Ko [11] modified viscosity model the roughness-affected viscosity (μ_R) increases exponentially from the tube centerline to the wall. At the centerline, the roughness viscosity is assumed to be zero, and at the wall it reaches its maximum value. The average height of the surface roughness dictates the dominance of this additional frictional effect. In Fig. 1, the effect of relative roughness on the roughness viscosity is shown for a Hedsrom number of zero, which would characterize zero yield stress. As can be seen from Fig. 1, as the relative surface roughness increases, the roughness viscosity increases significantly. The total viscosity is increased by 54% near the wall with 8% roughness as compared to viscosity in the centerline of the tube.

Comparison between the experimentally measured and predicted friction factors is shown in Fig. 2. It is clearly seen that the effect of wall roughness plays an important role on the friction factor even in the laminar flow conditions [10–12]. The dashed line indicates theoretical friction factor for Newtonian fluid, which is known as $f\,\mathrm{Re}=16$. From Fig. 2, it can be concluded that there is a good agreement between the predictions of the present study and the experimental friction factor data.

Figure 3 shows the velocity profiles for different relative surface roughness values and a constant He number of 1000. The dashed curve represents the theoretical laminar Bingham plastic flow velocity profile. As in the case of He=0, the peak velocity (or plug velocity) decreases considerably with increasing roughness. For the cases considered in Fig. 3, peak velocity reduces by 7.2%, 15.5%, and 23.2% compared to the conventional theory for relative roughness of 2%, 4%, and 8%, respectively.

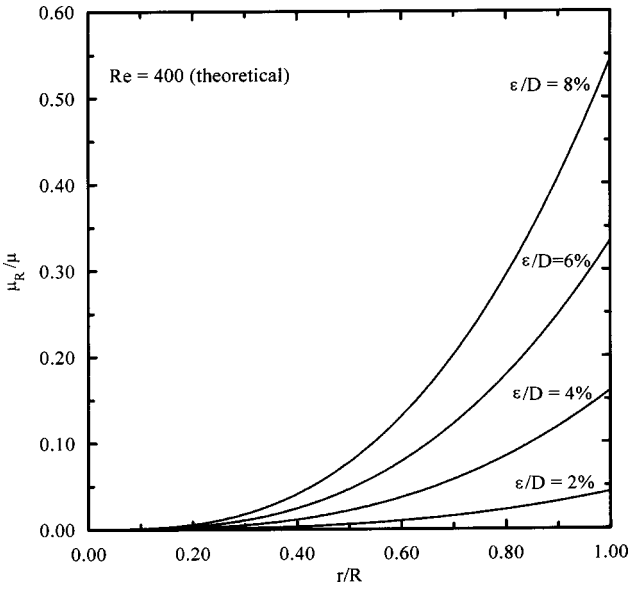

Fig. 1 Effect of relative roughness height on the roughness viscosity

Figure 4 shows nondimensional velocity profiles for different He numbers at a constant relative roughness of 4%. The results indicate that the effect of surface roughness on the velocity profile increases with increasing Hedsrom number. Particularly, for high He numbers, the shear flow is trapped into a small gap between plug flow and the tube wall. This increases the velocity gradient at the wall, $(d\bar{u}/d\bar{r})_{\bar{r}=1}$ and it results in increased effect of the roughness, as it is clear from Eq. (5). From Fig. 4, with smooth tube surfaces, it is seen that for high yield stresses (or He number), deviation from the velocity profile increases. For lower He numbers, as expected, the shear flow region increases due to reduction in the plug region and the percentage deviation of the plug velocity for the rough tube from the one for smooth tube reduces.

The flow behavior of a fluid through microtubes can be interpreted in terms of flow friction. Theoretically, laminar flow friction coefficient is given by

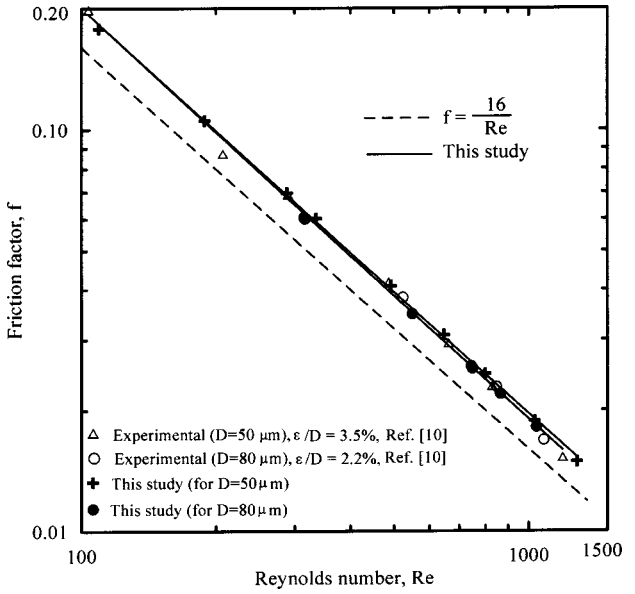

Fig. 2 Comparison among theoretical, experimental, and model results for He=0

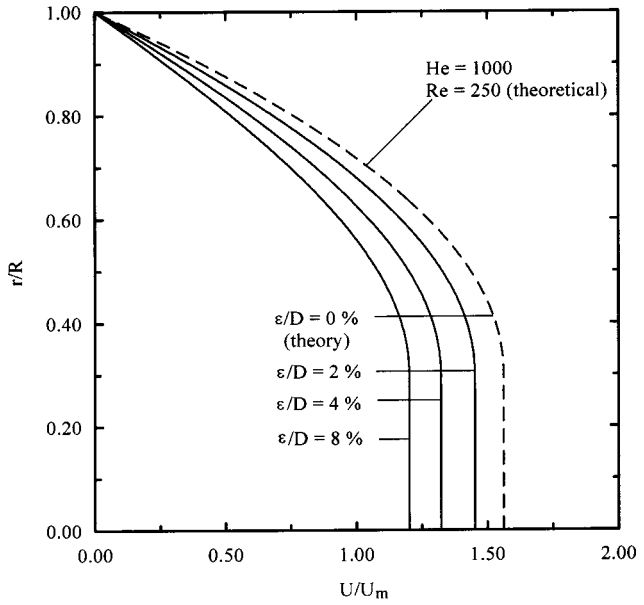

Fig. 3 Effect of relative roughness on velocity profile for He =1000

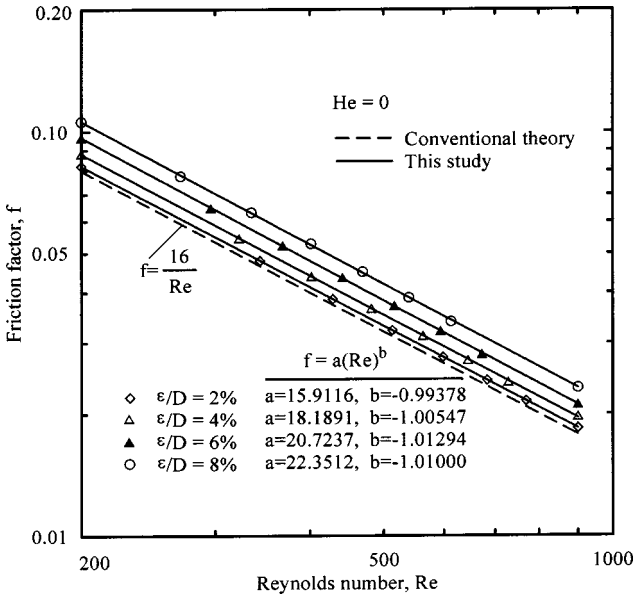

Fig. 5 Effect of relative roughness on friction factor for He=0

$$f = a\,\mathrm{Re}^{b}, \tag{6}$$

where $a=16$ and $b=-1$, respectively, and it does not depend on surface roughness for Newtonian fluid flow in a macrotube. For microtubes, in order to examine the effect of wall roughness, the dependency between the flow friction coefficient (f) and Reynolds number (Re) is plotted for various relative wall roughnesses as shown in Fig. 5, for He=0. For comparison, the theoretical flow friction factor is also plotted in the same figure. It is clear from Fig. 5 that all predicted friction factors using the model presented in this paper are well above the conventional laminar flow line within the range of the Re numbers considered. This can be attributed to the fact that the friction factor, i.e., pressure drop, in microchannels is considerably higher than the predictions based on the conventional laminar flow theory. This is presumably due to fact that the relative roughness height becomes comparable relative to the tube size. It is also reported in the literature [6,11] that the departure from the conventional theory increases with increasing Reynolds number for a Newtonian fluid. Results shown in Fig. 5 indicate that a friction factor for a tube of 4% relative roughness increases by 10.6% compared to the smooth tube for Re=100, while this increase is 17.2% for Re=1000. Considering Eq. (6), the results demonstrate an increase in the multiplier a with increasing relative roughness, while b, the slope in the log-log scale, remains nearly unchanged. This is clear from the fact that f vs Re lines are parallel to each other, indicating about the same slope.

Figure 6 illustrates the variation of friction coefficient with Reynolds number as a function of He. The results show that the difference between friction factors for different He decreases with increasing Re. On the other hand, deviation of friction factor for a

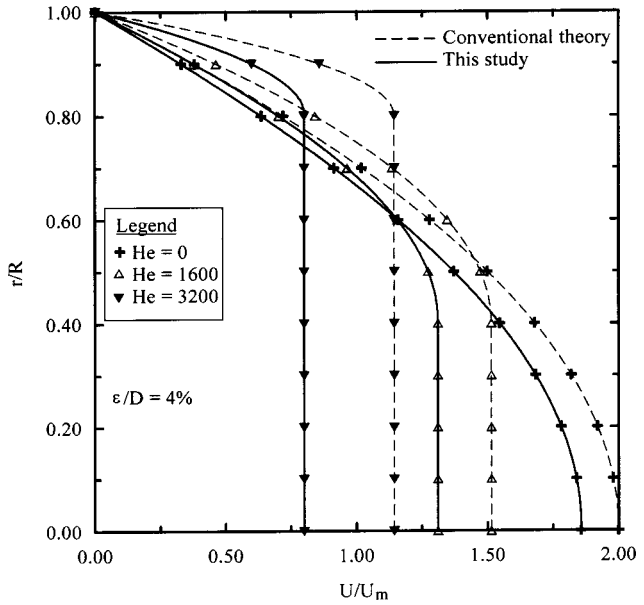

Fig. 4 Effect of He number on velocity profile for a relative roughness of 4%

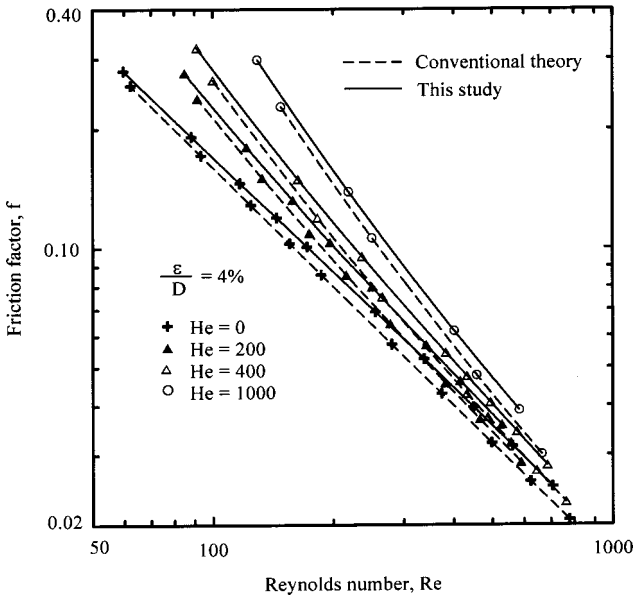

Fig. 6 Effect of He number for constant relative roughness of 4%

rough tube from a smooth one increase with increasing Reynolds number with the exception of He=1000. This is probably due to the increase in the interactions between fluid particles and irregular wall surface as discussed before. The deviation also increases with increasing roughness as expected.

4 Conclusions

The flow characteristics of liquids modeled by the Bingham plastic constitutive relation through microtubes were numerically studied. The wall roughness effect in a microtube was characterized by using a roughness-viscosity model. This model is used to modify the laminar Bingham plastic flow equations in microtubes by introducing a location dependent apparent viscosity.

The numerical results presented in this paper show that the flow friction in microtubes is considerably larger than the predictions of the conventional theory based on uniform viscosity. The departure from the conventional laminar flow theory is also dependent upon fluid yield stress, which is characterized by the Hedsrom number. Therefore, the combined effects of wall roughness and the yield stress appear to have a considerable impact on the flow behavior through microtubes.

Acknowledgments

One of us (T.E.) has been supported by *The Scientific and Research Council of Turkey* (TUBITAK) to conduct this research under NATO B1 international scholarship program. TUBITAK's support is gratefully acknowledged. Also, the authors would like to thank Gregory Hitchcock for his suggestions on the manuscript.

References

[1] Havenhill, D., and Wolke, P. J., 1991, "Magnetic Suspensions for Space Applications," NASA CP-10066.
[2] Eostein, A. H., 1997, "Micro-Heat Engines, Gas Turbines, and Rocket Engines, The MIT Microengine Project," AIAA-97-1773, 28th AIAA Fluid Dynamics Conference.
[3] Pfhaler, J., Harley, J., Bau, H., and Zemel, J., 1991, "Gas and Liquid Flow in Small Channels," *Micromechanical Sensors, Actuators, and Systems*, ASME, New York, DCS, Vol. 32, pp. 49–60.
[4] Peng, X. F., Peterson, P., and Wang, B. X., 1994, "Frictional Flow Characteristics of Water Flowing Through Rectangular Microchannels," Exp. Heat Transfer, **7**, pp. 249–264.
[5] Mala, G. M., and Li, D., 1999, "Flow Characteristics of Water in Microtubes," Int. J. Heat Fluid Flow, **20**, pp. 142–148.
[6] Weilin, Q., Mala, G. M., and Li, D., 2000, "Pressure-Driven Water Flows in Trapezoidal Silicon Microchannels," Int. J. Heat Mass Transfer, **43**, pp. 353–364.
[7] Judy, J., Maynes, D., and Webb, B. W., 2002, "Characterization of Frictional Pressure Drop for Liquid Flows Through Microchannels," Int. J. Heat Mass Transfer, **45**, pp. 3477–3489.
[8] Papautsky, I., 1999, "Metallic Microinstrumentation for Biomedical Applications," PhD. dissertation, University of Utah.
[9] Garimella, S. V., and Sobhan, C. B., 2003, "Transport in Microchannels—A Critical Review," Annu. Rev. Heat Transfer, **13**, pp. 1–50.
[10] Mala, G. M., 1999, "Heat Transfer and Fluid Flow in Microchannels," Ph.D. dissertation, University of Alberta, Canada.
[11] Mekle, C. L., Kubota, T., and Ko, D. R. S., 1974, "An Analytical Study of the Effects of Surface Roughness on Boundary Layer Transition," AF Office of Scientific Res. Space and Missile Sys. Org., Report No. AD/A004786.
[12] Tani, I., 1969, "Boundary Layer Transition. Annual Reviews of Fluid Mechanics," Vol. 1, Annual Reviews, Tiago, Palo Alta, CA, Vol. 1.

The Vibration Response of a Cantilevered Rectangular Cylinder in Cross-Flow Oscillation

Mizuyasu Koide
Life Engineering Research Center, Niigata Sangyo University, 4730 Karuigawa, Kashiwazaki, Niigata, 945-1393, Japan
e-mail: mkoide@life-eng.nsu.ac.jp

Yuuki Kubo
Toray Engineering Co., Ltd., Seta3-3-25, Ootsu, Shiga, 520-2134, Japan
e-mail: yuki_kubo@toray-eng.co.jp

Tsutomu Takahashi
Department of Mechanical Engineering, Nagaoka University of Technology, 1603-1 Kamitomioka, Nagaoka, Niigata, 940-2188, Japan
e-mail: ttaka@mech.nagaokaut.ac.jp

László Baranyi
Department of Fluid and Heat Engineering, University of Miskolc, H-3515, Miskolc-Egyetemváros, Hungary
e-mail: arambl@uni-miskolc.hu

Masataka Shirakashi
Department of Mechanical Engineering, Nagaoka University of Technology, 1603-1 Kamitomioka, Nagaoka, Niigata, 940-2188, Japan
e-mail: kashi@mech.nagaokaut.ac.jp

[DOI: 10.1115/1.1792255]

Introduction

It is well known that a large-amplitude oscillation called galloping [1–3] is generated, in addition to Kármán vortex excitation, for rectangular cylinders supported perpendicularly to a uniform flow when the slenderness b/d is in the range of 0.6 to 2.8 (d=height, b=streamwise length of the rectangular cross-section). The basic aerodynamic excitation mechanism of the cross-flow galloping of a rectangular cylinder is explained by the quasi-steady nonlinear aerodynamic theory developed by Parkinson et al. [4]. In this theory, the relative attack angle plays an important role in the excitation mechanism of galloping. Also, as was shown by Deniz and Staubli [5], the attack angle of a fixed rectangular cylinder strongly affects the vortex shedding frequency and lift.

Although the mechanism of pure cross-flow oscillation for a circular and rectangular cylinder is becoming clear, as seen in the recent paper [6], a slight difference in support conditions may affect strongly the oscillation behavior. The specific aim of this paper is to present the effect of attack angle fluctuation on the cross-flow oscillation behavior of a rectangular cylinder supported by a cantilever plate-spring system.

Contributed by the Fluids Engineering Division for publication in the JOURNAL OF FLUIDS ENGINEERING. Manuscript received by the Fluids Engineering Division August 6, 2003; revised manuscript received March 15, 2004. Associate Editor: H. Johari.

Experimental Apparatus and Measurements

Three rectangular cylinders with an equal height, $d=26$ mm, and a slenderness of $b/d=0.5$, 1.0, and 2.0 were used. These were chosen since $b/d=0.5$ is less than the galloping range and $b/d=2.0$ is higher than the Kármán vortex excitation range. Hereafter, the rectangular cylinders with $b/d=0.5$, 1.0, and 2.0 are expressed as Cylinder I, Cylinder II, and Cylinder III, respectively.

Experiments were carried out in a blow-down type wind tunnel with a measuring section of 320(H)×320(W)×1000(L) mm as shown in Fig. 1. The turbulence level in the measuring section was less than 0.6%. The cylinder was placed in the wind tunnel horizontally, perpendicular to the free stream. The blockage ratio was 8%. The cylinder was supported at both ends outside the measuring section. End plates were attached to the cylinder to remove influence of flow through slots on the sidewalls of the measuring section [7].

In order to investigate the influence of attack angle fluctuation superimposed on cross-flow oscillation, i.e., Kármán vortex excitation and galloping, the cylinder was supported by cantilever plate springs in three ways as shown in Fig. 2. When the cylinder is supported by the twin plate spring as in Fig. 2*a*, its motion is almost purely translational in the z direction. When the cylinder is supported by the single plate spring, a geometrical attack angle α_g is superposed due to angular deflection at the end of a cantilever beam. Thus α_g fluctuation is generated synchronizing with cylinder displacement Z. The phase difference ϕ between α_g and Z is zero (i.e., ''in-phase'') when the cylinder is supported against the flow as in Fig. 2*b*, and $\phi=\pi$ (''anti-phase'') when the cylinder is supported following the flow as in Fig. 2*c*. The magnitude of geometrical attack angle α_g is given by $|\alpha_g|=3|Z|/(2l)$, where l is the cantilever beam length. The absolute value of α_g reaches 6° at $Z=5$ mm, the maximum displacement in this experiment. The natural frequency f_n, the effective mass m_e, and the logarithmic damping factor δ were determined through a free damping oscillation experiment in otherwise quiescent air. These parameters, as well as the cantilever length l and the spring constant k, were virtually equal for all the cylinders and irrespective of the way of support, as shown in Table 1.

A ring type vortex anemometer [8] was applied to measure the free stream velocity U within an uncertainty of ±3%. The laser displacement meter measured the displacement Z at one end of the cylinder outside the measuring section, as shown in Fig. 1, and its uncertainty was ±2%. The vortex shedding frequency f_v was obtained by applying FFT analysis to the streamwise fluctuating velocity u detected by a hot wire probe at a location in the near wake of the cylinder ($x=2b$, $z=1d$, see Fig. 1). Since the velocity signal u includes turbulence, the spectrum of u was averaged over 20 data and the vortex shedding frequency f_v was taken to be the frequency at the maximum peak of the averaged spectrum. Thus, the uncertainty in f_v is estimated to be around 2%.

Results and Discussion

The nondimensional vortex shedding frequency f^* and nondimensional root-mean-square (rms) value of displacement, Z_{rms}/d, are plotted against the reduced velocity V_r in Figs. 3–5 for the three cylinders supported by three different ways shown in Fig. 2. In one run of the wind tunnel experiment, V_r was first increased stepwise from the lowest value of around 2.5 to the highest value of around 20 by increasing the free stream velocity U, and then decreased again to the lowest nondimensional velocity. The corresponding Reynolds number Re is from 2000 to 16,000. In these figures, open symbols are for increasing V_r and solid symbols for decreasing V_r, respectively. When the twin plate spring was used, the oscillation behavior showed only a slight difference between

cases of ''in-phase'' and ''anti-phase'' settings, confirming that the cylinder motion is purely translational in these settings.

Cylinder I ($b/d=0.5$). Figure 3 shows f^* and $Z_{\rm rms}/d$ versus V_r of Cylinder I for (a) pure cross-flow oscillation ($\alpha_g=0$), (b) ''in-phase'' α_g, and (c) ''anti-phase'' α_g.

For the pure cross-flow oscillation shown in Fig. 3*a*, a sharp maximum peak in $Z_{\rm rms}/d$ appears at $V_r\approx 7$, showing the occurrence of Kármán vortex excitation. The frequency of this large amplitude oscillation is equal to the natural frequency f_n of translational motion. The nondimensional vortex shedding frequency f^* is equal to unity over a considerable range of nondimensional velocity around maximum oscillation, showing that the lock-in phenomenon is occurring there. The oscillation behaviors for the increasing V_r and the decreasing V_r agree well, which shows that the effect of hysteresis is insignificant in the pure cross-flow oscillation of Cylinder I. Galloping did not occur on Cylinder I when $\alpha_g=0$.

The lower oscillation peak at around $V_r=8$ is not due to the translational oscillation but caused by rotational oscillation around the x axis (see Fig. 1), since the phases of the displacement Z at both ends of the cylinder are anti-phase, as confirmed by measur-

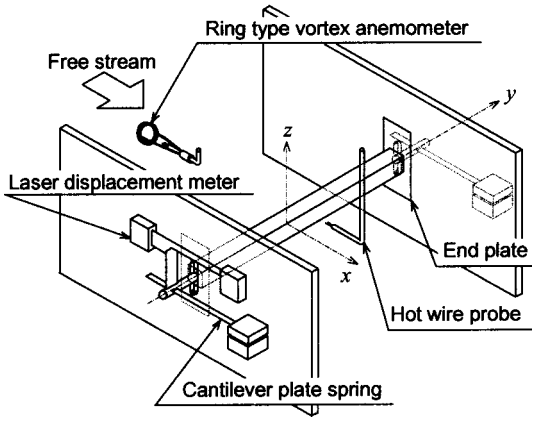

Fig. 1 Arrangement of the experimental apparatus and the coordinate system

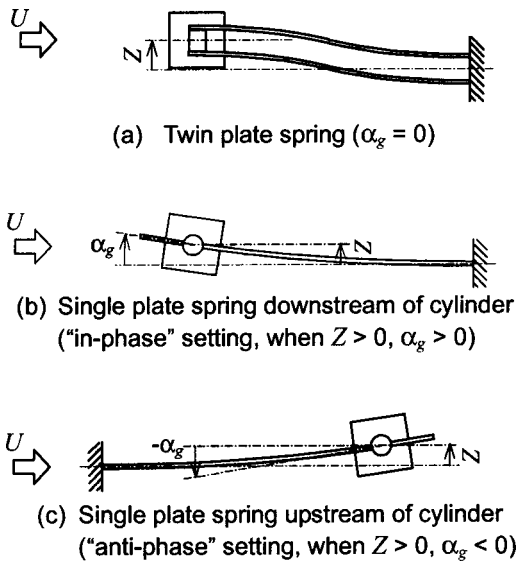

Fig. 2 Cylinder support method by cantilever plate spring and relationship between α_g and Z (flow direction is from left to right)

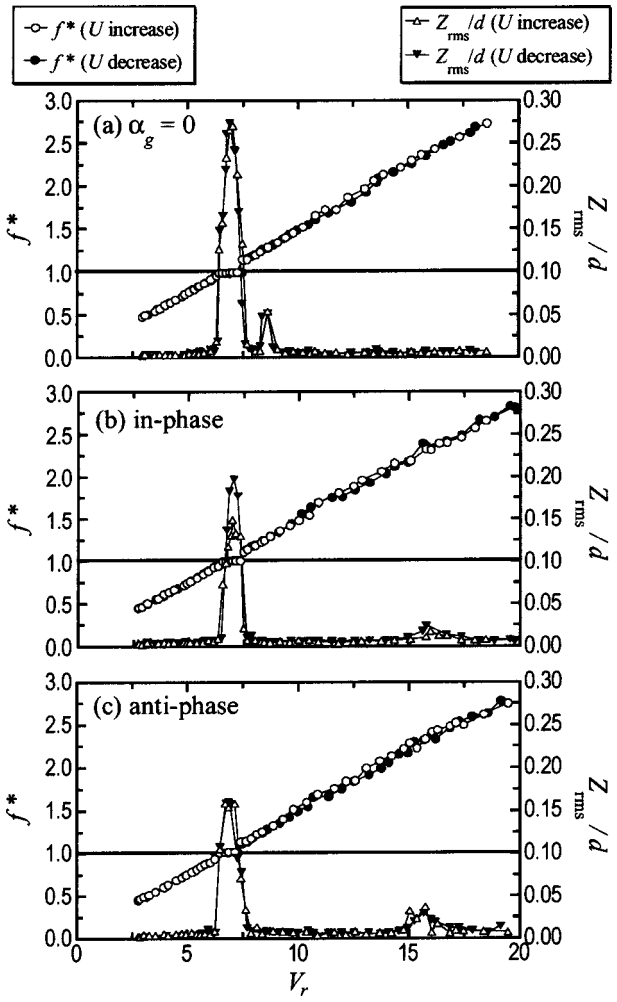

Fig. 3 f^* and $Z_{\rm rms}/d$ versus V_r for $b/d=0.5$

Table 1 Characteristics of the oscillating system

	Cylinder	b/d	k [N/m]	f_n [Hz]	m_e [kg]	δ
Single-plate spring	I	0.5	1260	17.0	0.11	0.011*1, 0.011*2
	II	1.0		16.7*1, 17.0*2		0.012*1, 0.011*2
	III	2.0		17.0		0.013*1, 0.012*2
Twin-plate spring	I	0.5	1310	17.0	0.12	0.013
	II	1.0		17.0		0.010
	III	2.0		17.0		0.012

*1''In-phase'' setting.
*2''Anti-phase'' setting.

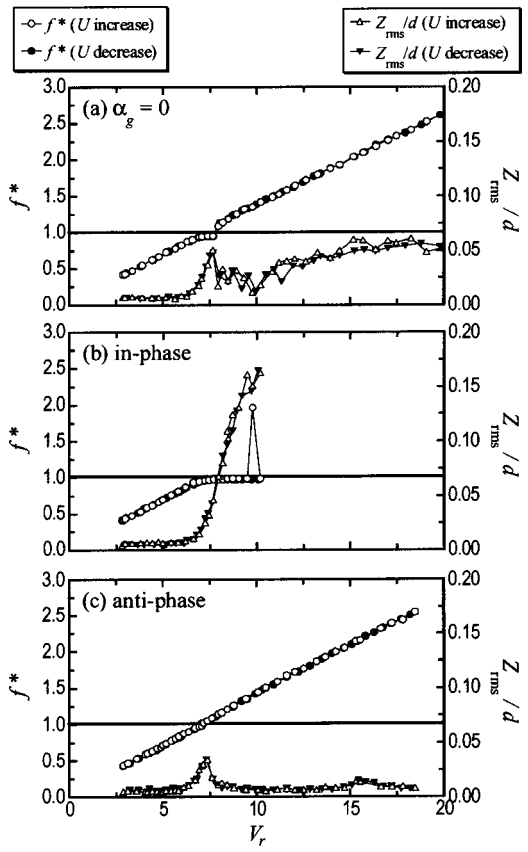

Fig. 4 f^* and Z_{rms}/d versus V_r for $b/d=1.0$

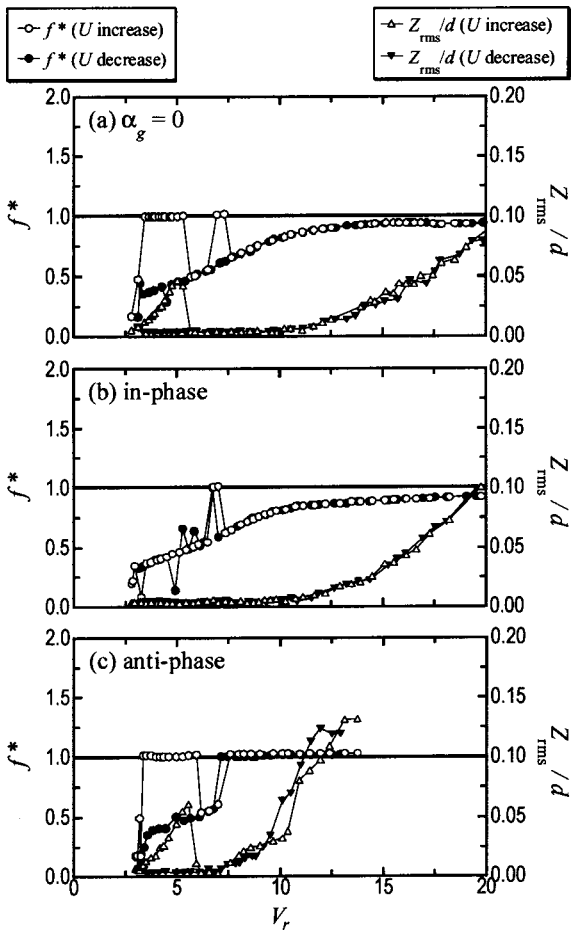

Fig. 5 f^* and Z_{rms}/d versus V_r for $b/d=2.0$

ing Z at both ends of the cylinder simultaneously. Furthermore, the oscillation frequency at this lower peak is confirmed to be equal to the natural frequency of the rotational mode oscillation around the x axis.

When "in-phase" or "anti-phase" α_g is superimposed, the oscillation behavior of Cylinder I is essentially equivalent to the pure cross-flow oscillation, as seen in Figs. 3*b* and 3*c*, except that the maximum Z_{rms}/d value becomes a little lower and the second peak in Z_{rms}/d at $V_r=8$ disappears while a much lower peak appears near $V_r=16$ instead. The latter effect is caused by the shift of the natural frequency of the rotational oscillation mode due to the support method.

Galloping does not occur on Cylinder I whether α_g exists or not. As a result, it is shown that the attack angle fluctuation α_g affects neither Kármán vortex excitation nor the galloping of Cylinder I, which has a slenderness smaller than the critical value.

Cylinder II ($b/d=1.0$). Figure 4 shows the oscillation behavior of Cylinder II. In the case of Cylinder II with $\alpha_g=0$, both Kármán vortex excitation and galloping are induced in different nondimensional velocity ranges, as seen in Fig. 4*a*. The large oscillation over the range of $V_r=7-8$ accompanied by lock-in phenomenon, i.e., the nondimensional vortex shedding frequency f^*, continues to be unity, showing the occurrence of Kármán vortex excitation. When the nondimensional velocity V_r is increased beyond this range, the oscillation amplitude decreases significantly and f^* returns to the value for the cylinder at rest, which shows that the Kármán vortex excitation ends at around $V_r=8$. When V_r is increased further, Z_{rms}/d begins to increase again while f^* is not equal to unity but proportional to V_r. The oscillation frequency is always equal to f_n while the cylinder oscillates. These behaviors of f^* show that cylinder oscillation shifts to galloping. Thus, in the case of Cylinder II with $\alpha_g=0$, both Kármán vortex excitation and galloping occur in their respective nondimensional velocity ranges.

Figures 4*b* and 4*c* show that the oscillation behaviors of Cylinder II with "in-phase" and "anti-phase" setting are dramatically different from the case of pure cross-flow oscillation ($\alpha_g=0$). As seen in Fig. 4*b*, the Z_{rms}/d of Cylinder II with "in-phase" setting traces that of Cylinder II with $\alpha_g=0$ until $V_r\approx 8$, where the Kármán vortex excitation is maximum in the case of $\alpha_g=0$. However, Z_{rms}/d continues to increase with V_r with an almost constant slope beyond $V_r\approx 8$ up to the maximum value of the experimental range at $V_r=10$. Throughout the region of large oscillation, the cylinder oscillates at its natural frequency f_n and the velocity spectrum S_u has a dominant peak at the frequency $f_v=f_n$, i.e., $f^*=1$, showing the occurrence of lock-in. However, S_u also had a peak at $2f_v$ in the large oscillation range as seen in the plot for f^* (dislocated plot, $f^*=2$) in Fig. 4*b*. Hence, the nondimensional velocity regions of Kármán vortex excitation and galloping can be no longer clearly distinguished by f^* and Z_{rms}/d in the case of in-phase α_g.

In the case of Cylinder II with "anti-phase" setting, in contrast, the Kármán vortex excitation is considerably suppressed and the lock-in region almost disappears, as seen in Fig. 4*c*. In addition, the galloping is almost completely suppressed.

The hysteresis in oscillation behavior of Cylinder II is also insignificant, as the case of Cylinders I, whether α_g is superimposed or not.

Thus, the influence of α_g on the oscillation behavior of Cylinder II is pronounced and its effects are in contrast depending on the phase difference between α_g and Z generated by the support

system. When α_g is in-phase with Z, both Kármán vortex excitation and galloping are strongly enhanced. In contrast, vortex excitation is significantly suppressed when α_g is anti-phase with Z, and galloping is almost entirely suppressed.

Cylinder III ($b/d=2.0$). Cylinder III with $\alpha_g=0$ shows the occurrence of two different oscillations with increasing V_r, i.e., low-velocity excitation in the range of $V_r=3-6$ and galloping in a higher nondimensional velocity range, say $V_r>12$, as seen in Fig. 5*a*. Kármán vortex excitation does not occur since the slenderness is larger than the Kármán vortex excitation region [9]. Since the range of V_r for the low-velocity excitation is much lower than the value of V_r at which $f^*=1$, i.e., $V_r=12$, its mechanism is not a synchronization between the cylinder oscillation and the periodic vortex shedding. Although f^* is equal to unity in this region and it seems to be lock-in, the peak in S_u at f_n is caused by velocity fluctuation due to the large cylinder oscillation. The galloping occurs when $V_r>12$ and the amplitude grows with V_r at an increasing gradient, showing the typical divergent character of galloping. When V_r is decreased, Z_{rms}/d traces the same curve in the galloping region but low-velocity excitation is not observed at all. This hysteretic behavior of the low-velocity excitation of Cylinder III is more pronounced compared with other excitations described in this paper, and it shows a strong nonlinearity of the low-velocity excitation.

In the case of Cylinder III with ''in-phase'' setting (Fig. 5*b*), the low-velocity excitation completely vanishes, while galloping is not affected by the superposition of α_g. In contrast, in the case of Cylinder III with ''anti-phase'' setting (Fig. 5*c*), the behavior of the low-velocity excitation including hysteresis is not affected by the superposition of α_g, while galloping occurs at a lower nondimensional velocity and its amplitude grows with V_r much more rapidly than in the case of $\alpha_g=0$. A sudden jump of f^* to unity appears at around $V_r=7$ in Figs. 5*a*–5*c*. This might be lock-in, but the cylinder oscillation is small at this V_r. Hence, the relation of the sudden jump of f^* to the oscillation is still to be investigated.

Conclusions

In this study, the cross-flow oscillation of a rectangular cylinder supported by a cantilever plate-spring system was investigated using a wind tunnel. Three kinds of supports were tested, which introduce different relationships between the geometrical attack angle α_g and cylinder displacement Z: (i) pure cross flow oscillation ($\alpha_g=0$), (ii) the phase difference ϕ between α_g and Z is zero (in-phase), and (iii) $\phi=\pi$ (anti-phase). Three rectangular cylinders with the slenderness of $b/d=0.5$, 1.0, and 2.0 were used to investigate the influence of α_g on Kármán vortex excitation and galloping.

The superposition of α_g has essentially no influence on the Kármán vortex excitation irrespective of b/d and ϕ, when the slenderness $b/d=0.5$ (Cylinder I). In the case of Cylinder II ($b/d=1.0$), the Kármán vortex excitation is considerably suppressed and the galloping is also completely suppressed when the cylinder is supported with ''anti-phase'' setting. In contrast, when the cylinder was supported with ''in-phase'' setting, the oscillation increases continuously beyond the nondimensional velocity V_r for the maximum amplitude of Kármán vortex excitation with $\alpha_g=0$, leading to galloping much larger than in the case of $\alpha_g=0$. In the case of Cylinder III ($b/d=2.0$), the influence of anti-phase α_g on the galloping of Cylinder III is opposite to that of Cylinder II, since the onset of galloping shifts to a considerably lower nondimensional velocity and its amplitude grows rapidly with V_r. However, the in-phase α_g does not affect the galloping on Cylinder III.

The above results show that the effect of attack angle fluctuation strongly depends on the slenderness b/d and ϕ, and it is stronger on galloping than on Kármán vortex excitation.

Acknowledgments

The support provided by the Hungarian Research Foundation (OTKA Project No. T 042961) is gratefully acknowledged by L. Baranyi.

Nomenclature

- b = streamwise length of rectangular cross section
- d = height of rectangular cross section
- f_n = natural frequency
- f_v = vortex shedding frequency
- f^* = nondimensional vortex shedding frequency ($=f_v/f_n$)
- k = spring constant
- m_e = effective mass
- Re = Reynolds number ($=Ud/\nu$, ν: kinematic viscosity)
- U = free stream velocity
- u = streamwise fluctuating velocity
- V_r = Reduced velocity [$=U/(f_nd)$]
- Z = displacement of rectangular cylinder
- α_g = geometrical attack angle due to deflection of cantilever
- δ = logarithmic damping factor

References

[1] Nakamura, Y., and Hirata, K., 1994, ''The Aerodynamic Mechanism of Galloping,'' Trans. J. Soc. Aero. Space Sci., **36**, No. 114, pp. 257–269.
[2] Bearman, P. W., and Obasaju, E. D., 1982, ''An Experimental Study of Pressure Fluctuations on Fixed and Oscillating Square-Section Cylinder,'' J. Fluid Mech., **119**, pp. 297–321.
[3] Chen, J. M., and Liu, C. H., 1999, ''Vortex Shedding and Surface Pressures on a Square Cylinder at Incidence to a Uniform Air Stream,'' Int. J. Heat Fluid Flow, **20**, pp. 592–597.
[4] Parkinson, G. V., and Brooks, N. P. H., 1961, ''On the Aeroelastic Instability of Bluff Cylinders,'' J. Appl. Mech., **28**, pp. 252–258.
[5] Deniz, S., and Staubli, T. H., 1997, ''Oscillating Rectangular and Octagonal Profiles: Interaction of Leading- and Trailing-Edge Vortex Formation,'' J. Fluids Struct., **11**, pp. 3–31.
[6] Khalak, A., and Williamson, C. H. K., 1999, ''Motions, Forces and Mode Transitions in Vortex-Induced Vibrations at Low Mass-Damping,'' J. Fluids Struct., **13**, pp. 813–853.
[7] Shirakashi, M., Ishida, Y., and Wakiya, S., 1985, ''Higher Velocity Resonance of Circular Cylinder in Cross Flow,'' Trans. ASME J. Fluids Eng., **107**, pp. 392–396.
[8] Koide, M., Takahashi, T., and Shirakashi, M., 2001, ''Development of a Ring-Type Vortex Anemometer for Low-Velocity Wind Tunnel Experiments,'' Bull. JSME, **67**, 657, B, pp. 1105–1111.
[9] Nakamura, Y., Hirata, K., and Urabe, T., 1991, ''Galloping of Rectangular Cylinders: Effects of a Downstream Splitter Plate,'' *Proc. of the 5th Int. Conf. on Flow Induced Vibration*, 20–22 May, Brighton, pp. 453–458.

The Response of a Turbulent Boundary Layer to Concentrated Suction Applied Through a Pair of Porous Wall Strips

O. Oyewola, L. Djenidi, and R. A. Antonia
Discipline of Mechanical Engineering, School of Engineering, The University of Newcastle, NSW, 2308, Australia

[DOI: 10.1115/1.1792273]

Introduction

Considerable effort has been devoted to the control of natural laminar-turbulent transition using various techniques, e.g., Refs. [1–4]. Out of all the techniques tested, suction has been found useful not only for delaying transition, but also for postponing separation [5,6]. For example, Gad-el-Hak [6] mentioned the possibility of maintaining laminar flow downstream of a spanwise slot through the combination of massive suction with other various control strategies. Also, Lingwood [7], in his review mentioned the work of Pfenninger and Bacon [8], who studied the control of transition in a laminar boundary layer. They found that suction stabilizes the attachment-line flow at the leading edge of swept wings. The possibility of reducing the skin friction through suction was also addressed [5,9], and in particular, the application of suction on a turbulent boundary layer through a single narrow porous wall strip or open slit has been widely studied for quite a number of reasons, e.g., see Refs. [9], [10–14]. For example, Merigaud et al., [11], and Pailhais et al. [13] have suggested that the application of suction to the turbulent boundary layer on the fuselage of an airplane may alleviate the likely contamination of the leading edge of a swept wing by the fuselage. Under certain conditions, relaminarization can be achieved immediately downstream of the strip [9,12]. Antonia, Zhu, and Sokolov [9] studied the effect of concentrated wall suction, applied through a short porous wall strip, on a low Reynolds number turbulent boundary layer. They showed that, when the suction rate is sufficiently high, pseudo-relaminarization occurs almost immediately downstream of the suction strip. Further downstream, there is transition followed by a slow return to a fully turbulent state. Further, Oyewola, Djenidi, and Antonia [12,15] showed that both the suction rate, σ ($\equiv V_w b/\theta_0 U_1$, where V_w is the suction velocity, b is the effective width of the strip, θ_0 is the momentum thickness of the boundary layer at the leading edge of the porous strip with no suction, and U_1 is the free stream velocity), and the momentum thickness Reynolds number, R_θ, played an important role in the relaminarization process. They argued that the ratio $R_{\theta 0}/\sigma$ should not exceed an (as yet undetermined) critical value if relaminarization is to occur. They also suggested that the retransition which follows the relaminarization could be controlled. They proposed that a series of suction strips could produce an effective means for controlling both the relaminarization and re-transition.

The present work exploits this suggestion and extends the work of Oyewola, Djenidi, and Antonia [12,15]. The main objective of this study is to assess the response of a turbulent boundary layer to a concentrated wall suction applied through two successive porous strips. The second strip is placed at a streamwise location where local recovery from the upstream suction strip first begins (see Ref. [16]). Skin friction estimates and results for the effectiveness of the suction as measured by the gain and expenditure of energy, are presented. They are compared with those obtained when suction is applied through the first strip only.

Contributed by the Fluids Engineering Division for publication in the JOURNAL OF FLUIDS ENGINEERING. Manuscript received by the Fluids Engineering Division September 10, 2003; revised manuscript received May 12, 2004. Associate Editor: S. L. Ceccio.

Experimental Details

Measurements were made in a newly constructed boundary layer wind tunnel, driven by a single-inlet 15 kW centrifugal fan, which is able to deliver up to a free stream velocity of 40 m/s. Air enters the working section (Fig. 1) through a two-stage two-dimensional diffuser into the 1.6×0.9 m^2 settling chamber. The chamber consists of six evenly spaced wire mesh screens and a 5 mm aluminum honeycomb. The settled air then flows through a 9.5:1 two-dimensional contraction. A turbulent boundary layer developed on the floor of the rectangular working section (see schematic arrangement in Fig. 1) after it was tripped at the exit from the contraction using a 100 mm roughness strip. Tests showed that the boundary layer was fully developed at the suction strip location. The two-dimensionality of the flow was checked by measuring mean velocity profiles at a number of spanwise locations for some streamwise locations. There were no systematic spanwise variations (maximum deviation was within $\pm4\%$ of the centerline velocity).

Two 3.25 mm thick porous strips of streamwise length 40 mm and made of sintered bronze with pore sizes in the range 40–80 μm or $(0.4-0.9)\nu/U_{\tau 0}$ (where $U_{\tau 0}$ is the friction velocity with no suction and ν the kinematic viscosity) was mounted flush with the test section floor. Allowing for the width of the mounting recess steps, the effective width (=b) of the strip was 35 mm. The suction velocity (V_w) was assumed to be uniform over the porous surface; this assumption seems reasonable if the variation in the permeability coefficient of the porous material is $\pm3\%$.

The second porous strip is placed at a streamwise location of $x/\delta_0\approx10$; $\delta_0(\approx30$ mm) is the boundary layer thickness at the leading edge of the first strip unperturbed. Measurements with only the first strip activated showed that the perturbed boundary layer started to recover from this position [12,15]. The free-stream velocity U_1 is 3.25 m/s and the corresponding initial momentum thickness Reynolds number $R_{\theta 0}$ ($\equiv U_1\theta_0/\nu$, where θ_0 is the unperturbed boundary layer momentum thickness at the leading edge of the first strip) is 750. At this location C_{f0} is 0.0048.

The suction rate was 3.3 over the first strip (σ_1) and 2.0 over the second strip (σ_2). In order to assess the effectiveness of the strips, measurements were also made for $\sigma=5.5$ applied through the first strip only. The combined suction (volumetric) flow rate Q_c ($=Q_1+Q_2$, where Q_1 and Q_2 are the flow rates for the first and second strips, respectively) over two strips is less than that for one strip with $\sigma=5.5$. The effect of suction is quantified by measuring the local wall shear stress downstream of each suction strip. The local wall shear stress was measured with a Preston tube with an outer diameter of 0.72 mm (calibrated in a fully developed turbulent channel flow using a similar method to that described in Ref. [17]) and a static tube located approximately 35 mm above it at the same x position. Using a propagation of error analysis, the uncertainty in the channel flow measurements of local wall shear stress was estimated to be $\pm4\%$. Pressure differences were measured with a MKS Baratron pressure transducer; the output of this instrument was averaged after digitizing at 400 Hz for approximately 120 s. The uncertainty in measuring the skin friction was about $\pm5\%$. This was estimated by measuring the skin friction 10 times, using records of about 60 s in each case, at several streamwise locations downstream of the strips. At each location, the uncertainty was $\pm5\%$ of the mean value.

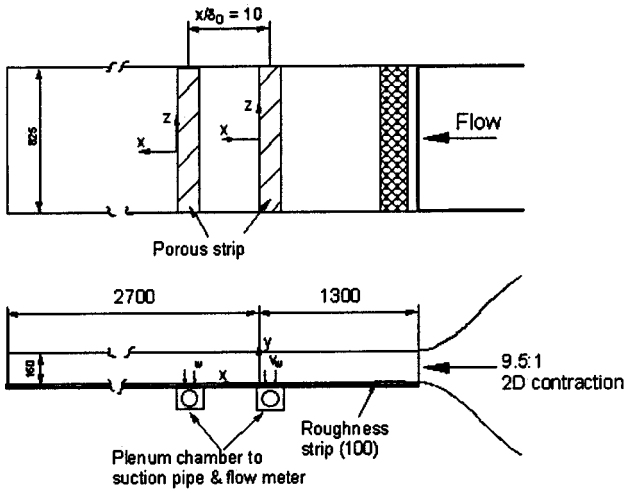

Fig. 1 Schematic arrangement of the test section (dimensions in mm)

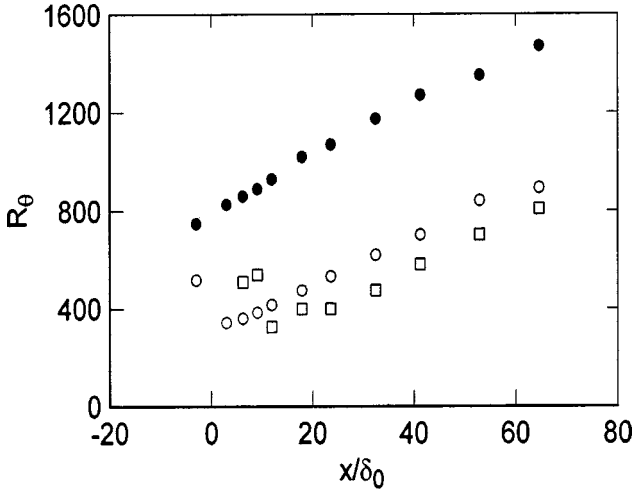

Fig. 3 Streamwise variation of momentum thickness Reynolds number (R_θ). ●: σ=0; □: two strips; ○: one strip.

Skin Friction Coefficient

The skin friction coefficient is plotted in Fig. 2, with reference to the no-suction case (C_{f0}) when the two strips are active ($\sigma_1 = 3.3$ and $\sigma_2 = 2.0$). The variation of C_f when suction is applied at the first strip only (σ=5.5) is also shown. The figure clearly shows that the second strip helps to maintain the value of C_f below that for no-suction over a larger downstream distance. Also, as expected, the use of a second strip causes C_f to rise locally. However, the magnitude of C_f at $x/\delta_0 = 12$ is smaller than C_{f0}. This can be an interesting result in a practical context. Indeed, it suggests that a series of successive strips with appropriately selected suction rates could help keep C_f below C_{f0} for a significant streamwise distance.

In the present case, the use of the second strip increases the total skin friction reduction relative to that obtained with one strip (the areas comprised between the curves and the horizontal line corresponding to σ=0 are 4.473 for one strip, and 6.132 for two strips). The reason why the second suction increases the streamwise distance over which C_f is reduced is related to the reduction in the Reynolds number downstream of the first strip (Fig. 3). This explains why the second rise in C_f is less pronounced than the first. The suction from the second strip is effective since it acts on a boundary layer with a lower Reynolds number and with a near-wall region that has been strongly interfered with Ref. [18] showed, via flow visualizations, that the low-speed streaks are less agitated when suction is applied. This is not surprising since the streaks are closely associated with the ejections and sweeps which are responsible for most of the shear stress in the inner layer [19]. The reduction suggests that the drag-producing events are weakened by suction. The second application of suction would act on a dynamically ''weakened'' boundary layer, and therefore provide a more effective means of control than with only one strip.

This delaying effect of the second strip on the recovery of the boundary layer was already noticeable in Fig. 3, where the minimum value of R_θ occurs at $x/\delta_0 \approx 20$ for two strips and $x/\delta_0 \approx 8$ with one strip. The minimum value of R_θ is nearly the same in each case.

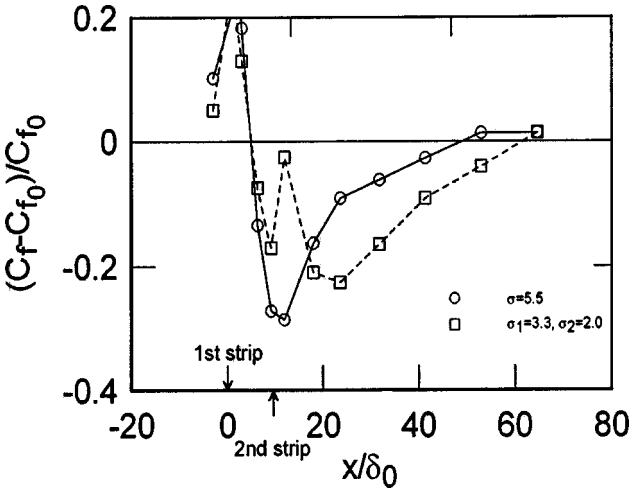

Fig. 2 Streamwise variation of skin friction coefficient. □: two strips; ○: one strip.

Energy Consideration

It is evident from Fig. 2 that suction reduces the skin friction over a significant distance downstream. Indeed, we estimated that there is an overall reduction in skin friction relative to the no suction case. However, considering that the suction rates used in the present experiment are relatively high, one may expect that the energy required to drive the suction is unlikely to balance the energy gained via the frictional reduction.

To quantify this balance, the power ratio P_D/P_{in}, where P_D is the power associated with the frictional reduction, and P_{in} the power used to achieve the specified suction rates, has been determined.

P_D is estimated from the relation

$$P_D = (D_0 - D_s)U_1,$$

where D_S and D_0 are the frictional drag forces with and without suction.

The input mechanical power is given by

$$P_{in} = \Delta p Q_w,$$

where Δp is the pressure drop across the porous strip, and Q_w is the volumetric flow rate associated with the suction.

To determine Δp, a sample of porous material similar to that used for the porous strip was mounted in a pipe. The pressure drop Δp across the sample was measured for various flow rates.

Figure 4 shows the measured ratio $(P_{in} - P_D)/P_{in}$ for various suction flow rates when one strip was used. Also show in the figure is the value of this ratio when two strips were used. Negative values of this ratio would indicate a net energy gain, i.e., that the energy gained as a result of the frictional drag outweighs the

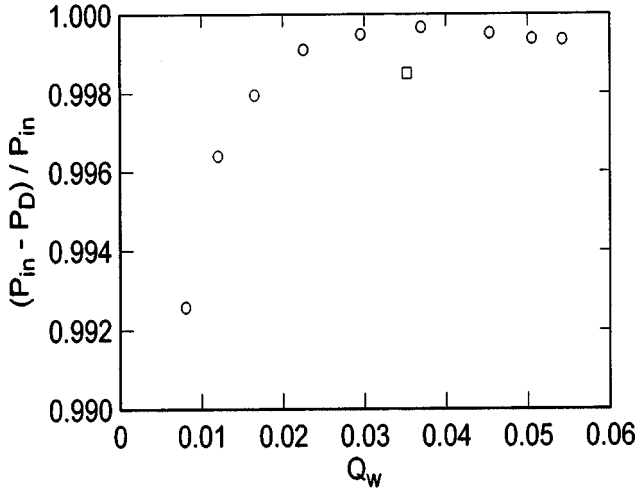

Fig. 4 Measured $(P_{in}-P_D)/P_{in}$ versus flow rate Q_w. □: two strips; ○: one strip.

energy used to achieve the reduction. While the value of $(P_{in} - P_D)/P_{in}$ for two strips is lower than those of one strip of higher flow rates, the plot shows that the present method for reducing the frictional drag does not generate such a saving of energy. Only a very small portion of the input energy is recovered by the drag reduction. This somewhat disappointing result suggests that the use of porous strips on their own is unlikely to be an effective means of controlling the frictional drag of a turbulent boundary layer.

However, there may be other more significant advantages, for example, in controlling the boundary layer over an aircraft wing. Here, the form drag is the major contributor to the total drag. In this case suction will not only reduce the form drag, but may help increase the lift by delaying separation and/or postponing the laminar-turbulent transition. In this respect, the data in Fig. 4 indicate that it would be more efficient and economical to use a series of porous strips with low and gradually reduced suction rates, where the first strip acts mainly to reduce the Reynolds number so that subsequent strips become more effective.

Concluding Remarks

The effect of suction, applied through two porous wall strips, on a turbulent boundary layer has been examined with the use of Preston tube measurements. The second strip was placed at the streamwise location where the maximum reduction of the skin friction occurred due to the first strip. The skin friction measurements revealed that the use of a second strip can significantly extend the relaminarization zone downstream of the first strip. The extent of the zone may reflect a structural change in the near-wall layer. Because it is acting on an already weakened boundary layer (the Reynolds number downstream the first strip is reduced by 33% relatively to the no suction case), the second strip is more effective in controlling the layer. The implication is that the use of a series of judiciously positioned strips can provide a relatively efficient means for controlling the turbulent boundary layer. Note though that, as indicated by the energy balance in Fig. 4, this technique does not appears to be effective in reducing the skin friction alone. However, it is expected that its use on an aircraft wing may lead to additional advantages as it should not only help to reduce the total drag but may also increase the lift.

Acknowledgment

The support of the Australian Research Council is gratefully acknowledged.

References

[1] Biringen, S., 1984, "Active Control of Transition Using Suction-Blowing," Phys. Fluids, **27**, pp. 1345–1358.
[2] Klingman, B. G. B., Boiko, A. V., Westin, K. J. A., Kozlov, V. V., and Alfredsson, P. H., 1993, "Experiments on Stability of Tollmien-Schlichting Waves," Eur. J. Mech. B/Fluids, **12**, pp. 493–514.
[3] Cathalifaud, P., and Luchini, P., 2000, "Algebraic Growth in Boundary Layers: Optimal Control by Blowing and Suction at the Wall," Eur. J. Mech. B/Fluids, **19**, pp. 469–490.
[4] Reed, H., Saric, W. S., and Arnal, D., 1996, "Linear Stability Theory Applied to Boundary Layers," Annu. Rev. Fluid Mech., **28**, pp. 389–428.
[5] Gad-el-Hak, M., 1989, "Flow Control," Appl. Mech. Rev., **42**, pp. 261–293.
[6] Gad-el-Hak, M., 1998, "Flow Control: Fundamental and Practices," Lecture notes in Physics, M. Gad-el-Hak, A. Pollard, and J.-P. Bonnet, eds., Springer, pp. 1–154.
[7] Lingwood, R. J., 1997, "On the Effects of Suction and Injection on the Absolute Instability of the Rotating-Disk Boundary Layer," Phys. Fluids, **9**, pp. 1317–1328.
[8] Pfenninger, W., and Bacon, J. W., 1969, "Amplified Laminar Boundary Layer Oscillations and Transition at the Front Attachment Line of 45° Swept Flat-Nosed Wing With and Without Boundary Layer Suction," in *Viscous Drag Reduction*, C. S. Wells, ed. (Plenum, New York), pp. 85–94.
[9] Antonia, R. A., Zhu, Y., and Sokolov, M., 1995, "Effect of Concentrated Wall Suction on a Turbulent Boundary Layer," Phys. Fluids, **7**, pp. 2465–2475.
[10] Antonia, R. A., Fulachier, L., Krishnamoorthy, L. V., Benabid, T., and Anselmet, F., 1988, "Influence of Wall Suction on the Organized Motion in a Turbulent Boundary Layer," J. Fluid Mech., **190**, pp. 217–240.
[11] Merigaud, E., Anselmet, F., Fulachier, L., Pailhas, G., and Cousteix, J., 1996, "Reduction of Parasitic Effects Related to the Turbulent Boundary Layer on the Fuselage Using Slot Suction," *Emerging Techniques in Drag Reduction*, K.-S. Choi, K. K. Prasad, and T. V. Truong, eds., pp. 263–280.
[12] Oyewola, O., Djenidi, L., and Antonia, R. A., 2001, "Effect of Wall Suction on a Turbulent Boundary Layer: Reynolds Number Dependence," *Proceedings of 14th Australasian Fluid Mechanics Conference*, Adelaide, B. B. Dally, ed., pp. 239–243.
[13] Pailhas, G., Cousteix, J., Anselmet, F., and Fulachier, L., 1991, "Influence of Suction Through a Slot on a Turbulent Boundary Layer," *8th Symposium on Turbulent Shear Flows*, Munich, pp. 18-4-1 to 18-4-6.
[14] Sano, M., and Hirayama, N., 1985, "Turbulent Boundary Layer With Injection and Suction Through a Slit; First Report: Mean and Turbulent Characteristics," Bull. JSME, **28**, pp. 807–814.
[15] Oyewola, O., Djenidi, L., and Antonia, R. A., 2003, "Combined Influence of the Reynolds Number and Localised Wall Suction on a Turbulent Boundary Layer," Exp. Fluids, **35**, pp. 199–206.
[16] Oyewola, O., Djenidi, L., and Antonia, R. A., 2003, "Effect of Suction Applied Through a Pair of Porous Wall Strips, on a Turbulent Boundary Layer," *3rd International Symposium on Turbulence and Shear Flow Phenomena*, Sendai Japan, June 25–27, 2003, pp. 887–892.
[17] Shah, D. A., and Antonia, R. A., 1989, "Scaling of the Bursting Period in Turbulent Boundary Layer and Ducts Flows," Phys. Fluids, **A1**, pp. 318–325.
[18] Djenidi, L., Vincent, A., Gall, P.-E., and Antonia, R. A., 2002, "Effect of Wall Suction on the Structure of a Turbulent Boundary Layer," *Proceedings of the 11th Int. Symp. on Application of Laser Techniques to Fluid Mechanics*, Lisbon, Portugal, 8–11 July, 23-1 (available on CD ROM, Ponteiromágico, electronic edition, LDA, Lisbon).
[19] Bradshaw, P., and Langer, C. A., 1995, "Nonuniversality of Sublayer Streaks in Turbulent Flow," Phys. Fluids, **7**, pp. 2435–2438.